# SCHLIEREN METHODS

by L.A. VASIL'EV

Translated by A. BARUCH

ISRAEL PROGRAM FOR SCIENTIFIC TRANSLATIONS
NEW YORK · JERUSALEM · LONDON · 1971

Distributed by

KETER INC., NEW YORK
KETER PUBLISHING HOUSE, JERUSALEM
KETER PUBLISHERS LTD., LONDON

SBN 7065 1100 X

IPST Cat. No. 2302

This book is a translation from Russian of
TENEVYE METODY
Izdatel'stvo "Nauka"
Moskva 1968

# FOREWORD

Schlieren methods have gained widespread acceptance in the study of transparent inhomogeneities. Several thousand papers have been written on the subject during the past century. The state of the art at various time periods has been satisfactorily

S. A. Abrukov [3], D. Holder and R. North [92], and others. Recently, however, the theory and the experimental methods of application of the schlieren methods have undergone a substantial change, namely, the diffraction theory has been developed considerably, many new quantitative methods have appeared, improved methods of calculation of volume inhomogeneities have been introduced, and the application of these methods has been expanded. Consequently, there has arisen a need to generalize the existing results, to describe the contemporary level of development of the methods, and to demonstrate the possibilities which they offer to the investigators in various branches of science and engineering. The present book is directed to this need.

Schlieren instruments and methods used in microscopic studies are not treated in this book. The statement of the problem is, however, sufficiently general to allow the application of many of its conclusions to microscopy.

There exist at present many methods of measurement similar to the schlieren methods. These include the interferometers with a diffraction grating, frequently using a schlieren attachment. The similarity is purely superficial, however. The sole function of the diffraction grating in the interferometer is to split the light beams and to create two coherent light sources. It can be satisfactorily replaced by a system of semitransparent mirrors. Such methods are valuable because they permit converting the inexpensive and widely-used schlieren instrument into an interferometer. The schlieren instrument can also be used for other purposes, such as the study of luminescence; the corresponding methods, however, are not examined in this book.

The phenomena in which phase changes in a transmitted wave are primarily caused by the object being studied extend beyond the scope of optics. As a result, schlieren instruments have found applications in other branches of science — in X-rays, ultrasonics, radio engineering, etc. An electronic-optical analog of the schlieren methods is used in the study of weak magnetic fields. The working techniques and the instrumentation, as well as numerous specific features, are different when applied to each of these fields. We shall accordingly restrict ourselves to the analysis of the schlieren phenomena in the field of optics.

Since it is the parameters connected with the refractive index gradient which are of decisive importance in conducting the experiment, and not the angles of light deviation in the inhomogeneities or the wave front shifts, we have included in this book a section on the methods of calculation of volume inhomogeneities. These analytical methods of calculation are common to a large number of optical and other phenomena, but manifest peculiar characteristics when applied to schlieren measurements.

The book is mainly based on scientific papers published by the author; relevant works of other scientists are also cited. Thus, §20, §58, §61, §62 and in part §53, §54, §56, and §57 repeat, at times verbatim, the findings of V. S. Sukhorukikh; §39 is based on the work of S. M. Belotserkovskii, V. S. Sukhorukikh, and V. S. Tatarenchik.

I. V. Obreimov, V. A. Yakovlev, M. M. Skotnikov, S. M. Raiskii, and above all, V. S. Sukhorukikh, took an active part in the discussion of the book in the course of its preparation. The author is grateful for their numerous helpful suggestions.

*L. A. Vasil'ev*

# TABLE OF CONTENTS

*Part I The Geometrical Theory of Schlieren Methods*

## *Part II The Diffraction Theory of Schlieren Methods*

# INTRODUCTION

Hundreds of scientists of different nationalities have contributed to the development of schlieren methods over more than a century. Initially, the basic work was conducted in Western Europe, mainly in France and Germany. Recently, the center of scientific studies in this area has shifted to the USSR. We shall sketch here the main stages in the development of schlieren methods.

The schlieren method was suggested by the French astronomer Léon Foucault [83] in 1858 as a means of quality control in the manufacture of large astronomic objectives of high resolving power. In this sense it is known to this day as the *Foucault knife-edge method.*

In 1864, the German physicist, August Töpler, applied this method to the study of gaseous inhomogeneities [130]. In effect, he uncovered a new application of the already-known Foucault method, but the great value of the results obtained and the increasingly large role played by gas dynamics in the general development of science have served to attach Töpler's name to this method.

Up to the 20th century, the optical quality tests and the study of gaseous inhomogeneities were the sole areas for the application of schlieren methods. With the advent of the 20th century, schlieren methods underwent considerable development. They acquired a physical interpretation, based on the laws of wave optics. Rayleigh [116] and Obreimov [41] calculated independently the diffraction distribution of the illumination in the image plane of the schlieren instrument, working on the assumption that the wave shape in the object plane is a piecewise-linear function of the coordinates. A large number of later investigations were based on these fundamental studies, and their importance has increased in recent years, in connection with the development of the diffraction theory of the schlieren methods.

The scope of the schlieren methods was also drastically expanded. They were used to study all types of transparent inhomogeneities. Centrifugation, microscopy, the study of convective air flow in heat-exchange processes, the analysis of hydrodynamic phenomena, quality control of optical glass, and the study of crystals of different minerals constitute some of the new applications of schlieren methods.

Finally, a transition was effected from qualitative to quantitative measurements. Numerous papers were published on the subject of the light wave front shape after its passage through an inhomogeneity, and of the relevant inhomogeneity parameters related to it — the refractive index gradient, the shape of the mirror or lens, etc. Of particular importance were the studies of Maksutov [34–37], who developed the quantitative methods of the focal filament and the curved-stop photometric method, and also improved practical work techniques using schlieren instruments.

H. Schardin contributed considerably to the development of schlieren methods. He suggested many new methods for quantitative and qualitative measurements, and developed procedures for calculating symmetrical inhomogeneities. His treatise [121] summarized the development of schlieren methods up to 1940.

Today the theory and the experimental techniques of schlieren methods are continuing to develop rapidly. Ostroumov developed the defocused grid method [42–44] and applied it to the study of thermal, hydrodynamic, and diffusion phenomena. Skotnikov obtained valuable results for gas-dynamic studies from the utilization of schlieren phenomena. Abrukov [1–5] used the diffraction phenomena in a schlieren instrument for the quantitative study of optical inhomogeneities.

Sukhorukikh [51–54] was the first to develop the diffraction theory of the methods of the filament and the slit, the defocused grooved
and photometric methods applicable to cases when the wav.
object plane is a second-order function of the coordinates. He suggested methods for measuring the angle of rotation of a plane wave and the derivative of the angle of light deviation in the case of a cylindrical wave, and conducted a detailed theoretical and experimental analysis of the interferometric schlieren method. His outstanding work will undoubtedly have a significant effect on the subsequent development of schlieren methods.

Holder and North [91, 92], Barnes [66–68], and Otmennikov and Ershov [17, 19] contributed to the improvement of the qualitative and quantitative methods of gas-dynamic studies. These scientists refined to a high degree of accuracy the numerous methods of schlieren measurements used on large industrial premises with a high level of vibrations and intense heat fluxes, and obtained results on the density distribution in various gas flows.

Considerable attention has been paid to the analytical methods of calculation of complex gaseous inhomogeneities. Skotnikov and Likhushin used a linear approximation to the distribution function of the light deviation angles; in later works [31, 32] a calculation method based on a quadratic approximation was developed.

In addition to the axisymmetric inhomogeneities, attempts are being made with increasing frequency to analyze objects of more complex shape. The leading work in this respect is [8], in which methods for the calculation of axisymmetric bodies under various angles of attack were developed.

Accurate schlieren measurements are impossible without high-quality instruments. These have to satisfy rigorous requirements as regards measurement precision, adaptability to different conditions, resistance to vibrations, etc. Among recent designs, we can mention that of Th. Zobel [136–137]. The most important contribution to the design of schlieren instruments was made, however, by Efimov. The Soviet-made instruments TE-19, TE-20, IAB-453 and others developed by Efimov (in cooperation with other scientists) are first-class equipment which can be used in very refined experiments.

There is some confusion concerning the terminology of schlieren methods. They are variously called *schlieren methods*, *Töpler methods*, *strioscopic methods*, *Foucault methods*, or *shadow methods*. We reserve here the term *shadow methods* to refer to the method developed by V. Dvořak, in which the optical inhomogeneity is illuminated by a point light source, and some section of the light beam beyond the inhomogeneity is observed. It should be noted, however, that some Soviet authors apply the name *shadow methods* to all the *schlieren methods*, referring to the Dvořak method as the *luminous point method*.

The scope of the schlieren methods is not clearly delineated either. In the West, these methods generally include those by means of which measurements can be conducted in transparent inhomogeneities. This results in the combining of methods based on different physical principles such as polarization, interference, etc. Soviet authors, on the other hand, frequently restrict their scope to methods based on the measurement of the angle of light deviation. This approach eliminates the diffraction schlieren methods and the methods of measurement of the wave front curvature, but makes use of the interference methods and some polarization methods.

We shall consider as *schlieren methods* the methods possessing the following common features:

1) The inhomogeneity is visualized by means of a viewing diaphragm causing phase or amplitude changes in a part of the light beam, which result in a redistribution of the illumination in the image plane. This redistribution provides definite indications concerning the character of the inhomogeneity and some of its parameters. This is the main feature which distinguishes *schlieren methods* from the *shadow methods*, where no additional diaphragm is used, and from the interferometric and polarization methods, where the entire light beam suffers phase or polarization changes.

2) The change of illumination is examined in a plane conjugate to the plane of the inhomogeneity (unlike the *shadow method*).

The measured magnitude is generally the angle of light deviation in the inhomogeneity, although in many cases other parameters can be measured as well, such as the wave front shift or curvature.

In real experiments, deviations from the basic features of the *schlieren methods* are frequently observed. Thus, in the case of extended inhomogeneities, not all the object points can be simultaneously conjugate with the image plane, and some of them are defocused. The image formation can then be treated from the points of view of both the *schlieren* and *shadow methods*. Usually, however, the effect of these deviations is small and can be considered as an error in measurement.

The diaphragm causing the amplitude and phase changes in a part of the light beam will be called the *viewing diaphragm*. It can have different shapes: Foucault knife-edge, phase plate, curved stop, grid, etc.

Schlieren methods differ according to the shape of the diaphragm, its position, and the method used for interpreting the photograph obtained. These differences are generally indicated by a proper name, e.g., *photometric knife-edge and slit standard method*, *defocused point grid method*, etc. In those cases where, generally speaking, the distinctive features do not require emphasis, the full term is abbreviated, for example, the *focal filament method*. Sometimes traditional terms are retained as the generic names. For example, the *phase contrast methods* as a group include the more recent *phase grid methods*, *photometric focal phase-knife method*, etc.

In our treatment, the basic magnitude measured is the angle of deviation of the light beam. It will be called simply the *angle of deviation*, or the *angle of light deviation*. The other terms used in the text are generally accepted and require no additional explanation.

# I

# QUALITATIVE SCHLIEREN METHODS

## 1. PRINCIPLES OF THE SCHLIEREN METHOD

The first schlieren method, which was suggested by Foucault [83] and has remained to this day the basic method for qualitative measurements, consists of the following: a point light source $S$ (Figure 1) is set at some distance from the objective, the reflector, or the refractor $O_1$; a plate with sharp straight edge $K$, called the Foucault knife-edge, is placed in the image plane. If the objective is free of aberrations and the transmitted wave is strictly spherical, we obtain a sudden, uniform extinction of the image by moving the knife-edge at right angles to the optical axis at the instant it covers the light source image. If some sections of the objective distort the wave front, the light from these sections will produce an image of the luminous point at a different

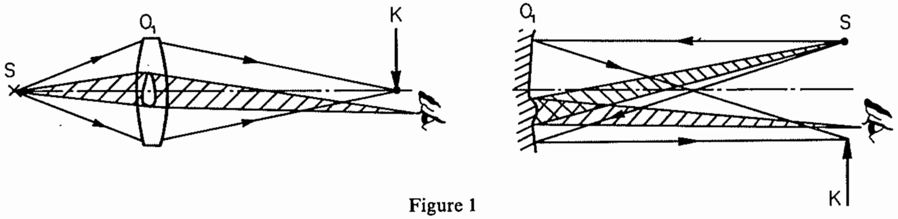

Figure 1

The principle of the schlieren method.

place. As a result, at the moment that the main image of the light source is covered by the knife-edge, and the entire field is dark, some light from the optical inhomogeneity will nevertheless reach the observer's eye. The inhomogeneity will appear illuminated against a dark background. When the knife-edge is rotated through 180° and moved toward the optical axis, the inhomogeneity will appear dark against a bright background.

In real optical systems, different field points deflect the light through different angles. If the objective being studied is theoretically split into a large number of areas, each of these areas forms an elementary image of the source. Each area is extinguished at the moment that the knife-edge covers the respective light source image. Glass defects and surface finish inaccuracies become visible. The object appears as if it were lighted from the side.

If the point light source is replaced by an extended source, the source image is covered by the knife gradually and not instantaneously. The illumination caused by field points deflecting the light through different angles will then vary. Thus the areas forming the image of the light source at point *E* (Figure 2) will be dark, the areas deflecting the source image to *A* will be bright, and the areas forming the source image at points *B*, *C*, *D* will be of intermediate brightness in relation to *A* and *E* (with *B* brighter than *D*, and *C* darker than *B*). A gradual change in the illumination is observed corresponding to the change in the angle of light deviation in the inhomogeneity.

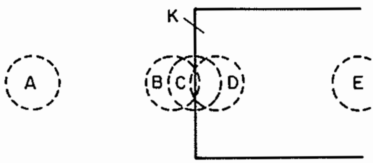

Figure 2

Image plane of the light source. *K* is the knife-edge; *A*, *B*, *C*, *D*, and *E* are images of a circular light source formed by rays coming from different parts of the objective.

The sensitivity of the method depends on the light source size. Thus the field areas corresponding to points *B*, *C*, and *D* differ only slightly in illumination. By using a sufficiently small light source, we obtain a much greater difference between the illuminations at these points. Point *D* is completely dark, while at *B* the entire luminous flux will avoid the knife-edge.

Since the source image shift depends on the angle of deviation in the inhomogeneity, the change in the light wave shape caused by the object can be estimated from the distribution of illumination in the schlieren pattern.

If a knife-edge is used as the viewing diaphragm, the image illumination is affected only by shifts of the source image perpendicular to the knife-edge. If the image shifts along the knife-edge, there is no change in the illumination. A schlieren instrument with a knife-edge therefore makes it possible to distinguish between points that differ in the value of the projection of the angle of light deviation on the plane perpendicular to the knife-edge.

The source image shift is due to the change in the wave front shape. Poor quality of the objective is not the only factor producing this distortion. The same effect can also be caused by any optical inhomogeneity which intercepts the light beam. The different points of such an object will appear differently illuminated, depending on how they deflect the light.

Maksutov's suggestion [35] to replace the point light source by a slit source marked a significant advance, making it possible to obtain a much larger light flux without loss of sensitivity. By increasing the light flux, we reduce the exposure time and can study in detail various high-speed processes, such as the flight of a projectile, the motion of a shock wave, etc. The reduction of the exposure time is also helpful in steady-state processes, since errors caused by variations of the instrument calibration with the time due to fluctuations in temperature, atmospheric pressure, etc., are correspondingly reduced.

The advantages of the slit source as opposed to the circular source become more pronounced as the aperture width (the source diameter) decreases. Thus for a slit height of 10 mm and slit width of 1, 0.1, and 0.01 mm, the transmitted light flux is larger by a factor of 3.9, 39, and 390, respectively, than in the case of a half-covered light source, whose diameter corresponds to the same sensitivity. The slit source is therefore most helpful when it is most needed — at high sensitivities and low light fluxes. At present a point source is used only when required by specific features of the measurements. Some examples will be considered below.

## 2. BASIC SYSTEMS OF SCHLIEREN MEASUREMENTS

Numerous optical systems suitable for schlieren measurements are currently available. Their large number is due to the wide range of problems and the particular requirements they impose on the results of the measurements. In cases of large and bulky objects which are not fixed in the same place (glass disks of diameter larger than 1.5 m) it is more expedient to have a portable instrument, adjusting its position relative to the disk, than to move the object toward the instrument. In wind tunnel studies the fixed mounting of the instrument is the most expedient procedure.

The instrument design also depends on the required sensitivity. Thus when measuring the velocity of a powerful shock wave, the simplest arrangements are used with a minimum number of relatively coarse components. On the other hand, in the case of inhomogeneities which only slightly deflect the light, the optical system, the instrument design, and the mounting are considerably more complicated.

The design of most instruments is more complex than that shown in Figure 1. An additional objective is usually introduced, forming an image of the inhomogeneity on the screen. The main objective could be used in this case, but such an arrangement would increase the instrument size and make difficult the utilization of different image scales.

In addition, schlieren photographs require, especially at high sensitivity, a very bright light source with straight edges. Since such a source is difficult to obtain, the usual procedure consists of forming an intermediate image of the source, which is limited by a slit. The introduction of a condenser objective also helps to eliminate scattered light.

the [illegible] spreading

The basic optical designs will now be briefly described. Figure 3 represents one of the first systems. It is mainly suitable for qualitative observations. Its advantages are simplicity, and ease of manufacture and adjustment. A single large lens is rarely used as the main objective. Normally, and particularly for exact measurements, a complex optical system is used instead, which is corrected for various aberrations. This system will be symbolically represented in our drawings by a single optical element. A disadvantage of systems using a refractor is the large value of the aberration, especially in the case of a large field.

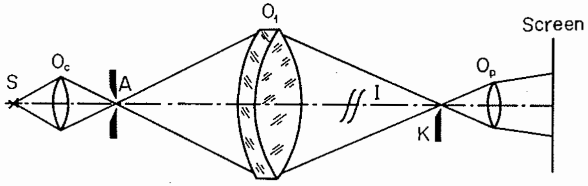

Figure 3

Optical design of a lens schlieren instrument. $O_c$ condenser objective, $A$ slit aperture, $I$ inhomogeneity, $O_p$ photographic objective, $S$ source.

Figure 4 represents a system frequently used for qualitative studies. A high-quality reflector is easier to manufacture than a refractor, particularly one of large dimensions. In addition, mirror objectives are free from chromatic aberrations.

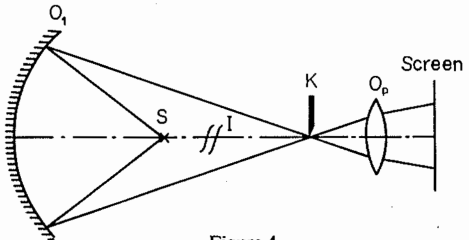

Figure 4

System with mirror objective.

It is inefficient to mount the light source and the condenser system on the optical axis, since this leads to the darkening of a considerable part of the field. The variant represented in Figure 5 is used more frequently. The mirror $M$ is not large; it occupies a considerably smaller part of the field than the illuminating system in the preceding variant. But in this case as well, the central part is inaccessible to measurement.

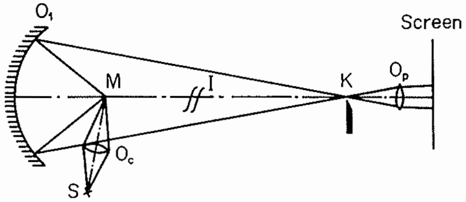

Figure 5

System using a small revolving mirror.

A frequently used system is shown in Figure 6. In this system the light source and the receiving photographic part are positioned symmetrically with respect to the optical axis of the mirror.

To reduce the aberrations of the main objective, the image and the light source are placed one next to the other, and one of the knife-edge faces serves as a mirror

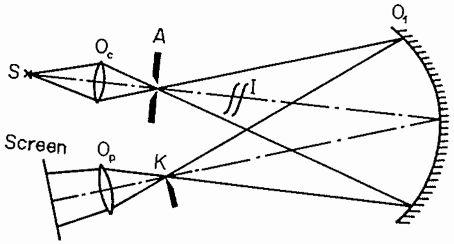

Figure 6

System of a symmetrical schlieren instrument.

(Figure 7). In this case the knife-edge is, in fact, the element forming the sharp edge of the light source image. The sensitivity of this system is higher, resulting from the double passage of the beam through the inhomogeneity. This advantage, however, is lost when studying transparent objects, which deflect the light through large angles. In this case the ray is deflected considerably from its direct path during the reverse passage. The narrow and sharp inhomogeneities are split, and the resolving power of the instrument is reduced. The system in Figure 7 is therefore used only for studying weak inhomogeneities.

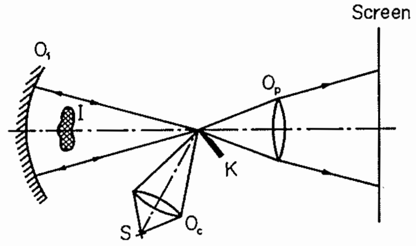

Figure 7
The use of a mirror knife.

If a still higher sensitivity is required, use is made of systems that provide for multiple passage of the ray through the inhomogeneity (Figure 8). The sensitivity is increased by a factor equal to the number of passages of the light beam through the inhomogeneity. Such instruments are, however, difficult to use due to their great sensitivity to vibrations and air oscillations. Schardin [121] points out that even the vibrations caused by the passage of vehicles at a considerable distance from the building can considerably affect the image illumination. The instrument is difficult to adjust and has a low resolving power, since the ray does not follow the same path during its repeated passages. These drawbacks explain why little use is made of instruments that function according to Figure 8.

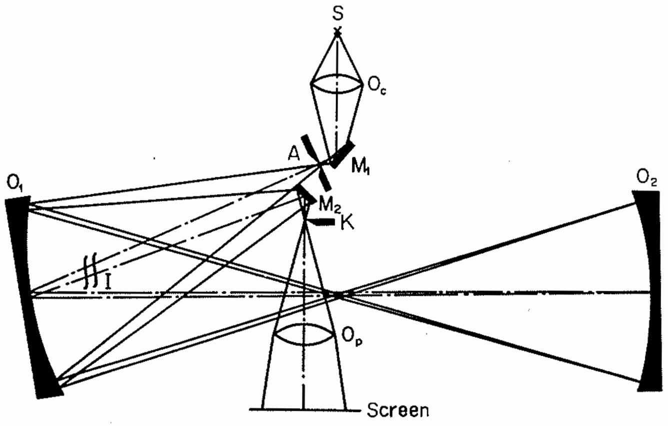

Figure 8
Optical system of an instrument where the inhomogeneity is traversed four times by the light beam.

As previously mentioned, schlieren instruments with a knife-edge can determine only the distribution of the projections of the angles of light deviation on the plane perpendicular to the knife-edge. The entire field of angles of deviation can be measured by instruments analogous to those used in creating a stereoscopic image. They function as two independent units each viewing the inhomogeneity at a small angle to the other. This design is also applicable to cases wherein one arm is adjusted for measuring weak objects, and the other for measuring strong ones. In the first, the knife-edge fully covers the slit image, and, in the second, the coverage is only slight. The difference in the directions of observation is virtually non-existent, since the angle between the two arms can be made small in view of the large focal length of the main objective. In real systems it does not exceed 1°. To measure the projections of the angles of light deviation on different planes, it is possible to set a rotating system in one of the arms, such as that represented by Figure 9.

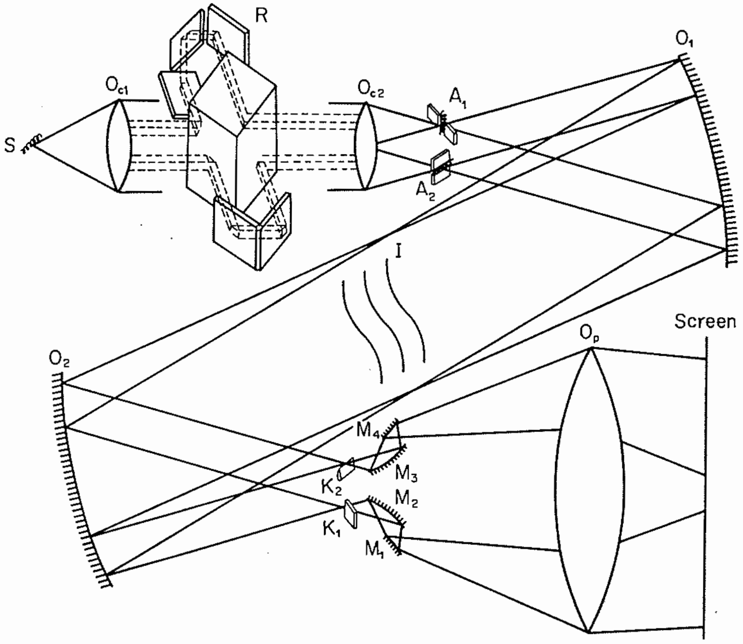

Figure 9
Double schlieren instrument for the simultaneous measurement of two components of the angles of light deviation in different directions. *R* is the mirror system rotating one of the images of the light source through 90°.

The use of a converging or a diverging light beam is inconvenient for quantitative investigations, since identical inhomogeneities shift the slit image to a different extent, depending on their location in the beam section. Since, in actual experiments, it makes little sense to use two schlieren instruments, one for qualitative measurements and the other for quantitative ones, the most widely used instruments are those in which the inhomogeneity is placed in a parallel beam. Such a modification can be applied to all the systems described. For examples see Figures 10 and 11.

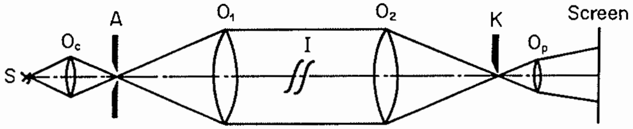

Figure 10
Lens instrument with parallel rays.

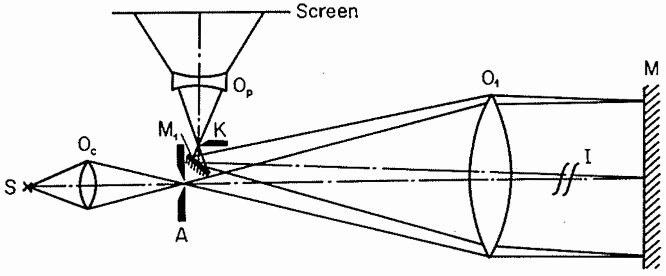

Figure 11
Mirror instrument with parallel rays and double passage of the light through the inhomogeneity.

The most widely used system is the so-called Z-system (Figure 12), in which two identical objectives are placed opposite each other. The condenser and the photographic unit are located on different sides of the optical axis. A characteristic aberration of this system is astigmatism. In order to minimize the latter, it is necessary to reduce the angle $\alpha$. But the size of the objective is determined by the size of the inhomogeneity. The increase of the focal length is similarly not always desirable, since it leads to an increase in the instrument size. Accordingly, astigmatism is normally eliminated by placing specially designed correcting lenses near the focal point.

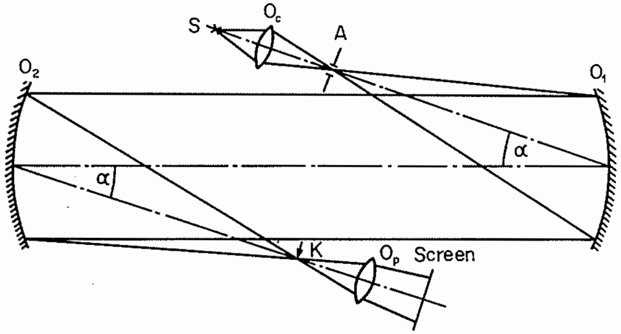

Figure 12
Schlieren Z-system.

If the inhomogeneity is highly elongated in one of the directions, and measurements in both directions are equally important to the experimenter, cylindrical lenses are employed. Such lenses are used in studies of the boundary layers in a supersonic flow, shock waves, surface phenomena of thermodiffusion, etc.

The schlieren instruments used in aerodynamics are, as a rule, large and unwieldy. Considerable difficulties arise in connection with their installation. To make the instrument more compact, use is made of multiple reflections of the light beam by means of plane mirrors. Such improvements, however, adversely affect the sensitivity of the instrument, cause an increase in the number of patches, and in parasitic light intensify the effect of vibrations, etc. It is therefore advisable to use the simplest system compatible with the space available. Such systems are found to be more sensitive and more reliable.

It is frequently expedient to use a part of the object being studied as one of the components of the schlieren instrument. In Figure 13 such a function is fulfilled by the turbine wheel *W*, which serves as a reflecting mirror. In [114] the piston of an internal combustion engine served the same purpose. The use of such instruments when applicable is more efficient than the manufacture of models from transparent materials, and frequently offers the only possible method of investigation.

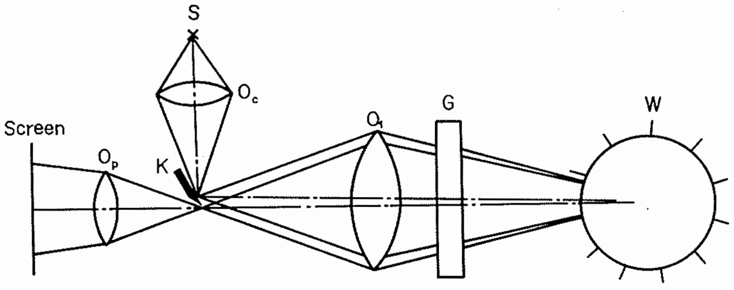

Figure 13
Determining the characteristics of the flow past a turbine wheel by schlieren measurements. *G* is the protective glass of the working chamber.

The basic systems described above represent only a small number of the great variety of existing optical systems. There is no need, however, to describe each one, since virtually all the different systems can be reduced to fit one of those described above. Some of them are based on a combination of several basic systems, or of individual elements from different basic systems, the aim being to satisfy simultaneously different requirements (for instance, small size and high sensitivity). Such combined systems normally possess, however, the same advantages and drawbacks as the constituent basic systems.

## 3. SENSITIVITY AND RANGE OF MEASUREMENT

The *sensitivity* of a measuring instrument is defined as the ratio of the increment in the instrument reading to the increment in the value of the parameter being measured, thus

$$S = \frac{dK}{d\rho}. \tag{3.1}$$

$K$ and $\rho$ can have different physical meanings. In the case of an ammeter, $K$ is the deflection of the instrument needle, and $\rho$ is the current strength causing this deflection.

The parameters $K$ and $\rho$ have different meanings for the different types of schlieren instruments. In the photographic method, the recorded magnitude is the optical density of the photographic emulsion $D$, and the measured parameter is normally the angle $\varepsilon$ of light deviation in the inhomogeneity. Therefore

$$S_p = \frac{dD}{d\varepsilon}. \tag{3.2}$$

But since $D$ is linked with the image illumination $I$ and the emulsion characteristics by the relation

$$D = \gamma \log I - b, \tag{3.3}$$

wherein $\gamma$ is the contrast factor of the emulsion and $b$ is a constant, we have

$$S_p = \frac{\gamma dI}{I d\varepsilon}. \tag{3.4}$$

In the visual observations, the effect of the light on the eye will be determined by the magnitude

$$E = c \log I, \tag{3.5}$$

where $c$ expresses the contrast sensitivity of the eye. The measurement sensitivity is then equal to

$$S_v = \frac{c dI}{I d\varepsilon}. \tag{3.6}$$

As noted in both the visual and the photographic methods of observation, the sensitivity is linked with the image contrast, which is determined by the value of the relative change of the light intensity in the image.

In the photoelectric method, the dc component is cut off by the ac amplifier. The recorded magnitude in this case is the signal amplitude, linearly related to the absolute change of the light intensity in the image

$$S_{\text{ph}} = \frac{c_1 dI}{d\varepsilon}, \tag{3.7}$$

where $c_1$ is a constant determined by the slope of the characteristic curve of the photomultiplier and by the recorder.

The magnitudes $dI/Id\varepsilon$ and $dI/d\varepsilon$ will be frequently used instead of the sensitivities defined above. Their advantage lies in the possibility of comparing different methods without entering into the question of the properties of the human eye or of the photographic material. It should be kept in mind, however, that the transition from these magnitudes to the true sensitivity entails multiplication by a factor which depends on the properties of the receiver and the method used. Furthermore, this factor is constant only in a limited illumination range, outside of which it may vary. In some cases a different magnitude is recorded, such as the color change or the shift of the shadow from the filament.

We shall examine the connection between the sensitivity and the adjustment parameters of the schlieren instrument for the most widely used photometric method of the knife-edge and the slit.

The screen illumination can be considered proportional to the area of the light source image not covered by the knife-edge. When a rectangular slit is used,

$$I = B\xi h, \tag{3.8}$$

where $B$ is a constant depending on the source luminance, the system absorption, etc., and $\xi$ and $h$ are, respectively, the width and height of the part of the slit image not covered by the knife-edge.

A deflection of the light in the inhomogeneity through the angle $\varepsilon$ shifts the light source image by the amount $\delta = \varepsilon f$, where $f$ is the distance from the inhomogeneity to the knife-edge for systems similar to those shown in Figures 3 to 8. If a parallel beam system is used, $f$ will be the second focal length of the main objective of the receiving part.

When the measured angles are small, the sensitivities are represented by the following expressions:

$$S_p = \frac{\gamma f}{\xi}, \tag{3.9}$$

$$S_{\text{ph}} = c_1 B h f. \tag{3.10}$$

It would follow that the sensitivity could be increased without limit by reducing the width of the open part of the slit image. This is not so in practice, due to diffraction, the aberrations, and the decrease of the contrast sensitivity of the receiver at low image illuminations. Formula (3.9) is applicable only to relatively large widths of the open part of the slit image, when these limitations do not appear.

The introduction of the concept of sensitivity and the establishment of its functional relationship with the adjustment parameters of the schlieren instrument make possible a correct selection of the experimental conditions. Thus if the photographic method of observation is used and the object of study is an inhomogeneity which produces a slight deviation of the light beam, it is necessary to use the smallest possible width of the open part of the slit image. In photoelectric recording, the source image brightness should be increased in order to increase the sensitivity.

By means of the formulas defining the sensitivity, it is also possible to calculate the minimum angle of deviation which causes the smallest measurable change in the parameter being recorded; and, consequently, to define the limits of applicability of the schlieren instrument at different adjustments.

The range of angles of deviation which cause a definite change in the recorded magnitude (in our case, the image illumination or the photographic density of the emulsion) is called the *range of measurement* of a schlieren method. The range depends on the size of the light source. Indeed, if the inhomogeneity shifts the source image so much that it is completely covered by the knife-edge (or completely uncovered), any further change in the angle of deviation will have no effect on the image illumination and the parameters dependent upon it. Curves of the illumination as a function of the angle of light deviation in the inhomogeneity for different shapes of the source and the stop are shown in Figure 14.

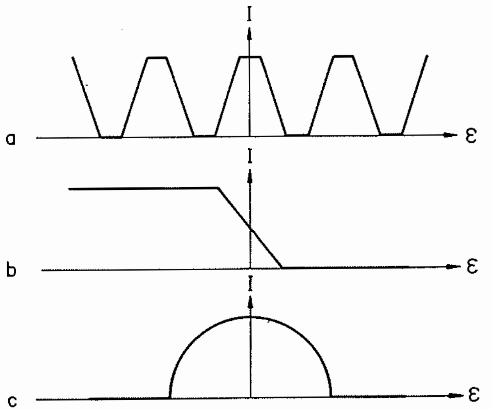

Figure 14

Image illumination as a function of the angle of light deviation: *a* slit source and amplitude grating; *b* slit source and knife-edge; *c* circular source and narrow slit stop.

Strictly speaking, the range should be defined as the segment of the $\varepsilon$ axis on which a monotonic change in illumination takes place. If, however, the distribution of deviation angles in the inhomogeneity is known beforehand, it is possible to make use of other illumination ranges as well; additional data will then be required to choose one value from several possible alternatives. In some cases, it is possible to use the intrinsic continuity of the field of deviation angles, and in other cases, additional coarse measurements are required.

For some quantitative investigations the measurement range is chosen not in the region of angles corresponding to some given change in the illumination, but where the dependence of the illumination on the deviation angle has a certain suitable form. Thus if we use a stop with curved edges, the quantity of light passing through it will vary when the slit image moves away from the curved zone and becomes partially limited by straight lines. The law governing this variation will not correspond to our working formulas. The measurement range of the methods using these formulas for quantitative analysis will therefore be restricted to the segment on which the image of the illuminating slit is limited by curved edges.

The receiver properties must be taken into account in defining the range of measurement. Thus if a wide slit is used, the range, defined as the region of regular change in the illumination, will be very large. But the actual limits of measurement are considerably narrower. Indeed, when photographic recording methods are used, we shall have overexposure at the moment the slit image is deflected to such an extent that it becomes excessively uncovered; while the field illumination will continue to change with the change in the angle of deviation, no further blackening of the emulsion will result. Similar phenomena take place at open parts of the slit, which are too narrow when the optical densities are in the region of underexposures. Since all receivers have definite threshold sensitivity and saturation limits, measurements can be conducted only in a specific range of illumination values.

The total measurement range is determined by the superposition of the illumination range and the receiver ranges. In a correct application of the method these two magnitudes must fit; otherwise, the total range of measurement may considerably contract, possibly dropping down to zero.

## 4. USES OF QUALITATIVE METHODS

The wide-scale uses of the schlieren method started immediately after its discovery. Its popularity was due to its simplicity, clarity, and accuracy. Maksutov provides an example illustrating the accuracy of the schlieren method [35]; it is possible to measure the surface curvature of a mercury mirror subjected to the action of the force of gravity alone, and thus to determine the radius of the Earth to the first decimal place. The studies conducted by various authors [48, 121] demonstrate that this method reliably records light deflection up to tenths of an angular second.

As mentioned earlier, the first application of schlieren measurements was in the manufacture of optical instruments for astronomic studies. Schlieren methods made it possible to estimate the quality of an objective and its different surfaces during the manufacturing process. The objective could be examined by zone, and decisions on shape alterations could be taken with a view to obtaining high-quality images. It became possible to alter purposefully the manufacturing methods, and, consequently, to improve the quality of telescope objectives. The method of objective retouching (the manual correction of different portions of the surface) developed as a result and led to the production of first-class objectives, which have played an important part in astronomic studies. The development of the schlieren method contributed thus to the growth of astronomic optics.

The method was later applied to the study of photographic and similar objectives. It made possible a rapid experimental study of the different types of aberrations, and a localization of the objective areas mainly responsible for the various aberrations. The comparison of the experimental results with those predicted by the aberration theory proved to be of considerable value.

The method is successfully applied to glass manufacture control in optical plants. By determining the glass quality before processing, it became possible to make purchases according to grades and thus avoid the expenditure of resources and labor in the manufacture of critical components from low-quality glass. It also became possible to initiate a study of the causes of inhomogeneity.

Drawing strips and other deviations from the flat shape of the surface which appear during rolling play an important part in the manufacture of sheet glass. These defects are of importance even when the glass is used for everyday needs (eye-glasses, windowpanes, etc.) but become critical with regard to various technical applications of glass. Thus if the glass support of photographic plates possesses such defects, the layer thickness of the poured emulsion will be uneven. As a result, the correspondence between the image illumination and the optical density of the photographic material will be unbalanced. Schlieren methods, by visualizing surface distortions, make it possible to evaluate the influence of distortions and to prevent them.

The method has reached its highest development in the study of processes in gases. It became particularly useful in recent years in connection with the development of supersonic jet technology. It enabled the determination of the profiles of shock waves moving from different portions of the models or the gas-dynamic installations, and the characterization of their interaction with solid objects, the gas flow, and with each other. Schlieren photographs led to conclusions concerning the quality of the nozzles, the uniformity of the stream field, and the possibility of simulating the conditions existing during high-velocity flight in the atmosphere. The study of the air flow past models sheds light on many phenomena occurring during flight. Such studies are frequently of a quantitative value, although they are classified as qualitative schlieren studies.

Schlieren methods are also used for visualizing subsonic gas streams. Artifices are frequently used in this regard, such as heating a part of the stream and tracking the motion of the heated zone, or introducing ultrasonic or weak sonic shock waves in the flow. A disadvantage of these methods is the necessity of deciding in each case to what extent the physical features of the phenomenon are distorted by the introduction of the additional disturbances.

The schlieren methods are of considerable use in the study of transient phenomena, such as explosions, processes in shock tubes, flutter, etc. [22]. The use of a schlieren instrument in conjunction with a cinecamera or some other receiver for studying the time picture of the process makes it possible not only to detect transient transparent inhomogeneities, but also to determine the frequency and amplitude of the fluctuations and to pinpoint more precisely the degree of instability [17, 123].

By recording in two consecutive points of the instrument field or, alternatively, using two instruments, it becomes possible to measure the velocity of motion of the inhomogeneities — shock waves, flames, etc. The schlieren methods are the most suitable for this purpose, since the density changes to which the schlieren instrument reacts are the primary factor in the formation of the wave, appearing earlier than the glow, or the ionization, which lags behind the shock front. If the density changes in the shock wave are extensive, it is possible to use instruments whose main objective is a photographic objective or a simple lens. These are supplied in the form of small attachments — transducers rigidly adjusted to the same sensitivity, which facilitate the utilization of the instruments and increase their reliability.

The other studies of gaseous inhomogeneities are very similar in the manner in which they utilize schlieren methods. Such are the studies of the phenomena of thermodiffusion, the convective fluxes about heated bodies, the flow past turbine blades, the different processes which take place in internal combustion engines, etc.

Schlieren methods are being widely used in the study of hydrodynamic phenomena as well. Since the angles of deviation in liquids are large, the schlieren installations here are substantially different from the gas-dynamic systems, e.g., relatively coarse lenses are used, and the stops are of large size. The motion of jets, the development and propagation of waves, the interaction of waves with bodies, and many other details are clearly seen on the photographs.

The use of schlieren methods in chemistry is characterized by a number of specific features. They are used in the study of the dissolution, mixing, and other related effects. The application of these methods in centrifugation offers a swift means for distinguishing between zones that differ in the value of the refractive index, and for determining changes in the density or the chemical composition. It is sufficient to conduct the measurements in one direction — along the liquid column. Accordingly, the schlieren methods of the cylindrical lens, the scale, the inclined slit, etc., are frequently used.

The utilization of schlieren methods in crystallography makes possible the observation of the growth of crystals and of the distribution of substance in the growing crystal. Disturbances in the crystal structure and transparent inserts undetectable by simple observation are studied [39].

In acoustics, schlieren methods are used in the study of the propagation of sonic and ultrasonic vibrations. The quality of sound insulation, the properties of resonators, the acoustic properties of the premises — all these problems, as well as many others, can be solved by the application of schlieren methods.

Most microscopic preparations are transparent, and, therefore, the problem of their visualization must be solved before they can be investigated. The schlieren methods in which both phase and amplitude changes are introduced in the light flux by means of an additional stop are the most successful in this respect. They are preferable to methods in which visualization is achieved by the introduction of dyes or substances altering the conditions of life and the properties of the preparation.

There are some ingenious and originally unforeseen applications of the schlieren methods. It was suggested in [96] that they be used for obtaining a large-screen television picture. According to this procedure, light from a bright light source (Figure 15) is sent to the mirror cylinder *C*, covered by an oil film; it is reflected from the mirror and, after passing through a grating, falls on the screen. A modulated cathode ray, originating from the electron gun *EG* and focused by the electronic optics *EO*, whose intensity is proportional to the brightness of the transmitted image, is directed at the oil film. The forces of repulsion between the electrons falling on the oil film cause it to bend, the radius of curvature and the height of the irregularities depending on the intensity of the electron ray. A light ray deflected from the curved portions is not stopped by the diaphragm, and therefore these portions appear bright while the remaining image is dark. The schlieren image of the inhomogeneities of the oil surface, corresponding to the image transmitted by the television set, is observed on the screen. The advantage of this method as compared with the fluorescent screen method is that it gives a much brighter image, since the brightness is determined here by the intensity of the light source, which can be made sufficiently powerful.

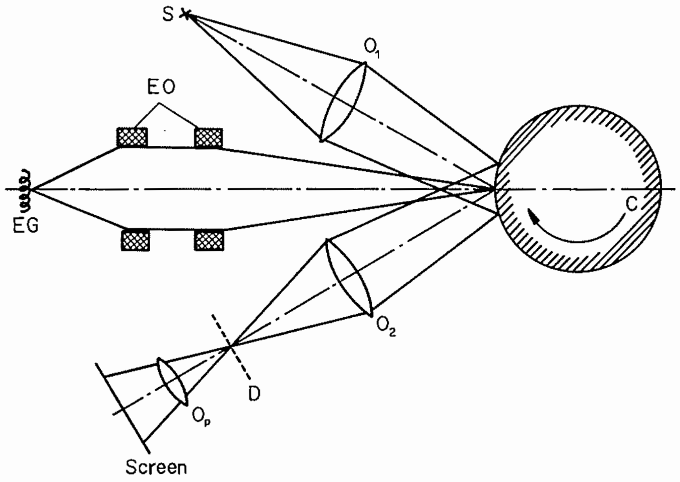

Figure 15

A schlieren method for obtaining a large-screen television picture.

Instead of oil it is possible to use a film of some organic material, which will melt when subjected to the electron ray. Such a modification makes it possible to preserve the image for a long period. It is also used today for microfilming books and documents.

Methods analogous to the schlieren methods have been developed in other branches of science as well, including X-rays, electronic microscopy, electrical engineering, etc. For example, consider the visualization of low-density gaseous streams by an electronic schlieren instrument [38, 108]. The beam of electrons emitted by the electron gun is collimated by electromagnetic lenses, then passes through the object under scrutiny, and is collected by the electromagnet objective of the receiving part. The main beam is intercepted by a stop placed at the point of convergence of the electrons. The electrons deflected by the inhomogeneity are not intercepted and reach the screen, on which the object image is formed.

In spite of the complete external similarity between the optical and electronic schlieren instruments, there exists a basic difference in their application to the study of a gaseous flow. In the optical variant, the angle of deviation depends on the refractive index gradient, while in the electronic instrument the distribution of the angles of deviation of the particles is determined by the collisions of electrons with atoms and is independent of the number of interacting particles. In the optical variant, the reduction in the density of the gaseous inhomogeneity leads to a reduction in the angle of light deviation. To preserve the image contrast it is therefore necessary to preserve the width of the open part of the source image, which enhances diffraction and aberration. When an electronic instrument is used, the density decrease does not affect the deviation angle, but only leads to a reduction in the number of scattered electrons. Since the problem of recording few electrons has been successfully solved, this method responds to very small density changes, corresponding to pressures as low as $10^{-4}$ mm mercury.

The same electronic method is successfully applied to the study of the configuration of weak magnetic and electric fields. In this case the transition to weak fields reduces the deviation angle, which causes difficulties similar to those encountered in the optical variant.

This brief survey demonstrates that the area of application of schlieren methods is wide and varied. However, the various methods share similar basic features. Concepts such as sensitivity and range retain their meaning, and the same quantitative methods are used in both cases. It seems therefore expedient to examine the schlieren methods in a general context, selecting examples from different areas. This makes it possible to discover the general laws of the methods, to compare the various means of their application, and to select the optimum method for any given problem. The specific features of the solution of individual problems will be examined only insofar as they are common to a wide range of problems, i.e., of a fundamental character.

# II

# QUANTITATIVE ZONE METHODS

## 5. SLIT IMAGE SHIFT CAUSED BY LIGHT DEVIATION

Qualitative schlieren photography yields valuable information on optical inhomogeneities. Schlieren photography can, however, be also used for determining the shape of the light wave front after its passage through the inhomogeneity, and therefore for establishing the refractive index distribution inside the inhomogeneity. Inasmuch as the latter problem is quite complex, it will be examined separately. We shall restrict ourselves to methods of determination of light deviation angles.

As noted above, the change in illumination in the image plane of the schlieren instrument is a function of the shift of the slit image in the focal plane of the main objective of the receiving part. The shift is caused by the deflection of the light rays in an optically inhomogeneous medium.

For systems with parallel rays (Figure 16), the displacement of a ray in the principal plane of the main objective of the receiving part is $bc = s \tan \varepsilon$. It follows from the similarity of the triangles *kde* and *kbc* that in the focal plane of the main objective the ray is shifted by the amount

$$\delta = f \tan \varepsilon. \tag{5.1}$$

Since the angles of deviation are usually small, especially in gaseous inhomogeneities, the tangent of the deviation angle can be replaced by the angle itself with sufficient accuracy:

$$\delta = \varepsilon f. \tag{5.2}$$

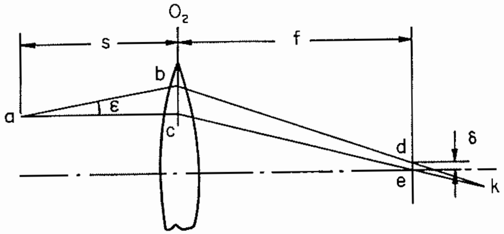

Figure 16
Calculation of light shift in the focal plane of the main objective in systems with parallel beam:
*acek* undeflected ray; *abdk* deflected ray.

The displacement of the slit image and the change in illumination of the object image are independent of the position of the inhomogeneity in the parallel light beam and of the distance from the point of origin to the optical axis of the system. This simplifies the processing of the results, since the spatial position of the inhomogeneity is frequently one of the unknowns of the problem. Furthermore, the inhomogeneities are usually somewhat stretched in the direction of the optical axis.

If the object is placed in a converging beam (Figure 17), then

$$\delta = \left[s \tan \alpha \left(1 + \frac{h^2}{s^2}\right)\right] : \left[1 + \frac{h}{s} \tan \varepsilon\right]. \tag{5.3}$$

For small angles of deviation (5.3) reduces to:

$$\delta = \varepsilon s \left(1 + \frac{h^2}{s^2}\right). \tag{5.4}$$

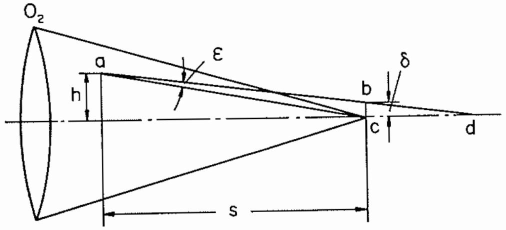

Figure 17
Ray displacement in systems with non-parallel beam.

In this case $\delta$ depends on the spatial position of the inhomogeneity. In most cases the relative aperture is not large, since only in such a situation can the aberrations be made small ($h/s < 0.1$ even for the extreme points of the field). It follows that the second term can usually be ignored, reducing (5.4) to

$$\delta = \varepsilon s. \tag{5.5}$$

There are cases (high-precision measurements, or measurements with high-speed lenses) when this approximation is not acceptable; as a result the mathematical treatment is extremely complicated.

Formula (5.5) is similar in form to formula (5.2), which is derived for a parallel beam. However, whereas $f$ is a constant magnitude, $s$ depends on the position of the inhomogeneity, and varies from point to point in an extended object. Inhomogeneity zones which deflect light through the same angle but are differently located in space will appear illuminated in varying degrees. This complicates the processing of the measurement results, and has prevented the use of convergent beams for quantitative measurements. Such beams have, however, several advantages in the study of weak processes: these advantages include the small number of patches, the possibility of using systems with a minimum number of optical components, better aberration properties, etc. The quantitative study of such phenomena necessitates the use of formula (5.5). The inconvenience and the errors of the numerical calculation are occasionally offset by the possibility of increasing the measurement sensitivity and accuracy.

## 6. ASSESSMENT OF INHOMOGENEITIES

The first attempts of quantitative application of the schlieren methods involved a gradual decrease of the measurement sensitivity, until the inhomogeneity disappeared. If the contrast sensitivity of the receiver was known, it was possible to determine the maximum angle of light deviation by such an operation. Thus, if points differing in brightness by 5% can be distinguished visually, and if the inhomogeneity becomes invisible at a slit width of 1 mm, the maximum shift of the slit image in this inhomogeneity will be 0.05 mm, which, for $f = 2000$ mm, corresponds to an angle of deviation of $2.5 \times 10^{-5}$ rad.

This method is useful for assessing the quality of optical components — objectives, mirrors, lenses, glass, etc. It permits components to be classified into different precision groups. It is not suitable, however, for studying in detail the physical processes within an inhomogeneity or for improving the quality.

Another group of methods for studying the properties of optical inhomogeneities is the immersion methods. In the latter, the object is placed in a salt solution or in a mixture of two liquids. The refractive index of the medium is changed gradually by varying the amount of the solute or the ratio between the mixture components. Thus the particular composition which renders the inhomogeneity invisible is established. In this composition the refractive indices of the liquid and the inhomogeneity are equal. The refractive index of the liquid is determined with a refractometer or by the schlieren method (by placing the liquid in a wedge-shaped cuvette and measuring the slit image displacement). The method is used for determining the refractive index of transparent objects of irregular shape.

The study of the object as a whole yields negligible information on the structure of the inhomogeneity. To fill this need, Ritchey [118] suggested the use of the zone method of measurement. According to this method, the diaphragm *D* was placed on the objective or some other component. The surface of the diaphragm was divided into a number of zones (Figure 18). The knife-edge was brought in line consecutively with the focus of each zone. The difference between the readings giving the knife position along the optical axis for each of the zones determined the longitudinal aberrations of the given area of the objective, and therefore the shape of the wave front or the mirror surface. While a Ritchey diaphragm is useful for determining the surface shape, it lowers the sensitivity of the schlieren measurements by reducing the number of measurement points. The increase of the size of each zone decreases diffraction effects and increases the accuracy of setting of the knife-edge in relation to each zone.

Maksutov suggested a separation of the zones by ruling lines on the glass or by drawing several wires in front of the object studied. This modification increased the sensitivity of the measurements [35].

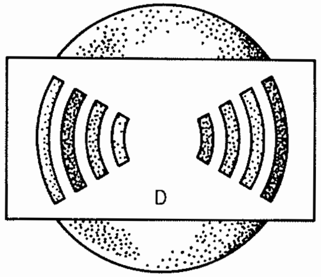

Figure 18
Ritchey diaphragm.

A drawback of the zone methods is the time required for carrying out the measurements, which demand great care and high accuracy. These methods are therefore used only for objects whose properties remain constant for long periods. Another drawback is the small number of measurement points. With an increase in the number of zones, the eye becomes incapable of distinguishing between highly similar but separate areas, and there is no further increase in the accuracy of shape measurement. Due to these drawbacks, zone methods are used only for rough orientation measurements.

# 7. STUDY OF THE DIFFERENT SECTIONS OF AN INHOMOGENEITY

When studying centrifugation processes, it is necessary to investigate the refractive index distribution along the liquid column. This investigation yields information on the chemical composition of the mixture, the rate of separation of the different components, the diffusion processes, etc. The method used most extensively is that of the inclined slit and the cylindrical lens [129]. One of the possible optical systems [62] is shown in Figure 19.

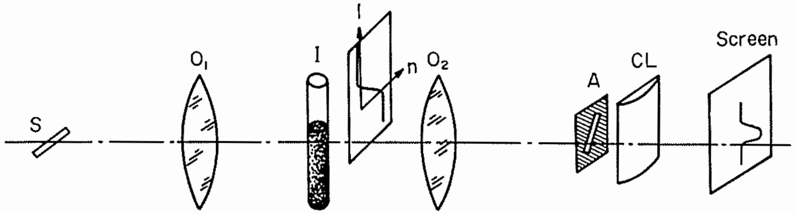

Figure 19
Layout of the cylindrical lens method [62].

A slit light source *S* is placed in the focal point of the collimating objective. As usual, this source can be a slit limiting the intermediate image of a luminous body. Between the collimating objective $O_1$ and the receiving objective $O_2$, the inhomogeneity *I* is placed, whose parameters vary in one direction only. It is necessary to adjust the instrument so that the slit image will be perpendicular to this direction. In the focal point of the receiving objective the inclined slit *A* is placed, forming some angle with the image of the illuminating slit. Behind the slit is placed the cylindrical lens *CL* and, if necessary, the photographic optics. The parameters of the optical system of the receiving part are selected in such a way that horizontal sections located on the object plane and vertical sections in line with the inclined slit are projected simultaneously on the screen. A curve plotting the distribution of the refractive index *n* along the inhomogeneity *I* is placed near the object.

If there is no inhomogeneity, all the light rays pass through the same portion of the inclined slit, and a luminous straight line is observed on the screen. When an inhomogeneity is introduced, the slit image produced by the deflected rays shifts. A different portion of the inclined slit will now be illuminated, and the luminous band on the screen bends. The value of its displacement at some point of the image is equal to

$$l' = \varepsilon f \mu \cot \alpha, \tag{7.1}$$

where $\alpha$ is the angle between the inclined slit and the image of the illuminating slit, $\mu$ is the scale of the image of the inclined slit sections produced by the cylindrical lens, $\varepsilon$ is the angle of light deviation at the conjugate point in the inhomogeneity.

The sensitivity of the method is equal to

$$S = \frac{dl'}{d\varepsilon} = f\mu \cot \alpha. \tag{7.2}$$

Theoretically, it can be increased by decreasing $\alpha$. In practice, this is ruled out by the finite width of the slit and by aberration and diffraction phenomena. Angles smaller than 10° are rarely used.

The width of the luminous band depends on the width of the inclined slit. Again, this width cannot be made very small, due to the aberrations of the cylindrical lens, the diffraction phenomena, and insufficient lighting. This method is mainly used for studying phenomena in liquids, where the angles of deflection are large. It is rarely used for weaker processes.

There are numerous modifications of this method, which differ according to the position of the inclined slit and of the cylindrical lens.

Similar problems are encountered in other branches of science as well. Thus, when studying photographic objectives, it is necessary to know the shape of the light wave front in some section after passing through the objective. To this end, the crossed prisms method [45] is used, one of whose variants is represented in Figure 20. The first half of this system functions as the ordinary schlieren instrument for color images described in §9. The sole difference is that a slit diaphragm $D$, placed in the object plane, is used to limit the part of the inhomogeneity which is to be studied. In the absence of the second prism $P_2$, a bright band would appear on the screen plane, whose color would depend on the instrument adjustment and the angles of light deviation at each point of the inhomogeneity section being considered.

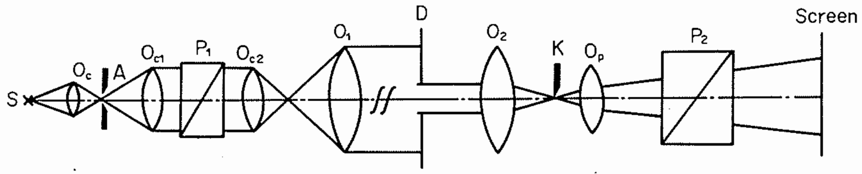

Figure 20
The method of crossed prisms.

The second prism, placed between the viewing diaphragm and the screen, deflects light at right angles to the given section. The light deviation angle in the second prism is different for the different points of the section, and depends on the prism dispersion and on the colors of the point considered. The amplitude of the curve displayed on the screen is determined by the angle of light deviation in the inhomogeneity.

The method is simple and convenient to employ. While fulfilling the same need as the method using the inclined slit and the cylindrical lens, it is superior in practical applications.

The methods described above are widely used for one-dimensional inhomogeneities. Once the relationship between the displacement of a point of the curve on the screen and the angle of light deviation in the inhomogeneity has been established, either by calculation or by calibration, the measurements are simplified to a measurement of the amplitude at each point of the section. The rapidity and ease of processing make these methods convenient for tentative measurements and for quality control of manufactured articles.

## 8. FOCAL KNIFE-EDGE AND FOCAL FILAMENT

Methods for establishing curves of equal angles of deviation are widely used in practical measurements. These methods use a knife-edge placed in the focal plane of the main objective of the receiving part parallel to the illuminating slit image. Areas deflecting the light rays whose light is stopped by the knife-edge will seem dark, while the remaining field will be bright. The boundary between light and shadow defines the locus of the images of points which deflect light through an angle corresponding to the distance between the knife-edge and the illuminating slit. By taking photographs at different positions of the knife-edge, it is possible to determine the field of angles of light deviation in the entire object.

Although the focal knife-edge method is very simple, it has not found wide application. Due to the finite width of the illuminating slit, the boundary of the shadow area is blurred. In addition, the apparent boundary between black and white can move under different conditions of photographic processing (or different illumination conditions in the case of visual observation). The reduction of the slit width is accompanied by an increase in the influence of diffraction phenomena; a system of fringes appears on the shadow boundary, considerably complicating the interpretation of the photographs.

Most of these drawbacks were eliminated by replacing the Foucault knife-edge with an opaque filament. While the filament shadow is blurred, due to the finite width of the source and to diffraction, it is usually symmetrical, with the shadow center corresponding to the locus of points deflecting the light through an angle which corresponds to the distance extending from the middle of the illuminating slit to the middle of the filament.

In the case of strongly bent waves the filament shadow is thin. For almost plane waves, on the other hand, the filament shadow covers a considerable part of the field and the possibility of error in the determination of its centerline is considerable.

Figures 21 and 22 show photographs obtained with vertical and horizontal filaments in the study of free convection from a heated cylinder in the atmosphere. The photographs in each figure differ regarding the position of the viewing filament with respect to the slit image. By processing a series of such photographs it is possible to obtain the distribution of the angles of light deviation in two mutually perpendicular directions over the entire instrument field and thus to determine the wave front shape and all the parameters connected with it.

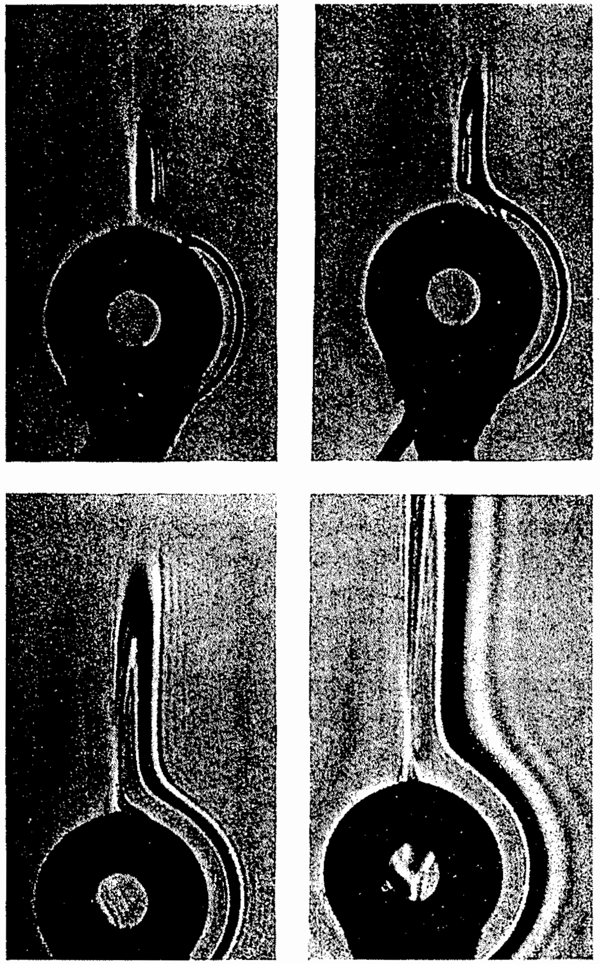

Figure 21
Convective flow about a heated cylinder — vertical viewing filament.

The study of the supersonic gas flow past a wing [21] represents an example of of the application of the method of the focal filament. The experiments were conducted in a plane-flow wind tunnel. The wing model was mounted so that its generatrices coincided with the line along which the flow properties were constant, and was kept parallel to the optical axis of the schlieren instrument.

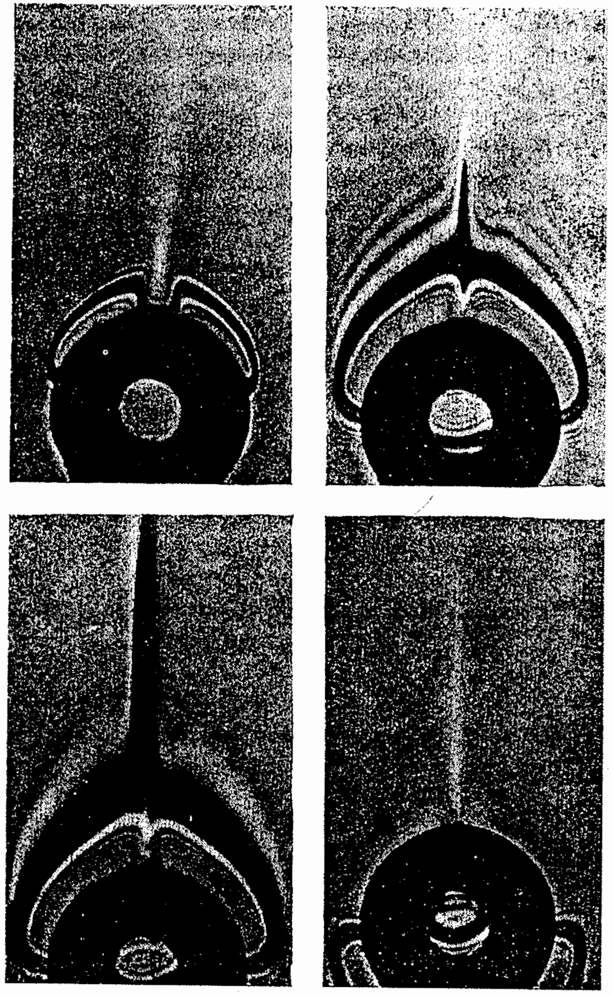

Figure 22
Convective flow about a heated cylinder — horizontal viewing filament.

Sample photographs of two series of experiments, in which the horizontal and vertical components of the deviation angles were measured, are shown in Figures 23 and 24.

The processing consisted of measuring the coordinates of the centers of the filament shadows. From the analysis of two series of photographs, it was possible to construct the distribution of the angles of light deviation in two mutually perpendicular directions (Figures 25 and 26). Since the deviation angle is linearly related to the density gradient of the gas stream, these curves represented curves of equal density gradient in directions $x$ and $y$. The values in parentheses in the figures represent the angles; the values preceding the parentheses represent the density gradients.

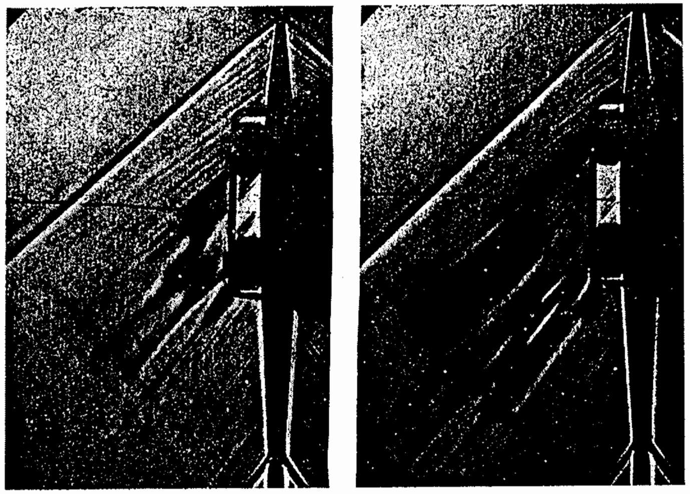

Figure 24

Flow past a plane wing — horizontal filament.

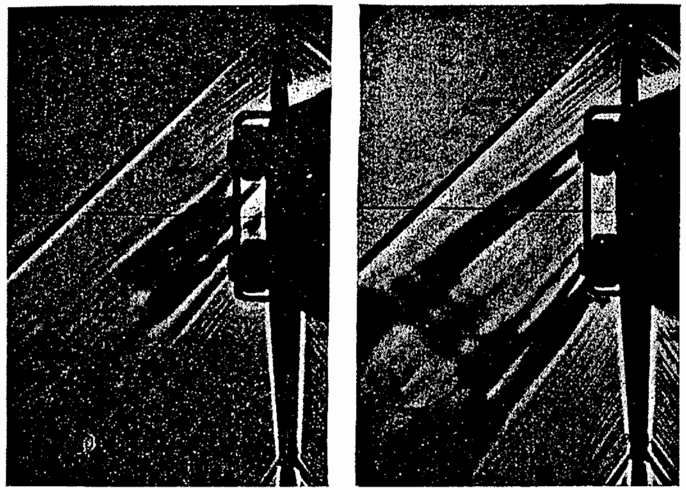

Figure 23

Flow past a plane wing — vertical filament.

The conversion to density values was accomplished by numerical integration of the gradients over the sections $x$ = const and $y$ = const. The theoretical and experimental density distributions are represented in Figures 27 and 28. To obtain the absolute values, the figures must be multiplied by $10^{-3}\,\mathrm{kg\cdot sec^2/m^4}$. The two distributions are seen to coincide satisfactorily. The existing differences are explained by the difference between the actual and ideal conditions; these differences are, however, small and exceed only slightly the margin of error of the experiment.

The study mentioned above established the advantages and drawbacks of the focal filament method. This method can be used for steady-state processes in which the angles of light deviation are relatively large ($> 5 \times 10^{-5}$ rad), and the inhomogeneity size is considerable. In zones where the derivative of the angle of light deviation is small, the filament shadow broadens and the measurement error increases. The error in the determination of the density gradients is variable and fluctuates between 1.5 and 10%. A considerable advantage of this method is the simplicity of the experimental procedure and of the processing.

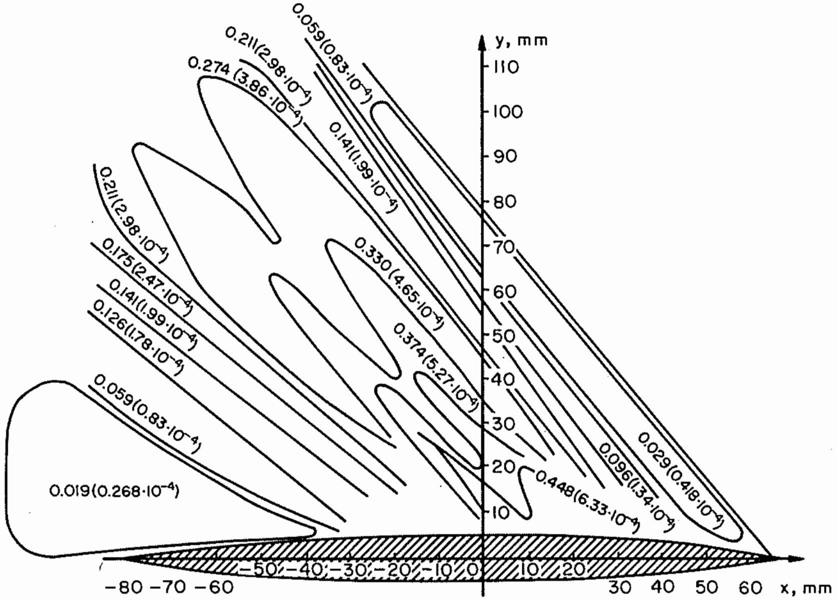

Figure 25

Curves of equal light deviation angles and equal density gradients in the horizontal direction.

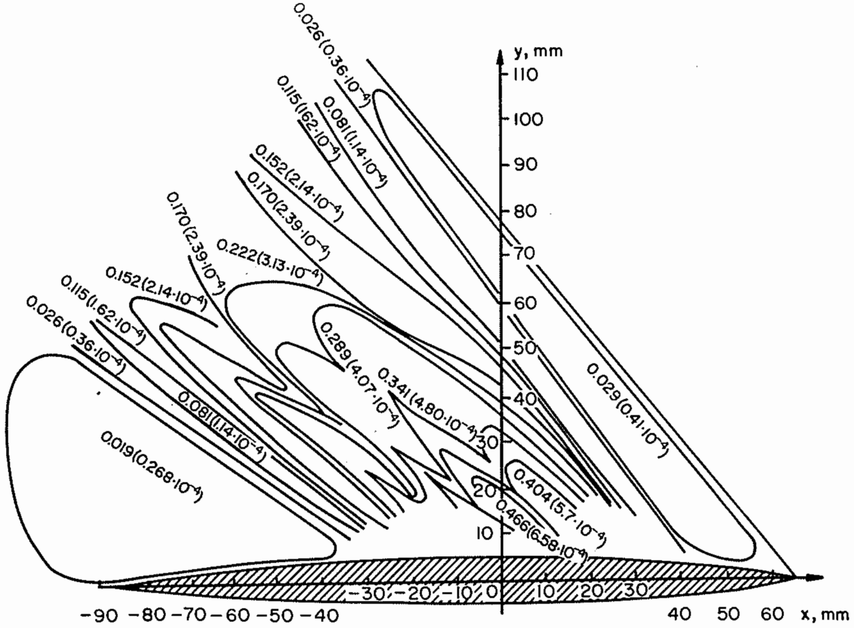

Figure 26

Curves of equal light deviation angles and equal density gradients in the vertical direction.

Attempts were made to use the negative version of the method just described, replacing the focal filament by a focal slit. This method has not been widely adopted, however, since the observation of a single bright line against a dark background complicates the correlation of the locus of points of equal deviation angles with the coordinate frame of the object field.

There is a shorter procedure for obtaining the same experimental data, consisting of setting up a system of filaments in the focal plane. A grating with equidistant grooves is normally used for this purpose. A system of shadows then appears in the inhomogeneity image, each a locus of points of equal deviation angles. While this method seems much superior to the preceding one, it has been used only for hydrodynamic measurements at large angles of light deviation. It is not suitable for weak inhomogeneities because 1) it is difficult to correlate the different shadows with specific grooves; 2) the distance between the grooves must be sufficiently large to prevent the overlapping of the diffraction patterns produced by adjacent shadows, which decreases the number of shadows in the inhomogeneity image. In order to conduct a more detailed study of the inhomogeneity it is then necessary to take a series of photographs, and this obviates the advantage of the method, compared to the focal filament method.

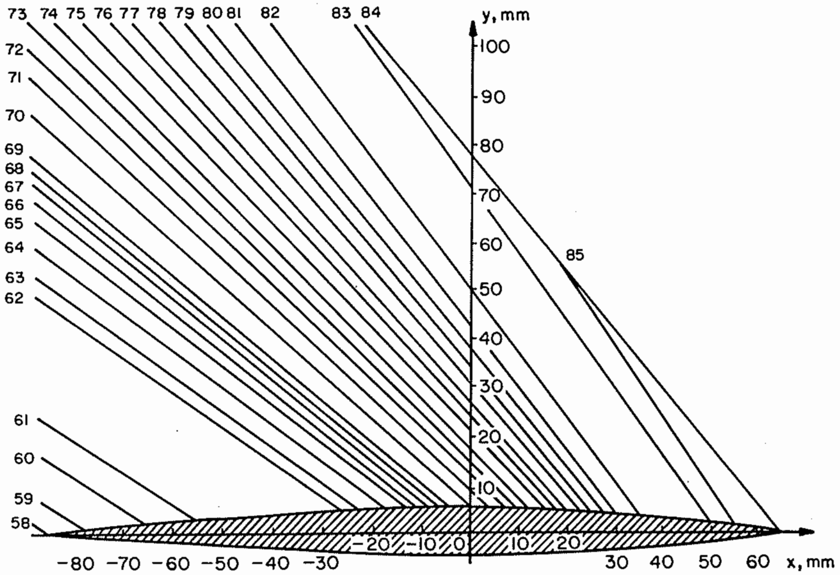

Figure 27

Theoretical distribution of gas flow density about a plane wing.

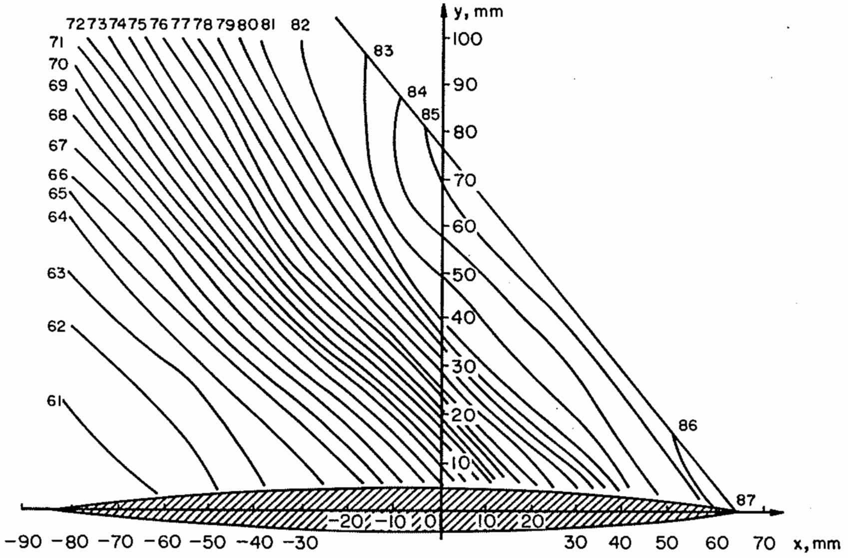

Figure 28

Distribution of gas flow density about a plane wing. Obtained experimentally by the slit and filament method.

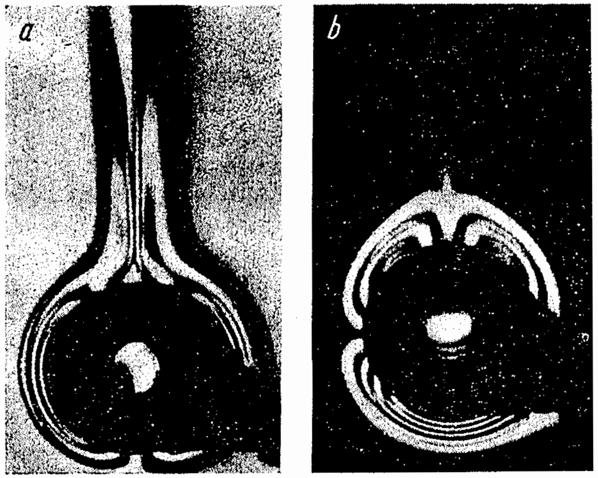

Figure 29
Photographs of the convective flow about a cylinder: *a* vertical grooves; *b* horizontal grooves.

Figure 29 shows photographs of the same convective flow as in Figures 21 and 22, with a grating placed at the focus. Under these conditions we can obtain the shadows of three grooves.

# III

# *SOME SPECIAL SYSTEMS*

## 9. COLOR METHODS

Color-image methods represent a further development of the ordinary schlieren methods. The first color-image system used a range of colored filters (transparent tinted glasses) placed in the focal plane of the main objective of the receiving part. In the absence of an inhomogeneity, light from different points passes through the same filter, and, as a result, the entire field appears identically colored. The introduction of an inhomogeneity causes the deflected rays to pass through different filters. The image of all the points which deflect the light beam through the same angle has the same color.

The two types of filters most widely used are a set of strips of colored glass, and a circular plate with differently colored sectors (see Figure 30, where the solid line represents the light source image, and the dotted line is the shifted image).

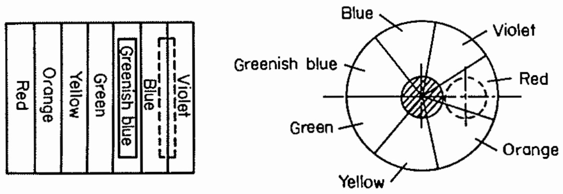

Figure 30
Sets of colored filters used for obtaining a color image.

A slit source is used with the colored strips. Since the lines of equal color in these filters are parallel, the displacement of the slit image along a strip does not alter the image color; the method records only the change of the component of the angle of light deviation in the direction perpendicular to the lines of equal color.

A circular light source is used with the circular filter. In this case the image color changes when the source image shifts in any direction. Theoretically, it is possible to measure both the magnitude and the direction of the angle of deviation with such a filter, for instance, by determining the intensity ratios of the different monochromatic radiation fluxes at every point of the image with the aid of spectral methods. Such measurements are complex, however, and, consequently, this method is not used in practice.

The measurement range is limited by the range of deviation angles for which the source image remains within the filter area. Its value is

$$D = \frac{L + 2l}{f}, \tag{9.1}$$

where $L$ is the width of the colored part, and $l$ the width of the source image.

The narrower the light source image and the higher the sensitivity of the methods described, the closer the different colors in the filter. It is usually advisable to use a light source image whose width is more or less equal to that of the colored strips.

If the slit is too narrow, changes in the angle of deviation which allow the slit image to remain within the limits of the same strip will not be accompanied by a color change. If the slit is too wide, the image contrast diminishes. Other factors affecting the selection of the source image size are the image illumination and the number of colors which can be distinguished.

The sensitivity of the above methods of color illumination cannot be increased to a high extent, since color filters with very thin strips or sectors are difficult to manufacture. Accordingly, the system shown in Figure 31 is used in measurements for which a high sensitivity is required. The light from the slit source $S$ is collimated by the condenser $O_c$ and falls on the prism $P$. The objective $O_{c1}$ forms the spectrum $Sp$, which functions as a light source for the system to its right side. The spectrum is formed at the focus of the main objective of the illuminating part; its image, formed by the main objective of the receiving part, is covered by a stop — a filament, a slit, or a knife-edge. If a filament or a knife-edge is used, its width is roughly equal to the width of one color in the spectrum.

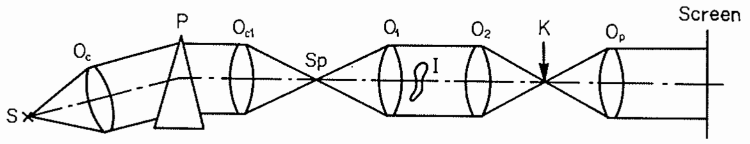

Figure 31
Optical system of the color schlieren instrument.

In the absence of inhomogeneities the field is illuminated uniformly, and its color corresponds to the mean color of the rays traversing the viewing diaphragm. A different color corresponds to each angle of deviation.

Since the spectrum width is easily reduced, a considerably higher sensitivity can be achieved than in the preceding variants. Most attachments for color photography manufactured for schlieren instruments are based on this system. Their design features will now be described. Since the objectives $O_c$ and $O_{c1}$ and the prism $P$ contribute to the formation of the spectrum, they are not permitted any noticeable aberrations. Experience has established that photographic objectives can be used as condensers; they provide a satisfactory spectrum sufficient for studying inhomogeneities deflecting the light rays by as little as $10^{-5}$ rad.

A prism with parallel faces (Figure 32), composed of two kinds of glass having the same refractive index for yellow light, is used as a dispersive element. The two types of glass have different dispersions, the refractive index for red light being larger in one component, and that for blue light in the other. The yellow light is not deflected on passing through such a prism, and the blue and red lights are deflected in different directions. This prism intercepting a parallel beam is virtually free of aberrations. No deviation of the beam as a whole takes place when it is used, which facilitates the actual construction of the system. This point is of considerable importance when the experimenter himself has to build the attachment.

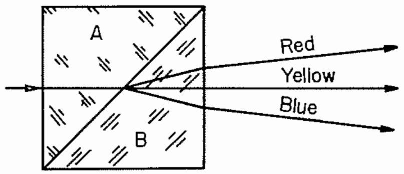

Figure 32
Prism for obtaining a color image.

In order to vary the width of the spectrum, it is convenient to position two prisms which can be rotated in opposite senses about the optical axis. The spectrum width will then vary from zero, when the angle between the prisms is 180°, to twice the width afforded by a single prism.

A schematic cross section of the color attachment for the Soviet-made IAB-451 instrument is shown on Figure 33 [11]. The condensers $O_c$ project the light source on the slit $A$. Focusing is achieved by moving the forward lens by rotating the ring $R$, and focusing control is provided by the total reflection of prism $P$. The slit is placed in the focus of the objective $O_p$, which directs a parallel beam at the two prisms. The

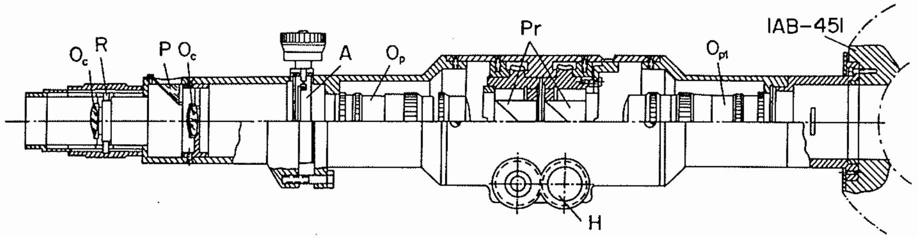

Figure 33
Color attachment for the Soviet-made IAB-451 instrument.

angular width of the spectrum depends on the angle of rotation of the prisms; rotation is achieved by means of the handles *H*. The second objective $O_{p1}$ projects the color of the slit *A* onto the illuminating slit of the schlieren instrument. Regular photographic objectives can be used as $O_p$ and $O_{p1}$. The 45° reflecting prism *Pr* provides a spectrum of angular size of up to 1° 50′; used in combination with an appropriate objective (Soviet-made Yu-11) it ensures a spectrum 4.3 mm wide.

The advantages of this attachment lie in the simplicity of its manufacture and of its optical calculation. The only parts which have to be ordered from specialized optical workshops are the prisms. The remaining optical parts are simply purchased, while the mechanical components can be manufactured by any workshop. The attachment is used to obtain relatively accurate measurements. If the homogeneity produces pronounced deviation of the light rays, the design becomes simpler, since the standards of the optical parts and the adjustment accuracy are less exacting.

Sample photographs obtained with the aid of the attachment are shown in Plates I through IV.

The measurement range is equal to the sum of the angular widths of the spectrum and the slit or filament. In the ordinary schlieren method, the spectrum width is virtually equal to the slit width. There are, however, some exceptions. If the stop is a filament, the relationship between the angles of deviation and the photographic density is not single-valued. The portions of the object which deflect the slit image to positions symmetrical with respect to the filament center are equally illuminated. This ambiguity is eliminated in the color-image method.

If a narrow slit is used as the viewing diaphragm, the sensitivity is equal to

$$S = \frac{d\lambda}{d\varepsilon} = f\frac{d\lambda}{d\xi}. \tag{9.2}$$

It is inversely proportional to the dispersion of the prism used. The smallest measurable angle of light deviation in the inhomogeneity is equal to

$$\Delta\varepsilon = \frac{d\xi}{d\lambda}\frac{\Delta\lambda}{f}, \tag{9.3}$$

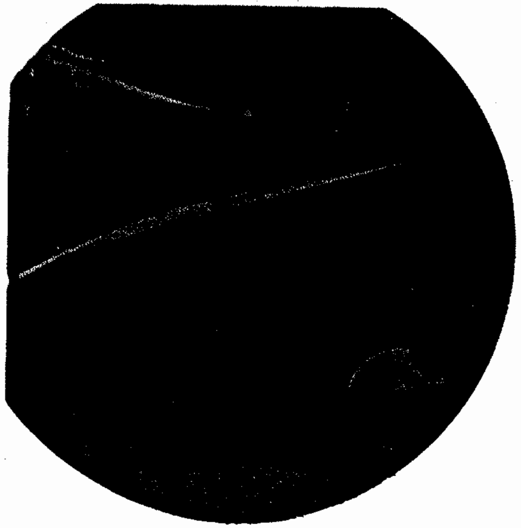

Plate I

Plate II

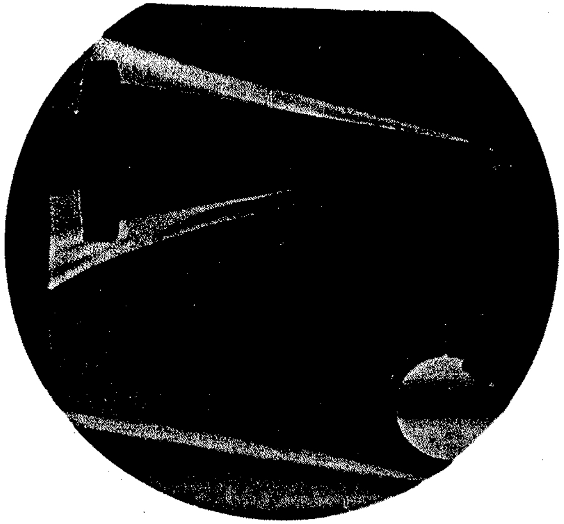

Plate III

Plate IV

where $\Delta\lambda$ is the minimum wavelength difference which gives an observable color difference. Assuming that this wavelength difference is equal to 200 Å, the minimum angle of deviation which can be observed for a spectrum 0.3 mm wide is about $10^{-5}$ rad. If a filament is used, the light variation in the image is somewhat different.

The minimum spectrum width depends on the aberrations and on the diffraction. The distance in the spectrum between adjacent distinguishable colors must be larger than the scattering disk representing the image of an infinitesimal light source in the focal plane. For the Soviet-made IAB-451 and TE-19 instruments the minimum width is 0.15 mm; the reduction of this value leads to poor color purity, and does not increase the sensitivity.

Color schlieren methods are suitable for quantitative measurements as well. In this regard, the differently colored areas of the image must be correlated with the corresponding position of the spectrum image relative to the diaphragm. The visual differentiation of the colors in the image is, however, difficult, particularly if it has to be conducted at many points of the object. Photographic measurements of this type, although possible, have not been conducted; this is probably due to the imperfections of the color photography method, which does not allow a faithful reproduction of all color shades.

A second method for obtaining quantitative results requires a light filter in the receiving-part illuminator [80]. A curve appears on the photograph, whose axis corresponds to the locus of points of equal deviation angle. By using different light filters we can obtain the entire field of deviation angles. This method is similar to the slit-and-filament and the slit-and-slit methods. The color pictures can be photographed with different light filters on a black-and-white film, which simplifies the processing. The method in this form has no comparative advantages and, accordingly, has not been widely used.

The most efficient method is the method of standards in color photography, consisting of placing a standard object of known deflection properties (a system of wedges or a lens — a *schliere*) in some point of the field which is free from inhomogeneity. By comparing the color distribution in the standard object and in the inhomogeneity, we can correlate each color with a particular angle of deviation. The method is, therefore, quite convenient for a rapid estimation of the size of the inhomogeneities.

The distortion of colors during film development and printing does not affect the measurement error, since this method does not require perfect identity between the color of the image point and its shadow on the positive or negative. It is only necessary that the points in the image on which radiation of a given color falls appear identically shaded on the photograph. Since these points are located on the same photograph and have been processed under the same conditions, this is easily achieved. Thus Plates I and II of the color insert represent photographs of the same object, but with different instrumental adjustment and processing of the material. As a result, the prints are differently colored, but the correspondence between the colors in the field and in the lens has been preserved. Therefore all these photographs yield the same results.

The color photography method has advantages as compared with other methods if exact measurements of the distribution of deviation angles are required. The measurement error in this case is larger than when using photometric measurement methods. Nevertheless, the method possesses specific advantages for assessing inhomogeneities and making tentative measurements of the distribution of deviation angles. It retains the most precious attribute of the photometric methods, namely, the visualization of the overall pattern of the inhomogeneity and the possibility of measuring the angle of deviation at any point of the object. The quantitative processing is also a simple matter. It does not require densitometric or other specialized instrumentation. When wedges are used, the photograph is simply examined, and the colors are identified. If a standard lens is used, it is also possible to measure the distance from the color strip in the standard lens to the lens center. Accordingly, it can be considered a semiquantitative method permitting the evaluation of the angles of light deviation.

Due to the relatively low sensitivity of color films available at present, difficulties are encountered in the application of the color-image schlieren methods to the study of weak transient processes. New photographic materials and more powerful light sources are urgently needed in order to be able to utilize the color-image methods on a large scale.

## 10. STEREOSCOPIC SYSTEMS

The ordinary schlieren instruments, in which the light source is small compared with the focal length of the main objective of the collimator, have a large depth of focus. Opaque objects on the optical axis are seen sharply from virtually any distance. Thus if the object is at a distance of 1 m from the ideal focus of the IAB-451 instrument, operating with a 1 mm slit, each of the object points will be represented by a circle of confusion 0.17 mm in diameter (for an image scale of 1 : 3).

The change in the image illumination is independent of the position of the inhomogeneity along the optical axis. This is convenient for the quantitative study of plane or axisymmetric objects, since the mathematical processing of the results and the transition from the overall deflections of a ray traversing the inhomogeneity to the values of the refractive index gradient at any point of the inhomogeneity become extremely simple. This same property, however, complicates the study of complex asymmetric bodies, since the superposition of the shadow patterns of different inhomogeneities or of portions of the same object lying at different positions along the optical axis of the instrument makes it impossible to determine the shape and position of the different elements.

Several means are known for overcoming this difficulty. In a number of studies [119, 132] the inhomogeneity was simultaneously photographed by several schlieren instruments, each of which was placed at a different angle with respect to the inhomogeneity (Figures 34 and 35). In order to determine the spatial distribution of the inhomogeneity, the processing of such photographs necessitates the use of stereoscopes. The pinpoint accuracy depends on the angle between the axes of the instruments utilized.

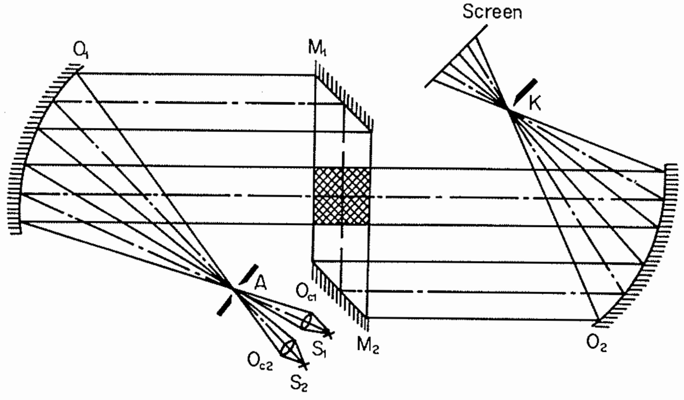

Figure 34

Dual instrument for the simultaneous observation of the inhomogeneity in two mutually perpendicular directions.

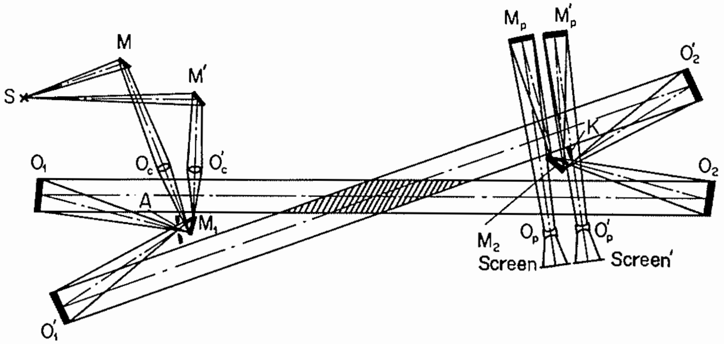

Figure 35

Double instrument for the simultaneous observation of the inhomogeneity in two directions, forming an acute angle.

The second possibility for determining the location of the inhomogeneities consists of utilizing a single instrument which can be rotated through different angles [112]. An example of such a system is represented in Figure 36. If the photographs are shot at different positions of the instrument, they are processed in the same way as when photographing with several instruments. If the object is photographed continuously on a still or movie film while the instrument is being rotated, the interpretation technique changes. A drawback of this method is the difficulty of applying it to the study of transient processes.

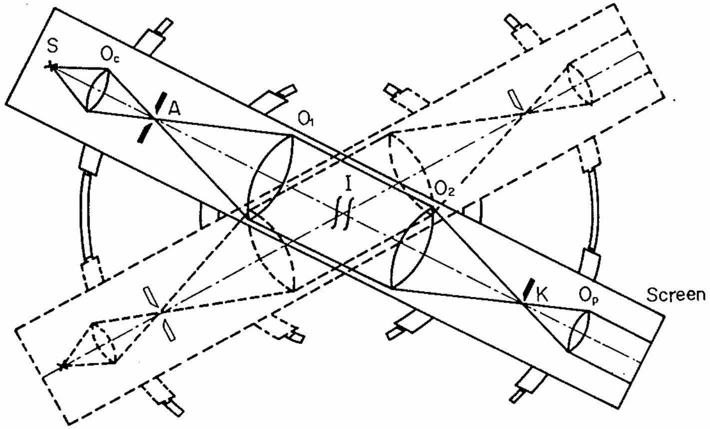

Figure 36

Design of an instrument which can be rotated through different angles.

An ingenious application of this arrangement is described in [100]. The light source was set at the end of an airplane wing, and the receiving part of the schlieren instrument was placed in the cabin. In flight, the light source moved in a vertical direction. The film was either still or moving. In the first variant, a complex pattern of superposed schlieren images, taken at different viewing angles, appeared on the photograph. The second variant yielded a series of photographs, each of which corresponded to projection at a different angle. The shock wave shape was determined by processing these photographs, and the shape changes caused by the irregularity of the wing profile were analyzed.

One of the widely used methods of stereoscopic observation uses a schlieren instrument with a multiple-slit light source [82, 94, 111]. The optical arrangement is represented by Figure 37. A large-size light source $S$ is projected by the condenser objectives $O_{c1}$ and $O_{c2}$ onto the grid $D_1$, representing a system of apertures on an opaque background. While the size, shape, and arrangement of the apertures can be arbitrary, the simplest and most convenient solution is to use a series of parallel or radial transparent slits separated by opaque spaces. The grid is placed in the first focal plane of $O_1$ — the main objective of the illuminating part of the schlieren instrument. In the second focal plane of $O_2$ the viewing diaphragm $D_2$ is placed, representing the negative image of the grid $D_1$. The camera objective projects the image of some section of the inhomogeneity $I$ on the screen.

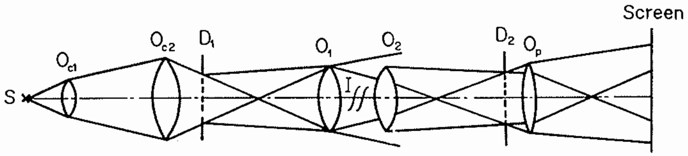

Figure 37

Design of a stereoscopic schlieren instrument with a multiple-slit light source.

The grids $D_1$ and $D_2$ are aligned in such a way that the image of each slit source of $D_1$ is partially obscured by an opaque spot of $D_2$. As a result, every slit of $D_1$ forms, together with the opaque spot of $D_2$ corresponding to it, a system analogous to the light-source-and-knife-edge system of the ordinary schlieren instrument. The entire arrangement represents a set of ordinary schlieren instruments placed at some angle to each other. The inhomogeneity images created by the different "instruments" are superposed, creating a complex pattern.

From the collimator emerge parallel beams, forming with the optical axis an angle $\varepsilon = h_i/f$, where $h_i$ is the distance from the corresponding source aperture to the axis. Through every point of the working space passes a light beam of angular aperture

$$\varepsilon \approx \tan \varepsilon = \frac{L}{f}, \tag{10.1}$$

where $L$ is the grid size.

The inhomogeneity points lying outside the ideal focal plane are represented by a circle of confusion of diameter

$$D = l\varepsilon\mu, \tag{10.2}$$

where $\mu$ is the image scale, and $l$ the distance from the given point of the inhomogeneity to the ideal focal plane. The circle of confusion increases with the increase of $l$, and the visibility of the object becomes poorer, until the object is blurred completely for some value of $l$. The distance between two objects just blurring to invisibility from different sides of the ideal focal plane is termed the *depth of focus*.

The arrangement with a multiple-slit light source has a light beam aperture considerably larger than ordinary schlieren instruments. This leads to a decrease in the depth of focus. Only a specific narrow region of the object plane is sharply represented. A spatial determination of the inhomogeneity parts becomes possible.

The configuration of the focusing schlieren instrument is more complex than that of the ordinary schlieren instrument. In the first instance it is considerably more expedient to use a two-lens condenser. In the second instance, the use of a grid instead of the knife-edge and slit leads to substantial alterations.

The design of the illuminating part of the focusing schlieren instrument is based on the following principles: 1) the image of the light source on the illuminating grid must completely fill the working area of $D_1$ and must be as bright as possible; 2) the main objective must not vignette the light beams emerging from $D_1$. These requirements are fulfilled if the size of the luminous part of the light source is equal to the size of the illuminating grid, and the rim of $O_c$ is projected on $O_1$.

If the second principal plane of $O_{c2}$ coincides with $D_1$, these requirements are satisfied for objectives $O_{c1}$ and $O_{c2}$ of lower speed. Then

$$\frac{d_{O_{c1}}}{f_{O_{c1}}} = (\mu_1 + 1)\frac{d_{O_1}}{f}, \tag{10.3}$$

$$\frac{d_{O_{c2}}}{f_{O_{c2}}} = \frac{L}{f_{O_1}}\left(\frac{d_{O_1}}{d_{O_{c1}}} + 1\right), \tag{10.4}$$

where $\mu_1 = h/l$ is the linear magnification with which the light source is projected onto $D_1$; the magnitudes $d_{O_{c1}}$, $f_{O_{c1}}$, $d_{O_{c2}}$, $f_{O_{c2}}$, $d_{O_1}$, $f_{O_1}$ are, respectively, the diameters and the focal lengths of the objectives $O_{c1}$, $O_{c2}$, $O_1$. When the objectives $O_{c1}$ and $O_{c2}$ are of lower speed, it is necessary to select light sources with a large luminous area. The larger the light source, the wider the parameters of the focusing system.

In designing the receiving part it is necessary to keep in mind that different light beams emerge at different angles from $D_1$. Only that part of the inhomogeneity through which pass all the beams emerging from the different slits of the grid will be uniformly illuminated. Furthermore, the light beams must not be cut off by the rim of $O_2$. To satisfy this requirement and the additional one of uniform illumination of the entire inhomogeneity, we must have

$$d_{O_2} = d_{O_1} + \frac{La}{f_{O_1}}. \tag{10.5}$$

It is difficult to obtain an objective $O_2$ with such a diameter, especially since $O_1$ is normally large as well, due to the necessity of studying large fields. The optimal solution is apparently $d_{O_1} = d_{O_2}$. If the system is focused on the middle point of the inhomogeneity between the objectives, the uniformly illuminated area is

$$d = d_{O_1} - \frac{(a \pm \Delta)L}{2f_{O_1}}, \tag{10.6}$$

where $\Delta$ is the depth of focus.

The illumination of the other portions of the field is variable, and the inhomogeneity details that appear are difficult to study. The size of the uniformly illuminated portion can be taken as the size of the working field. For $f_{O_2} = f_{O_1}$ the objective $O_p$ must not be smaller than $D_2$; the focal length of the camera objective is determined from the required image scale.

By means of the equations obtained it is possible to calculate the focusing system from the given parameters of the object studied. The distance $a$ between $O_1$ and $O_2$ is determined by the length of the inhomogeneity. In wind-tunnel measurements it is usually determined by the distance between the protective windows of the wind tunnel. The diameter of the main objectives is determined by the size of the inhomogeneity. The depth of focus $\Delta$ is determined by the accuracy required in determining the position of each part of the inhomogeneity. The focal lengths $f_{O_1}$ and $f_{O_2}$ are selected on the basis of the sensitivity required of the instrument.

To achieve adequate sensitivity in the system, all the objectives except $O_{c1}$ must be anastigmats. A high-speed achromatic lens can be used as $O_{c1}$. When an instrument of average sensitivity is assembled from ready-made optical elements, it is expedient to use the Soviet-made objectives I-51, I-52, and I-13, which are mass-produced.

The illuminating and viewing grids must have slits with a high optical density, and the dark and bright spots must coincide precisely in the focal plane of the main objective of the receiving part. Mechanical methods can be used for manufacturing the grids, but the best procedure is to use a photographic method. The negative of the illuminating grid is drawn to a larger scale on a special Whatman sheet and photographed on a plate. The illuminating grid is then placed in the instrument, and a new photographic plate is placed at its image in the focal plane of the main objective of the receiving part, followed by the exposure. The viewing grid thus obtained allows to a considerable extent for the aberrations of the system and for inaccuracies in the manufacture of the illuminating grid.

The grid shape is of considerable importance. The slits being discrete, every point of the inhomogeneity is illuminated by a series of narrow beams (Figure 38). The circle of confusion likewise receives discrete illumination. If the grid is made of parallel slits, the band structure of the blurred image detracts somewhat from the focusing effect. This drawback can be eliminated by using a grid of concentric circles. In this case the disappearance of the image is smoother and the depth of focus decreases. More complex grid shapes are seldom used, since additional difficulties arise in the manufacture and adjustment of the grids and in the interpretation of the results.

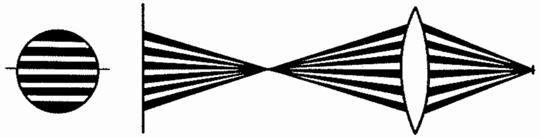

Figure 38

Illumination of every point of the inhomogeneity and point of the image when the light source is a grid.

The selection of the grid shape depends to a certain extent on the direction of the angle of light deviation which is recorded by the instrument. An arrangement using a grid of parallel lines measures only angles of deviation perpendicular to the grid lines. If a grid of concentric circles is used, the change in the image illumination is the same when the light is deflected in any direction.

The required width of the slits and the distance between them are also determined on the basis of the above factor. The grid period must correspond to the measurement range, since otherwise the correspondence between the light deflection and the image illumination will not be single-valued.

Figure 39 shows photographs of an air jet heated to 60° and discharged into the atmosphere at an excess pressure of 0.1 atm. The jet diameter at the nozzle throat is 1.5 mm. The light source was a PRK-4 mercury lamp, with a luminous area of 15 × 1.2 cm. The width of the illuminating grid $L$ was 2 cm. Under each of the photographs is indicated the distance $l$ from the object to the ideal focal plane. For $l = 0$ the jet image is sharp; the air flow is clearly visible. For $l = 2$ cm the object boundaries are blurred, and the inhomogeneity is observed very weakly. For $l = 4$ cm the jet becomes almost completely invisible; its tip is seen as a blurred spot of indefinite shape. If the grid width is changed by some factor, the distances $l$ for which such photographs are obtained are changed by the same factor. When the grid is replaced by a single slit, photographs taken even at a considerable distance from the ideal focal plane are virtually identical to those taken when the object is in that plane.

It is difficult to indicate the exact value of $\Delta$, since it depends on the character of the objects studied. Initially, weak inhomogeneities of small size disappear, after which stronger ones as well become blurred. Since a gas jet is the most important object, we can consider that $\Delta = 8$ cm.

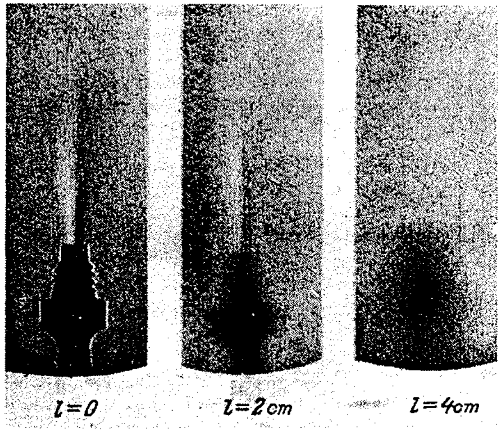

Figure 39
Photographs obtained by a schlieren instrument with a multiple-slit source.

The sensitivity of a focusing instrument is generally lower than that of the ordinary systems, due to the strong increase of the aberrations at the field edge and to inaccuracies in the manufacture and overlapping of the grids. The method is therefore used only for studying relatively strong inhomogeneities. Another drawback is the difficulty of using focusing systems for quantitative studies. The main objects of study are complex inhomogeneities of large size, in which the shape and position of different characteristic parts have to be determined.

By using converging beams it becomes possible to study strong inhomogeneities, of a size larger than the diameter of the objectives (Figure 40). The maximum size which can be studied is determined by the size of the illuminating grid, which can be easily increased in some cases. This property is frequently considered the basic one [74].

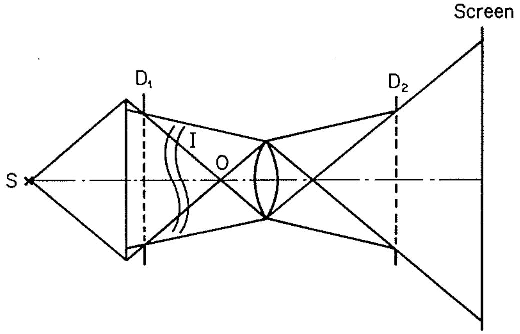

Figure 40
Instrument for the study of large inhomogeneities.

The above system is also used as a method of quality control monitoring defects in lenses and protective glasses, extraneous fluxes, etc.

The use of an extended light source makes it possible to use powerful lamp sources and to utilize their light flux more fully than in ordinary systems. As a result inhomogeneities can be observed under strong extraneous light.

Very few instruments have been manufactured as yet for the industrial study of large-size inhomogeneities, and the theoretical and experimental material assembled to date is insufficient for their definitive evaluation. It is, nevertheless, clear that they can be of considerable aid in some cases.

## 11. PHOTOELECTRIC RECORDING

A time resolution of the process is necessary in the study of transient processes, such as explosions, combustion, etc. This time resolution can be achieved by photoelectric recording of the schlieren instrument readings. The simple arrangement is shown in Figure 41 [17]. The field of an ordinary schlieren instrument is partially obscured by the stop *D*. Only a small area remains open, in which any changes in the angle of light deviation can be ignored. Behind the knife-edge is placed a photocell (or a photomultiplier for weak light fluxes), which receives the light flux unimpeded by the knife-edge. The deflection of the light by the part of the inhomogeneity facing the slit causes a change in the light flux falling on the photomultiplier. As a result, the current flowing through the photomultiplier will change. These changes in current are recorded by an oscillograph. If we examine the straight portion of the characteristic curve of the recording system, the pulse amplitude on the screen will be proportional to the light flux, which is determined by the angle of light deviation.

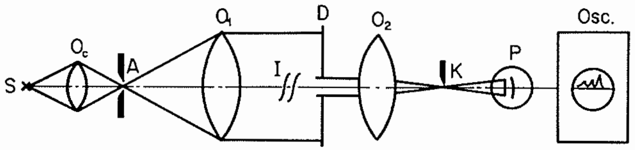

Figure 41
Photoelectric method for recording the readings of a schlieren instrument.

To minimize the averaging of the deviation angles over the finite part of the inhomogeneity facing the slit, it is necessary to reduce the slit aperture. This improves the resolution of the instrument in space and time, but reduces its sensitivity as a result of the diffraction phenomena. If the width of the diffraction maxima is much larger than the width of the geometrical image of the slit, the illumination distribution in the direction perpendicular to the knife-edge is determined by the equation

$$I(\xi) = c^2 \left( \frac{\sin \frac{k}{f} l\xi}{\frac{k}{f} l\xi} \right)^2, \tag{11.1}$$

where $c$ is a constant, $\xi$ is the coordinate in the focal plane of the receiving part perpendicular to the knife-edge, $l$ is the slit width in the same direction, $k = 2\pi/\lambda$, $\lambda$ is the wavelength, and $f$ is the second focal length of the main objective of the receiving part.

The instrument readings depend on the total intensity of the incident light (the light not stopped by the knife-edge). The intensity is equal to

$$J = \int_{\xi_0}^{\infty} I d\xi, \tag{11.2}$$

where $\xi_0$ is the knife-edge coordinate.

The sensitivity for photoelectric measurements is determined by the magnitude

$$\frac{dJ}{d\varepsilon} = If = \frac{c^2 f \sin^2 \frac{k}{f} l\xi_0}{\left( \frac{k}{f} l\xi_0 \right)^2}. \tag{11.3}$$

The sensitivity is highest for $\xi_0 = 0$, i.e., when the knife-edge covers half the diffraction pattern.

If a slit whose width is much smaller than the diffraction image is used, the sensitivity is proportional to the magnitude

$$\frac{dI}{d\varepsilon} = \frac{2c^2 f^3}{k^2 l^2 \xi_0^3} \left( \frac{k}{f} l\xi_0 \sin \frac{k}{f} l\xi_0 \cos \frac{k}{f} l\xi_0 - \sin^2 \frac{k}{f} l\xi_0 \right). \tag{11.4}$$

The sensitivity curve for this case is represented on Figure 42. The abscissae give

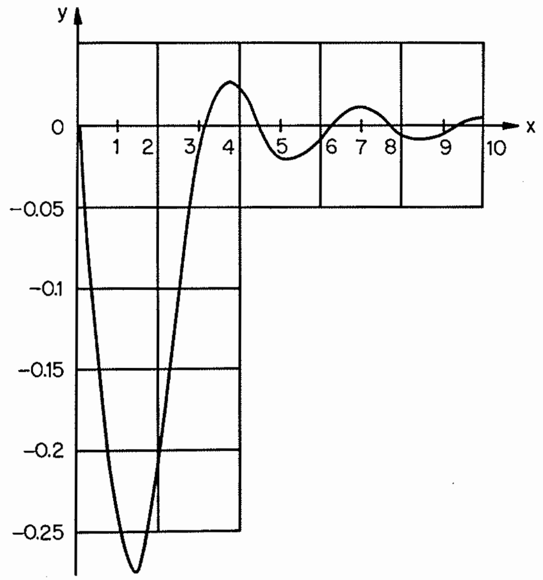

Figure 42
Sensitivity of photoelectric measurements for an aperture in the object plane.

$kl\xi_0/f$ and the ordinate is $\sin x\,(x\cos x-\sin x)/x^3$. It follows from this curve that the sensitivity is maximum for $kl\xi_0/f \approx 1.3$.

In practical work the slit width is selected on the basis of the expected size and character of the inhomogeneities. It is usually equal to several millimeters or fractions of a millimeter. The size of the diffraction pattern in the focal plane of the main objective of the receiving part is also roughly equal to fractions of a millimeter or several millimeters (for the IAB-451 instrument). It is larger than the width of the geometrical image of the illuminating slit. Therefore, in the study of weak inhomogeneities the measurement sensitivity is determined by the diffraction phenomena and is lower than the sensitivity achieved with a completely open instrument field.

The glow or absorption of the object studied plays a substantial role in the processing of the results. An additional experiment is usually conducted in order to estimate the influence of this factor. The viewing diaphragm is displaced to permit free passage of the light deflected by the inhomogeneity and to ensure that only the absorption or glow affect the value of the oscillograph signal. For small displacements of the viewing diaphragm and operation on the straight portion of the characteristic curve, the pulse corresponding to the light deflection is determined by subtracting from the total pulse the amplitude of the signal expressing the combined action of glow and absorption.

There are papers [77, 117] in which a slit whose size is much larger than the fine details of the inhomogeneity has been used as a beam-defining aperture. In this case, the signal amplitude is determined by the integral illumination of the aperture area. This method is convenient when studying plane inhomogeneities. If such an inhomogeneity covers part of the aperture, the variation of the light flux on the photocell is expressed by the formula

$$J = c\left[\xi_0 l + f\int_0^{x_0} \varepsilon(x)\,dx\right], \tag{11.5}$$

where $l$ is the aperture width, $x_0$ is the coordinate where the inhomogeneity begins, and $c$ is a constant. The direction of the $x$ axis coincides with the direction of motion of the inhomogeneity and is perpendicular to the knife-edge.

Since the angle of light deviation in plane inhomogeneities is linearly related to the gradient of the logarithm of the refractive index of the gas, equation (11.5) can be transformed to

$$J = c\{\xi_0 l + Lf\,[\ln n(x_0) - \ln n(0)]\}, \tag{11.6}$$

where $L$ is the size of the inhomogeneity along the instrument axis, $n(x_0)$ and $n(0)$ are the refractive indices of the gas at point $x_0$ and in the undisturbed region, respectively.

In gases $(n-1)$ is small and we can expand the logarithms in power series as follows:

$$J = c\left\{\xi_0 l + Lf\,[n(x_0) - n(0)] - \frac{Lf}{2}\,[(n(x_0)-1)^2 - (n(0)-1)^2] + \dots\right\}. \tag{11.7}$$

In most cases the quadratic terms are small compared with the leading terms — the third term in (11.7) is smaller than the second term by a factor of $1/(n-1)$, and can therefore be ignored. Taking into account the Gladstone–Dale relation, we obtain

$$J = c\left\{\xi_0 l - \frac{Lf}{K}\,[\rho(0) - \rho(x_0)]\right\}, \tag{11.8}$$

where $K$ represents the Gladstone–Dale constant. If we then proceed to operate on the straight portion of the characteristic curve, the signal amplitude will be a linear function of the gas density (the refractive index) in the inhomogeneity, which simplifies the conversions considerably.

The preceding calculation was based on the relationships that obtain in geometrical optics. It is correct, generally speaking, since the limiting slit used in this design is generally sufficiently large. If the slit is small, the inhomogeneity varies sharply, or the instrument is adjusted to a high sensitivity. In this case, it is necessary to allow for the diffraction phenomena, which introduce considerable complication.

The absolute change of the light flux intensity here is larger than in the preceding arrangement, while the relative change is smaller. This design is less suitable than the preceding one for photographic recording of the signal, but is better suited to photoelectric recording. In fact, due to the cutting off of the DC component by the AC amplifiers, the sensitivity will be higher. A reduction of the sensitivity is caused only by the high value of the constant component of the illumination, which magnifies noise and reduces the value of the minimum illumination change which can be recorded.

The influence of the diffraction phenomena in the first configuration can be eliminated by changing the location of the slit limiting the size of the object observed and placing it in the inhomogeneity image. In this arrangement, the diffraction redistribution of the intensity at the edges of the light beam emerging from the limiting slit is of no importance, since the integral value of the photocathode illumination is independent of the diffraction (if the diffraction angles are considerably smaller than the angular size of the photocathode, which is almost invariably true). The limitations of the method imposed by the diffraction phenomena on the inhomogeneity and the viewing diaphragm are the same as in the ordinary method of the knife-edge and the slit. They are examined in Part II of the book. This method is applicable to most objects studied by means of schlieren instruments, since it is fairly easy to make the slit so small as to make the angle of deviation virtually constant on the viewed portion of the inhomogeneity. Due to the high sensitivity of photomultipliers, insufficient lighting does not limit the reduction of the slit width. In conducting measurements with mass-produced instruments, it is advisable to use attachments similar to the one described in [11].

The shock tube measurements described in [17] represent an example of the application of the photoelectric method of recording the readings of the schlieren instrument. The general layout of the experiment is represented on Figure 43. After

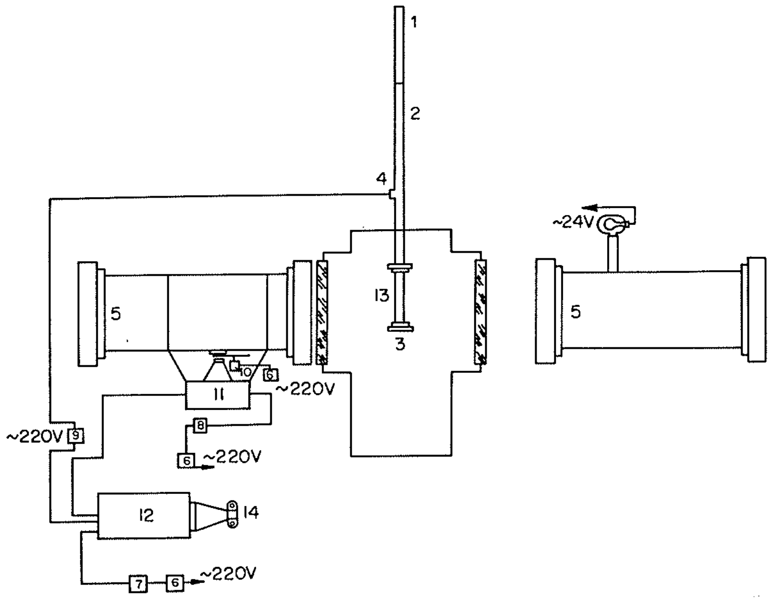

Figure 43

Schlieren instrument with photoelectric recording for studying the processes in a shock tube: 1) high-pressure compartment; 2) low-pressure compartment; 3) nozzle; 4) gage triggering the pulse oscillograph; 5) illuminating and receiving parts of the schlieren instrument; 6) voltage stabilizer; 7) rectifier; 8) high-voltage rectifier; 9) time delay; 10) mechanical chopper of the light flux; 11) photoelectric attachment to the schlieren instrument; 12) pulse oscillograph; 13) transparent compartment of the shock tube; 14) camera.

the diaphragm separating the high- and low-pressure compartments 1 and 2 is ruptured, a shock wave propagates along compartment 2. When it reaches the gage 4, the latter transmits a signal to the variable time delay 9, which triggers the pulse oscillograph several microseconds before the wave reaches the portion studied in the shock tube. By varying the delay and the sweep it is possible to obtain an image of any portions of the process with the necessary degree of resolution.

The measurement range depends not only on the slit width and the slit and knife-edge configuration, but also on the size and position of the straight portions of the characteristic curves of the different components of the electronic unit connecting the photomultiplier with the oscillograph. In the example considered the range was $3 \times 10^{-5}$ rad (angles of light deviation between $-1 \times 10^{-5}$ rad and $+2 \times 10^{-5}$ rad were measured).

The first result of the experimental studies was the confirmation of the concepts relating to the structure and the characteristic zones of the flow in the shock tube.

The typical oscillogram on Figure 44, obtained with a sweep of 100 $\mu$sec, shows a sharply rising shock-wave front, followed by the region of non-equilibrium processes $t_1$, the working gas sample $t_2$, the driver–driven interface, and the region of uniform parameters of the driver gas $t_3$.

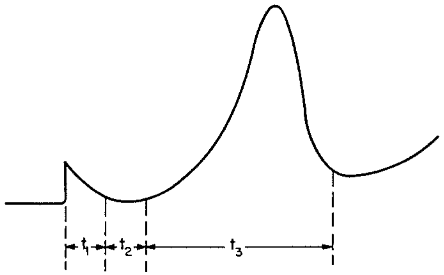

Figure 44

A characteristic oscillogram obtained in a shock tube by the single-slit method.

One of the important problems in the investigation of physical processes in a shock tube is the determination of the velocity of the shock wave and the gas particles following from it. The gas has different velocities at different parts of the flow (the shock wave, the working gas sample, the zone of uniform parameters of the driver gas, the driver–driven interface, etc.). For some regions it is calculated theoretically, while for other regions the calculation is difficult and must be based on very rough approximations. The direct measurement of the gas velocity at different parts of the stream is, therefore, of considerable interest both in testing the theory and in understanding the phenomena in the shock tube.

The velocity measurement is based on the photoelectric recording of the schlieren instrument readings in two sections through the flow. If a single instrument is used, two slits are used with the inhomogeneity image, and the light from each slit falls on a different photomultiplier connected to its own input of the oscillograph. From the oscillogram (Figure 45) two signals are obtained, representing the consecutive

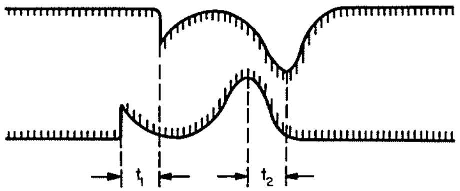

Figure 45

Oscillograms obtained in velocity measurements.

recording of the same process at two points of the field. Each pulse has the time base marks of the quartz generator. The velocity of every part of the flow can be found by measuring the time shift between analogous portions of the two signals. When a satisfactory time resolution has been achieved, it is possible to obtain a sufficiently small measurement base, so that the flow parameters will be virtually constant over it. The photoelectric method is superior in this respect to the photographic method, since the difficulty of obtaining high filming speeds and insufficient sensitivity of the photographic emulsions restrict the application of the photographic methods and make impossible the execution of studies under low-density conditions.

The shock-wave velocity $\tilde{u}$ has been plotted on Figure 46 as a function of the logarithm of the pressure drop across the diaphragm. The divergence between the experimental and theoretical results (the latter are represented by the solid line) is probably due to the use of the ideal gas equations in the calculations. A satisfactory agreement is observed between the results obtained by ionization gages (crosses) and by schlieren measurements (circles). The scatter in the velocity values is due to the inaccuracy in the measurement of the initial data. In fact, when the high pressure is 100 atm and the low pressure is 1 mm mercury, an error of 0.1 mm mercury in the measurement of the low pressure causes an error of 200 m/sec in the measurement of the velocity. The error in the measurement of the velocity was mainly determined by the accuracy of measurement of the time interval between the corresponding points of the two signals.

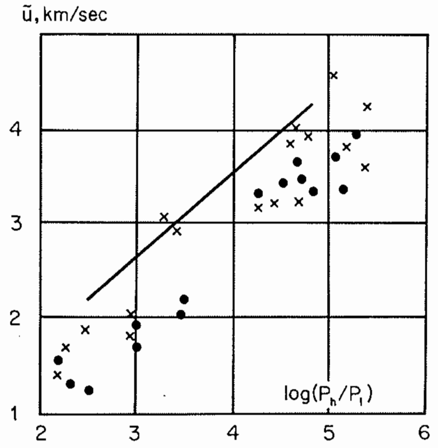

Figure 46

Results of the measurement of the shock-wave velocity.

Figure 47 compares the results of the measurement of the contact-surface velocity $v_c$ with the theory. The characteristic points of the contact region are less prominently pronounced than in the shock wave, and as a result the error in the velocity was very considerable: it actually was equal to the velocity of the shock wave.

It was established in several studies [75, 85, 102] that the measurement of the velocity by schlieren methods is superior in several respects to other methods. While the schlieren instrument reacts to a change in the density of the gaseous stream, methods based on the measurement of the glow or the ionization depend on magnitudes whose change lags behind the shock wave. In addition, by means of schlieren methods it is possible to measure not only the velocity of the shock or of separate luminous zones, but also the velocity of motion of the tailing regions.

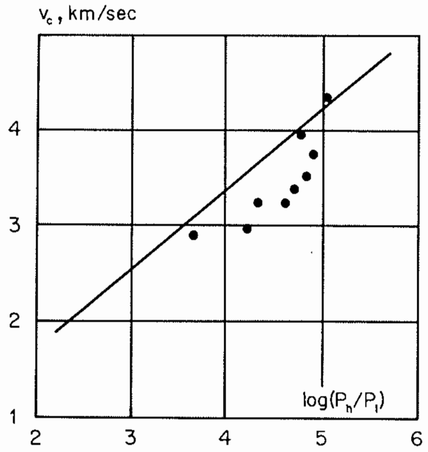

Figure 47

Results of the measurement of the contact-surface velocity.

For moderate sensitivities it is convenient to use miniature schlieren instruments (~20 mm diameter) shaped as gages which can be directly fastened to the tube. These gages are simple and reliable, and do not necessitate frequent adjustment [89].

The measurement of the working flow duration $T$ is of considerable importance for gas-dynamic measurements in the shock tube. According to the theory of the ideal shock tube $T = l/6\,\tilde{u}$, where $l$ is the length of the low-pressure compartment from the diaphragm to the point of observation. The allowance for dissociation and heat exchange reduces considerably the length of the working gas sample. Its value is established by measuring on an oscillogram similar to that in Figure 44 the length of the zone with density gradient close to zero. The results are presented in Figure 48. The comparison of the experimental and theoretical results indicates that there are many factors not adequately treated by the existing theories, which are responsible for a shortening of the working gas sample. An interesting fact is the constancy of the sample length in the high-pressure region.

One of the causes of this shortening is the existence of a combustion zone at the interface when using hydrogen-air and similar mixtures. To test this assumption, the air was replaced by nitrogen; this resulted in a certain lengthening of the working flow region at low pressures.

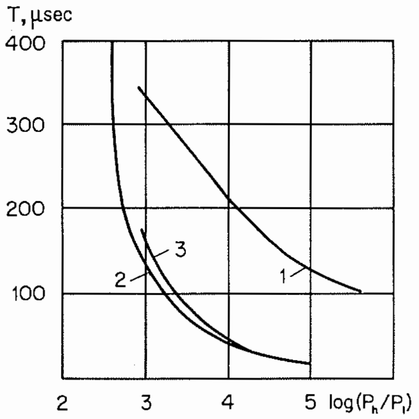

Figure 48

Measurement of the working flow duration: 1) theoretical curve; 2) experiment, the working gas is air; 3) experiment, the working gas is nitrogen.

The glow was regarded 1) as parasitic light, and 2) as object of study. In the first case, it was possible to suppress the parasitic light by using a slit instead of the knife-edge or by using light filters. In carrying out such experiments, a stop cutting off the lamp light from one of the recording slits was placed in the collimating part of the instrument. One of the signals of the oscillograph described only the glow, and the other only the variation of the refractive index, or the total effect of the glow and the light deflection.

It was possible to detect the gas glow behind the shock wave and the glow of the impurities. The gas glow is located directly behind the shock wave. Its duration is roughly equal to the length of the working gas sample. The intensity of the glow of the second type drops sharply in each successive experiment conducted on the same day (Figure 49). The impurities in the tube are apparently swept by the flow in the vacuum-chamber.

The location of the second glow maximum coincides with the position of the maximum angle of deviation. This indicates that the main heating of the impurities takes place in the contact region. The duration of the glow of second type considerably exceeds the region of variation of the refractive index; the cooling of the heated impurities occurs in hydrogen. On some oscillograms, the appearance of a third glow maximum is observed, whose meaning has not yet been satisfactorily explained, mainly because of its excessive variability.

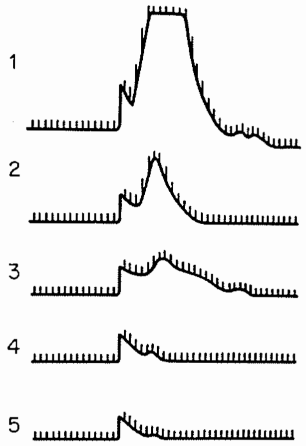

Figure 49

Photoelectric recording of the shock-tube glow. A series of experiments conducted in the course of a single day under the same conditions.

The signal amplitude can be connected quantitatively with the value of the angle of light deviation in the inhomogeneity, if it is assumed that the refractive index gradient is constant over the entire area of the portion cut by the slit. For this purpose, a series of calibration photographs are taken at different positions of the knife-edge with respect to the slit image. The light is modulated by a chopper (revolving disk with a set of holes, electronic circuit, etc.). From the photographs obtained a curve is plotted of the signal amplitude $A$ as a function of the coordinate $\xi$ of the knife-edge position (Figure 50). The knife-edge is then placed in position $\xi_1$, at which the signal amplitude is $A_0$, and a working experiment is conducted. All the remaining optical and electric parameters of the system remain unchanged.

In processing the photographs, the amplitude of the working signal $A_p$ is measured from $A_0$; the point on the calibration curve corresponding to the total amplitude of the working and initial pulses is determined. Subsequently, the displacement of the slit image $\xi_2 - \xi_1$ which led to this change in the amplitude is determined from the graph. If the working portion of the calibration curve is a straight line, the shape of the oscillograph signal corresponds to the function $\varepsilon(x)$. In these measurements the angle of light deviation is found by multiplying the signal amplitude at every point

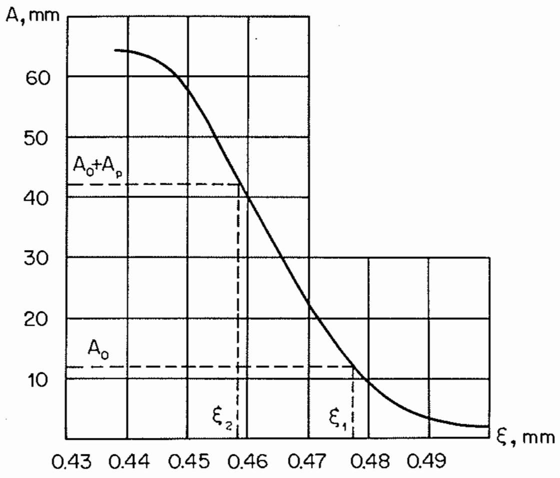

Figure 50

Signal amplitude as a function of the knife-edge position.

by a constant coefficient. By integrating the curve obtained it is possible to ascertain the value of the refractive index at every point of the flow.

The main difficulty in obtaining quantitative data is the problem posed by the compression shock. The width of the compression shock is normally much smaller than the width of the slit, and therefore the assumption that the angle of deviation is constant is not justified. The diffraction phenomena operating within the shock play an essential part. Two means for overcoming this difficulty exist at present: the development of diffraction schlieren methods and theoretical determination of the gas parameters at any point of the flow behind the shock.

The most interesting region of quantitative application of the schlieren methods is the first part of the working (driver) gas, in which non-equilibrium phenomena take place. Equilibrium is reached when the refractive index becomes constant. From the shape and length of the curve fall-off it is possible to determine the rate of establishment of the equilibrium.

The distribution of the gas flow density along the tube axis was determined by the method described. In the region of non-equilibrium processes it was possible to determine the dissociation rate constant for nitrogen and to obtain a value for the refraction of atomic nitrogen that agrees satisfactorily with the results of the measurements of other authors and with theoretical results. These measurements are described in §43.

The application of the schlieren photoelectric method to the preceding case was very fruitful, since it gave in a single experiment information on the general pattern

of the flow, the velocities of the shock wave and the contact surface, the glow of the flow and the impurities, the dissociation processes, the duration of the working flow, and the distribution of the refractive index in the gas flow.

The method opens new possibilities in the study of more complex processes, such as systems of waves moving in close formation. In such cases it is almost irreplaceable. High-speed photography would also have given the variation with time of a large field of angles of deviation, but with a poorer time resolution and an enormous increase in measurement work. The schlieren photoelectric method is one of the most promising methods in the study of transient processes.

## 12. PHASE CONTRAST

In 1934, the Dutch physicist F. Zernike [134, 135] suggested placing in a microscope a phase plate introducing an additional phase shift in a part of the light beam. This method, which was suitably called the phase contrast method, proved to be extremely fruitful and helped to solve a number of previously insoluble problems linked with the study of transparent objects.

The principle of the phase contrast method cannot be understood from the point of view of the geometrical ray theory used in the explanation of the other schlieren methods. One has now to consider aspects of the wave theory of light.

The phase contrast method can be understood basically by using the vector approach [56, 63–65]. Let the light disturbance in the object plane be represented by the vector $OM$ (Figure 51). The vector length is proportional to the magnitude of the light disturbance; the direction determines the wave phase. If the object has a transmission coefficient $1/q$ and introduces an additional phase difference $\theta$, the light passing through this section will be represented by the vector $OC$ of length

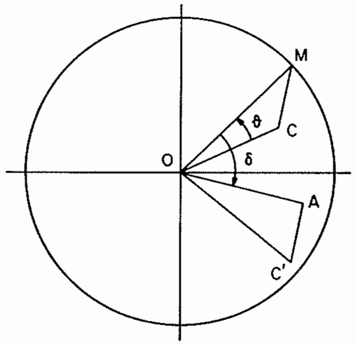

Figure 51

Vector diagram explaining the phase contrast method.

$OM/\sqrt{q}$, rotated through an angle $\theta$ with respect to $OM$. The vector $OC$ is represented as the sum of two vectors, $OM$ and $MC$, corresponding to the "direct" and "diffracted" light. It is considered in the following treatment that the phase plate changes the amplitude and the phase of the incident phase beam, decreasing the amplitude by a factor of $\sqrt{\tau}$ and shifting the phase by $\delta$. It is assumed that all these changes concern the "direct" light only, while the diffracted light remains unchanged.

The resulting light wave oscillation at the conjugate point of the inhomogeneity image is represented as the sum of the light beam $OA$ changed by the phase plate and the diffracted beam $AC' = MC$ traversing without change.

By means of the vector diagram it is possible to discern the common features of the methods using amplitude and phase plates. The change in the amplitude, as well as the change in the phase, can be represented by adding some vector of a different phase to the main vector. In the case of an amplitude plate the phase difference is 180°, while for a phase plate it can assume arbitrary values.

It is possible to derive, on the basis of the vector theory, the dependence of the image illumination on the characteristics of the inhomogeneity. If the object does not absorb light, we have $OC = OM$ and $q = 1$. Without a phase (or amplitude) plate the object will be invisible. When a phase plate is introduced, the sum of the vectors $OA$ and $AC'$ produces a vector of amplitude differing from the initial amplitude. The completely transparent object becomes visible.

The calculation of the square of the vector $OC'$ for a vector $OM$ of unit length leads to the basic formula of the vector theory:

$$I = 1 + \frac{1}{q} + \frac{1}{\tau} - \frac{2\cos\delta}{\sqrt{\tau}} - \frac{2\cos\theta}{\sqrt{q}} + \frac{2\cos(\delta-\theta)}{\sqrt{q\tau}}. \tag{12.1}$$

There arises the question of how to introduce additional phase and amplitude changes in the direct light without affecting the diffracted light. To resolve this problem, a peculiar feature of the light distribution in the focal plane of the main objective is used. The direct light, limited only by the aperture of the main objective, provides an almost correct image of the illuminating slit, while the diffracted light is deflected through large angles due to the small size of the object studied and forms a wide diffraction pattern. If, therefore, the phase plate coincides with the light source image, it introduces changes in almost all the direct light rays, while affecting only a minor fraction of the diffracted light.

Actually, the assumption that the phase plate effect is selective is only partially true. The image obtained in the focal plane can be represented (Figure 52) as the sum of two diffraction images, obtained from the main objective of the receiving part I and from the object II, respectively. Since both images are, strictly speaking, infinitely wide, the edges of the focal plane aperture cut off a part of the two beams. In addition, by introducing the phase plate in the main beam, we introduce changes in the diffracted light as well. It follows that the assumptions of the vector theory are not completely satisfied. The resulting error can be estimated only on the basis of the diffraction theory, allowing for the wave phenomena at the rim of the main objective, at the edges of the inhomogeneity, and at the boundaries of the focal plane aperture. This question is treated in Part II.

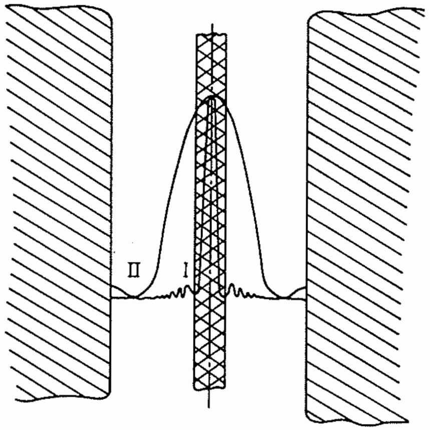

Figure 52
Relative position of the filament, the edge of the exit pupil of the instrument, and the diffraction images of the light source in the phase contrast method.

Using formula (12.1), it is possible to calculate the range and the sensitivity of the phase contrast method. The measured magnitude is the increment of the optical path of the light in the inhomogeneity. The method sensitivity for photoelectric measurements is equal to

$$S_{\text{ph}} = \frac{2}{\sqrt{q}}\left(\sin\theta + \frac{\sin(\delta-\theta)}{\sqrt{\tau}}\right), \tag{12.2}$$

which reduces for small values of $\theta$ to

$$S_{\text{ph}} = \frac{2\sin\delta}{\sqrt{q\tau}}. \tag{12.3}$$

It is seen from (12.3) that the sensitivity is maximum for $\delta = \pm\pi/2$, i.e., for a phase plate introducing an additional path difference of $\lambda/4$.

In visual and photographic observations we have for $q = 1$ and small $\theta$

$$S = 2\sqrt{\tau}\sin\delta. \tag{12.4}$$

The sensitivity is maximum for $\tau = \infty$.

It should be noted that the maximum sensitivity condition $\delta = \pi/2$, is correct only when the phase plate introduces changes in the entire main beam without affecting the diffracted beam. If the amplitude-phase changes are otherwise introduced, this condition is altered. Thus if the phase plate is a knife, the angle of light deviation in the inhomogeneity becomes the measured magnitude, and the condition of maximum sensitivity will be $\delta = \pm \pi$.

The methods of manufacturing amplitude-phase plates are more complex and varied than the methods of manufacturing amplitude plates. Different physical laws and different technical approaches are applied in their production. The most widely used shapes are the ring, the strip, the cross, and the half-plane. The first method for the manufacture of plates was suggested by F. Zernike [135]. In a layer of Canadian balsam placed between two glass plates, a collodium cellophane film cut in the form of a ring, a half-plane, etc., was introduced. The near equality of the refractive indices of the film and the Canadian balsam ensures small phase differences between light passing through the film and avoiding it, even though relatively thick plates are used (they are easy to manufacture).

A plate utilizing the polarization properties of cellophane was used in [104]. Light linearly polarized at 45° to the ring axis falls on a phase plate analogous to the one described above. The light which has passed through the cellophane is polarized at a right angle with respect to the light which has passed through the Canadian balsam. By placing an analyzer behind the plate, it becomes possible to alter the ratio between the amplitudes of direct and diffracted light. The same effect can be obtained if the ring and the remaining part of the plate are made from dextrorotatory and levorotatory quartz, respectively [127].

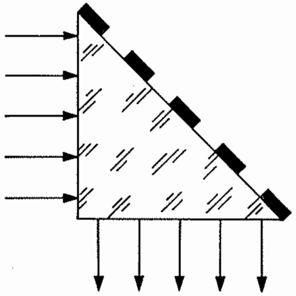

Figure 53
Phase plate.

Rytov used the phase plate represented on Figure 53 [49]. Metal layers are applied to the prism surface. Since the phase shift upon reflection from the metal differs from the shift at the glass–air boundary, the wave is deformed following reflection.

A similar prism was used by M. Franson and G. Nomarski [84]. An incident light wave was deformed upon reflection due to the finite thickness of the metallic layer. Since light is partially polarized upon reflection from glass, the ratio of amplitudes of the direct and reflected light can be changed by placing a polarizer and an analyzer before and after the plate.

Plates made by spraying various materials on glass supports are widely used, particularly transparent dielectric coatings. Thin metal layers are added at times for purposes of absorption.

In [103] a diaphragm was used made of a wedge-shaped plate divided into three parts by parallel cuts (Figure 54). If the middle wedge is aligned with the side wedges, the optical path lengths for rays lying in a plane parallel to the wedge angle are equal. By displacing the middle wedge it is possible to change the phase of the light falling on the middle plate. For a wedge angle of 0.5′ and $n = 1.5$, a displacement of 1 mm corresponds to a phase difference of $0.15\,\lambda$.

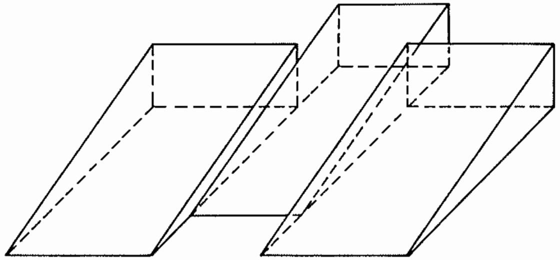

Figure 54
A three-wedge phase diaphragm.

The phase contrast method was also used in connection with infrared and ultraviolet sources. Infrared radiation did not lead to a substantial improvement in the results, but the ultraviolet radiation, on the other hand, did give interesting and promising results.

The first method for obtaining a color image of the inhomogeneity was suggested by F. Zernike. It was based on the use of a phase plate having the same refractive index as the surrounding medium for some range of wavelengths, and differing from it in the value of the dispersion in such a way that in the violet region of the spectrum, the refractive index of the plate was higher than that of the medium; the opposite was true for the red region. The contrast between the different points of the image will therefore depend on the wavelength of the light illuminating the inhomogeneity. When white light is used, the different points of the image become differently colored. There also exist many other means for obtaining color phase contrast.

A valuable survey of the methods of phase contrast and the necessary instrumentation is presented in [49, 56].

## 13. INTERFEROMETRIC SCHLIEREN INSTRUMENTS

The combined use of schlieren and interference instruments seems very interesting and promising. Interferometers react to the change of the optical path length of the ray, a fact which makes them at times more advantageous than schlieren instruments in quantitative measurements. The schlieren methods react to a change in the gradient of the optical path length, which makes them more suited to the determination of the shape and geometry of the shock waves, rarefaction zones, and similar details. It follows that interferometers are more sensitive for some types of problems, and schlieren instruments for other types.

The simultaneous use of these two types of instruments seems highly advantageous. Combined interference-schlieren systems were created to exploit this advantage. Interferometers in which the auxiliary arm is blocked by an opaque slide, and a knife-edge is placed in the focal plane of the main objective, are frequently used. Instead of blocking the auxiliary arm, it is also possible to transmit the light source image formed by this arm far behind the knife-edge. If the angles of light deviation in the inhomogeneity are not large, pure schlieren images are obtained. In instruments of this type it is possible to obtain, in turn, schlieren and interference patterns.

The knife-edge can be placed in one of the receiving parts of the interferometer (Figure 55). The other receiving part will then produce a pure interference pattern, while the image in the arm with the knife-edge is more complex and has a mixed interference–schlieren character [78]. Two beams interfere in the latter, one of which, the working beam, is partially cut off by the knife-edge. Depending on the magnitude of the angles of light deviation in the inhomogeneity and the instrument adjustment, the image obtained will approximate either an interference image or a schlieren one.

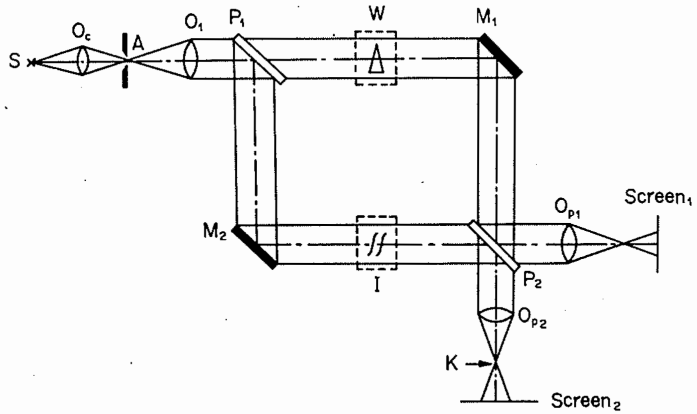

Figure 55
Interferometer with an attachment giving an interference-schlieren image.

Finally, the third type of instrument (Figure 56) [137] uses a mirror, which directs part of the light beam to the knife-edge. In such instruments it is possible to obtain schlieren and interference images simultaneously.

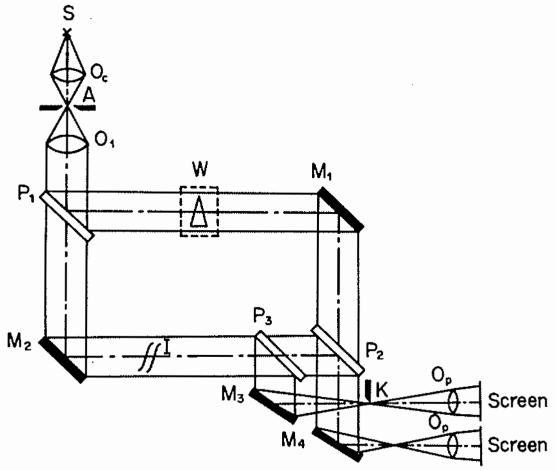

Figure 56
Interference-schlieren instrument with separate interference and schlieren images.

Interferometric systems (shift, interferometers, polarization interferometers, etc.) are frequently designed on the basis of schlieren instruments. The conversion of the schlieren instrument into an interferometer is achieved with the aid of attachments to the illuminating and receiving parts which split and recombine the light beam in the schlieren instrument. If the beams move apart a considerable distance, so that the disturbed wave interferes with the plane wave, we obtain a two-beam image, but the field of view is at least halved as compared with the field of the schlieren instrument.

As an example, consider the system represented in Figure 57 [46, 47], in which a diffraction grating is used. The image of the portion of the instrument field in which the inhomogeneity is situated is combined with the portion in which there is no inhomogeneity. The first image is obtained in a diffraction maximum order zero or minus one, and the second in the maximum of order + 1. In other systems the superposition is realized by means of a Fresnel biprism, polarization prisms, and other devices.

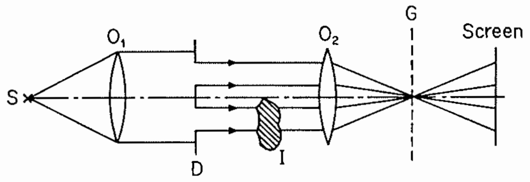

Figure 57

Interferometer with a diffraction grating.

A system widely used recently is one in which the wave disturbed by the inhomogeneity is split into two waves. One is shifted a small distance with respect to the other. The waves are then recombined and on the screen is observed the interference of two equally deformed waves, shifted through a small distance. As a result the interpretation of the pattern obtained becomes considerably changed. Thus if the shift is very small, the refractive index gradient is determined.

These systems are pure interference systems and have nothing in common with the schlieren systems. They are built, however, on the basis of the widely used schlieren instruments, which are much less expensive than the wide-field interferometers used in gas-dynamic measurements. Their use makes possible a rapid conversion of the schlieren instruments into an interferometer and vice versa, and thus eliminates the necessity of using two different instruments. Such interferometers withstand vibrations better than the commonly used Mach–Zehnder interferometer, since they do not lead the beams over large distances and have no components which act independently on one of the interfering beams. The same basic components participate in the formation of each of the beams. The extraneous effects are therefore the same for the two arms.

There are also systems in which the schlieren instrument acts as an interferometer. Such are the systems using a focal filament. This similarity is purely superficial, however, and is based on the fact that the diffraction pattern is, in some cases, very similar to the interference pattern. Strictly speaking, the position of the light intensity extrema is not perfectly correlated with the increment of the optical path length in the inhomogeneity, which is a multiple of a half-integer number of wavelengths. Under certain conditions it is, however, possible to neglect this inaccuracy and to consider the pattern as a pure interference pattern. A complete analysis of this measurement system necessitates examination of the diffraction phenomena taking place in the inhomogeneity and the beam defining apertures. A detailed description of this method will therefore be considered in Part II.

## 14. SCHLIEREN INSTRUMENTS WITH FLASH LIGHT SOURCES AND CINECAMERAS

The properties of various optical inhomogeneities change with time. Some processes which seem initially stationary are found to be unstable upon closer examination. Such are the phenomena in wind tunnels, where high-frequency fluctuations are frequently observed against the background of a steady-state flow. Such objects are studied with the aid of flash light sources and high-speed cinecameras, which record the processes with very short exposures, so that the process properties remain fairly constant during each exposure. The flash light sources available at present make it possible to reduce the exposure to $10^{-6}$–$10^{-7}$ sec, depending on the sensitivity of the schlieren instrument.

A specific feature of the flash light sources for schlieren measurements is the requirement of relatively high power, especially when studying weakly deflecting inhomogeneities, since it is necessary to block the illuminating slit image and, consequently, to reduce the mean illumination of the image. The increase of the flash source power leads to a lengthening of the flash time. A standard procedure for increasing the flash power is to increase the spark gap; as a result the brightness remains the same, and the total energy of the flash increases. This procedure, however, is not suitable for schlieren instruments, since the diameter of the open part of the light source image is limited by the method sensitivity, and the possible slit length by the system aberrations. In order to improve the light characteristics of the source it is therefore necessary to increase the brightness of the luminous body, e.g., by achieving the discharges at high filling-gas pressures or in water, and by using gases which have a high light yield.

The schlieren photographs obtained with flash light sources are usually of a high quality, frequently higher than the quality of photographs obtained with continuous sources, since vibrations, the instability of the instrument adjustment and the particular process under study do not affect the image sharpness. Single flash photographs cannot describe the entire process, however, since they isolate it only in one moment of time. A natural development of this system was, therefore, the successive utilization of a series of flashes. The first systems of this type (Figure 58) [76, 122] used several flash sources with common control, synchronizing the flashes with the process and with each other. A series of separate schlieren photographs are obtained as a result. The optical system constitutes a set of several schlieren instruments. This arrangement makes possible the photographing during very brief intervals of up to $10^6$ frames per second with an exposure of $10^{-7}$ sec. A drawback of these instruments is that each instrument sees the inhomogeneity at a different angle. In addition, the number of frames in such a camera is not large.

An attempt was made to eliminate parallax in the viewing of narrow moving inhomogeneities — shock waves. Several spark gaps were arranged in a series, and

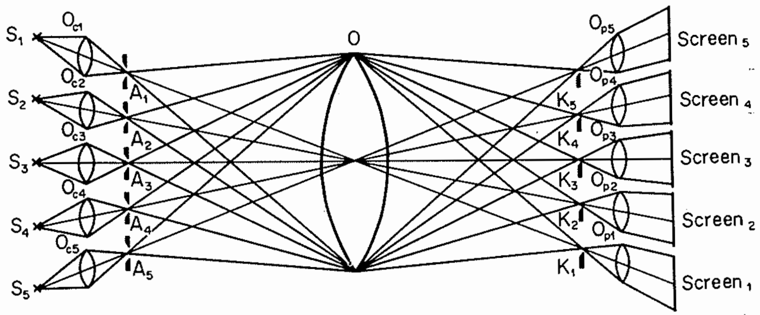

Figure 58

System with several flash light sources.

all were projected simultaneously on the inlet slit of a system of condensers (Figure 59). The consecutive flashes produced a schlieren image on the same place, but due to the motion of the object during the time interval between two frames, several separate images of the wave were obtained.

The same effect is obtained by repeated discharges of the same light source. Since some time is necessary in this case for recharging the supply source and deionizing the spark gap, the speed of photography is lower than in the case when several sources are used. This is most clearly seen with the high-power light sources used in highly sensitive measurements.

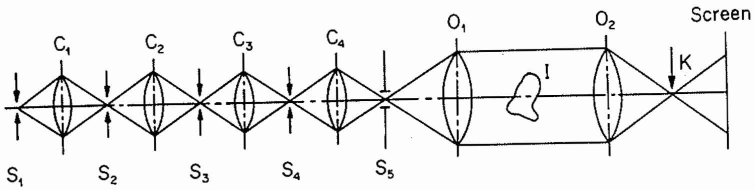

Figure 59

Arrangement for viewing shock waves.

In the study of complex processes, the superposition of a series of successive pictures on the same frame becomes impossible, and therefore a movie film is used. The difficulty of obtaining high film speeds limits the shooting rate. Nevertheless, rates as high as $4 \times 10^5$ frames per second can be attained [50].

Using a flash light source, photographs can be taken at the highest possible speed [121]. Such a method consists of splitting the light into several beams (Figure 60). The first beam propagates in the usual manner toward the image. The second beam is reflected by an additional mirror before reaching the image. The time during which the light travels the additional distance constitutes the interval between frames. By this method it is possible to obtain shooting speeds higher than $10^9$ frames per second.

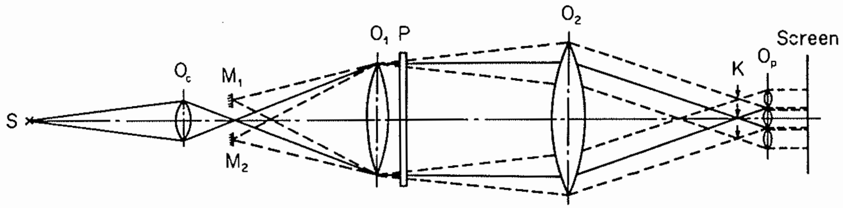

Figure 60

Arrangement for obtaining high shooting speeds.

Systems utilizing flash light sources are not suitable for the study of self-luminous objects. The spark is bright but of short duration. The glow of the object, even if considerably weaker, acts on the receiver over a long period of time and, as a result, affects the film to a greater extent than the spark. The effect of parasitic light increases and measures must be taken to counteract it. The attempt to reduce the influence of the glow by creating a shutter with an exposure time larger than that of the light pulse, and at the same time sufficiently small for eliminating extraneous light, has met with considerable difficulties. It is difficult to synchronize these shutters with the spark and the processes under study. Various types of shutters using different physical principles have been developed, but they have not as yet found a wide application.

Similar results can be obtained by using Kerr cells and similar electro-optical shutters. This method has also not found a wide application, due to the complexity of cell manufacture and the inevitability of a certain, although negligible, passage of light through the closed cell.

Spark cameras are used whenever the exposure time of each frame must be very short or the shooting speed must be high. Ordinary cinecameras, in which time resolution is achieved by moving the film, rotating a mirror or prism, etc., are also widely used.

The use of relatively low-speed cameras (up to several thousand frames per second) does not present many differences compared with ordinary photography. The differences lie basically in the method of attaching the cinecamera to the schlieren instrument and in the elimination of the influence of the vibrations caused by the camera. If a standard cinecamera is attached to the instrument, some difficulties arise in the design of the transition optics.

Somewhat more complex is the question of the use of schlieren instruments with ultrahigh-speed cameras [55]. These instruments are complex devices, and have many peculiar features which complicate their application in conjunction with schlieren instruments. Many cameras have multiple small pupils, while schlieren instruments utilize only one pupil. It is possible, in principle, to split the beam optically and use all the pupils, but such arrangements are not used in practice. As a result, the camera is not fully exploited and the shooting speed is considerably lower than the maximum. The small size of the pupil of many high-speed cameras enhances the diffraction phenomena and reduces the measurement range.

In view of the complexity of the individual methods and the difficulty of processing, only qualitative schlieren methods are used at present with cinecameras. Examples of the combined use of schlieren instruments and high-speed cameras are described in [30, 79]. In order to transfer to quantitative measurements it is necessary to solve problems connected with the constancy of the exposure from frame to frame, elimination of vibrations, simplification and automation of processing, etc.

# IV

# *DEFOCUSED GRID METHODS*

## 15. FUNDAMENTALS OF THE METHODS

The defocused grid methods derive from the qualitative method of V. Ronchi [48] for studying aberrations of optical components. As a qualitative method, the Ronchi method was inferior to other methods, but the simplicity of its application and of processing results made it suitable for the quantitative study of the light wave shape.

The method was subsequently developed by other scientists. Numerous improvements and additions transformed it from a qualitative into a quantitative method. Ostroumov [42–44] suggested that it be applied to the study of hydrodynamic processes and was the first to use a grid of mutually perpendicular lines, by means of which the angles of light deviation in two directions could be simultaneously measured. Defocused grids were successfully used in [57] for studying the properties of a gaseous flow. Sukhorukikh [26, 51, 52] developed the diffraction theory of the method, based on the parameters affecting the pattern in the image plane and on the experimental study of the influence of these parameters on the particular pattern. The defocused grid method has been successfully applied to the study of photographic and microscopic objectives [60, 105].

The term *defocused grid methods* is used today to characterize the group of methods in which the angle of deviation is established by measuring the displacements of the shadows from a grid of opaque spots, each surrounded by a transparent area. The methods of this group differ according to the shape and location of the grid and the procedure for processing the photographs.

In general, the shape and arrangement of the opaque spots and the clear spaces in the grid can be quite arbitrary. The grid can be a system of concentric circles, a set of arbitrary apertures or screens. To ensure that the light source size does not cause a blurring of the shadow edges, it is, however, necessary to use point or near-point light sources when using grids of arbitrary shape. This reduces the amount of light in the image, and in many cases complicates the application of the method. In addition, in quantitative measurements it is necessary to identify the points of the image plane corresponding to the same point of the grid before and after the introduction of the inhomogeneity, which is most easily accomplished with grids of parallel dark bands; accordingly, such grids or gratings (Figure 61) are the most widely used. The distance $p$ between the centers of the dark bands will be termed the *grating spacing*, and the width of the dark line $d$ will be termed the *groove width*. Other types of grids will be examined separately.

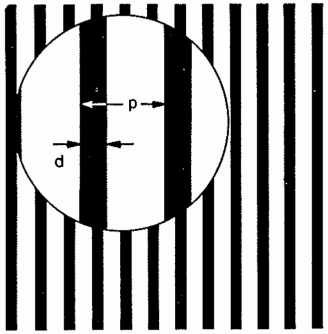

Figure 61
A schlieren grating.

One possible application of defocused grids is represented in Figure 62. The grating is placed at a specified distance from the main objective. The light beams, falling on the opaque spots of the grating, are stopped, and shadows of the opaque elements are formed on the screen as a result. If an optical inhomogeneity appears in the instrument field, the shadows of the grooves are shifted, altering their shape.

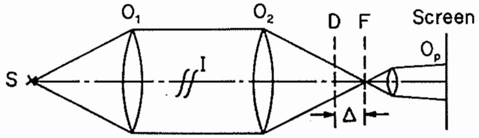

Figure 62
A system with a defocused grid.

As in all the other qualitative and quantitative methods, defocused grids can be used in various types of schlieren instruments such as instruments with a parallel beam, autocollimating instruments, converging beams, etc. The main features and requirements of the methods are, however, the same for all types. We shall, accordingly, examine the parallel beam arrangement, which is most widely used, although it is more expedient at times to use other types of schlieren instruments.

The detailed distribution of the illumination in the image plane is of no interest to the investigator using defocused grid methods. The only magnitude necessary for determining the distribution of the angles of light deviation in the inhomogeneity is the shadow shift. The distribution of the illumination affects the measurements only insofar as it complicates or simplifies the localization of any specific point of the image. When a wide light source is used, the shadows become blurred and less distinguishable, and their position is more difficult to determine accurately; this does not affect, however, the fundamentals of the method. If the illumination is highly non-uniform over the field as a result of the absorption of light by the inhomogeneity, aberrations of the condenser, or any other reason, the contrast of the shadows will be different at different areas of the field, but the shift of the shadows will be the same for the same angle of deviation. This feature of the defocused grid methods makes possible their utilization in cases when other methods are inapplicable (such as those processes in which glow changes abruptly and intensely over the field).

An important advantage of this method is the simplicity of interpretation. In many cases no complex instrumentation is required; a ruler and measuring compasses suffice. Figure 63 represents a characteristic photograph obtained by this method in the study of the inhomogeneities of the glass base of a photographic plate.

There are several varieties of the method, differing according to the location of the viewing diaphragm. In addition to the position considered above, it can be placed directly before or behind the object, and also near the inhomogeneity image. The first method is widely used in the study of hydrodynamic phenomena, and in centrifugation processes where it is known as the *scale method*. The method of placing the diaphragm near the image is termed the *remote grid method*.

Both these methods are basically similar to the defocused grid method, but are suited to the study of inhomogeneities deflecting light through large angles. The different methods have different working formulas, since the individual parameters of the system are taken as the base, but the transition between the various formulas can be made with ease.

If the optical system of the instrument is complex, the diaphragm can be placed between any two optical components along the ray path from the light source to the inhomogeneity image. In each position, it is possible to find a single-valued correspondence between the shadow shift and the angle of light deviation in the inhomogeneity.

If a grating is used as the diaphragm, and there is no inhomogeneity, the shadows

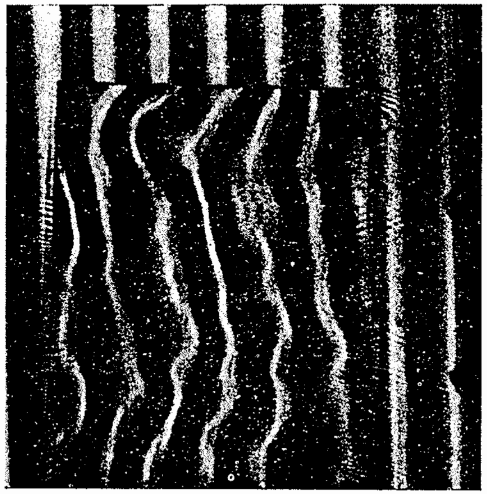

Figure 63
Photograph of the glass of a photographic plate obtained by the defocused grid method.

of the grooves are equidistant straight lines, their number equal to the number of grooves inside the light cone. According to the laws of geometrical optics, the shadows should form a succession of sharp dark and bright bands, with a narrow transition region on the boundaries between light and dark area due to the finite width of the light source and to the aberrations of the optical system. When the magnitude of the defocusing is increased, the width of the dark and light bands should decrease without any distortion in their structure.

The actual situation differs considerably from this description. The structure of the bands is complex and is normally determined by diffraction phenomena. Only in rare cases is it possible to use the approximation of geometrical optics. If the grating is very near the focus, the shadows represent wide and blurred bands; with the increase in the distance between the grating and the focus the shadows come nearer, and their diffraction structure becomes clearer (Figure 64).

With the further displacement of the grating away from the focus the pattern becomes more complex. The side maxima of the adjacent grooves overlap, until finally a point is reached when the number of observed shadows is twice the number of grooves. For a certain value of Δ the image is almost extinguished, and the contrast becomes considerably poorer. With the further increase of the defocusing the image is restored, but with the dark and bright bands interchanged. Unlike direct images, in which the distribution of the illumination as a whole coincides with that predicted by geometrical optics, these images can be referred to as reverse images. Inasmuch as these phenomena are basically diffraction phenomena, they are treated in more detail in Part II.

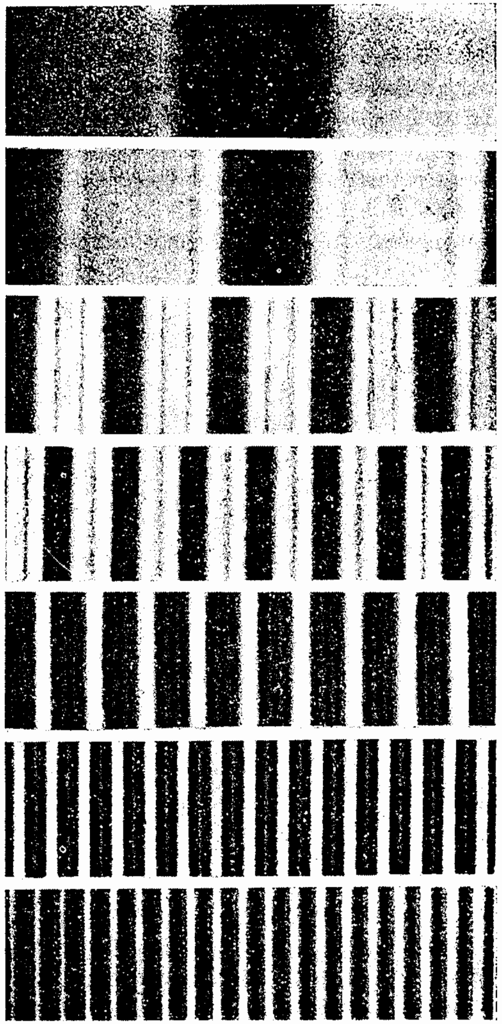

Figure 64
Contraction of the shadows with the increase of the defocusing.

## 16. BASIC ANALYTICAL RELATIONS

We shall now determine the relationship between the shift of the groove shadow and the angle of light deviation in the inhomogeneity. If there is no optical inhomogeneity, the light beam passing through point *a* of the object plane (Figure 65) meets the grid *D* at point *g* and reaches the point *c* of the image plane conjugate with *a*. When an inhomogeneity is introduced, the beam passes along *adec* and meets the grid at point *e*. Before the introduction of the inhomogeneity we observed at *c* the shadow of some specific area of the grid (point *g*); after the introduction of the inhomogeneity we observe another part of the diffraction pattern at the same point.

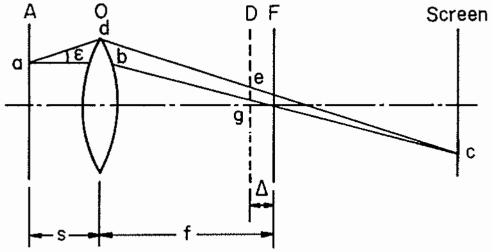

Figure 65

Derivation of the relation between the angle of light deviation in the inhomogeneity and the ray shift in the grating.

The relation between the angle of deviation and the ray displacement in the grating is found from the similar triangles *dbc* and *egc*. Setting $eg = \delta$ and taking into account that $bd = \varepsilon s$ and that points *a* and *c* are conjugate, we obtain

$$\varepsilon = \frac{\delta}{f + \dfrac{\Delta}{f}(s - f)}. \tag{16.1}$$

The defocusing Δ is measured from the focus. It is positive if the grid is placed between the focal plane and the main objective, and negative if the grid is placed closer to the screen than to the focal plane. The quantities *s* and *f* are considered positive.

The displacement of the ray on the grid leads to a shift of the groove shadow in the image plane. We have

$$\frac{\delta}{\delta_p} = \frac{\Delta(s - f)}{f^2}, \tag{16.2}$$

where $\delta_p$ is the displacement of the groove shadow on the photograph. Using the expression for the image scale, we rewrite (16.2) in the form

$$\delta_p = \frac{\delta \mu f}{\Delta}. \tag{16.3}$$

The combination of (16.3) and (16.1) yields

$$\varepsilon = \frac{\delta_p}{\mu\left(s - f + \dfrac{f^2}{\Delta}\right)}. \tag{16.4}$$

Since *f* and *s* are usually of the same order of magnitude, and Δ is considerably smaller than either, (16.4) can often be transformed to

$$\varepsilon = \frac{\delta_p \Delta}{\mu f^2}. \tag{16.5}$$

The following relationship is used in some cases:

$$\frac{\delta}{\delta_p} = \frac{p}{p_p}, \tag{16.6}$$

where $p_p$ is the grating spacing on the photograph without the inhomogeneity. It is then possible to measure *p* and $p_p$ instead of Δ and μ. In this case

$$\varepsilon = \frac{\delta_p p}{p_p f}. \tag{16.7}$$

We can find by means of these formulas the angle of light deviation in the inhomogeneity from the displacement of the groove shadow on the photograph relative to its original position. As the grating is one-dimensional, it is not the angle of deviation itself that is measured, but only its projection on the plane perpendicular to the grooves. The measurement is as follows: the field is photographed twice for the same adjustment of the schlieren instrument, once without the inhomogeneity — zero photograph, and then with the inhomogeneity — working photograph. In order to measure the shadow displacement, a coordinate axis is placed in the object field, and its image is obtained on every photograph. The contour of the instrument field or the model can be used in some cases as reference points for measuring the relative displacement; this method of measurement is, however, not convenient in a majority of cases.

On each photograph the distance from the coordinate axis to the center of the groove shadow in the direction perpendicular to the axis is measured. The band displacement obtained is substituted in (16.4), (16.5), or (16.7), and from the resulting formula the component of the angle of deviation in the inhomogeneity points corresponding to the position of the center of the groove shadow on the working photograph is calculated.

If the inhomogeneity does not occupy the entire instrument field and a part of the shadows remains undistorted, it is possible to measure the displacements from the straight lines representing continuations of the axes of symmetry of the undisturbed portions of the bands. In this type of measurement no zero photograph is necessary.

One of the difficult tasks is the correlation of the shadows on the zero and working photographs. If the inhomogeneities are complex, the shadows are mixed up, or split and even change places. Special measures may be taken in order to facilitate the correlation: some grooves are made thicker or thinner, a gap is made in some grooves or the bright spaces between the grooves are colored in different colors (particularly in visual observations). In some instances, the distribution of the angles of deviation is first estimated, and more accurate measurements are conducted subsequently. This makes it possible to correlate the shadows on the zero and working photographs and to select with accuracy the required defocusing and the grating parameters.

The groove shadows form a complex diffraction pattern. But, as was demonstrated by Sukhorukikh, up to the first reversal, the centers of symmetry of the diffraction pattern, coinciding with light intensity, minima or maxima, are the locus of points corresponding to the rays passing through the centers of the grooves or the transparent spaces.

If the diffraction structure of the shadows on both the zero and the working photograph follows the same pattern, the application of the method is relatively simple. If the wave front curvature changes considerably, frequently we have a situation in which some areas of the photograph are occupied by "direct" shadows, and others by "reverse" shadows, while the shadows of the zero photograph are all located before the first reversal, or are at least all of the same type. In processing such photographs it is necessary to take the middle of the dark and bright spaces, alternately, as the center line of the groove shadow. Practical measurements have established the possibility of such a procedure, which is, however, more complex than in the preceding case.

When reverse patterns are used, a larger number of shadows than in the direct case is obtained for the same sensitivity. The development of a method for processing reverse patterns and its justification are, therefore, of interest for future studies.

The parameters which must be known in order to conduct the measurements are $s$, $f$, and $\Delta$ (or $\mu$, $p$, and $p_p$). The value of $f$ is determined with sufficient accuracy by the manufacturer and is included in the technical description of the instrument. The value of $s$ is found by measuring the distance from the object plane on which the camera is focused to some reference point of the instrument. The accuracy of this measurement is generally sufficient, inasmuch as the contribution of $s$ in determining $\varepsilon$ is small.

The method of determination of $\Delta$ is somewhat more complex. Generally, the grating is first placed in the focal plane, and then shifted to its working position; the value of the displacement is measured on a scale. The main inaccuracy of this measurement is the error of setting the grating in the focal plane. It is frequently assumed that the grating has been properly set in the focus if the groove shadows are no longer visible. The error of this setting in the focus is

$$d\Delta = \frac{pf}{2D}, \tag{16.8}$$

where $D$ is the diameter of the main objective of the receiving part. For $D = 230$ mm, $f = 1918$ mm, and $p = 0.1$ mm we obtain $d\Delta = 0.4$ mm. This error is substantial in the case of a small defocusing, and consequently, it is necessary to use the same method as for the setting of a knife-edge (by examining the uniformity of the screen darkening as a result of the gradual covering of the slit image by the grating groove). This method is of insufficient practical accuracy for all measurements.

It is expedient at times to find $\Delta$ from the formula

$$\frac{p}{p_p} = \frac{\Delta}{\mu f}. \tag{16.9}$$

## 17. SENSITIVITY, RANGE AND FREQUENCY OF MEASUREMENTS

The sensitivity of the method is defined as

$$S = \frac{d\delta_p}{d\varepsilon} \tag{17.1}$$

and is equal to

$$S = \frac{\mu f^2}{\Delta}. \tag{17.2}$$

The sensitivity can theoretically be made infinitely large by increasing $\mu$ and $f$, or by decreasing $\Delta$. This is, however, accompanied by an increase of the shadow width on the photograph, i.e., by a decrease of the number of points at which the angle of deviation can be measured, and also by a considerable reduction in the accuracy of determination of the shadow centerline. This can apparently be prevented by reducing the grating spacing. The contribution from the diffraction phenomena increases as a result, thereby diminishing the shadow contrast, reducing the accuracy of measurement of their centerline, and complicating the correlation.

If we assume that the minimum value of the defocusing is the position at which only two shadows appear in the image, the maximum sensitivity will be

$$S_{\max} = \frac{\mu f R}{p}, \tag{17.3}$$

where $R$ is the radius of the main objective of the receiving part. For $\mu = 1$, $f = 1918$ mm, $R = 115$ mm, $p = 0.1$ mm the sensitivity is $S_{\max} = 2.2 \times 10^6$. In practice the sensitivity is considerably lower, since measurements in two sections only do not satisfy. Furthermore, the increase of the observed width of the groove is accompanied by an increase in the error of determination of the shadow centerline.

The problem of the range of the defocused grid method, i.e., of the range of deviation angles which can be measured by this method, is more complex. Theoretically, restrictions on the measurement range are imposed only by the size of the grid and the diaphragms transmitting the light beam. In practice, however, the limit is reduced far earlier. Experience shows that in many cases the groove shadows lose their contrast and are difficult to interpret if the groove displacement is larger than several grating spacings. If this magnitude is taken arbitrarily as the measurement range, we have

$$\mathcal{R} = \frac{Np}{f}. \tag{17.4}$$

The measurement range is also affected in some cases by the condition that all the inhomogeneity areas studied must give diffraction patterns of the same type as on the zero photograph. This question has not been sufficiently studied to date and, consequently, it is impossible to determine the range restrictions imposed by this condition.

The number of groove shadows in the image plane depends on the wave front curvature. Let the incident light wave have a radius of curvature $R_x$ in the section parallel to the optical axis and to the $x$ axis, and $R_y$ in the section through the $y$ axis. From the similar triangles whose vertices are at the points of convergence of the meridional and sagittal rays, we find the correspondence between the points of the grating plane and the image plane:

$$x' = \frac{\xi f^2}{(s - f)\left\{\Delta + \frac{1}{R_x}[f^2 + \Delta(s - f)]\right\}}, \tag{17.5}$$

$$y' = \frac{\eta f^2}{(s - f)\left\{\Delta + \frac{1}{R_y}[f^2 + \Delta(s - f)]\right\}}. \tag{17.6}$$

If the grating grooves form an angle $\alpha$ with the $x$ axis, the equation of the groove centerlines will be

$$\eta = \frac{np}{\sin\alpha} + \xi \tan\alpha, \tag{17.7}$$

where $n$ assumes integer values. The centerline of the zero groove coincides with the origin of coordinates.

The equation for the centerlines of the groove shadows is obtained by substituting (17.5) and (17.6) in (17.7):

$$y' = \frac{npf^2}{\sin\alpha(s - f)\{f^2 + \Delta(s - f)V_{yy}\}} + \frac{x' \tan\alpha V_{xx}}{V_{yy}}, \tag{17.8}$$

where

$$V_{xx} = \frac{1}{R_x} + \frac{\Delta}{f^2 + \Delta(s - f)} \quad \text{and} \quad V_{yy} = \frac{1}{R_y} + \frac{\Delta}{f^2 + \Delta(s - f)}$$

are functions defining the curvature of the wave front in the grating plane in sections parallel to the $\xi$ and $\eta$ axes.

With the aid of equation (17.8) it is possible to determine the ratio of curvatures of the wave front in sections parallel to $\xi$ and $\eta$ axes in the grating plane and to find the curvature of the cylindrical wave in the inhomogeneity plane.

The distance between the centerlines of the shadows of adjacent grooves is equal to

$$p_{\text{p}} = \frac{pf^2 V_{xx}}{(s - f)[f^2 + \Delta(s - f)]\, V_{yy}\sqrt{V_{yy}^2 \cos^2\alpha + V_{xx}^2 \sin^2\alpha}}. \tag{17.9}$$

If the incident wave is plane ($R_x = R_y = \infty$), equation (17.9) reduces to (16.3).

By an equation similar to (17.9) it is possible to find the geometrical width of the groove shadow as well. This relationship, however, is usually inapplicable, since the width of the groove shadow is mainly determined by diffraction phenomena.

By combining (16.3), (16.6), (17.2), and (17.4) it is possible to obtain a formula relating the measurement range, the frequency of measurements (the distance between the shadow centers in the image) and the sensitivity. It has the form

$$Np_{\text{p}} = S\mathcal{R}. \tag{17.10}$$

If we wish to measure angles of deviation of the order of $10^{-4}$ rad at image points distant 5 mm from each other, for $N = 2$ the measurement sensitivity cannot be higher than $10^5$ mm/rad. Given the sensitivity, we can find the minimum angle which can be measured for a given shift of the shadow. Thus if we can measure a band shift of 0.5 mm, the smallest measurable angle is $5 \times 10^{-6}$ rad.

The defocused grating method suggested by Ostroumov [44] will now be evaluated. If the grating becomes just visible when the first diffraction maxima overlap, we may write

$$\frac{\lambda}{p} = \frac{p_p}{f}. \tag{17.11}$$

The condition of the groove shifting by one grating spacing is

$$f\frac{dL}{dy} = p, \tag{17.12}$$

where $L$ is the length of the optical path of the light in the inhomogeneity. By combining these equations we obtain

$$p_p\frac{dL}{dy} = \lambda. \tag{17.13}$$

In inhomogeneities which displace the ray through one grating spacing, the difference between optical paths for rays lagging by one spacing is equal to $\lambda$ when the grating is correctly used. The sensitivity of the method is the same as for interference measurements, in which the shift of the interference maximum is measured.

By means of the above equations it is possible to select the instrument adjustment parameters (the sign and magnitude of the defocusing and the grating spacing) suitable for measuring angles of deviation of given magnitude with the desired sensitivity and frequency.

The inhomogeneities that are actually measured are very complex. The defocused grid methods measure only the projection of the angle of deviation on the plane perpendicular to the grating grooves. It follows that the parameters of the grating suitable for studying a given inhomogeneity and the maximum sensitivity vary for different orientations of the grating. By varying the angle between the direction of the grating grooves and the selected direction in the object plane we can derive the following benefits: 1) to attain a situation in which the most important parts of the inhomogeneity are measured with adequate sensitivity, while the maximum angles of deviation remain within the measurement range; 2) to adjust the instrument in such a way that the filament shadow on the working photograph lies on the areas of the inhomogeneity image where it is most essential to obtain measurements in a large number of points. It is thus possible to ensure that the shadow on the working photograph will lie on some preselected section.

In the study of the boundary layer, measurements in sections perpendicular to the model surface are the most important. It is necessary to find an angle of setting of the grating grooves for which the filament shadow lies near the section perpendicular to the boundary. These measurements are of interest for the study of similar processes; they indicate the importance of allowing for the grating inclination and its influence on the accuracy and sensitivity of the measurements, and the reliability of the results of schlieren measurements.

## 18. CROSSED-LINES GRID AND POINT GRID

A defocused grating is suitable only for measuring the projection of the angle of light deviation on the plane perpendicular to the grating grooves. In order to measure the entire field of deviation angles it is necessary to conduct two experiments (or two series of experiments), readjusting the instrument for the angles in the other direction. The accuracy is adversely affected by any variation in the parameters of the inhomogeneity in the course of the experiment and between experiments, all the processes studied being non-stationary to a certain extent. Thus the surface of the astronomic objective mirror "breathes", the flow in the wind tunnel shimmers, and the burner flame fluctuates.

The usual procedure for obtaining the necessary values at a given time consists of the combination in a single unit of two schlieren instruments, measuring the angles in different directions. This procedure complicates the instrument and raises its price; furthermore, the light transmission is reduced, the amount of parasitic light

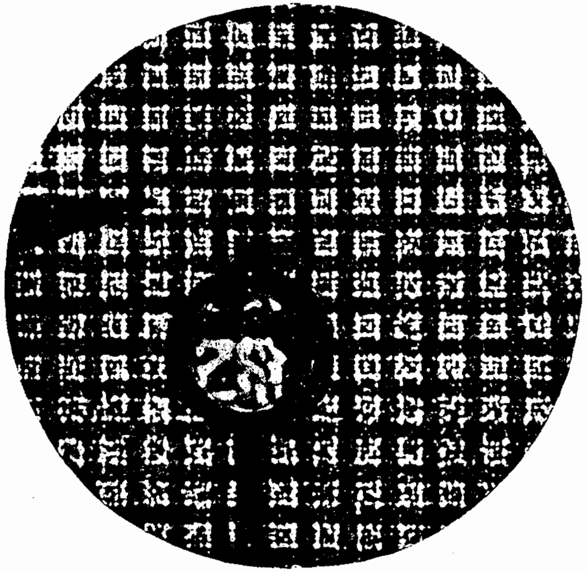

Figure 66
Diffraction pattern of the shadows from a crossed-lines grid.

increases, the instrument becomes more sensitive to vibrations, adjustment is complicated, etc.

Ostroumov [42] suggested using a grid made of two perpendicular systems of grooves. By means of such a grid it is possible to measure simultaneously two mutually perpendicular components of the angle of light deviation, and hence recover the entire field of angles of deviation. An improvement of the crossed-lines grid method lay in the utilization of two mutually perpendicular slits as a light source. This reduced the shadow contrasts somewhat, but increased the total illumination of the image several times (as compared with a point source), making it possible to study transient processes.

Diffraction phenomena considerably affect the images obtained by this method; the pattern is highly complicated as a result and its interpretation becomes difficult. Figure 66 shows a characteristic diffraction pattern of shadows of a crossed-lines grid.

A grid of points was suggested [12, 16] for the simultaneous measurement of the magnitude and direction of the angle of light deviation. The grid consisted of opaque spots separated by transparent spaces (Figure 67). The centers of the spots are located at the points of intersection of two systems of equidistant, mutually perpendicular lines. The shadows of the opaque spots appear on the screen; they constitute complex diffraction patterns, whose centers coincide with those of the shadows of the points according to geometrical optics. Figure 68 shows typical shadow patterns for different defocusings. If the wave curvature varies for different directions, the spot shadows are elongated (Figure 69).

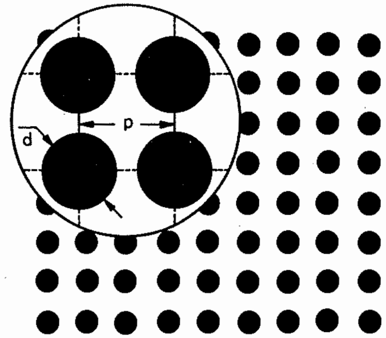

Figure 67
Point grid.

In the method of defocused grids, the normal measurement process consists of obtaining two photographs (the zero and the working photographs), in establishing the correspondence between the centers of the shadows on the two photographs, and in measuring the displacement of the center of each shadow.

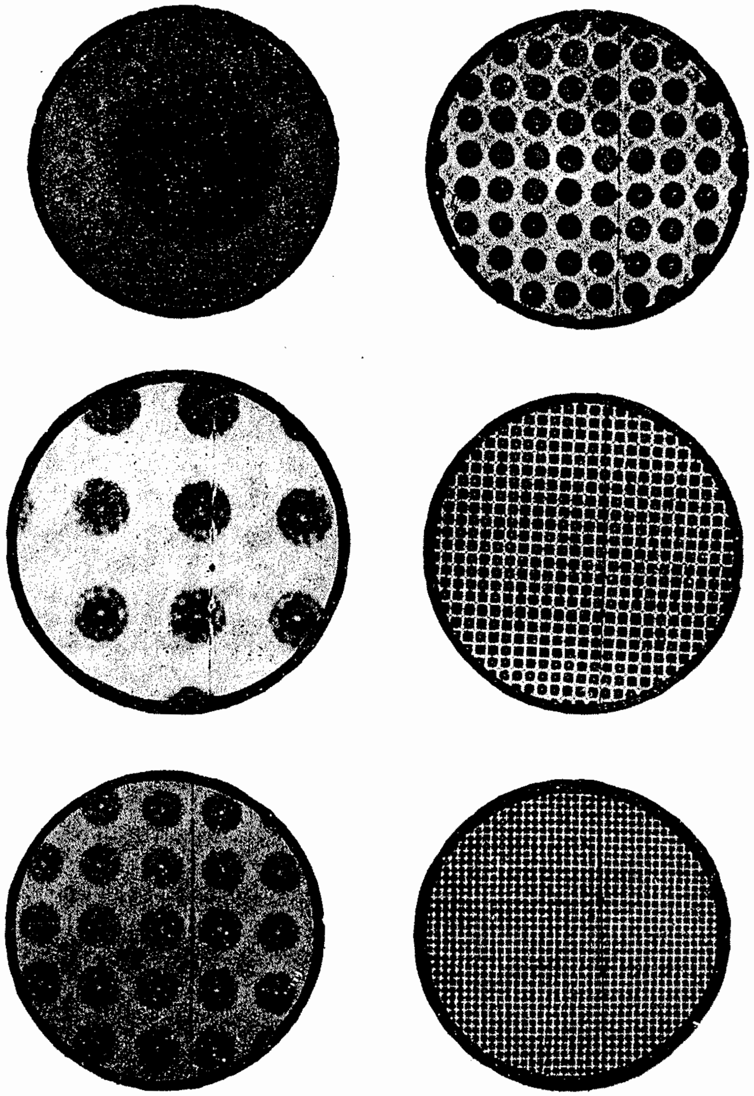

Figure 68
Schlieren patterns for various defocusings of the point grid.

The grid parameters are selected on the strength of the characteristics of the object of study. Grids of 0.1–2 mm spacing are used for wind-tunnel measurements, while for hydrodynamic measurements the grid spacing can increase to several centimeters.

By means of this method it is possible to determine simultaneously the magnitude and the direction of the angle of light deviation. We can study complex phenomena such as flutter, explosion, etc. The measurements are conducted with a single schlieren instrument.

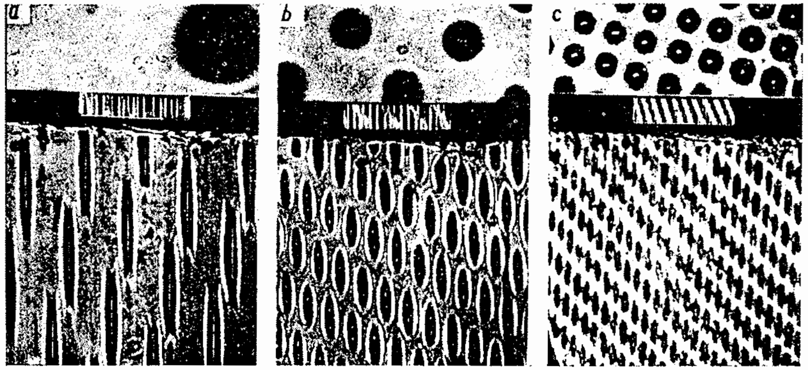

Figure 69

Schlieren patterns of a point grid for a light wave differently curved in different directions.

The application of the method with double instruments yields an additional advantage: it allows a more thorough study of processes with regions that differ greatly in the value of the refractive index gradients (the angles of light deviation). A weakly defocused dense grid is mounted in one of the arms, and the regions producing slight deflection are measured with a high sensitivity. The other arm accommodates a strongly defocused sparse grid, and angles of deviation are measured which lie outside the range of measurement of the first arm.

The method was tested experimentally on the IAB-451 instrument [16] for a convective air flow about a horizontal cylinder heated to 74°C.

The point grid method is most convenient for the study of time-dependent processes. Nevertheless, a steady-state process was selected as the inhomogeneity. To preserve the stability of the convective air flows, the heated cylinder was mounted in an insulated volume between the receiving and collimating parts of the instrument. This approach made possible a comparison of the point grid method with other pretested methods, which can be used in this case with maximum accuracy.

The cylinder surface temperature was controlled by varying the voltage on the heating coil. The high thermal conductivity of the material and the uniform placing

of the coil ensured isothermal surface conditions. Vibrations and sharp temperature changes were avoided by placing the installation in a basement. The working temperature conditions (surface temperature of 74°) provided a range of deviation angles $2 \times 10^{-4}$–$26 \times 10^{-4}$ rad, which roughly corresponds to the usual deviations in wind tunnels. The camera was focused on the middle of the cylinder.

A photograph obtained by the point grid method is represented on Figure 70.

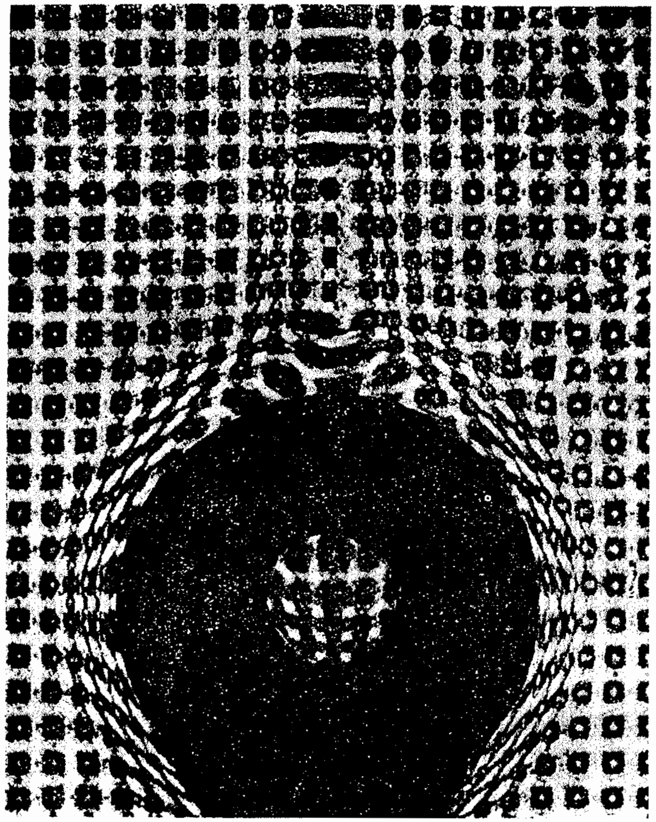

Figure 70

A photograph of convective air flow about a cylinder, taken by the point grid method.

The displacements of the shadow points and the angles of light deviation $\varepsilon$ were measured in both vertical and horizontal directions. The resulting distributions of the components of the deviation angles in these directions are shown on Figures 71 and 72.

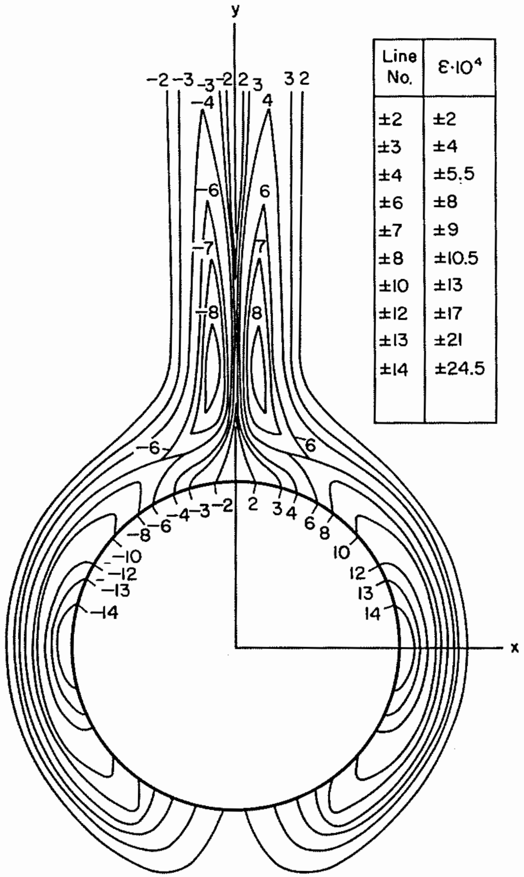

| Line No. | ε·10⁴ |
|---|---|
| ±2 | ±2 |
| ±3 | ±4 |
| ±4 | ±5.5 |
| ±6 | ±8 |
| ±7 | ±9 |
| ±8 | ±10.5 |
| ±10 | ±13 |
| ±12 | ±17 |
| ±13 | ±21 |
| ±14 | ±24.5 |

Figure 71

Components of the deviation angles in the vertical direction for the model shown on Figure 70.

The comparison of the results with data of similar measurements conducted under identical conditions by the focal-filament and defocused-grating methods showed excellent fit within the limits of error of the methods, equal to $\pm 10^{-4}$ rad. All the methods had the same accuracy and sensitivity under the given conditions. But while some 30 photographs were necessary for obtaining valid results by the focal-filament method, the defocused grating method required two photographs, and the point grid method only a single photograph.

From the field of deviation angles, the temperature distribution about the cylinder (Figure 73) was determined. The transition from the angles of light deviation to temperatures was achieved by the formula

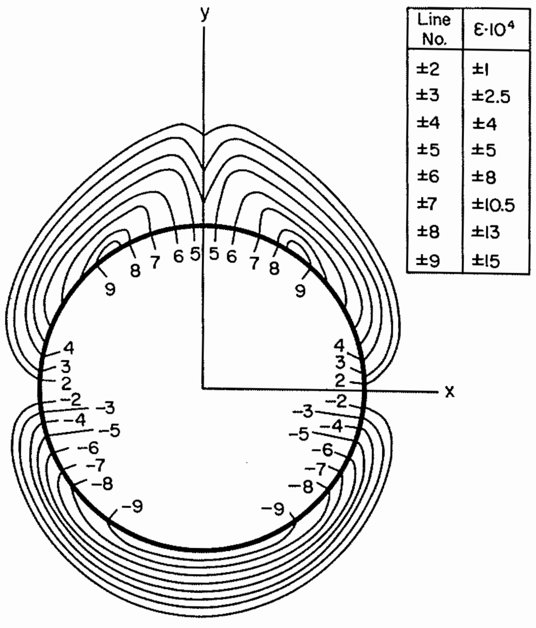

| Line No. | ε·10⁴ |
|---|---|
| ±2 | ±1 |
| ±3 | ±2.5 |
| ±4 | ±4 |
| ±5 | ±5 |
| ±6 | ±8 |
| ±7 | ±10.5 |
| ±8 | ±13 |
| ±9 | ±15 |

Figure 72

Components of the deviation angles in the horizontal direction for the model shown on Figure 70.

$$T(x) = T_\infty \left[ 1 + \frac{1}{(n_\infty - 1) L} \int_\infty^x \varepsilon(x)\, dx \right], \qquad (18.1)$$

where $T(x)$ is the temperature at the point $x$, $T_\infty$ and $n_\infty$ are, respectively, the temperature and the refractive index in the undisturbed parts of the field, and $L$ is the length of the inhomogeneity along the optical axis of the instrument. Numerical integration was carried out from regions without convective flows where the temperature could be measured with an accuracy of 0.1° by a mercury thermometer. The curves of the deviation angles were extrapolated to the region near the cylinder surface and to the region of small deviation angles at the interface between the disturbed and the undisturbed gas. The temperature distribution obtained was compared with the theoretical distribution and with the thermocouple measurements (Figure 74). The optical and theoretical curves agree satisfactorily, while the thermocouples give lower values, a fact explained by the difference between the temperature of the thermocouple junction and the air temperature.

Although extremely valuable as an illustration, measurements of the air tempera-

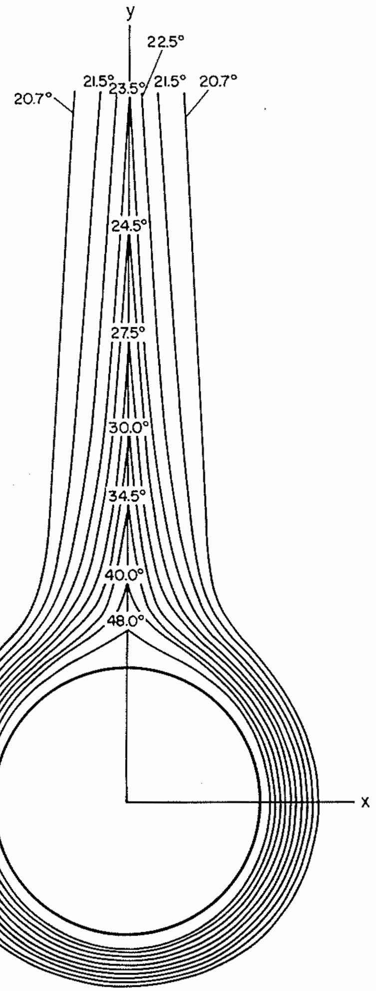

Figure 73

Temperature distribution in a convective air flow about a cylinder (cf. Figure 70).

ture about the cylinder do not provide a definite answer to the question of the accuracy of the point grid method, due to the approximations in the theoretical calculation and the considerable error in temperature measurements by thermocouples. To establish the accuracy of the method, the temperature of the cylinder surface was measured. Here the thermocouple accuracy was at least 0.5°, and the

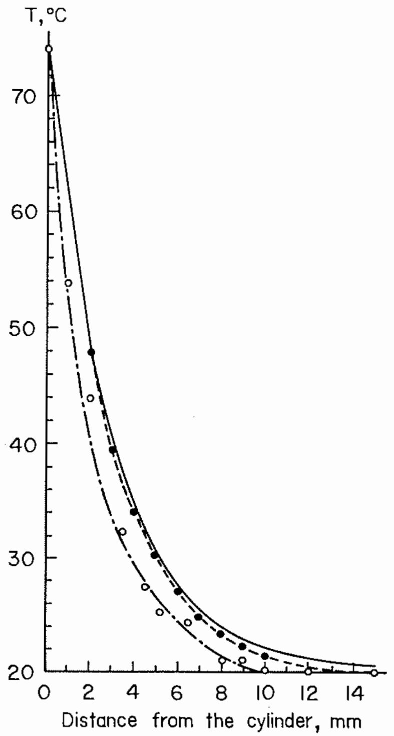

Figure 74

Temperature distribution along the $x$ axis. The solid line is the theoretical curve, the dotted line represents measurements by the point grid method, and the dash-dotted line represents thermocouple measurements.

error of the defocused grid method was at its maximum, since it included errors of the extrapolation at the cylinder surface. The measurements were conducted for different points of the cylinder surface, described by the angle $\phi$ about the $x$ axis (Figure 75). The error of the method under the above conditions, which can be broadly taken as the mean error for measurements of deviation angles of this magnitude, is 2°, i.e., 3% of the measured magnitude.

The main difficulty consists in correlating the elements of the pattern given by the inhomogeneity with the original pattern, and in determining the areas of the diffraction pattern corresponding to the locus of the centers of the point shadows. A shadow reversal took place in many areas. This phenomenon is similar to the reversal phenomenon in grating grooves: the center of the point's diffraction pattern corresponds to the intensity maximum and not the minimum.

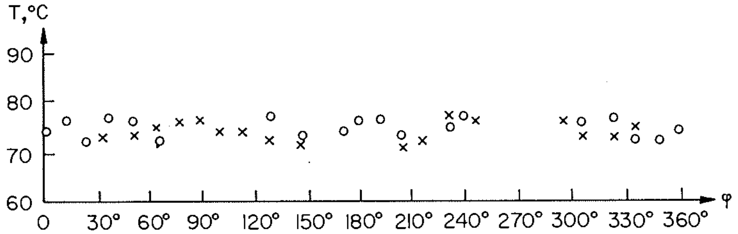

Figure 75
Measurement of the temperature at different points of the cylinder surface by the point grid method. The circles represent calculation along the sections $y$ = const, the crosses calculation along the sections $x$ = const.

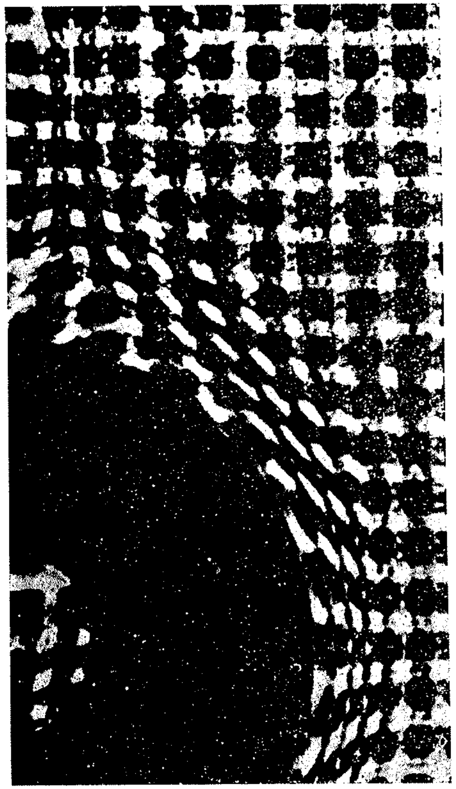

Figure 76
Photograph of convective air flow near the cylinder.

Both direct and reverse diffraction patterns were used. The locus of the centers of the point shadows on the working photographs was provided by a line drawn through the centers of the black points in the region of direct patterns and through the centers of the white spaces in the region of reverse patterns. Interpolation is used in the intermediate zones, where the diffraction pattern is highly complicated (either the pattern is obliterated or the number of shadows is doubled). An experiment was conducted in which the pattern on the zero photograph was reversed. To increase the number of measured points, both the displacements of the point shadows and the displacements of the clear spaces were measured. The results turned out to be identical with the results obtained from photographs located entirely in the region before the first reversal.

When point grids are used, the interpretation of processes with reversal is complicated by the discrete pattern of the point shadows. In difficult cases an additional experiment has to be conducted with a grooved grating, which gives the continuous motion of the center of the diffraction pattern of each groove and permits determining the exact places where reversal occurs. Thus it is possible to establish the correspondence between the points of the zero and the working photographs.

Figure 76 is a photograph of a complex schlieren pattern showing how shadow reversal works in the point grid method.

## 19. SCALE METHOD AND REMOTE GRID METHOD

In order to measure large angles of deviation, the grating must be placed far from the focus. Thus an angle of $5 \times 10^{-3}$ rad falls inside the measurement range of a grating with a 5 mm spacing (for $f = 2 \times 10^3$ mm). In order to obtain 20 shadows in a field of 20 cm, the grating must be placed at a distance of 1 m from the focus, which is unfeasible for the existing designs. The Soviet-made IAB-451 instrument has a maximum defocusing of about 30 mm, and TE-19 has 150 mm.

Many processes cause substantial deflection of light, and as a result it is frequently suggested that the existing instruments must be modernized in order to increase the defocusing. To fulfill these requirements in the arrangement described with the diaphragm placed at the second focus of the main objective of the receiving part, we must increase the effective diameter of the photographic objective substantially, in order not to cut off the light. This leads to a reduction of the resolving power. By making the objective more complicated, we reduce the transmission coefficient and increase the amount of parasitic light. It seems, therefore, difficult to create an instrument satisfying simultaneously the requirements of the highest quality for studying weak processes and the possibility of using the method of defocused grids for studying strong processes.

The distinctive characteristic of the method of defocused grids is the removal of the diaphragm from the focal plane, and the presence or absence of optical components in the space between the grid and the focal plane is not a critical factor. For the study of strong processes it is therefore advisable to use the remote grid method and the scale method — varieties of the defocused grid method in which the viewing diaphragm is placed either at the inhomogeneity image or at the object itself [97, 98]. Since the object plane and the image plane are conjugate, these methods were originally designed for different purposes. The scale method was proposed and used for studying phenomena in centrifuges, while the remote grating method was used for gas-dynamic studies. These cases correspond to setting the defocused grid at large distances from the focal plane. The placing of the grid in the object plane corresponds to a defocusing of $+\infty$, and in the image plane to a defocusing of $-\infty$.

The displacement of the groove shadow following the deviation of the ray through an angle $\varepsilon$ by the inhomogeneity is equal in the remote grid method to

$$\delta = \varepsilon l \mu, \tag{19.1}$$

where $l$ is the distance from the grating to the image plane, and $\mu$ the image scale. With the aid of (16.6) we obtain from (19.1)

$$\varepsilon = \frac{\delta_p p}{p_p l \mu}. \tag{19.2}$$

For the scale method

$$\varepsilon = \frac{\delta_p}{\mu l}. \tag{19.3}$$

The sensitivity of the methods is equal to

$$S_{r.g.} = \frac{p_p l \mu}{p}, \tag{19.4}$$

$$S_{sc} = \mu l. \tag{19.5}$$

The scale method and the defocused grid method will now be compared. Their sensitivities are equal for

$$l = \frac{f^2}{\Delta}. \tag{19.6}$$

The sensitivity of the remote grid method is equal to that of the defocused grid method for

$$l = \frac{\mu^2 f^2}{\Delta}. \tag{19.7}$$

The scale method and the remote grid method can be used with the existing schlieren instruments by introducing additional attachments for fitting the grating between the instrument and the object, as well as in the body of the photographic attachment.

## 20. MEASUREMENT OF THE DERIVATIVE OF THE LIGHT DEVIATION ANGLE IN THE CASE OF A CYLINDRICAL WAVE

The defocused grid methods can be used to determine more than the angle of light deviation. If the wave is cylindrical, it is possible to use these methods in measuring the derivative of the angle of deviation as well. The theoretical basis and the experimental development of the method are attributed to Sukhorukikh [52], whose results we shall now describe.

Let the wave front vary only in the direction of the $x$ axis,

$$z = P(x). \tag{20.1}$$

The direction of the cylindrical surface generatrix is considered to be known. A defocused filament is placed in the receiving part of the instrument at an angle $\psi$ to the wave surface generatrix. The derivative of the angle of light deviation $P_{xx}(x)$, is determined by measuring the angle $\omega$ between the tangent to the geometrical axis of the diffraction pattern and the light wave generatrix:

$$P_{xx}(x) = \frac{\Delta}{f^2 + \Delta(s+f)} \left( \frac{\tan\omega}{\tan\psi} - 1 \right). \tag{20.2}$$

For mirror–meniscus systems, equation (20.2) takes the following form, due to the change of the signs of $f$ and $\Delta$:

$$P_{xx}(x) = \frac{\Delta}{f^2 - \Delta(s-f)} \left( 1 - \frac{\tan\omega}{\tan\psi} \right). \tag{20.3}$$

The main random errors in the measurement of $P_{xx}(x)$ are due to the inaccuracies in the determination of $\omega$, $\psi$, and $\Delta$:

$$\frac{\delta P_{xx}(x)}{|P_{xx}(x)|} = \sqrt{\left[ \frac{\cos\psi}{\cos\omega \cdot \sin(\omega-\psi)} \right]^2 \cdot \delta^2\omega + \left[ \frac{\sin\omega}{\sin\psi \cdot \sin(\omega-\psi)} \right]^2 \delta^2\psi + \frac{\delta^2\Delta}{\Delta^2}}. \tag{20.4}$$

For small $\psi$ the error is large for almost any $\omega$. With the increase in $\psi$ the error decreases, and the range of $\omega$ values which can be measured increases.

It is advisable to place the filament in such a way that the angle $\psi$ will be large. The filament defocusing must be selected in order to reduce the effect of the error in $\omega$. For this purpose, it is recommended that a trial experiment be conducted by means of which the inhomogeneity characteristics can be estimated. If we take

$$\left|\frac{\cos\psi}{\cos\omega\cdot\sin(\omega-\psi)}\right| = \left|\frac{\sin\omega}{\sin\psi\cdot\sin(\omega-\psi)}\right| = 0.5,$$

$$\delta\omega = 3^\circ, \quad \delta\psi = 1^\circ, \quad \frac{\delta\Delta}{\Delta} = 0.01,$$

we obtain

$$\frac{\delta P_{xx}(x)}{|P_{xx}(x)|} = 0.03.$$

Here the error is smaller than the measurement errors when $P_{xx}$ is determined by differentiating the experimental distribution of the deviation angles.

In the experimental development of the method, the curvature of a light wave formed with the aid of a special cuvette was measured. Error estimates assessment established the validity of the theoretical calculations.

The method can also be used when the generatrix of the wave surface is not at a right angle to the undeflected rays, but then $P_{xx}(x)$ must be interpreted as the derivative of the angle between the undeflected rays and the projections of the deflected rays on the $Oxz$ coordinate plane. If the direction of the generatrix is not known, an additional experiment is conducted in which the filament is placed in the focal plane. For any orientation of the filament the geometrical axis of the diffraction pattern will then be located in the direction of the projection of the generatrix on the $Oxy$ plane.

# V

# PHOTOMETRIC METHODS

## 21. BASIC CONCEPTS

The main drawback of the defocused grid methods is that they measure only a discrete set of angles of deviation, corresponding to the centerlines of the diffraction patterns of the grooves or the bright spaces of the grating. This is insufficient for many physical studies. In qualitative studies, the discreteness of the observed field complicates the determination of the shape and the character of the inhomogeneity. Furthermore, the accuracy of the defocused grid method is not high. It became necessary, therefore, to develop quantitative methods of studying transparent inhomogeneities which would be capable of measuring deviation angles at any point of the field with a high sensitivity. Such are the photometric methods.

Their basic common feature is the use of an extended self-luminous body as a light source. A knife-edge partially covering the light source image is placed in the focal plane of the main objective of the receiving part. If an optical inhomogeneity lies in the object plane, the source image is displaced, and the amount of light blocked by the knife-edge changes, causing a change in the illumination of the observed point on the screen or the photographic plate. If different parts of the inhomogeneity deflect light through different angles, they will cause different displacements of the source image. Therefore, so long as the knife-edge continues to cover a part of the source image, a definite illumination of the screen will correspond to each angle of deviation. It becomes possible in principle to determine the angle of deviation by measuring the screen illumination or some related magnitude.

The quantitative photometric methods thus coincide basically with the qualitative methods described earlier. The difference consists of additional measurements which determine the schlieren image illumination. An important question to be considered is the accuracy of these measurements and the correspondence between the angle of light deviation and the image illumination.

The photometric methods can be classified into several groups, differing according to the shape of the viewing diaphragm and the method of determination of the light deviation angle. In some cases the inhomogeneity is compared with a standard object of known deflection properties, called a *schliere*. By determining the correspondence between the points of the two objects which give the same effect (the same screen illumination), we find the angle of deviation in the inhomogeneity being studied. These are the *standard photometric methods.*

It is also possible to follow a different procedure, i.e., to calculate what change in the screen illumination will correspond to every angle of deviation, allowing for the shape and brightness distribution of the light source and the shape of the viewing diaphragm; and then, by measuring the absolute value of the illumination or its relative variation, to find the deviation angle. These are the *absolute photometric* methods.

The absolute photometric methods were the last to be developed and utilized in practice, due to the difficulty of measuring the illumination. The illumination is generally estimated from the degree of blackening (or photographic density) of the emulsion. The blackening, however, depends on many factors other than the illumination, such as the development conditions, the developer, etc. In addition, the total measurement error is affected by inaccuracies in the diaphragm manufacture, non-uniformity of the source brightness, and photometric errors.

The basic features of the application of these methods will now be described.

In the *absolute photometric methods* it is necessary to relate the illumination at every point of the image to the angle of light deviation at the conjugate point of the inhomogeneity. This can be achieved if a number of conditions are satisfied.

1. According to Lambert's law, the brightness of the source image at points emitting rays at an angle $\omega$ to the optical axis is proportional to $\cos^4 \omega$. In order that the non-uniformity in the illumination caused by this phenomenon may be smaller than 1%, the extreme points of the light source must be viewed at an angle not larger than 4° to the optical axis. As a rule, this requirement is fulfilled by a wide margin in the existing long-focal schlieren instruments. In the Soviet-made IAB-451, TE-19, TE-20 and other instruments the extreme points of the source are viewed at an angle of no more than 0.5° to the optical axis. The error does not exceed 0.02% in this case.

2. The light source must be of uniform brightness. As will be seen later, in some cases uniform brightness should be maintained only in one direction of the extended light source, while in other cases the brightness must be uniform in all directions. The calculation of the illumination from the angle of light deviation in the inhomogeneity is based on the assumption of uniform source brightness. If this assumption is not satisfied, absolute photometric methods cannot produce accurate results. While it is possible in principle to allow for the non-uniformity of the illumination by constructing the distribution function of the light intensity of the receiving part, this is generally a difficult and inexpedient approach. It is considerably more efficient to use light sources having a uniform brightness over the surface of the luminous body.

3. The deflected rays must not be stopped by the objective rims and other stops, apart from the main viewing diaphragm placed in the focal plane of the main objective.

4. The shape and transparency of the focal plane stop must be well known. Deviations from the shape assumed in the theoretical calculation of the illumination lead to measurement errors.

5. The largest and smallest measured angles of deviation must lie inside the working range, since only in that range is there a one-to-one correspondence between the angle of deviation and the degree of emulsion blackening.

While the first and third conditions are normally met, the fulfillment of the other conditions must be examined in each individual case.

The *standard methods* have somewhat different conditions of applicability. While requirements 3 and 5 still apply, the other conditions do not substantially affect the accuracy of the results. On the other hand, it is necessary to know exactly the distribution of deviation angles in the standard schliere and its light absorption. In addition, the requirements regarding the uniform illumination of the instrument are stricter, since corresponding points in the schliere and the inhomogeneity are measured in different areas of the field.

There are two types of standard methods: the *standard lens method*, and the *standard wedge method*, differing according to the schliere used as the standard object. There also exists a method in which the inhomogeneity is photographed through a standard schliere. This method is called the semicompensated photometric method.

## 22. THE CURVED-STOP METHOD

The curved-stop method was suggested by Maksutov [35], and it constitutes the first quantitative photometric method. Although originally a standard method, it was developed as an absolute photometric method.

This method uses as a viewing diaphragm an opaque plate with transparent aperture (Figure 77), whose curved edges *AC* and *A′C′* are bounded by the curve

$$\eta = ca^{\xi/h}. \tag{22.1}$$

As will be seen in what follows, this curve shape makes the sensitivity independent of the value of the measured angle of deviation, reduces the influence of vibrations, and simplifies the processing of the results.

The light source is a luminous slit. The stop is set in the second focal plane of the main objective in such a way that its axis of symmetry is perpendicular to the slit

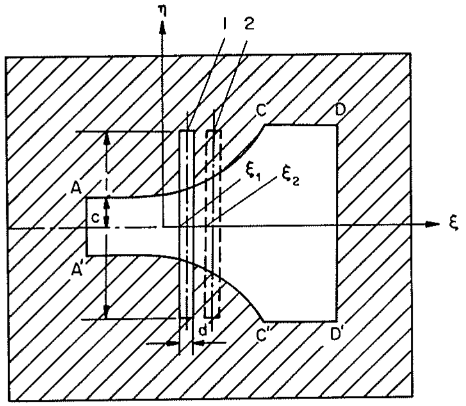

Figure 77
Curved stop: 1 and 2) original and displaced slit images.

image. This is achieved in practice by placing the side $DD'$ parallel to the light source image. The stop cuts off the rays from the slit extremities, and transmits only the central rays. The shift of the source image produced by the inhomogeneity causes a change in the length of the open portion of the slit.

Thus it can easily be observed that when the slit image is displaced a distance $h$, its open part increases by a factor $a$. The magnitude $h$ is termed the pitch of the stop. The smaller the pitch, the steeper the curve and the larger the relative increment in illumination obtained for the same shift. The magnitude $a$, which determines the factor by which the illumination changes when the image is shifted through one pitch, is termed the *multiplicity of the stop.* The magnitude $c$ determines the smallest value of the aperture and the minimum illumination of the image.

If the coordinate of the left edge in the initial position is $\xi$, the illumination of any field point will be

$$I_1 = B\int_{\xi_1}^{\xi_1+d} \eta d\xi, \tag{22.2}$$

where $d$ is the slit width and $B$ a coefficient allowing for the source brightness, the system absorption, etc. In a physical sense, equation (22.2) corresponds to the assumption that the illumination is proportional to the open part of the slit image.

When an inhomogeneity is interposed, the slit image moves to position $\xi_2$, which has to be determined. The illumination of point $\xi_2$ changes as a result to

$$I_2 = B\tau\int_{\xi_2}^{\xi+d} \eta d\xi, \tag{22.3}$$

where $\tau$ is constant for the given point of the image, its value depending on the absorption or emission of the inhomogeneity.

The optical densities of the emulsion corresponding to these illuminations will be·

$$D_1 = \gamma \log I_1 - b, \tag{22.4}$$

$$D_2 = \gamma \log I_2 - b, \tag{22.5}$$

where $\gamma$ is the emulsion contrast factor, and $b$ is a constant.

By substituting (22.2), (22.3) in (22.4), (22.5) and subtracting (22.4) from (22.5) we obtain (allowing for (22.1))

$$\xi_2 - \xi_1 = \frac{(D_2 - D_1 - \gamma \log \tau)\, h}{\gamma \log a}. \tag{22.6}$$

Taking into account that $\xi_2 - \xi_1 = \varepsilon f$, we reduce (22.6) to the form

$$\varepsilon = \frac{(D_2 - D_1 - \gamma \log \tau)\, h}{\gamma f \log a}. \tag{22.7}$$

In the absence of absorption (22.7) reduces to

$$\varepsilon = \frac{(D_2 - D_1)\, h}{\gamma f \log a}. \tag{22.8}$$

It is thus possible to determine the angle of light deviation at every point of the inhomogeneity from the measurement of the optical density of the emulsion on the zero and the working photograph. If the object absorbs or emits light, two additional photographs are necessary, taken with a remote diaphragm with and without an inhomogeneity. It is then possible to determine the value of $\tau$, since, if the deflected rays are not stopped, all the changes in the illumination will be due only to absorption. The density of the negative at the same point of the image will satisfy the condition

$$D'_2 - D'_1 = \gamma \log \frac{I'_2}{I'_1} = \gamma \log \tau. \tag{22.9}$$

By substituting (22.9) in (22.6) we obtain

$$\varepsilon = \frac{[D_2 - D_1 - (D'_2 - D'_1)]\, h}{\gamma f \log a}. \tag{22.10}$$

These formulas are valid if the inhomogeneity does not displace the slit image beyond the curved portion of the stop, and all the optical densities lie within the linear section of the characteristic curve of the emulsion.

The measurement range depends on the position of the stop with respect to the slit image and on the selection of the exposure. Both an insufficient length of the curved portion of the stop and an insufficient latitude of exposure of the emulsion can restrict the range. If a high-$\gamma$ film is selected, with a latitude of exposure considerably smaller than $n \log a$, the working range will be limited by the latitude of exposure. An underexposure or overexposure of the emulsion truncates the working range from one side. The working range is the overlap segment of the ranges associated with the limited size of the curved portions of the stop and the insufficient latitude of exposure.

To obtain the maximum possible sensitivity for a given measurement, the minimum and the maximum angles of deviation must deflect the slit image to the edges of the curved portion of the stop, and the corresponding photographic densities must correspond to the ends of the linear part of the characteristic curve. The value of the working range is then

$$\mathscr{R} = \frac{nh}{f} \tag{22.11}$$

and the latitude of exposure is

$$\mathscr{L} = n \log a, \tag{22.12}$$

where $n$ is the number of pitches accommodated by the projection of the curved portion of the stop on the $\xi$ axis and $\mathscr{L}$ is the width of the photographic material.

The sensitivity of the curved stop method is equal to

$$S = \frac{dD}{d\varepsilon} = \frac{\gamma f \log a}{h} = \frac{\gamma \mathscr{L}}{\mathscr{R}}. \tag{22.13}$$

From (22.11) and (22.12) we obtain

$$S_{\mathrm{max}} = \frac{D_{\mathrm{max}} - D_{\mathrm{min}}}{\mathscr{R}}, \tag{22.14}$$

where $D_{\mathrm{max}}$ and $D_{\mathrm{min}}$ are, respectively, the maximum and the minimum densities (corresponding to the ends of the linear part of the characteristic curve).

If the emulsion is specified, it is possible to determine from (22.14) the sensitivity of measuring the angles of deviation inside a given range. Equation (22.14) also shows that it is always expedient to use emulsions and processing conditions giving the largest possible difference between the maximum and the minimum densities.

The experimental conditions are selected as follows:

1. The film and the processing conditions giving a maximum difference $D_{\mathrm{max}} - D_{\mathrm{min}}$ are selected. The $\gamma$ and the latitude of exposure of the film are determined.

2. The conditions of light deviation in the object being studied are approximately estimated.

3. The sensitivity of measuring this distribution of deviation angles with such an emulsion is found from (22.14).

The necessary stop parameters are determined from (22.14) and (22.12).

The actual accuracy, characterized by the relative or absolute errors of measurement of the angles of deviation, depends on the background, the diffuseness of the stop edges, the optical density of the aperture and the background, inaccuracies in the manufacture of the stop, errors in the measurement of the emulsion $\gamma$, etc.

We shall estimate the main sources of errors and their effect on the measurement accuracy.

a) Curved stops are manufactured photographically as a rule. The optical density of the emulsion layer surrounding the transparent portion cannot be infinitely large. Some light from the slit zones projected on the "opaque" area traverses the stop and reaches the inhomogeneity image. This additional light, not provided for in the calculation, introduces an error in the measurement.

Let the transparent portion of the stop and the "opaque" background have constant optical densities $\tau_1$ and $\tau_2$. The image illumination will be

$$I_1 = B \cdot 10^{-\tau_2} \left( ld - 2 \int_{\xi_1}^{\xi_1 + d} \eta d\xi \right) + 2B \cdot 10^{-\tau_1} \int_{\xi_1}^{\xi_1 + d} \eta d\xi, \tag{22.15}$$

where $l$ is the slit length. If the width of the slit image is considerably smaller than the pitch of the stop, then

$$I_1 = B \cdot 10^{-\tau_2} d \left[ l - 2ca^{\xi_1/h} (1 - 10^{\tau_2 - \tau_1}) \right]. \tag{22.16}$$

If the inhomogeneity shifts the slit image to position $\xi_2$, the illumination at that point will be

$$I_2 = B \cdot 10^{-\tau_2} d \left[ l - 2ca^{\xi_2/h} (1 - 10^{\tau_2 - \tau_1}) \right]. \tag{22.17}$$

The measured and true angles of deviation are, respectively,

$$\varepsilon_{\mathrm{m}} = \frac{h}{f \log a} \log \frac{I_2}{I_1}, \tag{22.18}$$

$$\varepsilon_{\mathrm{t}} = \frac{\xi_2 - \xi_1}{f}. \tag{22.19}$$

Let $\varepsilon_{\mathrm{t}} - \varepsilon_{\mathrm{m}} = \Delta\varepsilon$. Then,

$$\frac{\Delta\varepsilon}{\varepsilon_{\mathrm{t}}} = -\frac{h}{(\xi_2 - \xi_1) \log a} \left[ \log \left( \frac{la^{-\xi_2/h} - 2c}{2c \cdot 10^{\tau_2 - \tau_1}} + 1 \right) - \log \left( \frac{la^{-\xi_1/h} - 2c}{2c \cdot 10^{\tau_2 - \tau_1}} + 1 \right) \right]. \tag{22.20}$$

Since

$$\frac{la^{-\xi_1/h}-2c}{2c\cdot 10^{\tau_2-\tau_1}} \ll 1 \quad \text{and} \quad \frac{la^{-\xi_2/h}-2c}{2c\cdot 10^{\tau_2-\tau_1}} \ll 1,$$

equation (22.20) reduces to

$$\tau_2-\tau_1 = \log\frac{l\varepsilon_t}{2ca^{\xi_1/h}\,\Delta\varepsilon}. \tag{22.21}$$

For $c = 0.2$ mm, $l = 10$ mm, $a = 2$, $\xi_1 = 2h$, $\Delta\varepsilon/\varepsilon_t = 10^{-3}$ we obtain $\tau_2-\tau_1 = 3.8$. For $\Delta\varepsilon/\varepsilon_t = 10^{-2}$ we obtain $\tau_2-\tau_1 = 2.8$.

It follows that in order to eliminate the error due to the transparency of the stop background, the difference between the optical densities of the background and the aperture must be no less than 3.0–3.5.

b) In photographically-manufactured stops, the aperture density cannot be made uniform over the whole area of the curved portion. As a result, the intensity of the transmitted light does not correspond exactly to the position of the slit image.

If the optical density of the aperture is not uniform, then

$$\varepsilon_m = \frac{h}{f\log a}\log\frac{\displaystyle\int_{\xi_2}^{\xi_2+d}\int_{-ca^{\xi_2/h}}^{ca^{\xi_2/h}} 10^{-\tau(\xi,\,\eta)}\,d\xi d\eta}{\displaystyle\int_{\xi_1}^{\xi_1+d}\int_{-ca^{\xi_1/h}}^{ca^{\xi_1/h}} 10^{-\tau(\xi,\,\eta)}\,d\xi d\eta}. \tag{22.22}$$

Writing $\tau(\xi, \eta) = \tau_{av} \pm \delta$, and remembering that the size of the density variations is of the same order as the width of the slit image, we obtain

$$\varepsilon_m = \frac{\xi_2-\xi_1}{f} + \frac{2\delta h}{f\log a}. \tag{22.23}$$

By combining (22.23) with (22.19) we obtain

$$\delta = \frac{\Delta\varepsilon f\log a}{2h}. \tag{22.24}$$

The source brightness must fulfill a condition similar to (22.24),

$$\frac{\Delta B}{B} = \frac{\Delta\varepsilon f\ln a}{2h}, \tag{22.25}$$

where $B$ is the source brightness, $\Delta B$ are admissible brightness fluctuations, causing an error $\Delta\varepsilon$. For $\Delta\varepsilon = 10^{-6}$ rad, $f = 2000$ mm, $a = 2$, and $h = 0.1$ mm, we obtain $\Delta B/B = \delta\ln 10 = 7\times 10^{-3}$.

While the condition (22.24) for $\delta$ is easily fulfilled, the requirement for $\Delta B/B$ is very restrictive. It cannot be achieved if the light source is a DRSh mercury discharge lamp or a coil filament lamp. Satisfactory results are obtained with the PRK-4 mercury discharge lamp, if the instrument slit is aligned with the lamp, and with strip filament lamps. When such light sources are used, the relative brightness fluctuations over the area of a slit 6 mm high and 0.1 mm wide do not exceed 1%.

c) Due to drawing inaccuracies, limited resolving power of the reproducing objective, etc., the curved aperture edge does not correspond exactly to the law $\eta = ca^{\xi/h}$. As an example, Figure 78 represents a photomicrograph of a portion of the curved stop of the TE-19 instrument. Since the deviations from the specified shape are small, the limiting curve can be written in the form

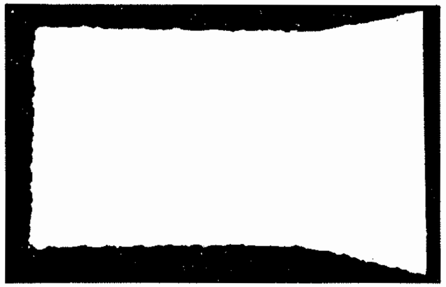

Figure 78

Photomicrograph of a narrow portion of a curved stop. Magnification 80 ×.

$$\eta = ca^{\xi/h} + \psi(\xi), \tag{22.26}$$

where

$$\psi(\xi) \ll \eta. \tag{22.27}$$

The substitution of (22.27) in (22.18) yields

$$\varepsilon_m = \frac{h}{f\log a}\log\frac{\displaystyle\int_{\xi_2}^{\xi_2+d}[ca^{\xi/h} + \psi(\xi)]\,d\xi}{\displaystyle\int_{\xi_1}^{\xi_1+d}[ca^{\xi/h} + \psi(\xi)]\,d\xi}. \tag{22.28}$$

Replacing $\psi(\xi)$ by $\psi_{av}$, introducing the concept of average value of the deviation from the specified shape, and making use of (22.19), we obtain the formula

$$\psi_{av} = \frac{\Delta\varepsilon cfa^{\xi_1/h}}{2h}. \tag{22.29}$$

Condition (22.29) can be satisfied only for a stop that is manufactured with sufficient accuracy. If $ca^{\xi_1/h} = 2$ mm, $f = 2000$ mm, $h = 0.5$ mm, and $\Delta\varepsilon = 10^{-6}$ rad, the value of $\psi_{\mathrm{av}}$ must be smaller than $4 \times 10^{-3}$ mm. It was assumed in the derivation of (22.29) that the mean size of the zones of deviation of the curve from the ideal curve is larger than the width of the slit image. If the zones are narrower, the deviations average out and the requirements regarding the quality of stop manufacture become less exacting.

d) In order to obtain the distribution of the light deviation angles, it is necessary to make photometry of the zero and the working photographs and to determine the $\gamma$ of the emulsion used. The photometric errors and the errors in the determination of the $\gamma$ enter the measurement error:

$$\frac{\Delta\varepsilon}{\varepsilon} = \frac{d\gamma}{\gamma} + \frac{d(D_2 - D_1)}{D_2 - D_1}, \tag{22.30}$$

where $d\gamma$ and $d(D_2 - D_1)$ are the errors in the determination of $\gamma$ and $D_2 - D_1$. Inaccurate positioning of the zero and the working photograph during the photometry can be included in the error of determination of the optical density.

The total measurement error is equal to the sum of the errors resulting from the preceding factors:

$$\left(\frac{\Delta\varepsilon}{\varepsilon}\right)_{\mathrm{tot}} = \sum_{i=1}^{N} \left(\frac{\Delta\varepsilon}{\varepsilon}\right)_i. \tag{22.31}$$

Each of the $(\Delta\varepsilon/\varepsilon)_i$ must be considerably smaller than $(\Delta\varepsilon/\varepsilon)_{\mathrm{tot}}$, which is the permissible measurement error.

The examination of the main errors of the curved-stop method leads to the conclusion that the actual error cannot be reduced below $2 \times 10^{-6}$ rad. This value is larger than the error of the knife-edge and slit photometric method, and is roughly equal to the error of the defocused grid methods. Due to the relatively large error, the method cannot be used for the study of weak processes, e.g., in rarefied gases. It can, however, be successfully used for studying inhomogeneities deflecting the light by more than $5 \times 10^{-5}$ rad.

The manufacture of the stop presents a problem, since a high accuracy is required. Photographic manufacture is the best procedure. The profile is first drawn on a 100:1 scale on moist Whatman paper stretched on a frame. The maximum error allowed in the drawing is 0.3 mm. In order to avoid ghosts during photographing, a dull paint such as gouache is used in drawing. To protect the stop from damage, it must be bonded onto a glass cover.

The stop size is determined by the following factors:

1. The minimum aperture is determined by the diffraction phenomena, the source brightness and the accuracy of the aperture drawing. In instruments for gas-dynamic measurements it should be of the order of tenths of a millimeter.

2. The maximum aperture cannot be very large, due to the difficulty of a uniform illumination of the slit and to system aberrations. In the Soviet-made IAB-451, TE-19, and TE-20 instruments the aperture diameter should be about 1 cm. A larger aperture would lead to a loss in accuracy. In addition, it is difficult to find a material that possesses a large difference between the optical densities on the linear section of the characteristic and also has a sufficiently wide latitude of exposure.

## 23. THE KNIFE-EDGE AND SLIT METHOD

The second method of absolute photometry is the knife-edge and slit method. Let the knife-edge cover the slit image in the zero position in such a way that only a part of the slit width $\xi_1$ remains open. If the brightness of the slit image in the direction perpendicular to the knife-edge is assumed to be constant, the illumination of any point of the image is

$$I_1 = \xi_1 \int_{\eta_1}^{\eta_1 + l} B(\eta)\, d\eta. \tag{23.1}$$

The function $B(\eta)$, allowing for the source luminance and the system absorption, is different at different field points and is constant in time; $\eta_1$ and $\eta_1 + l$ are the coordinates of the slit edges on the $\eta$ axis, and $l$ is the length of the slit image. The density at this point is determined from (22.4).

If the inhomogeneity deflects the light through the angle $\varepsilon$, the slit image is displaced by $\delta = \varepsilon f$, and the illumination at the same point of the inhomogeneity image becomes

$$I_2 = (\xi_1 + \delta) \int_{\eta_1}^{\eta_1 + l} B(\eta)\, d\eta. \tag{23.2}$$

By combining the equations for the optical densities, we obtain

$$\varepsilon = \frac{\xi_1}{f}\left(10^{(D_2 - D_1)/\gamma} - 1\right). \tag{23.3}$$

Thus in this method as well, the angle of light deviation in the inhomogeneity can be determined from the difference between the densities in the zero and the working photograph. While our calculation was based on the assumption of constant source brightness, a similar result can also be obtained for sources with variable brightness. In this case $I = I(t)$, and the optical density is given by

$$D_1 = \gamma \log \xi_1 \int_0^T \int_{\eta_1}^{\eta_1 + l} B(\eta, t)\, d\eta\, dt, \tag{23.4}$$

where $T$ is the total exposure. Since

$$\int_0^T B(t)dt = \text{const}, \tag{23.5}$$

the calculation gives a result identical to (23.3).

The sensitivity of the method is

$$S = \frac{\gamma}{\xi_1/f - \varepsilon}. \tag{23.6}$$

In this method, unlike the curved-stop method, the sensitivity depends on the value of the measured deviation angles. By selecting $\xi_1$ it is possible to adjust the instrument in order to achieve maximum sensitivity at the field points of greatest interest. In actual measurements, the sensitivity must be highest for small deviation angles, when

$$S = \frac{\gamma f}{\xi_1}. \tag{23.7}$$

The sensitivity of the method depends on the emulsion $\gamma$ and the angular size of the open part of the source image. By using high-$\gamma$ emulsions it is possible to increase the sensitivity.

According to the preceding theoretical explanation, the sensitivity can be made arbitrarily large, since no restrictions are imposed on $\gamma$, $f$ and $\xi_1$. In actual measurements there exists a sensitivity limit, determined by the brightness of the light sources, the aberrations of the system, the diffraction phenomena, etc. Different factors dominate under different conditions. A detailed examination of the effect of each of these factors will be given in the corresponding sections. We wish only to mention here that it is possible to achieve conditions under which the width of the open part of the slit will not be larger than $2 \times 10^{-2}$ mm. Taking $\gamma = 4$ (high-$\gamma$ emulsions are rare and normally possess a speed too low for schlieren measurements), we obtain the maximum attainable sensitivity

$$S = 4 \cdot 10^5. \tag{23.8}$$

Objects deflecting the light through $2.5 \times 10^{-7}$ rad will give a difference of 0.1 in the emulsion density. To compare the sensitivity obtained with that of the preceding method, we divide (23.7) by (22.13):

$$\frac{S_k}{S_{cs}} = \frac{h}{\xi_1 \log a}. \tag{23.9}$$

The two methods will be of equal sensitivity if $h = \xi_1 \log a$. For $a = 2$ this condition becomes $h = 0.3\,\xi_1$. The pitch of the stop must be three times smaller than the width of the open part of the slit image. While it is relatively easy to obtain $\xi_1 = 0.02$ mm, the manufacture and use of stops with a pitch of 0.007 mm does not seem practicable. It is observed from this example that the actual sensitivity obtainable by the knife-edge and slit method is much higher than that of the curved-stop method.

Consider the question of the measurement range of the method. It is easily observed that the field illumination changes only for deviation angles satisfying the condition

$$\frac{d-\xi_1}{f} > \varepsilon > -\frac{\xi_1}{f}, \tag{23.10}$$

i.e., only when the knife-edge covers the slit image partially. In the case of a completely uncovered or a completely covered slit, the screen illumination remains constant (or almost constant, since the quantity of scattered and diffracted light can vary).

Another factor restricting the measurement range is the latitude of exposure of the film. Indeed, if the deflection of the slit image takes us into the underexposure or overexposure region, no change in optical density will accompany a further variation of the light deviation angle. The minimum and maximum angles of deviation that can be measured are related to the latitude of exposure by the equation

$$\log \frac{\xi_1 + \varepsilon_{\max} f}{\xi_1 + \varepsilon_{\min} f} = \mathscr{L}. \tag{23.11}$$

This formula, together with (23.7) and the width of the working range, defines the relationship between sensitivity and range. Thus if deviation angles of one sign are measured (the slit image is uncovered by the inhomogeneity) we can take

$$\varepsilon_{\min} = 0, \quad \mathscr{R} = \varepsilon_{\max}.$$

Then

$$\mathscr{R}S = \gamma(10^{\mathscr{L}} - 1). \tag{23.12}$$

The knife-edge and slit method is, in this case, considerably more expedient than the curved-stop method. In fact, dividing (23.12) by (22.13), we find that the ratio of working ranges for the same sensitivity (or the ratio of sensitivities for the same range) is equal to $(10^{\mathscr{L}} - 1)/\mathscr{L}$. For $\mathscr{L} = 2$ this value is equal to 50; for $\mathscr{L} = 1$ it is roughly equal to 10.

If deviation angles of the opposite sign are measured (the slit is covered), the measurement range is virtually equal to $\xi_1/f$, and the product of the range and the sensitivity is equal to $\gamma$. In this case, when using films with $\mathscr{L} > 1$, the curved-stop method is more convenient in terms of the $\mathscr{R}S$ value.

If the deviation angles are symmetrical about zero, and the knife-edge covers half the slit image, then $\mathscr{R} = 2\xi_1$, and the relation of the range, determined by the slit width, to the sensitivity is

$$\mathscr{R}S = 2\gamma f. \tag{23.13}$$

It follows from this analysis that the method is most convenient for measuring deviation angles of the same sign. In this case the knife-edge is placed so that the light deviation by the inhomogeneity will "open" the slit image. The width of the open part of the slit is selected in order to achieve sufficient sensitivity for measuring small deviation angles, and a range embracing all the expected deviation angles.

Some of the important sources of error of the curved-stop method are irrelevant here. Knife-edges are metallic as a rule, and are, therefore, totally opaque. In addition, the straight knife-edge can be manufactured with an accuracy better than 0.001 mm. This accuracy is sufficient for virtually all measurements.

Other sources of error remain important, however. Foremost among them is the constancy of the brightness within the area of the source image. But while, in the preceding case, the brightness had to be constant along the slit, here it must be constant only in the direction perpendicular to the knife-edge. The requirements pertaining to the accuracy of measurement of the differences in the emulsion density between the zero and the working photograph and to the determination of the emulsion $\gamma$ become more exacting.

It is observed from the comparison of the two methods that each has its particular domain of application. Since the measurement range and the sensitivity are independent of the position of the slit image, the curved-stop method is convenient in cases when the instrument is liable to vibrate and the slit image moves all the time. In some cases it is also more expedient for measuring deviation angles larger than $5 \times 10^{-5}$ rad. Furthermore, a distinctive feature of the curved-stop method is the simplicity of its mathematics, the measured deviation angles being proportional to the optical densities of the emulsion. The distribution of the optical densities is also the curve of the deviation angles, and in many cases the final curve of the density gradient of the gaseous flow or other measured quantity.

On the other hand, small angles of light deviation have to be measured with the maximum attainable sensitivity of the schlieren instrument, or if the measurements take place in the absence of vibrations, and the initial position of the knife-edge with respect to the slit image is well known, the knife-edge and slit method is preferable.

## 24. STANDARD METHODS

The schlieren photometric methods most widely used today are the standard methods, in which the inhomogeneity is compared with an object of known deflection properties (a schliere). It is assumed in the comparison that two areas of the object field deflecting light equally must have equally illuminated images.

The schliere is usually a set of wedges or a small-curvature lens. When a set of wedges is used, the respective images are uniformly illuminated. The points of the object image having the same illumination (the same optical density of the emulsion) as the image of a given wedge deflect the rays through the same angle as the standard wedge. A drawback of this method is that only a discrete set of angles of deviation, corresponding to the set of wedges, can be measured; the other angles have to be determined by interpolation. Furthermore, to achieve high accuracy, the number of wedges must be sufficiently large, and their size must be very small in order not to take up a considerable part of the object field. The diffraction effects increase as a result, and the accuracy of measurement drops. This question will be treated in more detail in Part II.

A spherical lens is frequently used as the standard object. The distribution of deviation angles in it is known. If the focal length of the lens is equal to $f_l$, each point will deflect the light through the angle

$$\varepsilon = \frac{r_i}{f_l}, \tag{24.1}$$

where $r_i$ is the distance from the given point of the lens to its optical center. If the light deviation in one direction only is important (for instance, $x$), relation (24.1) takes the form

$$\varepsilon_x = \frac{x_i}{f_l}, \tag{24.2}$$

where $x_i$ is the component of $r_i$ along the $x$ axis.

The standard object is photographed together with the inhomogeneity as a rule. This imposes additional requirements on the technique used in conducting the experiment. For example, it is necessary to find sections of the instrument field which do not deflect the light rays, and it is there that the standard object must be positioned. In many cases, e.g., when studying large inhomogeneities, this requirement is difficult to satisfy. Two photographs have to be taken in such a case: one with the inhomogeneity, and the other with the standard object. This leads, however, to additional errors, connected with the instability of the source brightness and the instrument adjustment. In actual experiments it is necessary to choose between these two methods after estimating their respective errors.

In measuring small angles of deviation or in accurate studies, it is frequently necessary to allow for the additional absorption in the standard object. If the transparency of the standard object is $\eta$, the illumination of its image will be equal to

$$I_l = B\eta\left(\xi_1 + \frac{xf}{f_l}\right), \tag{24.3}$$

and the equation for the angle of deviation will be

$$\varepsilon = \frac{(\eta-1)\,\xi_1}{f} + \frac{\eta x}{f_l}, \tag{24.4}$$

where $x$ is as before the projection, in the direction of the measured angle of deviation, of the segment between the center of the standard lens and the lens point at which the optical density is the same as at the relevant point of the inhomogeneity, and $\xi_1$ is the width of the slit image not covered by the knife-edge.

As indicated by Skotnikov, the width of the open slit can be eliminated from the calculation by finding a point in the standard lens with the same illumination as that of the image of a field point which does not deflect light. At this point,

$$I_1 = B\xi_1, \tag{24.5}$$

and its coordinate is determined from the formula

$$x_1 = \frac{\xi_1(1-\eta)\,f_l}{\eta f}. \tag{24.6}$$

By combining (24.6) with (24.4) we obtain

$$\varepsilon = \frac{\eta}{f}(x-x_1). \tag{24.7}$$

The additional absorption in the lens can be allowed for in this way. It is, however, necessary to keep in mind that this procedure is not accurate and leads to additional measurement errors.

The transparency of the standard schliere is usually assumed to be uniform over the entire surface, although in fact the angles of light incidence on the lens and the glass thickness are different at different points. To estimate tentatively the value of the error introduced by this approximation, we shall calculate $\eta$ for the center and the edge of an uncoated plane-convex lens of 6 cm diameter, 8 mm thickness and $f = 10$ m with $n = 1.5$. For the center, $\eta \approx 0.91$; for the edge, $\eta$ differs from the value at the center by 0.01%. Such an error can obviously be dismissed.

The absorption in the standard schliere complicates the working procedure. Accordingly, small objects are frequently studied by the semicompensated photometric method. In this method the inhomogeneity is photographed through the standard lens. The arrangement of the lens and the objective must be such that the object will occupy only a part of the lens, while the remaining part is free. The processing consists of finding the points of equal density in the image of the object and in the unobscured parts of the standard object. The angle of deviation is found from the formula

$$\varepsilon = \frac{l}{\mu f_l}, \tag{24.8}$$

where $l$ is the distance (in the image) between the points of equal density in the free part of the lens and in the object, and $\mu$ is the image scale. This method does not require corrections for the absorption in the standard object, but it is applicable only when the inhomogeneity occupies part of the instrument field. It is sometimes expedient to take two photographs: one with the inhomogeneity, photographed through the standard lens, and the second with the standard lens alone, without the inhomogeneity. This procedure can also be used for the study of large objects, but it leads to additional errors due to the variability of the experimental conditions with time.

The use of standard objects with a known distribution of angles of deviation is not obligatory. It is possible to specify a number of standard illuminations (optical densities of the emulsion). In this case a number of zero photographs are taken, each corresponding to a given position of the knife-edge with respect to the light source image. This set of photographs with different values of the optical density will be referred to as the *gray scale*, or the *density scale*.

The knife-edge is then set in some middle position with respect to the light source, and the inhomogeneity is photographed. The optical densities on the working photograph are compared with the density scale. If the densities are equal, the angle of deviation will be

$$\varepsilon = \frac{\xi_2-\xi_1}{f}, \tag{24.9}$$

where $\xi_1$ and $\xi_2$ are the knife-edge coordinates relative to the light source image with which the density scale and the working photograph are taken, respectively. To eliminate the discreteness in the measured angles of deviation and to simplify the processing, a curve $D = f(\xi)$ is plotted, and the angles of light deviation are thus determined.

A common feature of the standard methods, which constitutes a distinct advantage as compared with the other photometric methods, is that they are independent from the non-uniformity of the slit image illumination, and the regularity of the stop shape. While these deviations from ideal conditions lead to some change in sensitivity, they barely affect the measurement accuracy, since the curve $D = f(\varepsilon)$ remains monotonic.

The largest errors are due to inaccurate manufacture of the standard object and to errors in the determination of points of equal optical density.

The standard methods have some drawbacks compared with the absolute photometric methods. The points of equal density compared are located in different parts of the photograph. As a result the measurement error includes the error due to the non-uniform illumination of the instrument field and the non-uniform exposure time over the photograph. Thus the standard methods are generally not superior in accuracy to the absolute photometric methods.

The standard objects are normally standard wedges or spherical surfaces. They must be manufactured with sufficient accuracy, especially for high-sensitivity measurements. The most accurate methods of optical quality control are the schlieren and the interferometric methods. Deviations of the standard objects from the ideal shape are determined by the error of the schlieren methods used in monitoring.

Interesting possibilities are offered by the use of standard objects of a different type. In [95] the standard object was a gas-filled soap bubble. Unfortunately, the authors say nothing about the control and manufacturing accuracy of that standard object, but application of such new physical ideas can lead to the appearance of high-quality reference objects. In this case the quantitative measurement methods can be highly accurate.

As in the ordinary photometric methods, the sensitivity depends on the illumination distribution in the source image and on the shape of the stop. In addition, the accuracy of measurement of the deviation angles also depends on the distribution of the angles of deviation in the standard object. If the gradient of the deviation angles in the standard object is large, two similar angles will correspond to two close points in the standard image, and the distance between these points will be measured with a large error. Long-focal lenses are accordingly used as standard objects, since they have a small gradient of deviation angles. On the other hand, the standard schliere must simulate all the angles obtaining in the real inhomogeneity. The optimum solution accommodating these contradictory requirements is to use a lens in which the largest and the smallest angles of deviation correspond to the largest and the smallest angles obtaining in the real inhomogeneity. The measurement range is then equal, for a symmetrical inhomogeneity, to

$$\mathcal{R} = \frac{2R}{f_l}, \tag{24.10}$$

where $R$ is the radius of the standard lens. In the case of a non-symmetrical inhomogeneity it is necessary to select a lens with $R = \varepsilon_{\max} f_l$, where $\varepsilon_{\max}$ is the maximum (in absolute value) angle of deviation of the light ray in the inhomogeneity.

## 25. IMAGE ILLUMINATION

The screen plane illumination is of utmost importance in the use of photometric methods. In practical schlieren work, considerable time is lost in choosing the normal exposure, at which all the optical densities of the emulsion fall on the linear part of the characteristic curve. Precious time would be saved if it were possible to calculate the normal exposure (as a function of the speed of the emulsion).

Furthermore, knowledge of the illumination is necessary for determining the minimum angle of light deviation in the inhomogeneity which can be measured by the schlieren instrument. In order to measure small angles of deviation it is necessary to reduce severely the width of the open part of the slit image, and, consequently, to increase the measurement sensitivity. The image illumination is reduced as a result. We must, therefore, either increase the exposure time or work in the region of underexposures. During underexposure, the slope of the characteristic curve becomes smaller, and the measurement sensitivity is reduced. The increase of the exposure time leads to a time-averaging of the measurement results.

These phenomena are particularly important in the study of low-intensity transient processes, which necessitates both a good time resolution and a high sensitivity of the schlieren measurements.

The image illumination can be determined by the formula

$$E = \frac{I\alpha^2\xi\tau\mu'}{16\pi l R^2 \mu^2}, \tag{25.1}$$

where $I$ is the luminous flux of the light source, in lumens, $\alpha$ is the aperture of the main objective of the schlieren instrument ($\alpha \approx 2R/f$), $\xi$ is the width of the open part of the slit image, $\tau$ is the transmission coefficient of the optical system, $l$ is the mean width of the light source in the direction perpendicular to the slit, $R$ is the radius of the main objective, $\mu$ is the scale of the inhomogeneity image, and $\mu'$ is the scale of the source image.

This formula is based on certain simplifying assumptions, i.e., the light source is assumed to radiate uniformly in all directions, and the aperture of the main objectives is the smallest of the apertures limiting the luminous flux.

The magnitude $l$ is determined with sufficient accuracy for filament lamps which have an incandescent body of regular geometrical shape. In the case of mercury discharge lamps, on the other hand, the luminous body does not have a regular geometrical shape; in addition, the brightness distribution over the discharge is non-uniform. In these cases $l$ is defined as some mean size of the luminous body.

With the aid of formula (25.1) it is possible to find the optimal conditions for the projection of the luminous body on the illuminating slit of the schlieren instrument.

The equation for the sensitivity of measurements yields

$$E = \frac{I\tau\gamma\mu'}{4\pi\mu^2 S L f}, \tag{25.2}$$

where $L$ is the size of the light source image in the direction perpendicular to the knife-edge.

To obtain maximum illumination in the schlieren image, the light source should be projected on the slit with the largest possible magnification. It is, however, necessary to keep in mind that, first, the increase of the source image is accompanied by an increase of main objective aberrations, and, second, the image cannot be made larger than the slit. Last, for a condenser objective of given speed, the aperture of the illuminating beam decreases with the increase of the image scale. And yet, the beam aperture must not be smaller than the aperture of the main objectives, in order to fill the instrument completely. This requirement must be fulfilled with a comfortable margin in order to facilitate the adjustment.

Due to all these factors, it is not possible to increase the image brightness substantially by changing the source image scale, although attempts have been made to vary this parameter. When searching for the optimum, we should allow for the specific conditions (shape and size of the luminous body, required range and sensitivity of the measurements). In most cases the optimal solution is $\mu' = 1$ (this is, in fact, the solution used in the Soviet-made instruments IAB-451, TE-19, and TE-20).

To determine the exposure time necessary for obtaining normally exposed negatives, we should take into account the emulsion characteristics. The speed of the emulsion is usually defined as the inverse of the exposure providing a density of 0.2 higher than the fog. The speed is thus linked with the other characteristics of the emulsion by the formula

$$s = 10^{(b-0.2)/\gamma}. \tag{25.3}$$

By combining (25.3) with the equation for the optical density of the emulsion, we obtain

$$D - 0.2 = \gamma \log Ets, \tag{25.4}$$

where $t$ is the exposure time, and $E$ is defined by (25.1). By combining (25.4) and (25.1) we obtain an equation for the exposure time which is a function of the required density:

$$t = \frac{16\pi l R^2 \mu^2}{I\alpha^2 \xi \tau s \mu'^2} 10^{(D-0.2)/\gamma}. \tag{25.5}$$

The results of the calculation of the exposure time for the IAB-451 and TE-19 instruments are represented on Figure 79. The transmission coefficient for IAB-451 was taken equal to 0.25, for TE-19 to 0.06. The speed of the Mikrat-200 film was taken equal to 4 with $\gamma = 3.2$. For the A-2 film, $s = 140$ units with $\gamma = 0.95$. The luminous flux of the K-10 filament lamp was taken equal to 650 lumens, and that of the DRSh-250 mercury discharge lamp to $10^4$ lumens.

It is seen that when IAB-451 instrument is combined with K-10 lamp and A-2 film, the open part of the slit can be reduced to 0.02 mm at exposure times longer than $10^{-2}$ sec. This is almost sufficient for all schlieren measurements, since aberrations and diffraction phenomena prevent work with narrower open slits. Thus processes allowing an exposure time longer than 0.01 sec can be studied at the maximum sensitivity of the schlieren instrument.

The situation is different in the study of transient processes, requiring ultrahigh speed cinecameras or flash light sources. The exact calculation in such a case is not given here, since its practical value is doubtful in view of the large variety of light sources and cinecameras used. Experience demonstrates that in the study of objects with an exposure time shorter than 1 $\mu$sec, it is difficult to reduce the width of the open part of the slit below 0.1 mm, which makes impossible the study of objects deflecting the light rays by less than $5 \times 10^{-6}$ rad.

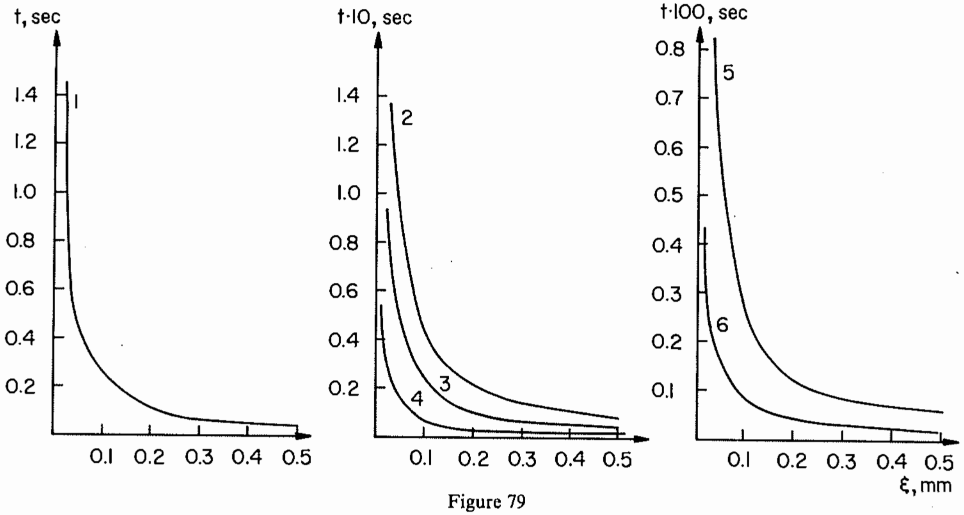

Figure 79

The exposure time as a function of the width of the open part of the slit image for different instruments, light sources and films: 1) TE-19, K-10, Mikrat-200; 2) IAB-451, K-10, Mikrat-200; 3) TE-19, K-10, A-2; 4) IAB-451, K-10, A-2; 5) TE-19, DRSh-250, A-2; 6) IAB-451, DRSh-250, A-2.

When the schlieren pattern is observed visually, the increase of the instrument sensitivity is accompanied by an increase in the image contrast. Simultaneously, however, the image illumination and the contrast sensitivity of the eye decrease. Finally, at very low image illuminations, a point is reached when the drop of the contrast sensitivity of the eye is larger than the increase in the sensitivity resulting from the reduction in the width of the open part of the slit image. The eye no longer notes inhomogeneities which it could observe earlier. It follows that there do exist a minimum size of the open slit and a smallest measurable angle of deviation in the inhomogeneity, characteristic for the instrument–eye system.

The capacity of the eye to distinguish between objects is determined by the threshold contrast, which is expressed by the formula

$$K_{\text{th}} = \frac{\Delta B}{B}, \tag{25.6}$$

where $B$ is the mean brightness of the field against which the object is observed, and $\Delta B$ is the minimum brightness increment between the background and the object for which the eye still distinguishes the object. The empirical relationship between the value of the threshold contrast and the background brightness for different angular sizes $d$ of the object is represented on Figure 80 [40].

The parameters of the individual human eye affect the threshold sensitivity substantially. They differ considerably from person to person. The pupil size, for instance, varies between 1.5 and 8 mm. We shall base our calculations on a "standard" eye, having the following mean parameters: refractive index of the lens, 1.33; radius of curvature of the refracting surface, 5.7 mm; first focal length, 17.1 mm; second focal length, 22.8 mm; power of the lens, 58.48 dioptres; and radius of curvature of the retina, 9.7 mm.

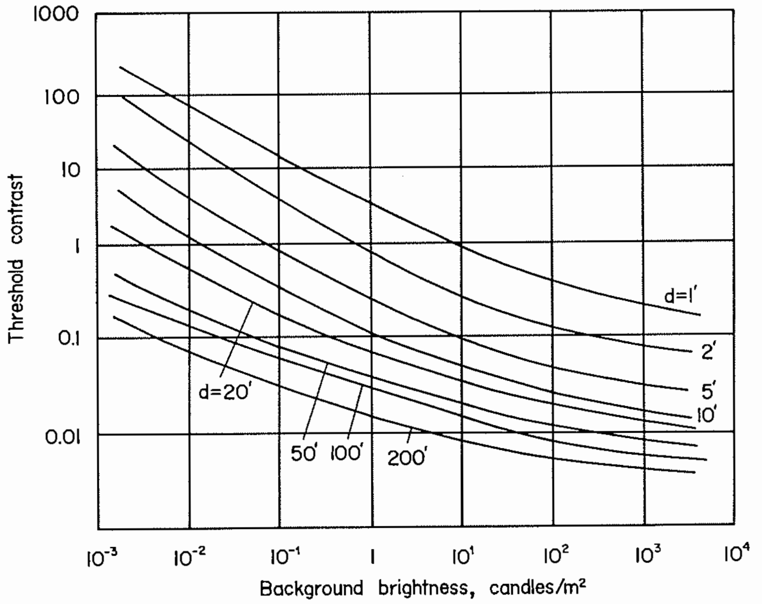

Figure 80

Threshold contrast as a function of the background brightness for different angular dimensions of the object.

We shall calculate the width of the open part of the slit image for which the illumination is such that the threshold contrast is 1% or 5% for different instruments and light sources. It is seen from Figure 80 that these values of the contrast are obtained for $B = 8$ candles/m² and $B = 6 \times 10^{-2}$ candles/m². The calculation by formula (25.2) leads to the results given in Table 1.

The values of $\xi_{\min}$ given in Table 1 are the minimum values of the width of the open slit for which the relationship between the image illumination and the light stimulus in the eye is still described by the Weber–Fechner law. In this case the angle of light deviation can be derived from the brightness ratios in the image. In parts of the image having a lower illumination, this relationship becomes more complicated.

Table 1

| Instrument | Light source | Values of $\xi_{\min}$ in mm for | | | |
|---|---|---|---|---|---|
| | | $B = 8$ candles/m², $\Delta B/B = 1\%$ | | $B = 6 \cdot 10^{-2}$ candles/m², $\Delta B/B = 5\%$ | |
| | | Frosted glass | Magnifying glass 5 × | Frosted glass | Magnifying glass 5 × |
| IAB-451 | K-10 | 1.65 | $5 \cdot 10^{-3}$ | 0.012 | $4 \cdot 10^{-4}$ |
| | DRSh-250 | 0.16 | $5 \cdot 10^{-4}$ | $10^{-3}$ | $4 \cdot 10^{-6}$ |
| TE-19 | K-10 | 2.6 | $8 \cdot 10^{-3}$ | 0.02 | $6 \cdot 10^{-5}$ |
| | DRSh-250 | 0.25 | $7.5 \cdot 10^{-4}$ | 0.002 | $6 \cdot 10^{-6}$ |

It was assumed in the calculations that the effective brightness of the image on frosted glass is double the brightness of a screen scattering the light uniformly in all directions. This is so because 70% of the light incident on frosted glass reaches the observer and also because the observations are made in an almost perpendicular direction to the frosted glass plane, and in this direction the quantity of light is larger than in other directions.

As we see from Table 1, the observation of the image on a frosted glass does not always lead to the desired results. The minimum permissible slit width in this case is fairly large, especially for the linear section of the eye characteristic. This section is the most convenient for observations, since at lower illuminations the eye requires a long time to adapt to the weak light and to acquire maximum contrast response. The minimum width of the lens in this case is tenths of a millimeter, which is insufficient for many processes.

It is considerably more expedient to conduct the observations through a magnifying glass, which increases the image illumination on the retina to a large extent. In the calculation of the maximum instrument sensitivity compatible with the brightness requirements, it is necessary to take into account the small aperture of the light beam illuminating the inhomogeneity. The eye pupil does not restrict the light beams coming from the inhomogeneity. The final formula for the minimum width of the open part of the slit image whose illumination corresponds to the linear section of the eye characteristic is

$$\xi_{\min} = \frac{4\pi^2 L f^2 r_e^2 B_{\min} \mu^2 \mu_l^2}{625 I \tau}, \tag{25.7}$$

where $r_e$ is the eye pupil radius and $B_{\min}$ is the minimum brightness corresponding to the straight portion of the curve. For $\Delta B/B = 1\%$ it is equal to 8 candles/m$^2$ just as in the preceding case; for $\Delta B/B = 5\%$, $B_{\min} = 6 \times 10^{-2}$ candles/m$^2$.

It is observed that here the insufficient brightness of the light source does not restrict the sensitivity. The minimum width of the open part of the slit image is considerably smaller than the widths usually met in practice. The maximum sensitivity of measurements is limited by other factors, such as aberration, diffraction, etc.

By means of a similar calculation it is possible to determine the minimum angle of deviation which can be measured in the visual method of observation. It is equal to

$$d\varepsilon = \frac{\xi_1 (\Delta B/B)}{f}. \tag{25.8}$$

Since $B$ (and thus also $\Delta B$) depends on $\xi_1$, the illumination parameters, and the properties of the eye, it is possible to construct the function $d\varepsilon = f(\xi_1)$ giving the smallest measurable angle for different widths of the open slit. It follows from the calculation that, even for a relatively poor case (TE-19 with K-10), the increase of the instrument sensitivity with the reduction of the slit width exceeds the decrease in the contrast sensitivity of the eye down to a width of 0.01 mm. Narrower slits are not used in practice.

With a magnifying glass, the eye virtually always functions under ideal conditions.

## 26. APPLICATION OF PHOTOMETRIC METHODS

Each of the quantitative photometric methods has its specific difficulties in practical applications. Thus the absolute photometric methods necessitate repeated determinations of the emulsion $\gamma$, since it is variable along the same spool of film.

The following method of conducting the experiment was found to be convenient: a series of graded attenuators is prepared, each in the form of a strip with sections of different photographic density. The attenuators are contact-printed on the film on which the schlieren pattern will be photographed. The "zero" and "working" photographs are taken in such a way that they are located inside windows formed by the attenuators (Figure 81).

The attenuators can be prepared in different ways — by sputtering with silver, from gray glass, by photographing a gray scale, etc. The densities of the grades are measured with a densitometer. They should be chosen so as to ensure a constant density difference between adjacent grades.

A photometric measurement is taken of each attenuator, and the density of each grade is determined. The $\gamma$ is equal to the slope factor of the linear portion of the characteristic plotting the density of the images of the scale grades on the test film as a function of the density of the original strip grades themselves (Figure 82). The $\gamma$ is determined for each of the seven strips. If all the $\gamma$ values coincide, we can be fairly certain that the zero and the working photographs have the same $\gamma$.

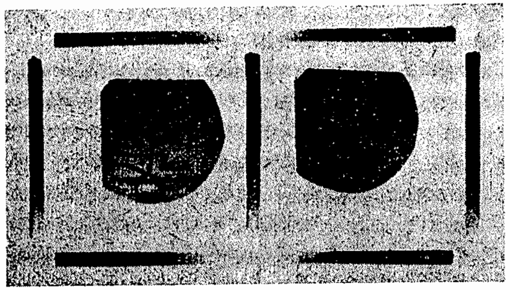

Figure 81

Experimental photographs in the absolute photometric method.

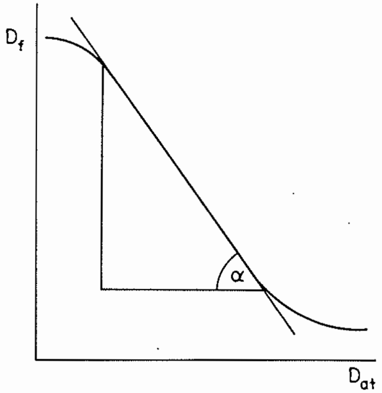

Figure 82

Determination of $\gamma$.

In this way $\gamma$ can be determined with a much higher accuracy than when a single attenuator is used. The measurement error is 0.03–0.05.

It should be kept in mind that the emulsion $\gamma$ depends on the spectral composition of the light source and the exposure time. The attenuators, therefore, have to be contact-printed under the same conditions as when the zero and the working photographs are shot, with the same light source and the same exposure.

If the shooting and developing conditions are standardized, the $\gamma$ need not be measured each time, and may be considered as constant for the entire batch of film. In this case it is necessary, however, to conduct control measurements of $\gamma$ for different film strips out of the same batch, in order to check its constancy. In addition, uniform development conditions (composition of the developer, freshness, temperature, and development time) must be ensured for all the photographs.

Experience shows that the constancy of $\gamma$ under industrial conditions is questionable; the fluctuations of $\gamma$ are larger than the measurement accuracy in each photograph (0.05) and, therefore, this method is normally used for studies which do not require a high measurement accuracy.

It is convenient to use a pen-and-ink recording microphotometer for measuring the zero and the working photographs. In such experiments photometric tracings are taken for the relevant sections on the zero and the working photographs (curves 4 and 3 in Figure 83) together with the dark-current tracing of the photocell, which serves as the reference line. The coordinates of the various points are then measured. The difference between the optical densities is equal to the logarithm of the ratio of the distances from each of the curves to the reference line:

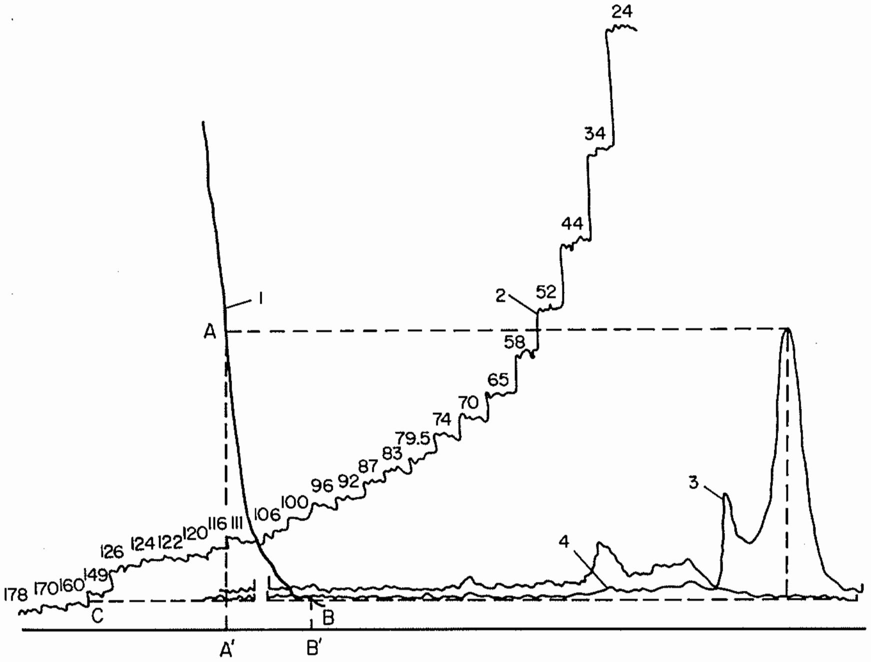

Figure 83

A microphotometer tracing: 1) reference lens; 2) photometry of a graded attenuator; 3) section of the working photograph; 4) section of the zero photograph.

$$D_2 - D_1 = \log(y_2/y_1). \tag{26.1}$$

This method is useful when the distribution of deviation angles is not known in advance. It is then possible to find on the microphotometer tracing the characteristic points at which the angles of light deviation should be determined. It is inconvenient, however, when the distribution of the measurement points in the section is known and their position has been established. In this case, the recording stage and the subsequent processing consume much more time than in point-by-point photometry. Furthermore, the accuracy is lower than with the last method.

A pen-and-ink recording microphotometer can also be used for processing photographs taken with a standard lens or wedge. The section of the working photograph and the section of the standard lens or wedge (curve 1 of Figure 83) perpendicular to the knife-edge are recorded. The advantages and drawbacks of the pen-and-ink microphotometer are the same as in the previous case.

When standard methods are used, the main sources of error are the nonuniformity of the illumination of the instrument field and differences in the exposure time over the photograph due to the finite speed of the shutter. In accurate measurements it is necessary, therefore, to take a zero photograph without the inhomogeneity and the standard lens and to check the constancy of the optical density. If the density is found to vary, a correction must be introduced in the measurements. In this case, we have to measure the difference between the optical densities of the points of the zero photograph corresponding to the points of the inhomogeneity and the standard lens where the image illumination is the same. The angle of deviation is then equal to

$$\varepsilon = \eta \cdot 10^{(D_1' - D_1)/\gamma}\left[\frac{\xi_1}{f} + \frac{x}{f_l}\right] - \frac{\xi_1}{f}. \tag{26.2}$$

For $D_1' = D_1$, formula (26.2) reduces to the ordinary formula of the standard methods (24.4). The coefficient $\eta \cdot 10^{(D_1' - D_1)/\gamma}$ is equivalent to the $\eta$ for a uniformly illuminated field, but it varies from point to point, which complicates the measurements considerably. In practical studies this coefficient is usually close to unity and, accordingly, it is frequently advisable to use the simplified formula (24.2) with tentative measurements.

An interesting application of the photometric schlieren methods is the quantitative study of moving shock waves. Flash light sources are used to photograph these objects. The wave travels a finite distance during the flash duration, and its image is consequently blurred. It is possible, however, to determine the refractive index gradient in the shock wave.

The difference between the optical densities at a point of the blurred schlieren image of the wave and the corresponding point of the zero photograph is given by (in the knife-edge and slit method)

$$D - D_0 = \gamma \log \frac{\int E(t)[\xi_0 + \varepsilon_x(t) f]\,dt}{\int \xi_0 E(t)\,dt}, \tag{26.3}$$

where $E(t)$ describes the time dependence of the flash source brightness, and $\varepsilon_x(t)$

expresses the time dependence of the angles of deviation in the direction $x$, perpendicular to the knife-edge.

Let the knife-edge be set so that the direction of the measured component of the angles of deviation coincides with the direction of motion of the compression shock; equation (26.3) is then transformed to

$$D-D_0 = \gamma \log \left[ 1 + \frac{\dfrac{f}{\xi_0}\displaystyle\int E(t)\frac{dn}{dt} L \frac{dt}{dx}\, dt}{\displaystyle\int E(t)\, dt} \right]. \tag{26.4}$$

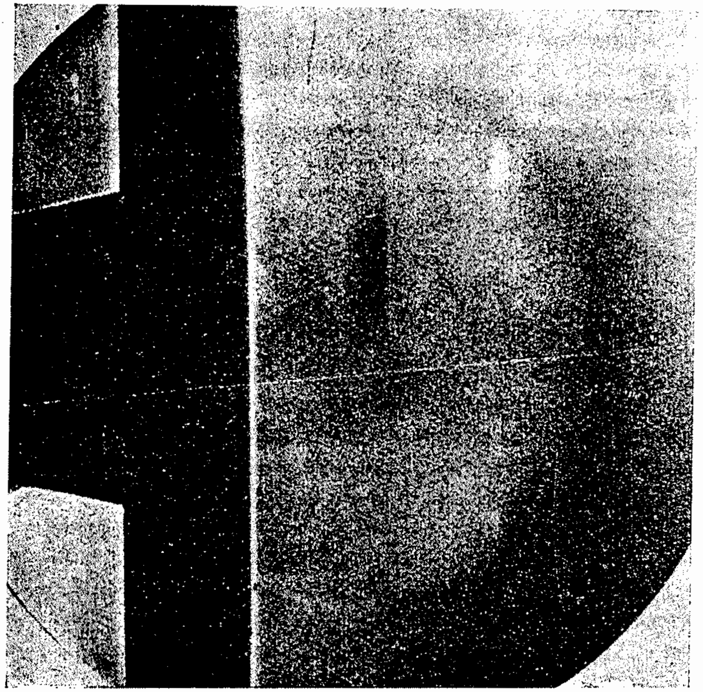

Figure 84

Photograph of gas flow from a shock tube.

Let the velocity of the moving inhomogeneity be constant for the duration of the light flash and let the time for the inhomogeneity to cross an image point be considerably shorter than the flash duration. It can be assumed in this case that the source brightness varies insignificantly during the passage of the wave through the image point. Then

$$D-D_0 = \gamma \log \left[ 1 + \frac{f E_0 L \Delta n}{\xi_0 v I} \right], \tag{26.5}$$

where $E_0$ is the source brightness at the time of passage of the wave through the measured point, $\Delta n$ is the variation of the refractive index in the compression shock,

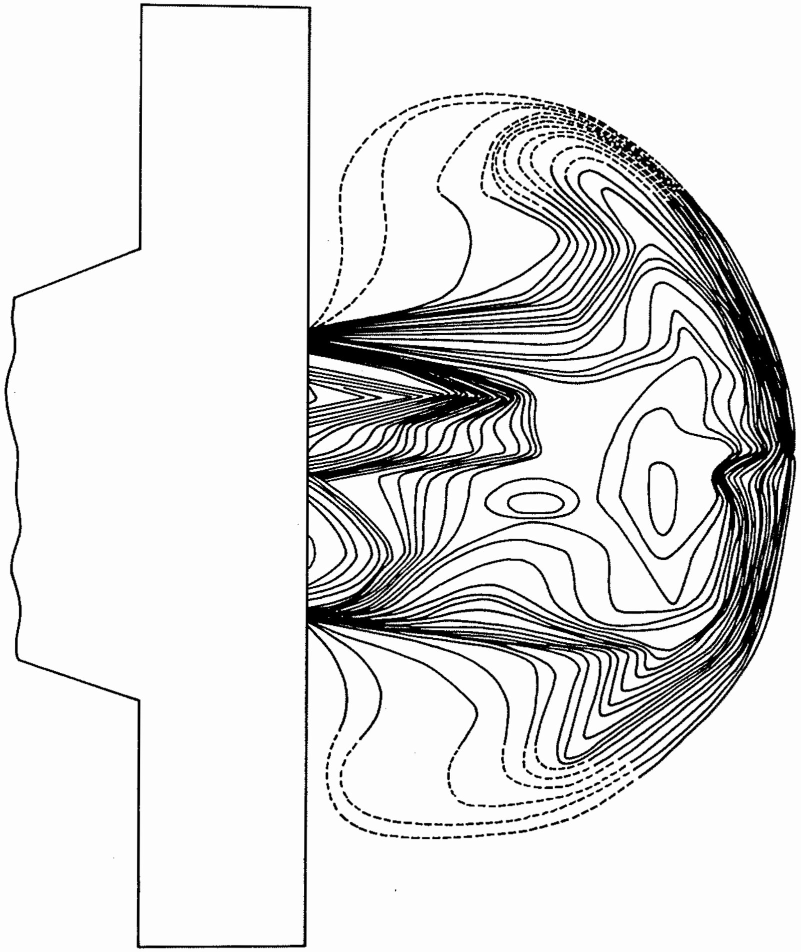

Figure 85

Density distribution in the gas flow shown on Figure 84.

$v$ is the velocity of the inhomogeneity, and $I = \int E(t)\,dt$ is the integrated flash intensity. It is convenient to conduct the measurements at the point where $E$ is maximum. This point is easily found.

In practical measurements it is convenient to transform (26.5) into an explicit function of the measured parameter:

$$\Delta n = \left(10^{(D-D_0)/\gamma} - 1\right)\frac{\xi v I}{f L E_0}. \tag{26.6}$$

Diffraction phenomena must be allowed for in measurements of this type, since the measurements are taken in the region of fast changes of the wave front. This method should be used, therefore, when the moving inhomogeneity is sufficiently wide, and when a sufficiently large source giving a sharp image of the inhomogeneity cannot be obtained.

An example of the practical application of the quantitative photometric method of the knife-edge and the slit is the measurement of the gaseous flow from a shock tube. The process is brief and, accordingly, a spark of effective duration of 2 $\mu$sec was used. The wave velocity was roughly equal to 5 km/sec. One of the photographs obtained is shown on Figure 84. Qualitative measurements give the shape of the shock wave and the contact surface, and the extent of the zone of uniform parameters in the driver gas. From the quantitative measurement of the angles of light deviation, we find the gas density distribution in the flow, as represented on Figure 85. The comparison of the schlieren pattern with the curve of gas density distribution demonstrates that the absolute photometric methods eliminate the illumination non-uniformities caused by poor quality of the protective glasses and by other similar factors.

# VI

# SOVIET-MADE SCHLIEREN INSTRUMENTS

## 27. IAB-451

IAB-451 is the schlieren instrument which is most widely used in the USSR today. It is based on Maksutov's design. The instrument layout is represented in Figure 86. The instrument consists of two units — the illuminating part (collimator) and the receiving part. Each unit is a metallic tube 240 cm long with a maximum diameter of 320 mm. The weight of each tube is approximately 150 kg.

A carriage, supporting a slit and a condenser with a light source, is attached to the collimating unit. A similar carriage in the receiving unit carries the knife-edge attachment and the attachment for observing and photographing the schlieren image and viewing the illuminating slit image. The length of the condenser attachment together with the projection lamp housing is 300 mm.

Either the K-10 filament projection lamp (50 W, 12 V) or the DRSh-250 high-pressure mercury discharge lamp can be used as the light source $S$. Suitable lamp housings ensuring the necessary ventilation and alignment controls are included in the instrument set. Power is supplied through a transformer. Whenever necessary, the instrument can operate with other light sources, such as flash lamps, unconfined sparks, etc. The power supply and the control circuitry for such light sources are built by the user. To permit operating with an unconfined spark, the instrument is supplied with an additional long-focus lens, making it possible to set the illuminating assembly at a considerable distance from the condenser lenses. This is done to avoid damaging the surface of the first lens by the spark discharge.

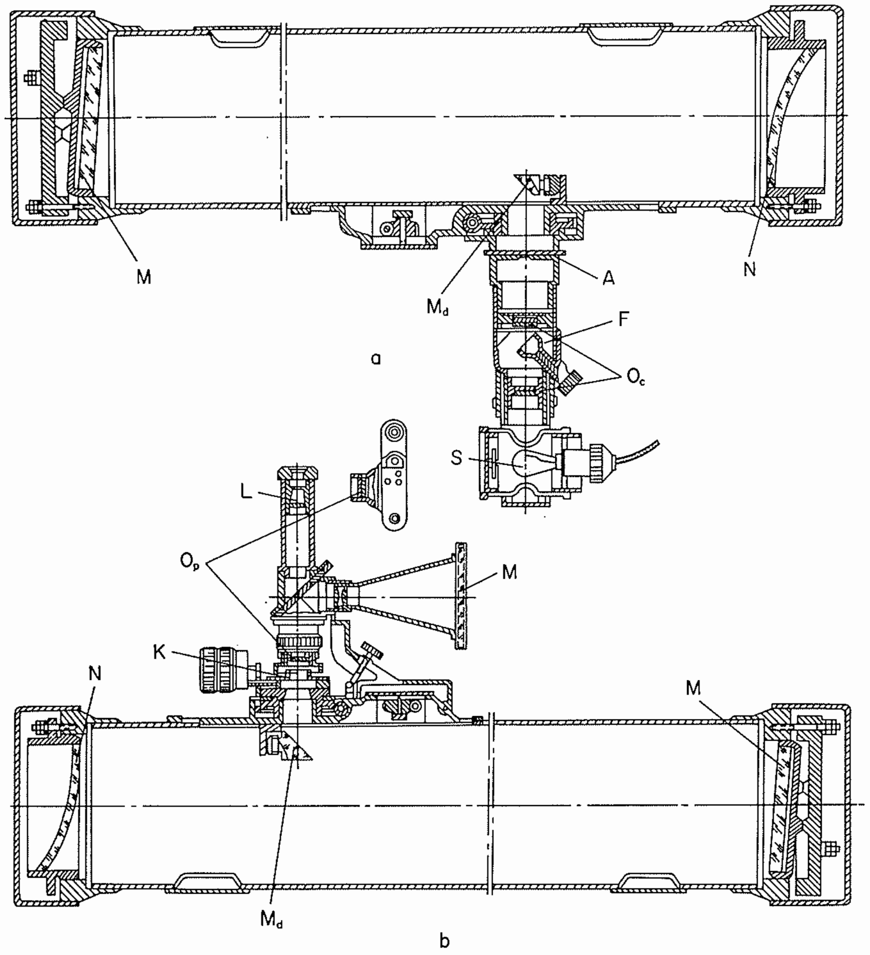

Figure 86

The optical system of the Soviet-made schlieren instrument IAB-451: *a* illuminating unit, *b* receiving unit.

The condenser is a system of two objectives $O_c$, made of two bonded lenses, 23 mm in diameter and 65 mm focal length. The second objective projects the image of the luminous part of the light source — the lamp filament or the discharge gap — on the entrance slit aperture $A$ of the instrument. The first objective can be moved along the optical axis of the instrument, focusing the source image on the slit. For visual adjustment control, a prism is mounted between the second condenser lens and the slit. It enables us to see the light source image on the outer surface of the slit cheeks, facilitates the centering of the image on the slit, and allows coarse focusing of the source image.

A revolving drum with light filters $F$ is placed between the condenser lenses and the parallel light beam; it alternately inserts the different filters, which are 3 mm thick and are made of different grades of glass (ZhZS-12, ZhS-18, and KS-14). The transmittance curves of these filters are represented in Figure 87. In practical work, light filters are frequently used in adjustment operations, e.g., when observing the slit image in the focal plane of the main objective of the receiving unit; without a light filter the eye is dazzled and the adjustment accuracy is considerably poorer. They are little used in actual experimental work; their only function in this case is to decrease the total luminous flux (in some photoelectric measurements) or to isolate a limited spectral region (when using diffraction methods). Usually, however, special filters are used for the latter purpose, which can isolate any strong line of the source.

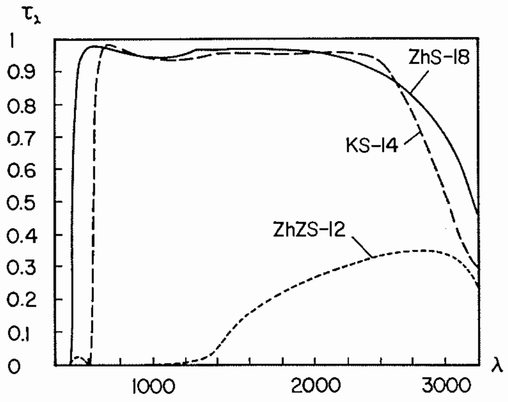

Figure 87

Transmittance curves of the light filters in the IAB-451. The wavelengths are in millimicrons.

The entrance slit aperture $A$ of the schlieren instrument can be varied between 0 and 3 mm with a reading accuracy of 0.01 mm. Its length is 25 mm; it can be stopped by a stepped diaphragm to 2, 4, 6, 8 mm, and by a wedge diaphragm to any size from 0 to 10 mm. Instead of a slit aperture, we can use point grids with hole diameters of 3, 1, 0.3, 0.1 mm.

The slit can be rotated through 360° about the optical axis together with the condenser attachment. The accuracy of measurement of the angle of rotation is 6′. The entire condenser attachment, together with the diagonal mirror $M_d$ is mounted on a carriage which can be moved by 25 mm in either direction, with an accuracy of 0.01 mm, along the body of the instrument. The slit aperture thus can be brought to the focal plane of the main objective of the illuminating unit.

The light reflected from the diagonal mirror $M_d$ falls on the main objective of the illuminating unit. A similar objective is also used in the receiving unit. The optical system of the objective is shown in Figure 88. The objective (see Figure 86) comprises the mirror $M$ and the meniscus $N$, manufactured in such a way that they both are parts of larger components. The light diameter (and accordingly the maximum size of the inhomogeneities which can be studied with this instrument) is 230 mm. The focal length is 1917.6 mm. The presence of a meniscus with surfaces of almost equal curvature reduces considerably the aberration of the spherical mirror.

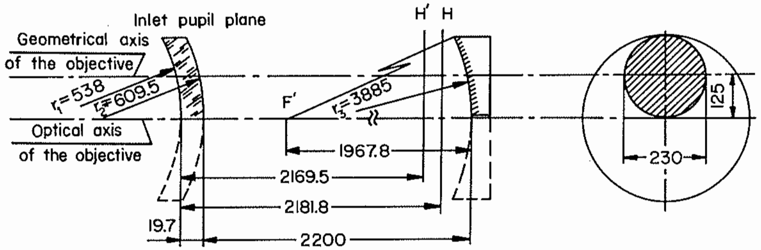

Figure 88

Schematic cross section through the objectives in the IAB-451.

The main objectives of the receiving and the collimating unit are cut and mounted opposite each other so that their nonsymmetrical aberrations cancel. The total aberration of the instrument is thus smaller than the aberration of each of its parts.

The inhomogeneity can be bracketed between a pair of protective glasses, which is helpful for processes in vacuum or when mechanical protection is required.

The mirror and the meniscus can be moved for the purpose of alignment. Covered openings are provided in the instrument body, through which the instrument can be cleaned and the diagonal mirrors are aligned. Supporting rings and pads on the instrument fit into the pedestal supports.

The angles of the light beam axis to the optical axis is the same in the receiving and the collimating unit. The IAB-451 is thus a parallel-beam Z-type instrument.

The light reflected from the diagonal mirror $M_d$ of the receiving unit reaches the Foucault knife-edge $K$. Filaments of various thicknesses may be used instead of the knife-edge. The knife-edge can be rotated through 280° about the optical axis, with a reading accuracy of 6′, and thus set parallel to the illuminating slit image for any position of the slit.

The knife-edge is removable. It is held in special recesses and fastened by holding pawls. The fastening is symmetrical, and the knife-edge can be rotated through 180° and fixed on either side of the illuminating slit image without using the rotating device.

The knife-edge attachment is mounted together with the photographic unit and the second diagonal mirror on a carriage similar to the collimator carriage. By moving it along the instrument body, we can bring the knife plane to coincide with the illuminating slit image plane focal position of the knife-edge in the receiving unit) or impart a certain defocusing to the viewing diaphragm. The displacement limits are ± 25 mm from the mean position, with a reading accuracy of 0.1 mm.

The photographic unit of the instrument is set on a hinged bracket, attached to the carriage. The optical unit consists of two lenses $O_p$. The first lens is positive with $f' = 136.2$ mm and a light diameter of 27 mm. It can be moved ± 20 mm along the optical axis, giving a sharp image of objects situated at distances between 200 and 4000 mm from the end of the receiving unit tube. The image scale is somewhat altered as a result. The calculations are carried out for the mean position of the inhomogeneity, at a distance of 2000 mm from the tube end. The second lens is part of a removable photographic attachment. There are two such attachments. One of them is a standard Soviet-made *Zorkii* camera with $f' = -51.31$ mm and image diameter of 24 mm. The second attachment gives an image 80 mm in diameter; it uses a lens with $f' = -199.95$ mm and a 9 cm × 12 cm film.

A revolving holder is mounted between the lenses of the photographic objective, permitting the insertion of a semitransparent or a completely reflecting mirror. By covering the aperture with an opaque mirror, we can conduct observations in each arm in turn. The insertion of a semitransparent mirror makes possible simultaneous viewing or photographing of the schlieren image by two observers or two cameras. Simultaneous photography on two different scales or simultaneous observation and photography are also possible.

The standard exposures of the *Zorkii* camera are used for the 24 mm film. With 80 mm film, a shutter giving exposures from 1 sec to 0.004 sec is used.

The instrument is also provided with lens caps, hoods for the condenser and the photographic unit and magnifying glasses for monitoring the knife-edge setting.

The exit aperture of the receiving unit is 40 mm in diameter. As a result, only inhomogeneities deflecting the light by no more than 36′ can be viewed. A restriction on large deviation angles is also imposed by the rim of the first photographic lens. It vignettes the parts of the field which deflect light by 24′ if they are located at the center of the instrument field, and by 19′ if they lie at the periphery. (This calculation was made for a zero curvature of the wave front. If the wave front has a considerable curvature and shifts the point of convergence of the rays in the direction opposite to the direction of defocusing of the diaphragm, the maximum angles of light deviation in the inhomogeneity which can be measured by this schlieren instrument may be much smaller.) This measured range is sufficient for most gas-dynamic processes, the angles of deviation being much smaller than the limiting value.

The original IAB-451 is a limited-purpose instrument and is unsuitable for application with many of the methods. Its great advantage lies in the possibility of separating easily the condenser and the photographing unit from the main objectives. As a result, various optical or mechanical attachments, each intended specifically for work with a single method, can be designed and used with the instrument. Examples are the previously described attachments for color schlieren photography, for large defocusing, for photoelectric recording, a measuring microscope, various cinecameras, etc. [11]. A variety of attachments make the instrument suitable for almost all types of schlieren measurements, without appreciably increasing its price. The attachments can be built by any mechanical workshop. The improved instrument in which these refinements are introduced is designated IAB-453 (see §29).

## 28. TE-19

The TE-19 is much more versatile and much smaller in size than the IAB-451. It was designed by a team headed by V. K. Efimov. The optical system was designed by N. N. Gubel. The light diameter of the main objectives is 150 mm, the focal length 1500 mm.

The optical system of the instrument is shown in Figure 89. Like other types of mass-produced schlieren instruments, TE-19 is made of two separate units — a collimator with a light source and a receiving part. However, the overall dimensions of the instrument are considerably reduced owing to multiple refractions in the main objectives of the two units and the use of objectives consisting of separated elements. Dimensions of the collimating unit: length 950 mm, height together with the illuminator 1150 mm, width 400 mm; dimensions of the receiving unit: 950 mm × × 400 mm × 400 mm. The combined weight of the two units is 200 kg.

Because of its smaller size, the TE-19 is more convenient in practical work. The instrument does not require a special support, it becomes easier to manipulate the test object, and additional measuring instrumentation can be installed on the same premises. This is undoubtedly a great advantage of this instrument.

The instrument has three lamp housings, two lateral and one on top. Incandescent lamps and high-pressure mercury discharge lamps can be used in each of the lateral lamp housings. Mercury discharge lamps are not used in the top lamp housing, since according to the manufacturer's specifications they can burn in a vertical position only. The much wider range of light sources than for the preceding instrument provides a better fit to the conditions of different experiments.

The lamp housings are interchangeable. They are equipped with a spherical reflector placed behind the light source, which nearly doubles the light flux. An additional adjustment is required, however: the image of the luminous body formed by the reflector must be as near as possible to the light source, since only in this case is it possible to sharply project both images on the slit and to achieve a satisfactory uniformity of the field illumination. Each lamp housing is provided with the necessary alignment controls. Cooling of the housing surface is enhanced with the aid of fins, so that these sources can be used continuously over long periods.

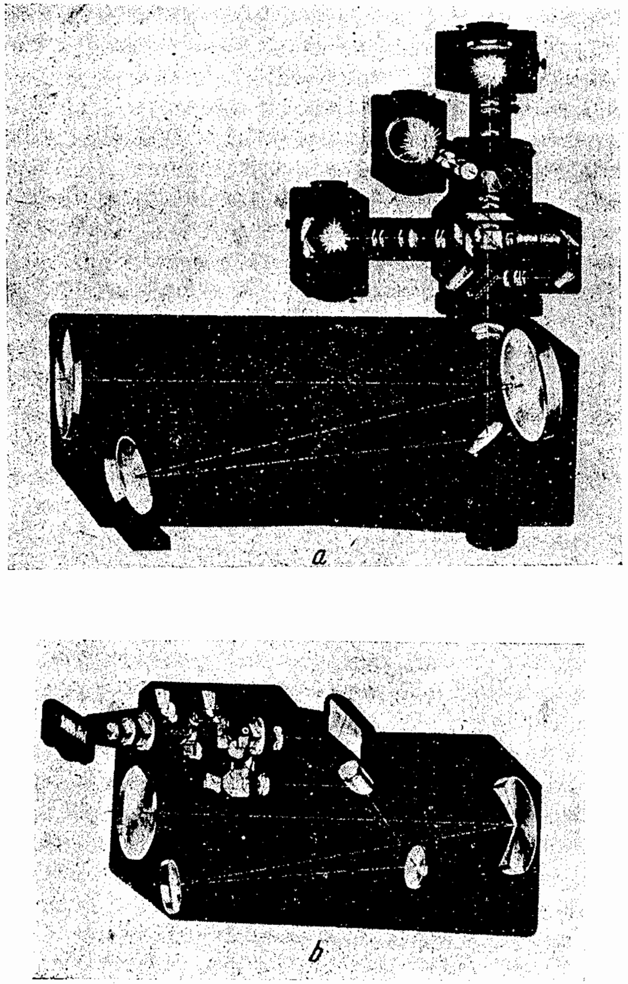

Figure 89
The optics of the Soviet-made TE-19 instrument: *a* illuminating unit, *b* receiving unit.

The two-lens condenser projects the image of the luminous body on the entrance slit. One of the lateral lamp housings has a permanent slit assigned to it. The second slit may alternately receive illumination from the top housing or the second lateral housings. The switchover is effected by interposing a diagonal mirror in the light beam. The light sources are thus easily interchanged (by remote control if necessary).

The first lens of the condenser is covered by interference filters having a transmission half-width of about 20 Å. The wavelengths transmitted by the basic set of filters were selected so as to make possible work with the mercury lines and other frequently used spectral regions. Some filters can be ordered by the experimenter according to his particular requirements.

Polaroids are provided in the side arms of the illuminator. The planes of polarization in the two arms are mutually perpendicular.

The height of each slit can be altered in steps of 2 mm from 2 to 10 mm; the slit width can be varied continuously between 0 and 2 mm with an accuracy of 0.01 mm.

Having passed through the slit, the light reaches a splitting block, and then the two light beams are delivered to the main objective of the collimator. By introducing a mirror on the other side of the splitting block, we activate the color attachment, which disperses the slit image into a spectrum and projects it in the position originally occupied by the slit image. Therefore, with a correctly aligned instrument, no additional adjustment is needed when the ordinary image is replaced with a color pattern. The spectrum width can be altered between 0 and 30 mm by rotating the Amichi prisms in opposite directions. Color photography methods thus can be applied in the entire range of deviation angles measurable by this schlieren instrument. The color attachment can function only with one of the lateral light housings.

The entire illuminator can be rotated through 100°, and we can therefore use the instrument for different angles of slit inclination relative to the object. The rotation is effected either by means of a handwheel or by remote control, with an accuracy of 6′.

The collimating and the receiving units use identical main objectives, made of two spherical mirrors and an afocal compensator. The objectives form a Z-type system, reducing substantially the coma and the distortion of the point image in the focal plane of the receiving unit. The afocal compensators are set near the focal planes of the main objectives. The positive lenses of the compensators are moved at right angles to the optical axis until the astigmatism is corrected. The compensators also lead to a substantial decrease in the spherical aberration.

The objective mirrors are decentered, and the image of the slits in the receiving unit is therefore inclined. The image plane of the illuminating slits is made to coincide with the knife plane by inclinating the illuminator slits between 15 and 18°.

The quality of the optical system of the collimating and the receiving units depends on the combined effect of the two units and can be defined by the maximum size of the disk of confusion in the focal plane of the receiving unit. Strictly speaking, the schlieren instrument performance is affected only by the aberrations in the direction perpendicular to the knife-edge. Therefore, the objective should be characterized not only by the maximum size of the disk of confusion, but also by its shape and the energy distribution in the disk. However, the knowledge of the maximum size of the disk of confusion is sufficient for estimating the upper-bound sensitivity for all measurements. The angular diameter of the disk of confusion for points on the axis is equal to 0.9″, and the linear diameter is 0.007 mm. For points an angular distance of 8′, which corresponds to a distance of 3.5 mm from the optical axis, the aberrations vary between 4″ and 11″ for different directions. Note that the actual distribution and the magnitude of the aberrations depend on the instrument adjustment, and are therefore different for different instruments of the same type.

We can assume that the average aberrations for a 7 mm long slit are roughly equal to 6″, and the instrument can thus measure deviation angles as small as 0.5″. If this sensitivity is insufficient in high-precision measurements, we must reduce the slit size. The sensitivity can be increased in some cases by selecting the knife-edge position in such a way that the astigmatic aberrations stretch point images in the direction parallel to the knife-edge. In this case, the sensitivity is not determined by the maximum magnitude of the aberrations, but by some smaller figure. Naturally, in order to elucidate the possibility of increasing the sensitivity in this way, we have to know the distribution of the instrumental aberrations and the distribution of the angles of light deviation in the inhomogeneity.

The light emerging from the main objectives of the receiving part reaches the splitting block, whence the two beams are directed to the two arms of the receiving unit. A polaroid intercepts each beam. By a suitable orientation of the polaroid we can extinguish the light in one of the arms without considerably attenuating the light from the second working lamp. The image of one of the slits is extinguished. In the second arm, the other slit image is extinguished. Thus the image of the object in each arm of the photographic unit is illuminated by light from one of the two mutually perpendicular slits. The result is equivalent to an assembly of two schlieren instruments covering the same field. The unique feature of this design is that the light from the two instruments traverses the inhomogeneity at the same angle, which is unfeasible in systems where the light beams in each arm are split by means of prisms or mirrors only.

This two-in-one instrument produces a new qualitative effect: we can conduct simultaneous measurements in two mutually perpendicular directions. The ordinary schlieren instrument, which usually measures the angle of deviation in one direction only, does not give the instantaneous distribution of the refractive index in the inhomogeneity, whereas the combination instrument recovers this distribution. A shortcoming of this beam-splitting method is that the polarization system does not completely extinguish one of the slit images. Moreover, only half the extinguished slit image is covered by the knife-edge but most of the second slit image is obscured, especially in high-sensitivity measurements. As a result, the light coming from the extinguished slit image lowers the instrument sensitivity.

If the two slits are of length $L$, the polaroid reduces the brightness of the extinguished slit image to $1/n$ of the original value, and the exposed part of the slit is of width $\xi_0$, the total image illumination will be

$$I = BL\left(\frac{1}{2n} + \frac{\xi_0}{L}\right). \qquad (28.1)$$

The sensitivity of measurements is determined in this case by the expression

$$S = \frac{f}{L/2n + \xi_0}. \tag{28.2}$$

The relative drop in sensitivity compared with the ideal instrument is equal to

$$\frac{S_{\text{id}}}{S} = 1 + \frac{L}{2n\xi_0}. \tag{28.3}$$

For $L = 2n\xi_0$ the sensitivity is reduced by half. Modern instruments have $n \sim 100$. For $L = 10$ mm, this leads to difficulties when the width of the exposed part of the illuminating slit image reaches a few hundredths of a millimeter.

The light extinction by the polaroids is not uniform over the instrument field. Some parts of the field are brighter than others. This complicates the application of many quantitative methods of measurement, such as the method of standard inhomogeneities. Moreover, a partial depolarization of the light accompanies refraction from the mirrors. This complicates the qualitative and quantitative interpretation of the schlieren pattern and lowers the sensitivity.

The diameter of the exit pupil is 40 mm. This makes the instrument suitable for measuring inhomogeneities at the center of the field which deflect the light through 45′. The maximum angles of deviation which can be measured at the edge of the instrument field are much smaller, due to the vignetting caused by various optical components (most components have dimensions comparable with the width of the undeflected light beam). When using the method of defocused grids with the maximum attainable defocusing, restrictions are also imposed by the insufficient size of the camera objectives.

Two separate images of the object are obtained in the image plane, corresponding to different directions of the viewing diaphragm. Each image can be observed visually through an eyepiece. The insertion of an additional lens makes it possible to observe alternately the image plane of the inhomogeneity with the schlieren pattern and the plane of the viewing diaphragm with the illuminating slit image. The magnification of the replaceable eyepieces is 4 × or 8 ×. This gives considerable advantages in the adjustment of the instrument and makes possible an easy and accurate control of the adjustment stability in the course of the experiment.

By moving the mirrors apart, we can displace the point of convergence of the rays along the optical axis of the instrument. The displacement is smooth within ± 150 mm, with an accuracy of 0.1 mm.

The instrument set is provided with a number of different viewing diaphragms, which can be used instead of the knife-edge; these include filaments, grids, curved stops. The diaphragm fastening assembly permits rotating the diaphragms through 360° with an accuracy of 6′. The knife-edges are displaced within ± 15 mm from the optical axis with an accuracy of 0.01 mm.

Revolving mirrors alternately direct the image to the eyepiece for visual observation and to the photographic cameras.

Cinecameras or standard still cameras can be used as the photographic attachment. They can be activated by remote control, using electromagnets.

While the TE-19 has the advantages of compactness and versatility, it also has several drawbacks. 1) All the instrument attachments are mounted in the same housing. As a result, the customer cannot order a stripped-down model and must pay for the accessories which he may not need. 2) Due to the complexity of the instrument and the large number of optical components, it is beyond the user's power to align the instrument, as he was able to do with the IAB-451. Furthermore, the instrument goes frequently out of alignment and needs servicing by authorized technicians. 3) Due to the complicated design, it is difficult to modify the instrument and to adapt it to new measurement methods. 4) The light absorption coefficient is much higher than in simpler instruments.

## 29. IAB-453

Each of the two instruments described above has considerable drawbacks, which lower its value and make it inapplicable to some types of schlieren measurements. In our opinion, there exists a different and more promising procedure for developing schlieren instruments. It consists in designing a series of basic objectives for schlieren instruments, differing in the diameter of the field of view, the focal length, and the quality of the point image. The set of lenses can be relatively small. The objectives with parameters listed in Table 2 meet the requirements of most measurements.

Table 2

| $D$, mm | $f$, mm | $R$ |
|---|---|---|
| 50 | 500 | 2.5″ |
| 100 | 1000 | 1.2″ |
| 200 | 2000 | 0.5″ |
| 400 | 4000 | 0.3″ |

Simplified objectives with the same $f$ and $D$, made of simpler and cheaper optical components, can be used for lower quality measurements. Rejects of high-quality objectives can also be sold for such measurements.

A number of attachments are manufactured, each intended for a specific measurement method: photoelectric recording, color schlieren photography, high-speed photography, etc. Each attachment is designed in such a way that it can be used with minimum alterations with any main objective of the receiving or collimating units.

The existence of a range of objectives and standardized attachments enables each investigator to select the methods and instrument parameters which are the most suitable for his experiment. The possibility to order a custom-made instrument assembled of standard components makes this instrument highly attractive from the points of view of price and versatility. The standardization of the components is also advantageous to the manufacturer. Furthermore, the fact that to each method correspond its own exclusive components makes the instrument highly accurate and easy to operate. Finally, the instrument will not be made obsolete by the development of new schlieren methods, since all one has to do is to design some suitable new attachments. The use of interchangeable attachments offers wide possibilities for the improvement of schlieren methods and the development of new measurement techniques.

We shall describe in this section the IAB-453 instrument, designed on the basis of these principles by a team headed by V. K. Efimov and V. G. Koskovskii. The instrument is the first of a projected series, which is to satisfy all the needs of schlieren measurements. Preliminary calculations show that it satisfies the requirements of the experimenters better than all other existing instruments. The IAB-453 is an improved version of the IAB-451; a technical description of the improvements and the underlying principles is given in [3, 11, 20].

The basic layout of the instrument is the same as that of the IAB-451. It consists of two parts accommodating identical mirror–meniscus objectives, which serve as main objectives of the collimating and the receiving units. Mobile carriages are provided outside the two tubes; the carriage in the collimating unit bears a removable illuminator, and the carriage in the receiving unit a removable hinged bracket and the knife-edge attachment. The interchangeable attachments are connected to the two units of the instrument.

The basic dimensions and characteristics of the instrument are similar to those of the IAB-451. The field of view diameter is 230 mm, the focal length of the main objectives is 1904.3 mm, the depth of focus is 4 m from the receiving unit exit; the weight of each tube is 150 kg, its length is 2.5 m, and its maximum diameter 32 cm.

The instrument is intended for measuring light deviation angles between 0 and 25′ in optical inhomogeneities. The maximum sensitivity attained with photographic measurements (for $\gamma = 2$) is $2 \times 10^5$, so that inhomogeneities deflecting the light by an angle of $5 \times 10^{-7}$ rad or 0.1″ are visualized with a contrast of 10% (if we do not consider errors due to diffraction phenomena and external causes).

The main objective is a mirror–meniscus system, designed by N. N. Gubel. The image quality over the field was improved, at the cost of a certain deterioration of the quality of the point image on the optical axis, by introducing afocal compensators similar to those used in [133b]. As a result, we can use longer illuminating slits without a marked decrease in sensitivity, which leads to an increase in the actual sensitivity of the instrument for transient processes, requiring flash sources or high-speed cinecameras.

In the IAB-451 the aberrations of the objectives in the receiving and the collimating units cancel out, whereas in the new setup each unit is corrected separately. The Z-shaped design is thus replaced by a more convenient arrangement: the experimenter is free to rotate each tube about its optical axis until he finds the best position for conducting the measurements.

The basic components are fastened in the same way as in the IAB-451, since this system has proved itself on the whole. Some improvements have been introduced, however. The sealing of the rims (especially of the meniscus rim) has been improved. To reduce the effect of vibrations, the rims of the meniscus and the mirror are clamped radially from three directions.

The carriage was made more massive. It can be displaced along the axis by ± 150 mm from the zero position. "Coarse" and "fine" controls have been introduced. The carriage has fixtures for setting up various interchangeable multipurpose attachments.

The principal optical axis of the mirror–meniscus objective does not coincide with the geometrical axis of the instrument, being distant 125 mm from the axis. The center of the object being studied lies on the geometrical axis of the instrument, and therefore all the attachments are set on the geometrical axis. The knife and the slit image are situated at the intersection of the geometrical and the optical axes; they are perpendicular to the optical axis, while making an angle of 4° with the geometrical axis. As a result, the plane of the slit image and the knife plane coincide. The carriage moves along the geometrical axis, and therefore the defocusing of the instrument does not affect the position of the inhomogeneity image on the screen.

The multipurpose applications of the instrument made necessary the use of various light sources. Ordinary incandescent lamps with a coil filament are the most convenient for instrument alignment and in qualitative studies not requiring a high time resolution. They are sufficiently stable and simple in use. However, such lamps are unsuitable for exact quantitative studies, since the filament does not possess a uniform brightness in the direction perpendicular to the illuminating slit image. Ribbon-filament incandescent lamps are used in such experiments. Since the luminous part of the ribbon defined by the slit is of fairly uniform brightness, absolute photometry is used with a much higher accuracy with these light sources.

Due to their low luminance, incandescent lamps cannot be used when the schlieren instruments work in conjunction with high-speed cinecameras, since they necessitate longer exposures than those corresponding to the linear part of the emulsion characteristic. High-pressure mercury discharge lamps, which possess a much higher luminance, are used in such cases; they will work with motion picture cameras giving up to $10^6$ frames/sec for a 0.2 mm wide illuminating slit image.

Finally, we must also consider transient processes. Flash sources are frequently convenient for their study, since they can be easily synchronized with the process and yield a higher resolution than that obtained with a high-speed cinecamera. Flash lamps giving flashes of duration between 0.1 $\mu$sec and 1 msec can be used with the IAB-453. The control systems of these lamps are manufactured separately from the instrument set, in accordance with the particular problems to be treated.

The varied range of light sources permits using the schlieren instrument for practically all types of studies. Provision has also been made for synchronizing the flash lamps with cinecameras; in this case the lamps operate in the stroboscopic mode with a flashing rate equal to the camera rate. Such arrangements are used if we film the process at a relatively low rate using a short exposure time for each frame.

The light sources are placed in two lamp housings, fastened to the two arms of the illuminating unit. The two lamp housings and a switch mirror, alternating between the two light sources, is a highly useful feature. Indeed, the alignment of the receiving unit (setting the viewing diaphragm in the image plane of the illuminating slit, setting the knife-edge parallel to the slit image, etc.) is very difficult when a flash light source is used; in this setup, we can align the unit with an incandescent lamp, and then switch over to the flash source. Furthermore, it becomes possible to control the adjustment stability. In addition, by replacing the reflecting mirror with a semitransparent one, we can use two light sources simultaneously; by using two flash lamps, we can obtain two images of moving objects and transparent inhomogeneities on the same frame, and so determine their velocity.

The light source can be displaced within ± 10 mm in the lamp housing, and as a result its image produced by the condenser can be rapidly brought to coincide with the illuminating slit of the instrument. The image is focused by displacing the condensers in each of the arms. Focusing accuracy is controlled through a window with a prism and a semitransparent mirror through which the position of the light source image on the slit can be observed. Crossed polaroids can be used to reduce the light flux in the case of high-luminance sources; such flux attenuation is needed to achieve a more accurate adjustment.

Light filters are placed between the two lenses of the condenser. Green, yellow, and red glass filters and interference filters are included in the instrument kit. Filters can also be placed in the receiving unit of the instrument in front of most photographic attachments.

The main slit of the schlieren instrument has a maximum height of 10 mm and an aperture range between 0 and 3 mm with a reading accuracy of 0.01 mm. Stops are provided in the slit planes, varying the slit height in discrete steps to 1, 2, 4, 6, 8, 10 mm. It is also possible to use round stops 3, 1, 0.3, 0.1, 0.03, 0.01 mm in diameter. The slit height is reduced when working with a light source whose points are located near the optical axis of the system. This decreases the experiment errors connected with aberrations of the main objective, inaccurate manufacture of the knife-edge, and adjustment errors. Round sources are used in the determination of the direction of the light deviation angles in an inhomogeneity, for instance when using the method of point grids.

The instrument can also be ordered with a high-precision slit, having an aperture range from 0 to 0.4 mm with an adjustment accuracy of 0.001 mm. The high quality of the slit edges makes this slit much more convenient for use with the diffraction and photometric methods, and especially in absolute photometry. The measurement sensitivity is somewhat increased, and the errors caused by curved edges of the slit, nonparallel cheeks, inaccurate determination of the uncovered part of the illuminating slit image, etc., become smaller.

The illuminating unit (Figure 90) can be rotated together with the slit through 270° about the geometrical axis, and therefore the instrument can be used for different orientations of the illuminating slit with respect to the instrument field. A measurement accuracy of 6′ suffices for almost all measurements. By disconnecting the fine control, we can rapidly bring the slit to the required position. The rotation is facilitated through the use of bearings.

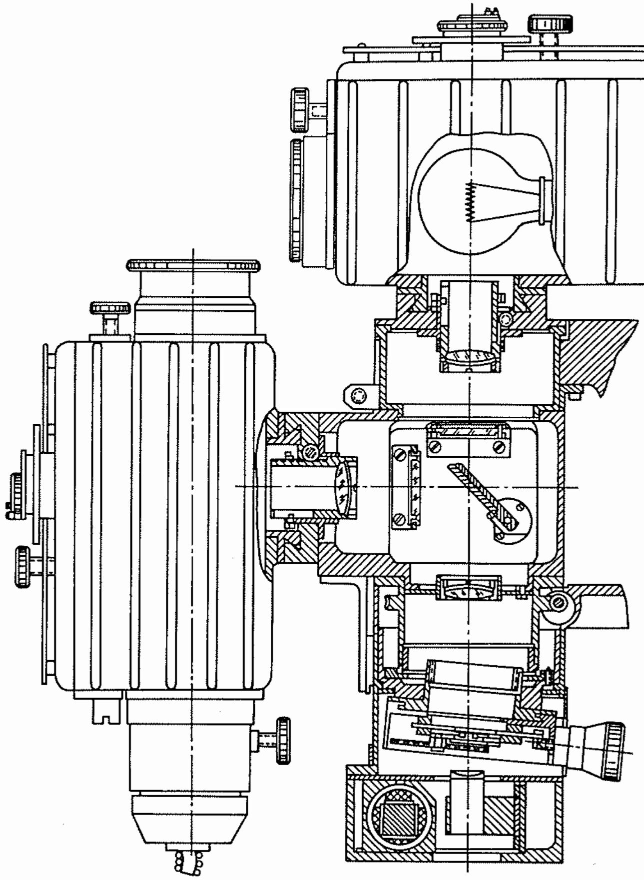

Figure 90

The illuminating unit of the IAB-453.

A color-photography attachment is mounted between the illuminator and the main objective of the collimator. The spectrum formed by the prisms is observed in the focal plane of the main objective of the collimating unit. The schlieren system is converted to a color system by a simple rotation of the prisms; there is almost no need for an additional adjustment.

When working under standard conditions, the color photography accessories do not participate in the formation of the schlieren pattern. This improves the quality of the schlieren instrument, since it increases the light transmittance of the instrument and reduces the possibility of misalignment in the course of the experiment.

The spectrum width is controlled by rotating the prisms about the optical axis. The prisms are turned in opposite directions symmetrically with respect to the zero position. If the prisms are set in the same position, the spectrum width is maximum; if they are rotated through 180°, the spectrum width is zero, and we observe an undispersed slit image, somewhat weakened by the absorption of light in the color attachment. The maximum width of the spectrum, defined as the distance between the lines at 4342 Å and 6563 Å, is equal to 10 mm, which corresponds to a measurement range of $5 \times 10^{-3}$ rad.

The total transverse aberrations of the color attachment do not exceed 0.02 mm. These aberrations fix a lower bound of $10^{-5}$ rad for the angles of light deviation which can be measured with the aid of this unit.

The carriage mobility permits accurate mounting of the illuminating slit (or of its spectral dispersed image) in the focal plane of the main objective of the collimating unit. This is usually superfluous, however; by setting the carriage in its middle position, according to the manufacturer's instructions, we bring the slit to coincide with the focus with sufficient accuracy.

The receiving unit carriage is similar to the collimator carriage. It carries the knife-edge attachment, provided with suitable controls.

The viewing diaphragm, set in the knife-edge attachment, can be displaced by ± 25 mm perpendicular to the optical axis, with a reading accuracy of 0.01 mm. It can also be rotated through 360° about the optical axis, with a reading accuracy of 6′. Since the diaphragm also can be displaced along the geometrical axis together with the carriage, it is easy to set it in the required position with respect to the illuminating slit image. The specific setting procedure depends on the method used and is described in the appropriate sections.

Besides the knife-edge, several other types of viewing diaphragms can be used. The IAB-453 is provided with a set of curved stops with a pitch of 0.1, 0.2, 0.3, 0.6, 1.5, 3 mm, which measure deviation angles from 0 to $6 \times 10^{-3}$ rad with a sensitivity (for $\gamma = 2$) between $9 \times 10^3$ and $3 \times 10^2$. The multiplicity of all the stops is equal to 2, the smallest value of the gap is 0.4 mm. We can also use a phase knife-edge, introducing an additional path difference of $\lambda/2$.

The instrument is equipped with a set of filaments 0.01, 0.02, 0.04, 0.08, 0.16, 0.5, 1, 2 mm wide, which are used in the methods of focal filament, color photography, and diffraction interferometry. A 20 mm high slit of width variable between 0 and 3 mm (with an accuracy of 0.01 mm) can be used with the filaments. The instrument is also supplied with gratings of 5, 2, 1, 0.5, 0.2, 0.1 mm spacing. The ratio of the grating spacing to line width is 2. Point grids with the same spacing and with point diameters equal to the line width of the grating are also included in the kit. The grids are shifted from the focus by moving the receiving unit carriage, which can be displaced by ± 150 mm from the zero position. The grids also can be set in front of the diagonal mirror at a distance of 150 mm from the place where the knife-edge is set. Thus the position of the grid with respect to the focal plane can be altered between + 150 and − 300 mm.

The knife-edge can be replaced by a diffraction grating, transforming the schlieren instrument into an interferometer.

The instrument is also supplied with a range of standard lenses, of focal lengths of 2, 6, 20, 60, 150, 200 m, for use with standard schliere methods. The size of each lens is 60 mm. The range of angles given by the lenses covers the range of the schlieren instrument. Since the focal length of the lens affects only the sensitivity and the measurement range, both of which are known approximately in each experiment, a relatively large tolerance, equal to 10%, is allowed for this quantity. The focal length is measured with an accuracy of not less than 2% (for long-focus lenses) and is marked on the lens rim. When photographing standard schliere and conducting actual measurements, the origin of coordinates is taken at the center of the lens. To facilitate these measurements, the lens center is marked with an opaque disk, clearly observed on the photograph.

A right-angled prism manufactured with an accuracy of 10″ is used for monitoring the parallel setting of plane models to the optical axis of the instrument.

One of the important operations in the highly sensitive knife-edge and slit method is the setting of the knife-edge parallel to the slit image and the accurate measurement of the size of the uncovered part of the slit. A microscope mounted on the receiving unit carriage is used to that end. The microscope magnification is 45 ×, and the field of view is 0.2 m. The width of the uncovered part of the slit image is measured with an accuracy of $3\mu$ by an eyepiece micrometer. The microscope is set in such a way that the inaccuracy in the position of the microscope objective with respect to the knife-edge and the eyepiece focusing error will not introduce an error larger than $2\ \mu$ in the measurement of the width of the uncovered part of the slit image.

The possibility of measuring the width of the uncovered part of the slit image prior to the actual measurements does not always meet with unanimous approval, since the position of the image can change in the course of the measurements due to vibrations, heating of the instrument, or other causes. In order to record such displacements of the image, the microscope is equipped with a camera which photographs the slit image simultaneously with the object. A prism set in the microscope objective cuts a length of 1–2 mm from the illuminating slit image. The remaining light forms a schlieren image. With this attachment, we not only control the constancy of the relative position of the knife-edge and the slit image, but also measure the size of the open part at the instant when the photograph is taken. By placing a high-speed camera or a photoelectric system behind the microscope eyepiece, we can record the time variation of the slit image position, which is particularly important when studying vibrations and determining their influence on the schlieren instrument readings.

A retractable hinged bracket attached to the carriage supports a housing with two yokes to which the photographing devices and eyepieces are attached. The first lens of the photographic objectives, which is the same for all the photographic attachments used, is placed inside the housing. The attachment is focused, with this lens on the inhomogeneity. A hinged mirror directs the light in turn to each of the two receiving units. A semitransparent mirror can be used instead of the reflecting mirror, in which case simultaneous photographs can be shot in the two arms of the instrument. The general view of the receiving unit is shown in Figure 91.

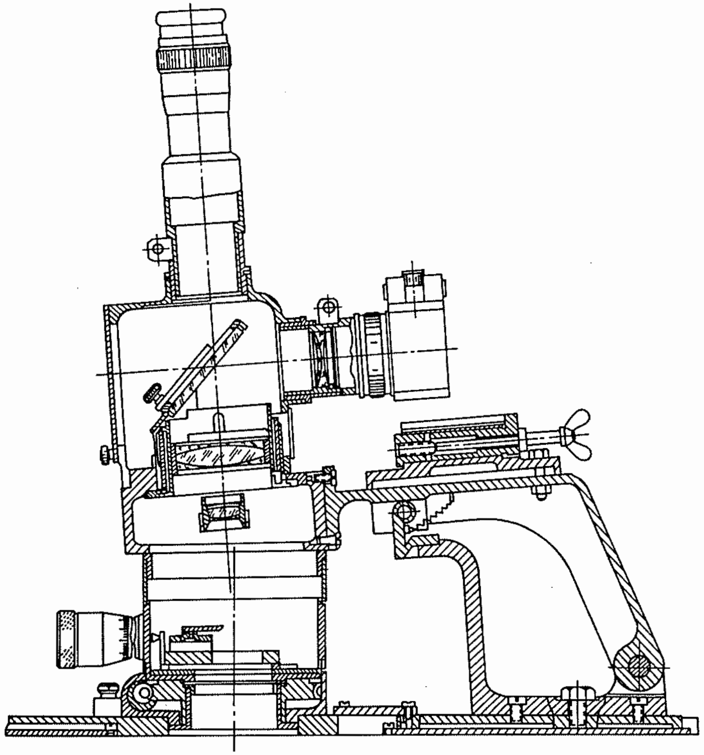

Figure 91
The receiving unit of the IAB-453.

All the focusing and mirror changing operations are conducted after the protective cover is thrown open by pulling the outside handle. An additional lens is similarly introduced, projecting the image of the knife plane instead of the inhomogeneity plane. This lens is necessary when adjusting the instrument. It is convenient to replace the photographic attachments by visual observation eyepieces, with a magnification of 5 × or 10 ×. The rapid insertion of an additional lens is very advantageous, since it permits finding the dependence of the schlieren pattern on the knife-edge position with respect to the slit.

Attachments for photographing the inhomogeneity can be mounted anywhere on the body of the instrument. They give a field image of 24, 60, and 120 mm. The use of attachments of different scales is essential, when the diffraction phenomena are weak and the resolving power is determined by the aberrations of the photographic objective and the emulsion graininess. If the source brightness is sufficient for obtaining the image of a large inhomogeneity, it is efficient to use large-frame attachments, since the number of details in the image will be greater than with other attachments. On the other hand, an attachment with a small frame is efficient in the case of inadequately bright sources or for a strong diffraction phenomena.

The instrument can also be supplied with a photorecorder, which comprises a light hollow drum geared to an electric motor. A film strip approximately one meter long is wound on the inner surface of the drum. With the aid of a prism, an image 24 mm in diameter is projected onto the film. Usually, the schlieren instrument field is limited by a slit when using the recorder. The linear velocity of the film can be varied between 20 and 185 m/sec. The recorder dimensions are 550 mm × × 350 mm × 420 mm, its weight is 50 kg; it is therefore necessary to mount it on a separate pedestal in the receiving unit of the instrument. A synchronizing device emits a signal for every revolution of the drum or at 10° intervals during each revolution. It is used when the recorder operates with shutters or flash light sources.

A two-channel photoelectric attachment has been designed for the study of transient processes. This is a separate attachment, connected to the receiving unit of the schlieren instrument. The optical system of this attachment forms an image of the instrument field 60 mm in diameter. Two slits are used to cut small portions from the image. The slit width can be altered between 0 and 2 mm with an accuracy of 0.01 mm. The height of the slits can be made equal to 1, 2, or 3 mm. A light pipe transfers the light from each slit to the cathode of a photomultiplier. A cathode follower is mounted alongside the photomultiplier. The two blocks with slits and photomultipliers can be displaced independently of each other along the same guiding line perpendicular to the optical axis. The guiding line can be translated or rotated about the optical axis. Each of the slits can be brought by these operations to any point of the schlieren image. As is usual in photoelectric recording, the signal from each photomultiplier is delivered to the input of a two-beam oscillograph or to a separate oscillograph. The photoelectric recording system used in the IAB-453 permits recording the illumination changes at two points of the process under study.

It is possible to achieve almost any time resolution up to $10^{-7}$ sec. This is quite sufficient for most schlieren measurements.

The IAB-453 thus can be used with all the current schlieren methods. From this point of view, it is superior even to the universal TE-19. But, unlike with the latter instrument, each method is implemented independently of the others. This constitutes a substantial advantage in practical work: the instrument adjustment is simplified, the difficulties connected with extraneous effects, ghosts, light scattering, etc., decrease.

The design of the instrument as a basic unit plus specialized attachments for the different methods makes it easily adaptable to the implementation of new schlieren and similar methods. Polarization and interferometric methods of viewing optical inhomogeneities, can be easily implemented with the instruments.

## 30. QUALITY OF THE SCHLIEREN INSTRUMENT COMPONENTS

Size and aberration calculations of the schlieren instruments and the main requirements regarding the quality of the optical and mechanical components are not unlike those usually encountered in optical instruments manufacture. However, there exist several distinctive features characteristic of the schlieren instruments, which are discussed below.

In the first place, the schlieren instrument is made of two units. The first and basic unit shapes the light wave front passing through the inhomogeneity and forms an image of the light source at the viewing diaphragm. Its main components are the diaphragm stopping the intermediate image of the light source formed by the condenser; the main objectives of the receiving and collimating parts; the protective windows restricting the inhomogeneity; the viewing diaphragm. The second unit contains the light source and the condenser objectives, also the photographic objectives and the recording instrumentation.

The size and the precision of the illuminating and the viewing diaphragms and of the main objectives are interrelated; they depend on the values of the light deviation angles in the inhomogeneity. The instruments used in practice are most varied. Strong explosion waves are studied with mirrors from large-diameter projectors, which are of relatively poor optical quality. The velocity of motion of strong waves in shock tubes is measured using small-diameter photographic objectives. Gaseous objects and precision components of astronomical optics are studied by means of instruments using long-focus astronomical objectives, with resolving power almost equal to the diffraction limit of resolution. Such instruments are widely used, and they are applied to schlieren studies in almost all the branches of science and engineering. Their main components are large mirrors whose shape remains ideal up to $\frac{1}{4}$ or $\frac{1}{10}$ of the light wavelength.

The required manufacturing precision is determined by the character of the inhomogeneity and the method of measurement used. With defocused grids or absolute photometry, the initial bending of the wave front is allowed for and hardly affects the measurement error. Standard comparison methods have more exacting requirements. In practice, however, every instrument is used with various methods. Therefore the deviations of the wave front from a plane wave should always be considerably smaller than the smallest measured angles of light deviation in the inhomogeneity.

Additional requirements are imposed by the necessity of operating the instrument over long periods of time. The external reflecting coat, made of silver, aluminium, or rhodium, must be sufficiently durable to withstand cleaning or washing. The coat may be covered with a special protective film. Nevertheless, the cleaning of large mirrors is a complex operation and should not be performed too often. Under industrial conditions special measures must be taken to protect the instrument from dust, oil drops, etc. A tightly fitting hood, when used correctly, will minimize the necessity of cleaning the main mirrors, even in a very soiled atmosphere.

Particular attention must be paid to the selection, control, and maintenance of the performance parameters of the protective glasses. Their optical properties must ensure a good point image in the focal plane of the main objective of the receiving unit. The glasses, however, may be wedge-shaped or even introduce a constant curvature of the wave front, since these distortions are easily corrected by displacing the knife-edge along the optical axis. Deviations of the refractive index of the glass from its nominal value, light absorption, and double refraction are of no significance, and the glass may be of poor quality in terms of these characteristics. As regards optical homogeneity, however, the glass must be of the highest quality. It must be entirely free of knots. Bubbles in the glass are somewhat less critical, but the standards here are nevertheless exacting.

Since the protective glasses are subjected to mechanical or chemical effects, their strength and chemical stability under the action of specific reagents must satisfy certain requirements. Particular attention should be paid to the aging of the protective glasses. The surface properties change under the continued action of fast particles and a periodically changing pressure: there appear minute craters, microfractures, surface deposits. As a result, the optical and mechanical properties of the glasses are altered. A provision must therefore be made for protective screens in the design of instruments. Periodical check of the glasses is also very important.

The quality of the condenser and the photographic unit is almost the same for maximum sensitivity instruments and for less accurate ones. The main function of the condenser is to illuminate uniformly the instrument field through the illuminating aperture. The condenser aperture must be somewhat larger (by a factor of 1.5 to 2) than the aperture of the main objectives. The quality of the objectives is determined by the uniformity of the source luminance. Simple objectives of low resolving power can be used as condensers. The quality of the optical components of the photographic unit depends on the resolving power of the instrument. A high quality is usually necessary, which calls for suitably corrected photographic objectives, giving a resolution of 40–60 lines/mm at the center of the field. The schlieren image being usually $\frac{1}{3}$ to $\frac{1}{10}$ of the inhomogeneity, the resolution in the object plane is roughly equal to 10 lines/mm. We must remember when designing schlieren instruments that deflected rays may be intercepted by the rim of the photographic objectives. This effect is particularly strong at the periphery of the instrument field, since the objectives are placed at a fixed distance from the focal plane of the main objective. This factor leads to a considerable increase of the light diameter of the photographic objectives.

Less exacting demands are imposed on the mechanical components of the schlieren instruments. Particular attention should only be paid to the fastening of the main objectives, which must permit an initial alignment of the instrument and then keep the optical components rigidly in position to prevent vibrations. The only mechanical displacement which requires very high precision in the course of the experiment is the motion of the knife-edge (or any other viewing diaphragm) in the direction perpendicular to the optical axis. We must use a micrometer screw with a reading accuracy of 0.01 mm at least. An accuracy of the order of 0.1 mm suffices for the other moving components. This precision usually can be achieved without particular difficulty.

## 31. LIGHT SOURCES

The light sources used in schlieren measurements are incandescent lamps, high-pressure gaseous discharge lamps, and flash lamps. The choice of the particular source depends on the type of the inhomogeneity and the aims of the experiment. Projector lamps are usually used in visual and photographic observations of lengthy processes. As we saw in §25, a maximum measurement sensitivity is achieved in this case. A regular incandescent lamp is convenient for most measurements. It is sufficiently bright, and the light fluctuations resulting from the use of an AC power source are small. The only exception are the methods of absolute photometry, in which the luminous body must possess a high luminance constancy in the direction of displacement of the illuminating slit image. It is convenient to use ribbon-filament in such measurements. The central brightness of the luminous body of these lamps is constant to within 1%.

The insufficient luminance of incandescent lamps affects practical measurements in two cases. The first is the case of transient processes, when very short exposure times or high-speed cinecameras are necessary. High-pressure mercury or xenon discharge lamps are usually used in this case. The second case is when monochromatic light is necessary. One of the strongest emission lines is then isolated by light filters (for instance, the green line of mercury). This combination makes it possible to greatly step up the image illumination compared to that obtained with continuous-spectrum sources.

A shortcoming of the gaseous discharge lamps is the shift of the discharge gap in the course of combustion, which is frequently as large as 1 mm. This is particularly troublesome in quantitative and high-sensitivity measurements. Different portions of the discharge gap thus appear in the part of the illuminating slit image not covered by the knife-edge. Moreover, the luminance of the luminous volume is highly nonuniform.

Flash light sources are being widely used [10] for various problems. We often need a single shot with a very brief exposure time. Either flash lamps or sparks are used to this end. An exposure time as short as 2 to 10 $\mu$sec is usually achieved without particular difficulty. The total quantity of light during the flash is usually sufficient to produce an adequate darkening of an average-speed emulsion with about 0.05 mm of the illuminating slit image remaining uncovered. Shorter exposure times are difficult to attain. In the first place, the inductance of the discharge circuit — the leads and the capacitors — must be radically lowered. Ceramic capacitors made of barium titanate and similar materials are frequently used. The quantity of light emitted by the flash is greatly reduced, however, and it becomes necessary to use high-speed emulsions and leave more than 0.1 mm of the slit image uncovered (for the IAB-451 instruments). The properties of the gas in which the discharge takes place begin to exert a strong influence. Discharge in high-pressure hydrogen is used for very brief exposures. Experience shows that it is possible to manufacture sources and discharge circuits giving a spark of duration of $10^{-7}$ sec whose intensity is sufficient to produce schlieren images with a sensitivity of the order of $10^4$ (for $\gamma = 2$). Flash sources with shorter exposure times are very seldom used.

One of the specific features of the use of flash sources is the necessity of synchronizing the flash with a certain phase of the process. The synchronism is usually achieved with the aid of a triggering transducer which generates a trigger signal at a certain instant (e.g., when the shock wave passes near the transducer, simultaneously with the ignition pulse, etc.) and a time delay element which energizes the light source a specified time after the reception of the transducer pulse. If the rate of the process changes between experiments, and we are interested in photographing the same phase of the process (thus, in a shock tube we mainly need pictures of the model in the zone of uniform parameters of the working gas), a more complicated time delay circuit is used, comprising two triggering transducers at a certain distance from each other. The delay time is automatically set proportional to the time interval between the signals from these two transducers. Such a circuit allows for possible velocity changes.

The discharge channel of an unconfined spark changes its position between flashes. This is inconvenient for schlieren measurements, especially for quantitative ones. To avoid this difficulty, the discharge channel is confined artificially, using discharge in a capillary tube, discharge between two quartz or glass plates, etc. The only drawback of such designs is the destruction of the wall material by the powerful pulse.

The sensitivity of photomultipliers is sufficient for almost all schlieren measurements. Some difficulties arise only when working with instruments of low light transmission coefficient (TE-19) with the uncovered part of the illuminating slit image narrower than 0.1 mm.

The spectral sensitivity is of much smaller importance, since most measurements are conducted with light sources of a sufficient spectral width. It is important only in some diffraction measurements and when the properties of the source and the emulsion must be matched. The dependence of the spectral sensitivity on the wavelength is plotted in Figure 92. These data, however, are tentative. The actual parameters must be measured under the same conditions as when photographing the schlieren image of the inhomogeneity.

Photocells, and mainly photomultipliers, are used in photoelectric recording. The signal generated in each of these instruments is proportional to the light flux, and

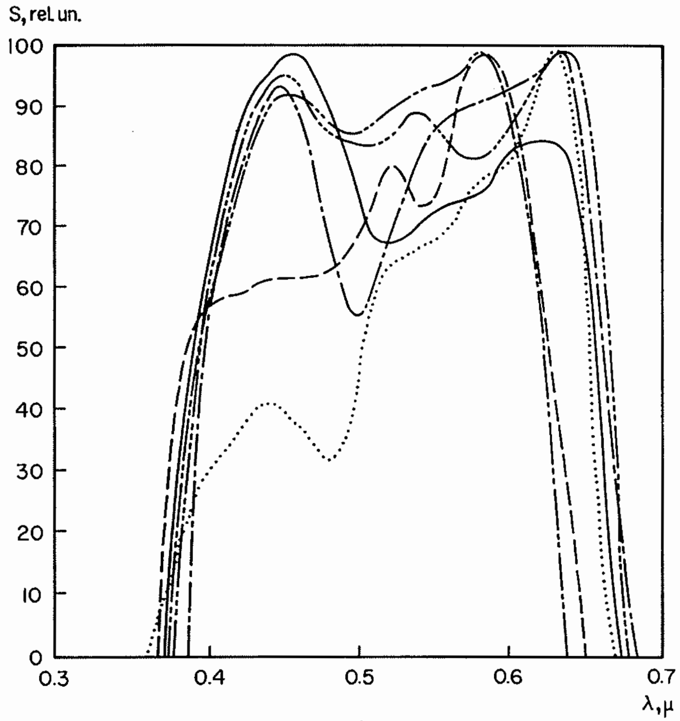

Figure 92

Spectral sensitivity of Soviet-made films as a function of $\lambda$: dotted curve — Mikrat-300, solid curve — FT-12, dash-dotted curve — oscillographic film, dash-double dot — RF-3, dash-triple dot — M3, A, C, dashed curve — B-type film.

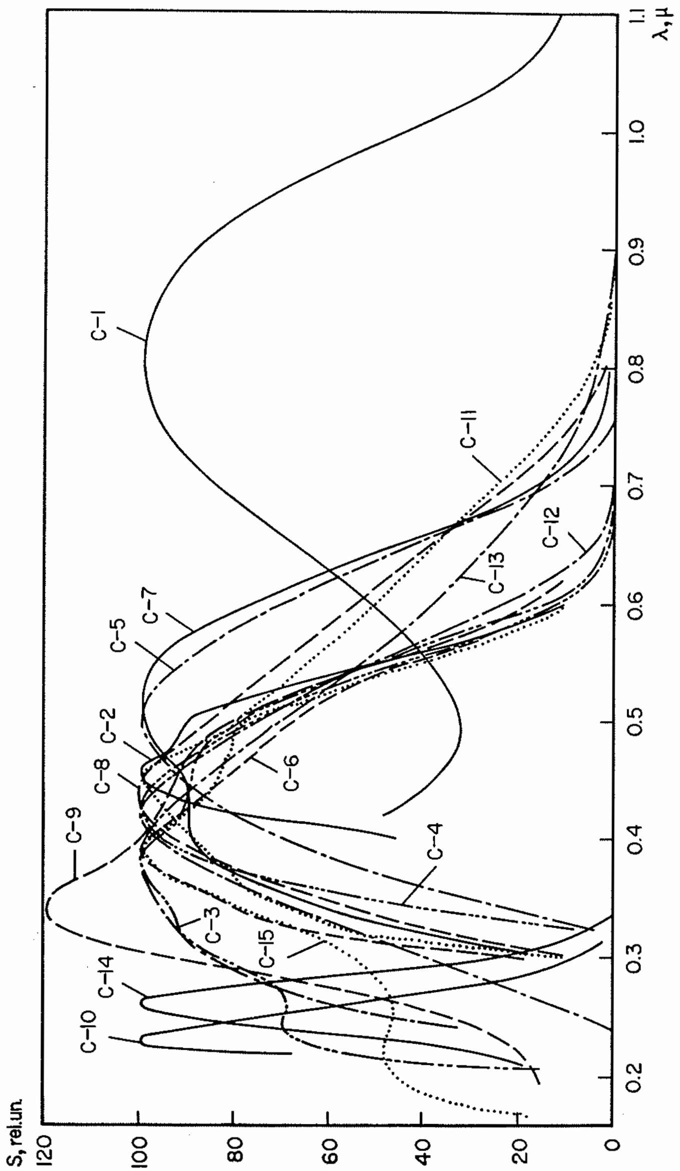

Figure 93

Relative sensitivity of various photocathodes.

this proportionality simplifies the processing of the results. The measurement sensitivity is determined by the integrated sensitivity of the photocell, and the minimum recorded light flux depends on the dark current.

As a rule, vacuum photocells are used in schlieren instruments with high-speed main objectives in low-sensitivity measurements. Photomultipliers are used at high sensitivities.

The relative spectral sensitivity of the photoelectronic instruments depends on the type of the photocathode used (Figure 93).

# VII

# MOUNTING AND ADJUSTMENT OF SCHLIEREN INSTRUMENTS

## 33. ALIGNMENT

The instrument must be aligned before it is put into operation. It is supplied in a dismantled form, separate containers being used for the different optical components. Therefore, the first operation consists in assembling and aligning the instrument.

The actual alignment procedure depends on the type of schlieren instrument used. The TE-19 and TE-20 instruments can be aligned only by specialists; the IAB-451 and IAB-453 instruments, on the other hand, can be aligned by the user. We shall therefore describe in greater detail the alignment for the IAB-451.

The working space necessary for instrument alignment is 7 m × 2 m. The receiving and the illuminating units are aligned separately; they are then matched, and the quality of the point image is checked.

One of the units is mounted on a pedestal at the middle of the working area. The pedestal must have controls for instrument leveling. A level gage is placed on a scraped area of the instrument. The instrument is then displaced and the body is rotated about the axis until this area becomes horizontal. If several instruments have to be aligned, it is more efficient to level the pedestal.

A guide rail with an autocollimating eyepiece is provided on one side of the instrument, and on the other an optical tube with illuminator, which forms the image of the cross-hairs at different distances from the tube. The problem is to align the optical axis of the instrument. To that end, frames with cross-hairs are placed at the two ends of the instrument body, at a distance of 117 mm from its geometrical axis. The vertical axis of each frame must coincide with the plumb. The optical axis is set 10 mm farther from the center than the line through the centers of the two cross-hairs. The optical tube is mounted so that its optical axis coincides with the centers of the cross-hairs. To this end, the cross-hairs are projected on each frame in turn. The tube is shifted and inclined until the cross image is made to coincide with the two cross-hairs for the same position of the tube.

After the illuminating tube has been aligned, the frames are removed and the guide rail is set so that the line of motion of the cross-hairs in the autocollimating eyepiece coincides with the tube axis. This is achieved when the centers of the cross-hairs in the eyepiece and of the cross-hairs image coincide for any position of the eyepiece on the rail. The eyepiece is then moved 10 mm away from the instrument center. As a result of all these operations, the center of the eyepiece cross-hairs lies on the optical axis of the instrument for any position of the eyepiece on the rail.

Next, the optical components of the instrument must be mounted in such a way that the centers of curvature and the foci will be located on the optical axis, fixed by the eyepiece cross-hairs. First, a revolving diagonal mirror is mounted. A bushing with glass on which two cross-hairs are traced is placed in the exit opening. The side cross-hairs is at a distance of 9.3 mm from the central cross-hairs, and it corresponds to the point through which passes the ray displaced 10 mm from the optical axis, i.e. from the center of the luminous beam of the illuminating tube. The optical tube is focused in such a way that the cross-hairs image appears on the bushing wall. The cross-hairs centers are then made to coincide by rotating and inclining the diagonal mirror.

Next, the spherical mirror and the meniscus are mounted. The mirror is inserted in a fitting socket, and is brought into position by means of adjusting screws, so that the cross-hairs of the autocollimating eyepiece coincides with its image formed by reflection from the spherical mirror. The menisci are aligned in the same way. The search for an autocollimated image presents some practical difficulties.

The point of coincidence of the cross-hairs with its image from the meniscus is at a distance of 608 mm from the tube exit, and the point of coincidence with its image from the mirror is at a distance of 1655 mm. These distances determine the necessary size of the rail when mounting the spherical mirror and the meniscus.

This ends the instrument alignment proper. The accuracy of the illuminating slit setting is controlled by a plane mirror, which gives an autocollimated image of the point formed by a microscope. The microscope is focused on the slit and on the autocollimated image of the point, and the slit position is adjusted until they are both clearly visible at the same time. The setting is then equal to 0.1 mm, which, as will be seen below, considerably exceeds the required accuracy.

The same procedure is followed for aligning the second unit of the instrument. The quality of the instrument as a whole is checked against a luminous point image. To this end, a microscope with an illuminator giving an image of a luminous point $< 0.01$ mm in diameter in the slit plane is placed in the illuminating part. The image of this point in the receiving unit is observed by means of a second microscope. The point image must be a small circle. On the axis the point image must have a distinct diffraction structure.

The energy distribution in the diffraction disk of confusion has a decisive influence on the quality of the schlieren instrument. Therefore, if the instrument is intended for very accurate experiments, it is advisable to photograph the point at different distances from the axis. By observing and analyzing photometrically the image, we can best estimate the instrument quality and select the size and the position of the illuminating slit for which the aberrations are minimum.

Thus auxiliary aligning equipment is necessary for the full alignment of the schlieren instrument: an illuminating tube on a pedestal, a cross-hairs, a bushing, a guide rail with an autocollimating eyepiece, an autocollimating microscope, a plane mirror, and a microscope. It should be borne in mind that this equipment serves only for fixing the optical axis in space and determining the position of the centers and the foci of the mirror and the meniscus on the axis. A different alignment equipment and procedure can therefore be used. Thus if we have to align a single instrument, we may use a longer alignment procedure and, replacing the illuminating tube by a level gage, avoid any special equipment. The most important operation remains the alignment quality control.

## 34. MOUNTING

Schlieren measurements are being used on an increasing scale in complex installations, requiring a large staff, numerous motors, machines, and other industrial equipment. The transition from laboratory to industrial conditions is particularly noticeable when the schlieren instruments are used for gas-dynamic measurements. The instruments are mounted in large industrial premises together with functioning motors, pumps, and similar objects.

As a result, the effect of extraneous disturbances increases considerably. Whereas the sensitivity of the schlieren instrument under laboratory conditions is limited only by aberrations and diffraction phenomena, here vibrations and heat fluxes become predominant. Particular attention should be paid to methods of mounting the instrument intended to decrease these effects. Each of the disturbing factors will now be separately examined.

The strongest effect is that of vibrations. The method to be used for protecting the instrument from vibrations depends on the frequency and the amplitude of vibrations, and on the deflection of light in the inhomogeneity. The problem is particularly difficult if the inhomogeneity deflects the light through a small angle and the instrument must operate at a high sensitivity. Thus if the instrument must measure deviation angles as small as 1″, the slit image must not move by more than $10^{-3}$ mm in the course of the experiment. This is a very exacting requirement, and several preventive measures must be taken in order to fulfill it.

Practice shows that there is always a tendency to improve with time the accuracy of the measurements. Therefore, the instrument must be mounted in such a way that its vibrations are minimum.

Note that a simultaneous shift of the two units of the schlieren instrument will not lead to a displacement of the slit image, and therefore will not distort the results of schlieren measurements. Only relative displacements of the instrument units are of importance.

A vibration-free seating, set on a cushion of air or some other vibration damping material (sand, sawdust, etc.) is essential under these conditions, supporting both the receiving and the illuminating unit. No vibration-conducting objects should be located in the space separating this seating from the common seat of the machines.

As a rule, the use of a separate seating is insufficient for the complete prevention of vibrations. In addition, the two units must be set on a single rigid truss mounted on shock absorbers. Satisfactory results were obtained with shock absorbers made of several layers, each differing from the adjacent one in its elasticity and stopping vibrations of a given frequency.

Even this is not sufficient in some cases. Residual vibrations pass through the protective system and lead to a displacement of the illuminating slit image, reducing the accuracy of the schlieren measurements.

Working experience with the IAB-451 and TE-19 shows that the vibrations of the different components are easily eliminated by the introduction of fastening elements (screws). To prevent relative vibrations of the receiving and the collimating units, particular attention should be paid to their rigid fastening on a common pedestal.

When mounting the instrument, it is necessary to study the influence of vibrations and estimate their quantitative effect. Continuous-trace photography can be used to this end, but the photoelectric recording of vibrations is more convenient. The setup used is similar to that described above. A transducer transforming the light intensity fluctuations into electric fluctuations is set behind the schlieren instrument knife-edge; this transducer can be a photoresistor, a photocell, or a photomultiplier. The signal generated by the transducer is recorded on an oscillograph. Since low-frequency vibrations (lower than 1 kHz) are the most important ones, it is convenient to use a loop oscillograph. To determine the vibration frequency, a signal from a signal generator is fed to the second input of the oscillograph. The signal amplitude can be easily related to the deviation of the illuminating slit image. To this end, the pattern is photographed for different positions of the knife-edge with respect to the slit image. A curve of the signal amplitude as a function of the slit image displacement is plotted on the strength of these photographs. This method has two advantages: first, it records directly the displacement of the illuminating slit image, i.e., the quantity which affects the sensitivity and the error of the schlieren instruments; second, it is graphic, attractively simple, and its results can be rapidly processed. These advantages make the photoelectric recording method superior to the continuous-trace photography.

We shall describe the fastening of the IAB-451 as an example of vibration protection.

The instrument was set on a single pedestal made of two channels. A vibrator was placed under one of the edges, generating vibrations between 20 and 300 Hz with an amplitude of up to 0.1 mm. First, an experiment was conducted without fastening the instrument. When the vibrator was started, the instrument tubes started to rotate in opposite directions, and the illuminating slit image was displaced by several centimeters in a few seconds. This shows that the intensity of the applied disturbances considerably exceeds the strength of the vibrations usually met in industrial conditions. Next, the instrument was fastened by means of a rubber band which pressed the tubes of the receiving and illuminating parts to the support. Because of its large friction coefficient, the rubber band markedly hinders the rotation of the instrument tubes about the axis. For a rubber band tension of 100 kg, the total slit image displacement decreased to 0.1 mm. The increase of the tension to 800 kg decreased the displacement to 0.01 mm, and its further increase to 2500 kg reduced the displacement to 0.002 mm. Therefore, this fastening method reduces the influence of vibrations almost to zero and the sensitivity is determined by other sources of error. The final results are summarized in Table 4.

Table 4

| Fastening of the tubes to the pedestal | Rotation of the tubes | Slit-image displacement, mm/min | | | |
|---|---|---|---|---|---|
| | | high-frequency vibration | change of the illuminating slit position | knife-edge motion | total displacement |
| Without fastening | | | | | $\geqslant$ 1 mm |
| Fastening with a tension of 100 kg | 0.03 | 0.01 | 0.01 | 0.05 | 0.1 |
| Fastening with a tension of 800 kg | 0.01 | < 0.001 | < 0.001 | 0.001 | 0.01 |
| Fastening with a tension of 3000 kg | < 0.001 | < 0.001 | < 0.001 | < 0.001 | 0.001 |

Parameters of the vibrations: frequency 20–70 cycles/sec, amplitude 0.05 mm.

Naturally, the method just described is far from being the only possible method; it is not even the best one. The results indicate, however, that the instrument by relatively simple means can be made vibration-proof to such an extent that even in case of very strong vibrations the ultimate sensitivity is determined by other factors. On the other hand, when the instrument is mounted in industrial premises without the use of a tested vibration protection, the vibration limitations become fundamental and determine the maximum possible sensitivity of the instrument and the limits of its applicability.

The second condition of reliable functioning of the instrument is its insulation from heat and from sound vibrations, which cause deformation of the air medium in the instrument and between the instrument and the object of study. The schlieren instrument readings are almost equally affected by all the disturbances in the field of view of the instrument lying at different distances along the optical axis. The air density fluctuations in the instrument lead to a displacement of the slit image similar to that produced by light deviation in the inhomogeneity. Small density fluctuations are particularly dangerous, since they greatly interfere with the identification and interpretation of the object. If the angle of deviation produced by the additional disturbances is almost constant over the entire instrument field, such errors lead only to a change in the measurement sensitivity and have a much smaller effect than small inhomogeneities for the same values of the angle of deviation.

The theoretical evaluation of the influence of thermal and convective flows is difficult. We shall describe here an experimental study of these factors, conducted for the IAB-451 [20]. The local thermal effects were studied by heating the instrument body with an incandescent lamp. The body temperature changed in 10 min from 21° to 36°. The rate of heating was constant (1.5 deg/min). The schlieren pattern of the instrument field was regularly photographed on a Mikrat-200 film. The displacement of the illuminating slit image was determined by the photometric method of the knife-edge and the slit.

The slit image displacement strongly depends on the point at which heat is applied (Figure 94). Heating near the meniscus displaces the slit image by 0.01 mm when the body is heated by 3° C. Heating near the main objective mirror displaces the slit image by 0.15 mm when the body is heated by 4° C. Thus, heating near the mirror affects the measurements twenty times more strongly than heating near the meniscus. Therefore, the main cause of the slit image displacement is to be sought in the thermal deformations of the different components of the instrument, and not in the convective flows.

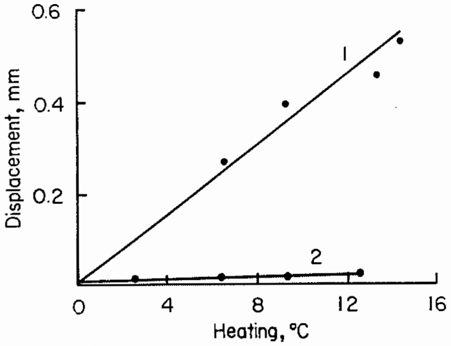

Figure 94

Displacement of the illuminating slit image when the body of the IAB-451 is heated near the mirror (1) and near the meniscus (2).

The minimum light deviation angles measured with this instrument are about 0.1″. Aberrations of the optical system and diffraction phenomena prevent the measurement of smaller angles. Therefore, the thermal effects will be negligible if the external heating does not lead to a slit displacement larger than $10^{-3}$ mm. If the maximum effect taking place during heating near the main objective mirror is taken as a measure of the thermal disturbance, we reach the conclusion that the instrument body must not be heated by more than 0.02° in the course of the experiment. As a rule, the schlieren instrument body is sufficiently massive, and the heat sources are weak, so that this requirement is satisfied relatively easily. Experiments show that if we protect the instrument by a 4 cm layer of porous insulation, heating for 30 min by this same incandescent lamp does not lead to a displacement of the slit image larger than $10^{-3}$ mm.

Thus this protection represents a complete solution of the problem, in spite of its simplicity. However, special measures must be taken to prevent the instrument temperature from rising by more than 0.02° C. In fact, the instrument is exposed in industrial conditions to various heat sources: nearby incandescent lamps (including the lamp of the schlieren instrument itself), convective heat flows from running motors, sun rays accidentally falling on the instrument, etc. It follows that an instrument without thermal insulation cannot be used for high-sensitivity precision experiments in industrial conditions.

The thermally insulating layer represents a good protection both against acoustic vibrations and against air flows.

It is convenient to use a hood for insulating the space between the instrument and the test object. For the hood to reliably protect the instrument from acoustic and thermal factors, it must be made from a sufficiently thick layer of porous insulant ($\sim$ 4 cm), attached to a rigid base. Slits and gaps are not allowed. The hood must be fastened tightly to the instrument on one side, and to the chamber containing the object on the other. The fastening is most reliably done by means of screwed flanges. Since the working chamber may vibrate, one of the hood components must be flexible, to prevent the transmission of vibrations from the working chamber to the instrument.

A high-sensitivity instrument should be mounted as follows (Figure 95): a common pedestal for the illuminating and the receiving units of the schlieren instrument is mounted on shock absorbers on a vibration-insulated seating. The schlieren instrument units, thermally and acoustically insulated by a porous sheathing, are rigidly fixed to the pedestal. The space between the instrument and the object is likewise insulated with the aid of a compact hood, having a flexible gap for the absorption of the vibrations coming from the working chamber. The complexity of

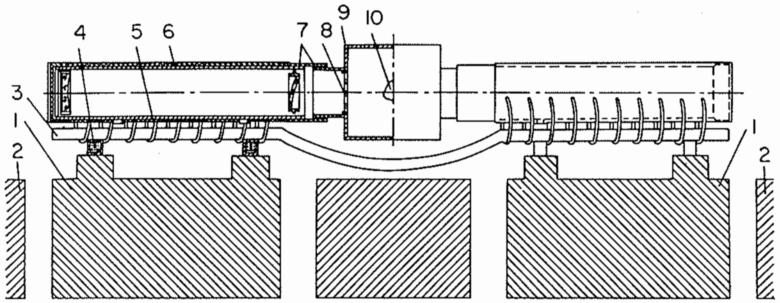

Figure 95

The mounting of a high-sensitivity schlieren instrument near a large aerodynamic installation:

1 vibration-insulating seating of the schlieren instrument; 2 foundation of the premises; 3 common rigid pedestal of the collimating and the receiving units; 4 shock absorbers; 5 rubber band fastening the instrument to the pedestal; 6 sound and heat insulating jacket; 7 periscopic lens hood; 8 protective glass; 9 working chamber of the installation; 10 observed inhomogeneity.

the installation is more than made up by the reliability of the measurements and the possibility of operating at the maximum sensitivity of the schlieren instrument.

If the premises are vibration-free, or if the experiments are tentative, a simpler mounting system is permitted, with some of the protective elements omitted. The selection of the mounting system is dictated by the specific conditions and aims of the experiment.

## 35. ELEMENTS OF ADJUSTMENT

We have assumed so far that the optical and the mechanical systems of the schlieren instrument completely satisfy the basic requirements of schlieren methods: the source is in the focus of the main objective of the collimator, the viewing diaphragm coincides with the source image, etc. In practice, however, the schlieren instrument is adjusted by devices and methods which lead to various errors. In addition, it is inherently impossible to conduct certain operations with the required accuracy. Thus, we say that the plane of the inhomogeneity is projected on a screen or a photographic plate. And yet most of the test objects are extended along the optical axis, so that only one section of the inhomogeneity is conjugated with the screen plane, while all the other parts of the inhomogeneity are projected on the screen in a defocused form. It follows that the problem of elucidating the necessary accuracy of instrument adjustment is one of the most important tasks in understanding the operation of schlieren instruments.

There is a second side to this question. It is important to determine the necessary adjustment accuracy, since a superfluously high accuracy only complicates the practical work and prolongs the experiment unnecessarily. Different stages of the adjustment procedure have been repeatedly described in the literature (cf. [3, 35, 58]).

The schlieren instrument adjustment starts with the mounting of the light source. Usually the luminous body does not have sharp boundaries or regular geometrical shape. Therefore, in exact qualitative and especially quantitative measurements, we use as a light source the image of the real source projected on the illuminating slit of the instrument. The slit cuts a portion of regular geometrical shape from the image, which is convenient for processing and analyzing the results. The first operation is thus to project the image of the luminous body on the slit. First, the source image is brought to coincide with the slit by means of the control screws, and then one of the condenser lenses is displaced until the image is moved to the slit plane. A coarse control of the focusing sharpness and the correctness of the image position is accomplished by visual inspection of the illuminating slit, conducted through special windows. The fine control is accomplished by observing the slit position through a microscope or a magnifying glass. The components are aligned so that the edges of the slit and the luminous body appear equally sharp and the slit cuts the necessary portion of the luminous body image.

The focusing accuracy depends on the source shape and the uniformity of the source luminance. If the luminous body is extended and uniformly bright, a poor focusing accuracy will suffice, since even then the schlieren instrument field will be illuminated with sufficient uniformity. If, on the other hand, the light source has portions which differ markedly from the rest of the luminous body, the defocusing will lead to a nonuniform illumination of the field. The adjustment method described makes it possible to bring the image plane of the luminous body to coincide with the illuminating slit plane with an accuracy of up to tenths of a millimeter, which is sufficient for all the practicable light sources (flash lamps, sparks, high-pressure mercury discharge lamps, incandescent lamps) and for almost all slit widths (up to 0.03 mm).

The mounting of the illuminating slit in the collimator focus is another of the adjustment operations. It is assumed in all the calculations that light emerges from the collimator as an ideally parallel beam. Actually, the slit is at a certain distance from the focus, and as a result the light wave in the object plane is slightly curved. This leads to some additional undesirable effects and measurement errors.

If the light ray passes at some angle to the object plane, and the camera is focused at the middle of the object, the region near the boundary will appear darker (Figure 96). The size of the darker zone depends on the position of the object and the ideal focal plane, on the width of the object and on the light front curvature. It is determined by the expression

$$\Delta y = \frac{yl}{f^2}\,\Delta f. \qquad (35.1)$$

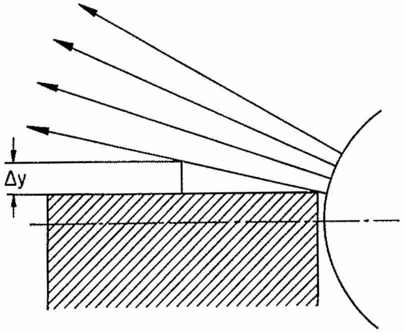

Figure 96

Ray path in the object plane with a defocused light source.

This effect is noticeable if $\Delta y$ is larger than the maximum resolvable distance. We shall evaluate this condition numerically. If $y = 10$ cm, $\Delta y = 10^{-3}$ cm, $l = 10$ cm, $f = 200$ cm, then $\Delta f = 0.4$ cm. As we see, the requirements regarding the mounting accuracy of the illuminating slit are not particularly exacting.

Because of the noncoincidence of the illuminating slit and the collimator focus, the edge of the field is cut by the receiving unit objective. This truncating effect is expressed by

$$\Delta R = \frac{Ra}{f^2}\Delta f, \tag{35.2}$$

where $a$ is the distance between the receiving and the illuminating units, $R$ is the radius of the main objectives. For a maximum field truncation of 0.1 cm we obtain $\Delta f = 2$ cm for $R = 10$ cm, $f = 200$ cm, $a = 200$ cm.

The third error caused by the inaccurate mounting of the illuminating slit leads to a breakdown of the quantitative relationship between the angle of light deviation in the inhomogeneity and the shift of the slit image. In fact, the slit image will be projected not in the focal plane of the collimator, but in some other plane distant $\Delta f$ from it (up to terms of second order). In quantitative measurements we assume as before that $\delta = \varepsilon f$, whereas in this case

$$\delta = \varepsilon f\left(1 - \frac{s-f}{f^2}\Delta f\right), \tag{35.3}$$

where $s$ is the distance from the inhomogeneity to the first principal plane of the receiving unit objective. If the error must not exceed 0.5%, we obtain $\Delta f = 1$ cm (for $s = 4 \times 10^2$ cm, $f = 200$ cm).

The analysis of the phenomena taking place when the illuminating slit is inaccurately set in the collimator focus shows that the focusing can be achieved with an accuracy of ± 3 mm. This is a very low accuracy, which is covered with a wide margin in the manufacturer's instrument alignment. We can therefore dispense with any additional adjustment under practical conditions. The carriage with the illuminating slit is set in the position indicated by the manufacturer. The mechanical manufacture and the alignment accuracy give an error not larger than ± 1 mm in slit focusing, which satisfies the requirements to be met by the schlieren instrument.

The instrument must be mounted so that the light rays traverse the object in a given direction. If a plane inhomogeneity is studied, the optical axis of the instrument should be directed along a line of equal parameters of the flow. A right-angled prism can be used usually to this end (Figure 97). The support plane is brought to coincide with the plane relative to which the instrument is oriented — a plate, the chamber wall, etc. If the optical axis of the instrument is parallel to this plane, the image of the illuminating slit formed by the rays passing through the alignment device will coincide with the fundamental image. The images separate in cases of nonparallel alignment. The adjustment method calls for observing the illuminating slit image in the focal plane of the main objective of the receiving unit. The two slit images are brought into coincidence by moving the collimator tube. This procedure ensures that the optical axis of the instrument is parallel to any plane with an accuracy of about 1′, which is much higher than what the experiment requires.

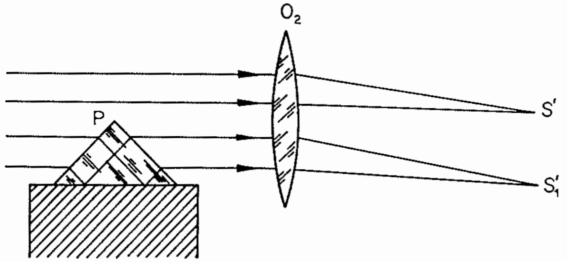

Figure 97

A right-angled prism used to align the optical axis parallel to the supporting plane of the object.

The exact alignment of the illuminating slit in a given direction is necessary because an instrument with a slit source measures only deviation angles in the direction perpendicular to the slit. Knowledge of the direction of the deviation angles is necessary for the subsequent processing of the photographs. Thus when studying axisymmetrical inhomogeneities, the schlieren instrument is adjusted so as to measure the angles of light deviation in the parallel and perpendicular directions to the axis of symmetry of the inhomogeneity. Skotnikov suggests the following procedure for aligning the instrument slit in the necessary direction: a lens is placed in the image plane (the schliere lens used for measurements by standard methods can be used to that end), and the knife-edge is rotated until the diffraction pattern observed in the lens reaches maximum sharpness. To ensure good visibility, a sufficiently narrow slit is selected (0.01–0.03 mm). The direction of the diffraction bands coincides with the direction of the illuminating slit. The slit and the knife-edge are then rotated until the diffraction bands in the lens are aligned in the required direction. If the slit must be set parallel to some component of the optical inhomogeneity which is not visible in the preliminary adjustment, a simultaneous photograph is taken of the diffraction pattern in the lens and of the inhomogeneity, and the angle between the diffraction pattern and the given direction is measured on the photograph; the slit is then rotated through this angle. This method is particularly convenient if the slit must be aligned relative to a transient inhomogeneity. The alignment accuracy of the illuminating slit on the basis of the diffraction pattern in the extra lens is usually sufficient for any experiment.

A similar method without a standard lens is sometimes used. The knife-edge is defocused and its diffraction pattern is observed. In this case, however, the knife-edge can be aligned only relative to opaque edges, since the visibility of the optical inhomogeneities is much poorer. In addition, this method incorporates errors of the mechanical defocusing system. Its only advantage lies in the absence of an additional lens.

The next operation in schlieren instrument adjustment is the matching of the illuminating and the receiving units. The optical axes of the two units must coincide. Inclination and displacement of one axis relative to the other may reduce the instrument field, change the working range, and alter the aberration characteristics of the instrument.

In the TE-19, the coincidence of the optical axes is controlled by means of cross-hairs in each of the instrument units, which are used for assembling the optical system. They are observed through a theodolite. In the IAB-451 and IAB-453, this operation is conducted differently: a rim is fitted on the exit aperture, with a cross-hairs whose center coincides with the aperture center. The height of the illuminating slit is stopped (or a point grid is used). The receiving unit is then fitted until the luminous point image coincides with the center of the cross-hairs. Frequent use is made of the coincidence of the axis of rotation of the knife-edge with the center of the exit aperture. In this case, the receiving unit is fitted until the point image touches the edge for any position of the knife (usually for two vertical positions, with the knife-edge above and below, and for two horizontal positions). Since devices for tilting the receiving unit are usually independent for vertical and horizontal displacements, it is convenient to move the luminous point first along one coordinate and then along another. When the axes are matched, the receiving unit is translated parallel to itself until the beam emerging from the collimator fills the light aperture of the receiving unit. The observation is conducted with a wide open illuminating slit, which increases the quantity of light and facilitates the adjustment.

Let us question the accuracy of these operations. If the axes are not parallel, the instrument range is shifted and the aberration characteristics deteriorate. If the aperture radius is 20 mm, an error in the inclination causing a displacement of 1 mm of the source image will change by 5% the value of the largest measurable angle. Since the aperture size is made with a certain margin, it becomes clear that this factor does not impose substantial restrictions on the adjustment accuracy. Another factor is more important. The shift of the point position has an adverse effect on the aberration quality of the point image. If a slit source is used, its points lying far from the optical axis will be imaged with poorer quality than the central points. A total shift of the slit image $\frac{1}{10}$ of its length does not lead as a rule to a substantial deterioration of the results. If point sources (or short slits) are used, the permissible displacement is determined by the distance at which the image quality deteriorates insignificantly. For the existing systems of instruments, the angular size of the zone in which the aberrations are almost equal to the aberrations for a point on the axis is 1–2′, which corresponds to a linear size of approximately 1 mm.

It follows from the above that the optical axes of the illuminating and the receiving units must be parallel to within 1′. The image of a point source in the focal plane of the receiving unit must lie at a distance not greater than 1 mm from the optical axis. A higher accuracy does not lead to a substantial improvement of the results.

The matching of the optical axes affects almost only the truncation of the field of view. Since the wave front from a point source can be regarded as plane with satisfactory accuracy over the entire instrument field, the aberrations change negligibly and can be neglected. The field truncation does not impose special adjustment requirements, either. Thus a displacement of 3 mm is unnoticeable for an instrument with a field of the order of 200 mm.

It should be noted that all the adjustment procedures leading to the coincidence of the optical axes of the receiving and collimating units give an accuracy wholly sufficient for the measurements.

The next step is to align the viewing diaphragm relative to the light source image. In the knife-edge and slit method, the knife must be brought to coincide with the plane of the slit image, and the knife-edge must be parallel to the slit edges at a given distance from them. In the curved-stop method, the stop plane is brought to coincide with the slit image plane, which should be perpendicular to the stop axis lying on a specified portion of the curve. When using defocused grids, they are oriented with respect to the slit image and set at a specified distance from the focal plane.

We will examine this adjustment step for the knife-edge and slit method. First, the knife must be brought to coincide with the illuminating slit image. A defocusing of the knife-edge leads to a nonuniform illumination of the field. For a field point situated at a distance $r$ from the field center in the direction perpendicular to the knife-edge, a displacement $\Delta$ is roughly equivalent to a shift $\Delta r/f$ of the knife-edge. Field points lying on the same side of the optical axis as the knife-edge appear darker for defocusing toward the main objective and brighter when the knife-edge is moved behind the focus.

The sensitivity of the method becomes different for different points of the field.

This leads to great inconveniences in practical measurements. Optical disturbances of equal magnitude produce different effects if they are located at different distances from the geometrical axis. The defocusing factor is particularly large at high sensitivities. The relative change of the illumination in the instrument field is equal to

$$\frac{\Delta I}{I} = \frac{2r\Delta}{f\xi_0}. \tag{35.4}$$

If an illumination nonuniformity of 5% is admissible for a 0.05 mm wide slit, we obtain from (35.4) that the defocusing must not exceed $2.5 \times 10^{-2}$ mm for an instrument field of 100 mm. To achieve this high accuracy, we use the phenomenon of uniform field darkening when the knife-edge is moved perpendicular to the optical axis. If the knife-edge is in position *A* (Figure 98), the direction of image darkening is opposite to the direction of knife-edge motion; if it is in position *C*, darkening occurs along the knife-edge motion. If we take a sufficiently narrow slit (~ 0.03 mm) and by moving the carriage align the knife-edge so that the darkening is uniform over the entire field area, we achieve the necessary accuracy of knife-edge focusing, since the eye readily senses an illumination nonuniformity of the order of 5–10%.

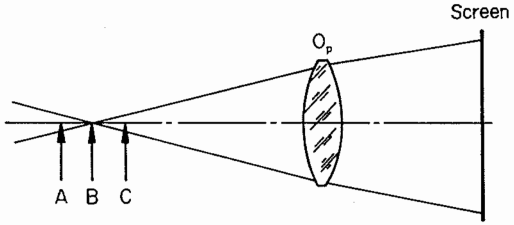

Figure 98

Focusing the knife-edge.

A high-precision focusing of the knife-edge makes sense only if the knife plane is parallel to the plane of the illuminating slit image. Indeed, for a slit length of 10 mm, a departure of 30′ from perfect parallel alignment of the planes leads to a defocusing of $5 \times 10^{-2}$ mm for the extreme points when the central point of the slit is in focus. The mechanical manufacture errors can reach a considerable value. Therefore, in precision measurements, we must check the coincidence of the planes. To this end, a slit diaphragm *D* (Figure 99) cutting a portion of the illuminating slit *A* is placed in the focal plane. We then check by the method described above whether there exists a certain position of the knife-edge for which all the parts of the slit are in focus. If there is no such position and opposite parts of the slit are defocused in different directions, we must tilt the knife until its plane coincides with the slit image. In precision instruments, the parallel alignment of the planes is checked only once in the course of the preliminary alignment of the instrument. There are cases when the plane of rotation of the knife does not coincide with the slit image plane, so that the rotation of the knife breaks the instrument adjustment and causes a defocusing of different parts of the slit. The value of this error must be checked when aligning the instrument. To reduce this error, the instrument should have fine controls which bring the knife plane to coincide with the slit image. This is usually achieved by moving the carriage along the optical axis and tilting the knife (or the illuminating slit).

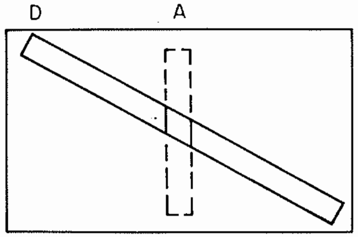

Figure 99

Checking the coincidence of the knife plane and the slit image plane.

Other diaphragms are set in the focal plane of the main objective in exactly the same way as the knife-edge. In the curved-stop method, the straight edge of the stop perpendicular to the axis of symmetry serves as a knife-edge in the adjustment process; in the filament and grid methods, the edge of the opaque line serves as a knife-edge. The same operation, although with a lower accuracy, is used in the defocused grid methods, where it is applied to establish the position from which the defocusing is measured.

The method described is convenient and sufficiently reliable for the majority of the experiments. The adjustment quality can be determined with an accuracy which is sufficient for reliably establishing whether the error affects the results of the high-accuracy measurements.

The next step involves setting the knife-edge parallel to the edge of the illuminating slit image (the coarse adjustment is generally carried out before the knife is set in the focus, since the accuracy of the knife-edge focusing is improved if the knife is parallel to the slit image). The previous relationship between the knife position and the image illumination does not hold if the knife-edge is not parallel to the illuminating slit edge, and it becomes difficult to determine the width of the uncovered part of the illuminating slit image. An error is thus introduced in the quantitative methods.

Let the slit be rotated through an angle $\alpha$ (Figure 100). The screen illumination will then be equal to

$$J_1 = Bl\left(\xi_1 + \frac{l \tan \alpha}{2}\right), \tag{35.5}$$

where $\xi_1$ is the width of the uncovered part of the slit image in the direction perpendicular to the narrow part of the slit.

If the inhomogeneity rotates the wave front through an angle $\varepsilon$ in the direction perpendicular to the knife-edge, the screen illumination becomes equal to

$$J_2 = Bl\left(\xi_1 + \frac{l \tan \alpha}{2} + \frac{\varepsilon f}{\cos \alpha}\right). \tag{35.6}$$

The angle of light deviation can be found from the formula

$$\varepsilon = \frac{J_1 - J_2}{J_1 f} \cos \alpha \left(\xi_1 + \frac{l \tan \alpha}{2}\right). \tag{35.7}$$

Usually, however, the width of the uncovered part of the slit is measured in the direction perpendicular to the knife-edge. Let this measurement be conducted at a distance $h$ from the point of intersection of the lower edge of the slit image with the knife-edge. It is then assumed when measuring the angle of deviation that

$$\varepsilon_m = \frac{J_2 - J_1}{J_1 f} \frac{\xi_1 + h \tan \alpha}{\cos \alpha}. \tag{35.8}$$

The relative error of determination of the angle of light deviation is equal to

$$\kappa = 1 - \frac{\xi_1 + h \tan \alpha}{\cos^2 \alpha \, (\xi_1 + \frac{1}{2} l \tan \alpha)}. \tag{35.9}$$

Since $\alpha$ is small, we can transform (35.9) to

$$\kappa = \frac{\alpha}{\xi_1}\left(\frac{l}{2} - h\right) + \frac{\alpha^2 h l}{2\xi_1^2}. \tag{35.10}$$

The width of the uncovered part of the slit image must be measured at the middle. If the measurement is conducted at one of the edges, the requirements of parallel alignment are much more exacting. The effect of nonparallel alignment is the greatest in the case of high-sensitivity measurements.

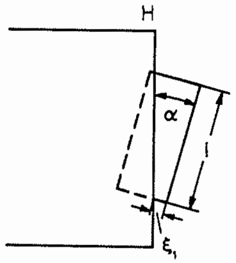

Figure 100

Setting the knife-edge parallel to the slit edge.

If $l/2 - h = 0.5$ mm, $\xi_1 = 0.2$ mm, $\alpha = 10'$, the measurement error is equal to $\kappa = 1.5\%$.

In practice, the parallel alignment of the knife-edge relative to the slit edge is established visually. A difference of 0.01 mm in the slit width at the ends is reliably detected for a slit width of 0.05 mm. For a slit length of 10 mm, this leads to an accuracy of 3′ in the measurement of the angle $\alpha$. Since in practice the width of the uncovered part of the slit image is measured at slit points situated at a distance of not more than one millimeter from the center, such adjustment accuracy suffices even in precision experiments. When the width of the uncovered part of the slit image is reduced, it is necessary to conduct the measurements closer to the middle.

The error due to nonparallel alignment is substantial only for the methods of absolute photometry. When schliere are used, it affects the sensitivity only. However, since a change of about 10% in sensitivity is virtually of no consequence, a coarser adjustment is permissible in these cases.

In the defocused grid methods, the parallel alignment of the slit image relative to the grid lines is important because the sharpness of the shadows and the accuracy of determination of their center depend on it. A different adjustment procedure is used in this case: the grid is rotated, and the shadows of the lines are observed on the screen. The grid is set in a position which ensures shadows of maximum clarity. This method is very simple and sufficiently accurate.

The concluding stage in the instrument adjustment procedure consists in focusing the camera on the inhomogeneity. The aperture of the illuminating beam in the schlieren instrument is small. For a 10 mm long slit, the angle of divergence is a mere 18′. Attempts to focus the photographic attachment using the sharpness of the opaque edge placed in the object plane do not lead to satisfactory results, since the object appears sufficiently sharp even for a considerable defocusing.

H. Schardin [121] suggested focusing the camera on the strength of the shape of the diffraction pattern produced at an opaque edge. If the knife covers the slit image, a bright fringe appears at the edge of objects; this fringe is split if the camera is defocused, and gives a single diffraction peak only in case of exact focusing. This method is somewhat more accurate, but it is difficult to make a detailed observation of the diffraction pattern.

The following procedure is the simplest and the most accurate. A light source (usually a portable incandescent lamp) is placed in the plane where the inhomogeneity is expected to be. The camera is adjusted so that the image of the lamp filament is clearly visible on the screen. Since the aperture of the light rays forming the filament image is large, the focusing can be done with a high accuracy. The large amount of light likewise simplifies the adjustment.

If the viewing diaphragm is removed, transparent inhomogeneities in the object plane will not be visible on the screen in case of correct focusing. Note that the inhomogeneities must not be too strong, since for large deviation angles the light rays may be cut off by the exit pupil rim, which will play in this case the part of the viewing diaphragm.

Extended inhomogeneities are frequently observed. In this case, a complete invisibility of the inhomogeneity cannot be made completely invisible. The optimal focusing is then sought, i.e., the position of minimum visibility; in many axisymmetrical objects, the optimal focusing is achieved by focusing on the middle of the inhomogeneity. When studying more complex processes, the ideal focal plane can be displaced. The condition of invisibility of the inhomogeneity in the absence of the diaphragm is not the only condition in selecting the ideal focal plane. Refraction problems become decisive when the light is deflected through large angles. In these cases, the ideal focal plane is selected so as to make the largest possible part of the inhomogeneity accessible to measurements and to ensure that the illumination-distribution in the screen plane corresponds as accurately as possible to the distribution of light deviation angles in the inhomogeneity.

# VIII

# *METHODS OF CALCULATION OF INHOMOGENEITIES*

## 36. PASSAGE OF LIGHT THROUGH AN ISOTROPIC MEDIUM

The schlieren methods measure the change in the shape of the light wave front after its passage through an inhomogeneity. In order to determine the inhomogeneity characteristics, we must, therefore, ascertain the relationship between this quantity and the properties of the optical inhomogeneities. This problem is easily solved in the case of mirror optical systems; the relationship between the wave shape change and the mirror irregularities is readily found. The study of transparent objects, in which the light beam passes through zones of different refractive indices, is more difficult; it necessitates an examination of the question of light propagation in an isotropic medium.

Our analysis will be based on the electromagnetic theory of light [9]. The Maxwell equations for an isotropic, non-magnetic and non-conducting medium are

$$\begin{aligned} &\operatorname{curl} \boldsymbol{H} - \frac{\varepsilon}{c}\dot{\boldsymbol{E}} = 0, \qquad \operatorname{div} \boldsymbol{E} = 0, \\ &\operatorname{curl} \boldsymbol{E} - \frac{1}{c}\dot{\boldsymbol{H}} = 0, \qquad \operatorname{div} \boldsymbol{H} = 0, \end{aligned} \tag{36.1}$$

where $\boldsymbol{E}$ is the electric field vector, $\boldsymbol{H}$ is the magnetic field vector, $c$ is the light velocity, and $\varepsilon$ is the dielectric constant of the medium. The elimination of the electric or the magnetic field vector from these equations yields a wave equation for every component of the other vector, or

$$\Delta E - \frac{\varepsilon}{c^2}\ddot{E} = 0, \tag{36.2}$$

where $\Delta = \partial^2/\partial x^2 + \partial^2/\partial y^2 + \partial^2/\partial z^2$ is the Laplacian.

Consider the case of simple harmonic oscillations, described by the function $f(x, y, z)e^{ikct}$. Equation (36.2) reduces for such oscillations to

$$\Delta f + k^2 n^2 f = 0, \tag{36.3}$$

where $n = \sqrt{\varepsilon}$ is the refractive index.

We introduce a wave of the form

$$f = U(x, y, z)e^{ikL(x, y, z)}, \tag{36.4}$$

where $L(x, y, z)$ is an almost linear function, and $U(x, y, z)$ is a slowly varying function. The substitution of this expression in (36.3) yields

$$k^2 U(n^2 - |\operatorname{grad} L|^2) + ik(U\Delta L + 2 \operatorname{grad} U \cdot \operatorname{grad} L) + \Delta U = 0. \tag{36.5}$$

We shall now derive the equations of geometrical optics. Since geometrical optics is valid for large $k$, we can drop all the terms of (36.5) except the first, obtaining

$$|\operatorname{grad} L|^2 = n^2. \tag{36.6}$$

Introducing a unit vector $\boldsymbol{S}$ normal to the surface $L = \text{const}$, we obtain

$$\int_1^2 n dS = L(2) - L(1). \tag{36.7}$$

From (36.7) follows the Fermat principle, which can be written in the form

$$\delta_1 \int n dS = 0. \tag{36.8}$$

The light paths corresponding to the Fermat principle must satisfy the Euler equations, namely,

$$\begin{aligned} \frac{d}{dS}\left(n\frac{dx}{dS}\right) &= \frac{dn}{dx}; \\ \frac{d}{dS}\left(n\frac{dy}{dS}\right) &= \frac{dn}{dy}; \\ \frac{d}{dS}\left(n\frac{dz}{dS}\right) &= \frac{dn}{dz}. \end{aligned} \tag{36.9}$$

On interfaces they satisfy the law of refraction.

Introduce Cartesian coordinates, with the $z$ axis directed along the light ray. We shall consider the case of gaseous inhomogeneities, where light deviations are small. We can disregard the bending of the light ray in the inhomogeneity, and assume that the light propagates along a straight line deviating only slightly from the unperturbed light path in the absence of inhomogeneity.

Under these assumptions the Euler equations reduce to

$$\begin{aligned} \frac{d^2x}{dz^2} &= \left[1 + \left(\frac{\partial x}{\partial z}\right)^2 + \left(\frac{\partial y}{\partial z}\right)^2\right]\left[\frac{d \ln n}{dx} - \frac{dx}{dz}\frac{d \ln n}{dz}\right], \\ \frac{d^2y}{dz^2} &= \left[1 + \left(\frac{\partial x}{\partial z}\right)^2 + \left(\frac{\partial y}{\partial z}\right)^2\right]\left[\frac{d \ln n}{dy} - \frac{dy}{dz}\frac{d \ln n}{dz}\right]. \end{aligned} \tag{36.10}$$

We can derive from (36.10) equations for the additional phase difference and deflection caused by the optical inhomogeneity [58], namely,

$$\tau(x, y) \approx \frac{1}{c}\int_{z_1}^{z_2} [n(x, y, z) - n_0] dz, \tag{36.11}$$

$$\tan \varepsilon_x \approx \int_{z_1}^{z_2} \frac{d \ln n(x, y, z)}{dx} dz, \tag{36.12}$$

$$\tan \varepsilon_y \approx \int_{z_1}^{z_2} \frac{d \ln n(x, y, z)}{dy} dz. \tag{36.13}$$

Here $z_1$ and $z_2$ are the coordinates of the entrance and exit points of the light in the optical inhomogeneity.

The equations are quite general: they are applicable to all methods measuring a quantity which is a result of the action of different parts of the object, with different values of the relevant parameter. Similar problems occur in interferometry, in spectroscopy, in X-ray and $\gamma$-ray studies, and in many other branches of science and engineering. The theory described in this chapter is applicable to all these methods.

## 37. CALCULATION OF PLANE INHOMOGENEITIES

Equations (36.11) to (36.13) define the functional relationships for the angles of light deviation and the additional phase difference resulting from the passage of light through an inhomogeneity with a known refractive index distribution. In practical measurements we have to solve the inverse problem, i.e., to determine the refractive index distribution from the measurements of the angles of light deviation or the additional phase difference. Equations (36.11) to (36.13) cannot be solved in a general manner, since we can have various functional expressions for the refractive index distribution, giving the same final value for the angle of light deviation. Therefore, we have to impose restrictions on the shape of the inhomogeneity when solving specific problems.

The phenomena studied are simplest in the case of an inhomogeneity of simple shape, and can thus be investigated in a pure form. Accordingly, models of simple geometry are widely used in experimental physics.

The simplest objects are inhomogeneities where the refractive index is constant in some direction. Let this direction coincide with the optical axis of the instrument. The functions $\partial n/\partial x$ and $\partial n/\partial y$ are then independent of the coordinate $z$, and expressions (36.12) and (36.13) reduce to

$$\varepsilon_x = \frac{1}{n_0}\frac{\partial n}{\partial x}(z_2 - z_1), \tag{37.1}$$

$$\varepsilon_y = \frac{1}{n_0}\frac{\partial n}{\partial y}(z_2 - z_1). \tag{37.2}$$

By elementary transformations we obtain from (37.1) and (37.2) expressions for the refractive index gradients:

$$\frac{\partial n}{\partial x}(x, y) = \frac{n_0 \varepsilon_x(x, y)}{L}, \tag{37.3}$$

$$\frac{\partial n}{\partial y}(x, y) = \frac{n_0 \varepsilon_y(x, y)}{L}, \tag{37.4}$$

where $L$ is the light path length in the inhomogeneity.

Thus the field of angles of light deviation obtained in schlieren measurements of plane inhomogeneities can be transformed to the field of refractive index gradients in the inhomogeneity. The refractive index values are found by integrating the distribution of the refractive index gradients. In order to determine the absolute values of the refractive index, we must know its value at some point along the path of integration. Thus

$$n(x, y) = n(x_0, y) + \int_{x_0}^{x} \frac{\partial n}{\partial x}(x, y)\,dx. \tag{37.5}$$

These relationships are valid for a medium with a continuously varying refractive index. They must be modified, however, if the medium has interfaces involving a discontinuous change in the refractive index.

Plane discontinuities along the optical axis of the instrument should be invisible in the schlieren image according to geometrical theory. Their appearance is due to diffraction phenomena. Information on such discontinuities can, therefore, be obtained only by studying the diffraction patterns. This problem will be treated in Part II. When using the ordinary means of analysis, the refractive index increment should be determined by interferometric measurements, by calculations from the shock or interface angle, or by measurements carried out in the part of the inhomogeneity at the interface.

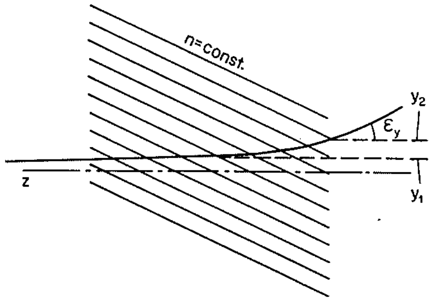

Figure 101
Light deviation in a plane inhomogeneity.

This difficulty can be avoided if the optical axis of the instrument does not coincide with the line of equal refractive indices in the plane inhomogeneity. In such measurements (Figure 101) the angle of light deviation in the inhomogeneity is determined by the variation of the refractive index along the light path inside the inhomogeneity:

$$\varepsilon_y = \frac{L}{y_2 - y_1}\,[n(y_2) - n(y_1)]. \tag{37.6}$$

The refractive index increment (e.g., in a compression shock) can be found from two photographs of the inhomogeneity taken at two different angles between the optical axis and the lines of equal refractive indices (one of which is 0°). Using (37.5) and (37.6), the refractive index difference between the light entrance and exit points is determined on each photograph. The difference between the two values obtained defines the "shock intensity" — the refractive index increment.

## 38. AXISYMMETRICAL INHOMOGENEITIES

Inhomogeneities with axial symmetry constitute another group of inhomogeneities for which adequate methods for the computation of the refractive index distribution have been developed.

Let the axis of symmetry of the inhomogeneity be perpendicular to the optical axis of the instrument, pointing along the $x$ axis. The light beam is then confined to the plane $x$ = const, and we can ignore the dependence of the refractive index on $x$. Every section $x$ = const is calculated separately.

Transforming equations (36.12) and (36.13) to cylindrical coordinates, we obtain integral Abel equations

$$(\varepsilon_y)_j = \frac{2}{n_0}\int_{r_j}^{R} \frac{\partial n}{\partial r}\frac{r_j dr}{\sqrt{r^2-r_j^2}}, \tag{38.1}$$

$$(\varepsilon_x)_j = \frac{2}{n_0}\int_{r_j}^{R} \frac{\partial n}{\partial x}\frac{r dr}{\sqrt{r^2-r_j^2}}. \tag{38.2}$$

Several methods are available for solving these equations. The first method to have been developed is approximative.

H. Schardin [120] suggested splitting the axisymmetrical inhomogeneity into a number of rings. Figure 102 shows a cross section $x$ = const through an inhomogeneity split in this way with the ring zones marked. Since the inhomogeneity parameters in this cross section depend only on $r$, we can assume that they change insignificantly in a narrow ring. Schardin assumed that $\partial n/\partial r$ and $\partial n/\partial x$ are constant in each ring. On this assumption, we can split each of the integrals in (38.1) and (38.2) into a sum of integrals, factoring out the refractive index gradient, namely,

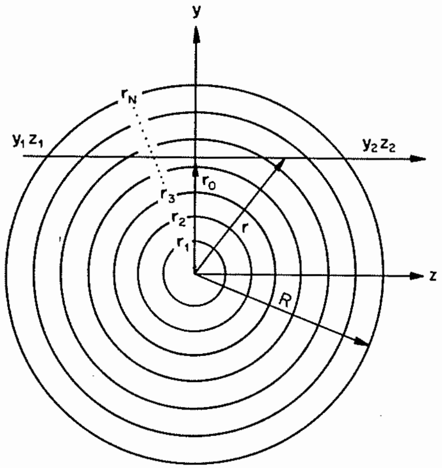

Figure 102

Ring zones of an axisymmetrical inhomogeneity.

$$(\varepsilon_y)_j = \frac{2}{n_0}\sum_{i=j}^{N-1}\left(\frac{\partial n}{\partial r}\right)_i \int_{r_{i-1}}^{r_i} \frac{r_j}{\sqrt{r^2-r_j^2}}\,dr, \tag{38.3}$$

$$(\varepsilon_x)_j = \frac{2}{n_0}\sum_{i=j}^{N-1}\left(\frac{\partial n}{\partial x}\right)_i \int_{r_{i-1}}^{r_i} \frac{rdr}{\sqrt{r^2-r_j^2}}. \tag{38.4}$$

After integration we obtain

$$(\varepsilon_y)_j = \frac{2}{n_0}\sum_{i=j}^{N-1}\left(\frac{\partial n}{\partial r}\right)_i r_0 \ln \frac{r_i+\sqrt{r_i^2-r_j^2}}{r_{i-1}+\sqrt{r_{i-1}^2-r_j^2}}, \tag{38.5}$$

$$(\varepsilon_x)_j = \frac{2}{n_0}\sum_{i=j}^{N-1}\left(\frac{\partial n}{\partial x}\right)_i \left[\sqrt{r_i^2-r_j^2}-\sqrt{r_{i-1}^2-r_j^2}\right]. \tag{38.6}$$

These formulas are a system of linear equations for $\partial n/\partial r$ and $\partial n/\partial x$. There are two possible procedures for solving them. The first procedure is an iterative solution: the empirical value of $\varepsilon_{N-1}$ is substituted in the first equation, and the value of $(\partial n/\partial x)_N$ is found. This value and $\varepsilon_{N-2}$ are substituted in the second equation, and $(\partial n/\partial x)_{N-1}$ is determined. The procedure is continued until the value of $(\partial n/\partial x)_j$ is ascertained from the last equation. This procedure is quite cumbersome. Furthermore, all the values of $(\partial n/\partial x)$ had to be found in each beam section, and a single omission would prevent the continuation of the process. Accordingly, a different procedure was developed, in which equations (38.5) and (38.6) are first solved for $(\partial n/\partial x)$ or $(\partial n/\partial r)$. The coefficients of $\varepsilon_j$ are calculated beforehand. The experimental angles of deviation for the different ring zones are then substituted in these equations.

The number of rings depends on the accuracy desired. The accuracy is improved with the increase in the number of rings, since the assumption of constant gradient inside each ring is better satisfied for smaller rings. However, since $\varepsilon_j$ are experimental quantities, measured with some error, the number of rings should be increased only so long as the error stemming from the inaccurate measurement of $\varepsilon_j$ remains smaller than the error caused by the assumption of constant gradient. The determination of the optimal number of rings is a difficult problem, which has not been satisfactorily solved to date. The method has not been widely used, due to the large error resulting from the stepwise approximation of the refractive index gradient distribution.

The error is reduced by assuming that the gradient in each ring is a linear function of the radius, namely,

$$\frac{\partial n}{\partial r}(r) = \frac{\partial n}{\partial r}(r_i) + \frac{\left[\frac{\partial n}{\partial r}(r_{i+1}) - \frac{\partial n}{\partial r}(r_i)\right][r-r_i]}{r_{i+1}-r_i}. \tag{38.7}$$

Equations (38.1) and (38.2) again reduce to a system of linear equations, solved as demonstrated above.

The most widely used methods of calculation are based on the conversion of the Abel integrals to a form which can be solved for the unknown function.

Multiplying both sides of (38.1) and (38.2) by $1/\sqrt{r_i^2-r^2}$ and integrating over $r_i^2$, we obtain after simple manipulations

$$\phi(\bar{r}_i) = \frac{1}{\pi R}\left[\frac{f(1)}{\sqrt{1-\bar{r}_i^2}} - \int_{\bar{r}_i}^{1} \frac{df(\bar{r})/d\bar{r}}{\sqrt{\bar{r}^2-\bar{r}_i^2}}\,d\bar{r}\right], \tag{38.8}$$

$$\bar{r}_i = r_i/R, \qquad \bar{r} = r/R.$$

Here $\phi = (1/\bar{r})\ (dn/d\bar{r})$ and $f = \varepsilon_y/\bar{r}$ for the equation obtained from (38.1), and $\phi = dn/dx$ and $f = \varepsilon_x$ for the equation corresponding to (38.2) ($n_0$ is taken equal to 1).

Since the light ray tangent to the inhomogeneity at the point $y = R$ is not deflected, $f(1) = 0$, and equation (38.8) reduces to

$$\phi(\bar{r}_i) = -\frac{1}{\pi R}\int_{\bar{r}_i}^{1} \frac{df(\bar{r})/d\bar{r}}{\sqrt{\bar{r}^2-\bar{r}_i^2}}\,d\bar{r}. \tag{38.9}$$

This equation is undoubtedly more advantageous than the initial equations: it is solved for the unknown function.

The first methods for the solution of (38.9) were based on graphic integration. They were widely used in Germany in interferometric studies. A similar method was suggested by Brinkman [72] for spectral measurements. Special planimeters were designed for speedier and easier calculations.

Today, it is the numerical methods that are most widely used. They are based on the substitution of a function of known analytical form for the empirical function in the integrand. The simplest procedure is to assume that the empirical function is constant in each ring. In this case equation (38.9) reduces to a system of linear equations from which the values of the refractive index gradient at the ring boundaries can be determined:

$$\phi(r)_i = \sum_{j=i}^{N} \alpha_j f_j. \tag{38.10}$$

The coefficients $\alpha_j$ are calculated beforehand on a computer and arranged in the form of a triangular table. It remains only to find the values of the angle of light deviation or the shifts of the interference fringes at the points corresponding to the ring boundaries, substituting the results in the given equations.

The analytical methods were found to be more convenient than the graphic methods since they are simpler to process. Furthermore, they are better suited to machine computation.

Superficially, equations (38.10) are very similar to Schardin's equations. Actually, the empirical function is smoother than the refractive index distribution or the gradient distribution. Therefore, the approximation of this function leads to smaller errors than those resulting from the approximation of the original function.

An approximation of the empirical function allowing for the deviation angle increment due to the refraction at the interface between two media was used in cases when axisymmetrical density discontinuities (discontinuous changes of the refractive index) occur in the inhomogeneity:

$$\frac{\varepsilon_y}{\bar{y}} = A\ln\frac{1+\sqrt{1-\bar{y}^2}}{\bar{y}} + B\bar{y},$$

$$\varepsilon_x = A\sqrt{1-\bar{y}^2} + B\bar{y}. \tag{38.11}$$

The accuracy of the calculation methods is considerably increased by the introduction of (38.11).

A shortcoming of these methods is that the inhomogeneity must be split into a large number of rings, since the approximation error is large for a small number of rings, particularly near the points where the empirical function has a considerable curvature. The increase in the number of rings complicates the calculations, since the number of terms in the triangular table increases by a factor of $N^2$.

The empirical function was approximated in [70, 88] by a polynomial whose degree is determined by the function curvature. This method has not been widely used due to the difficulty in its programming for machine computation. We shall describe a method based on a parabolic approximation of the empirical function [32].

Equations (38.1) and (38.2) have the following form in reduced coordinates:

$$f(\bar{r}_i) = 2\int_{\bar{r}_i}^{1} \phi(\bar{r})\,\frac{\bar{r}d\bar{r}}{\sqrt{\bar{r}^2-\bar{r}_i^2}}. \tag{38.12}$$

The transformation of variables $\bar{r}_i^2 = 1-z$, $\bar{r}^2 = 1-\xi$ yields

$$f(\sqrt{1-z}) = \int_{0}^{z} \phi(\sqrt{1-\xi})\,\frac{d\xi}{\sqrt{z-\xi}}. \tag{38.13}$$

Multiply the two sides of (38.13) by $1/\sqrt{u-z}$ and integrate over $z$ from 0 to $u$, changing the order of integration on the right-hand side. Reverting to the old variables, we obtain after differentiation with respect to $\bar{r}_i$

$$\phi(\bar{r}_N) - \phi(\bar{r}_i) = -\frac{1}{\pi}\,\frac{d}{\bar{r}_i d\bar{r}_i}\int_{\bar{r}_i}^{1} f(r)\,\frac{\bar{r}d\bar{r}}{\sqrt{\bar{r}^2-\bar{r}_i^2}}. \tag{38.14}$$

Since the integral in (38.14) is a smoother function than $f(\bar{r})$, it is advisable to differentiate the right-hand side with respect to $\bar{r}_i$ after the approximate integration. In the author's opinion, this can considerably increase the accuracy of the method.

Due to some specific features of the solution of equation (38.14), we shall present separate calculation procedures for the measurement of $dn/dx$ (this is the quantity determined in interferometric, spectral, and other measurements) and for the measurement of $dn/dr$.

In the first case we have

$$\frac{dn}{dx}(r_i) - \frac{dn}{dx}(r_N) = -\frac{1}{\pi\bar{r}_i}\frac{d}{d\bar{r}_i}\int_{\bar{r}_i}^{1}\frac{\varepsilon_x(\bar{r})\bar{r}d\bar{r}}{\sqrt{\bar{r}^2-\bar{r}_i^2}}. \tag{38.15}$$

We shall first calculate

$$\psi(\bar{r}_i) = \frac{1}{\pi}\int_{\bar{r}_i}^{1}\frac{\varepsilon_x(\bar{r})\bar{r}d\bar{r}}{\sqrt{\bar{r}^2-\bar{r}_i^2}}, \tag{38.16}$$

after which we shall describe a method for differentiating the tabular function $\psi(\bar{r}_i)$.

As is usual, we divide the cross section of the axisymmetrical inhomogeneity into $N$ rings, and assume that the function $\varepsilon_x(\bar{r})$ can be approximated inside each zone by a quadratic polynomial. To construct the approximating quadratic polynomial, we must have the values of the function $\varepsilon_x(\bar{r})$ in a minimum of three points. We select a system of equidistant tabular points, i.e., $\varepsilon_x(\bar{r})$ is taken at two boundary points and at the middle of the ring. The $j$-th ring will be the ring extending from point $\bar{r}_j$ to point $\bar{r}_{j+1}$; $\bar{r}_i$ will then run through the set of values $\bar{r}_i = i/2N$ (here $i = 1, \ldots, 2N-1$). If $i$ is even, the segment contains an integral number of rings. This case corresponds to the determination of the unknown function at the boundary points of the ring. If the number $i$ is odd (determination of the function in the middle of the ring), the number of rings will be half-integral. Under these assumptions, equation (38.16) is written in the following form for even and odd $i$, respectively:

$$\psi(\bar{r}_i) = \frac{1}{\pi}\sum_{j=i/2}^{N-1}\int_{\bar{r}_{2j}}^{\bar{r}_{2j+2}}\varepsilon_x(\bar{r})\frac{\bar{r}d\bar{r}}{\sqrt{\bar{r}^2-\bar{r}_i^2}}, \tag{38.17}$$

$$\psi(\bar{r}_i) = \frac{1}{\pi}\left[\sum_{j=i/2}^{N-3/2}\int_{\bar{r}_{2j}}^{\bar{r}_{2j+2}}\varepsilon_x(\bar{r})\frac{\bar{r}d\bar{r}}{\sqrt{\bar{r}^2-\bar{r}_i^2}} + \int_{\bar{r}_{2N-1}}^{1}\varepsilon_x(\bar{r})\frac{\bar{r}d\bar{r}}{\sqrt{\bar{r}^2-\bar{r}_i^2}}\right]. \tag{38.18}$$

We represent the approximating function in each ring by a Lagrange polynomial

$$\varepsilon_x(\bar{r}) = \sum_{k=1}^{n} l^{(k)}\varepsilon_x(\bar{r}_k), \tag{38.19}$$

where

$$l^{(k)} = \frac{(\bar{r}-\bar{r}_1)(\bar{r}-\bar{r}_2)\ldots(\bar{r}-\bar{r}_{k-1})(\bar{r}-\bar{r}_{k+1})\ldots(\bar{r}-\bar{r}_n)}{(\bar{r}_k-\bar{r}_1)(\bar{r}_k-\bar{r}_2)\ldots(\bar{r}_k-\bar{r}_{k-1})(\bar{r}_k-\bar{r}_{k+1})\ldots(\bar{r}_k-\bar{r}_n)}, \tag{38.20}$$

and $\varepsilon_x(\bar{r}_k)$ are known values of the empirical function $\varepsilon_x(\bar{r})$. When the Simpson formula is used (equidistant tabular points and parabolic approximation), we have $n = 3$. Let

$$F_j(\bar{r}) = (\bar{r}-\bar{r}_j)(\bar{r}-\bar{r}_{j+1})(\bar{r}-\bar{r}_{j+2}). \tag{38.21}$$

We obtain

$$l_j^{(k)} = \frac{F(\bar{r})}{(\bar{r}-\bar{r}_{j+k-1})F(\bar{r}_{j+k-1})}, \tag{38.22}$$

$$\varepsilon_x(\bar{r}) = \sum_{k=1}^{3}\frac{F(\bar{r})}{(\bar{r}-\bar{r}_{j+k-1})F'(\bar{r}_{j+k-1})}\varepsilon_x(\bar{r}_{j+k-1}). \tag{38.23}$$

The substitution of (38.23) in (38.17) yields

$$\psi(\bar{r}_i) = \sum_{j=i/2}^{N-1}\sum_{k=1}^{3}\alpha_{ij}^{(k)}\varepsilon_x(\bar{r}_{2j+k-1}), \tag{38.24}$$

where

$$\alpha_{ij}^{(k)} = \frac{1}{\pi F(\bar{r}_{2j+k-1})}\int_{\bar{r}_{2j}}^{\bar{r}_{2j+2}}\frac{F(\bar{r})\bar{r}d\bar{r}}{(\bar{r}-\bar{r}_{2j+k-1})(\bar{r}^2-\bar{r}_i^2)^{1/2}} \quad (k = 1, 2, 3). \tag{38.25}$$

Thus, the problem of calculating the function $\psi(\bar{r})$ has been reduced to the calculation of the coefficients $\alpha_{ij}^{(k)}$. Substituting (38.21) in (38.25) and integrating, we obtain

$$\begin{aligned}\alpha_{ij}^{(1)} = \frac{2N^2}{\pi}\Bigg[&(\bar{r}_{j+2}^2-\bar{r}_i^2)^{1/2}\left(-\frac{1}{6}\bar{r}_{2j+2}^2 + \frac{1}{2}\bar{r}_{2j+1}\bar{r}_{2j+2} + \frac{2}{3}\bar{r}_i^2\right)-\\ &-(\bar{r}_{2j}^2-\bar{r}_i^2)^{1/2}\left(\frac{1}{3}\bar{r}_{2j}^2 - \frac{1}{2}\bar{r}_{2j}\bar{r}_{2j+1} - \frac{1}{2}\bar{r}_{2j}\bar{r}_{2j+2} + \bar{r}_{2j+2}^2 + \frac{2}{3}\bar{r}_i^2\right)-\\ &-\frac{\bar{r}_i^2}{2}(\bar{r}_{2j+1}+\bar{r}_{2j+2})\ln\frac{\bar{r}_{2j}+(\bar{r}_{2j}^2-\bar{r}_i^2)^{1/2}}{\bar{r}_{2j+2}+(\bar{r}_{2j+2}^2-\bar{r}_i^2)^{1/2}}\Bigg],\end{aligned} \tag{38.26}$$

$$\begin{aligned}\alpha_{ij}^{(2)} = -\frac{4N^2}{\pi}\Bigg[&(\bar{r}_{2j+2}^2-\bar{r}_i^2)^{1/2}\left(-\frac{1}{6}\bar{r}_{2j+2}^2 + \frac{1}{2}\bar{r}_{2j}\bar{r}_{2j+2} + \frac{2}{3}\bar{r}_i^2\right)-\\ &-(\bar{r}_{2j}^2-\bar{r}_i^2)^{1/2}\left(-\frac{1}{6}\bar{r}_{2j}^2 + \frac{1}{2}\bar{r}_{2j}\bar{r}_{2j+2} + \frac{2}{3}\bar{r}_i^2\right)+\\ &+\frac{\bar{r}_i^2}{2}(\bar{r}_{2j}+\bar{r}_{2j+2})\ln\frac{\bar{r}_{2j}+(\bar{r}_{2j}^2-\bar{r}_i^2)^{1/2}}{\bar{r}_{2j+2}+(\bar{r}_{2j+2}^2-\bar{r}_i^2)^{1/2}}\Bigg],\end{aligned} \tag{38.27}$$

$$\begin{aligned}\alpha_{ij}^{(3)} = \frac{2N^2}{\pi}\Bigg[&(\bar{r}_{2j+2}^2-\bar{r}_i^2)^{1/2}\left(\frac{1}{3}\bar{r}_{2j+2}^2 - \frac{1}{2}\bar{r}_{2j}\bar{r}_{2j+2} - \frac{1}{2}\bar{r}_{2j+2}\bar{r}_{2j+1} +\right.\\ &\left.+\bar{r}_{2j}\bar{r}_{2j+1} + \frac{2}{3}\bar{r}_i^2\right) + (\bar{r}_{2j}^2-\bar{r}_i^2)^{1/2}\left(-\frac{1}{6}\bar{r}_{2j}^2 + \frac{1}{2}\bar{r}_{2j}\bar{r}_{2j+1} + \frac{2}{3}\bar{r}_i^2\right)+\\ &+\frac{\bar{r}_i^2}{2}(\bar{r}_{2j}+\bar{r}_{2j+1})\ln\frac{\bar{r}_{2j}+(\bar{r}_{2j}^2-\bar{r}_i^2)^{1/2}}{\bar{r}_{2j+2}+(\bar{r}_{2j+2}^2-\bar{r}_i^2)^{1/2}}\Bigg].\end{aligned} \tag{38.28}$$

The values of the function $\varepsilon_x(\bar{r})$ at the boundary points of the rings, with the exception of points $\bar{r}_i$ and 1, figure twice in equation (38.28). The function $\varepsilon_x(\bar{r})$ at a boundary point is multiplied by the third coefficient $\alpha_{ji}$ of the $j$-th ring and the first coefficient of the adjacent $(j+1)$-th ring. When tabulating the coefficients, it is convenient to introduce in the tables the sum of the third coefficient of each ring and the first coefficient of the next ring. We can then write (38.24) in the form

$$\psi(\bar{r}_i) = \sum_{\mu=i}^{2N-1} \beta_{i\mu}\varepsilon_x(\bar{r}_\mu), \tag{38.29}$$

where

$$\beta_{i\mu} = \alpha_{ij}^{(2)}, \qquad \mu = 2j+1$$

when the parities of $\mu$ and $i$ do not coincide, and

$$\beta_{i\mu} = \alpha_{i,\,j+1}^{(1)} + \alpha_{ji}^{(3)}, \qquad \mu = 2j+2$$

when the parities of $\mu$ and $i$ are equal.

If $\bar{r}_i$ runs through the values $i/2N$ $(i = 1, \ldots, 2N-1)$, the values of the function $\psi(\bar{r}_i)$ are obtained in a system of equidistant points $i/2N$.

To determine the required magnitude

$$\left(\frac{dn}{dx}\right)_{r_i} - \left(\frac{dn}{dx}\right)_0 = -\frac{1}{\bar{r}_i}\frac{d}{d\bar{r}_i}\psi(\bar{r}_i) \tag{38.30}$$

we differentiate $\psi(\bar{r}_i)$ with respect to $\bar{r}_i$. We first approximate the function $\psi(\bar{r})$ by a Lagrange polynomial:

$$\psi(\bar{r}) = \sum_{k=1}^{3} \frac{F(\bar{r})}{(\bar{r}-\bar{r}_{i+k-2})F(r_{i+k+2})}\psi(\bar{r}_{i+k-2}). \tag{38.31}$$

By differentiating, we determine $d\psi(\bar{r})/dr$ at the point $\bar{r}_i$:

$$\left.\frac{d\psi(\bar{r})}{d\bar{r}}\right|_{\bar{r}=\bar{r}_i} = N[-\psi(\bar{r}_{i+1}) + \psi(\bar{r}_{i-1})]. \tag{38.32}$$

Substituting (38.32) in (38.30), we obtain

$$\left(\frac{dn}{dx}\right)_{r_i} - \left(\frac{dn}{dx}\right)_0 = \frac{N}{\bar{r}_i}[\psi(\bar{r}_{i-1}) - \psi(r_{i+1})]. \tag{38.33}$$

When determining the refractive index from the gradient in the radial direction, we must take into account that

$$n(\bar{r}_i) - n_0 = -\int_{\bar{r}_i}^{1}\frac{dn}{d\bar{r}}\,d\bar{r}. \tag{38.34}$$

There is no necessity in this case to differentiate the two sides with respect to the inferior limit, since the density difference is directly determined in what follows.

Equation (38.34) can be transformed to

$$n(\bar{r}_i) - n_0 = \frac{1}{\pi}\int_{\bar{r}_i}^{1}\frac{\varepsilon_r d\bar{r}}{(\bar{r}^2-\bar{r}_i^2)^{1/2}}. \tag{38.35}$$

The approximation of the empirical function and the calculation of the integral are conducted in the same way as in the determination of the refractive index gradient from the values of $\varepsilon_x$. The only difference is that the integrand numerator does not contain $\bar{r}$. Performing calculations, we obtain

$$\begin{aligned}\alpha_{ij}^{(1)} = \frac{2N^2}{\pi}\Bigg[&(\bar{r}_{2j+2}^2-\bar{r}_i^2)^{1/2}\left(-\bar{r}_{2j+1} - \frac{1}{2}\bar{r}_{2j+2}\right) + \\ &+ (\bar{r}_{2j}^2-\bar{r}_i^2)^{1/2}\left(\bar{r}_{2j+1} + \bar{r}_{2j+2} - \frac{1}{2}\bar{r}_{2j}\right) - \\ &- \left(\bar{r}_{2j+1}\bar{r}_{2j+2} + \frac{\bar{r}_i^2}{2}\right)\ln\frac{\bar{r}_{2j} + (\bar{r}_{2j}^2-\bar{r}_i^2)^{1/2}}{\bar{r}_{2j+2}^2 + (\bar{r}_{2j+2}^2-\bar{r}_i^2)^{1/2}}\Bigg],\end{aligned} \tag{38.36}$$

$$\begin{aligned}\alpha_{ij}^{(2)} = -\frac{4N^2}{\pi}\Bigg[&(\bar{r}_{2j+2}^2-\bar{r}_i^2)^{1/2}\left(-\frac{1}{2}\bar{r}_{2j+2}-\bar{r}_{2j}\right) + \\ &+ (\bar{r}_{2j}^2-\bar{r}_i^2)^{1/2}\left(\frac{1}{2}\bar{r}_{2j} + \bar{r}_{2j+2}\right) - \left(\bar{r}_{2j}\bar{r}_{2j+2} - \frac{\bar{r}_i^2}{2}\right)\ln\frac{\bar{r}_{2j} + (\bar{r}_{2j}^2-\bar{r}_i^2)^{1/2}}{\bar{r}_{2j+2} + (\bar{r}_{2j+2}^2-\bar{r}_i^2)^{1/2}}\Bigg],\end{aligned} \tag{38.37}$$

$$\begin{aligned}\alpha_{ij}^{(3)} = \frac{2N^2}{\pi}\Bigg[&(\bar{r}_{2j+2}^2-\bar{r}_i^2)^{1/2}\left(\frac{1}{2}\bar{r}_{2j+2}-\bar{r}_{2j+1}-\bar{r}_{2j}\right) + \\ &+ (\bar{r}_{2j}^2-\bar{r}_i^2)^{1/2}\left(\frac{1}{2}\bar{r}_{2j} + \bar{r}_{2j+1}\right) - \\ &- \left(\bar{r}_{2j}\bar{r}_{2j+1} + \frac{\bar{r}_i^2}{2}\right)\ln\frac{\bar{r}_{2j} + (\bar{r}_{2j}^2-\bar{r}_i^2)^{1/2}}{\bar{r}_{2j+2} + (\bar{r}_{2j+2}^2-\bar{r}_i^2)^{1/2}}\Bigg],\end{aligned} \tag{38.38}$$

$$n_0 - n(r_i) = \sum_{j=1/2}^{N-1}\sum_{k=1}^{3}\alpha_{ij}^{(k)}\varepsilon_i(\bar{r}_{2j+k-1}). \tag{38.39}$$

Like (38.29) equation (38.39) can be written in the form

$$n(r_i) - n(0) = \sum_{\mu=1}^{2N-1}\beta_{i\mu}\varepsilon_r(\bar{r}_\mu). \tag{38.40}$$

The coefficients calculated for the determination of $dn/dx$ and $n(r)-n(0)$ when the inhomogeneity is divided into 25 rings are tabulated in Tables I and II of the inset.

The section $x = \text{const}$ of the axisymmetrical inhomogeneity is divided into 25 rings of equal size, and $\varepsilon_x$ or $\varepsilon_y$ are determined at the middle point and at the two boundary points of the rings (odd values of $j$ correspond to the middle of the ring, and even values to the boundary points). To find $\rho(r_i)-\rho(0)$ or $(\partial n/\partial x)_i$, we take the column of coefficients for the given $i$, and add up the product of each of the coefficients multiplied by the angle of deviation, measured at the point whose number corresponds to the value of the coefficient.

The tables can also be used for calculating an axisymmetrical inhomogeneity split into less than 25 rings. The table used for that purpose is the triangle cut from the basic table along the $(2N-1)$-th line. When calculating $dn/dx$, the result obtained must be multiplied by $N/25$. This leads to a loss of accuracy in the outside rings, particularly for inhomogeneities in which the angles of deviation change greatly in those rings.

By using quadratic approximation and numerical differentiation of a tabular function, we can attain the specified accuracy with a considerably smaller number of rings. The time to process the experimental results is considerably reduced as a result.

The presentation of the coefficients in tabular form facilitates the use of high-speed computers for calculations.

The refractive index of axisymmetrical inhomogeneities can be determined directly from the results of schlieren measurements, using the same simple procedure as in interferometry.

If the function describing the refractive index is discontinuous (e.g., in the case of a shock wave), $\varepsilon(\bar r) \to \infty$ for $\bar r = 1$. This singularity can be isolated by representing $f(\bar r)$ as a sum

$$f(\bar r_i) = 2\int_{\bar r_i}^{1} \frac{\phi(\bar r)\,\bar r\,d\bar r}{\sqrt{\bar r^2-\bar r_i^2}} + V(\bar r_i), \qquad (38.41)$$

where the function $\phi(\bar r)$ is determined by the variation of the refractive index gradient inside the inhomogeneity, and $V(\bar r_i)$ is a function of the angles of deviation due to the refractive index discontinuity. It is expedient to determine $V(\bar r_i)$ on the strength of the following approximation for the function of the deviation angles in the last ring:

$$\varepsilon(\bar r) = \frac{A\bar r}{\sqrt{1-\bar r^2}} + B(1-r) + Cr(1-r). \qquad (38.42)$$

The coefficients $A$, $B$, and $C$ in (38.42) are determined from the values of $\varepsilon(\bar r)$ at the three tabular points of the last ring, $\bar r_{2N-1/2}$, $\bar r_{2N-1}$ and $\bar r_{2N-2}$.

This method leads to a considerable increase in the accuracy of calculation of inhomogeneities with axisymmetrical phase discontinuities, reducing the problem to the preceding one of the calculation of smoothly changing inhomogeneities.

Table I

| | | | | | | | | |
|---|---|---|---|---|---|---|---|---|
| 1 | 3.4246 | | | | | | | |
| 2 | 6.5239 | 3.1131 | | | | | | |
| 3 | −2.9438 | 5.1648 | 2.8245 | | | | | |
| 4 | −3.3331 | 2.3983 | 4.4100 | 2.5932 | | | | |
| 5 | −0.3834 | −2.6509 | −2.0673 | 3.9125 | 2.4072 | | | |
| 6 | −0.7678 | −0.3218 | −2.2544 | −1.8415 | 3.5528 | 2.2548 | | |
| 7 | −0.2444 | −0.6367 | −0.2794 | −1.9902 | −1.6755 | 3.2771 | 2.1273 | |
| 8 | −0.3805 | −0.2065 | −0.5515 | −0.2490 | −1.7990 | −1.5471 | 3.0570 | 2.0188 |
| 9 | −0.1414 | −0.3245 | −0.1807 | −0.4912 | −0.2261 | −1.6529 | −1.5441 | 2.8761 |
| 10 | −0.2311 | −0.1222 | −0.2855 | −0.1619 | −0.4461 | −0.2081 | −1.4368 | −1.3590 |
| 11 | −0.0924 | −0.2013 | −0.1084 | −0.2567 | −0.1475 | −0.4108 | −0.1936 | −1.4417 |
| 12 | −0.1562 | −0.0812 | −0.1795 | −0.0980 | −0.2345 | −0.1361 | −0.3823 | −0.1816 |
| 13 | −0.0652 | −0.1383 | −0.0729 | −0.1628 | −0.0898 | −0.2167 | −0.1269 | −0.3588 |
| 14 | −0.1130 | −0.0582 | −0.1247 | −0.0665 | −0.1496 | −0.0832 | −0.2022 | −0.1191 |
| 15 | −0.0485 | −0.1013 | −0.0527 | −0.1140 | −0.0613 | −0.1389 | −0.0778 | −0.1901 |
| 16 | −0.0856 | −0.0438 | −0.0922 | −0.0484 | −0.1054 | −0.0570 | −0.1300 | −0.0732 |
| 17 | −0.0375 | −0.0776 | −0.0400 | −0.0849 | −0.0449 | −0.0982 | −0.0534 | −0.1224 |
| 18 | −0.0672 | −0.0342 | −0.0712 | −0.0370 | −0.0789 | −0.0419 | −0.0922 | −0.0504 |
| 19 | −0.0299 | −0.0614 | −0.0315 | −0.0659 | −0.0344 | −0.0738 | −0.0394 | −0.0871 |
| 20 | −0.0542 | −0.0275 | −0.0567 | −0.0292 | −0.0615 | −0.0323 | −0.0695 | −0.0373 |
| 21 | −0.0244 | −0.0499 | −0.0255 | −0.0528 | −0.0274 | −0.0578 | −0.0305 | −0.0658 |
| 22 | −0.0446 | −0.0226 | −0.0463 | −0.0238 | −0.0495 | −0.0258 | −0.0546 | −0.0289 |
| 23 | −0.0203 | −0.0413 | −0.0210 | −0.0433 | −0.0223 | −0.0467 | −0.0244 | −0.0518 |
| 24 | −0.0374 | −0.0189 | −0.0386 | −0.0197 | −0.0408 | −0.0211 | −0.0442 | −0.0231 |
| 25 | −0.0172 | −0.0348 | −0.0177 | −0.0362 | −0.0186 | −0.0386 | −0.0200 | −0.0420 |
| 26 | −0.0318 | −0.0160 | −0.0327 | −0.0166 | −0.0342 | −0.0176 | −0.0366 | −0.0190 |
| 27 | −0.0147 | −0.0297 | −0.0151 | −0.0308 | −0.0157 | −0.0324 | −0.0167 | −0.0349 |
| 28 | −0.0274 | −0.0138 | −0.0280 | −0.0142 | −0.0291 | −0.0149 | −0.0309 | −0.0160 |
| 29 | −0.0127 | −0.0257 | −0.0130 | −0.0265 | −0.0135 | −0.0277 | −0.0142 | −0.0295 |
| 30 | −0.0238 | −0.0120 | −0.0243 | −0.0123 | −0.0251 | −0.0128 | −0.0264 | −0.0136 |
| 31 | −0.0111 | −0.0225 | −0.0113 | −0.0230 | −0.0117 | −0.0329 | −0.0122 | −0.0253 |
| 32 | −0.0209 | −0.0106 | −0.0213 | −0.0108 | −0.0219 | −0.0112 | −0.0229 | −0.0118 |
| 33 | −0.0098 | −0.0198 | −0.0100 | −0.0202 | −0.0102 | −0.0210 | −0.0108 | −0.0220 |
| 34 | −0.0186 | −0.0092 | −0.0188 | −0.0096 | −0.0192 | −0.0098 | −0.0202 | −0.0102 |
| 35 | −0.0086 | −0.0176 | −0.0088 | −0.0178 | −0.0092 | −0.0186 | −0.0096 | −0.0192 |
| 36 | −0.0166 | −0.0082 | −0.0168 | −0.0086 | −0.0172 | −0.0086 | −0.0178 | −0.0092 |
| 37 | −0.0078 | −0.0158 | −0.0078 | −0.0160 | −0.0080 | −0.0164 | −0.0084 | −0.0170 |
| 38 | −0.0148 | −0.0074 | −0.0148 | −0.0076 | −0.0154 | −0.0078 | −0.0157 | −0.0080 |
| 39 | −0.0070 | −0.0142 | −0.0072 | −0.0144 | −0.0072 | −0.0148 | −0.0174 | −0.0152 |
| 40 | −0.0134 | −0.0068 | −0.0136 | −0.0068 | −0.0138 | −0.0070 | −0.0141 | −0.0072 |
| 41 | −0.0064 | −0.0128 | −0.0064 | −0.0130 | −0.0066 | −0.0132 | −0.0067 | −0.0136 |
| 42 | −0.0122 | −0.0062 | −0.0122 | −0.0062 | −0.0124 | −0.0064 | −0.0127 | −0.0066 |
| 43 | −0.0058 | −0.0166 | −0.0058 | −0.0118 | −0.0060 | −0.0120 | −0.0060 | −0.0124 |
| 44 | −0.0110 | −0.0055 | −0.0112 | −0.0056 | −0.0112 | −0.0058 | −0.0115 | −0.0058 |
| 45 | −0.0054 | −0.0106 | −0.0054 | −0.0108 | −0.0054 | −0.0108 | −0.0055 | −0.0112 |
| 46 | −0.0102 | −0.0052 | −0.0102 | −0.0052 | −0.0104 | −0.0052 | −0.0105 | −0.0054 |
| 47 | −0.0048 | −0.0097 | −0.0048 | −0.0098 | −0.0048 | −0.0100 | −0.0050 | −0.0102 |
| 48 | −0.0092 | −0.0043 | −0.0092 | −0.0048 | −0.0096 | −0.0048 | −0.0098 | −0.0048 |
| 49 | −0.0065 | −0.0094 | −0.0066 | −0.0096 | −0.0067 | −0.0098 | −0.0069 | −0.0098 |
| $i$ / $j$ | 2 | 3 | 4 | 5 | 6 | 7 | 8 | 9 |

|  |  |  |  |  |  |  |  |  |  |
|---|---|---|---|---|---|---|---|---|---|
| 02 |  |  |  |  |  |  |  |  |  |
| 34 | 0.0397 | 0.9722 |  |  |  |  |  |  |  |
| 47 | 0.0528 | 1.3142 | 0.9612 |  |  |  |  |  |  |
| 71 | 0.0145 | −0.6208 | 1.2988 | 0.9504 |  |  |  |  |  |
| 14 | 0.0268 | −0.6432 | −0.6134 | 1.2838 | 0.9398 |  |  |  |  |
| 07 | 0.0113 | −0.0798 | −0.6356 | −0.6064 | 1.2696 | 0.9298 |  |  |  |
| 93 | 0.0204 | −0.1582 | −0.0788 | −0.6282 | −0.5996 | 1.2554 | 0.9201 |  |  |
| 72 | 0.0092 | −0.0524 | −0.1564 | −0.0780 | −0.6210 | −0.5928 | 1.2419 | 0.9106 | −0.8920 |
| 80 | 0.0170 | −0.0836 | −0.0518 | −0.1546 | −0.0770 | −0.6142 | −0.5865 | 1.2229 | 2.4023 |
| 59 | 0.0117 | −0.0463 | −0.0862 | −0.0728 | −0.1580 | −0.1174 | −0.6029 | −0.7948 | 0.6607 |
|  | 41 | 42 | 43 | 44 | 45 | 46 | 47 | 48 | 49 |

# 39. INHOMOGENEITIES OF COMPLEX SHAPE

The most difficult case is the calculation of the refractive index distribution in an inhomogeneity of a general, unknown shape. No single-valued relationship can be established in this case between the function determining the angle of light deviation at the exit from the inhomogeneity and the refractive index distribution inside the inhomogeneity.

The existing studies of such inhomogeneities are based on raying the working space of the instrument in several directions. It was shown in [27] that by taking three photographs with raying along the three coordinate axes, respectively, we can find the spatial distribution of the refractive index in the inhomogeneity (provided the functions defining this distribution along lines parallel to the axes can be expressed by quadratic polynomials). If the distribution function is represented by a polynomial of a higher degree, we must increase the number of rayings; however, this procedure is not generally used at present due to technical difficulties.

A method for determining the spatial distribution of the refractive index gradient when the unknown function can be approximately considered as constant or linearly varying in some rectangular zone was developed in [6, 7]. The refractive index in each of the rectangular regions was determined by several rayings.

If the object is transparent, we can select the inclination of the light beam to the lines partitioning the inhomogeneity in such a way that a single raying will suffice for calculating the refractive index distribution. The number of rayings must be increased in the case of an opaque body.

This method has been found suitable for measurements in gas-dynamic plants, but its utilization has remained limited. The question of the experimental error and the suitability of the method in the case of an inhomogeneity of almost regular shape has similarly remained unanswered.

The necessity of developing experimental methods for studying objects of complex shapes is increasingly being felt with the advance of science. New computing possibilities are offered by the rapid development of electronic computers; it is no longer necessary to render the final formulas in a simple form suitable for manual calculation. As a result, a new trend has appeared in the development of methods of analysis of complex objects. It consists of developing methods for calculating specific classes of inhomogeneities, in which certain restrictions are imposed on the refractive index distribution function.

Thus the paper by Belotserkovskii, Sukhorukikh, and Tatarenchik [8] describes a method of spatial determination of the density in gaseous flows around axisymmetrical bodies under angles of attack. We shall describe this method for the case when the density distribution between the bow wave and the body (or some other inner plane) is continuous (Figure 103). The $x$ axis is directed along the velocity of the undisturbed flow. The raying direction is parallel to the planes $x$ = const. Let

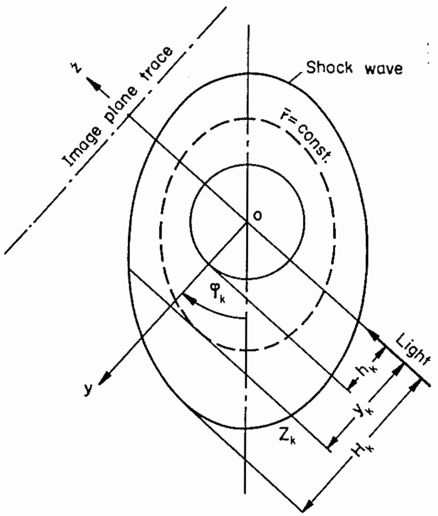

Figure 103

Section $x$ = const of an inhomogeneity formed around a cone under an angle of attack.

contours of the shock wave and the inner boundary of the region being studied be described in these section planes by the equations

$$R = R(\gamma), \qquad t = t(\gamma), \tag{39.1}$$

where $\gamma$ is the polar angle reckoned from the lower vertical axis to the left (from the symmetry plane of the inhomogeneity).

We introduce the relative radial coordinate

$$\bar{r} = \frac{r(\gamma)-t(\gamma)}{R(\gamma)-t(\gamma)}. \tag{39.2}$$

It is equal to 0 at the inner boundary of the flow, and to 1 at the outer boundary. Let the flow have one symmetry plane, and let the angles $\gamma$ be measured from it. The density distribution along the lines $r$ = const of the section $x$ = const can then be expressed by the trigonometric series

$$\bar{\rho}(\bar{r}, \gamma) = \frac{\rho}{\rho_\infty} = \sum_{m=0}^{q-1} \rho_m(\bar{r}) \cos^m \gamma. \tag{39.3}$$

The general problem is simplified under these assumptions. It is now necessary to determine the functions $R = R(\gamma)$, $t = t(\gamma)$, and $\rho_m(\bar{r})$ from the results of optical measurements by raying from several directions. The number $q$ of terms in expansion (39.3) is selected depending on the expected flow pattern, and can be adjusted in the course of the study. The number of raying directions must be no smaller than $q$.

---

If the light ray equations in a Cartesian frame with axis $z_k$ coinciding with the direction of the $k$-th raying are

$$x = x(z_k), \qquad y = y(z_k), \tag{39.4}$$

the result of the schlieren measurements is the field of derivatives

$$\frac{dx}{dz_k} \quad \text{and} \quad \frac{dy_k}{dz_k} \tag{39.5}$$

in the plane of exit of the light from the disturbed region. Schlieren measurements can also be used to determine the quantities $H_k$ and $h_k$, characterizing the outer and inner boundaries of the disturbed region.

The variations of the derivatives are related to the gas density:

$$\frac{\partial\bar{\rho}}{\partial x} = \mu_k \frac{d^2x}{dz_k^2} + \frac{\partial}{\partial z_k}\left(\bar{\rho}\,\frac{dx}{dz_k}\right), \qquad \frac{\partial\bar{\rho}}{\partial y_k} = \mu_k \frac{d^2y_k}{dz_k^2} + \frac{\partial}{\partial z_k}\left(\bar{\rho}\,\frac{dy_k}{dz_k}\right), \tag{39.6}$$

where

$$\mu_k = \frac{\rho_0}{(n_0-1)\rho_\infty}.$$

Expressing the Cartesian partial derivatives of the density function in polar coordinates and integrating the equations along the light trajectory, under the assumption that the rays are only slightly deflected from the straight lines $y_k$ = const, we obtain

$$\int_{z_{k1}}^{z_{k2}} \left[\frac{\partial\bar{\rho}}{\partial x} + A\frac{\partial\bar{\rho}}{\partial\bar{r}} + B\frac{\partial\bar{\rho}}{\partial\gamma}\right] dz_k = (\mu_k + \bar{\rho}_2)\left[\left(\frac{dx}{dz_k}\right)_2 - \left(\frac{dx}{dz_k}\right)_1\right] + \left(\frac{dx}{dz_k}\right)_1 (\bar{\rho}_2 - \bar{\rho}_1); \tag{39.7}$$

$$\int_{z_{k1}}^{z_{k2}} \left[\frac{\cos(\gamma-\phi_k)}{R-t}\frac{\partial\bar{\rho}}{\partial\bar{r}} - \frac{\sin(\gamma-\phi_k)}{t+\bar{r}(R-t)}\frac{\partial\bar{\rho}}{\partial\gamma}\right] dz_k = (\mu_k + \bar{\rho}_2)\left[\left(\frac{dy_k}{dz_k}\right)_2 - \left(\frac{dy_k}{dz_k}\right)_1\right] + \left(\frac{dy_k}{dz_k}\right)_1 (\bar{\rho}_2 - \bar{\rho}_1). \tag{39.8}$$

Here

$$A(x, \bar{r}, \gamma, \alpha) = -\frac{1}{R-t}\left\{\tan\alpha\cos\gamma + \frac{\partial t}{\partial x} + \bar{r}\frac{\partial}{\partial x}(R-t) + \frac{\tan\alpha\sin\gamma}{t+\bar{r}(R-t)}\left[\frac{\partial t}{\partial\gamma} + \bar{r}\frac{\partial}{\partial\gamma}(R-t)\right]\right\}; \tag{39.9}$$

$$B(x, \bar{r}, \gamma, \alpha) = \frac{\tan\alpha\sin\gamma}{t+\bar{r}(R-t)}; \tag{39.10}$$

the subscripts 1 and 2 correspond to the initial and final points of the ray trajectory in the disturbed region; the derivative $\partial\bar{\rho}/\partial x$ is taken for constant values of $r$ and $\gamma$.

Using (39.3), we obtain the following equations for the functions $\rho_m(x, \bar{r})$ and their derivatives:

$$\sum_{m=0}^{q-1}\int_{z_{k1}}^{z_{k2}}\left[\left(\frac{\partial\rho_m}{\partial x}+A\frac{\partial\rho_m}{\partial\bar{r}}\right)\cos\gamma-mB\rho_m\sin\gamma\right]\cos^{m-1}\gamma\,dz_k=$$

$$=(\mu_k+\bar{\rho}_2)\left[\left(\frac{dx}{dz_k}\right)_2-\left(\frac{dx}{dz_k}\right)_1\right]+\left(\frac{dx}{dz_k}\right)_1(\bar{\rho}_2-\bar{\rho}_1); \tag{39.11}$$

$$\sum_{m=0}^{q-1}\int_{z_{k1}}^{z_{k2}}\left[\frac{\cos(\gamma-\phi_k)\cos\gamma}{R-t}\frac{\partial\rho_m}{\partial\bar{r}}+\frac{\sin(\gamma-\phi_k)\sin\gamma}{t+\bar{r}(R-t)}m\rho_m\right]\cos^{m-1}\gamma\,dz_k=$$

$$=(\mu_k+\bar{\rho}_2)\left[\left(\frac{dy_k}{dz_k}\right)_2-\left(\frac{dy_k}{dz_k}\right)_1\right]+\left(\frac{dy_k}{dz_1}\right)_1(\bar{\rho}_2-\bar{\rho}_1). \tag{39.12}$$

These equations are supplemented by the equation obtained by integrating $\partial\bar{\rho}/\partial z_k$ along the $z_k$ axis

$$\sum_{m=0}^{q-1}\int_{z_{kl}}^{z_{k2}}\left[\frac{\sin(\gamma-\phi_k)\cos\gamma}{R-t}\frac{\partial\rho_m}{\partial\bar{r}}-\frac{\cos(\gamma-\phi_k)\sin\gamma}{t+\bar{r}(R-t)}m\rho_m\right]\cos^{m-1}\gamma\,dz_k=\bar{\rho}_2-\bar{\rho}_1. \tag{39.13}$$

The equations obtained for $k = 1, 2, \ldots, q$ form a system of $3q$ equations with $3q$ unknown functions $\rho_m$, $\partial\rho_m/\partial\bar{r}$, and $\partial\rho_m/\partial x$.

The quantities $(dx/dz_k)_{1,2}$ and $(dy_k/dz_k)_{1,2}$ in (39.11) and (39.12) correspond to the boundaries of the region of continuous variation of the density and do not include the rotation of the light rays in the shock wave.

To calculate the corrections, we introduce the subscripts 0 and 3, corresponding to the position before the entry into and after the exit from the shock wave. The quantities $(dx/dz_k)_0$ and $(dy_k/dz_k)_0$ can be considered equal to zero; the schlieren apparatus measures the differences

$$\left(\frac{dx}{dz_k}\right)_3-\left(\frac{dx}{dz_k}\right)_0 \quad\text{and}\quad \left(\frac{dy_k}{dz_k}\right)_3-\left(\frac{dy_k}{dz_k}\right)_0.$$

Introduce a right-hand triad of unit vectors $\mathbf{l}_1$, $\mathbf{l}_2$ and $\mathbf{l}_3$, directing $\mathbf{l}_1$ along the $x_1$ axis, $\mathbf{l}_2$ along the polar ray $\gamma = \text{const}$ in the plane $x = \text{const}$, and $\mathbf{l}_3$ along the tangent to the line $r = \text{const}$ in the same plane. The unit vector $\mathbf{V}$ of the outer normal to the shock wave surface, and the unit vector $\mathbf{l}_{k0}$ of the ray penetrating the shock wave along the $z_k$ axis can now be written as

$$\mathbf{V}=\frac{-\left(\dfrac{\partial R}{\partial x}\right)_1\mathbf{l}_1+\mathbf{l}_2-\dfrac{1}{R}\dfrac{\partial R}{\partial\gamma}\mathbf{l}_3}{\sqrt{1+\left(\dfrac{\partial R}{\partial x}\right)_1^2+\left(\dfrac{1}{R}\dfrac{\partial R}{\partial\gamma}\right)^2}}, \tag{39.14}$$

$$\left(\frac{\partial R}{\partial x}\right)_1=\frac{\partial R}{\partial x}+\tan\alpha\left(\cos\gamma+\sin\gamma\frac{1}{R}\frac{\partial R}{\partial\gamma}\right), \tag{39.15}$$

$$\mathbf{l}_{k0}=\sin(\gamma-\phi_k)\,\mathbf{l}_2-\cos(\gamma-\phi_k)\,\mathbf{l}_3. \tag{39.16}$$

The cosine of the angle $\beta_0$ between the vectors $\mathbf{l}_{k0}$ and $\mathbf{V}$ is equal to

$$\cos\beta_0=\mathbf{V}\mathbf{l}_{k0}=\frac{\sin(\gamma-\phi_k)+\cos(\gamma-\phi_k)\dfrac{1}{R}\dfrac{\partial R}{\partial\gamma}}{\sqrt{1+\left(\dfrac{\partial R}{\partial x}\right)_1^2+\left(\dfrac{1}{R}\dfrac{\partial R}{\partial\gamma}\right)^2}}. \tag{39.17}$$

After its passage through the shock wave, the light ray propagates in the direction $\mathbf{l}_{k1}$. The sine of the angle $\beta_1$ between the vectors $\mathbf{l}_{k1}$ and $\mathbf{V}$ is

$$\sin\beta_1=\sin\beta_0\frac{1+\mu_k}{\bar{\rho}_1+\mu_k}. \tag{39.18}$$

The vector $\mathbf{l}_{k1}$ is expressed by $\mathbf{l}_{k0}$ and $\mathbf{V}$ as

$$\mathbf{l}_{k1}=\frac{\sin\beta_1}{\sin\beta_0}\mathbf{l}_{k0}+\frac{\sin(\beta_0-\beta_1)}{\sin\beta_0}\mathbf{V}. \tag{39.19}$$

Representing the vector $\mathbf{l}_{y_k}$ as a vector product

$$\mathbf{l}_{y_k}=[\mathbf{l}_1\mathbf{l}_{k0}], \tag{39.20}$$

we find $(dx/dz_k)_1$ and $(dy_k/dz_k)_1$ as

$$\left(\frac{dx}{dz_k}\right)_1=\mathbf{l}_{k1}\mathbf{l}_1=-\frac{\dfrac{\sin(\beta_0-\beta_1)}{\sin\beta_0}\left(\dfrac{\partial R}{\partial x}\right)_1}{\sqrt{1+\left(\dfrac{\partial R}{\partial x}\right)_1^2+\left(\dfrac{1}{R}\dfrac{\partial R}{\partial\gamma}\right)^2}}; \tag{39.21}$$

$$\left(\frac{dy_k}{dz_k}\right)_1=\mathbf{l}_{k1}\mathbf{l}_{y_k}=\left(\frac{\sin(\beta_0-\beta_1)}{\sin\beta_0}\right)\frac{\cos(\gamma-\phi_k)-\sin(\gamma-\phi_k)\dfrac{1}{R}\dfrac{\partial R}{\partial\gamma}}{\sqrt{1+\left(\dfrac{\partial R}{\partial x}\right)_1^2+\left(\dfrac{1}{R}\dfrac{\partial R}{\partial\gamma}\right)^2}}. \tag{39.22}$$

A similar examination of the ray rotation upon leaving the shock wave yields equations for $(dx/dz_k)_2$ and $(dy_k/dz_k)_2$:

$$\left(\frac{dx}{dz_k}\right)_2 = l_{k2}l_1 = \frac{\sin\beta_2}{\sin\beta_3}\left(\frac{dx}{dz_k}\right)_3 - \frac{\sin(\beta_3-\beta_2)}{\sin\beta_3}\frac{\left(\dfrac{\partial R}{\partial x}\right)_1}{\sqrt{1+\left(\dfrac{\partial R}{\partial x}\right)_1^2+\left(\dfrac{1}{R}\dfrac{\partial R}{\partial \gamma}\right)^2}}; \qquad (39.23)$$

$$\left(\frac{dy_k}{dz_k}\right)_2 = \frac{\sin\beta_2}{\sin\beta_3}\left(\frac{dy_k}{dz_k}\right)_3 + \frac{\sin(\beta_3-\beta_2)}{\sin\beta_3}\frac{\cos(\gamma-\phi_k)-\sin(\gamma-\phi_k)\dfrac{1}{R}\dfrac{\partial R}{\partial \gamma}}{\sqrt{1+\left(\dfrac{\partial R}{\partial x}\right)_1^2+\left(\dfrac{1}{R}\dfrac{\partial R}{\partial \gamma}\right)^2}}, \qquad (39.24)$$

where $\beta_2$ and $\beta_3$ are the angles between the light ray and the normal to the wave before and after the exit from the shock wave.

The right-hand sides of equations (39.11) and (39.12) can be determined with the aid of formulas (39.21) through (39.24).

To simplify the equations, we divide the range of $r$ into $j$ parts by the tabular points

$$\bar{r}_i = 1 - i\Delta\bar{r} = 1 - \frac{i}{j} \qquad (i = 1, 2, \ldots, j), \qquad (39.25)$$

assuming that $\partial\rho_m/\partial\bar{r}$ and $\partial\rho_m/\partial x$ are constant within each segment $\bar{r}_i \leqq \bar{r} \leqq \bar{r}_{i-1}$ namely,

$$\left(\frac{\partial\rho_m}{\partial\bar{r}}\right)_{\bar{r}_i+\frac{1}{2}\Delta\bar{r}} = \rho_{mi}^{\bar{r}}, \qquad \left(\frac{\partial\rho_m}{\partial x}\right)_{\bar{r}_i+\frac{1}{2}\Delta\bar{r}} = \rho_{mi}^{x}. \qquad (39.26)$$

Writing inside the segment

$$\rho_m(\bar{r}) = \rho_{mi} + \rho_{mi}^{\bar{r}}\left[\bar{r} - \left(\bar{r}_i + \frac{\Delta\bar{r}}{2}\right)\right], \qquad (39.27)$$

we transform the system of integral equations (39.11)–(39.13) into a system of algebraic linear equations. By solving it for the gas density gradients in each zone of the inhomogeneity, we can determine the local values of these parameters in inhomogeneities of the same shape.

We observe that the procedure used in [8] is analogous to the method of calculation of axisymmetrical inhomogeneities; the form of the function is specified in some narrow range of the coordinates. However, the shape of the approximation zone and the form of the function are selected in accordance with the type of the inhomogeneity and reflect the true variation of the parameters. This increases considerably the accuracy of the method compared with the more general methods based on the formal partitioning of the space, without taking into account the specific characteristics of the object. This trend seems very promising. Similar methods for other classes of objects will probably be developed in the near future.

## 40. REFRACTION

Light propagates inside the inhomogeneity along a curved trajectory, which can have quite a complicated shape. In the computing methods, we replace this curved trajectory by a straight line with some mean angle of deviation. As a result, an error is introduced in the determination of the coordinates of different points of the object.

To find these errors, we shall calculate the light path in a plane inhomogeneity. We assume for the sake of simplicity that the object parameters vary only in the $y$ direction. This reduces (36.10) to the one equation

$$\frac{d^2y}{dz^2} = \left[1 + \left(\frac{dy}{dz}\right)^2\right]\frac{d\ln n}{dy}. \qquad (40.1)$$

Assuming a small angle of deviation and slow variation of the function $n(y)$ whose values are close to one (these assumptions are valid for gaseous inhomogeneities), we reduce (40.1) to the form

$$\frac{d^2y}{dz^2} = \frac{dn}{dy}. \qquad (40.2)$$

In order to be able to use this equation, we require an expression for the refractive index. As a first step, let us approximate it by a linear function of the coordinate

$$\frac{dn}{dy} = A + By. \qquad (40.3)$$

The integration of (40.2) then yields the following equation for the light path in the given medium:

$$y = \frac{A(e^{\sqrt{B}z}-1)^2}{2Be^{\sqrt{B}z}}. \qquad (40.4)$$

In deriving (40.4) we assumed that the light enters the inhomogeneity at $y = 0$ and initially propagates along the $z$ axis. Since $\sqrt{B}z$ is small, we may frequently use the approximate equation

$$y = \frac{Az^2}{2}\left(1 + \frac{Bz^2}{12}\right). \qquad (40.5)$$

If the second term between parentheses is small compared to the first term, we can simplify (40.5) further and take the ray shift to be mainly determined by the constant component of the refractive index gradient,

$$y_1 = \tfrac{1}{2}AL^2, \qquad (40.6)$$

where $L$ is the light path length in the inhomogeneity and $y_1$ is the difference between the $y$ coordinates of the light entrance and exit points.

This error is substantial for sharply varying inhomogeneities such as shock waves, boundary layers, etc. The shift is small as a rule in smoothly varying objects. Its evaluation for the inhomogeneity represented in Figures 23 and 24 established that the curvature of the refractive index distribution function is the maximum at the middle of the object, where the light shift is 0.2 mm.

To reduce the error caused by the light shift in plane inhomogeneities or to eliminate it completely, we must focus the schlieren camera on the middle of the object.

Another error is due to the passage of light through zones with different values of the refractive index gradient, since we assumed that this quantity is constant along the entire light path.

The differential equation for the angle of light deviation is

$$d\varepsilon = \frac{dn}{dy}\,dz. \tag{40.7}$$

Since $dy/dz$ is the tangent of the angle the light ray makes with the $z$ axis, we have

$$\tan\varepsilon\, d\varepsilon = dn, \tag{40.8}$$

whose solution yields

$$\ln\cos\varepsilon = n - n_0, \tag{40.9}$$

or, to a certain approximation,

$$\varepsilon^2 = 2(n - n_0). \tag{40.10}$$

We can determine from this equation the mean value of the refractive index gradient

$$\left(\frac{dn}{dy}\right)_{\mathrm{av}} = \frac{\varepsilon^2}{2y_1}. \tag{40.11}$$

We assume in the calculations that

$$\frac{dn}{dy} = \frac{\varepsilon}{L}. \tag{40.12}$$

The relative error in the determination of the refractive index gradient is

$$\kappa = 1 - \frac{2y_1}{\varepsilon L}. \tag{40.13}$$

Allowing for the curvature of the light trajectory, we have the following expression for $\varepsilon$:

$$\varepsilon = LA\left(1 + \frac{BL^2}{6}\right). \tag{40.14}$$

The substitution of (40.14) and (40.5) in (40.13) yields

$$\kappa = \frac{L^2}{12}\,\frac{d^2n}{dy^2}, \tag{40.15}$$

where $B$ has been replaced by $d^2n/dy^2$.

We shall estimate the approximate value of this error for the inhomogeneity represented in Figures 23 and 24. The second derivative is maximum at the middle of the model, where it is equal to $5.6 \times 10^{-8}\ \mathrm{mm}^{-2}$. The error at these points is equal to 0.2%, which is negligible. Obviously, however, an assessment based on (40.15) must be performed in every calculation, since a small increase in the second derivative suffices for causing an error of a few per cent.

Such calculations for axisymmetrical flows are complicated and have not been conducted so far. The allowance for the refractive shifts of the light rays in this case has been based on the assumption that the deviation is the largest on the inhomogeneity–shock wave interface, and that inside the inhomogeneity the light can be considered to propagate along a straight line.

As a rule, the shock wave surface is piece-wise approximated by conical surfaces, the assumption being that light entering a certain part of the cone does not leave it within the inhomogeneity.

The shift of the light ray resulting from the bending of its path inside the object can be estimated just as in the case of a plane object. However, this is usually not necessary, the quantities in question being small compared with the refraction in the shock wave.

By means of this simplified model of the axisymmetrical object we can calculate the error in the angle of deviation introduced by the assumption that the light continues propagating in the initial direction, and determine the portions of the inhomogeneity in which this error is substantial.

## 41. ERRORS OF SCHLIEREN MEASUREMENTS

Errors can occur in quantitative schlieren measurements at different stages of the measurement process, and can be due to different factors. The first group of errors are the experimental errors, due to vibrations, non-uniform illumination of the slit image in the receiving part of the schlieren instrument, variation of the emulsion properties, etc. The causes of these errors are highly varied and depend on the specific features of the method used.

The second group of errors are the computational model errors, due to the difference between the real body and the ideal geometrical shape (plane or axisymmetrical) assumed in the calculation of the refractive index distribution. It is very difficult to estimate this error, and it is even more difficult to introduce suitable corrections in the working formulas, especially since many shapes are irregular and change in a random manner in time and space. In practice, the shape irregularity is generally estimated by taking schlieren photographs at different positions of the inhomogeneity. The study of the schlieren pattern of the inhomogeneity-free flow is of great importance in gas-dynamic measurements.

An additional source of errors occurs in the calculation of axisymmetrical objects, caused by the approximation of the sought function. We shall calculate the resulting error for the two most widely used methods, based, respectively, on linear and quadratic approximation of the function.

Series-expanding the function defining the light deviation distribution in the section studied, we write

$$\varepsilon = \varepsilon_i + (y-y_i)\left(\frac{d\varepsilon}{dy}\right)_i + \frac{(y-y_i)^2}{2}\left(\frac{d^2\varepsilon}{dy^2}\right)_i + \frac{(y-y_i)^3}{6}\left(\frac{d^3\varepsilon}{dy^3}\right)_i + \ldots \qquad (41.1)$$

The linear approximation omits all but the first two terms of this series, and the quadratic approximation retains only the first three terms. The absolute error in the determination of the function will be equal in each case to the sum of the dropped terms.

The error of the linear approximation in the determination of $dn/dx$ is

$$\Delta_{ix} = \frac{1}{\pi}\sum_{j=i}^{N-1}\left(\frac{d^2\varepsilon_x}{dy^2}\right)_j \int_{y_j}^{y_{j+1}} \frac{(y-y_j)dy}{\sqrt{y^2-y_i^2}}. \qquad (41.2)$$

The evaluation of the integral leads to the expression

$$\Delta_{ix} = \frac{1}{\pi}\sum_{j=i}^{N-1}\left(\frac{d^2\varepsilon_x}{dy^2}\right)_j \left[\sqrt{y_{j+1}^2-y_i^2} - \right.$$

$$\left. - y_j \ln\frac{y_{j+1}+\sqrt{y_{j+1}^2-y_i^2}}{y_j+\sqrt{y_j^2-y_i^2}} - \sqrt{y_j^2-y_i^2}\right]. \qquad (41.3)$$

It is convenient in practical calculations to replace the function curvature by its sagitta (i.e., its deviation from the linear approximation in the middle, which is related to the curvature by the relationship

$$P_{ix} = \left(\frac{d^2\varepsilon_x}{dy^2}\right)_i \frac{R^2}{8N^2}. \qquad (41.4)$$

By allowing for this expression and passing to reduced coordinates we obtain

$$\Delta_{ix} = \frac{8N}{\pi R}\sum_{j=i}^{N-1} P_{ix}\left[\sqrt{(j+1)^2-i^2} - \right.$$

$$\left. - j \ln\frac{j+1+\sqrt{(j+1)^2-i^2}}{j+\sqrt{j^2-i^2}} - \sqrt{j^2-i^2}\right]. \qquad (41.5)$$

If the calculation according to (41.3) is difficult and we need only an estimate of the error, we can use the mean sagitta over the integration range

$$\Delta_{ix} = \frac{8N}{\pi R}(P_{ix})_{\text{av}}\sum_{j=i}^{N-1}\left[\sqrt{(j+1)^2-i^2} - \right.$$

$$\left. -j \ln\frac{j+1+\sqrt{(j+1)^2-i^2}}{j+\sqrt{j^2-i^2}} - \sqrt{j^2-i^2}\right]. \qquad (41.6)$$

In the case of the quadratic approximation, the error will depend on the value of the third derivative of the empirical function. Integration of the fourth term in (41.1) leads to the following error:

$$\Delta_{ix}^{\text{q}} = \frac{1}{2\pi}\sum_{j=i}^{N-1}\left(\frac{d^3\varepsilon_x}{dy^3}\right)_j \left[\left(\frac{y_i^2}{2}+y_j^2\right)\ln\frac{y_{j+1}+\sqrt{y_{j+1}^2-y_i^2}}{y_j+\sqrt{y_j^2-y_i^2}} + \right.$$

$$\left. + \left(\frac{y_{j+1}-4y_j}{2}\right)\sqrt{y_{j+1}^2-y_i^2} + \frac{3y_j}{2}\sqrt{y_j^2-y_i^2}\right]. \qquad (41.7)$$

To determine the third derivative, we partition the zone $(j, j+1)$ into three equal parts and measure the angle of light deviation at the end points of these parts. Substituting the corresponding values of $y$ and $\varepsilon$ in (41.1), we obtain three equations for the three unknown derivatives. Their solution yields

$$\left(\frac{d^3\varepsilon}{dy^3}\right)_j = 27\left(\frac{N}{R}\right)^3 [(\varepsilon_{j+1}-\varepsilon_j)-3(\varepsilon_{j+2/3}-\varepsilon_{j+1/3})]. \qquad (41.8)$$

Substituting (41.8) in (41.7) and changing over to reduced coordinates, we obtain

$$\Delta_{ix}^{\text{q}} = \frac{27N}{2\pi R}(K_{ix})_{\text{av}}\sum_{j=i}^{N-1}\left[\left(\frac{i^2}{2}+j^2\right)\ln\frac{j+1+\sqrt{(j+1)^2-i^2}}{j+\sqrt{j^2-i^2}} + \right.$$

$$\left. + \left(\frac{1-3j}{2}\right)\sqrt{(j+1)^2-i^2} + \frac{3j}{2}\sqrt{j^2-i^2}\right], \qquad (41.9)$$

where

$$K_{ix} = [(\varepsilon_{j+1,\,x}-\varepsilon_{j,\,x})-3(\varepsilon_{j+2/3,\,x}-\varepsilon_{j+1/3,\,x})]_{\text{av}}. \qquad (41.10)$$

Radial changes of the refractive index are calculated by (38.37), where the empirical function itself, and not its derivatives, figures in the integrand. In every other aspect, formula (38.37) is similar to formula (38.9). The calculation error in the case of a linear approximation is described by the equation

$$\Delta_{ir} = \frac{4}{\pi}(K_{ix})_{\text{av}} \sum_{j=i}^{N-1} \left[ \left(\frac{i^2}{2} + j^2\right) \ln \frac{j + 1 + \sqrt{(j+1)^2 - i^2}}{j + \sqrt{j^2 - i^2}} + \right.$$

$$\left. + \left(\frac{1-3j}{2}\right)\sqrt{(j+1)^2 - i^2} + \frac{3j}{2}\sqrt{j^2 - i^2} \right]. \qquad (41.11)$$

The error in the quadratic approximation is

$$\Delta^{q}_{ir} = \frac{9}{2\pi}(K_{ir})_{\text{av}} \sum_{j=i}^{N-1} \left[ -\left(\frac{11}{6}j^2 - \frac{5}{6}j + \frac{1}{3} + \frac{2}{3}i^2\right)\sqrt{(j+1)^2 - i^2} + \right.$$

$$\left. + \frac{11j^2 + 4i^2}{6}\sqrt{j^2 - i^2} + \frac{j(2j^2 + 3i^2)}{2} \ln \frac{j + 1 + \sqrt{(j+1)^2 - i^2}}{j + \sqrt{j^2 - i^2}} \right]. \qquad (41.12)$$

The values of the sums in (41.6), (41.9) and (41.12) have been plotted in Figure 104. A quick estimate of the error for the different cases of experimental studies is possible on the basis of these curves.

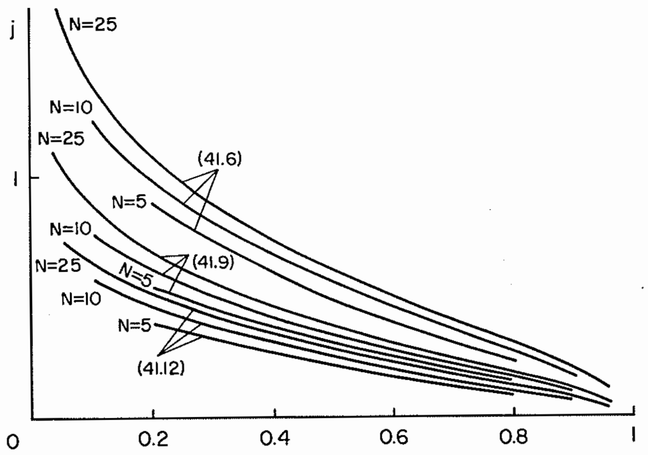

Figure 104

Curves of the sums in (41.6), (41.9), (41.12).

The comparison of the errors corresponding to the linear and the quadratic approximations demonstrates that in gas-dynamic measurements the use of a quadratic approximation lowers the error and makes it possible to reduce the number of zones by more than half.

On the strength of the equations derived, we can select the number of zones for which the error will not exceed some specified value for a given form of the function.

The required refractive index or refractive index gradient is found by adding separate elements, each of which is known with a certain accuracy, depending on the errors of the measurement method used. If we assume that all the angles of light deviation are measured with the same root-mean-square error $\Delta\varepsilon_m$, the total error of determination of the refractive index gradients will be

$$\Delta\varepsilon = \Delta\varepsilon_{\text{av}}\sqrt{\sum_i \alpha_i^2}\,, \qquad (41.13)$$

where $\alpha_i$ are the coefficients before the light deviation angles in the inhomogeneity. Expression (41.13) defines the maximum error value. Actually, the error is considerably smaller, due to the fact that the angle measurement errors have different signs at different points of the section.

Unlike the approximation error, this error increases with the increase in the number of zones. The value selected for $N$ thus should not be too large; the optimum value of $N$ is the value for which the measurement error is equal to the approximation error. The optimal number of zones depends on the value of the third derivative of the empirical function (or on the second derivative, determined by the function curvature, in the case of linear approximation) and on the measurement errors. Another factor which must be taken into account is the length of the calculations and the required accuracy of the final results.

# IX

# THE RELATION OF THE REFRACTIVE INDEX TO OTHER CHARACTERISTICS OF THE MEDIUM

## 42. GAS DENSITY DETERMINATION

The refractive index is a purely optical characteristic of the medium. While the determination of its value can be the final objective in certain cases, other parameters are generally more interesting. Thus in the study of diffusion or centrifugal separation, the most significant parameter is the chemical composition of the mixture at every point of the object; in the study of gaseous flow, it is the parameters of state — density, temperature, and pressure of the gas — that are the most important. As a result, the processing of the schlieren photographs does not end with the determination of the refractive index distribution.

The gas density can be determined from the refractive index. The derivation of the corresponding relation is based on an examination of the behavior of molecules in the field of the light wave, using the molecular theory of gases [28]. We assume that the wave field acts as the field of a capacitor on the gas. Draw a sphere of large enough radius around a molecule. The field acting on this molecule will be

$$\mathbf{F} = \mathbf{F}_1 + \mathbf{F}_2 + \mathbf{F}_3\,, \tag{42.1}$$

where $\mathbf{F}_1$ is the effective capacitor field, $\mathbf{F}_2$ is the field created by the gas inside the capacitor (excluding the sphere drawn around the molecule), and $\mathbf{F}_3$ results from the polarization inside the sphere. The first term of (42.1) can be represented in the form

$$\mathbf{F}_1 = \mathbf{E} + 4\pi\mathbf{P}\,, \tag{42.2}$$

where $\mathbf{P}$ is the polarization of the medium, and $\mathbf{E}$ is the external field. The field $\mathbf{F}_2$ can be represented as the sum of the fields of the charges induced on the capacitor plates and on the surface of the object:

$$\mathbf{F}_2 = -\,4\pi\mathbf{P} + \int_0^{\pi} \frac{\mathbf{P}\cos^2\theta}{r^2}\, 2\pi r^2 \sin\theta\, d\theta = -\frac{8}{3}\,\pi\mathbf{P}\,. \tag{42.3}$$

We assume in the calculation of $\mathbf{F}_3$ that the molecules are dipoles. Adding together all the molecules of the medium except the central one we obtain for each field component

$$(\mathbf{F}_3)_x = \mathbf{P}_x \left\{ -\sum_k \frac{1}{r_k^3} + \sum_k \frac{3x_k^2}{r_k^5} \right\} + 3\mathbf{P}_y \sum_k \frac{x_k y_k}{r_k^5} + 3\mathbf{P}_z \sum_k \frac{x_k z_k}{r_k^5}\,. \tag{42.4}$$

Averaging over a random distribution of the dipoles, we obtain inside the sphere (provided the number of dipoles is sufficiently large)

$$\mathbf{F}_3 = 0. \tag{42.5}$$

The substitution of (42.2), (42.3), and (42.5) in (42.1) yields

$$\mathbf{F} = \mathbf{E} + \frac{4\pi}{3}\,\mathbf{P}\,. \tag{42.6}$$

We can express the polarization as

$$\mathbf{P} = Na\mathbf{F}\,, \tag{42.7}$$

where $a$ is the polarizability of the molecules, and $N$ is the number of molecules per unit volume. Also

$$\varepsilon\mathbf{E} = \mathbf{E} + 4\pi\mathbf{P}\,. \tag{42.8}$$

Eliminating $\mathbf{F}$ and $\mathbf{P}$ between the last three expressions, and seeing that $\varepsilon = n^2$, we obtain

$$\frac{n^2 - 1}{n^2 + 2} = \frac{4\pi}{3}\,Na\,. \tag{42.9}$$

This is the well-known Lorentz–Lorenz equation.

The refractive index of gases is close to 1, and (42.9) can be transformed to

$$n - 1 = 2\pi Na\,. \tag{42.10}$$

The number of molecules per unit volume $N$ is expressed in terms of the density and the molecular weight of the gas, and (42.10) can be written in the form of the Gladstone–Dale equation

$$\frac{n - 1}{\rho} = K\,, \tag{42.11}$$

where $K$ is constant for a given gas.

This derivation of the Lorentz–Lorenz and Gladstone–Dale equations is based on the most elementary theory, which ignores a large number of factors. The variability of the wave field and the dependence of the polarizability on the external field frequency were not considered; the interaction between the light wave and the medium was disregarded, etc. The application of a more rigorous molecular theory and the examination of the phenomenon on the basis of quantum mechanics lead to somewhat different results. The molecular refraction of gases proves to be dependent on the temperature, due to the excitation of vibrational levels of molecules.

This effect was analyzed by Levin [33], who represented the molecule by an anharmonic oscillator of moderate vibrational energy and assumed a Boltzmann distribution of molecules over energy levels. The calculations lead to the result

$$\frac{n-1}{\rho} = K(1 + \beta T), \tag{42.12}$$

where $\beta$ is constant for a given gas. Estimates give $\beta = 10^{-6}$, which corresponds to the following temperature gradient of the refractive index:

$$\left(\frac{dn}{dT}\right)_{\rho=\mathrm{const}} \approx 5 \times 10^{-10}\ \mathrm{deg}^{-1}. \tag{42.13}$$

Measurements of the $CO_2$ refraction as a function of the temperature for this case give $(dn/dT)_{\rho=\mathrm{const}} = 3 \times 10^{-9}$. A satisfactory fit was observed between the theoretical and experimental results.

The corrections for the temperature dependence of the molecular refraction are meaningless in practical schlieren measurements, since the measurement errors caused by other factors are much greater. The quantum-mechanical calculation, which is more accurate than the approximate calculation, corroborates the validity of the Lorentz–Lorenz and Gladstone–Dale equations.

Experimental studies show that the above relations are achieved in practice with a high degree of accuracy. The value of $K$ remains constant within wide ranges of gas pressure and temperature. Thus for air at normal temperature, $K$ varies by no more than 0.5% when the pressure increases from 1 to 200 atm. The same is roughly true for other gases as well. Numerous experiments have also established that $K$ is independent of the temperature.

Equation (42.11) is frequently used in the form

$$\frac{n-1}{\rho} = \frac{n_0 - 1}{\rho_0}, \tag{42.14}$$

where $\rho_0$ and $n_0$ are, respectively, the density and the refractive index at normal temperature and pressure. By means of this expression we can easily determine the value of $K$ in different systems of units. The density is found from the molecular weight. The refractive index $n_0$ of different gases is given in Table 5 for the wavelength of 5893 Å. The table also lists the constants of the Cauchy dispersion equation

$$n - 1 = A\left(1 + \frac{B}{\lambda^2}\right), \tag{42.15}$$

from which the refractive index can be calculated for any other wavelength.

Table 5

| Gas | $(n_0 - 1) \cdot 10^4$ for 760 mm Hg and 0° C; $\lambda = 5893$ Å | $A \cdot 10^5$ | $B \cdot 10^{11}$ |
|---|---|---|---|
| Air | 2.92 | 28.71 | 5.67 |
| $O_2$ | 2.71 | 26.63 | 5.07 |
| $N_2$ | 2.98 | 29.06 | 7.7 |
| $H_2$ | 1.39 | 13.58 | 7.52 |
| Mercury vapors | 9.33 | 87.8 | 22.65 |
| Ne | 0.67 | 6.66 | 2.4 |
| Ar | 2.81 | 27.92 | 56 |
| He | 0.35 | 3.48 | 2.3 |
| Kr | 4.27 | 41.89 | 6.97 |
| Xe | 7.02 | 68.23 | 10.14 |
| $NH_4$ | 3.77 | 36.45 | 11.8 |
| $CO_2$ | 4.50 | 45 | 65 |
| NO | 2.95 | 29.5 | 74 |
| HCl | 4.46 | 43.56 | 8.7 |
| HBr | 5.77 | 56 | 11 |
| HI | 9.28 | 89 | 15 |
| $O_3$ | 5.11 | 48 | 23 |
| Cl | 7.61 | 74 | 10 |
| Water vapors | 2.52 | 24.35 | 8.72 |

All the values are given for dry gases. The refractive indices for wet gases are found by the formula

$$n_w = n_d - \frac{4.1 \times 10^{-5}\, m}{760}, \tag{42.16}$$

where $m$ is the partial pressure of water vapor in millimeters of mercury column.

## 43. STUDY OF MIXTURES

Mixtures of substances with different refractive indices are encountered in the study of diffusion and centrifugation of various gases. The refractive index gradient and the light deviation in the inhomogeneity are determined by the variation of the component concentrations in the object. The concentrations can be found because of the additivity of the refractions of the mixture components.

The refractive index can be expressed in terms of the polarizability and the component concentrations as

$$\frac{n^2 - 1}{n^2 + 2} = \frac{4\pi}{3}(N_1 a_1 + N_2 a_2 + \ldots). \tag{43.1}$$

Multiplying the two sides of (43.1) by $\bar{M}/\rho$, we obtain the mean refraction:

$$\bar{R} = \frac{n^2-1}{n^2+2}\left(\frac{\bar{M}}{\rho}\right) = \kappa_1 R_1 + \kappa_2 R_2 + \ldots, \tag{43.2}$$

where $\kappa_i$ and $R_i$ are the concentration and the refraction of the $i$-th component. Because of additivity, we can calculate the concentration of the components. Thus for a binary mixture

$$\kappa_1 = \frac{\bar{R}-R_2}{R_1-R_2}. \tag{43.3}$$

$\bar{R}$ is found by measuring the refractive index, the temperature, and the pressure of the mixture.

For a mixture of gases, the equation can be written in a simpler form:

$$(n-1)P = (n_1-1)P_1 + (n_2-1)P_2 + \ldots \tag{43.4}$$

The concentrations are determined with a high accuracy by the refractometric method. Thus the $CO_2$ impurity in nitrogen is determined with an error of 0.14%.

The measurement of a single value of the refractive index is insufficient for the analysis of multi-component mixtures. We must use the dispersion relation and measure the refractive index at several wavelengths. Two measurements suffice for a three-component mixture. The equations for determining the concentrations in this case are

$$\begin{aligned} \kappa_1 + \kappa_2 + \kappa_3 &= 1, \\ R_1\kappa_1 + R_2\kappa_2 + R_3\kappa_3 &= \bar{R}, \\ R'_1\kappa_1 + R'_2\kappa_2 + R'_3\kappa_3 &= \bar{R}'. \end{aligned} \tag{43.5}$$

The composition of these mixtures is determined with a lower accuracy than that of binary mixtures; the accuracy is, nevertheless, acceptable.

The principle of additivity of the refractions is not only valid in the case of a mixture of different components. In many cases, the polarizability of the molecules can be represented as the sum of the polarizabilities of their constituent atoms. As a result, we can use refractometry to determine the molecular structure, a fact of great importance in organic chemistry.

An example of the application of schlieren methods to the study of the composition of mixtures is provided by the determination of the degree of dissociation of nitrogen and air in a shock tube [17, 59]. The experimental method is the same as that described in the case of the quantitative photoelectric method.

By applying the analytical method to the zone of inhomogeneous parameters, we can ascertain the values of the refractive index gradient in the direction of the flow axis. Changes introduced by ionized atoms are neglected in the calculation of the refractive index, since the degree of ionization is small in the relevant temperature range (3000–5000°). Since the electronic excitation levels for nitrogen are high, the molecular refraction can be considered independent of temperature.

The total refractive index is equal to

$$n - 1 = K_N N_N + K_{N_2} N_{N_2}, \tag{43.6}$$

where $N_N$ and $N_{N_2}$ are, respectively, the parts of atomic and molecular nitrogen in unit volume. The value of $K_{N_2}$ is well known; it is $1.13 \times 10^{-23}$. The value of $K_N$ can be determined from (43.6), if the refractive index and the number of particles of each gas are known at some point of the mixture. The quantities $N_N$ and $N_{N_2}$ are related to the degree of dissociation by the equality

$$\alpha = \frac{\frac{1}{2}N_{N_2}}{\frac{1}{2}N_N + N_{N_2}}. \tag{43.7}$$

The degree of dissociation and the gas parameters in the shock tube flow may be calculated at two points upstream from shock wave. Directly behind the shock wave $\alpha = 0$, and in the region of thermodynamic equilibrium $\alpha = \alpha_{eq}$. The temperature and pressure at these points are calculated from the measured shock velocities and the initial conditions.

By using one of the boundary conditions, we can determine the refractive index at the initial point $n = n_0$. The refractive index at any other point of the flow is determined by numerical integration of the empirical curve $\partial n/\partial x = f(x)$. Experimental measurements give $\partial n/\partial x$ as a function of the time $t$. If we know the velocity of the gas particles $V$ at different points of the flow, we can pass from $\partial n/\partial x$ as a function of $t$ to $\partial n/\partial x$ as a function of $x$. In our experiments we took $V$ to be constant in the flow. From (43.6) and (43.7) we derive

$$K_N = \frac{n - 1 - K_{N_2}(1-\alpha)\, n_m}{2\alpha n_m}, \tag{43.8}$$

where $n_m$ is the number of particles per unit volume, and

$$n_m = \frac{N_N}{2} + N_{N_2}. \tag{43.9}$$

Since the value of $\alpha$ can be calculated reliably only in the equilibrium region, we excluded from our treatment those experiments in which the contact region extended over the zone of parameter inhomogeneity.

The experiments established that the empirical relation in the integration region can be represented by an exponential curve. This simplified considerably the numerical integration.

For atomic nitrogen we found $K_N = 1.04 \times 10^{-23}$, which fits the theoretical and experimental values. The determination of the reaction rate constant and the transient time similarly led to a satisfactory agreement with the theoretical values.

This example illustrates that schlieren measurement methods can be reliably used for the study of mixtures even when the execution of the experiment is beset by considerable difficulties. A much higher accuracy can be achieved in simpler cases.

## 44. MEASUREMENTS IN PLASMA

Recently, schlieren methods are being increasingly used for plasma studies [61]. The plasma polarization depends both on the bound and the free electrons. The two factors are independent, and in order to determine the refraction of an incompletely ionized plasma, we must examine the motion of a free electron in the field of the light wave and add to it the polarization caused by the bound electrons. If the absorption of the medium is small, the refractive index is determined by the expression

$$n^2 = 1 - \frac{e^2 N}{m\varepsilon_0(\omega^2 + \nu^2)} + \frac{e^2}{m}\sum_{i,k} N_i \frac{f_{ki}}{\omega_{ki}^2 - \omega^2}. \tag{44.1}$$

Here $N$ is the concentration of free electrons, $N_i$ is the concentration of the various particle species in the plasma (ions, atoms, or molecules), $e$ and $m$ are the charge and the mass of the electron, $\omega$ is the light frequency, $\omega_{ki}$ is the frequency of the $k$-th absorption band of the $i$-th particle species, $f_{ki}$ is the oscillator strength for the transition $k \to i$, $\nu$ is the frequency of collisions of free electrons with heavy particles.

The second term of (44.1) gives the refraction due to free electrons, and the third term gives the bound-electron refraction.

We can assume that $\omega$ is very large in the optical region. The free electrons make a negative contribution to the refractive index, and each of them acts roughly $(\omega_{ki}/\omega)^2$ times more strongly than an atom or an ion. Their influence already becomes substantial at ionizations of a few per cent. At high degrees of ionization the refraction is determined only by the free electrons, and the refractive index is less than 1. For this case we can write

$$n = 1 - \frac{\lambda^2 e^2 N}{2mc^2}, \tag{44.2}$$

where $c$ is the velocity of light. Since the classical radius of the electron is equal to

$$r = \frac{e^2}{mc^2} = 2.8 \times 10^{-13}\,\mathrm{cm}, \tag{44.3}$$

we obtain from (44.2)

$$n = 1 - 1.4 \times 10^{-13}\lambda^2 N. \tag{44.4}$$

If the concentration of free electrons is $10^{17}\,\mathrm{cm}^{-3}$, for $\lambda = 5 \times 10^{-5}$ cm the refractive index will differ by $1 \times 10^{-5}$ from 1. This value can be measured with sufficient accuracy by schlieren methods.

Thus in a strongly ionized plasma we can measure the concentration of free electrons by refractometric methods. A partially ionized plasma should be considered as a mixture of different particle species. If the number of particle species is small (two or three), we can find the concentration of each component.

A specific feature of plasma measurements is the strong glow of the hot plasma. Therefore, it is desirable to use the defocused grid methods. If more accurate photometric methods are necessary, we must either substantially increase the light source brightness, or restrict the plasma glow by means of light filters and special slits. Experience shows that if the plasma is not too dense, the influence of the plasma glow can easily be suppressed.

# X

# CALCULATION OF THE ILLUMINATION DISTRIBUTION IN THE IMAGE PLANE WITH ALLOWANCE FOR DIFFRACTION PHENOMENA

## 45. GENERAL DISCUSSION OF THE DIFFRACTION EFFECTS

The qualitative and quantitative analysis of schlieren photographs is almost always based on geometrical optics. However, the geometrical optics provides only first-order approximations, which do not consider the phenomena associated with the wave nature of light; as a result, the geometrical-optics equations are not valid in many cases of application of schlieren instruments. The diffraction phenomena frequently lead to a distribution of the illumination in the image plane substantially different from the simplified distribution calculated on the basis of geometrical optics. It becomes difficult, and at times altogether impossible, to draw conclusions regarding the shape of the inhomogeneity, the distribution of the angles of light deviation, and the relevant object parameters. Even if the diffraction changes in the illumination are barely noticeable and do not substantially affect the qualitative measurements, they introduce a marked error in the more accurate quantitative measurements.

Diffraction phenomena are clearly observed in schlieren studies. Schlieren photographs of a supersonic flow past models of various shapes, obtained for different instrument adjustments, are shown in Figures 105 through 107. The light maxima at the boundaries of the opaque objects are clearly visible on each photograph. A system of diffraction fringes near the compression shock is observed in Figure 105. These image details corroborate the well known experimental and theoretical deduction, according to which the influence of diffraction is particularly noticeable in

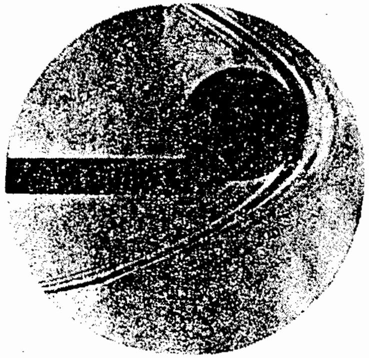

Figure 105

Photograph of the flow past a cylinder, taken by the method of the focal filament.

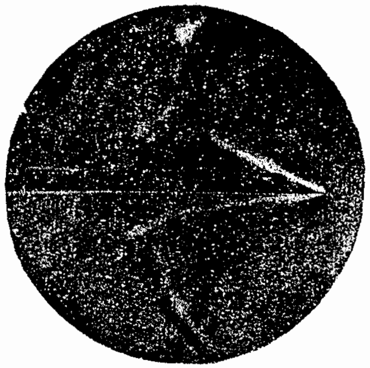

Figure 106

System of shock waves on a plate.

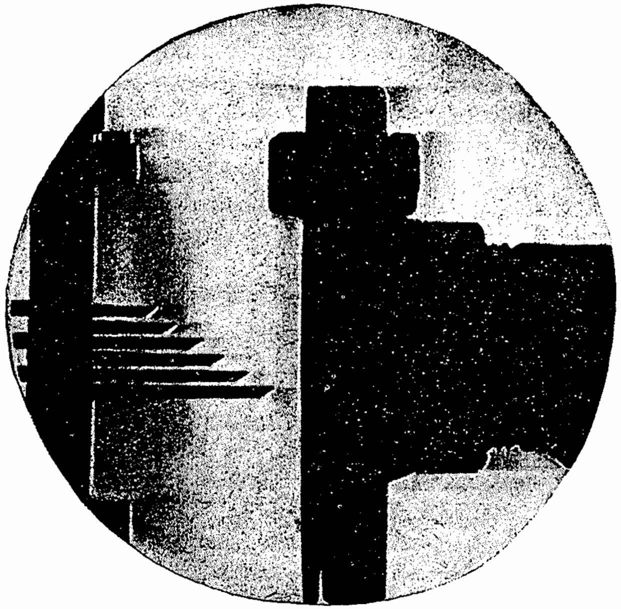

Figure 107

Measurement of the flow uniformity in a shock tube with a "comb".

places where the wave front suffers a discontinuity or a sharp deviation from linear propagation (after its passage through the inhomogeneity). In the parts of the field far from these places, the diffraction phenomena do not distort the schlieren pattern substantially, and do not hinder the execution of qualitative studies.

It is observed from the photographs that the influence of diffraction is a function of the shape and the character of the object, the method used, and the instrument adjustment. Thus on the photograph of Figure 107, taken with a vertical knife-edge, diffraction maxima are clearly noticeable only at the object edges which have a component parallel to the knife-edge. No diffraction maxima are formed at the edges perpendicular to the knife-edge.

The study of the schlieren photographs shows that the diffraction phenomena are most clearly observed with a high sensitivity of the schlieren instrument, i.e., when the uncovered part of the illuminating slit image in the focal plane is of small size. The larger the part of the image covered by the knife, the clearer and wider are the diffraction maxima and the stronger is their disturbing effect on the qualitative and quantitative measurements.

The calculation of the diffraction pattern is necessary for selecting the experimental conditions so the reduced results will correspond to reality with the desired accuracy.

Whereas in the study of "strong" optical inhomogeneities, deflecting the light through relatively large angles, the allowance for diffraction is necessary only in infrequent cases (e.g., the study of the boundary layer), in problems necessitating work at maximum sensitivity, the diffraction actually limits the possibility of using schlieren instruments. In many experiments with objects causing but a slight deflection, the schlieren methods are unable to visualize the inhomogeneities and are therefore inapplicable. Thus the question of the limit of applicability of schlieren instruments and of the means for attaining this limit should be considered. An increase in method sensitivity and the development of new methods for studying weak optical inhomogeneities become acutely necessary.

This problem can be solved in different ways. One of them is to calculate the image illumination in the schlieren instrument and in similar optical systems, to determine the sensitivity limit and to create new methods adapted to diffraction. This approach constitutes the subject matter of this part of the book. Another approach consists of creating new methods of study, basically different from the schlieren methods; this procedure necessitates separate treatment.

The diffraction phenomena interfere mainly with the use of schlieren methods based on geometrical optics. In this case the diffraction pattern is calculated in order to determine the limit of applicability of the methods and to select the optimum conditions for conducting the experiment. On the other hand, an attempt is made to make use of diffraction in the measurements. For this purpose a relation is established between the parameters of the diffraction pattern and the characteristic quantities of the inhomogeneity. Subsequently, an experimental method is developed which is best suited to utilizing these relations.

## 46. DERIVATION OF THE FUNDAMENTAL RELATIONS

The general problem of the effect of diffraction on the measurement results and the development of methods for utilizing the diffraction phenomena in the determination of the parameters of the optical inhomogeneity can be split into two independent parts. The first consists of calculating the illumination distribution in the image plane of the schlieren instrument by the methods of wave optics, and the second consists of determining the errors and limitations imposed by the diffraction phenomena and establishing techniques for harnessing diffraction.

The second problem is highly specific, depending on the method used, the shape of the object, and the aims of the experiment. It is therefore best treated in the corresponding special sections.

The first problem has been repeatedly examined, and can be formulated in a general manner. In the case of a schlieren instrument it was analyzed in considerable detail by Rayleigh [116], Obreimov [41], and Sukhorukikh [51].

We shall use the following simplified model of the schlieren instrument (Figure 108). A finite light source $S$, radiating isotropically in all directions, is placed in the focal plane of the main objective $O_1$ of the collimating part of the schlieren instrument, which has principal planes passing through the principal points $H_1$ and $H'_1$. The various points of the finite light source are defined by their coordinates $\xi'$, $\eta'$. Let the objective $O_1$ be free of aberrations; in that case, a plane light wave is emitted from it by each point of the source. Disregarding diffraction phenomena on the collimating objective rim, we consider an infinite plane light wave.

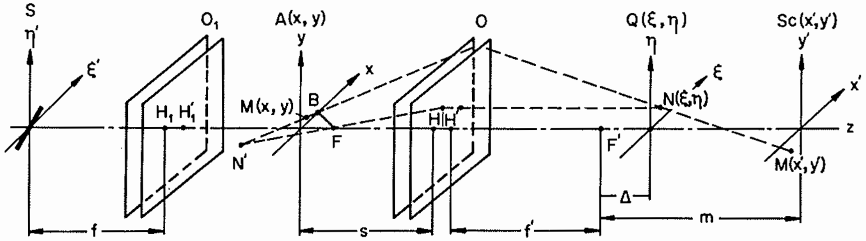

Figure 108
A model of the schlieren instrument.

The limiting diaphragm and the inhomogeneity are located in the object plane $A$ with coordinates $x$, $y$; they introduce amplitude and phase changes in the transmitted wave front.

After its passage through the plane $A$, the light reaches the main objective of the receiving part $O$, whose principal points are $H$ and $H'$ and foci $F$ and $F'$. The objective

$O$ is also assumed to be free of aberrations and sufficiently large in order not to restrict the light beam.

A viewing diaphragm causing additional amplitude and phase changes in the transmitted light wave is placed in the plane $Q(\xi, \eta)$ which lies near the focal plane $O$ or coincides with it. Different types of viewing diaphragms can be used, depending on the experimental conditions: Foucault knife-edge, phase filament, curved stop, etc. The distance from the plane $Q(\xi, \eta)$ to the second focal plane of the objective $O$ is defined by the segment $\Delta$.

The screen plane $Sc(x', y')$ with coordinates $x', y'$ is conjugate to the object plane $A$. The scale of the inhomogeneity image is defined by the distance from $A(x, y)$ to $O$ and the focal length of the objective $O$. These quantities also define the distance $m$ from the second focal plane of $O$ to the screen.

All the coordinate axes $(\xi', x, \xi, x')$ and $(\eta', y, \eta, y')$ are parallel to each other. The $z$ axes all coincide with each other and with the optical axis of the objectives $O_1$ and $O$.

The final aim of the calculation is to determine the illumination distribution in the screen plane $Sc$ for a given light source and known phase and amplitude changes introduced by the limiting diaphragm and the inhomogeneity in the plane $A(x, y)$ and by the viewing diaphragm in the plane $Q(\xi, \eta)$.

The instrumental model used in the calculation differs from most instruments available in practice. The main objectives of real instruments have aberrations and are of finite dimensions, the inhomogeneity is imaged by special photographic objectives, and the instruments have corrective lenses, mirrors, etc. However, the size of the additional optical elements can almost always be easily increased to the extent that the diffraction does not markedly change the illumination distribution in the image plane. In this case they affect only the numerical values of the parameters used in the calculation — the focal lengths of the objectives $O$ and $O_1$, the image scale, etc.

The size of the main objectives is large as a rule, and the diffraction from their edges has an effect in only a narrow zone of the $Sc(x', y')$ plane, located near the image of the boundaries of the instrument's working field. It is the diffraction in the object plane diaphragm and in the inhomogeneity which is of the greatest importance. Therefore, we can usually assume without much error that the objectives are infinitely large.

The assumption that the main objectives are aberration-free similarly does not lead to substantial restrictions, since their quality is almost always sufficiently high for the wave front distortions to be considerably smaller than those produced by the object. In the case of very weak inhomogeneities, it is the amplitude changes of the wave front produced by opaque objects in the $A(x, y)$ plane that are of decisive importance. Furthermore, the methods used most widely are based on the comparison of the schlieren pattern of the inhomogeneity with the schlieren pattern in the absence of inhomogeneity, and the aberrations are thus partly compensated.

The optical inhomogeneity is sometimes placed in a converging or a diverging light beam. This does not complicate the calculation considerably, since only the shape of the light wave front after its passage through the inhomogeneity is essential, and its determination is not considerably more difficult than in the case of a parallel beam.

The analysis of the above assumptions thus shows that they do not lead to substantial restrictions. The mathematical model adopted can be used for any schlieren measurements, since it allows for the most important factor — the diffraction in the inhomogeneity and the viewing diaphragm.

The light wave from any point of the source is described in the plane $A(x, y)$ by the function

$$S_A(\xi', \eta', x, y) = a_A(\xi', \eta', x, y)\, e^{ik[U(\xi', \eta', x, y)+ct]}, \tag{46.1}$$

where $a_A(\xi', \eta', x, y)$ is the magnitude of the amplitude, $k = 2\pi/\lambda$, $\lambda$ is the light wavelength, $U(\xi', \eta', x, y)$ is a function describing the phase distribution, $c$ is the light velocity, and $t$ is the time. At the points of the plane $A(x, y)$ where the gradient of the function $U(\xi', \eta', x, y)$ is small, the equation

$$z = U(\xi', \eta', x, y) \tag{46.2}$$

can be taken as the equation for the wave surface.

The function $U(\xi', \eta', x, y)$ can be represented in the form

$$U(\xi', \eta', x, y) = P_A(\xi', \eta', x, y) + \frac{\xi'}{f_1}x + \frac{\eta'}{f_1}y, \tag{46.3}$$

where $P_A(\xi', \eta', x, y)$ is the path difference introduced by the inhomogeneity. Since the quantities $\xi'/f_1$ and $\eta'/f_1$ are small, $P_A(x, y, \xi', \eta')$ will be considered independent of the variables $\xi'$ and $\eta'$.

The light disturbance in the plane $Q(\xi, \eta)$ can be found by applying the Huyghens–Fresnel principle, according to which every point of the wave surface can be considered as a source of secondary spherical waves. The light disturbance at any point of the plane $Q(\xi, \eta)$ caused by the element $dxdy$ of the plane $A(x, y)$ located near the point $(x, y)$ can be expressed as

$$dS_Q(\xi, \eta) = C_1 S_A(\xi', \eta', x, y)\, e^{-ikL[(x, y), (\xi, \eta)]}\, dx\, dy, \tag{46.4}$$

where $C_1$ is a constant, $L[(x, y), (\xi, \eta)]$ is the optical path length between the point $(x, y)$ of $A(x, y)$ and the point $(\xi, \eta)$ of $Q(\xi, \eta)$.

The overall light disturbance at the point $(\xi, \eta)$ is expressed by the superposition of the light disturbances contributed at this point by all the points of $A(x, y)$:

$$S_Q(\xi, \eta, \xi', \eta') = C_1 \int_{-\infty}^{\infty}\int_{-\infty}^{\infty} S_A(\xi', \eta', x, y)\, e^{-ikL[(x, y), (\xi, \eta)]}\, dx\, dy. \tag{46.5}$$

By applying once more the Huyghens–Fresnel principle, we can calculate the disturbance in the image plane:

$$S_{Sc}(x', y', \xi', \eta') =$$

$$= C_2 \int_{-\infty}^{\infty}\int_{-\infty}^{\infty} a_Q(\xi, \eta)\, e^{ikP_Q(\xi,\eta)}\, S_Q(\xi, \eta)\, e^{-ikL[(\xi,\eta),(x',y')]}\, d\xi\, d\eta\,, \qquad (46.6)$$

where $C_2$ is a constant, $a_Q(\xi, \eta)e^{ikP_Q(\xi,\eta)}$ is a function describing the amplitude and phase changes of the wave front introduced by the viewing diaphragm, and $L[(\xi, \eta), (x', y')]$ is the optical path length from the point $(\xi, \eta)$ of $Q(\xi, \eta)$ to the point $(x', y')$ of $Sc(x', y')$.

The illumination distribution in the image plane is given by the square of the modulus of the light disturbance distribution function:

$$I(x', y', \xi', \eta') = |S_{Sc}(x', y', \xi', \eta')|^2. \qquad (46.7)$$

All this is valid only for a single wave front, originating from an infinitesimal light source. However, in practical work, equations (46.1)–(46.7) are valid also for sources of finite width, made up of elementary radiators, provided the light source dimensions are so small that the function $S_A(\xi', \eta', x, y)$ is almost the same for each of the elementary waves. In this case we have in the image plane a superposition of a number of incoherent diffraction patterns shifted only slightly with respect to each other, and the image illumination at every point increases, while the illumination distribution remains as before. Such sources are called *infinitesimal* or *point* sources. As will be noted subsequently, the image illumination depends in some cases on amplitude and phase changes in one direction only, while the changes in other directions play no part. In such cases we can use slit light sources, and thus define infinitely thin slits.

If the light source is sufficiently large, the illumination distribution is determined by the superposition of many incoherent diffraction patterns shifted with respect to each other

$$J(x', y') = \int_{-\infty}^{\infty}\int_{-\infty}^{\infty} I(x', y', \xi', \eta')\, d\xi'\, d\eta'\,. \qquad (46.8)$$

Thus the calculation of the illumination distribution in the image plane of the schlieren instrument reduces to calculating the expression

$$J(x', y') = C_2 \int_{-\infty}^{\infty}\int_{-\infty}^{\infty} a_S(\xi', \eta') \left| \int_{-\infty}^{\infty}\int_{-\infty}^{\infty} a_Q(\xi, \eta)\, e^{ikP_Q(\xi,\eta)}\, e^{-ikL[(\xi,\eta),(x',y')]} \times \right.$$

$$\left. \times \int_{-\infty}^{\infty}\int_{-\infty}^{\infty} S_A(x, y, \xi', \eta')\, e^{-ikL[(x,y),(\xi,\eta)]}\, dx\, dy\, d\xi\, d\eta \right|^2 d\xi'\, d\eta'\,, \qquad (46.9)$$

obtained from (46.8) by the substitution of (46.7), (46.6), and (46.5). The quantity $a_S(\xi', \eta')$ is the distribution of the light source brightness.

Note that an auxiliary diaphragm is sometimes placed after the collimating part and before the object plane. The diffraction calculation in this case is basically the same, with only the order of integrations changed; the first integration is performed over the viewing diaphragm plane, and the second integration is performed over the object plane.

The functions $L[(x, y), (\xi, \eta)]$, $L[(\xi, \eta), (x', y')]$, $a_Q(\xi, \eta)$, and $P_Q(\xi, \eta)$ depend only on the method used and are easily found after the measurement procedure has been selected. The case of the function $P_A(x, y)$ is considerably more difficult, since it depends on the inhomogeneity and is actually the relationship which must be determined as a result of the experiment.

## 47. WORKING FORMULAS

The general formulas derived in the preceding section cannot be used when the functions $L[(x, y), (\xi, \eta)]$ and $L[(\xi, \eta), (x', y')]$ are known. We will determine them for the case when the viewing diaphragm is located near the second focus of the main objective of the receiving part or coincides with it. The method is similar to that used in [51].

Consider once more Figure 108. Here $M(x, y)$ and $N(\xi, \eta)$ are the points in the object plane and the diaphragm plane, the distance between which is to be determined; $M'(x', y')$ is the image of the point $M(x, y)$ formed by the main objective $O$ on the screen $Sc$.

In calculating the optical path length we take into account that in most cases the calculation of the light disturbance function in the screen plane is necessary for determining the illumination distribution. This means that in the expressions for $L[(x, y), (\xi, \eta)]$ and $L[(\xi, \eta), (x', y')]$ we can ignore the terms which are independent of the variables $x$, $y$, $\xi$, $\eta$, since their only effect concerns the phase of the light disturbance.

The value of $L[(x, y), (\xi, \eta)]$ is determined by the length $MN$. To calculate it, we use an artificial procedure. We construct the image of point $N(\xi, \eta)$ through the main objective, by taking two rays: one through $M(x, y)$, and the other originating from $N(\xi, \eta)$ and parallel to the optical axis (it passes through the first focus). Since $N'$ is the image of $N$, $N'MN = N'FN$. But $FN$ is independent of the coordinates of points $M$ and $N$, and can, therefore, be ignored.

Draw around point $N'$ a circle of radius $N'F$ and denote by $B$ its intersection with $N'M$. According to earlier explanation, the part of the optical path between points $M$ and $N$ which affects the intensity distribution is the segment $MB$. We shall take the length of this segment as the difference between $N'F$ and $NM$.

The coordinates of $N'$ in the object plane will then be

$$x_{N'} = -\xi f'/\Delta; \quad y_{N'} = -\eta f'/\Delta; \quad z_{N'} = -[f'^2 + \Delta(s + f')]/\Delta;$$

the coordinates of point $F$ will be $x_F = 0$, $y_F = 0$, $z_F = s + f'$. The sought difference will be

$$L[(x, y), (\xi, \eta)] =$$

$$= -n\left\{\sqrt{\left(\frac{-\eta f'}{\Delta} - y\right)^2 + \left(-\frac{\xi f'}{\Delta} - x\right)^2 + \left(-\frac{f'^2 + \Delta(s + f')}{\Delta}\right)^2} - \right.$$

$$\left. - \sqrt{\left(\frac{\eta f'}{\Delta}\right)^2 + \left(\frac{\xi f'}{\Delta}\right)^2 + \frac{f'^4}{\Delta^2}}\right\}. \qquad (47.1)$$

To simplify equation (47.1), we note that the last term of each of the expressions in the radicand is much larger than the other terms. We can, therefore, disregard terms of order $\xi^4/f'^4$ and $(\xi' + \Delta x)^4/[f'^2 + \Delta(s + f')]^4$ and write (47.1) in the form

$$L[(x, y), (\xi, \eta)] = n\,\frac{(s + f')(\xi^2 + \eta^2) - 2f'(y\eta + x\xi) - \Delta(x^2 + y^2)}{2[f'^2 + \Delta(s + f')]}. \qquad (47.2)$$

We determine the distance between the point $N(\xi, \eta)$ and any point of the image plane by the formula

$$L[(\xi, \eta), (x', y')] = n\sqrt{(x' - \xi)^2 + (y' - \eta)^2 + (m - \Delta)^2}. \qquad (47.3)$$

Using the smallness of the first two terms in the radicand, we find

$$L[(\xi, \eta), (x', y')] = -n\,\frac{(s + f')[\xi^2 + \eta^2 - 2x'\xi - 2y'\eta]}{2[f'^2 + \Delta(s + f')]}. \qquad (47.4)$$

Since $L[(\xi, \eta), (x', y')]$ is independent of $x$ and $y$, the term containing this magnitude can be moved into the inner integrands. The exponent in the integrand contains a quantity which can be obtained by adding (47.2) and (47.4):

$$L[(x, y), (\xi, \eta)] + L[(\xi, \eta), (x', y')] = \frac{-n}{2[f'^2 + \Delta(s + f')]} \times$$

$$\times\left\{\Delta(x^2 + y^2) + 2f'\left[\xi\left(x - \frac{s + f'}{f'}x'\right) + \eta\left(y - \frac{s + f'}{f'}y'\right)\right]\right\}. \qquad (47.5)$$

After these transformations, (46.9) can be written in the form

$$J(x', y') = C^2\int_{-\infty}^{\infty}\int_{-\infty}^{\infty} a_S(\xi', \eta')\left|\int_{-\infty}^{\infty}\int_{-\infty}^{\infty} a_Q(\xi, \eta)\,e^{ikP_Q(\xi, \eta)} \times\right.$$

$$\left. \times \int_{-\infty}^{\infty}\int_{-\infty}^{\infty} S_A(x, y, \xi', \eta')\,e^{W_1}\,dx\,dy\,d\xi\,d\eta\right|^2 d\xi'd\eta', \qquad (47.6)$$

where

$$W_1 = \frac{ikn}{2[f'^2 + \Delta(s + f')]}\left\{\Delta(x^2 + y^2) + 2f'\left[\xi\left(x - \frac{s + f'}{f'}x'\right) + \right.\right.$$

$$\left.\left. + \eta\left(y - \frac{s + f'}{f'}y'\right)\right]\right\}.$$

Formula (47.6) can be simplified in many cases. To make it more compact, without loss of generality, we can take the image scale to be $-1$ ($s = -2f'$).

If the viewing diaphragm is placed in the focus of the main objective of the receiving part, we have

$$J(x', y') = C^2\int_{-\infty}^{\infty}\int_{-\infty}^{\infty} a_S(\xi', \eta')\left|\int_{-\infty}^{\infty}\int_{-\infty}^{\infty} a_Q(\xi, \eta)\,e^{ikP_Q(\xi, \eta)} \times\right.$$

$$\left. \times \int_{-\infty}^{\infty}\int_{-\infty}^{\infty} S_A(x, y, \xi', \eta')\,e^{W_2}\,dx\,dy\,d\xi\,d\eta\right|^2 d\xi'd\eta', \qquad (47.7)$$

where

$$W_2 = \frac{ikn}{f'}[\xi(x + x') + \eta(y + y')].$$

For plane waves, with the viewing diaphragm placed in the focus of the main objective, the exponent in the integrand will be linear in each of the integration variables. If the diaphragm is displaced from the focus or the light wave curvature is introduced, quadratic terms appear in the exponent. Defocusing is equivalent to imparting a certain curvature to the light wave.

The working formulas are simplified if the amplitude and phase changes introduced by the inhomogeneity or the viewing diaphragm remain constant in some direction. To obtain these simplifications, we assume that the viewing diaphragm parameters are independent of the coordinate $\eta$. This situation is met in practice if a vertical knife-edge, a filament, or a grid are used as the diaphragm.

Under these assumptions the inner integrals over the variables $y$ and $\eta$ in (47.6) can be written in the form

$$\int_{\eta=-\infty}^{\infty}\int_{y=-\infty}^{\infty} \phi(x, y, \xi, \xi', \eta')\exp\left[\frac{ikn}{f' - \Delta}\eta(y + y')\right]dy\,d\eta. \qquad (47.8)$$

Integrating by parts with respect to the variable $y$, we obtain

$$\int_{-\infty}^{\infty}\left\{\frac{\phi\exp\left[\dfrac{ikn}{f' - \Delta}\eta(y + y')\right]}{\dfrac{ikn}{f' - \Delta}\eta} - \int\frac{\dfrac{\partial\phi}{\partial y}\exp\left[\dfrac{ikn}{f' - \Delta}\eta(y + y')\right]dy}{\dfrac{ikn}{f' - \Delta}\eta}\right\}d\eta. \qquad (47.9)$$

After the integration over $\eta$, we split the range of the variable $y$ into three parts, isolating a small zone near $y = -y'$. The integrals over the regions outside this isolated zone vanish. The isolated zone is small and we can assume when integrating that the function $\phi(x, y, \xi, \xi', \eta')$ has a constant value, equal to $\phi(x, -y', \xi, \xi', \eta')$. The integrals are then equal to

$$\frac{2\pi(f' - \Delta)}{kn}\phi(x, -y', \xi, \xi', \eta'), \tag{47.10}$$

and expression (47.6) reduces to

$$J(x', y') = \left[\frac{2\pi C(f' - \Delta)}{kn}\right]^2 \int_{-\infty}^{\infty}\int_{-\infty}^{\infty} a_S(\xi', \eta') \Bigg| \int_{-\infty}^{\infty} a_Q(\xi) e^{ikP_Q(\xi)} \times$$

$$\times \int_{-\infty}^{\infty} S_A(x, -y', \xi', \eta') e^{W_3}\, dx\, d\xi \Bigg|^2 d\xi'\, d\eta', \tag{47.11}$$

where

$$W_3 = \frac{ikn}{f' - \Delta}\left\{\frac{\Delta}{2f'}(x^2 + y'^2) + \xi(x + x')\right\}.$$

Thus if the viewing diaphragm is one-dimensional, the illumination of any point of the image is affected only by the phase and amplitude distribution at points of the object plane on the line passing through the conjugate point and perpendicular to the lines of constant value of the parameters of the viewing diaphragm. The phase and amplitude distribution in the other points of the object plane do not affect the illumination at the point considered.

This simplification is of great importance, since one-dimensional diaphragms are the most popular in schlieren measurements.

Similarly, if the inhomogeneity is one-dimensional, the illumination distribution in the image plane is affected only by the parameters of the viewing diaphragm along the straight line passing through the light source and perpendicular to the lines of constant values of the inhomogeneity parameters. This facilitates the study of diffraction phenomena in one-dimensional inhomogeneities with diaphragms of complex shapes.

If we use a one-dimensional diaphragm and a narrow-slit light source parallel to the line of constant diaphragm parameters, all the diffraction patterns produced by the different source elements located at different parts of the extended slit are identical. The overall diffraction pattern from the slit in this case is the same as from a point source, with the only difference that it is brighter.

With the aid of the above equations, we can calculate the illumination at any point of the schlieren image if we know the characteristics of the inhomogeneity, the parameters of the light source, and the amplitude and phase changes introduced by the viewing diaphragm. However, it is the inverse problem which has to be solved in practice: to determine the phase and amplitude distribution of the light wave after its passage through the inhomogeneity by measuring the illumination distribution in the image plane. A general procedure is known for solving the integral equation (47.6). It consists of taking the unknown function as constant in some small zone of the plane $A(x, y)$ (in more complicated methods, it is considered a linear or a quadratic function of the coordinates). In this case we obtain from (47.6)

$$J(x', y') = C^2 \int_{-\infty}^{\infty}\int_{-\infty}^{\infty} a_S(\xi' \eta') \Bigg| \sum_{i=1}^{N_1}\sum_{j=1}^{N_1} S_{A_{ij}} \int_{-\infty}^{\infty}\int_{-\infty}^{\infty} a_Q(\xi, \eta) e^{ikP_Q(\xi, \eta)} \times$$

$$\times \int_{-\infty}^{\infty}\int_{-\infty}^{\infty} e^{W_4}\, dx\, dy\, d\xi\, d\eta \Bigg|^2 d\xi'\, d\eta', \tag{47.12}$$

where

$$W_4 = \frac{ikn}{f' - \Delta}\left\{\frac{\Delta}{2f'}(x^2 + y^2) + \xi(x + x') + \eta(y + y')\right\}.$$

The integrals can be evaluated, since only known functions remain in the integrands. The integral equation is thus transformed into an algebraic equation. By measuring $J(x', y')$ in a sufficient number of points, we can obtain a system of algebraic equations from which $S_{A_{ij}}$ is determined anywhere in the object plane. This general method for analyzing the diffraction pattern has not been used thus far in practical schlieren measurements, due to the complexity of the schlieren pattern, the blurring of the characteristic diffraction details of the image as a result of the action of an extended light source, and insufficient measurement accuracy.

A simpler method is used at present, based on the fact that the illumination distribution at a given point of the image is affected only by the phase and amplitude distribution in some neighborhood of the conjugate point in the object plane. At a given adjustment of the instrument this neighborhood can be taken as sufficiently small for approximating $P_A(x, y)$ with a known function of the coordinates with one or several parameters, which are then found by comparing the experimental results with theoretical calculation.

Due to the complexity of calculations, $P_A(x, y)$ is usually given as a combination of straight lines or quadratic curves. Calculations in a more complicated form have been carried out only in [53]. However, as we shall note subsequently, valuable information can also be obtained from the illumination calculation based on the simplest form of the functional relationship $P_A(x, y)$.

The mathematical apparatus to be used and the methods of approximate calculation depend on the form of the function $P_A$. Therefore, in what follows we shall consider separately the questions connected with studies of plane waves, when $P_A$ is a linear function of the coordinates, of quadratic waves, when $P_A$ can be expressed by a second order equation, and of more complex wave front shapes.

# XI

# ERRORS IN THE STUDY OF PLANE WAVES

## 48. ERRORS OF THE PHOTOMETRIC KNIFE-EDGE AND SLIT METHOD

There are several factors limiting the accuracy and the sensitivity of schlieren instruments: vibrations of the instrument body and the mirrors, convective air currents in the instrument and between the instrument and the object, inaccuracies in the manufacture of the objective and the protective glasses, diffraction on the rims of the optical components and in the inhomogeneity, etc. From this list, it is the diffraction phenomena that actually determine the maximum accuracy of the schlieren methods. Although the errors caused by the other factors are continuously being reduced with advances in technology, diffraction phenomena cannot be eliminated. Their influence can be allowed for by calculating the diffraction pattern, but this leads to a considerable modification of the measurement method, involving a new range of phenomena.

The study of diffraction is most important when viewing small inhomogeneities or studying the processes near the boundary of the object, since in this case the changes in the image illumination caused by diffraction can become comparable to or larger than the effect of the inhomogeneity. Limitations of this type are most important and can considerably affect the measurement error or make it altogether impossible to obtain the required result. This problem is also of considerable practical interest, since by solving it we can decide whether very thin astronomical mirrors, low-density gaseous flows, and similar objects can be studied at all by

schlieren methods. The entire question of the sensitivity limit of schlieren methods and of the means for improving schlieren instruments becomes clearer. The diffractional redistribution of the light intensity introduces in the measurement result errors related to the neglect of the diffraction phenomena. Allowance for these errors and determination of the maximum sensitivity become possible only when the illumination distribution in the image plane is calculated by the wave-optical methods.

The standard schlieren method of the knife-edge and slit [15, 25, 116] was selected for a specimen calculation of the error introduced by diffraction phenomena. This method is particularly suitable for measuring small angles of deviation.

An opaque diaphragm having a rectangular cut with sides $2R$ and $2R_1$ parallel to the coordinate axes $x$, $y$ is placed in the object plane. Then

$$a_A(x, y)e^{ikP_A(x, y)} = \begin{cases} 0 & \text{for} \quad |x| > R \quad \text{or} \quad |y| > R_1, \\ e^{ik(\alpha x + \beta y)} & \text{for} \quad |x| < R \quad \text{and} \quad |y| < R_1, \end{cases} \tag{48.1}$$

where $\alpha$ and $\beta$ are the projections of the angle of rotation of the plane wave in plane $A$ on the planes $xOz$ and $yOz$. A knife partially covering the slit image is placed in the focal plane $Q(\xi, \eta)$. The knife-edge is parallel to the $\eta$ axis and intersects the $\xi$ axis at point $\xi = \xi_0$. In this case

$$a_Q(\xi, \eta)e^{ikP_Q(\xi, \eta)} = \begin{cases} 0 & \text{for} \quad |\eta| > r_1 \quad \text{or} \quad \xi < \xi_0 \quad \text{or} \quad \xi > r, \\ 1 & \text{for} \quad |\eta| < r_1 \quad \text{and} \quad \xi_0 < \xi < r. \end{cases} \tag{48.2}$$

Let the light source be a uniformly illuminated slit with edges having coordinates $\xi_1, \xi_2$ and $\eta_1, \eta_2$. We obtain

$$J(x', y') = C^2 \int_{\eta'=\eta_1}^{\eta_2} \int_{\xi'=\xi_1}^{\xi_2} \left| \int_{\xi=\xi_0}^{r} \int_{\eta=-r_1}^{r_1} \int_{x=-R}^{R} \int_{y=-R_1}^{R_1} e^{W_5}\, dx\, dy\, d\xi\, d\eta \right|^2 d\xi'\, d\eta', \tag{48.3}$$

where

$$W_5 = \frac{ik}{f}\{\xi(x + x') + \eta(y + y') + \alpha x f + \beta y f + x\xi' + y\eta'\}.$$

It is assumed in (48.3) and in all cases below that the focal lengths of the main objectives of the receiving and collimating part of the schlieren instrument are equal, i.e., that $-f_1 = f' = f$.

Noting that the integration variables can be separated, we write (48.3) in the form

$$J(x', y') = C^2 \int_{\xi'=\xi_1}^{\xi_2} \int_{\eta'=\eta_1}^{\eta_2} \left| \int_{\xi=\xi_0}^{r} \int_{x=-R}^{R} e^{W_6}\, dx\, d\xi \int_{\eta=-r_1}^{r_1} \int_{y=-R_1}^{R_1} e^{W_7}\, dy\, d\eta \right|^2 d\xi'\, d\eta' \tag{48.4}$$

where

$$W_6 = \frac{ik}{f}\{\xi(x + x') + \alpha x f + x\xi'\},$$

$$W_7 = \frac{ik}{f}\{\eta(y + y') + \beta y f + y\eta'\}.$$

Calculating all the inner integrals, we obtain

$$J(x', y') = \frac{C^2 f^4}{k^4} \int_{\xi'=\xi_1}^{\xi_2} \{[\mathrm{Ci}\,\beta_1(r + \alpha f + \xi') - \mathrm{Ci}\,\beta_1(\xi_0 + \alpha f + \xi') -$$

$$- \mathrm{Ci}\,\beta_2(r + \alpha f + \xi') + \mathrm{Ci}\,\beta_2(\xi_0 + \alpha f + \xi')]^2 + [\mathrm{Si}\,\beta_1(r + \alpha f + \xi') -$$

$$- \mathrm{Si}\,\beta_1(\xi_0 + \alpha f + \xi') - \mathrm{Si}\,\beta_2(r + \alpha f + \xi') + \mathrm{Ci}\,\beta_2(\xi_0 + \alpha f +$$

$$+ \xi')]^2\}\, d\xi' \int_{\eta'=\eta_1}^{\eta_2} \{[\mathrm{Ci}\,\alpha_1(r_1 + \beta f + \eta') - \mathrm{Ci}\,\alpha_1(-r_1 + \beta f + \eta') -$$

$$- \mathrm{Ci}\,\alpha_2(r_1 + \beta f + \eta') + \mathrm{Ci}\,\alpha_2(-r_1 + \beta f + \eta')]^2 +$$

$$+ [\mathrm{Si}\,\alpha_1(r_1 + \beta f + \eta') - \mathrm{Si}\,\alpha_1(-r_1 + \beta f + \eta') -$$

$$- \mathrm{Si}\,\alpha_2(r_1 + \beta f + \eta') + \mathrm{Si}\,\alpha_2(-r_1 + \beta f + \eta')]^2\}\, d\eta, \tag{48.5}$$

where

$$\beta_1 = \frac{k}{f}(R + x'), \qquad \alpha_1 = \frac{k}{f}(R_1 + y'),$$

$$\beta_2 = \frac{k}{f}(-R + x'), \qquad \alpha_2 = \frac{k}{f}(-R_1 + y'). \tag{48.6}$$

We note that the illumination at every point of the image depends on the distance of that point from the image of the working field boundaries and the distance of the source image from the viewing diaphragm boundaries. The quantities $R$, $R_1$, $r$, $\xi_0$, $\alpha$, $r_1$, $\beta$, $\xi_1$, $\xi_2$, $\eta_1$, and $\eta_2$ are significant only insofar as they alter these distances. Taking this into account, we can write $\alpha = \beta = \xi_0 = 0$ without any loss of generality.

The integrals in (48.5) cannot be evaluated analytically. However, in actual experiments with schlieren instruments, the parameters $r_1$, $\xi_0$, $r$, $\eta_0$ are connected by known relationships, which can be used to simplify (48.5). Normally, the width of the illuminating slit image is much smaller than the width of the focal plane slit aperture, so that $\xi_1, \xi_2 \ll r$. Taking this into account, and also seeing that $\beta_1 r$ and $\beta_2 r$ are sufficiently large, we reach the conclusion that the addition of $\xi'$, varying between $\xi_1$ and $\xi_2$, to $r$ in the arguments of the integral sines and cosines cannot substantially alter their values. Therefore, we can write without substantial loss of accuracy

$$\mathrm{Ci}\,\beta_1(r + \xi') = \mathrm{Ci}\,\beta_1 r, \qquad \mathrm{Si}\,\beta_1(r + \xi') = \mathrm{Si}\,\beta_1 r,$$

$$\mathrm{Ci}\,\beta_2(r + \xi') = \mathrm{Ci}\,\beta_2 r, \qquad \mathrm{Si}\,\beta_2(r + \xi') = \mathrm{Si}\,\beta_2 r. \tag{48.7}$$

By imposing similar requirements on the variation of $\eta$, we obtain $\eta_1, \eta_2 \ll r_1$. But $r_1$ is large. Therefore, we can drop terms of order of $1/\alpha_1(r_1 + \eta_0)$, $1/\alpha_2(r_1 + \eta_0)$, $1/\alpha_1(-r_1 + \eta_0)$, and $1/\alpha_2(-r_1 + \eta_0)$ in the asymptotic expansions of the integral sines and cosines, which are valid for large values of the arguments:

$$\mathrm{Si}\,(t) = \frac{\pi}{2} - \left(\frac{1}{t^2} - \frac{6}{t^4}\right)\sin t - \left(\frac{1}{t} - \frac{2}{t^3}\right)\cos t + \ldots, \tag{48.8}$$

$$\mathrm{Ci}\,(t) = \left(\frac{1}{t} - \frac{2}{t^3}\right)\sin t - \left(\frac{1}{t^2} - \frac{6}{t^4}\right)\cos t + \ldots \tag{48.9}$$

From these assumptions we obtain

$$\begin{aligned} \mathrm{Ci}\,\alpha_1(-r_1 + \eta') = \mathrm{Ci}\,\alpha_1(r_1 + \eta') = \mathrm{Ci}\,\alpha_2(-r_1 + \eta') &= \\ = \mathrm{Ci}\,\alpha_2(r_1 + \eta') &= 0, \\ -\mathrm{Si}\,\alpha_1(-r_1 + \eta') = -\mathrm{Si}\,\alpha_2(r_1 + \eta') = \mathrm{Si}\,\alpha_2(-r_1 + \eta') &= \\ = -\mathrm{Si}\,\alpha_1(-r_1 + \eta') &= \tfrac{1}{2}\pi. \end{aligned} \tag{48.10}$$

Formula (48.5) is reduced with the aid of (48.7) and (48.10) to

$$J(x') = \frac{4\pi(\eta_2 - \eta_1) C^2 f^4}{k^4} \int_{\xi'=\xi_1}^{\xi_2} \{[\mathrm{Ci}\, r\beta_1 - \mathrm{Ci}\,\xi'\beta_1 - \mathrm{Ci}\, r\beta_2 + \mathrm{Ci}\,\xi'\beta_2]^2 +$$

$$+ [\mathrm{Si}\, r\beta_1 - \mathrm{Si}\,\xi'\beta_1 - \mathrm{Si}\, r\beta_2 + \mathrm{Si}\,\xi'\beta_2]^2\}\, d\xi', \tag{48.11}$$

which gives after integration

$$J(x') = \frac{4\pi(\eta_2 - \eta_1) C^2 f^4}{k^4}\, \xi' \left\{\left[\mathrm{Ci}\,\xi'\beta_1 - \mathrm{Ci}\,\xi'\beta_2 - \mathrm{Ci}\,\beta_1 r + \mathrm{Ci}\,\beta_2 r -\right.\right.$$

$$\left. - \frac{\sin \xi'\beta_1}{\xi'\beta_1} + \frac{\sin \xi'\beta_2}{\xi'\beta_2}\right]^2 + \left[\mathrm{Si}\,\xi'\beta_1 - \mathrm{Si}\,\xi'\beta_2 - \mathrm{Si}\,\beta_1 r + \mathrm{Si}\,\beta_2 r +\right.$$

$$\left. + \frac{\cos \xi'\beta_1}{\xi'\beta_1} - \frac{\cos \xi'\beta_2}{\xi'\beta_2}\right]^2 + \frac{2\xi'(\beta_1 - \beta_2)\,\mathrm{Si}\,\xi'(\beta_1 - \beta_2) + 2\cos \xi'(\beta_1 - \beta_2)}{\xi'^2 \beta_1 \beta_2}$$

$$\left. - \frac{1}{\xi'^2}\left(\frac{1}{\beta_1^2} + \frac{1}{\beta_2^2}\right)\right\}\Bigg|_{\xi'=\xi_1}^{\xi'=\xi_2} \tag{48.12}$$

The illumination distribution for the case when the object plane diaphragm is a half-plane restricting the object field on one side is shown in Figures 109 and 110. The edge of the half-plane is parallel to the $y$ axis. The light source is an infinitely narrow luminous slit parallel to the $\xi'$ axis at a distance $\xi_1$ from it. The illumination

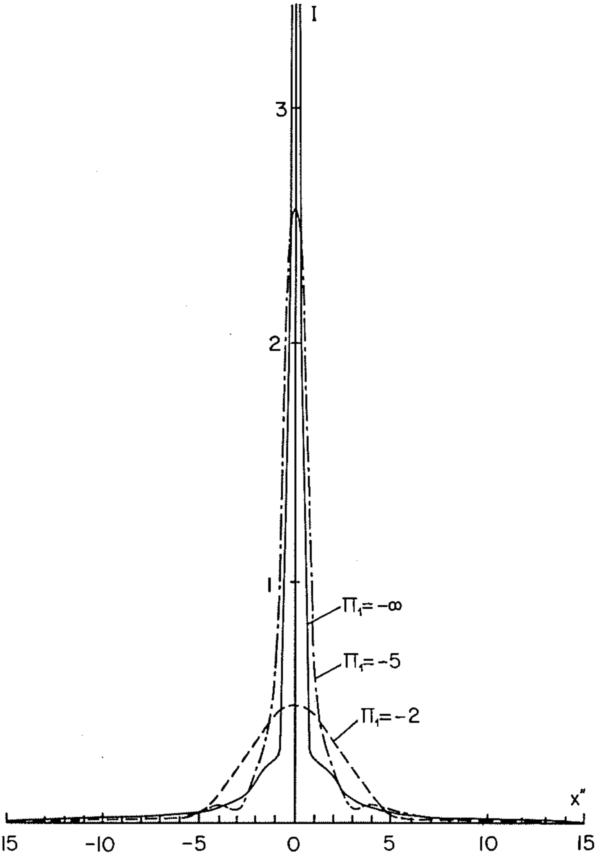

Figure 109

Illumination distribution at the edge of an opaque screen. The geometrical image of the slit is covered by a knife.

distribution was expressed by the integrand in (48.11), which under our assumptions has the form

$$J(x') = \left\{\left[\mathrm{Ci}\,\frac{kr}{f}(-R+x') - \mathrm{Ci}\,\frac{k\xi_1}{f}(-R+x')\right]^2 + \right.$$

$$\left. + \left[-\mathrm{Si}\,\frac{kr}{f}(-R+x') - \mathrm{Si}\,\frac{k\xi_1}{f}(-R+x') + \begin{pmatrix}\pi\\0\end{pmatrix}\right]^2\right\}, \qquad (48.13)$$

where $\xi_1$ is the coordinate describing the position of the source image (since $\xi_0 = 0$, $\xi_1$ is also the distance from the knife-edge to the illuminating slit image).

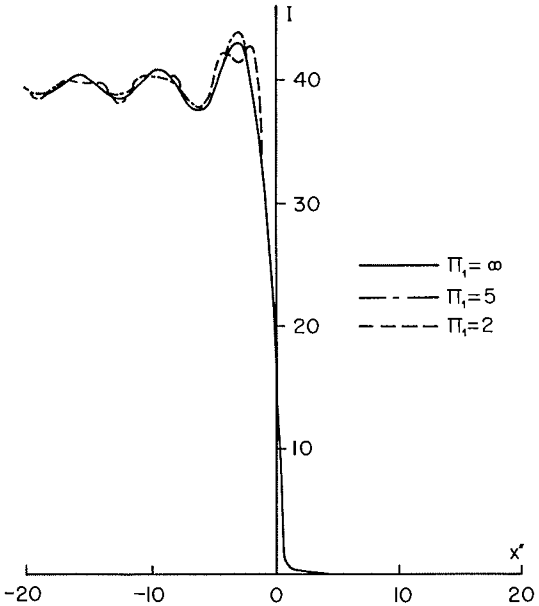

Figure 110

Illumination distribution at the edge of an opaque screen. The slit image is not covered.

The upper term ($\pi$) in parentheses obtains for $\xi_1 > 0$, and the lower term (0) for $\xi_1 < 0$. The origin of coordinates in the figures is chosen at the point where the image of the screen edge should be according to geometrical optics. The abscissa is related to the coordinate of the screen plane by the equality

$$x'' = \frac{2\pi}{\lambda f}\,\xi_1\,(-R + x')\,.$$

The curves are given for different values of the parameter $\Pi_1 = r/\xi_1$.

If the points considered are sufficiently far from the screen image, so that $(-R + x')\cdot kr/f$ is large, the illumination distribution depends on $x''$ only. We note that for an uncovered slit image ($\Pi_1 > 0$) the illumination distribution is virtually independent of the value of $\Pi_1$. If the source image is covered by the knife, the decrease of the absolute value of $\Pi_1$, leads to a reduction in the illumination at the center of the diffraction maximum located on the opaque edge.

All the possible illumination distribution curves in the screen plane are obtained from those shown in Figures 109 and 110 by altering the horizontal scale.

A decrease of the angular distance from the center of the diffraction pattern of the illuminating slit image to the knife-edge, an an increase of the wavelength involve an increase in the width of the diffraction maxima, which is proportional to $x''$.

To study the illumination distribution described by (48.12), we introduce the dimensionless magnitudes

$$\rho = \frac{k}{f}\xi' R; \quad \bar{x} = \frac{x'}{R}; \quad p = \frac{k}{f} rR; \quad C_3 = \frac{4\pi(\eta_2 - \eta_1)C^2 f^5}{k^5 R}.$$

Formula (48.12) is then transformed into

$$\begin{aligned} J = C_3\rho \Bigg\{ \Bigg[ & \mathrm{Ci}\,\rho(\bar{x}+1) - \mathrm{Ci}\,\rho(\bar{x}-1) - \mathrm{Ci}\,p(\bar{x}+1) + \mathrm{Ci}\,p(\bar{x}-1) - \\ & - \frac{\sin\rho(\bar{x}+1)}{\rho(\bar{x}+1)} + \frac{\sin\rho(\bar{x}-1)}{\rho(\bar{x}-1)}\Bigg]^2 + \Bigg[\mathrm{Si}\,\rho(\bar{x}+1) - \mathrm{Si}\,\rho(\bar{x}-1) - \\ & - \mathrm{Si}\,p(\bar{x}+1) + \mathrm{Si}\,p(\bar{x}-1) + \frac{\cos\rho(\bar{x}+1)}{\rho(\bar{x}+1)} - \frac{\cos\rho(\bar{x}-1)}{\rho(\bar{x}-1)}\Bigg]^2 + \\ & + \frac{4\rho\,\mathrm{Si}\,2\rho + 2\cos 2\rho}{\rho^2(\bar{x}^2-1)^2} - \frac{1}{\rho^2(\bar{x}+1)^2} - \frac{1}{\rho^2(\bar{x}-1)^2}\Bigg\}\Bigg|_{\rho=\rho_1}^{\rho=\rho_2} \end{aligned} \tag{48.14}$$

We note that in general, the illumination distribution in the image of a rectangular aperture depends, in the case of a wide source and a wide viewing slit, on three parameters: $\rho_1$, $\rho_2$, and $p$. However, in actual experiments, $r$ is usually large. Therefore, the diffraction phenomena at the edge of the viewing slit, located at $\xi = r$, affect only the illumination distribution at screen points very near the image of the object plane diaphragm edges. Ignoring these points, we can write $p = \infty$. We must also take into account that the influence of diffraction at the edge of the illuminating slit image covered by the knife is much smaller than the influence of diffraction at the uncovered edge. Therefore, we can write $\rho_2 = \infty$. We obtain finally

$$\begin{aligned} J = -C_3\rho_1 \Bigg\{ \Bigg[ & \mathrm{Ci}\,\rho_1(\bar{x}+1) - \mathrm{Ci}\,\rho_1(\bar{x}-1) - \frac{\sin\rho_1(\bar{x}+1)}{\rho_1(\bar{x}+1)} + \\ & + \frac{\sin\rho_1(\bar{x}-1)}{\rho_1(\bar{x}-1)}\Bigg]^2 + \Bigg[\mathrm{Si}\,\rho_1(\bar{x}+1) - \mathrm{Si}\,\rho_1(\bar{x}-1) - \binom{\pi}{0} + \\ & + \frac{\cos\rho_1(\bar{x}+1)}{\rho_1(\bar{x}+1)} - \frac{\cos\rho_1(\bar{x}-1)}{\rho_1(\bar{x}-1)}\Bigg]^2 + \frac{4\rho_1\,\mathrm{Si}\,2\rho_1 + 2\cos 2\rho_1}{\rho_1^2(\bar{x}^2-1)^2} - \\ & - \frac{1}{\rho_1^2(\bar{x}+1)^2} - \frac{1}{\rho_1^2(\bar{x}-1)^2}\Bigg\}. \end{aligned} \tag{48.15}$$

The upper term in parenthesis is taken for $|\bar{x}| < 1$, the lower term for $|\bar{x}| > 1$. Figure 111 shows curves of illumination distribution, calculated by (48.15) for the values of $\rho_1$ indicated in the figure; $\rho_1 = -\infty$ corresponds to geometrical optics.

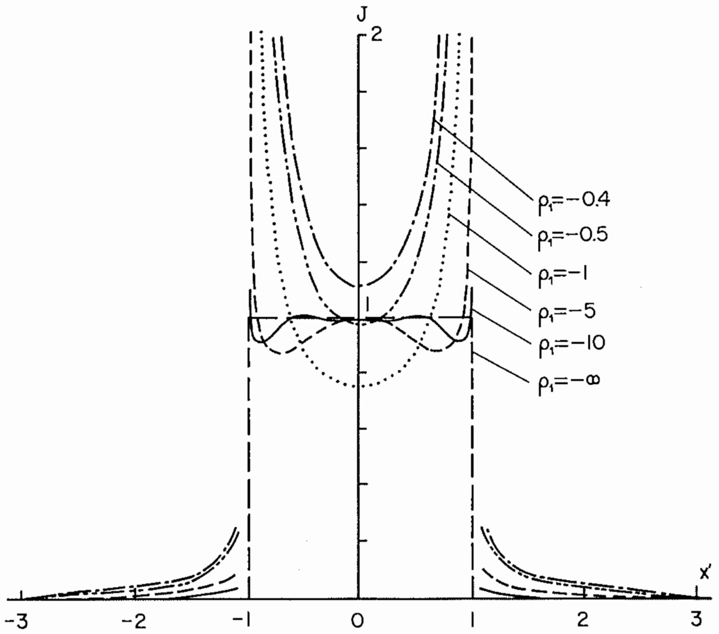

Figure 111

Illumination distribution calculated by (48.15).

The curves are normalized so that the intensity at the image center is always equal to one, i.e.,

$$-C_3\rho_1\left\{\left[2\,\mathrm{Si}\,\rho_1 - \pi + \frac{2\cos\rho_1}{\rho_1}\right]^2 + \frac{4\rho_1\,\mathrm{Si}\,2\rho_1 + 2\cos 2\rho_1 - 2}{\rho_1^2}\right\} = 1. \tag{48.16}$$

The case of a wide slit is similar to that of a narrow slit. The diffraction maxima become wider and grow with the decrease in the width of the uncovered part of the slit. However, unlike the distribution in the case of a narrow slit, here the diffraction pattern is somewhat smoothed by the superposition of numerous elementary patterns formed by light from different points of the source.

These phenomena were investigated experimentally with the IAB-451 instrument [15]. A diaphragm with a rectangular cut was placed in the object plane. A slit illuminated by a cineprojector was the light source. The illuminating slit image was partially covered by a knife. The slit image and the knife-edge were arranged parallel to the diaphragm edges. Thus the experimental layout closely follows our computing model. Since the instrument used was not ideal, a small object-plane diaphragm was selected (2 cm). As a result, the contribution from diffraction phenomena increased and their influence became much larger than the influence of aberrations. The experimental setup is similar to that described in [69a].

The photographs were processed photometrically in the direction perpendicular to the knife-edge; the results obtained are represented in Figure 112. The ordinates of the curves are proportional to $[J(x')]^a$, which is the deflection of the recording ray of the microphotometer. The values of the parameter $a$ depend on the $\gamma$ and the speed of the film used.

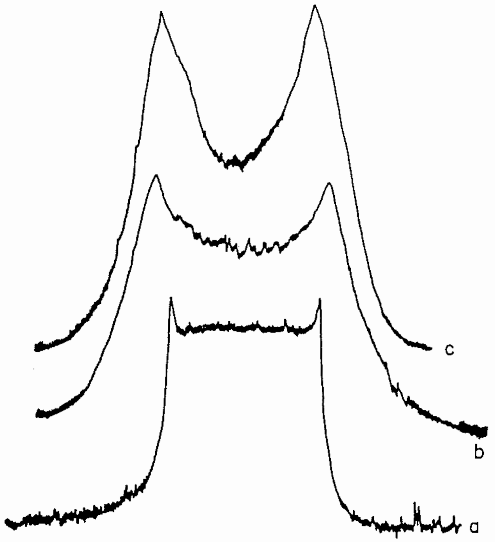

Figure 112

The broadening of the diffraction maxima with the narrowing of the uncovered part of the slit.

The results corroborate the theoretical conclusions concerning the enhancement of the diffraction phenomena with the narrowing of the uncovered part of the slit. Thus in Figure 112*a*, taken with a relatively wide uncovered part of the slit, the diffraction phenomena noticeably affect the illumination distribution only near the diaphragm edges. The narrowing of the uncovered part of the slit leads to the broadening of the diffraction maxima, which then fill a larger part of the diaphragm aperture image (Figure 112*b*). When the width of the uncovered part is reduced still further (Figure 112*c*), the illumination at the center differs substantially from that predicted by geometrical optics. The qualitative and quantitative comparison of the experimental and theoretical data established the validity of our calculations and their applicability to practical work with schlieren instruments.

We shall use the illumination distribution obtained in the image plane of the schlieren instrument for estimating the error of the photometric schlieren method

of the knife-edge and the slit introduced by the neglect of the diffraction phenomena.

Let the initial position of the slit be characterized by a width $\xi_1$ of the uncovered part of the slit image; the inhomogeneity shifts the slit image to a position where the width of the uncovered part is $\xi_2$. The true angle of deviation is then

$$\varepsilon_t = \frac{\xi_2 - \xi_1}{f}. \tag{48.17}$$

In real measurements, we use equation (26.3), in the derivation of which it was assumed that

$$\varepsilon_m = \frac{J_2 - J_1}{J_1}\frac{\xi_1}{f}, \tag{48.18}$$

where $J_1$ and $J_2$ are the illuminations of the measured field point obtained for the widths $\xi_1$ and $\xi_2$ of the uncovered part of the slit image. The relative measurement error in this case is

$$\kappa = \frac{\varepsilon_t - \varepsilon_m}{\varepsilon_t} = 1 - \frac{(J_2 - J_1)\xi_1}{J_1(\xi_2 - \xi_1)}. \tag{48.19}$$

Using expansions (48.8) and (48.9), we substitute in (48.19) $J_1$ and $J_2$ from (48.12). Assuming that more than half the slit image is covered, and dropping higher-order terms, we obtain

$$J_1(x') = \frac{16\pi^4(\eta_2 - \eta_1)C^2 f^4}{k^4}\left[\xi_1 + \frac{\beta_1 - \beta_2}{2\pi\beta_1\beta_2} - \frac{1}{\pi\xi_1}\left(-\frac{\sin\xi_1\beta_1}{\beta_1^2} + \frac{\sin\xi_1\beta_2}{\beta_2^2}\right)\right]. \tag{48.20}$$

At this point, we must distinguish between two cases.

1. The angle of light deviation is so small that the shift of the diffraction pattern on the working photograph with respect to the zero photograph is much smaller than the distance between the fringes. In this case, inserting in (48.19) the expression for $J_1$ from (48.20) and the expression for $J_2$ obtained in the same way, and further assuming that $\xi_2 - \xi_1 \ll \xi_1$, we obtain

$$\kappa = \frac{1}{\pi\xi_1}\left(\frac{\cos\xi_1\beta_1}{\beta_1} - \frac{\cos\xi_1\beta_2}{\beta_2}\right). \tag{48.21}$$

If the point studied is located near the edge of the object plane diaphragm at $x = R$, the maximum error is

$$\kappa = \frac{f}{\pi k\xi_1(x' + R)}. \tag{48.22}$$

If $\beta_1 = -\beta_2$ (the point studied is located near the middle of the object plane diaphragm), then

$$\kappa = \frac{2f}{\pi k\xi_1 R}. \tag{48.23}$$

Let us estimate the numerical value of the error. For $(x' + R) = 1$ mm, $f = 2 \times 10^3$ mm, $\lambda = 5 \times 10^{-4}$ mm, and $\xi_1 = 0.2$ mm, we obtain $\kappa = 0.25$, which is a very large error. This example shows that the diffraction phenomena cannot be disregarded in measurements near the object boundary.

If the diffraction maxima are not clearly observed due to the insufficient resolving power of the instrument, or if large angles of light deviation in the inhomogeneity are being measured, we can replace the rapidly oscillating functions $\sin \xi_1 \beta_1$ and $\sin \xi_1 \beta_2$ in the expression for the illumination by 1 and write (48.20) in the form

$$J_1(x') = \frac{16\pi^4(\eta_2 - \eta_1)C^2 f^4}{k^4}\left[\xi_1 + \frac{\beta_1 - \beta_2}{2\pi\beta_1\beta_2} - \frac{1}{\pi\xi_1}\left(\frac{1}{\beta_1^2} + \frac{1}{\beta_2^2}\right)\right]. \quad (48.24)$$

Substituting (48.24) and the analogous expression for $J_2$ in (48.19), we obtain for $\xi_2 - \xi_1 \ll \xi_1$

$$\kappa = \frac{(R^2 + x'^2)f^2\lambda^2}{2\pi^3\xi_1^2(R^2 + x'^2)^2}. \quad (48.25)$$

This expression, as (48.21), gives the field zones (for given parameters of the optical system) in which the angle of light deviation in the inhomogeneity can be measured with a relative diffraction error not exceeding $\kappa$.

For the case when a measurement with error $\kappa$ is possible only at the center of the field, while the error everywhere else is larger, expression (48.25) assumes the form

$$\kappa = \frac{f^2\lambda^2}{2\pi^3\xi_1^2 R^2}. \quad (48.26)$$

If the inhomogeneity point being considered is located near the edge of the diaphragm, then

$$\kappa = \frac{f^2\lambda^2}{4\pi^3\xi_1^2(R + x')^2}. \quad (48.27)$$

The physical meaning of equations (48.21) and (48.25) is easily understood. The increase in the diaphragm aperture or in the distance of the point from the opaque edge is accompanied by a decrease in the effect of diffraction; the distribution approaches the geometrical optics distribution, and the error diminishes. The decrease in the light wavelength has a similar effect.

When the width of the uncovered slit image increases, we obtain a superposition of diffraction patterns which are shifted relative to one another. If the angular distance (determined by the ratios $(\xi_2 - \xi_1)/f$ and $\xi_1/f$) between the axes of the extreme superimposed beams is large, a uniform illumination results from the superposition of many beams, and the observed distribution approaches the geometrical optics distribution. The diffraction phenomena become noticeable only if the knife-edge is located near the edge of the slit image; the error increases as the uncovered part of the slit is made narrower.

We can thus deduce that the width of the uncovered part of the slit should be large in order to ensure a small error. However, this is true only in part, since the increase in the width of the uncovered part involves a drop in the measurement sensitivity and in the contrast of the inhomogeneity image, which increases the measurement error of the image illumination (or of the difference in the optical densities of the emulsion).

By substituting (26.7) in (48.22) and (48.27), we obtain a relation between the diffraction error and the measurement sensitivity,

$$\kappa = \frac{S}{\pi k\gamma(R + x')}, \quad (48.28)$$

$$\kappa = \frac{S^2\lambda^2}{4\pi^3\gamma^2(R + x')^2}. \quad (48.29)$$

To determine the minimum angle of light deviation in the inhomogeneity which can be measured with a given diffraction error, we combine (48.22) and (48.27) with (26.3), using the series expansion of (26.3) in powers of the small quantity $(D - D_0)/\gamma$:

$$\varepsilon = \frac{(D - D_0)\ln 10}{\pi k\gamma\kappa(R + x')}, \quad (48.30)$$

$$\varepsilon = \frac{(D - D_0)\ln 10}{k\gamma\sqrt{\pi\kappa}(R + x')}. \quad (48.31)$$

For $(R + x') = 10$ mm, $D - D_0 = 0.02$, $\gamma = 2$, $\kappa = 0.1$, and $\lambda = 5.5 \times 10^{-4}$ mm we derive from (48.30) that the angle of $6.4 \times 10^{-7}$ rad or $1.3 \times 10^{-1}$ seconds of arc can be measured with an accuracy of about ten per cent (it follows from (48.31) that $\varepsilon = 7 \times 10^{-2}$ seconds of arc). This angle is considerably smaller than those usually met in practice. The minimum angles of deviation which can be measured at present in experimental conditions are much larger than this theoretical limiting value.

The example given illustrates the case when the wave front can be taken as plane over the entire instrument field. This approximation is inapplicable in many cases, and then the smallest measurable angle of light deviation in the inhomogeneity will be much larger. The influence of diffraction will be particularly strong if we study processes near an opaque boundary or an interface of two media. Thus if we measure the inhomogeneity parameters at a distance of 0.1 mm from the opaque boundary, we obtain $\varepsilon = 6 \times 10^{-5}$ rad for the same numerical values as in the preceding example. In such studies the diffraction error becomes larger than the errors due to other factors, and the calculation of the inhomogeneity characteristics from the diffraction pattern parameters presents an especially acute problem.

With the aid of the above formulas, we can determine the minimum distance from the diaphragm edge for which the angle of deviation can be measured with a given error. Thus for $\kappa = 0.1$, $\lambda = 5.5 \times 10^{-4}$ mm, $S = 10^5$, and $\gamma = 2$, we can conduct measurements only at points lying farther than 14 mm from the edge.

Note that in quantitative measurements the diffraction also interferes with the execution of the auxiliary operation — the measurement of $\xi_1$. We shall determine the magnitude of the resulting error. If the width of the uncovered part is determined to within $1/p$ of the radius of the Airy disk, the error will be equal to

$$\kappa' = \frac{d\varepsilon}{\varepsilon} = \frac{d\xi_1}{\xi_1} \approx \frac{\lambda f}{4R\xi_1 p}. \tag{48.32}$$

By comparing (48.32) and (48.23) we obtain

$$\kappa' = \frac{\pi^2 \kappa}{4p}. \tag{48.33}$$

If $\kappa = 0.1$, it is necessary for $\kappa' = 0.1$ that $p = 2.5$, i.e., that $\xi_1$ be measured with an accuracy of up to 0.4 of the Airy disk radius. This is a very complicated problem, which is difficult to solve by a direct measurement of the knife-edge distance from the slit edge. For such accurate measurements, we must make use of the slit image symmetry, and measure the knife-edge shift from the middle of the slit image.

Thus it would seem that the error due to the inaccuracy of the slit measurement is larger than the error of the illumination measurement. However, a basic consideration in practical measurements is that the restriction of the plane wave front in the working photograph is stronger than in the "zero" photograph. The "zero" photograph is restricted only by the main objective rim, while the plane zone on the working photograph is also restricted by the inhomogeneity elements. As a result, it is possible to measure the width of the uncovered part of the slit image for a considerably larger $R$ than that affecting the diffraction error of measurements.

If the auxiliary measurements are conducted for $R = R_1$, and the inhomogeneity restricts the plane front to $R_2$, then

$$\kappa' = \frac{\pi^2 R_1 \kappa}{4pR_2} \tag{48.34}$$

The error defined by (48.34) is small if the inhomogeneity strongly restricts the wave front ($R_1 \ll R_2$), i.e., when the diffraction error substantially affects the measurement results. If $R_1 \approx R_2$, then as a rule $\kappa \geqq \kappa'$ but in this case $\kappa$ is small and can be ignored.

We note from this analysis that the possibilities of the schlieren instruments are not fully utilized in the study of large-size gaseous inhomogeneities. These instruments are inherently capable of measuring angles of light deviation smaller than the smallest angles measured today. The reduction in the instrument accuracy is due to ambient vibrations, aberrations of the optical system, temperature fluctuations, fluctuations of the air density in the instrument and around it. It is clear that the sensitivity of schlieren instruments can be increased as follows:

*a*) All the optical components of the instrument must be insulated thermally. It has been experimentally established that a local increase in the temperature of some component by a fraction of a degree suffices to cause noticeable changes in the schlieren picture. The components connecting the optical elements with the instrument body are of particular importance in this respect; a thermoinsulating padding between them is obligatory.

*b*) Vibrations are the main enemy of schlieren instruments. If we wish to measure an angle of deviation with an absolute error of $\pm 10^{-7}$, the maximum permissible shift of the illuminating slit image in the course of the experiment is $2 \times 10^{-4}$ mm (for $f = 2 \times 10^3$ mm). Since the instruments are usually placed near running motors, the fulfillment of these requirements is obviously very difficult. To reduce vibrations, schlieren instruments must be manufactured in the form of integral structures, and not as a system of two different units (collimating and receiving), as is the case at present. A separate seating and an antivibration suspension system should be provided for when setting up the instrument.

*c*) In many cases, especially when studying transient processes, the main factor limiting the sensitivity is the insufficient brightness of the light sources. Therefore, we must envisage the use of high-pressure xenon lamps as light source, and of image converters as receivers. In addition to increasing the sensitivity, this combination will be extremely useful in the study of very short processes (of the order of $10^{-7}$ sec and shorter).

*d*) The schlieren instrument readings are almost equally affected by inhomogeneities at different points along the optical path of the beam. Therefore, we must take measures to prevent air density fluctuations in the instrument and between the instrument and the object. Generally, it is sufficient to seal the instrument; in some cases, when the influence of extraneous light sources or convective air currents is large, it becomes necessary to work in a partial or absolute vacuum.

*e*) The last factor contributing to a high resolving power of the instrument is high-quality optics. The resolving power of schlieren instruments is still considerably below the limiting resolution determined by the diffraction at the rim of the main objectives. A criterion of satisfactory optical quality is a point image equal to the diffraction circle of confusion.

Particular attention should be paid to the fact that the limiting sensitivity is related to the accuracy of the instruments recording the variation of the emulsion optical density. If we can record density changes of up to $10^{-4}$, the sensitivity limit of the schlieren instruments is shifted by two orders of magnitude. Therefore, to increase the schlieren sensitivity, we must increase the accuracy of measurement of the photographic density. It is necessary to use new high-$\gamma$ emulsions with uniform parameters over the surface, and differential microphotometers with an improved method for reading the results.

The above methods of increasing the schlieren sensitivity should be implemented only when working at maximum sensitivity, i.e., when studying inhomogeneities which produce a very slight deflection of the light beam. In less accurate measurements we can disregard the influences of some of the factors listed and settle for a lower sensitivity. Another factor of great importance is the specific environment in which the experiment is conducted, namely, the presence or absence of heat sources, the frequency and the amplitude of the vibrations, etc. Therefore, the methods for attaining the required sensitivity and accuracy must be selected after analysis of the working conditions of the instrument and the problems which have to be solved.

However, the diffraction limit has already been reached for many objects, in measurements conducted near discontinuities or sharp changes in the wave front linearity. In these cases, the question of utilizing the diffraction pattern for measurements or devising a basically different method of measurement becomes highly topical.

## 49. LIMITATIONS OF THE VECTOR THEORY OF THE PHASE CONTRAST

The basic features of the phase contrast method are generally explained in terms of the vector theory. As we observed, this theory is based on a number of inaccurate assumptions, which at times introduce substantial errors and restrict its applicability. In this section we shall analyze quantitatively, allowing for diffraction, the influence of these assumptions [23].

We shall use as a mathematical model the general diagram of the phase contrast method shown in Figure 113. To simplify the calculations, we take as our object a slit diaphragm of width $2a$, with a transmission coefficient $q$, which introduces an additional path difference $\nu$. The instrument field diameter is $2R$. A filament of width $2\xi_0$, with a transmission coefficient $\tau$, introducing an additional path difference $\delta$ is placed coinciding with slit source image. The inhomogeneity image is projected by the receiving part objective with main foci $H_2$ and $H'_2$ on the screen $Sc$.

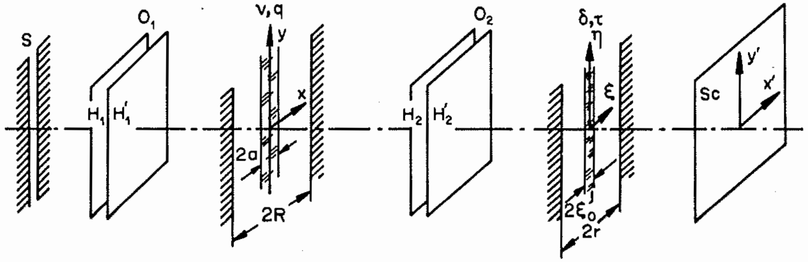

Figure 113

A diagram of the phase contrast method.

The calculation of the illumination distribution in the image plane by equation (47.7) leads to the expression

$$\begin{aligned}
I(x') = \left[\frac{2\pi C(f-\Delta)}{kn}\right]^2 \Bigg\{ \Bigg[ & \operatorname{Si}\frac{k}{f}r(R+x') - \operatorname{Si}\frac{k}{f}\xi_0(R+x') - \\
& - \operatorname{Si}\frac{k}{f}r(a+x') + \operatorname{Si}\frac{k}{f}\xi_0(a+x') + \operatorname{Si}\frac{k}{f}r(-a+x') - \\
& - \operatorname{Si}\frac{k}{f}\xi_0(-a+x') - \operatorname{Si}\frac{k}{f}r(-R+x') + \operatorname{Si}\frac{k}{f}\xi_0(-R+x') + \\
& + \frac{1}{\sqrt{q}}\cos\nu\left[\operatorname{Si}\frac{k}{f}r(a+x') - \operatorname{Si}\frac{k}{f}\xi_0(a+x') - \operatorname{Si}\frac{k}{f}r(-a+x') + \right. \\
& \left. + \operatorname{Si}\frac{k}{f}\xi_0(-a+x')\right] + \frac{1}{\sqrt{\tau}}\cos\delta\left[\operatorname{Si}\frac{k}{f}\xi_0(R+x') - \right. \\
& \left. - \operatorname{Si}\frac{k}{f}\xi_0(a+x') + \operatorname{Si}\frac{k}{f}\xi_0(-a+x') - \operatorname{Si}\frac{k}{f}\xi_0(-R+x')\right] + \\
& + \frac{1}{\sqrt{\tau q}}\cos(\delta+\nu)\left[\operatorname{Si}\frac{k}{f}\xi_0(a+x') - \operatorname{Si}\frac{k}{f}\xi_0(-a+x')\right]\Bigg]^2 + \\
& + \Bigg[\frac{1}{\sqrt{q}}\sin\nu\left[\operatorname{Si}\frac{k}{f}r(a+x') - \operatorname{Si}\frac{k}{f}\xi_0(a+x') - \operatorname{Si}\frac{k}{f}(-a+x')r + \right. \\
& \left. + \operatorname{Si}\frac{k}{f}\xi_0(-a+x')\right] + \frac{1}{\sqrt{\tau}}\sin\delta\left[\operatorname{Si}\frac{k}{f}\xi_0(R+x') - \right. \\
& \left. - \operatorname{Si}\frac{k}{f}\xi_0(a+x') + \operatorname{Si}\frac{k}{f}\xi_0(-a+x') - \operatorname{Si}\frac{k}{f}\xi_0(-R+x')\right] + \\
& + \frac{1}{\sqrt{\tau q}}\sin(\delta+\nu)\left[\operatorname{Si}\frac{k}{f}\xi_0(a+x') - \operatorname{Si}\frac{k}{f}\xi_0(-a+x')\right]\Bigg]^2\Bigg\}. \qquad (49.1)
\end{aligned}$$

Since the present theory is more general than the vector theory, we can derive from (49.1) the fundamental relation of the vector theory. In fact, by adopting the assumptions of § 12 and considering the focal and object plane diaphragms as infinitely large, while taking the inhomogeneity and amplitude-phase filament as sufficiently small, we obtain from (49.1) the already known equation (12.1), which has been derived from geometrical optics.

To estimate the error of the vector theory, we restrict ourselves to the first two terms in the asymptotic expansion of the functions

$$\mathrm{Si}\,\frac{k}{f}\,\xi_0(R + x'), \qquad \mathrm{Si}\,\frac{k}{f}\,\xi_0(-R + x'),$$

$$\mathrm{Si}\,\frac{k}{f}\,r(a + x'), \qquad \mathrm{Si}\,\frac{k}{f}\,r(-a + x')$$

for large values of the argument. $\xi_0(a + x')\cdot k/f$ and $\xi_0(-a + x')\cdot k/f$ should be so small that their integral sine can be approximated by the first terms of the exponential series.

Since $R$ and $r$ are large, the integral sines of the arguments containing these magnitudes are rapidly oscillating functions, and, therefore, in order to determine the maximum diffraction error, we set the cosines of these arguments equal to $\pm 1$.

We transform (49.1), chopping the terms of second order of smallness:

$$\begin{aligned} I(x') = \\ &= \left[\frac{2\pi C(f - \Delta)}{kn}\right]^2 \left\{1 + \frac{1}{q} + \frac{1}{\tau} + \frac{2\cos(\nu - \delta)}{\sqrt{q\tau}} - \frac{2\cos\delta}{\sqrt{\tau}} - \frac{2\cos\nu}{\sqrt{q}} + \right. \\ &\quad + \frac{4R}{\frac{\pi k}{f}\,\xi_0(R^2 - x'^2)}\left[-1 - \frac{1}{\tau} - \frac{\cos(\nu - \delta)}{\sqrt{q\tau}} + \frac{2\cos\delta}{\sqrt{\tau}} + \frac{\cos\nu}{\sqrt{q}}\right] + \\ &\quad + \frac{4a}{\frac{\pi k}{f}\,r(a^2 - x'^2)}\left[-1 - \frac{1}{q} - \frac{\cos(\nu - \delta)}{\sqrt{q\tau}} + \frac{2\cos\nu}{\sqrt{q}} + \frac{\cos\delta}{\sqrt{\tau}}\right] + \\ &\quad + \frac{4k\xi_0 a}{\pi f}\left[-1 - \frac{1}{q} - \frac{1}{\tau} - \frac{2\cos(\nu - \delta)}{\sqrt{q\tau}} + \frac{\cos\delta}{q\sqrt{\tau}} + \right. \\ &\quad \left.\left. + \frac{\cos\nu}{\tau\sqrt{q}} + \frac{2\cos\nu}{\sqrt{q}} + \frac{2\cos\delta}{\sqrt{\tau}} - \frac{\cos(\nu + \delta)}{\sqrt{\tau q}}\right]\right\}. \end{aligned} \tag{49.2}$$

Let us rewrite expression (49.2) for the case of pure phase changes of the wave front in the inhomogeneity and the filament. Taking into account that the diffraction is most significant when measuring small path differences, we use the expansion of cos $\nu$ and sin $\nu$ for small values of the argument, taking

$$\cos\nu = 1, \qquad \sin\nu = \nu. \tag{49.3}$$

Formula (49.2) reduces after these changes to

$$\begin{aligned} I(x') = \left[\frac{2\pi C(f - \Delta)}{kn}\right]^2 \{1 + 2\nu\sin\delta - (1 - \cos\delta)\,A - \\ - \nu\sin\delta(A + B + D)\}, \end{aligned} \tag{49.4}$$

where

$$A = \frac{4R}{\frac{\pi k}{f}\,\xi_0(R^2 - x'^2)}, \qquad B = \frac{4a}{\frac{\pi k}{f}\,r(a^2 - x'^2)}, \qquad D = \frac{4k\xi_0 a}{\pi f}.$$

Generally, the additional path difference introduced is measured by comparing the illumination of the object image with the illumination of the background or some standard of known parameters. An error is introduced in such measurements, since they do not allow for the shape and the size of the compared objects, and use the vector theory for comparing the illuminations. Let us estimate the magnitude of this error.

The background illumination achieved for $\nu = 0$ is equal to

$$I_0 = \left[\frac{2\pi C(f - \Delta)}{kn}\right]^2 \{1 - A(1 - \cos\delta)\}. \tag{49.5}$$

Combining (49.5) with (49.4), we obtain the following expression for the additional path difference introduced by the inhomogeneity, allowing for the maximum diffraction error:

$$\nu_{\text{dif}} = \left(1 - \frac{I}{I_0}\right)\frac{1}{[1 - \frac{1}{2}(A - B - D) - A\cos\delta]\,2\sin\delta}. \tag{49.6}$$

The vector theory uses the expression

$$\nu_{\text{vect}} = \left(1 - \frac{I}{I_0}\right)\frac{1}{2\sin\delta}. \tag{49.7}$$

The relative measurement error is therefore

$$\kappa = \frac{\nu_{\text{dif}} - \nu_{\text{vect}}}{\nu_{\text{dif}}} = \tfrac{1}{2}(A - B - D) - A\cos\delta. \tag{49.8}$$

The signs of $A$, $B$, and $D$ depend on the values of the cosines and the sines of large arguments: they cannot be determined and are independent. We therefore take the sum of the moduli

$$\kappa = \frac{|B| + |D| + |A(1 - 2\cos\delta)|}{2}. \tag{49.9}$$

For the central point of the field we obtain

$$\kappa = \left|\frac{2k\xi_0 a}{\pi f}\right| + \left|\frac{2}{\dfrac{\pi k}{f}\, ra}\right| + \left|\frac{2(1-2\cos\delta)}{\dfrac{\pi k}{f}\,\xi_0 R}\right|. \tag{49.10}$$

The error consists of the sum of several terms reacting differently to any change in the system parameters. Thus a decrease in the viewing filament width $\xi_0$ lowers the error associated with the partial screening of the diffracted beam together with the main beam and increases the error caused by ignoring the diffraction from the edges of the instrument field. Similar phenomena accompany a change of the object size. If the object is too small, the error caused by the finite size of the focal plane diaphragm and the partial screening of the diffracted beam increases, while the error due to the partial screening of the diffracted beam by the viewing diaphragm filament decreases.

The error can be minimized by selecting the suitable size of the screening filament and the object. The minimum error is achieved for

$$\xi_0 = \sqrt[3]{\frac{r(1-2\cos\delta)}{\dfrac{k^2}{f^2}R^2}}, \qquad a = \sqrt[3]{\frac{R}{\dfrac{k^2 r^2}{f^2}(1-2\cos\delta)}}. \tag{49.11}$$

The total error (for a phase plate introducing an additional phase difference of $\lambda/2$, i.e., for $\delta = \pi$) is thus

$$\kappa_{\min} \approx 1.5\sqrt[3]{\frac{\lambda f}{Rr}}. \tag{49.12}$$

With this expression we can estimate the error obtained for the most widely used optical systems. Thus for microscopes $R \approx 3$ mm, $r/f \approx 1/10$, this gives an error of 18%. For the schlieren instruments used in gas-dynamic studies, $R/f \approx 1/20$, $r = 20$ mm, and this leads to a minimum error of 10%. In the majority of cases, this error considerably exceeds the required measurement accuracy.

Roughly the same results are obtained when estimating standard methods of phase shift detection. In this case the error depends largely on the shape of the standard inhomogeneity. The greater the likeness between the standard and the object, the smaller is the diffraction error. However, the manufacture of a standard object similar to the object of study is a difficult problem in the majority of cases (this requires knowledge of the shape of the wave front after its passage through the inhomogeneity, i.e., we first have to solve the final problem), and it is therefore necessary to assess the maximum value of the error and see whether it coincides with the value derived.

The following conclusions can be drawn from the diffraction theory of phase contrast:

1) The results obtained in the vector theory are only tentative. The vector theory ignores the diffraction on the main objective rim, and the partial screening of the diffracted beam by the image plane diaphragm. The viewing diaphragm also affects a part of the diffracted beam. The results obtained by the phase-contrast method can be understood only from the point of view of the diffraction theory.

2) It is impossible to reduce the diffraction error below some limiting value, fluctuating between 10% and 15% for real optical systems, by changing the optical system parameters. This error can be reduced only by increasing the speed of the main objective and the size of the focal plane diaphragm and by using light of shorter wavelength. In any case, the minimum error is attainable only for objects of a certain size; inasmuch as the object size is usually fixed, the error exceeds the minimum value.

3) Since the errors in the quantitative measurement of the path difference by the phase-contrast method are too large, the only way of obtaining quantitative results by this method is to use the diffraction theory or to create standards as close as possible to the object being studied. Attempts to create standards for the study of microscopic objects have already been made [110]. This procedure, however, is inapplicable to gaseous objects, since only some very simple inhomogeneities can be simulated here. The question of the diffraction error of such measurements must be examined separately in each case.

## 50. COMPARISON OF THE KNIFE-EDGE AND SLIT METHOD WITH THE PHASE-KNIFE METHOD

Repeated attempts have been made recently to increase the sensitivity of schlieren methods. Many papers have suggested replacing the ordinary amplitude Foucault knife-edge by a phase knife [103].

We shall compare the two methods [24], basing the analysis on the diffraction theory, since from the point of view of geometrical optics both methods are infinitely sensitive and can be used for detecting infinitely small inhomogeneities.

The procedure for calculating the illumination of the schlieren image plane differs from the method used in § 48 in that the focal plane diaphragm causes both amplitude and phase changes in the incident light, instead of pure amplitude changes. The function $a_Q(\xi,\eta)\exp\{ikP_Q(\xi,\eta)\}$ thus has the form

$$a_Q(\xi,\eta)e^{ikP_Q(\xi,\eta)} = \begin{cases} 0 & \text{for } \xi < -r \text{ or } \xi > r, \\ 1 & \text{for } r > \xi > \xi_0, \\ \tau e^{-i\delta} & \text{for } \xi_0 > \xi > -r, \end{cases} \tag{50.1}$$

and the illumination distribution for a point source, defined by (47.7), can be written as

$$I_{\mathrm{ph}}(x') = \left[\frac{2\pi C(f-\Delta)}{kn}\right]^2 \{[(\mathrm{Ci}\,\beta_1 r - \mathrm{Ci}\,\beta_1\xi_0 - \mathrm{Ci}\,\beta_2 r + \mathrm{Ci}\,\beta_2\xi_0) \times$$
$$\times (1 - \tau\cos\delta) + \tau\sin\delta\,(-\,\mathrm{Si}\,\beta_1\xi_0 - \mathrm{Si}\,\beta_1 r +$$
$$+ \mathrm{Si}\,\beta_2\xi_0 + \mathrm{Si}\,\beta_2 r)]^2 + [(\mathrm{Si}\,\beta_1\xi_0 - \mathrm{Si}\,\beta_2\xi_0) \times$$
$$\times (1 - \tau\cos\delta) - (\mathrm{Si}\,\beta_1 r - \mathrm{Si}\,\beta_2 r)(1 + \tau\cos\delta) +$$
$$+ \tau\sin\delta\,(\mathrm{Ci}\,\beta_1\xi_0 - \mathrm{Ci}\,\beta_1 r - \mathrm{Ci}\,\beta_2\xi_0 + \mathrm{Ci}\,\beta_2 r)]^2\}\,. \tag{50.2}$$

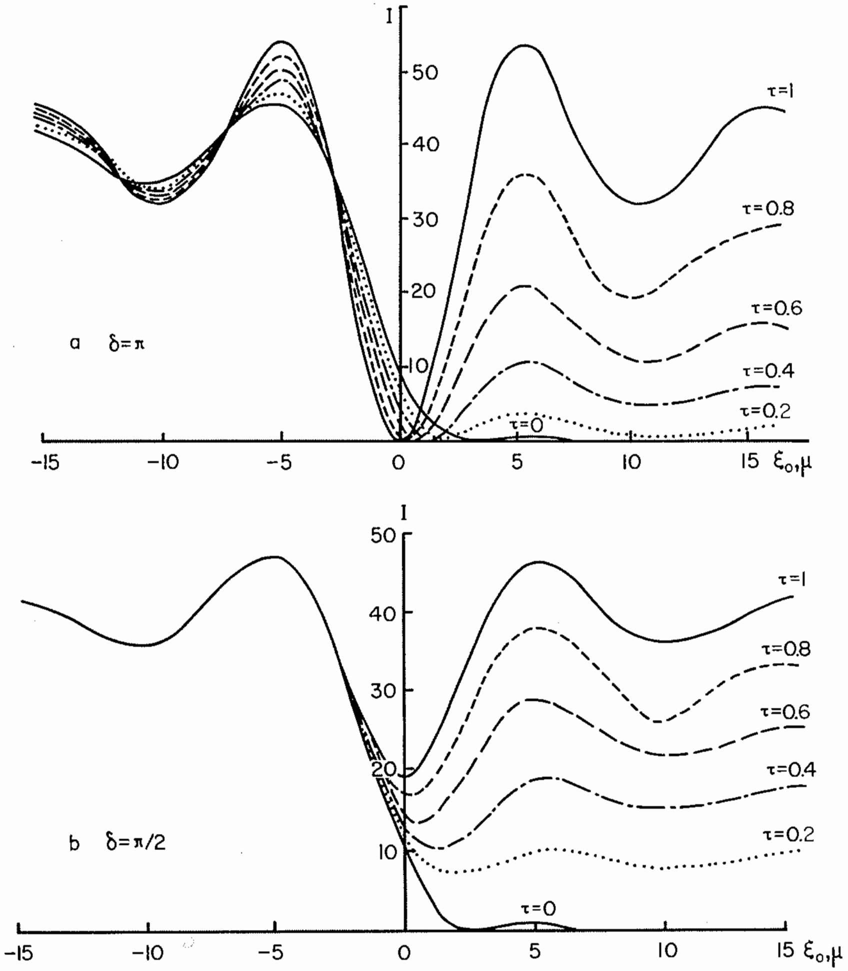

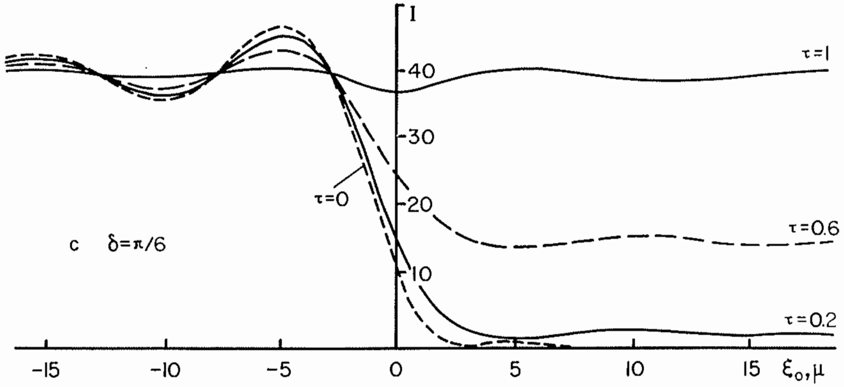

Figure 114

Illumination of the central field point as a function of the knife position.

When studying the image of field points situated not very close to the object plane diaphragm edges ($x' = R$ and $x' = -R$), we can disregard the effect of the focal plane diaphragm edges, located at $\xi = r$ and $\xi = -r$. The terms $\beta_1 r$ and $\beta_2 r$ then become so large that we can write with sufficient accuracy

$$\mathrm{Ci}\,\beta_1 r = \mathrm{Ci}\,\beta_2 r = 0\,, \qquad \mathrm{Si}\,\beta_1 r = -\,\mathrm{Si}\,\beta_2 r = \pi/2\,. \tag{50.3}$$

Equation (50.2) reduces then to

$$I_{\mathrm{ph}}(x') = \left[\frac{2\pi C(f-\Delta)}{kn}\right]^2 \{[(-\,\mathrm{Ci}\,\beta_1\xi_0 + \mathrm{Ci}\,\beta_2\xi_0)(1 - \tau\cos\delta) +$$
$$+ \tau\sin\delta\,(\pi - \mathrm{Si}\,\beta_1\xi_0 + \mathrm{Si}\,\beta_2\xi_0)]^2 + [(1 - \tau\cos\delta)(\mathrm{Si}\,\beta_1\xi_0 - \mathrm{Si}\,\beta_2\xi_0) +$$
$$+ \pi(1 + \tau\cos\delta) + \tau\sin\delta\,(\mathrm{Ci}\,\beta_1\xi_0 - \mathrm{Ci}\,\beta_2\xi_0)]^2\}\,. \tag{50.4}$$

Consider the curves plotting the illumination of the central field point ($x' = 0$) vs. the knife position with respect to the slit image for a fixed value of the other parameters (Figure 114). The slope of these curves determines the measurement sensitivity of the photoelectric recording methods. Note that the curves have a complicated character; the same illumination may correspond to different slope angles of the wave front. As a result, measurements become possible only in the range of deviation angles for which a single-valued variation of the illumination is observed. This is the working measurement range.

The curves with $\tau = 1$ correspond to a pure phase knife, which does not introduce amplitude changes in the incident light; $\tau = 0$ corresponds to the popular schlieren method of the knife-edge and the slit, when the knife stops the incident light completely. In intermediate cases the knife causes both amplitude and phase changes in the light flux transmitted in the region $-r < \xi < \xi_0$.

We see that if $\delta = \pi$ (Figure 114*a*), the sensitivity is maximum for $\tau = 1$. The sensitivity of the phase method is higher in this case than that of the amplitude method of the knife-edge and the slit. Any decrease in the absorption coefficient (which leaves $\delta = \pi$ unchanged) leads to an increase in the sensitivity. Note, however, that this increase in the sensitivity is accompanied by a contraction of the working range.

Figure 114*b* plots $I$ as a function of $\xi_0$ for $\delta = \pi/2$. The phase-contrast method in this case has a considerably lower sensitivity than the knife-edge and slit method for all values of the coefficient $\tau$. This reduction in the sensitivity with the deviation of the phase shift from $\lambda/2$ takes place fairly rapidly: phase plates with phase shift smaller than $2\pi/3$ offer no advantage in sensitivity over the knife-edge and slit method. We thus conclude that for the phase method to be more sensitive than the amplitude method in measuring small deviation angles over the maximum part of the instrument field space, the additional shift caused by it must differ negligibly from $\pi$.

If the additional phase shift introduced by the knife-edge (Figure 114*c*) is small ($\delta = \pi/6$), the sensitivity of the phase knife method is low and the method becomes inapplicable.

Since our main problem is to find methods with the highest attainable sensitivity, we shall assume in what follows that $\delta = \pi$ and $\tau = 1$. We then obtain from (50.4)

$$I_{\mathrm{ph}}(x') = 4C^2\left(\frac{2\pi(f-\Delta)}{kn}\right)^2[(\mathrm{Ci}\,\beta_1\xi_0 - \mathrm{Ci}\,\beta_2\xi_0)^2 + (\mathrm{Si}\,\beta_1\xi_0 - \mathrm{Si}\,\beta_2\xi_0)^2]. \tag{50.5}$$

The derivatives of illumination with respect to the distance of the knife-edge from the source image, which are proportional to the sensitivity of the schlieren methods with photoelectric measurements, are determined by differentiating (50.5) and the expression for the intensity in the knife-edge and slit schlieren method,

$$I_{\mathrm{s}}(x') = C^2\left(\frac{2\pi(f-\Delta)}{kn}\right)^2[(\mathrm{Ci}\,\beta_1\xi_0 - \mathrm{Ci}\,\beta_2\xi_0)^2 + (\pi - \mathrm{Si}\,\beta_1\xi_0 + \mathrm{Si}\,\beta_2\xi_0)^2], \tag{50.6}$$

obtained from (48.12) for $r \to \infty$. Apart from constant coefficients, these derivatives

have the form

$$\frac{dI_{\mathrm{ph}}(x')}{d\xi_0} = 8C^2\left[(-\mathrm{Ci}\,\beta_1\xi_0 + \mathrm{Ci}\,\beta_2\xi_0)\left(-\frac{\cos\beta_1\xi_0}{\xi_0} + \frac{\cos\beta_2\xi_0}{\xi_0}\right) + \right.$$
$$\left. + (-\mathrm{Si}\,\beta_1\xi_0 + \mathrm{Si}\,\beta_2\xi_0)\left(-\frac{\sin\beta_1\xi_0}{\xi_0} + \frac{\sin\beta_2\xi_0}{\xi_0}\right)\right], \tag{50.7}$$

$$\frac{dI_{\mathrm{s}}(x')}{d\xi_0} = 2C^2\left[(\pi - \mathrm{Si}\,\beta_1\xi_0 + \mathrm{Si}\,\beta_2\xi_0)\left(-\frac{\sin\beta_1\xi_0}{\xi_0} + \frac{\sin\beta_2\xi_0}{\xi_0}\right) + \right.$$
$$\left. + (\mathrm{Ci}\,\beta_1\xi_0 - \mathrm{Ci}\,\beta_2\xi_0)\left(\frac{\cos\beta_1\xi_0}{\xi_0} - \frac{\cos\beta_2\xi_0}{\xi_0}\right)\right]. \tag{50.8}$$

We have considered an aberration-free optical system, working with an infinitely narrow slit source. This approximation is not always valid in real measurements. The optical systems used in practice have some aberrations. Additionally, the real source has a finite width. The illumination distribution in the image plane for this case has to be found by additional integration over the various incoherent points of the extended light source.

The sensitivity at the central field point is given by

$$\frac{dJ_{\mathrm{ph}}}{d\xi_0} = 16C^2\left[\mathrm{Si}^2\left(\xi_0 + \frac{L}{2}\right)\beta - \mathrm{Si}^2\left(\xi_0 - \frac{L}{2}\right)\beta\right] \tag{50.9}$$

for the phase method, and

$$\frac{dJ_{\mathrm{s}}}{d\xi_0} = 4C^2\left\{\mathrm{Si}^2\left(\xi_0 + \frac{L}{2}\right)\beta - \mathrm{Si}^2\left(\xi_0 - \frac{L}{2}\right)\beta - \pi\left[\mathrm{Si}\left(\xi_0 + \frac{L}{2}\right)\beta - \right.\right.$$
$$\left.\left. - \mathrm{Si}\left(\xi_0 - \frac{L}{2}\right)\beta\right]\right\} \tag{50.10}$$

for the amplitude method. Here $\beta = kR/f$, $L$ is the source width.

Changing over to new variables $p = L\beta$ and $\bar{\xi} = \xi_0/L$, we obtain from (50.9) and (50.10)

$$\frac{dJ_{\mathrm{ph}}}{d\xi_0} = 16C^2\left[\mathrm{Si}^2\left(\bar{\xi} + \frac{1}{2}\right)p - \mathrm{Si}^2\left(\bar{\xi} - \frac{1}{2}\right)p\right], \tag{50.11}$$

$$\frac{dJ_{\mathrm{s}}}{d\xi_0} = 4C^2\left\{\mathrm{Si}^2\left(\bar{\xi} + \frac{1}{2}\right)p - \mathrm{Si}^2\left(\bar{\xi} - \frac{1}{2}\right)p - \right.$$
$$\left. - \pi\left[\mathrm{Si}\left(\bar{\xi} + \frac{1}{2}\right)p - \mathrm{Si}\left(\bar{\xi} - \frac{1}{2}\right)p\right]\right\}. \tag{50.12}$$

Functions (50.11) and (50.12) are plotted in Figures 115 and 116. In examining the latter, we note a substantial difference between the two methods. The family of curves representing the sensitivity in the knife-edge and slit method as a function of the knife position for different widths of the illuminating slit tends to a rectangle as the parameter increases *p* (Figure 116). This means that for a sufficiently large illumination slit, the sensitivity is constant, being independent of the knife position relative to the slit image, if the knife-edge covers the slit image partially. It is this property that determines the transition to geometrical optics. In this case, we may use quantitative methods in which the angle of light deviation in the inhomogeneity is found from the image illumination, and the actual position of the field point is disregarded.

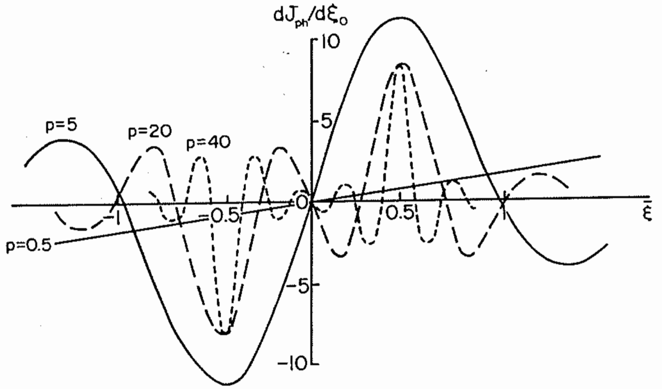

Figure 115
The plot of the function (50.11).

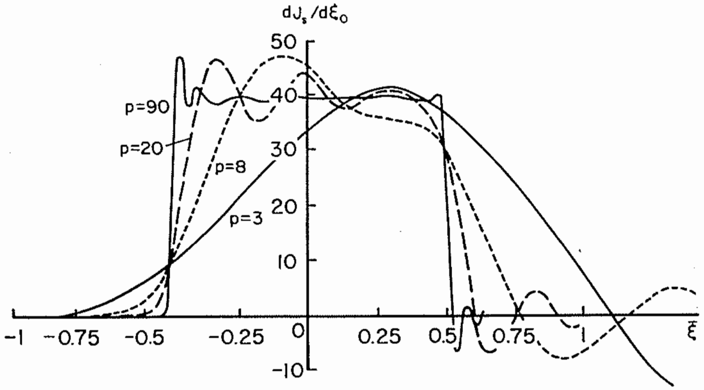

Figure 116
The plot of the function (50.12).

The transition to geometrical optics is impossible when using the phase-contrast method (Figure 115); the sensitivity is low if the phase knife is located between the slit edges. It is only when the slit image edge has moved past the edge of the phase knife that a change is observed in the light intensity in the image. For any source width, the measurement range is equal to the radius of the disk of confusion.

The manufacturing accuracy of the phase knife, the aberrations of the optical system, and the finite width of the light source substantially affect the sensitivity of the phase contrast method. Due to these factors, the theoretical sensitivity can be attained only under exceptionally favorable experimental conditions, using a precision phase plate and a carefully adjusted schlieren instrument.

Methods based on geometrical optics can be used with amplitude stops only. In the phase-contrast method the sensitivity goes to zero with the increase of the slit width, when the edge of the phase knife is located at the middle of the slit. The highly complicated diffraction pattern also affects the measurement range of the method. The range of the amplitude knife is determined by the slit width, while that of the phase knife is equal to the radius of the disk of confusion and cannot be markedly increased. This complicates the practical uses of the method considerably and reduces its value.

## 51. RESOLVING POWER OF SCHLIEREN INSTRUMENTS

Schlieren photographs can be analyzed qualitatively or quantitatively. The quantitative photometric methods measure the shift of the shadow from a defocused grid or the color; the angles of deviation are associated with the points at which the measurements were conducted. The qualitative analysis determines the shape of the inhomogeneity, its position and structure, e.g., the shape of the compression shock and its position with respect to the flying body, the exact boundary of the model and the rate of its displacement, etc.

However, in view of the limited resolving power, the light rays from a given point of the inhomogeneity do not converge at one point of the image plane, producing a circle of confusion which causes a certain measurement error. We do not find the true value of the deviation angle at every point, but instead a value averaged over the inhomogeneity area, equal to the area of the circle of confusion.

When determining the relative position of the model and the compression shock around it, the boundaries of the model and the shock are found with an error equal to the radius of the circle of confusion. Smaller size features cannot be detected at all.

Thus the accuracy (and frequently even the very applicability of schlieren methods) depends on the resolving power of the instrument, which can be defined as

$$R = \frac{1}{L}, \qquad (51.1)$$

where $L$ is the minimum distance between lines in the object plane at which the individual lines are resolved by the instrument ($L$ can be alternatively be defined as the effective width of the image of a thin line). $R$ is frequently expressed as the number of resolvable lines per unit length in the image plane. While this quantity is a useful characteristic of the photographic objective quality, the resolution in the object plane indicates more clearly the potential of the instrument as a whole. The resolving power is limited by the aberrations of the main objectives of the schlieren instrument and the photographic attachment, the quality of the emulsion, and diffraction phenomena.

The total image width can be approximately expressed as the sum of the widths contributed by each of the three factors above:

$$L = L_a + L_{ph} + L_d \,. \tag{51.2}$$

Defining the partial resolving powers

$$R_a = \frac{1}{L_a}, \quad R_{ph} = \frac{1}{L_{ph}}, \quad R_d = \frac{1}{L_d}, \tag{51.3}$$

we transform (51.1) to the form

$$\frac{1}{R} = \frac{1}{R_a} + \frac{1}{R_{ph}} + \frac{1}{R_d}. \tag{51.4}$$

In this section we shall evaluate the factors affecting the resolving power, determine the scope of influence, and indicate possible means for improving the resolving power [18]. Since the aberration and photographic resolution limits for schlieren instruments do not differ from similar problems in the general theory of optical instruments design, we need only the empirical numerical values of $R_a$ and $R_{ph}$ for several existing designs of schlieren instruments. The influence of diffraction is examined in greater detail, since the diffraction phenomena in the schlieren instrument differ somewhat from those generally met.

The measurements of the aberration resolution were conducted with a fully open focal plane diaphragm. As a result, it was possible to ignore the broadening of the line image caused by the wave nature of light. The values of $R_a$ obtained for the Soviet-made TE-19, TE-20, and IAB-451 instruments are listed in Table 6. The aberration resolution is the highest in TE-19 and IAB-451 operating with photographic attachments which give the maximum frame size for each instrument. Even in these cases, however, the instruments cannot resolve more than 10 lines/mm.

This resolution is insufficient in some cases, e.g., when studying the boundary layer; it has been suggested that in such cases a photographic attachment with variable magnification be used. A pancratic photographic system similar to that described in [71] was used to explore this possibility: the image scale could be varied continuously by moving the lens with respect to the screen. For a distance of 1 m between the screen and the knife-edge, the image scale $\mu$ varied from 0.17 to 1.54 for $f_1 = 135.8$ mm, $f_2 = -51.31$ mm (curve I in Figure 117) and from 0.17 to 0.46 for $f_1 = 135.8$ mm, $f_2 = -199.95$ mm (curve II). An increase of the resolution with the increase in scale is observed on both curves, but the effect is very small. Therefore, it does not seem efficient to use variable-magnification systems with aberrations satisfactorily corrected only for one image size. This improvement is meaningful only if the aberrations of the photographic optics are calculated.

Table 6

| Diameter of the photographic attachment frame, mm | TE-19 | | IAB-451 | | TE-20 | |
|---|---|---|---|---|---|---|
| | $R_a$ | $R_{ph}$ | $R_a$ | $R_{ph}$ | $R_a$ | $R_{ph}$ |
| 80 | | | 10 | 30 | | |
| 40 | 10 | 26 | | | 4.5 | 11.5 |
| 24 | | | 5 | 10 | | |
| 17 | 2.4 | 11 | | | 1 | 5.0 |
| 11 | 1.5 | 7.5 | | | 0.6 | 3.2 |
| 4 | 1.1 | 2.7 | 0.7 | 1.7 | 0.5 | 1.1 |

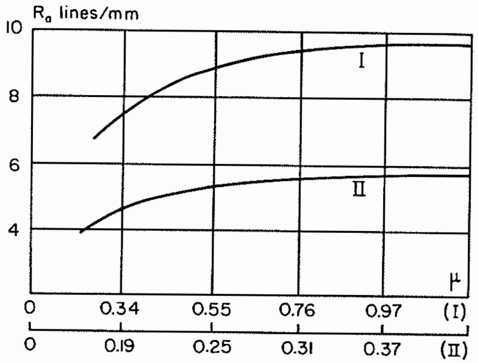

Figure 117

Aberration resolving power for a photographic attachment with variable magnification:

I attachment with large magnification; II attachment with small magnification.

The photographic resolution limit is determined by the emulsion grain size and the image scale $\mu$. If the emulsion resolution is equal to $R_1$, then

$$R_{ph} = R_1 \mu \,. \tag{51.5}$$

Some special emulsions have $R_1 \approx 300$ lines/mm, but their speed is too low for some schlieren measurements. The films most widely used in schlieren techniques (A-2, A-35, M3-2) have $R_1 \approx 100$ lines/mm. The values of $R_{ph}$ calculated from (51.5) for different $\mu$ and $R_a = 100$ lines/mm are given in Table 6. As with aberrations, the limitation of the resolving power by the emulsion is particularly noticeable when using cameras with small frame size.

The diffraction limitations of the resolving power were examined in [18] under the assumption that the incident light wave is plane, the optical system is aberration-free, and the light source is monochromatic. The object plane diaphragm was an infinitely long slit of width $2R$. The object consisted of two infinitely long parallel lines of width $2a$, with axes separated by $4a$ and parallel to the coordinate axis $y$ and to the diaphragm edges. The viewing (focal plane) diaphragm was a slit of width $2r$, symmetrical about the $\eta$ axis. The point source was located on the $z$ axis.

Under these assumptions we obtain from (47.11) the following expression for the illumination distribution in the screen plane:

$$I(x') = \frac{4C^2 f^4}{k^4}\left\{\pi + \mathrm{Si}\,\frac{k}{f}(-x' - 3a)r + \mathrm{Si}\,\frac{k}{f}(-x' + a)r - \right.$$
$$\left. - \mathrm{Si}\,\frac{k}{f}(-x' - a)r - \mathrm{Si}\,\frac{k}{f}(-x' + 3a)r\right\}^2. \qquad (51.6)$$

Equation (51.6) was obtained under the assumption that the diffraction at the edges of the object plane slit does not affect the line resolution.

Writing (51.6) in the form

$$I(x') = \frac{4f^4C^2}{k^4}\left\{\pi + \mathrm{Si}\,b\left(-\frac{x'}{a} - 3\right) + \mathrm{Si}\,b\left(-\frac{x'}{a} + 1\right) - \right.$$
$$\left. - \mathrm{Si}\,b\left(-\frac{x'}{a} - 1\right) - \mathrm{Si}\,b\left(-\frac{x'}{a} + 3\right)\right\}^2, \qquad (51.7)$$

we note that the illumination distribution depends only on the parameter $b$ and the reduced coordinate $x'/a$.

Curves calculated by (51.7) for different values of $b$ are plotted in Figure 118. The distribution corresponding to the geometrical optics ($b = \infty$) is represented by the thin solid line. If the dimensions of the line or the slit aperture in the $\xi, \eta$ plane are sufficiently large ($b \approx 10$), diffraction is noticeable at the line edges only. The effect of diffraction becomes more pronounced with the decrease in $b$, the maxima broaden and grow, and the line resolution diminishes. A further decrease in $b$ creates a uniform illumination in the image plane.

The following parameter can be adopted as a criterion of resolution:

$$\psi = \frac{I(0) - I(2a)}{I(0)}, \qquad (51.8)$$

where $I(0)$ is the illumination at the center of the bright space between lines ($x' = 0$) and $I(2a)$ is the illumination at the line center ($x' = 2a$). The dependence of $\psi$ on $b$ is represented in Figure 119.

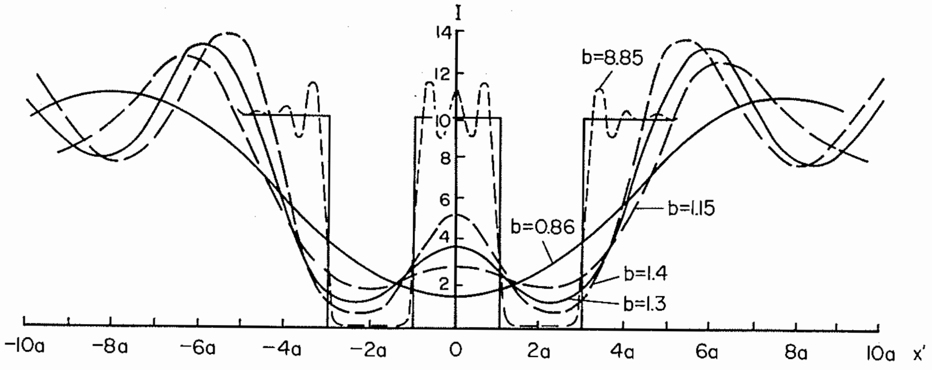

Figure 118

Illumination distribution calculated from (51.7).

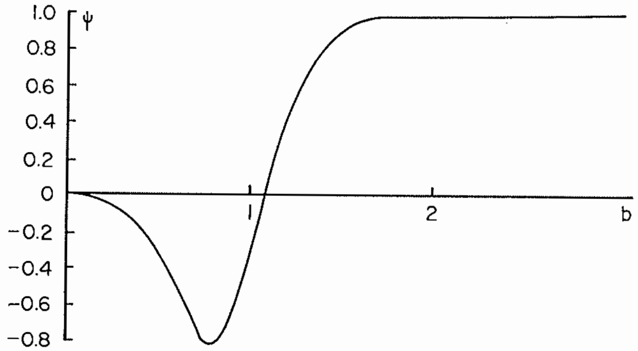

Figure 119

Resolution $\psi$ as a function of the parameter $b$.

For large values of $b$, when the diffraction hardly affects the line resolution, $\psi = 1$. The value of $\psi$ decreases with the decreases of $b$, and the difference in illumination between the line center and the center of the transparent gap diminishes. In addition, the illumination at points which should be dark according to the geometrical optics starts to exceed that in the bright space.

Defining the distribution with $\psi = 0.5$ as the resolution limit, we obtain

$$b = 1.2, \qquad (51.9)$$

which leads for $\lambda = 5.5 \times 10^{-4}$ mm, $f = 1918$ mm to

$$ar = 0.2\ \mathrm{mm}^2. \qquad (51.10)$$

Note that the curve $\psi = f(b)$ falls off from 1 to zero in a fairly narrow range of variation of $b$ (roughly from $b = 1.6$ to $b = 1.07$). As a result, the arbitrary definition of the resolution limit does not lead to considerable errors in the determination of the parameters for which the lines become unresolvable.

A focal plane slit symmetrical with respect to the illuminating slit image is seldom used as a viewing diaphragm in schlieren measurements. The viewing diaphragm generally is a Foucault knife-edge. In this case the resolving power depends on the part of the diffraction pattern, representing the illuminating slit image, which is covered by the knife. This arrangement is similar to oblique illumination in microscopes.

The calculation procedure in this case is similar to the one described above. The focal plane diaphragm is placed so that one of its edges is near the illuminating slit image, while the other is at a considerable distance from it. If we disregard the effect of the far edge of the viewing diaphragm, we derive

$$\begin{aligned} I(x') = \frac{C^2 f^4}{k^4}\Bigg\{\Bigg[&\mathrm{Ci}\, b_1\left(-\frac{x'}{a}-3\right)+\mathrm{Ci}\, b_1\left(-\frac{x'}{a}+1\right)- \\ &-\mathrm{Ci}\, b_1\left(-\frac{x'}{a}-1\right)-\mathrm{Ci}\, b_1\left(-\frac{x'}{a}+3\right)\Bigg]^2+ \\ &+\Bigg[\mathrm{Si}\, b_1\left(-\frac{x'}{a}-3\right)+\mathrm{Si}\, b_1\left(-\frac{x'}{a}+1\right)-\mathrm{Si}\, b_1\left(-\frac{x'}{a}+3\right)- \\ &-\mathrm{Si}\, b_1\left(-\frac{x'}{a}-1\right)+\left|\begin{matrix}0 & \text{for} & \xi_0>0\\ 2\pi & \text{for} & \xi_0<0\end{matrix}\right.\Bigg]^2\Bigg\}, \end{aligned} \tag{51.11}$$

where $b_1 = \xi_0 \cdot ka/f$, and $\xi_0$ is the knife-edge coordinate with respect to the slit image.

The form of the illumination distribution as a function of the dimensionless coordinate $x'/a$ depends on the parameter $b_1$.

Curves calculated from (51.11) are plotted in Figure 120. Curve 1 is the distribution corresponding to geometrical optics ($b_1 = \infty$). For large values of $b$, the distribution is very similar to that obtained in geometrical optics (curves 2, 3). For small $b$ the difference becomes large and the lines are not resolved (curves 4, 5). Unlike the cases considered above, illumination maxima appear at the line edges, which grow with the approach of the knife-edge to the slit image and interfere with the resolution. (The existence of maxima at the edge of an opaque body occasionally simplifies the schlieren pattern analysis, since the maxima fix the exact location of the boundary. However, in the general case, when the arrangement of the schlieren pattern details is unknown, the maxima reduce the resolution).

When the knife edge is sufficiently far from the slit image, the pattern is similar to the one discussed above.

A point source was assumed in the two preceding cases. However, the case of a source of finite dimensions is the most interesting in practice. The calculation of the intensity reduces to integration of an expression similar to (51.11), without any simplifying assumptions ignoring the effect of the edges of the focal plane and the object plane diaphragm. The calculation gives

$$\begin{aligned} I(x') = C^2\Bigg\{&\left[\sum_{i=1}^{6}\left((-1)^i\,\mathrm{Ci}\,\beta_i+(-1)^{i+1}\frac{\sin\beta_i}{\beta_i}+(-1)^{i+1}\,\mathrm{Ci}\,\alpha_i\right)\right]^2+ \\ &+\left[\sum_{i=1}^{6}\left((-1)^i\,\mathrm{Si}\,\beta_i+(-1)^i\frac{\cos\beta_i}{\beta_i}+(-1)^{i+1}\,\mathrm{Si}\,\alpha_i\right)\right]^2- \\ &-\sum_{i=1}^{6}\frac{1}{\beta_i^2}-2\sum_{i=1}^{5}\sum_{j=i+1}^{6}(-1)^{i+j}\frac{\cos(\beta_i-\beta_j)}{\beta_i\beta_j}+ \\ &+2\sum_{i=1}^{5}\sum_{j=i+1}^{6}(-1)^{i+j}\left(\frac{1}{\beta_i}-\frac{1}{\beta_j}\right)\mathrm{Si}\,(\beta_i-\beta_j)\Bigg\}\Bigg|_{\xi_0=\xi_1}^{\xi_0=L+\xi_1}, \end{aligned} \tag{51.12}$$

where

$$\beta_1 = \frac{k}{f}(-x'-3a)\xi_0, \quad \beta_2 = \frac{k}{f}(-x'-a)\xi_0,$$

$$\beta_3 = \frac{k}{f}(-x'+a)\xi_0, \quad \beta_4 = \frac{k}{f}(-x'+3a)\xi_0,$$

$$\beta_5 = \frac{k}{f}(-x'+R)\xi_0, \quad \beta_6 = \frac{k}{f}(-x'-R)\xi_0,$$

$$\alpha_1 = \frac{k}{f}(-x'-3a)r, \quad \alpha_2 = \frac{k}{f}(-x'-a)r, \quad \alpha_3 = \frac{k}{f}(-x'+a)r,$$

$$\alpha_4 = \frac{k}{f}(-x'+3a)r, \quad \alpha_5 = \frac{k}{f}(-x'+R)r, \quad \alpha_6 = \frac{k}{f}(-x'-R)r,$$

$\xi_1$ and $L + \xi_1$ are the coordinates of the edges of the illuminating slit image with respect to the knife-edge. Here $k$, $f$, $(\eta_2 - \eta_1)$ have been incorporated in $C^2$, which is consequently different from above. This method will be used in cases when the absolute value of the illumination is of no importance.

The illumination distribution and the limit of resolution depend on two parameters: the illuminating slit width $L$ and the distance from the knife-edge to the nearest edge of the slit (the width of the slit image which is not covered by the knife).

An increase in $\xi_1$ improves the resolution; an increase in the covered part of the slit image for $\xi_1 = \text{const}$ lowers the resolution.

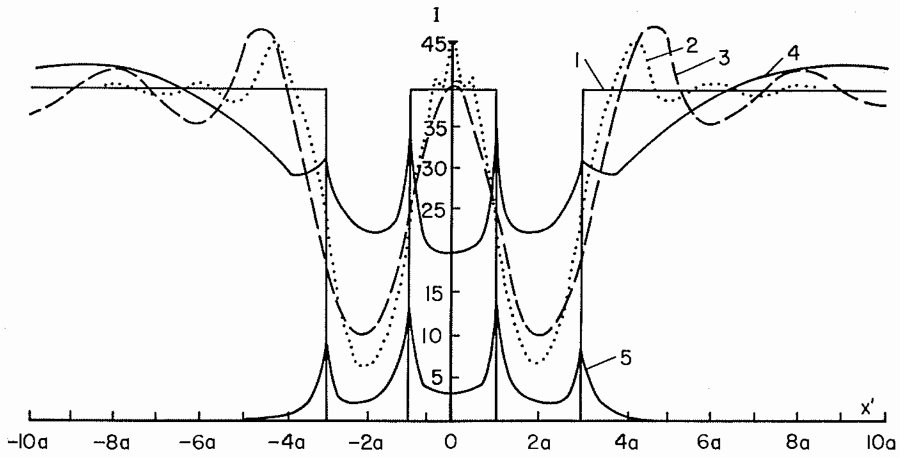

Figure 120

Curves calculated from (51.11).

The calculated illumination distribution curves are given in Figure 121. Curves 1 and 2 correspond to the same uncovered width of the illuminating slit image, but to slits of different width (wider for curve 1 than for curve 2). We see that the increase in the slit width enhances the illumination at the points where the image of the opaque lines is expected to form, and, therefore, reduces the line resolution.

A similar situation is observed when comparing curves 3 and 4, which were also obtained for the same uncovered width of the slit,(smaller than for curves 1 and 2) and slits of different widths.

Unlike the above cases of a wide slit partly covered by the knife, the background illumination in this case depends linearly on the knife position relative to the slit image. As a result, the resolution conditions will be different.

The dependence of $\psi$ on $b_2 = \xi_1 \cdot ak/f$ for $L = \text{const}$ (Figure 122) differs substantially from that shown in Figure 119, namely, there is no sharp drop in resolution, and this leads to a large error in the determination of the resolution limit. If we take as before $\psi = 0.5$ as the resolution condition, then

$$b_2 \geqq 0.52\,, \tag{51.13}$$

which corresponds for $\lambda = 5.5 \times 10^{-4}$ mm and $f = 1918$ mm to

$$a\xi_1 \geqq 0.09\ \text{mm}^2\,. \tag{51.14}$$

To compare the theoretical and experimental results, the diffraction patterns of two parallel lines were photographed on an IAB-451 instrument [18]. The illuminating slit width was 0.8 mm, the width of the lines and the bright space between them

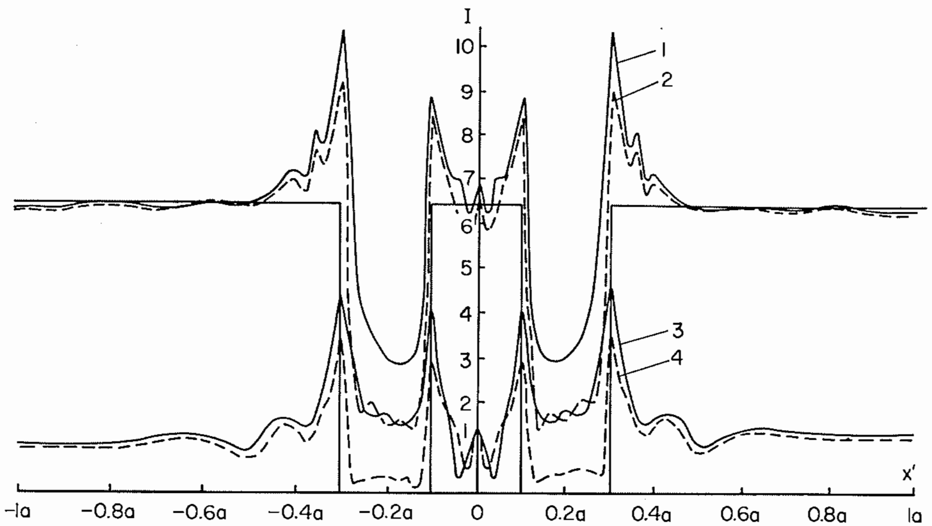

Figure 121

Curves calculated from (51.12).

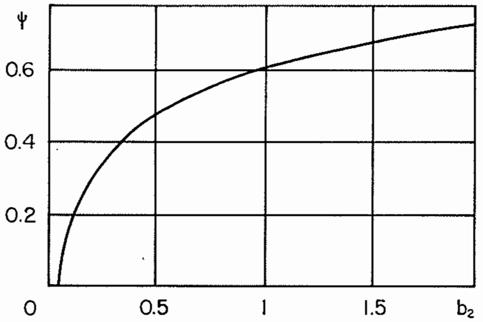

Figure 122

Resolution $\psi$ as a function of the parameter $b_2$.

2 mm. A photometric analysis of the photographs was conducted on the MF-4 recording microphotometer in the direction perpendicular to the lines. A series of photographs were obtained, corresponding to different positions of the knife with respect to the slit image (Figure 123).

For large distances between the knife-edge and the slit image (Figure 123*a*, $\xi_1 = 0.8$ mm), the pattern is almost that of geometrical optics. The diffraction is

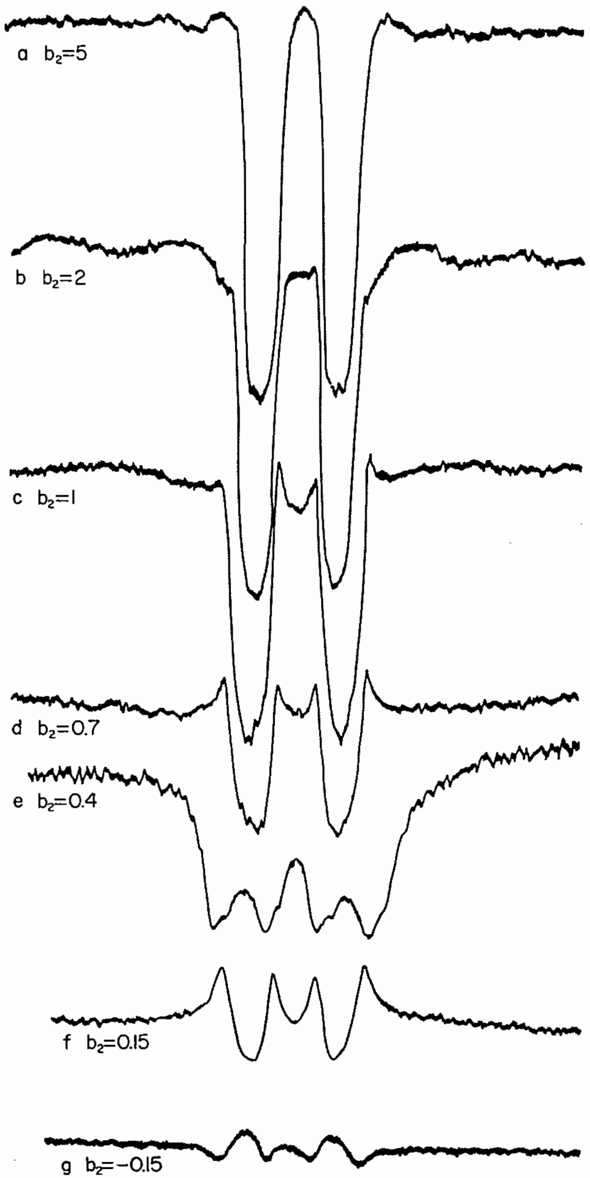

Figure 123

Microphotometer tracings of the illumination distribution on two parallel lines for different positions of the knife.

barely noticeable and hardly affects the resolution. The effect of diffraction increases with the approach of the knife-edge to the slit image. Clear maxima appear at the line edges, interfering with resolution. We note from the curves that the limit of resolution is attained between curves *d* and *e* of Figure 123, which roughly corresponds to

$$a\xi_1 = 0.07 \text{ to } 0.12\ \text{mm}^2. \tag{51.15}$$

This empirical value of the resolution limit coincides satisfactorily with the theoretical value calculated from (51.13), particularly if we take into account the smoothness of the curve in Figure 122 and the arbitrary definition of the criterion used for determining the resolution limit. With the further decrease of $\xi_1$ (Figure 123*g*) we obtain a system of four maxima at the line boundaries, whose brightness decreases as the slit is progressively covered.

The experimental patterns fit both qualitatively and quantitatively the theoretical curves. For each particular use of a schlieren instrument, we can determine the resolving power from the values obtained and establish which of the various factors is the most important.

When the photographic emulsion limits the resolution, magnifying attachments should be used, or, if this is difficult (as it is with superhigh-speed cinecameras), the source brightness should be increased or a better emulsion used. If aberrations in the instrument or attachments limit the resolution then a larger image scale should be used or the optics improved. If diffraction is the limiting factor then sensitivity must be reduced, with compensation made by increased emulsion $\gamma$. Increasing the image scale or suppressing the aberrations of the objective will not help if resolution is limited by diffraction.

Note that it is the diffraction which in most cases limits the resolving power of high-sensitivity measurements, particularly when schlieren instruments are used for accurate measurements. Thus with the IAB-451 instrument and a photographic attachment giving an image 24 mm in diameter, $R_a = 5$ lines/mm, and $R_{ph} = 10$ lines/mm. The combined effect of aberrations and of the emulsion grain size sets the resolution limit at 3.3 lines/mm. The diffraction limitations are less than the combined effect of these factors only if the uncovered width of the illuminating slit image is at least 1 mm, i.e., in the case of when the instrument shows very poor sensitivity. At higher sensitivities, the effect of diffraction exceeds the combined contribution of the other factors.

## 52. ERROR OF THE CURVED-STOP METHOD

In examining the diffraction error of the curved-stop method and similar methods, we encounter some peculiar features not met thus far. In the first instance, the viewing diaphragm is not one-dimensional, as in the preceding cases; which complicates the calculations. Moreover, the finite width of the illuminating slit image need not be considered here; the image can be assumed infinitely long and infinitely thin, and the diffraction at its edges can be disregarded. In practice, the illuminating slit length is always considerably greater than the stop aperture size, and, therefore, the assumption of infinite slit length does not involve substantial deviations from the experimental conditions.

Consider the diffraction at a straight opaque edge. The diffraction pattern is affected in this case only by the parameters of the viewing diaphragm in the direction perpendicular to the opaque edge. If we assume that a slit with edges at $x' = R$ and $x' = 0$ is placed in the object plane, and the image of the point source is at point $\eta = \beta f$, $\xi = \alpha f$ of the focal plane of the main objective, the light intensity distribution in the image plane will be given, apart from a constant coefficient, by the expression

$$\begin{aligned} I(x') = \Big[ & \mathrm{Ci}\,\frac{kx'}{f}\left(ca^{\alpha f/h} - \beta f\right) - \mathrm{Ci}\,\frac{kx'}{f}\left(-ca^{\alpha f/h} - \beta f\right) - \\ & - \mathrm{Ci}\,\frac{k(x'-R)}{f}\left(ca^{\alpha f/h} - \beta f\right) + \mathrm{Ci}\,\frac{k}{f}(x'-R)\left(-ca^{\alpha f/h} - \beta f\right)\Big]^2 + \\ & + \Big[\mathrm{Si}\,\frac{kx'}{f}\left(ca^{\alpha f/h} - \beta f\right) - \mathrm{Si}\,\frac{kx'}{f}\left(-ca^{\alpha f/h} - \beta f\right) - \\ & - \mathrm{Si}\,\frac{k}{f}(x'-R)\left(ca^{\alpha f/h} - \beta f\right) + \mathrm{Si}\,\frac{k}{f}(x'-R)\left(-ca^{\alpha f/h} - \beta f\right)\Big]^2 . \end{aligned} \tag{52.1}$$

We assumed here that the transparent aperture of the curved stop had edges of the form

$$\eta = ca^{\xi/h} \quad \text{and} \quad \eta = -ca^{\xi/h}.$$

If the light source is an infinitely long slit perpendicular to the axis of symmetry of the stop, we determine the illumination distribution in the image plane by integrating (52.1) over $\beta$ in an infinite range:

$$J(x') = \int_{-\infty}^{\infty} I d\beta . \tag{52.2}$$

Integrating by parts, we obtain

$$\begin{aligned} J(x') = \frac{1}{kx'}\Big\{ & 4\pi - 4\pi\cos 2a' - \frac{4\pi}{e} + \frac{4\pi\cos 2a'c}{e} + \\ & + 4a'\Big[\int_{-\infty}^{\infty} \frac{\mathrm{Ci}\,(y-a')\cos e(y+a') + \mathrm{Si}\,(y-a')\sin e(y+a')}{y+a'}\,dy + \end{aligned}$$

$$\begin{aligned} & + \int_{-\infty}^{\infty} \frac{\mathrm{Ci}\,e(y-a')\cos(y+a') + \mathrm{Si}\,e(y-a')\sin(y+a')}{y+a'}\,dy - \\ & - \int_{-\infty}^{\infty} \frac{\mathrm{Ci}\,(y-a')\cos(y+a') - \mathrm{Si}\,(y-a')\sin(y+a')}{y+a'}\,dy - \\ & - \int_{-\infty}^{\infty} \frac{\mathrm{Ci}\,e(y-a')\cos e(y+a') + \mathrm{Si}\,e(y-a')\sin e(y+a')}{y+a'}\,dy\Big]\Big\}, \end{aligned} \tag{52.3}$$

where

$$a' = \frac{kx'}{f}\,ca^{\alpha f/h}, \qquad e = \frac{x'-R}{x'} .$$

The remaining integrals are calculated by integrating over a parameter. The final illumination distribution is expressed by the formula

$$\begin{aligned} J(x') = \frac{1}{kx'}\Big[ & 4\pi - 4\pi\cos 2a' - \frac{4\pi}{e} + \frac{4\pi\cos 2a'c}{e} - \\ & - 8a\pi(\mathrm{Si}\,2a' - \mathrm{Si}\,2a'e)\Big]. \end{aligned} \tag{52.4}$$

Assuming that $a'$ is large (it is only in this case that the diffraction error is small and the geometrical optics is applicable), we can represent the integral sines by the first terms of the asymptotic series. Equation (52.4) reduces to

$$J(x') = \frac{4\pi^2 l}{f}\left(1 + \frac{f}{kx'l\pi} + \frac{f^2 \sin\dfrac{kx'}{f}\,l}{\pi k^2 x'^2 l^2}\right), \tag{52.5}$$

where $l = 2\,ca^{\alpha f/h}$.

We shall use this distribution for determining the diffraction error of the photometric methods. The relative error of the curved-stop method is determined by the expression

$$\kappa = \frac{\log(J_2/J_1)}{\log(l_2/l_1)} - 1 , \tag{52.6}$$

where $J_1$ and $J_2$ are, respectively, the image illumination before and after the introduction of the inhomogeneity; $l_1$ and $l_2$ are the lengths of the corresponding portions of the illuminating slit image which pass through the stop aperture. Substituting the expressions for $J_2$, $J_1$ according to (52.5) in (52.6), and taking into account the smallness of the diffraction error, we obtain

$$\kappa = \frac{f}{\pi k x' l_1} + \frac{f^2 l_1}{\pi k^2 x'^2 (l_2 - l_1)}\left[\frac{\sin\dfrac{kx'}{f}\,l_1}{l_1^2} - \frac{\sin\dfrac{kx'}{f}\,l_2}{l_2^2}\right]. \tag{52.7}$$

The second term is usually much smaller than the first term, so that

$$\kappa = \frac{f}{\pi k x' l_1}. \tag{52.8}$$

A similar expression is obtained for photometric methods in which an infinitely long slit is bounded by two straight edges placed at an angle to each other.

The diffraction errors of these methods are equal to the error of the knife-edge and slit method when the width of the uncovered part of the illuminating slit image in the knife-edge and slit method is equal to the length of the image portion passing through the stop aperture. However, whereas in the knife-edge and slit method the uncovered width of the slit image is related to the measurement sensitivity, in the wedge and curved-stop methods the sensitivity depends on the angle between the stop axis and the lines bounding the transparent segment. This difference complicates the comparison of these methods. We can only state that each of these methods should be applied under appropriate experimental conditions.

The error calculation is complicated if the diffracting edge lies at some angle to the axis of symmetry of the stop. However, the diffraction pattern will be approximately the same as in the previous case, with the only difference that the characteristic dimension determining the error will be the size of the stop aperture in the direction perpendicular to the edge. This dimension will have a different value for each point of the slit image, and we can adopt as a mean value the length of the aperture in the direction perpendicular to the edge for the middle point of the slit. Since knowledge of the diffraction error is necessary for estimating the accuracy of the measurements, the latter can be found only approximately. Therefore, the somewhat arbitrary determination of the error for inclined edges will not lead to a substantial distortion of the results.

# XII

# ALLOWANCE FOR THE LIGHT WAVE CURVATURE

## 53. THE SLIT AND FILAMENT METHOD

The illumination distribution in the image plane has been examined thus far assuming a plane light wave, with the viewing diaphragm placed in the focal plane of the main receiving objective. However, not all the schlieren methods can be described by this model. Thus if we use a focal filament, the filament shadow produced by a plane light wave will occupy the entire image plane, and the measurements become impossible. In this method, the light wave curvature must be taken into consideration. The case is similar when using defocused viewing diaphragms; in this case a quadratic relationship enters the function $L[(x, y), (\xi, \eta)]$. Moreover, the real wave front behind the inhomogeneity is complex, and its approximate description by plane surfaces is highly unsatisfactory. For these reasons it is necessary to refine the computing model so that it allows for the curvature of the light wave.

We start with the simplest case — the slit and filament method [35, 52]. The diffraction theory will be used, since the part of the image corresponding to the center of the geometrical shadow of the filament must be determined in the quantitative processing of the schlieren patterns. In real conditions, the shadow is a complex diffraction pattern, where the illumination distribution depends on the character of the inhomogeneity. The illumination changes caused by the diffraction phenomena could be mistakenly interpreted as the effect of the wave front deformation, leading to systematic errors. To avoid these errors, we need the dependence of the image plane illumination on phase and amplitude distribution in the object plane.

The calculation will be made for a point source located on a straight line passing through the optical axis at an angle $\psi$ to the $\xi'$ axis. The distance from the source to the optical axis is $l$.

The front of the light wave propagating behind the collimator can be described by the equality

$$z = x \tan \frac{l \cos \phi}{f} + y \tan \frac{l \sin \phi}{f}. \tag{53.1}$$

Since $l$ is small compared to $f$ (this condition is almost always satisfied in schlieren instruments; thus, in IAB-451, $l/f \leqq 1/200$), equation (53.1) can be simplified thus:

$$z = \frac{xl \cos \phi}{f} + \frac{yl \sin \phi}{f}. \tag{53.2}$$

An optical inhomogeneity distorting the light wave is placed in the object plane $A(x, y)$. Let the inhomogeneity alter the wave front shape to

$$z = \frac{xl \cos \phi}{f} + \frac{yl \sin \phi}{f} + \alpha_x x + \alpha_y y + \frac{P_{xx}}{2} x^2 + \frac{P_{yy}}{2} y^2 = U(x, y). \tag{53.3}$$

If the angles of inclination of the wave front to the object plane are so small that the quantities $(\partial z/\partial x)^2$ and $(\partial z/\partial y)^2$ can be ignored, equation (53.3) gives the phase distribution function in the $A(x, y)$ plane, apart from a constant factor (the refractive index of the medium).

We assume to first approximation that the objectives $O_1$ and $O_2$ are large and free from aberrations. Let there be no obstructions to the light passage in plane $A(x, y)$. An infinitely long filament of width $2t$, making an angle $\psi$ with the $\eta$ axis, is placed in the focal plane of the receiving part. The filament axis of symmetry passes through the origin of coordinates.

Under these assumptions, the light intensity in the screen plane will be described by the expression

$$I(x', y') = \left| C \int_{-\infty}^{\infty} \int_{\xi=\eta \tan \phi + t/\cos \phi}^{\eta \tan \phi - t/\cos \phi} \int_{-\infty}^{\infty} \int_{-\infty}^{\infty} e^{W_8} dx\, dy\, d\xi\, d\eta \right|^2, \tag{53.4}$$

where

$$W_8 = \frac{ik}{f} \{\xi(x + \mu x') + \eta(y + \mu y') + f U(x, y)\}.$$

When the coordinate frame is rotated in the $(\xi, \eta)$ plane through an angle $\alpha$, defined by the expression

$$\tan \alpha = \sqrt{\frac{A_{yy}}{A_{xx}}} \tan \phi \tag{53.5}$$

(one of the new coordinate axes then becomes parallel to the viewing filament), the variables separate and expression (53.4) is reduced to a Fresnel integral. The final expression for the intensity distribution in the screen plane is

$$I(x, y) = C^2 \{[1 - C(\xi_{11}) + C(\xi_{12})]^2 + [1 - S(\xi_{11}) + S(\xi_{12})]^2\}, \tag{53.6}$$

where

$$\xi_{11} = \sqrt{\frac{k}{\pi A_{ll}}} \left[\frac{l}{f} + \frac{t}{f} + \cos \phi (\alpha_x + \mu x' A_{xx}) + \sin \phi (\alpha_y + \mu y' A_{yy})\right], \tag{53.7}$$

$$\xi_{12} = \sqrt{\frac{k}{\pi A_{ll}}} \left[\frac{l}{f} - \frac{t}{f} + \cos \phi (\alpha_x + \mu x' A_{xx}) + \sin \phi (\alpha_y + \mu y' A_{yy})\right], \tag{53.8}$$

$$A_{ll} = A_{xx} \cos^2 \phi + A_{yy} \sin^2 \phi. \tag{53.9}$$

Transforming the coordinates so that

$$x_1 = \frac{l}{t} + \frac{f}{t} [\cos \phi (\alpha_x + \mu x' A_{xx}) + \sin \phi (\alpha_y + \mu y' A_{yy})], \tag{53.10}$$

we reduce (53.7) and (53.8) to the form

$$\varepsilon_{11,12} = \Pi(x_1 \pm 1). \tag{53.11}$$

The illumination distribution in the diffraction pattern of a defocused filament depends on one parameter,

$$\Pi = \frac{t}{f} \sqrt{\frac{k}{\pi A_{ll}}}. \tag{53.12}$$

The larger the value of this parameter, the closer is the distribution to the geometrical.

The illumination distributions for different values of the parameter $\Pi$ are shown in Figure 124. These distributions cover the entire variety of patterns which can be obtained for different filament thicknesses, different defocusings, and different curvatures of the light wave after its passage through the inhomogeneity.

In all cases, we are dealing with the ordinary Fresnel diffraction from a filament. The interpretation of these patterns is simple: the middle of the central bright diffraction band corresponds to the rays which pass through the center of the opaque line.

Significantly, $l$ and $\alpha_x$ do not affect the diffraction pattern; their change leads only to a shift of the shadow unaccompanied by any change in its structure. Therefore, we can set these parameters equal to zero in what follows. Similarly, wave front deformation is of importance only if the quantity $A_{ll}$ — the wave front curvature in the direction perpendicular to the filament — changes. This conclusion could be derived without a detailed calculation on the basis of the general results of §47.

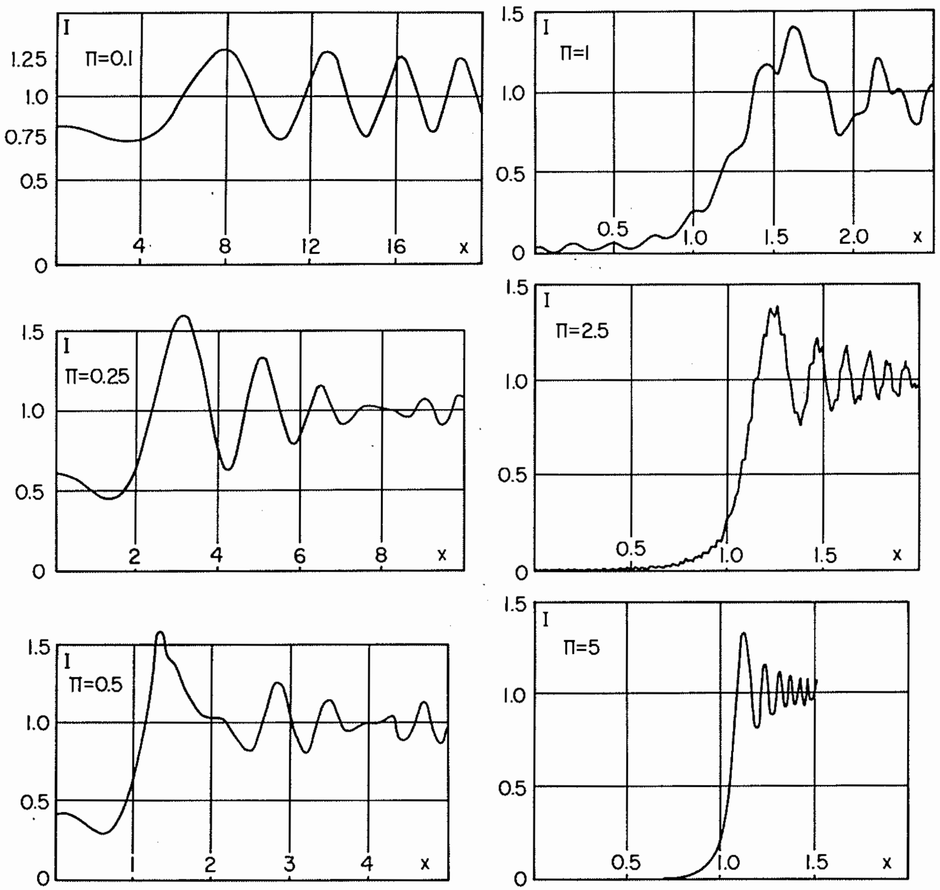

Figure 124

Illumination distribution in the defocused filament image for different values of the parameter Π.

We shall now conduct a more complicated calculation [52]. Consider an opaque screen in the object plane with its straight edge making an angle $\psi$ to the $x$ axis. let the wave surface equation be

$$z = \tfrac{1}{2}P_{xx}x^2 + \tfrac{1}{2}P_{yy}y^2 . \tag{53.13}$$

The filament is placed so that the angle between it and the $\xi$ axis is equal to $\psi$. The wave front in the filament plane is described by the formula

$$V(x, y) = \tfrac{1}{2}V_{xx}x^2 + \tfrac{1}{2}V_{yy}y^2 , \tag{53.14}$$

where

$$\begin{aligned} V_{xx} &= P_{xx} + \frac{\Delta}{f(f-\Delta)}, \\ V_{yy} &= P_{yy} + \frac{\Delta}{f(f-\Delta)}. \end{aligned} \tag{53.15}$$

The illumination in the screen plane is equal to

$$I(x', y') = \left| a - \frac{1}{\pi}\int_{[\phi_1(-y')+x']kt/(f-\Delta)}^{[\phi_2(-y')+x']kt/(f-\Delta)} e^{if(P)}\,\frac{\sin P}{P}\,dP\right|^2 , \tag{53.16}$$

$$\begin{aligned} f(P) = {} & \frac{1}{2}(V_{xx}\sin^2\psi + V_{yy}\cos^2\psi)\frac{(f-\Delta)^2}{kt^2}P^2 - \\ & -(V_{xx}\sin^2\psi + V_{yy}\cos^2\psi)\frac{(f-\Delta)x'}{t}P - \\ & -(V_{xx} - V_{yy})\sin\psi\cos\psi\,\frac{(f-\Delta)y'}{t}P ; \end{aligned} \tag{53.17}$$

$a$ is equal to 1 outside the opaque screen image and to zero elsewhere; $\phi_1$ and $\phi_2$ are functions determining the limits of integration in the object region.

From this point the calculation depends substantially on whether or not $V_{ll}$ vanishes. Let $V_{ll} \neq 0$ initially. We write then

$$f(P) = f(P_0) + \tfrac{1}{2}f''(P - P_0)^2 , \tag{53.18}$$

where

$$P_0 = \frac{kt}{f-\Delta}x' + \frac{kt}{f-\Delta}\,\frac{(V_{xx} - V_{yy})\sin\psi\cos\psi}{V_{ll}}\,y' , \tag{53.19}$$

$$\begin{aligned} f(P_0) = {} & -\frac{kV_{ll}}{2}x'^2 - \\ & -\frac{k}{2}\,\frac{(V_{xx} - V_{yy})^2\sin^2\psi\cos^2\psi}{V_{ll}}\,y'^2 - k(V_{xx} - V_{yy})\sin\psi\cos\psi\cdot x'y' , \end{aligned} \tag{53.20}$$

$$f'' = \frac{(f-\Delta)^2}{kt^2}V_{ll} . \tag{53.21}$$

Let

$$l = \frac{V_{ll}x' + (V_{xx} - V_{yy})\sin\psi\cdot\cos\psi\cdot y'}{\left|\sqrt{V_{xx}^2\sin^2\psi + V_{yy}^2\cos^2\psi}\right|} ; \qquad M = \sqrt{\frac{|V_{ll}|}{\lambda}} ;$$

$$K = \frac{\left|\sqrt{V_{xx}^2\sin^2\psi + V_{yy}^2\cos^2\psi}\right|}{V_{ll}} ; \qquad \mu = \frac{2t}{f-\Delta}\sqrt{\frac{1}{\lambda|V_{ll}|}} .$$

Here, $l$ is the distance from the point $x', y'$ to the geometrical axis. The sign of $l$ is determined as follows: replace the filament by a knife edge occupying for $\psi = 0$ the negative part of the $\xi$ axis; $l$ is then positive for points outside the geometrical shadow of the knife and negative for the shadow points.

In terms of the new parameters, expressions (53.19)–(53.21) are transformed to

$$P_0 = \pm\,\pi MK\mu l\,; \quad f(P_0) = \pm\,\pi M^2K^2l^2\,; \quad f'' = \pm\,\frac{2}{\pi\mu^2}. \tag{53.22}$$

The upper signs are taken for positive $V_{ll}$, and the lower signs for negative $V_{ll}$. Using (53.22), we obtain

$$I(l,h) = \left|\,a - \frac{\exp\{\mp\, i\pi M^2K^2l^2\}}{\pi} \times \right.$$
$$\left. \times \int_{-\infty}^{\pi M\mu h/\cos(\phi-\psi)} \exp\left\{\pm\, i\,\frac{(\mp\, P \mp \pi MK\mu l)^2}{\pi\mu^2}\right\} \frac{\sin P}{P}\,dP\,\right|^2, \tag{53.23}$$

where $h$ is the distance from the relevant point of the screen plane to the image of the screen edge. It is taken as positive for points outside the screen image and negative for the points of the image. The integration variable $P$ is positive for $\cos(\phi - \psi) < 0$ and negative for $\cos(\phi - \psi) > 0$.

The illumination distribution in the diffraction pattern is a function of the following three parameters:

$$P_1 = MKl = \frac{\left|\sqrt{V_{xx}^2 \sin^2\psi + V_{yy}^2\cos^2\psi}\,\right|}{\sqrt{\lambda\,|V_{ll}|}}\,l, \tag{53.24}$$

$$Q = \frac{Mh}{|\cos(\phi-\psi)|} = \sqrt{\frac{|V_{ll}|}{\lambda}}\,\frac{h}{|\cos(\phi-\psi)|}, \tag{53.25}$$

$$\mu = \frac{2t}{f-\Delta}\sqrt{\frac{1}{\lambda\,|V_{ll}|}}. \tag{53.26}$$

$P_1$ and $Q$ are the affine coordinates of the image points; $\mu$ is the affine parameter. Diffraction patterns with equal value of $\mu$ can be made congruent by an affine transformation. They are similar if the following four parameters are equal: $\mu$, $\psi$, $V_{yy}/V_{xx}$ and $\phi$. The scale of similar patterns is proportional to $\sqrt{\lambda/|V_{ll}|}$.

If the geometrical axis of the shadow is parallel to the image of the screen edge, the illumination distribution depends on one coordinate only — the distance $r$ between the geometrical axis and the screen edge image, or

$$r = h \pm l\,. \tag{53.27}$$

The positive sign is taken if the screen image and the knife edge shadow point in the same direction, and the negative sign if they point in opposite directions.

The illumination distribution is a function of three parameters, $P_1$, $\mu$, $\nu$. The parameter $\nu$ is defined by the expression

$$\nu = \frac{\left|\sqrt{V_{xx}^2\sin^2\psi + V_{yy}^2\cos^2\psi}\,\right|}{\sqrt{|V_{ll}|\,\lambda}}\,r\,. \tag{53.28}$$

$\mu$, $\nu$ are the similarity parameters of the diffraction patterns, whose width is proportional to

$$\frac{\sqrt{\lambda\,|V_{ll}|}}{\left|\sqrt{V_{xx}^2\sin^2\psi + V_{yy}^2\cos^2\psi}\,\right|}.$$

Consider the diffraction patterns formed when $V_{ll} = 0$. Then

$$f(P) = \mp\,\frac{f-\Delta}{t}\sqrt{|V_{xx}|\,|V_{yy}|}\,lP\,, \tag{53.29}$$

$$I(l,h) = \left|\,a - \frac{1}{\pi}\int_{-\infty}^{[kt/(f-\Delta)]\,[h/|\cos(\phi-\psi)|]} \exp\left\{\pm\, i\,\frac{f-\Delta}{t}\sqrt{|V_{xx}|\,|V_{yy}|}\,lP\right\} \times \right.$$
$$\left. \times\,\frac{\sin P}{P}\,dP\,\right|^2. \tag{53.30}$$

The illumination distribution depends on two parameters:

$$T = \frac{f-\Delta}{t}\sqrt{|V_{xx}|\,|V_{yy}|}\,l, \qquad u = \frac{kt}{f-\Delta}\,\frac{h}{|\cos(\phi-\psi)|}. \tag{53.31}$$

The diffraction patterns were studied on the Soviet-made IAB-451 schlieren instrument. The effective diameter of the objective was 220 mm; the focal length was $f = -1916$ mm. A mercury lamp with a filter isolating the green mercury line served as the light source. The collimator slit width was 0.02–0.03 mm. A cuvette with walls formed by a plane-parallel plate and a plane-convex cylindrical lens with radius of curvature of 2250 mm was placed at a distance of 3 cm from the object plane. A mixture of benzene and ethyl alcohol was poured into the cuvette. By changing the relative concentration of the mixture components, it was possible to change the radius of curvature of the cylindrical wave emerging from the cuvette. The wave formed was vertical.

The wave front curvature in the filament plane changed as a result of defocusing

$$V_{xx} = K_c - \frac{\Delta}{f^2 - \Delta(s-f)}, \qquad V_{yy} = -\,\frac{\Delta}{f^2 - \Delta(s-f)}, \tag{53.32}$$

where $K_c$ is the wave front curvature contributed by the cuvette. An opaque screen with a straight edge was placed in the object plane. Two beads were fastened on the filament at a distance of 100 mm from each other in order to measure the linear magnification.

A photograph of the diffraction pattern photograph is shown in Figure 125. At a distance from the screen image, we observe the usual Fresnel diffraction patterns of the filament. Closer to the screen image, the diffraction bands on one side of the geometrical axis are destroyed; the screen has no influence on the diffraction bands on the other side. The middle part of the shadow, including the central bright band, is destroyed. The general features of the partly destroyed pattern are independent of the value of $\mu$.

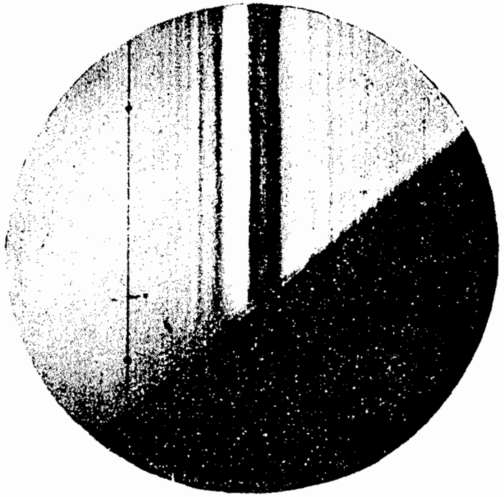

Figure 125

Shadow of a defocused filament near an opaque screen for $V_{xx}/V_{yy} = 1$.

Narrow whisper-like stripes are observed, crossing the Fresnel diffraction bands without affecting their shape.

To determine the position of the "destroyed" and "undestroyed" parts of the diffraction pattern, draw a straight line perpendicular to the filament and passing through the point of intersection of the geometrical axis with the image of the screen edge. The straight lines parallel to this line meet the geometrical axis or its continuation in the region of the screen image. The "destroyed" part is located in the region through which pass the lines intersecting the continuation of the geometrical axis. The "undestroyed" bands are located in the region through which pass the lines intersecting the geometrical axis.

Figure 126 shows patterns with the geometrical axis parallel to the screen image. The distance between the inner edges of the beads is 26 mm. If the screen is located far from the geometrical axis, it covers only individual diffraction bands. So long as the bright diffraction band next to the central band has not been completely covered by the screen image, we can determine the geometrical axis of the diffraction pattern, which virtually coincides with the middle of the central band. If the screen lies nearer, its influence becomes strong and it is impossible to determine the axis position.

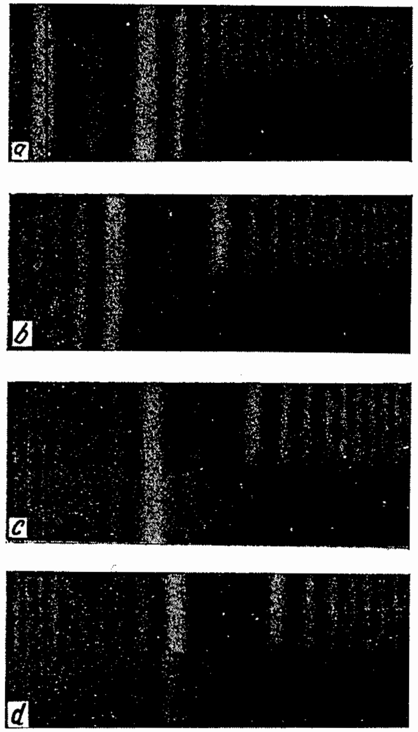

Figure 126

Diffraction patterns from a filament parallel to the edge of an opaque screen.

$V_{xx} = V_{yy} = 1.7 \times 10^{-6}\,\mathrm{mm}^{-1}, \mu = 0.34.$

*a* $v = 2.4$; *b* $v = 0.95$; *c* $v = 0.056$; *d* $v = -0.28$.

Consider what the shadows of the filament will be, if the object plane is transparent everywhere but is divided into two parts $\tau_1$ and $\tau_2$ separated by a straight boundary. The wave in $\tau_1$ is described by the equation $z = Z_1(x, y)$, and the wave in $\tau_2$ by the equation $z = Z_2(x, y)$. Here $Z_1$ and $Z_2$ are quadratic functions. The illumination in $\tau_1$ is thus equal to

$$I(l_1, l_2, \delta) = \left| 1 - \frac{1}{\pi} \int_{-\infty}^{\infty} \exp\left\{ i \left( \frac{P^2}{\pi\mu_1^2} \pm \frac{2}{\mu_1} M_1 K_1 l_1 P \right) \right\} \frac{\sin P}{P}\, dP + \right.$$
$$+ \frac{1}{\pi} \int_{\pi\mu_1 M_1 \delta}^{\infty} \exp\left\{ i \left( \frac{P^2}{\pi\mu_1^2} \pm \frac{2}{\mu_1} M_1 K_1 l_1 P \right) \right\} \frac{\sin P}{P}\, dP -$$
$$- \frac{1}{\pi} \exp\{ i [Z_2(-x', -y') - Z_1(-x', -y')] \} \times$$
$$\left. \times \int_{\pi\mu_2 M_2 \delta}^{\infty} \exp\left\{ i \left( \frac{P^2}{\pi\mu_2^2} \pm \frac{2}{\mu^2} M_2 K_2 l_2 P \right) \right\} \frac{\sin P}{P}\, dP \right|^2 . \tag{53.33}$$

Here $\delta$ is the distance from the relevant screen point to the image of the phase discontinuity along the $x'$ axis; $l_1$ and $l_2$ are the distances to the geometrical axes of the shadows for the waves $Z_1$ and $Z_2$, or for their continuation in the other region. The first two terms determine the Fresnel diffraction pattern, the third term describes the deviations caused by the restriction of the wave surface, and the fourth term represents the contribution of the wave from the bounded region $\tau_2$.

In the experimental study of these patterns, two square wedge-shaped glass plates of K-8 glass with wedge angles of 2′ 11″ and 1′ 04″ measuring 100 mm on a side were placed in the object plane. The plate thickness at the wedge base was 9.573 mm and 9.572 mm. The end faces of the plates were in contact. The photographs obtained for different values of $V_{xx}$ and $\mu$ and for different mutual positions of the plates are shown in Figure 127. In Figure 127*a* one of the plates is covered by the screen; the pattern observed in that case is the pattern near an opaque screen previously considered. If the screen is withdrawn, a new system of narrow curved bands appears — the result of interaction of the waves passing through the left and the right plate.

White light (Figure 128) produces a certain blurring of the diffraction bands.

When the filament is placed perpendicular to the plate edge, the diffraction pattern is not destroyed (Figure 129).

On the basis of this analysis we can suggest some practical recommendations regarding the processing of schlieren photographs obtained by the slit and filament method.

The middle of the central bright band is taken as the geometrical axis whenever the symmetry of the diffraction pattern is retained. At the edge of opaque objects, where the symmetry is broken, we must draw the geometrical axis along one of the undestroyed bands, preferably the one nearest the central band.

Consider as an example the photograph in Figure 130, taken with an inclined defocused filament to study the boundary layer on a plane plate. The viewing diaphragm was a wire grid, with a wire diameter of 0.25 mm. The distance between

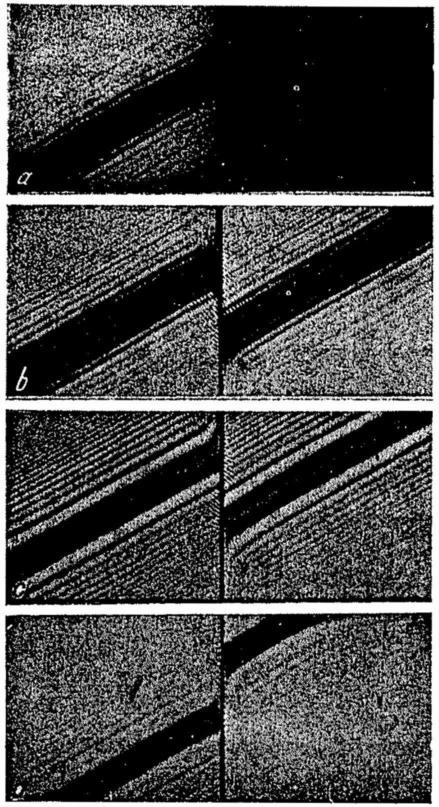

Figure 127

The shadow of a defocused filament near a discontinuity of the wave front obtained using a narrow light source. $V_{xx} = V_{yy} = 6.8 \times 10^{-6}\ \text{mm}^{-1}$; $\mu = 1.4$ (*a* and *b*); $\mu = 0.4$ (*c*) and $\mu = 0.7$ (*d*).

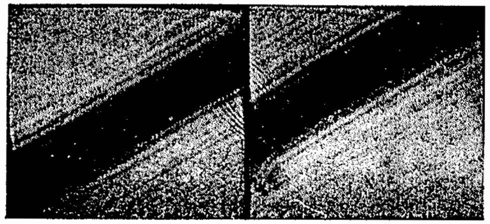

Figure 128

The shadow of a defocused filament near a discontinuity in the wave front obtained using a white light source.

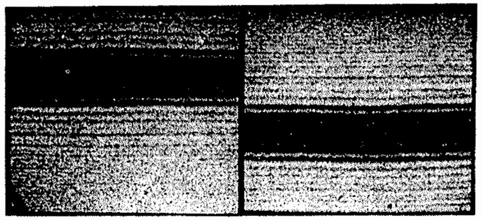

Figure 129
Diffraction patterns from a filament perpendicular to the plate edge.

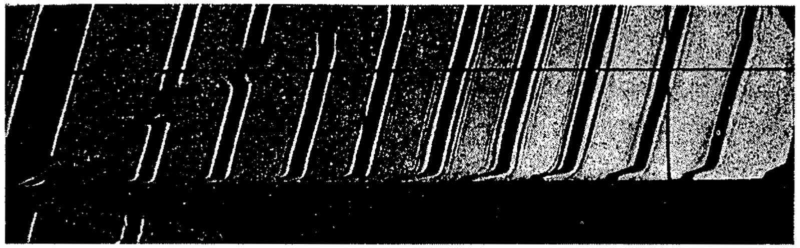

Figure 130
The boundary layer on a plate (defocused filament method).

adjacent wires was 4 mm; the grid defocusing was 450 mm. For these parameters, there was virtually no interaction between the diffraction phenomena of adjacent wires. As a result, the photograph shows the diffraction pattern of the individual filaments.

The undestroyed part of the shadow is on the right, where the shape of the bands is determined only by the light wave deformation. On the left, the diffraction from the plate causes an additional bending of the bands, and as a result of which the bands bend to follow the plate edge image.

This analysis of the diffraction pattern is very important, since it eliminates the suspicion that the light diffraction from the plate will cause bending of all diffraction bands, and, consequently, makes possible the quantitative processing of the results.

## 54. DEFOCUSED GRID

If the object field boundaries are ignored, the diffraction pattern illumination for the case of a defocused grid is calculated as for a filament, since the grid is nothing more than a set of parallel lines or grooves.

The expression for the illumination in the image plane is [26]

$$I(x) = \frac{1}{2}\Bigg\{\Bigg\{\sum_{N=-\infty}^{\infty} S[\Pi(x + 2\mu N - 1)] - \\ - \sum_{N=-\infty}^{\infty} S[\Pi(x + 2(N-1)\mu + 1)]\Bigg\}^2 + \Bigg\{\sum_{N=-\infty}^{\infty} C[\Pi(x + 2\mu N - 1)] - \\ - \sum_{N=-\infty}^{\infty} C[\Pi(x + 2(N-1)\mu + 1)]\Bigg\}^2\Bigg\}. \qquad (54.1)$$

Unlike (53.11), the illumination distribution depends on two parameters. One of them, Π, is the previous parameter, which determines the light intensity distribution in the diffraction pattern of the filament. The other, $\mu$, is new. It represents the ratio of the grid spacing to the opaque gap width.

On the basis of the preceding analysis of the diffraction patterns of an opaque line, we can draw some conclusions regarding the dependence of the light intensity distribution in the diffraction pattern of the grid on the value of Π.

For a large Π, the illumination distribution is close to the geometrical pattern. A certain difference is observed only at the ends of the lines. The diffraction region is broadened with the decrease in Π. For a small Π, the pattern differs sharply from the geometrical pattern. The diffraction shadows from adjacent lines superimpose, and a complex interaction pattern is observed on the screen. The lower the value of the parameter Π, the greater is the reduction in contrast between the line shadows in the schlieren image.

To conduct a more detailed analysis of the diffraction patterns from a defocused grid, we have to calculate the illumination distribution in the image plane using (48.1). The values of $S(x)$ and $C(x)$ can be calculated by expanding the Fresnel integrals in power and asymptotic series. For values of the arguments greater than 2, it is convenient to use the truncated asymptotic series:

$$S(x) \approx \pm\frac{1}{2} - \cos\frac{\pi}{2}x^2 \sum_{k=0}^{3} (-1)^k \frac{(4k)!\,x^{-(4k+1)}}{2^{2k}\pi^{2k+1}(2k)!} - \\ - \sin\frac{\pi}{2}x^2 \sum_{k=0}^{3} (-1)^k \frac{(4k+2)!\,x^{-(4k+3)}}{2^{2k+1}\pi^{2k+2}(2k+1)!}; \qquad (54.2)$$

$$C(x) \approx \pm\frac{1}{2} + \sin\frac{\pi}{2}x^2 \sum_{k=0}^{3} (-1)^k \frac{(4k)!\,x^{-(4k+1)}}{2^{2k}\pi^{2k+1}(2k)!} - \\ - \cos\frac{\pi}{2}x^2 \sum_{k=0}^{3} (-1)^k \frac{(4k+2)!\,x^{-(4k+3)}}{2^{2k+1}\pi^{2k+2}(2k+1)!}. \qquad (54.3)$$

Power series are frequently used for values of the arguments smaller than 2, or

$$S(x) = \sum_{k=0}^{9} \frac{(-1)^k (\pi/2)^{2k+1}}{(2k+1)!(4k+3)} x^{4k+3}, \qquad (54.4)$$

$$C(x) = \sum_{k=0}^{10} \frac{(-1)^k (\pi/2)^{2k}}{(2k)!(4k+1)} x^{4k+1}. \qquad (54.5)$$

This representation of the functions ensures the calculation of each of the Fresnel integrals with an accuracy not lower than 0.001.

Typical illumination distributions for the center of a grid with 20 opaque lines are shown in Figures 131–136 [26]. The analysis of the curves corroborates our description of the influence of the parameter Π. Furthermore, they make it possible to detect finer relations.

For $\mu = 2$ the diffraction pattern coincides almost completely with the Fresnel diffraction pattern at the edge of an opaque screen for Π greater than 10. "Ledges" associated with the influence of adjacent lines appear for $\Pi < 10$. The pattern progressively deviates from the geometrical distribution. For $\Pi \sim 1$, the first diffraction maximum is located at the pattern center. With the further decrease in Π, the illumination at the center of the space between the lines gradually decreases. Simultaneously, the light intensity at the center of the dark space increases. For $\Pi \sim 0.5$, these intensities are comparable; the dark lines virtually do not differ from the bright spaces, and a uniformly gray background is observed.

When Π decreases still further, the light maximum moves to the center of the dark line. A "reversal" of the bands occurs. The maximum intensity is attained for about $\Pi = 0.2$. Then a very sharp reverse process commences: an increase of the light intensity at the center of the transparent space and its decrease at the center of the dark line. The intensity distribution again reverts to normal for $\Pi \approx 0.18$. Several more reversals take place with the further decrease of Π, with the maximum intensity attained alternately at the line center and at the middle between the lines. The maxima become progressively smaller, and the image contrast continues to decrease. Finally, for $\Pi \sim 0.02$, the contrast is almost lost entirely. For $\Pi\mu > 0.5$, the illumination at the center of an extended grid shadow differs from the illumination in the case of an infinite grid by no more than 0.1, and for $\Pi\mu > 0.15$, by 0.3.

For $\mu = 2.0$ and $\lambda = 5 \times 10^{-4}$, we write (53.12) in the form

$$\Pi = \frac{p}{\sqrt{2\lambda\Delta}} = \frac{31.8\,p}{\sqrt{\Delta}}. \qquad (54.6)$$

The values of Π for grids with $\mu = 2$, different grid spacings $p$, and different defocusings Δ are given in Table 7 (see p. 277).

The diffraction patterns change similarly for other values of the parameter $\mu$.

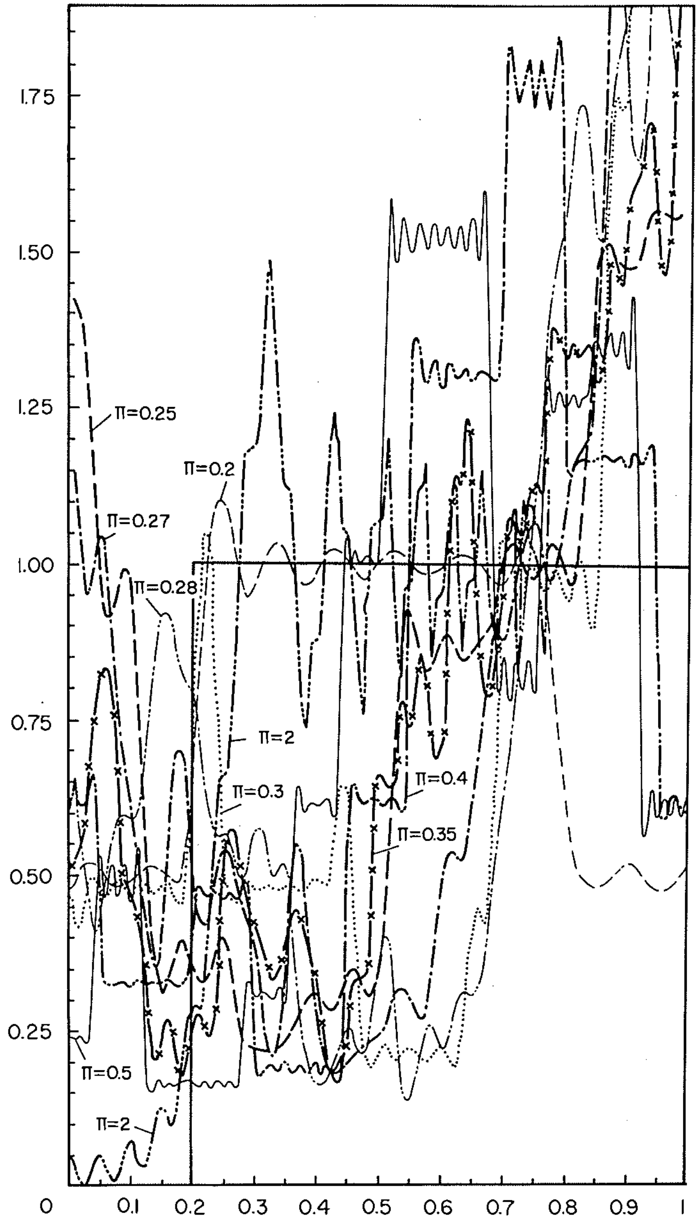

Figure 131

Illumination distribution in the image for a defocused grid with $\mu = 5$.

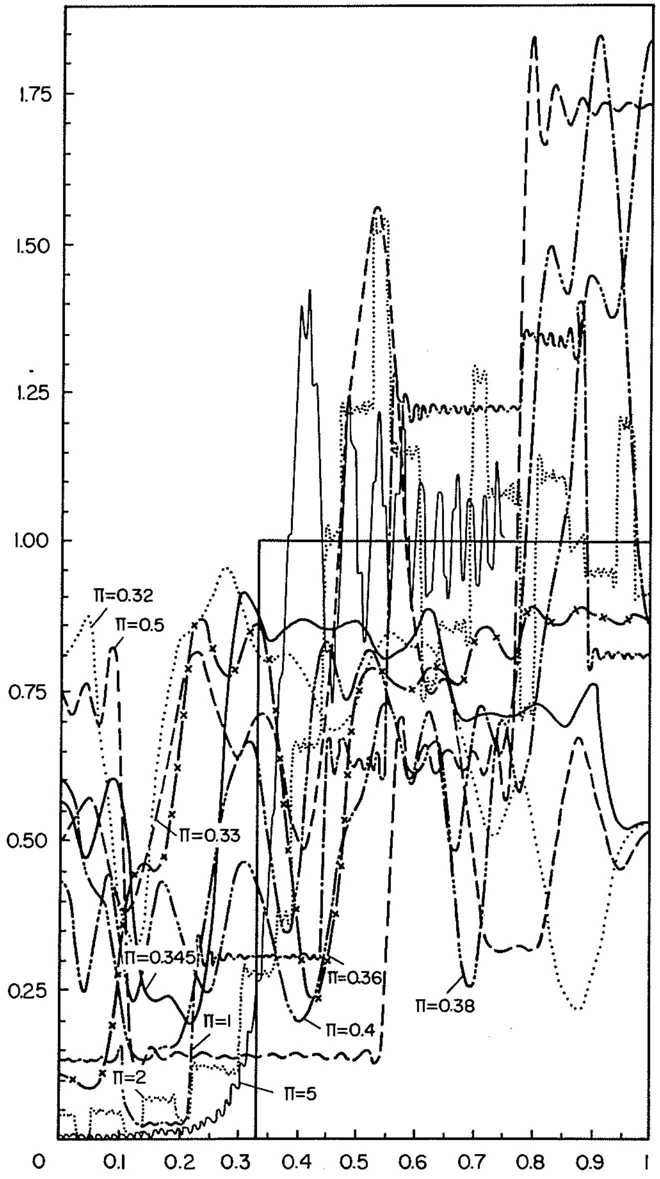

Figure 132
Illumination distribution in the image for a defocused grid with $\mu = 3$, for $\Pi$ between 5 and 0.32.

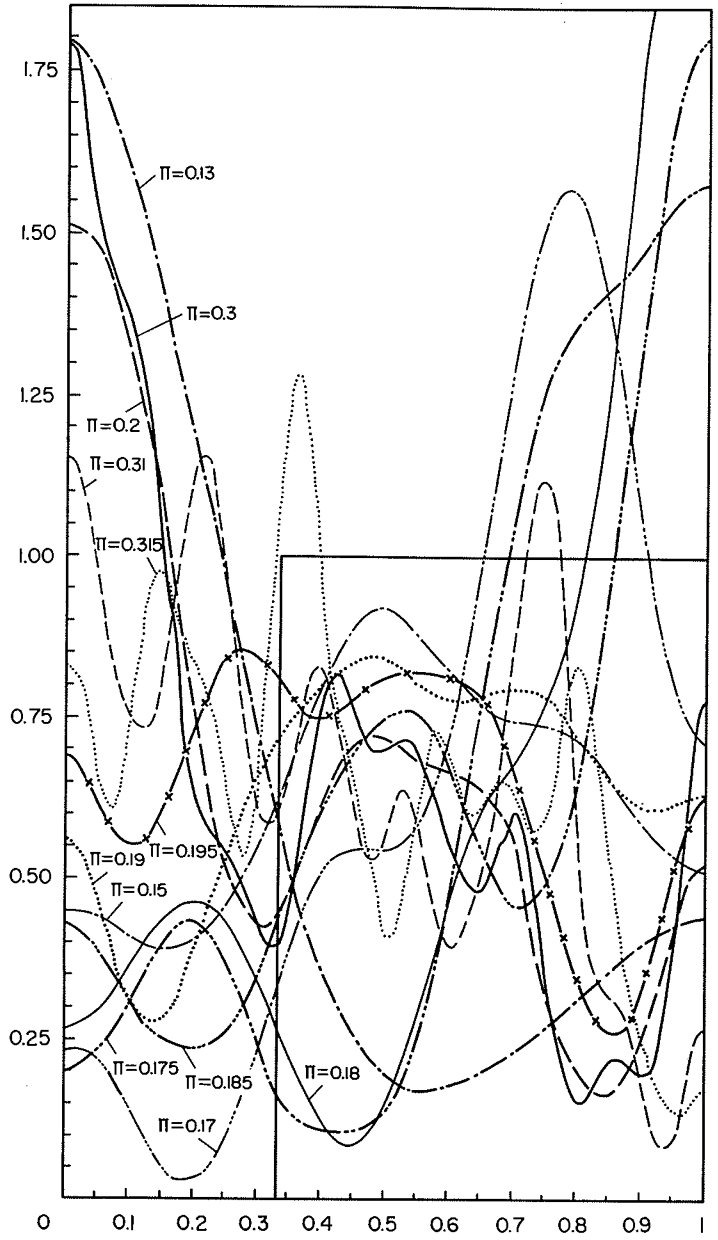

Figure 133
Illumination distribution in the image for a defocused grid with $\mu = 3$, for $\Pi$ between 0.315 and 0.13.

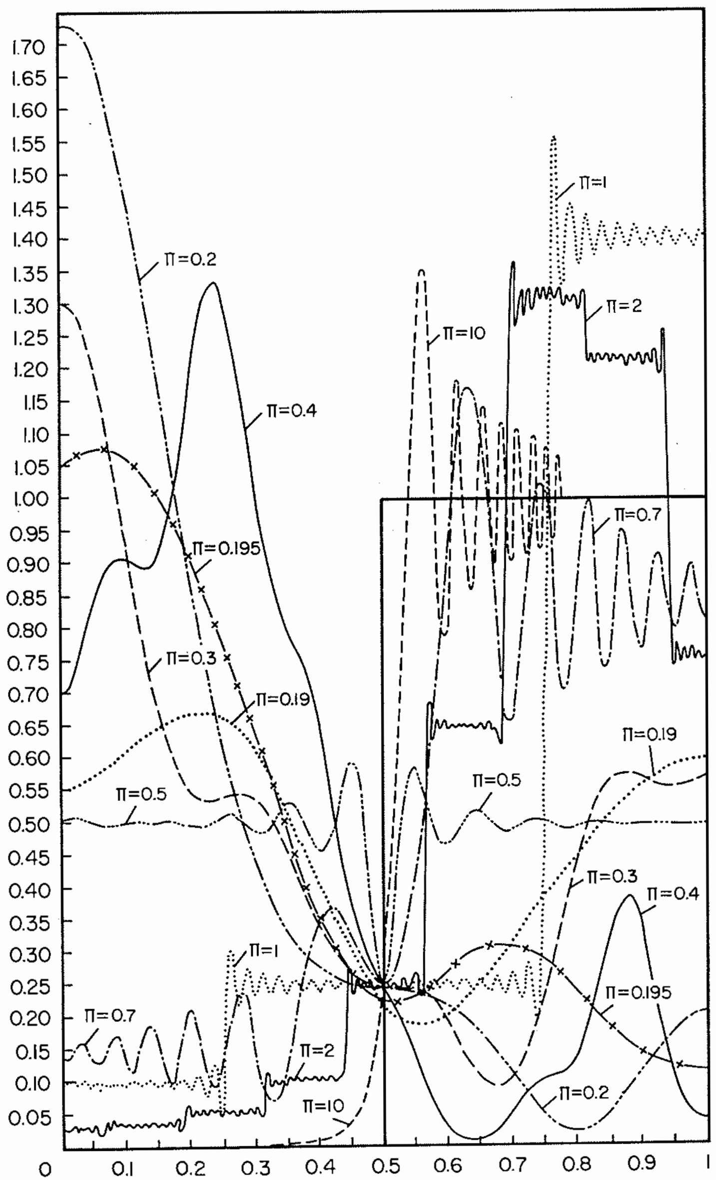

Figure 134

Illumination distribution in the image for a defocused grid with $\mu = 2$, for $\Pi$ between 10 and 0.19.

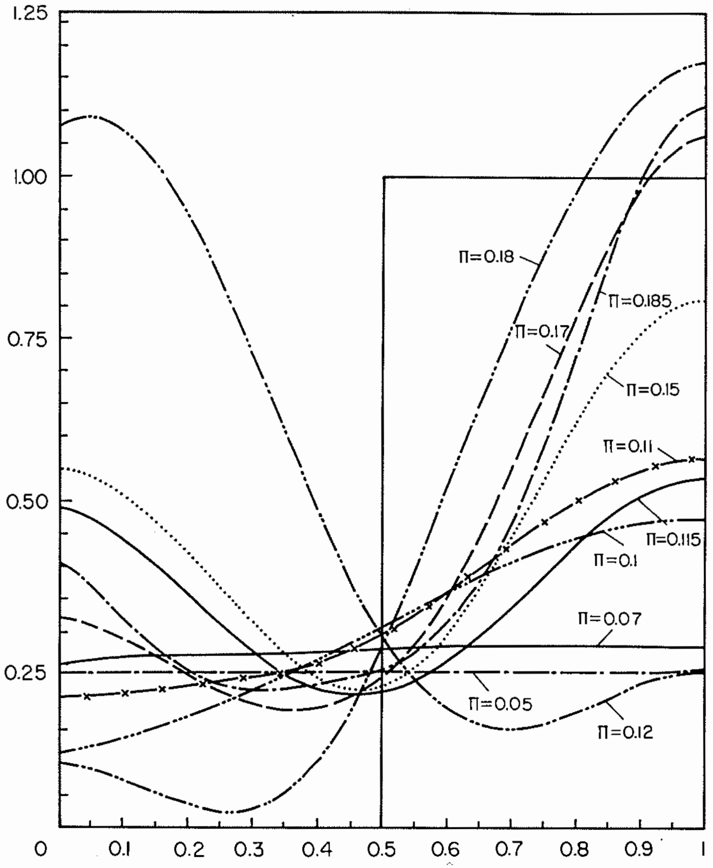

Figure 135

Illumination distribution in the image for a defocused grid with $\mu = 2$, for $\Pi$ between 0.185 and 0.05.

For $\mu > 2$, the same phenomena take place for smaller values of $\Pi$. Thus for $\mu = 3$, the first maximum is at the center for $\Pi = 0.5$; the first reversal takes place for $\Pi = 0.3$. For $\mu = 5$ the values of $\Pi$ corresponding to the central position of the maximum and the reversal are 0.3 and 0.1, respectively. In this case the contrast is not completely destroyed, and the maxima located between the line center and the center of the transparent space play a more important role.

For $\mu < 2$, the Fresnel pattern deteriorates much earlier. For $\mu = 1.5$, deviations are noticeable already for $\Pi = 10$, and for $\mu = 1.3$ — for $\Pi = 30$. A destruction of the contrast is not observed either. The reversals are much less distinct, the pattern becomes low-contrast for small $\Pi$ and is complicated by additional maxima.

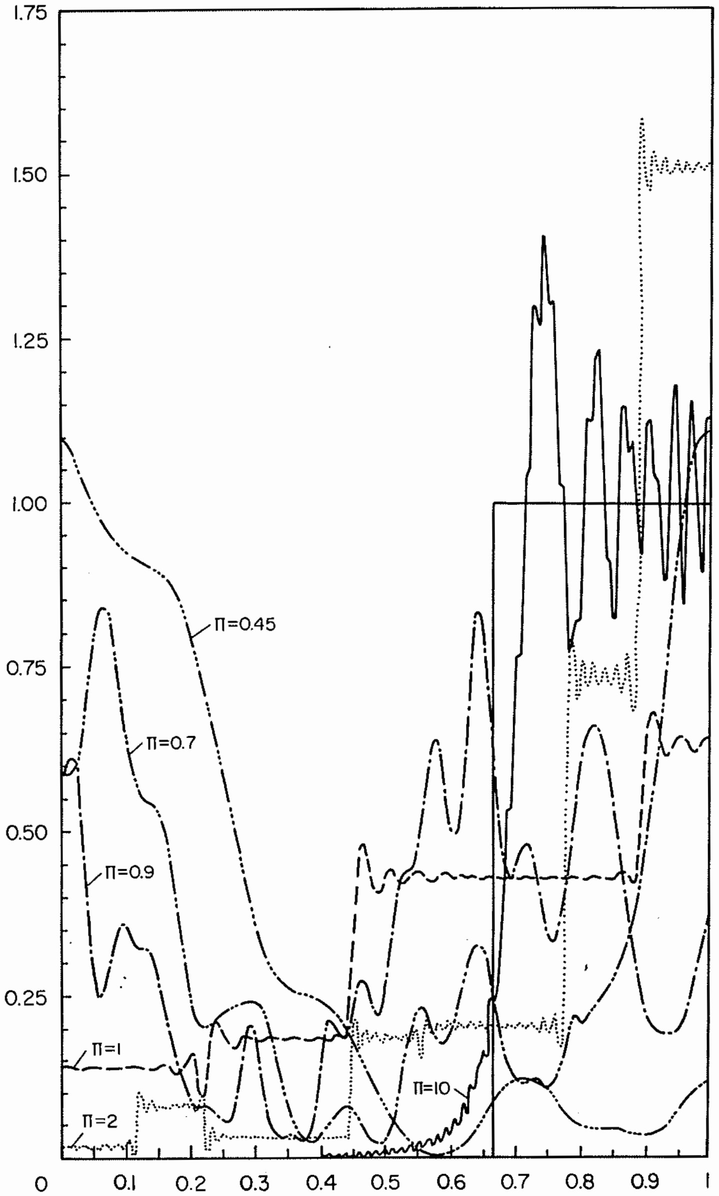

Figure 136

Illumination distribution in the image for a defocused grid with $\mu = 1.5$.

Table 7

VALUES OF THE PARAMETER Π FOR GRIDS WITH $\mu = 2$

| $p$, mm | Δ, mm | | | | | | | | | | | |
|---|---|---|---|---|---|---|---|---|---|---|---|---|
| | 0.1 | 0.2 | 0.5 | 1 | 2 | 5 | 10 | 20 | 50 | 100 | 200 | 500 |
| 0.1 | 10 | 7.1 | 4.5 | 3.2 | 2.9 | 1.42 | 1 | 0.7 | 0.45 | 0.32 | 0.22 | 0.14 |
| 0.2 | 20 | 14.1 | 9 | 6.4 | 4.5 | 2.85 | 2 | 1.4 | 0.9 | 0.64 | 0.45 | 0.28 |
| 0.5 | 50 | 35.3 | 22.5 | 15.9 | 11.2 | 7.12 | 5 | 3.5 | 2.2 | 1.6 | 1.12 | 0.71 |
| 1.0 | 100 | 71 | 45 | 32 | 22.5 | 14.2 | 10 | 7.1 | 4.5 | 3.2 | 2.25 | 1.42 |
| 2.0 | 200 | 141 | 90 | 64 | 45 | 28.5 | 20 | 14 | 9 | 6.4 | 4.5 | 2.85 |
| 5.0 | 500 | 353 | 225 | 159 | 112 | 71 | 50 | 35 | 22.5 | 15.9 | 11.2 | 7.12 |

The patterns with $\mu = 2$ differ from the others in that the illumination at the points corresponding to the line edge image (apart from grid boundary effects) is one quarter of the illumination in the gap between the lines in the geometrical distribution. The patterns with $\mu = 2$ are similar in this respect to the illumination patterns from an opaque screen.

The study and analysis of the patterns obtained bears out Sukhorukikh's conclusion [26] that the grid with $\mu = 2$ is the most effective. The identification of the shadows and the pinpointing of the line image centers are simplest with such grids.

We shall now consider the possibility of a quantitative analysis of the photographs taken with a defocused grid which gives pattern "reversal" over the entire field or some portions thereof.

If the wave curvature changes negligibly between the zero and the working photographs, and the light deviation angle in the inhomogeneity can be taken as constant over a sufficiently large section, a quantitative analysis is possible using any of the diffraction maxima of any diffraction pattern. This is true provided the parameter Π does not change so much that one reversal is replaced by another or the light maximum is substantially shifted relative to the line center. It follows from the analysis of Figure 133 that a change of Π from 0.2 to 0.18 is sufficient to bring about the next reversal; this change is related to the change of the wave front curvature by the equality

$$\frac{A_{II} - A'_{II}}{A_{II}} = 2\,\frac{\Pi - \Pi'}{\Pi}. \tag{54.7}$$

A 20 per cent change in $A_{II}$ for $\Pi \sim 0.2$ suffices for the pattern to revert from reversed to normal.

Reversed patterns for $\mu > 2$ are particularly difficult to account for, since in this case particular importance is attached to the light maxima whose position depends on the value of Π.

For these reasons, reversed patterns are used relatively seldom for quantitative measurements, and even then without a detailed analysis of the phenomena.

The relation between the parameters $\Pi$ and $\mu$ corresponding to the first reversal was derived in [51] by studying a long series of photographs, each taken for a different value of $\mu$. The value of $\Pi$ for which the first reversal of the diffraction pattern took place ($\Pi_0$) was determined. The results are given in Table 8.

Table 8

| $\mu$ | $\Pi_0$ | $\mu\Pi_0$ | $\mu$ | $\Pi_0$ | $\mu\Pi_0$ |
|---|---|---|---|---|---|
| 2 | 0.90 | 1.8 | 5 | 0.35 | 1.8 |
| 3 | 0.60 | 1.8 | 6 | 0.30 | 1.8 |
| 4 | 0.40 | 1.6 | 7 | 0.30 | 2.1 |

The product $\mu\Pi_0$ is virtually constant. The existing deviations are possibly caused by the inevitable subjectivity in the determination of $\mu_0$ from the photographs. Furthermore, a large part is played by photographic factors — the $\gamma$ and the latitude of exposure of the negative film and the photographic paper. However, the resulting error in the determination of $\Pi_0$ and $\mu\Pi_0$ is small and without practical importance.

Let us consider the possibility of using direct-type diffraction patterns with $\mu > \mu_0$ (before the first reversal) [51]. We began by determining the maximum density of shadow lines on the photograph (the number of lines in which the light deviation angles are measured).

The distance between adjacent shadow lines in the direction perpendicular to the grid lines is equal to

$$\delta = \Pi\mu\sqrt{\frac{\lambda}{V_{II}}}. \tag{54.8}$$

The minimum value of $\delta$ is attained for $\mu = \mu_0$. Since the product $\Pi\mu$ is virtually constant, the maximum number of lines is the same for grids with any $\mu$.

The number of shadow lines per unit length is

$$N = \frac{f\,|V_{II}|}{p}. \tag{54.9}$$

The value of $\Pi\mu$ must satisfy the condition $\Pi\mu > 1.8$, and therefore

$$p > 1.8f\sqrt{\lambda\,|V_{II}|}\cdot \tag{54.10}$$

For a plane wave (zero photograph)

$$p > 1.8\sqrt{\lambda\,|\Delta|}. \tag{54.11}$$

For the geometrical axes of the shadow lines on the zero and the working photographs to correspond, (54.10) and (54.11) must be satisfied simultaneously. This is ensured if (54.10) is satisfied and the sign of defocusing is so chosen that the geometrical axes draw closer together when the inhomogeneity is introduced.

The maximum number of shadows is equal to

$$N_{p\,\max} = \frac{\sqrt{|V_{II}|}}{1.8\sqrt{\lambda}}, \tag{54.12}$$

and on the zero photograph

$$N = \frac{\sqrt{|\Delta|}}{1.8f\sqrt{\lambda}}. \tag{54.13}$$

The error $\Delta\varepsilon$ in the determination of the angle of light deviation depends on the error $\Delta\delta$ in the coordinate of the geometrical axis. We can assume that on the zero photograph the coordinates are measured exactly. On the photograph with the inhomogeneity,

$$(\Delta\varepsilon) = V_{II}(\Delta\delta). \tag{54.14}$$

Using (54.14), we obtain

$$N_{p\,\max} = \frac{1}{1.8}\sqrt{\left|\frac{\Delta\varepsilon}{\lambda\Delta\delta}\right|}. \tag{54.15}$$

The minimum grid spacing which ensures the maximum number of experimental points is

$$p_{\min} = 1.8f\sqrt{\left|\frac{\lambda\Delta\varepsilon}{\Delta\delta}\right|}. \tag{54.16}$$

The actual wave fronts are considerably more complex than those assumed in our calculations. However, at every point of the field the wave front can be approximated by a quadratic surface, since the illumination of a given point in the image plane is determined by the parameters of a small portion of the wave front around the conjugate point in the object plane.

At the points of the inhomogeneity with maximum wave front curvature ($P_{II\,\max}$) we have, for a grid in the focal plane of the instrument and a proper choice of the line width,

$$\delta_{F\,\min} = \Pi_0\mu\sqrt{\frac{\lambda}{|P_{II\,\max}|}}. \tag{54.17}$$

Elsewhere in the inhomogeneity image, we similarly have direct-type diffraction patterns with the line spacing

$$\delta_F = \Pi_0\mu\frac{\sqrt{\lambda P_{II\,\max}}}{P_{II}}. \tag{54.18}$$

We can decrease $\delta$ by defocusing the grid and thus increasing the absolute value of the curvature. If $P_{ll} > 0$, the defocusing must be positive. After the defocusing

$$\delta_\Delta = \Pi_0 \mu \frac{\sqrt{\lambda\left(P_{ll\,\max} + \dfrac{\Delta}{f(f-\Delta)}\right)}}{P_{ll} + \dfrac{\Delta}{f(f-\Delta)}} . \tag{54.19}$$

Setting

$$\alpha = \frac{P_{ll}}{P_{ll\,\max}}, \quad \beta = \frac{\Delta}{f(f-\Delta)P_{ll\,\max}}, \tag{54.20}$$

we find the ratio

$$\frac{\delta_\Delta}{\delta_F} = \frac{\alpha\sqrt{1+\beta}}{\alpha+\beta}, \tag{54.21}$$

which shows how much $\delta$ is reduced by defocusing.

The increase in the number of measurement points is the more considerable, the larger the difference between the curvature $P_{xx}$ and the maximum curvature.

However, grid defocusing leads to an increase in the random measurement error

$$\Delta\varepsilon = \left(P_{xx} + \frac{\Delta}{f(f-\Delta)}\right)\Delta x . \tag{54.22}$$

The increase in the defocused grid error compared to that of the focal grid is given by

$$\frac{\delta\varepsilon_\Delta}{\delta\varepsilon_F} = \frac{\alpha+\beta}{\alpha} . \tag{54.23}$$

It is desirable that each of the ratios $\delta_\Delta/\delta_F$ and $\delta\varepsilon_\Delta/\delta\varepsilon_F$ be small. Their product is equal to

$$\frac{\delta_\Delta}{\delta_F}\frac{\delta\varepsilon_\Delta}{\delta\varepsilon_F} = \sqrt{1+\beta} . \tag{54.24}$$

It increases with the increase of $\Delta$, so the measurement error increases more rapidly than the number of experimental points. In order to reduce the measurement error, it is advisable to work with a small $\Delta$.

## 55. THE PHOTOMETRIC KNIFE-EDGE AND SLIT METHOD

The photometric knife-edge and slit method uses a Foucault knife-edge as a focal plane diaphragm instead of a filament or a grid. We shall calculate the corresponding illumination and determine the error resulting from the neglect of diffraction phenomena [25].

If we ignore the effect of the far edge of the knife (the one far from the slit image) and the diffraction from the object plane edges, the illumination distribution from a point source will be

$$I(x', y') = C^2\{[C(\xi_{12}) - \tfrac{1}{2}]^2 + [S(\xi_{12}) - \tfrac{1}{2}]^2\} . \tag{55.1}$$

A distinctive feature of the photometric knife-edge and slit method as compared with the filament and defocused-grid methods is the use of extended light sources. Therefore, an additional integration over the incoherent points of the extended source is required.

Let the illuminating slit image be perpendicular to the knife. Then the different points of the source will have different values of the parameter $l$. If the values $l = l_1$ and $l = l_2$ correspond to the source end points, the total light intensity is given by the expression

$$J(x', y') = \int_{l=l_1}^{l_2} I(x', y')\,dl . \tag{55.2}$$

Using the substitution of variables $l' = \xi_{12}$, we obtain

$$J(x', y') = C^2 f \sqrt{\frac{\pi(A_{xx}\cos^2\phi + A_{yy}\sin^2\phi)}{k}} \times$$

$$\times \int_{l_1'}^{l_2'} \{[C(l') - \tfrac{1}{2}]^2 + [S(l') - \tfrac{1}{2}]^2\}\,dl' . \tag{55.3}$$

Noting that

$$A_{ll} = A_{xx}\cos^2\phi + A_{yy}\sin^2\phi \tag{55.4}$$

is the curvature of the wave front in the plane perpendicular to the knife-edge, and

$$\sin\phi(\alpha_y + \mu y' A_{yy}) + \cos\phi(\alpha_x + \mu x' A_{xx}) = \varepsilon_l \tag{55.5}$$

is the angle of light deviation in the direction perpendicular to the knife-edge plane at the point of the wave front conjugate with $(x', y')$, we write

$$l_1' = \sqrt{\frac{k}{\pi A_{ll}}}\left(\frac{l_1}{f} + \varepsilon_l\right), \quad l_2' = \sqrt{\frac{k}{\pi A_{ll}}}\left(\frac{l_2}{f} + \varepsilon_l\right) \tag{55.6}$$

We obtain by integrating

$$J(x', y') = C^2 \left\{\tfrac{1}{2}l' - l'S(l') - \frac{\cos\frac{1}{2}\pi l'^2}{\pi} - l'C(l') + \frac{\sin\frac{1}{2}\pi l'^2}{\pi} + \right.$$

$$\left. + l'S^2(l') + l'C^2(l') + \frac{2}{\pi}\cos\tfrac{1}{2}\pi\, l'^2 S(l') - \frac{2}{\pi}\sin\tfrac{1}{2}\pi\, l'^2 C(l') \Big|_{l_2'}^{l_1'} \right\}. \qquad (55.7)$$

Rotating the image plane axes through the angle $\delta$, defined by the expression

$$\tan\delta = -\tan\phi \frac{A_{yy}}{A_{xx}}, \qquad (55.8)$$

we reduce the expression for the light intensity distribution in the image plane to the form

$$J(\bar{y}) = C^2 \{-\tfrac{1}{2}m - m\bar{y}[S(m\bar{y}) + C(m\bar{y}) - S^2(m\bar{y}) - C^2(m\bar{y})] +$$

$$+ m(\bar{y}+1)[S(m(\bar{y}+1)) + C(m(\bar{y}+1)) - S^2(m(\bar{y}+1)) -$$

$$- C^2(m(\bar{y}+1))] + \frac{\cos\frac{1}{2}\pi\, m^2(\bar{y}+1)^2}{\pi} - \frac{\cos\frac{1}{2}\pi\, m^2y^2}{\pi} +$$

$$+ \frac{2}{\pi}\cos\tfrac{1}{2}\pi\, m^2\bar{y}^2 S(m\bar{y}) - \frac{2}{\pi}\cos\tfrac{1}{2}\pi\, m^2(\bar{y}+1)^2\, S(m(\bar{y}+1)) -$$

$$- \frac{2}{\pi}\sin\tfrac{1}{2}\pi\, m^2\bar{y}^2 C(m\bar{y}) + \frac{2}{\pi}\sin\tfrac{1}{2}\pi\, m^2(\bar{y}+1)^2\, C(m(\bar{y}+1)) +$$

$$+ \frac{\sin\frac{1}{2}\pi\, m^2\bar{y}^2}{\pi} - \frac{\sin\frac{1}{2}\pi\, m^2(\bar{y}+1)^2}{\pi}\Bigg\}, \qquad (55.9)$$

where $\bar{y}$ is the reduced coordinate, and

$$m = \frac{l_2 - l_1}{f}\sqrt{\frac{k}{\pi A_{ll}}}. \qquad (55.10)$$

Thus the diffraction pattern in this case depends only on the parameter $m$, which depends in its turn on the angular width of the slit, the wave front curvature in the direction perpendicular to the knife-edge, and the wave length.

The theoretical illumination distribution curves for $m = 1$, 4, and 10 are shown in Figure 137. We note that the larger the value of the parameter $m$, the closer is the distribution to the geometrical. The experimental points completely fit the theoretical values.

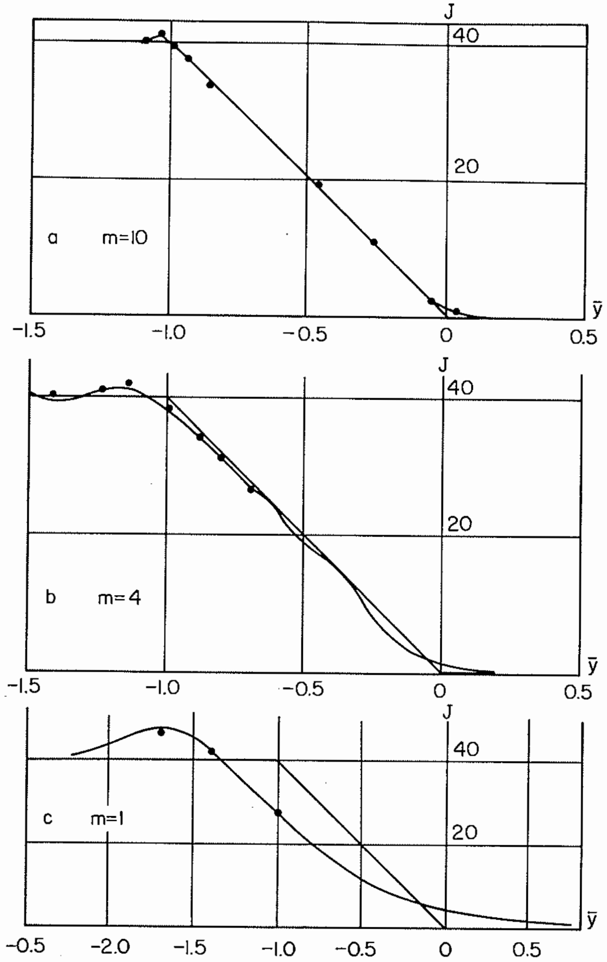

Figure 137

Illumination distribution in the image with the photometric knife-edge and slit method.

To determine the photometric method error, we ignore the points $\bar{y} = 0$ and $\bar{y} + 1 = 0$, and assume that $m\bar{y}$ and $m(\bar{y} + 1)$ are so large that terms of order of $1/(m\bar{y})^2$ and $1/[m(\bar{y} + 1)]^2$ can be dropped. Using the asymptotic expansions of the Fresnel integrals, we reduce (55.9) to the form

$$J(\bar{y}) = C^2\left\{2m\bar{y} + \frac{1}{\pi^2 m\bar{y}(\bar{y}+1)}\right\}. \qquad (55.11)$$

In geometrical optics,

$$J(\bar{y}) = C^2 \cdot 2m\bar{y}\,. \qquad (55.12)$$

Transforming (55.12), we obtain

$$J = C^2\left(\frac{l_1}{f} + \varepsilon_l\right). \qquad (55.13)$$

According to this geometrical optics formula, the image illumination at any point depends only on the uncovered width of the slit and the angle of inclination of the wave front at the conjugate point. This enables us to compare different inhomogeneities, stating that if the image illumination at two points is the same, the respective deviation angles are similarly equal.

Equation (55.13) also suggests a method for photometric determination of the deviation angle. Indeed, if

$$J_0 = C^2\,\frac{l_1}{f} \qquad (55.14)$$

corresponds to the absence of an inhomogeneity, and relation (55.13) applies when the inhomogeneity is introduced, we have

$$\varepsilon_l = \frac{l_1}{f}\left(10^{(D-D_0)/\gamma} - 1\right) \qquad (55.15)$$

for the working relation of the photometric knife-edge and slit method.

Actually, however, relation (55.13) is not correct because of the diffraction phenomena. The maximum deviation from this relation is given by (55.11). By comparing these magnitudes, we can determine the error of the photometric knife-edge and slit method. To calculate this error, we transform (55.11) as follows:

$$J = 2C^2\left(\frac{l_1}{f} + \varepsilon_l + \frac{A_{ll}}{2\pi k\left(\frac{l_1}{f} + \varepsilon_l\right)}\right) \qquad (55.16)$$

If we compare the distorted and the standard wave, with their different curvatures, we have at the points of equal light intensities

$$\frac{l_1}{f} + \varepsilon_l + \frac{A_{ll}(l_2 - l_1)}{2\pi k f\left(\frac{l_1}{f} + \varepsilon_l\right)\left(\frac{l_2}{f} + \varepsilon_l\right)} = \frac{l_1}{f} + \varepsilon_l' + \frac{A_{ll}'(l_2 - l_1)}{2\pi k f\left(\frac{l_1}{f} + \varepsilon_l'\right)\left(\frac{l_2}{f} + \varepsilon_l'\right)}. \qquad (55.17)$$

Denoting

$$\varepsilon_l' = \varepsilon_l + \Delta\varepsilon \qquad (55.18)$$

and seeing that

$$\Delta\varepsilon \ll \frac{l_1}{f} + \varepsilon_l \quad \text{and} \quad \Delta\varepsilon \ll \frac{l_2}{f} + \varepsilon_l\,, \qquad (55.19)$$

we obtain

$$\Delta\varepsilon = \frac{(A_{ll} - A_{ll}')(l_2 - l_1)}{2\pi k f\left(\frac{l_1}{f} + \varepsilon_l\right)\left(\frac{l_2}{f} + \varepsilon_l\right)}. \qquad (55.20)$$

Expression (55.20) gives the error of the standard photometric method, if we can ignore the diffraction at the edges of the inhomogeneities. The error is determined by the curvature difference between the standard and the actual inhomogeneities, the width of the uncovered and the covered part of the slit for the points, under comparison, and the ratio $\lambda/f$. If $l_1 = -1$ mm, $l_2 = 1$ mm, $A_{ll} = 10^{-4}\,\text{mm}^{-1}$, $\lambda = 5 \times 10^{-4}$ mm, $\varepsilon_l = 0$, $A_{ll}' = 0$, then $\Delta\varepsilon = 5 \times 10^{-6}$.

If the measurements are conducted by the semicompensated method, in which the inhomogeneity is examined through a standard lens, then $A_{ll} - A_{ll}'$ is equal to the wave curvature produced by the inhomogeneity.

The error obtained when a wedge is used as the inhomogeneity is the same.

We shall now determine the error of the absolute photometric knife-edge and slit method. Its geometrical formula

$$\varepsilon_l = \left(\frac{J}{J_0} - 1\right)\frac{l_1}{f}, \qquad (55.21)$$

while the formula allowing for the maximum diffraction effect is

$$\frac{J}{J_0} = 1 + \frac{\varepsilon_l f}{l_1} + \frac{A_{ll}(l_2 - l_1)}{2\pi k l_1\left(\frac{l_1}{f} + \varepsilon_l\right)\left(\frac{l_2}{f} + \varepsilon_l\right)}. \qquad (55.22)$$

The comparison of (55.21) and (55.22) yields

$$\Delta\varepsilon = \frac{A_{ll}(l_2 - l_1)}{2\pi k f\left(\frac{l_1}{f} + \varepsilon_l\right)\left(\frac{l_2}{f} + \varepsilon_l\right)}. \qquad (55.23)$$

The error of this method proved to be equal to the error of the semicompensated method or the method using a wedge. This is natural, since in all the three cases the distorted wave is compared with a plane wave. The specific features of the mathematics do not change the value of the error.

We can reduce the error by using standard lenses such that the curvature of the wave emerging from the standard lens is almost equal to the curvature of the wave after its passage through the inhomogeneity. Generally, however, it is difficult to choose a suitable lens without preliminary experiments. Furthermore, the complex inhomogeneities usually encountered in practice have variable curvature. Frequently the curvatures differ even in sign. Therefore, a lens which is satisfactory for one portion of the inhomogeneity may prove unsuitable for other points of the field. It is impractical to use a large number of lenses of different curvatures, since this only increases other errors, e.g., the errors connected with the non-uniform illumination of the instrument field. These errors may eventually exceed the diffraction error.

## 56. ALLOWANCE FOR OPAQUE BOUNDARIES

The calculation of the diffraction pattern in the image plane of a schlieren instrument involves considerable difficulties if the wave front in the object plane, in addition to being a quadratic function of the coordinates, is restricted by one or several opaque screens. This case is more general than those considered earlier and includes several of the previously obtained results.

The photographs in Figure 138 are an example of the diffraction patterns obtained in such a case. They were taken on the Soviet-made IAB-451 schlieren instrument with a knife-edge defocused by 25 mm, which corresponds to a wave curvature of $7 \times 10^{-6}\,\mathrm{mm}^{-1}$ in the object plane. The light source is narrow ($\sim 0.02$ mm), parallel to the knife-edge. The angle between the opaque edge in the object plane and the knife-edge is respectively equal to 30°, 60°, 90°, and 120°. The diffraction patterns from the opaque screen edge and the knife-edge overlap. If the angle between the knife-edge and the screen boundary is acute, "whiskers" bending to stretch along the surface appear in the pattern, and the distance between them increases as they approach to the knife-edge image. A region of destroyed diffraction bands appears on the photographs taken at an obtuse angle. The bands also bend along the opaque boundary.

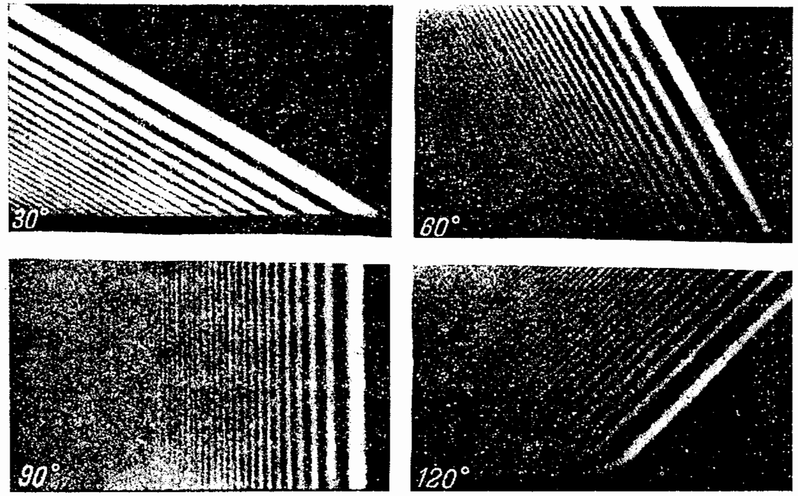

Figure 138

Diffraction patterns near an opaque screen obtained by the photometric knife-edge and slit method with a narrow light source.

These new phenomena are very important in the use of schlieren methods in various applied problems. Had we not established their geometrical origin, these curious features of the diffraction patterns could have been attributed to the optical inhomogeneities. Thus the bending of the bands along the surface could be erroneously associated with density changes in the boundary layer, etc.

The shape of the diffraction pattern depends largely on the width of the light source. Photographs taken at an angle of 30° under the same conditions as those of Figure 138, but with source widths of 0.05 mm and 0.1 mm, are shown in Figure 139. The contrast of the knife-edge diffraction bands decreases considerably. The bands become blurred and fewer in number. The diffraction bands of the opaque screen become somewhat more prominent.

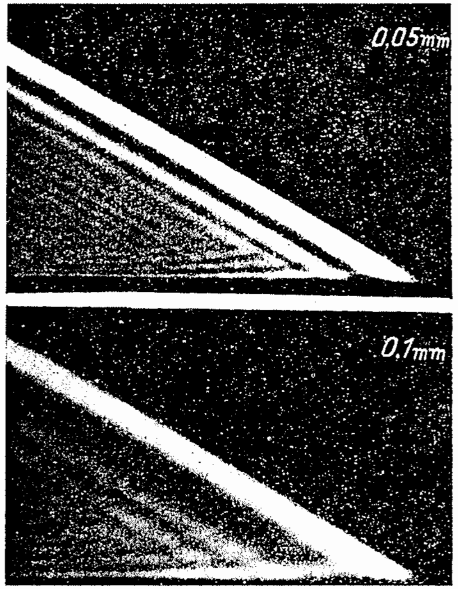

Figure 139

Diffraction patterns near an opaque screen obtained with a wide light source.

Let us calculate the light intensity distribution in the image plane of the schlieren instrument. We assume for the sake of simplicity that the opaque object-plane diaphragm is an infinitely long slit, with edges aligned along the lines $x = R$ and $x = -R$. The wave front parameters vary only in the direction $x$, and the wave front is described by the equation

$$z = \frac{xl}{f} + \alpha_x x + \frac{A_{xx}}{2} x^2. \tag{56.1}$$

The focal knife-edge is parallel to the $\eta$ axis and lies on the line $\xi = r_1$. The far edge of the knife lies on the line $\xi = r_2$.

The assumption of one-dimensionality does not lead to substantial restrictions in the calculation. As noted above, the results obtained under more general assumptions contain, instead of $\alpha_x$ and $A_{xx}$, quantities which determine the curvature and the angle of inclination of the wave front in the direction perpendicular to the knife-edge.

We have obtained for the light disturbance distribution function in the image plane after integrating over the variables $x$, $y$ and $\eta$:

$$S(x') = 2\pi f C e^{i\omega\tau} \sqrt{\frac{\pi}{kA_{xx}}} \times$$

$$\times \int_{r_2}^{r_1} \exp\left\{ ik \left[ -\frac{\mu\xi x'}{f} - \frac{\left(\frac{l}{f} + \alpha_x + \frac{\xi}{f}\right)^2}{2A_{xx}} \right] \right\} [C(t) + iS(t)] \Big|_{t=B_1}^{t=B_2} d\xi, \tag{56.2}$$

where

$$B_1 = \sqrt{\frac{kA_{xx}}{\pi}} \left[ -R + \frac{\frac{l}{f} + \alpha_x + \frac{\xi}{f}}{A_{xx}} \right], \quad B_2 = \sqrt{\frac{kA_{xx}}{\pi}} \left[ R + \frac{\frac{l}{f} + \alpha_x + \frac{\xi}{f}}{A_{xx}} \right].$$

This formula is easily transformed to

$$S(x') = C_1 \int_{B_3}^{B_4} \exp\left\{ -\frac{i\pi}{2} \left[ t + \sqrt{\frac{kA_{xx}}{\pi}} (-R + \mu x') \right]^2 \right\} \times$$

$$\times [C(t) + iS(t)] dt - \int_{B_5}^{B_6} \exp\left\{ -\frac{i\pi}{2} \left[ t + \sqrt{\frac{kA_{xx}}{\pi}} (R + \mu x') \right]^2 \right\} \times$$

$$\times [C(t) + iS(t)] dt = C_1(I_1 - I_2), \tag{56.3}$$

where

$$B_3 = \sqrt{\frac{k}{\pi A_{xx}}} \left( RA_{xx} + \frac{l}{f} + \alpha_x + \frac{r_2}{f} \right),$$

$$B_4 = \sqrt{\frac{k}{\pi A_{xx}}} \left( RA_{xx} + \frac{l}{f} + \alpha_x + \frac{r_1}{f} \right),$$

$$B_5 = \sqrt{\frac{k}{\pi A_{xx}}} \left( -RA_{xx} + \frac{l}{f} + \alpha_x + \frac{r_2}{f} \right),$$

$$B_6 = \sqrt{\frac{k}{\pi A_{xx}}} \left( -RA_{xx} + \frac{l}{f} + \alpha_x + \frac{r_1}{f} \right).$$

Let $r_1$ and $r_2$ be sufficiently large and of opposite signs, so that the variable $t$ in the integrals $I_1$ and $I_2$ takes large values and passes through zero. We divide each of the integrals $I_1$ and $I_2$ into three, isolating the region where $t$ passes through zero:

$$I_1 = \int_{-\Delta}^{B_4} + \int_{\Delta}^{-\Delta} + \int_{B_3}^{\Delta} = I_1' + I_1'' + I_1''', \tag{56.4}$$

$$I_2 = \int_{-\Delta}^{B_6} + \int_{\Delta}^{-\Delta} + \int_{B_5}^{\Delta} = I_2' + I_2'' + I_2'''. \tag{56.5}$$

Let the limits of integration be sufficiently wide for the Fresnel integrals to be expressed with the required accuracy by the first two terms of the respective asymptotic expansion.

The values of the variable $t$ in the integrals $I_1'$ and $I_2'$ are always negative and of large absolute value. After the replacement of the Fresnel integrals by the first terms of the asymptotic expansion, $I_1'$ and $I_2'$ are expressed in the form

$$I_1' = -\frac{1+i}{2} \left\{ C\left[ \sqrt{\frac{k}{\pi A_{xx}}} \left( \frac{l}{f} + \alpha_x + \frac{r_1}{f} + \mu x' A_{xx} \right) \right] - \right.$$

$$- iS\left[ \sqrt{\frac{k}{\pi A_{xx}}} \left( \frac{l}{f} + \alpha_x + \frac{r_1}{f} + \mu x' A_{xx} \right) \right] -$$

$$- C\left[ -\Delta + \sqrt{\frac{kA_{xx}}{\pi}} (-R + \mu x') \right] +$$

$$\left. + iS\left[ -\Delta + \sqrt{\frac{kA_{xx}}{\pi}} (-R + \mu x') \right] \right\} + \frac{\exp\{-\frac{1}{2}ikA_{xx}(-R + \mu x')^2\}}{\pi i} \times$$

$$\begin{aligned}
&\times \Bigl\{\mathrm{Ci}\, k(-R+\mu x')\Bigl(RA_{xx}+\frac{l}{f}+\alpha_x+\frac{r_1}{f}\Bigr)- \\
&-i\,\mathrm{Si}\, k(-R+\mu x')\Bigl(RA_{xx}+\frac{l}{f}+\alpha_x+\frac{r_1}{f}\Bigr)- \\
&-\mathrm{Ci}\sqrt{k\pi A_{xx}}\,(-R+\mu x')\Delta-i\,\mathrm{Si}\sqrt{k\pi A_{xx}}\,(-R+\mu x')\Delta\Bigr\}\,;
\end{aligned}\qquad (56.6)$$

$$\begin{aligned}
I'_2 = &-\frac{1+i}{2}\Bigl\{C\Bigl[\sqrt{\frac{k}{\pi A_{xx}}}\Bigl(\frac{l}{f}+\alpha_x+\frac{r_1}{f}+\mu x' A_{xx}\Bigr)\Bigr]- \\
&-iS\Bigl[\sqrt{\frac{k}{\pi A_{xx}}}\Bigl(\frac{l}{f}+\alpha_x+\frac{r_1}{f}+\mu x' A_{xx}\Bigr)\Bigr]- \\
&-C\Bigl[-\Delta+\sqrt{\frac{kA_{xx}}{\pi}}\,(R+\mu x')\Bigr]+iS\Bigl[-\Delta+\sqrt{\frac{kA_{xx}}{\pi}}\,(R+\mu x')\Bigr]\Bigr\}+ \\
&+\frac{\exp\{-\tfrac{1}{2}ikA_{xx}(R+\mu x')^2\}}{i\pi}\Bigl\{\mathrm{Ci}\, k(R+\mu x')\Bigl(-RA_{xx}+\frac{l}{f}+\alpha_x+\frac{r_1}{f}\Bigr)- \\
&-\mathrm{Si}\, k(R+\mu x')\Bigl(-RA_{xx}+\frac{l}{f}+\alpha_x+\frac{r_1}{f}\Bigr)- \\
&-\mathrm{Ci}\sqrt{k\pi A_{xx}}\,(R+\mu x')\Delta-i\,\mathrm{Si}\sqrt{k\pi A_{xx}}\,(R+\mu x')\Delta\Bigr\}.
\end{aligned}\qquad (56.7)$$

The integrals $I'''_1$ and $I'''_2$ are similarly evaluated, but the variable $t$ is always large and positive:

$$\begin{aligned}
I'''_1 = &\frac{1+i}{2}\Bigl\{C\Bigl[\Delta+\sqrt{\frac{kA_{xx}}{\pi}}\,(-R+\mu x')\Bigr]- \\
&-iS\Bigl[\Delta+\sqrt{\frac{kA_{xx}}{\pi}}\,(-R+\mu x')\Bigr]-C\Bigl[\sqrt{\frac{k}{\pi A_{xx}}}\Bigl(\frac{l}{f}+\alpha_x+ \\
&+\frac{r_2}{f}+A_{xx}\mu x'\Bigr)\Bigr]+iS\Bigl[\sqrt{\frac{k}{\pi A_{xx}}}\Bigl(\frac{l}{f}+\alpha_x+\frac{r_2}{f}+A_{xx}\mu x'\Bigr)\Bigr]\Bigr\}+ \\
&+\frac{\exp\{-\tfrac{1}{2}ikA_{xx}(-R+\mu x')^2\}}{\pi i}\times
\end{aligned}$$

$$\begin{aligned}
&\times\,\mathrm{Ci}\sqrt{k\pi A_{xx}}\,(-R+\mu x')\,\Delta-i\,\mathrm{Si}\sqrt{k\pi A_{xx}}\,(-R+\mu x')\,\Delta- \\
&-\mathrm{Ci}\, k(-R+\mu x')\Bigl(RA_{xx}+\frac{l}{f}+\alpha_x+\frac{r_2}{f}\Bigr)+ \\
&+i\,\mathrm{Si}\, k(-R+\mu x')\Bigl(RA_{xx}+\frac{l}{f}+\alpha_x+\frac{r_2}{f}\Bigr)\Bigr\}\,;
\end{aligned}\qquad (56.8)$$

$$\begin{aligned}
I'''_2 = &\frac{1+i}{2}\Bigl\{C\Bigl[\Delta+\sqrt{\frac{kA_{xx}}{\pi}}\,(R+\mu x')\Bigr]-iS\Bigl[\Delta+\sqrt{\frac{kA_{xx}}{\pi}}\,(R+\mu x')\Bigr]- \\
&-C\Bigl[\sqrt{\frac{k}{\pi A_{xx}}}\Bigl(\frac{l}{f}+\alpha_x+\frac{r_2}{f}+A_{xx}\mu x'\Bigr)\Bigr]+ \\
&+iS\Bigl[\sqrt{\frac{k}{\pi A_{xx}}}\Bigl(\frac{l}{f}+\alpha_{xx}+\frac{r_2}{f}+A_{xx}\mu x'\Bigr)\Bigr]\Bigr\}+ \\
&+\frac{\exp\{-\tfrac{1}{2}ikA_{xx}(R+\mu x')^2\}}{\pi i}\Bigl\{\mathrm{Ci}\sqrt{k\pi A_{xx}}\,(R+\mu x')\,\Delta- \\
&-i\,\mathrm{Si}\sqrt{k\pi A_{xx}}\,(R+\mu x')\,\Delta-\mathrm{Ci}\, k(R+\mu x')\Bigl(-RA_{xx}+\frac{l}{f}+\alpha_x+\frac{r_2}{f}\Bigr)+ \\
&+i\,\mathrm{Si}\, k(R+\mu x')\Bigl(-RA_{xx}+\frac{l}{f}+\alpha_x+\frac{r_2}{f}\Bigr)\Bigr\}.
\end{aligned}\qquad (56.9)$$

Setting $a=(-R+\mu x')\sqrt{kA_{xx}/\pi}$, we can write $I''_1$ in the form

$$I''_1=\int_{\Delta}^{-\Delta} e^{-i\pi(t+a)^2/2}\,[C(t)+iS(t)]\,dt\,. \qquad (56.10)$$

Integrating by parts and expanding the Fresnel integrals in an asymptotic series, we obtain

$$\begin{aligned}
I''_1 = &[C(t)+iS(t)]\,[C(t+a)-iS(t+a)]\Bigr|_{-\Delta}^{\Delta}- \\
&-(\pm)_1\frac{1-i}{2}\int_{\Delta}^{-\Delta} e^{i\pi t^2/2}\,dt-\frac{1}{\pi i}\int_{\Delta}^{-\Delta}\frac{\exp\{\tfrac{1}{2}i\pi a^2-i\pi a t\}}{t+a}\,dt\,.
\end{aligned}\qquad (56.11)$$

The sign $(\pm)_1$ is selected depending on the sign of $a$. We have finally

$$I''_1=[C(\Delta)+iS(\Delta)]\Bigl\{-C\Bigl[-\Delta+\sqrt{\frac{kA_{xx}}{\pi}}\,(-R+\mu x')\Bigr]+$$

$$+ iS\Big[-\Delta + \sqrt{\frac{kA_{xx}}{\pi}}(-R + \mu x')\Big] - C\Big[\Delta + \sqrt{\frac{kA_{xx}}{\pi}}(-R + \mu x')\Big] +$$

$$+ iS\Big[\Delta + \sqrt{\frac{kA_{xx}}{\pi}}(-R + \mu x')\Big] + (\pm)_1(1 - i)\Big\} +$$

$$+ \exp\{\tfrac{1}{2}ikA_{xx}(-R + \mu x')^2\} \times$$

$$\times \Big[\mathrm{Ci}\Big\{\sqrt{\pi kA_{xx}}\Big[-\Delta + \sqrt{\frac{kA_{xx}}{\pi}}(-R + \mu x')\Big](-R + \mu x')\Big\} -$$

$$- i\,\mathrm{Si}\Big\{\sqrt{\pi kA_{xx}}(-R + \mu x')\Big[-\Delta + \sqrt{\frac{kA_{xx}}{\pi}}(-R + \mu x')\Big]\Big\} -$$

$$- \mathrm{Ci}\Big\{\sqrt{\pi kA_{xx}}(-R + \mu x')\Big[\Delta + \sqrt{\frac{kA_{xx}}{\pi}}(-R + \mu x')\Big]\Big\} +$$

$$+ i\,\mathrm{Si}\Big\{\sqrt{\pi kA_{xx}}(-R + \mu x')\Big[\Delta + \sqrt{\frac{kA_{xx}}{\pi}}(-R + \mu x')\Big]\Big\}\Big]. \qquad (56.12)$$

Similarly

$$I_2'' = [C(\Delta) + iS(\Delta)]\Big\{- C\Big[-\Delta + \sqrt{\frac{kA_{xx}}{\pi}}(R + \mu x')\Big] +$$

$$+ iS\Big[-\Delta + \sqrt{\frac{kA_{xx}}{\pi}}(R + \mu x')\Big] - C\Big[\Delta + \sqrt{\frac{kA_{xx}}{\pi}}(R + \mu x')\Big] +$$

$$+ iS\Big[\Delta + \sqrt{\frac{kA_{xx}}{\pi}}(R + \mu x')\Big] + (\pm)_2(1 + i)\Big\} + \frac{\exp\{\tfrac{1}{2}ikA_{xx}(R + \mu x')^2\}}{\pi i} \times$$

$$\times \Big\{\mathrm{Ci}\sqrt{\pi kA_{xx}}(R + \mu x')\Big[-\Delta + \sqrt{\frac{kA_{xx}}{\pi}}(R + \mu x')\Big] -$$

$$- i\,\mathrm{Si}\sqrt{\pi kA_{xx}}(R' + \mu x')\Big[-\Delta + \sqrt{\frac{kA_{xx}}{\pi}}(R + \mu x')\Big] -$$

$$- \mathrm{Ci}\sqrt{\pi kA_{xx}}(R + \mu x')\Big[\Delta + \sqrt{\frac{kA_{xx}}{\pi}}(R + \mu x')\Big] +$$

$$+ i\,\mathrm{Si}\sqrt{\pi kA_{xx}}(R + \mu x')\Big[\Delta + \sqrt{\frac{kA_{xx}}{\pi}}(R + \mu x')\Big]\Big\}. \qquad (56.13)$$

The sign $(\pm)_2$ is selected depending on the sign of $(R + \mu x')\sqrt{kA_{xx}/\pi}$.

If $\Delta$ is neglected compared with $a$, $I_2''$ and $I_2'$ will go to zero.

The above integrals determine the light disturbance distribution in the image plane.

The expressions obtained are valid if the focal plane diaphragm is much larger than the light-filled aperture.

We shall now consider the opposite case, when one of the viewing diaphragm edges covers a part of the slit image, and the second edge does not cover it. Let the covered width be larger than $\Delta$, but not sufficiently large for ignoring the second term of the asymptotic expansion. We shall then have $I_1' = 0$, $I_1'' = 0$ in (56.4), and in the expression for $I_1'''$ the upper limit $\Delta$ is replaced with

$$\sqrt{\frac{k}{\pi A_{xx}}}\Big(RA_{xx} + \frac{l}{f} + \alpha_x + \frac{r_1}{f}\Big).$$

The integral $I_2$ remains unchanged.

We have for the light disturbance distribution function:

$$\frac{S(x')}{C_1} = \frac{1 + i}{2}\Big\{2C\Big[\sqrt{\frac{k}{\pi A_{xx}}}\Big(\frac{l}{f} + \alpha_x + \frac{r_1}{f} + \mu x' A_{xx}\Big)\Big] -$$

$$- 2iS\Big[\sqrt{\frac{k}{\pi A_{xx}}}\Big(\frac{l}{f} + \alpha_x + \frac{r_1}{f} + \mu x' A_{xx}\Big)\Big] -$$

$$- C\Big[-\Delta + \sqrt{\frac{kA_{xx}}{\pi}}(R + \mu x')\Big] + iS\Big[-\Delta + \sqrt{\frac{kA_{xx}}{\pi}}(R + \mu x')\Big] -$$

$$- C\Big[\Delta + \sqrt{\frac{kA_{xx}}{\pi}}(R + \mu x')\Big] + iS\Big[\Delta + \sqrt{\frac{kA_{xx}}{\pi}}(R + \mu x')\Big]\Big\} +$$

$$+ \frac{\exp\{-\tfrac{1}{2}ikA_{xx}(-R + \mu x')^2\}}{\pi i}\Big\{\mathrm{Ci}\Big[k(-R + \mu x')\Big(RA_{xx} + \frac{l}{f} +$$

$$+ \alpha_x + \frac{r_1}{f}\Big)\Big] - i\,\mathrm{Si}\Big[k(-R + \mu x')\Big(RA_{xx} + \frac{l}{f} + \alpha_x + \frac{r_1}{f}\Big)\Big] -$$

$$- \mathrm{Ci}\Big[k(-R + \mu x')\Big(RA_{xx} + \frac{l}{f} + \alpha_x + \frac{r_2}{f}\Big)\Big] +$$

$$+ i\,\mathrm{Si}\Big[k(-R + \mu x')\Big(RA_{xx} + \frac{l}{f} + \alpha_x + \frac{r_2}{f}\Big)\Big]\Big\} +$$

$$+ \frac{\exp\{-\tfrac{1}{2}ikA_{xx}(R + \mu x')^2\}}{\pi i}\Big\{- \mathrm{Ci}\Big[k(R + \mu x')\Big(- RA_{xx} + \frac{l}{f} +$$

$$\begin{aligned}
&+ \alpha_x + \frac{r_1}{f}\Big)\Big] + i\,\mathrm{Si}\Big[k(R + \mu x')\Big(- RA_{xx} + \frac{l}{f} + \alpha_x + \frac{r_1}{f}\Big)\Big] + \\
&+ \mathrm{Ci}\Big[k(R + \mu x')\Big(- RA_{xx} + \frac{l}{f} + \alpha_x + \frac{r_2}{f}\Big)\Big] - \\
&- i\,\mathrm{Si}\Big[k(R + \mu x')\Big(- RA_{xx} + \frac{l}{f} + \alpha_x + \frac{r_2}{f}\Big)\Big] + \\
&+ 2i\,\mathrm{Si}\,[\sqrt{k\pi A_{xx}}\,(R + \mu x')\,\Delta]\Big\} - [C(\Delta) + iS(\Delta)] \times \\
&\times \Big\{- C\Big[- \Delta + \sqrt{\frac{kA_{xx}}{\pi}}\,(R + \mu x')\Big] + \\
&+ iS\Big[- \Delta + \sqrt{\frac{kA_{xx}}{\pi}}\,(R + \mu x')\Big] - C\Big[\Delta + \sqrt{\frac{kA_{xx}}{\pi}}\,(R + \mu x')\Big] + \\
&+ iS\Big[\Delta + \sqrt{\frac{kA_{xx}}{\pi}}\,(R + \mu x')\Big] + (\pm)_2\,(1 - i)\Big\} - \\
&- \frac{\exp\{\frac{1}{2}ikA_{xx}(R + \mu x')^2\}}{\pi i}\Big\{\mathrm{Ci}\Big\{\sqrt{\pi kA_{xx}}\Big[- \Delta + \sqrt{\frac{kA_{xx}}{\pi}}\,(R + \mu x')\Big] \times \\
&\times (R + \mu x')\Big\} - i\,\mathrm{Si}\Big\{\sqrt{\pi kA_{xx}}\,(R + \mu x')\Big[- \Delta + \sqrt{\frac{kA_{xx}}{\pi}}\,(R + \mu x')\Big]\Big\} - \\
&- \mathrm{Ci}\Big\{\sqrt{\pi kA_{xx}}\,(R + \mu x')\Big[\Delta + \sqrt{\frac{kA_{xx}}{\pi}}\,(R + \mu x')\Big]\Big\} + \\
&+ i\,\mathrm{Si}\Big\{\sqrt{\pi kA_{xx}}\,(R + \mu x')\Big[\Delta + \sqrt{\frac{kA_{xx}}{\pi}}\,(R + \mu x')\Big]\Big\}\Big\}.
\end{aligned} \tag{56.14}$$

Let $|- R + \mu x'|$ and $|R + \mu x'|$ be considerably larger than $\Delta$. The illumination in the image plane is then given by the following expression (apart from a constant):

$$\begin{aligned}
I(x') = &\Big\{C\Big[\sqrt{\frac{k}{\pi A_{xx}}}\Big(\frac{l}{f} + \alpha_x + \frac{r_1}{f} + \mu x' A_{xx}\Big)\Big] + \\
&+ S\Big[\sqrt{\frac{k}{\pi A_{xx}}}\Big(\frac{l}{f} + \alpha_x + \frac{r_1}{f} + \mu x' A_{xx}\Big)\Big] -
\end{aligned}$$

$$\begin{aligned}
&- C\Big[\sqrt{\frac{kA_{xx}}{\pi}}\,(R + \mu x')\Big] - S\Big[\sqrt{\frac{kA_{xx}}{\pi}}\,(R + \mu x')\Big] + \\
&+ \cos\tfrac{1}{2}kA_{xx}(- R + \mu x')^2\Big\{- \frac{1}{\pi}\,\mathrm{Si}\Big[k(- R + \mu x') \times \\
&\times \Big(RA_{xx} + \frac{l}{f} + \alpha_x + \frac{r_1}{f}\Big)\Big] + (\pm)_1 \cdot \tfrac{1}{2}\Big\} - \\
&- C(\Delta)\Big[- 2C\Big[\sqrt{\frac{kA_{xx}}{\pi}}\,(R + \mu x')\Big] + (\pm)_2 \cdot 1\Big] + \\
&+ S(\Delta)\Big[S\Big(\sqrt{\frac{kA_{xx}}{\pi}}\,(R + \mu x') - (\pm)_2 \cdot 1\Big] - \sin\frac{kA_{xx}}{2}(- R + \mu x')^2 \times \\
&\times \Big(\frac{1}{\pi}\,\mathrm{Ci}\Big[k(- R + \mu x')\Big(RA_{xx} + \frac{l}{f} + \alpha_x + \frac{r_1}{f}\Big)\Big]\Big) + \\
&+ \cos\frac{kA_{xx}}{2}(R + \mu x')^2\Big((\pm)_2 \cdot \frac{1}{2} + \frac{1}{\pi}\,\mathrm{Si}\Big[k(R + \mu x')\Big(- RA_{xx} + \\
&+ \frac{l}{f} + \alpha_x + \frac{r_1}{f}\Big)\Big]\Big) - \sin\frac{kA_{xx}}{2}(R + \mu x')^2 \cdot \frac{1}{\pi}\,\mathrm{Ci}\Big[k(R + \mu x') \times \\
&\times \Big(- RA_{xx} + \frac{l}{f} + \alpha_x + \frac{r_1}{f}\Big)\Big]\Big\}^2 + \Big\{C\Big[\sqrt{\frac{k}{\pi A_{xx}}}\Big(\frac{l}{f} + \alpha_x + \frac{r_1}{f} + \\
&+ \mu x' A_{xx}\Big)\Big] - S\Big[\sqrt{\frac{k}{\pi A_{xx}}}\Big(\frac{l}{f} + \alpha_x + \frac{r_1}{f} + \mu x' A_{xx}\Big)\Big] - \\
&- C\Big[\sqrt{\frac{kA_{xx}}{\pi}}\,(R + \mu x')\Big] + S\Big[\sqrt{\frac{kA_{xx}}{\pi}}\,(R + \mu x')\Big] - \\
&- \sin\frac{kA_{xx}}{2}(- R + \mu x')^2\Big(- \frac{1}{\pi}\,\mathrm{Si}\Big[k(- R + \mu x') \times \\
&\times \Big(RA_{xx} + \frac{l}{f} + \alpha_x + \frac{r_1}{f}\Big)\Big] + (\pm)_1 \cdot \frac{1}{2}\Big) + \cos\frac{kA_{xx}}{2}(- R + \mu x')^2 \times \\
&\times \Big[- \frac{1}{\pi}\,\mathrm{Ci}\Big[k(- R + \mu x')\Big(RA_{xx} + \frac{l}{f} + \alpha_x + \frac{r_1}{f}\Big)\Big]\Big] -
\end{aligned}$$

$$- C(\Delta)\left[2S\left(\sqrt{\frac{kA_{xx}}{\pi}}(R + \mu x')\right) - (\pm)_2 \cdot 1\right] +$$

$$+ S(\Delta)\left[2C\left(\sqrt{\frac{kA_{xx}}{\pi}}(R + \mu x')\right) - (\pm)_2 \cdot 1\right] +$$

$$+ \cos\frac{kA_{xx}(R + \mu x')^2}{2}\left[\frac{1}{\pi}\operatorname{Ci}\left[k(R + \mu x')\left(- RA_{xx} + \frac{l}{f} + \alpha_x + \frac{r_1}{f}\right)\right]\right] -$$

$$- \sin\frac{kA_{xx}}{2}(R + \mu x')^2 \Bigl[(\pm)_2 \cdot \frac{1}{2} + \frac{1}{\pi}\operatorname{Si}\Bigl[k(R + \mu x') \times$$

$$\times \left(- RA_{xx} + \frac{l}{f} + \alpha_x + \frac{r_1}{f}\right)\Bigr]\Bigr]\Bigr\}^2 . \tag{56.15}$$

Expression (56.15) determines the illumination distribution in the case of an infinitely narrow light source.

In order to calculate the illumination distribution for a wide light source, we must integrate over $l$ from $l_1$ to $l_2$. These values of the integration variable determine the boundaries of the illuminating slit in the coordinate $\xi$. Remember that $l_1$ and $l_2$ are such that $l/f + \alpha_x + r_1/f + \mu x' A_{xx}$ reverses its sign inside the integration limits, while $RA_{xx} + l/f + \alpha_x + r_1/f$ remains positive all the time. We have

$$J(x') = \int_{l_2}^{l_1} I(l, x')dl . \tag{56.16}$$

This expression cannot be integrated in known functions. Therefore, unlike the restricted plane wave and the unrestricted quadratic wave, the illumination distribution of the restricted quadratic wave can be found only by numerical integration. This undoubtedly limits the applicability of this technique to practical measurements.

However, we can estimate the relative measurement error. The error is written in the form

$$\kappa = \frac{(J_2 - J_1)\xi_1}{J_1(\xi_2 - \xi_1)} - 1 . \tag{56.17}$$

Since the illumination in the image plane depends on the angle of light deviation and the wave front curvature, the change in the illumination during the experiment can be represented as a total differential

$$J_2 - J_1 = \frac{\partial J}{\partial \varepsilon} d\varepsilon + \frac{\partial J}{\partial A_{xx}} dA_{xx} . \tag{56.18}$$

Furthermore, $J_1 = 4\xi_1$, $\xi_2 - \xi_1 = f\,d\varepsilon$ (the substitution of the geometrical-optics expression for $J_1$ in the denominator alters negligibly the value of the error). After the substitution, we obtain for (56.17)

$$\kappa = \frac{1}{4f}\frac{\partial J}{\partial \varepsilon} + \frac{1}{4f}\frac{\partial J}{\partial A_{xx}}\frac{dA_{xx}}{d\varepsilon} - 1 . \tag{56.19}$$

The different terms in (56.19) affect the error differently. The first term is associated with the relative measurement error, and the second term with the absolute error,

Introducing in (56.15)

$$\varepsilon = \frac{l}{f} + \alpha_x + \mu x' A_{xx} , \tag{56.20}$$

we find:

$$\frac{\partial J}{\partial \varepsilon} = f[I(l_1) - I(l_2)] . \tag{56.21}$$

We insert (56.15) in (56.21) and simplify the expression by replacing the Fourier integrals and the integral sines and cosines with the first terms of the asymptotic expansion. Dropping the squares of small terms and the high-frequency intensity fluctuations, we obtain

$$\frac{\partial J}{\partial \varepsilon} = 4f\left\{1 + \frac{1}{\pi k(R - \mu x')\left[\dfrac{r_1 + \xi_1}{f} + (R - \mu x')A_{xx}\right]}\right\} . \tag{56.22}$$

To calculate $\partial J/\partial A_{xx}$, we simplify expression (56.15), writing it in the form

$$I(x') = 2\left\{C\left[\sqrt{\frac{k}{\pi A_{xx}}}\left(\frac{r_1 + \xi_1}{f}\right)\right] - \frac{1}{2}\right\}^2 +$$

$$+ 2\left\{S\left[\sqrt{\frac{k}{\pi A_{xx}}}\left(\frac{r_1 + \xi_1}{f}\right)\right] - \frac{1}{2}\right\}^2 +$$

$$+ \frac{1}{\left\{\pi k(- R + \mu x')\left[\dfrac{r_1 + \xi_1}{f} + (R - \mu x')\dfrac{A_{xx}}{2}\right]\right\}} -$$

$$- \frac{2\cos\left[k(- R + \mu x')\left[\dfrac{r_1 + \xi_1}{f} + (R - \mu x')\dfrac{A_{xx}}{2}\right]\right]}{\pi k(- R + \mu x')\left[\dfrac{r_1 + \xi_1}{f} + (R - \mu x')\dfrac{A_{xx}}{2}\right]} \times$$

$$\times\left\{C\left[\sqrt{\frac{k}{\pi A_{xx}}}\left(\frac{r_1+\xi_1}{f}\right)\right]+S\left[\sqrt{\frac{k}{\pi A_{xx}}}\left(\frac{r_1+\xi_1}{f}\right)\right]-1\right\}-$$

$$-\frac{2\sin\left[k(-R+\mu x')\left[\frac{r_1+\xi_1}{f}+(R-\mu x')\frac{A_{xx}}{2}\right]\right]}{\pi k(-R+\mu x')\left[\frac{r_1+\xi_1}{f}+(R-\mu x')\frac{A_{xx}}{2}\right]}\times$$

$$\times\left\{C\left[\sqrt{\frac{k}{\pi A_{xx}}}\left(\frac{r_1+\xi_1}{f}\right)\right]-S\left[\sqrt{\frac{k}{\pi A_{xx}}}\left(\frac{r_1+\xi_1}{f}\right)\right]\right\}. \tag{56.23}$$

The first two terms of (56.23) constitute the known expression for the image-plane illumination for a quadratic wave of infinitely large dimensions. Since the error is additive, the derivative $\partial J/\partial A_{xx}$ for these terms will be

$$\frac{\partial J'}{\partial A_{xx}}=\frac{2(l_2-l_1)}{k\pi\left(\frac{l_1}{f}+\varepsilon_l\right)\left(\frac{l_2}{f}+\varepsilon_l\right)}. \tag{56.24}$$

From among the other terms in (56.23), the largest is the fourth term, or more precisely its part obtained for

$$\sqrt{\frac{k}{\pi A_{xx}}}\,\frac{r_1+\xi_1}{f}<0\,.$$

Dropping the other terms, we obtain

$$\frac{\partial J''}{\partial A_{xx}}=\frac{4}{\frac{\pi k}{f}(R-\mu x')A_{xx}}. \tag{56.25}$$

The final expression for the maximum relative error due to the neglect of diffraction is

$$\kappa=\frac{1}{\pi k(R-\mu x')\left[\frac{r_1+\xi_1}{f}+(R-\mu x')A_{xx}\right]}+$$

$$+\frac{(l_2-l_1)dA_{xx}}{2k\pi f\left(\frac{r_1+\xi_1}{f}\right)\left(\frac{r_1+\xi_2}{f}\right)\varepsilon}+\frac{dA_{xx}}{\pi k(R-\mu y')A_{xx}\varepsilon}. \tag{56.26}$$

The absolute measurement error is

$$\delta\varepsilon=\frac{\varepsilon f}{\pi k(R-\mu x')\left[r_1+\xi_1+(R-\mu x')A_{xx}\right]}+$$

$$+\frac{(\xi_2-\xi_1)(A'_{xx}-A''_{xx})f}{(r_1+\xi_1)2\pi k(r_1+\xi_2)}+\frac{(A'_{xx}-A''_{xx})}{\pi k(R-\mu x')A_{xx}}. \tag{56.27}$$

The above expressions include, as a particular case, the previous formulas. By writing $A_{xx}=0$ in (56.27), we obtain (48.22), which determines the error in the case of a plane wave front. For $(R-\mu x')=\infty$ we obtain equation (55.20) for the error in the case of an unrestricted quadratic wave.

The illumination distribution in the image plane can be written in the form

$$J=\frac{1}{2\pi^2}\int_{-1}^{+1}\left|\int_{\eta(a+t-\omega)}^{\eta(a+t)}\int_{-\infty}^{b\pm z}e^{-i(z^2-y^2)}\,dz\,dy\right|^2dt\,. \tag{56.28}$$

The illumination distribution is a function of two variables, $a$ and $b$. The variable $a$ is defined by the relation

$$a=\frac{m_0}{f}\,\frac{1}{\alpha_0}, \tag{56.29}$$

where $m_0$ is the distance from the knife-edge to the middle of the illuminating slit image, and $\alpha_0$ is the angular half-width of the illuminating slit image. The variable $b$ is defined by

$$b=l\sqrt{\tfrac{1}{2}k\,|A_{ll}|}, \tag{56.30}$$

where $l$ is the distance from the image point to the screen edge image in the direction perpendicular to the knife-edge.

The parameters of the illumination distribution are given by

$$\eta=\alpha_0\sqrt{\frac{k}{2\,|A_{ll}|}},\qquad \omega=\frac{H}{f'}\,\frac{1}{\alpha_0}. \tag{56.31}$$

$H$ is the width of the viewing diaphragm aperture.

We take the plus sign in the upper limit of the inner integral in (56.28) if $A_{ll}$ and $\cos\phi$ ($\phi$ is the angle between the direction perpendicular to the object field boundary and the knife-edge) are of the same sign. For a spherical wave, we obtain diffraction patterns in which the edges of the bright space between the knife shadow and the screen image make an acute angle.

The minus sign is taken if $A_{ll}$ and $\cos\phi$ are of different signs. For a spherical wave, the angle between the knife-edge shadow and the screen image is then obtuse.

We calculated numerically the illumination distribution and studied its deviation from that predicted by geometrical optics. The difference between the illumination calculated by (56.28) and the illumination calculated from the formulas of geometrical optics is plotted in Figure 140. $\Delta E_+$ corresponds to the plus sign in the upper limit of the inner integral in (56.28), and $\Delta E_-$ to the minus sign. In the calculations by (56.28) we used

$$\eta = 4, \qquad \omega = 20.$$

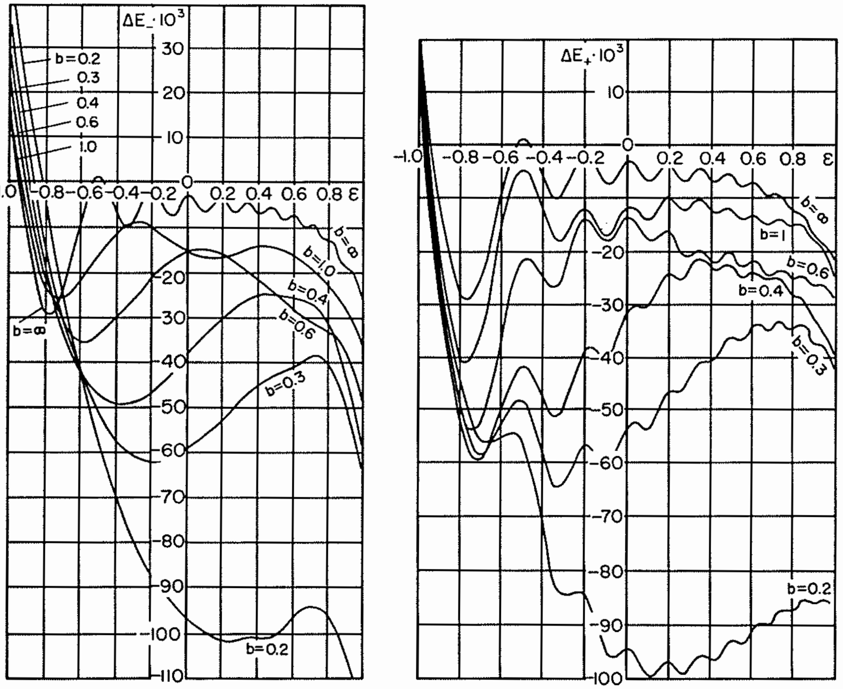

Figure 140

Difference between the diffraction and the geometrical illumination distributions.

## 57. DEFOCUSED POINT GRIDS

Consider the diffraction theory of the defocused point grid method [26]. We shall assume that the light wave in the object plane is a paraboloid. The object plane diaphragm and the point grid are assumed to be infinitely large. A monochromatic point source is used, located on the optical axis of the system. In this case, the illumination distribution in the image plane is given by the expression

$$J(x', y') = \left| e^{ikP(-x', -y')} - \frac{1}{\lambda^2 (f' - \Delta)^2} F_D \right|^2, \tag{57.1}$$

where

$$F_D = \iint_{\sigma_D} \exp\left\{\frac{ik}{f - \Delta}(\xi x' + \eta y')\right\} \Phi(\xi, \eta)\, d\xi\, d\eta, \tag{57.2}$$

$$\Phi(\xi, \eta) = \int_{-\infty}^{\infty} \int_{-\infty}^{\infty} \exp\left\{\frac{ik}{f - \Delta}[V^*(x, y) + \xi x + \eta y]\right\} dx\, dy, \tag{57.3}$$

$$V^*(x, y) = V(x, y)(f - \Delta). \tag{57.4}$$

The function $P(-x', -y')$ defines the wave shape in the object plane, $\sigma_D$ is the part of the viewing grid plane occupied by the opaque circles. The coordinate axes are directed along the symmetry planes of the wave surface.

To calculate (57.3), we series-expand the function $f(x, y) = V^*(x, y) + \xi x + \eta y$ in powers of $x - x_0$ and $y - y_0$:

$$f(x, y) = V^*(x_0, y_0) + \xi x_0 + \eta y_0 + \tfrac{1}{2}[V^*_{xx}(x - x_0)^2 + V^*_{yy}(y - y_0)^2]. \tag{57.5}$$

The values of $x_0$ and $y_0$ are determined from the relations

$$f_x(x_0) = V^*_x(x_0) + \xi = 0, \qquad f_y(y_0) = V^*_y(y_0) + \eta = 0. \tag{57.6}$$

If $V_{xx}$ and $V_{yy}$ are of the same sign, we have

$$\Phi = \frac{2\pi}{k\sqrt{|V_{xx}||V_{yy}|}} e^{\pm i\pi/2} \exp\left\{\frac{ik}{f - \Delta}[V^*(x_0, y_0) + \xi x_0 + \eta y_0]\right\}. \tag{57.7}$$

The upper sign in the exponential corresponds to positive values of $V_{xx}$ and $V_{yy}$, and the lower sign to negative values. Substituting (57.7) in (57.2) and omitting the zero subscripts of $x$ and $y$, we obtain

$$F_D = \frac{2\pi}{k\sqrt{|V_{xx}||V_{yy}|}} e^{\pm i\pi/2} \times$$
$$\times \iint_{\sigma_D} \exp\left\{\frac{ik}{f - \Delta}[V^*(x, y) + \xi x + \xi x' + \eta y + \eta y']\right\} d\xi\, d\eta. \tag{57.8}$$

Series-expanding the function $\phi(\xi, \eta) = V^*(x, y) + \xi(x + x') + \eta(y + y')$ in powers of $\xi - \xi_0$ and $\eta - \eta_0$, we find $\xi_0$ and $\eta_0$ from the relations

$$\xi_0 = -V^*_x(-x'), \qquad \eta_0 = -V^*_y(-y'). \tag{57.9}$$

For this choice of $\xi_0$ and $\eta_0$,

$$\phi_\xi(\xi_0) = \phi_\eta(\eta_0) = 0, \tag{57.10}$$

and the series has the form

$$\phi(\xi, \eta) = V^*(-x', -y') \pm \frac{1}{2}\left[\frac{1}{|V_{xx}^*|}(\xi - \xi_0)^2 + \frac{1}{|V_{yy}^*|}(\eta - \eta_0)^2\right]. \quad (57.11)$$

After the substitution of (57.11) in (57.18) we obtain

$$F_D = \frac{2\pi}{k\sqrt{|V_{xx}||V_{yy}|}} e^{\pm i\pi/2} e^{ikV(-x', -y')} g(x', y'), \quad (57.12)$$

where

$$g(x', y') = \iint_{\sigma_D} \exp\left\{\pm i \frac{k}{2(f - \Delta)}\left[\frac{1}{|V_{xx}^*|}(\xi - \xi_0)^2 + \frac{1}{|V_{yy}^*|}(\eta - \eta_0)^2\right]\right\} d\xi\, d\eta . \quad (57.13)$$

Let the centers of the grid circles be located at the vertices of a square grid of spacing $p$. Denote by $\psi$ the angle between the $O\xi$ axis and the line through the centers of the circles. If the origin of coordinates is placed at the center of the zero circle, the coordinates of the center of the $m, n$ circle are

$$\xi_{mn} = p(m\cos\psi - n\sin\psi), \qquad \eta_{mn} = p(m\sin\psi + n\cos\psi). \quad (57.14)$$

Expression (57.13) is transformed to

$$g(x', y') = \sum_{m=-\infty}^{\infty} \sum_{n=-\infty}^{\infty} g_{mn}, \quad (57.15)$$

where $g_{mn}$ is defined by (57.13), where the integrals are taken over the area of an opaque circle with subscripts $m$ and $n$.

Introducing new variables $\rho$ and $\theta$, which are the polar coordinates with the origin at the point $\xi_{mn}$, $\eta_{mn}$, we obtain

$$g_{mn} = \exp\left\{\mp i \frac{k}{2(f - \Delta)}\left[\frac{1}{|V_{xx}^*|}(\xi_{mn} - \xi_0)^2 + \frac{(\eta_{mn} - \eta_0)^2}{|V_{yy}^*|}\right]\right\} \times$$
$$\times \int_0^r \int_0^{2\pi} \exp\left\{\mp \frac{ik}{2(f - \Delta)}\left[2\rho\left(\frac{\xi_{mn} - \xi_0}{|V_{xx}^*|}\cos\theta + \frac{\eta_{mn} - \eta_0}{|V_{yy}^*|}\sin\theta\right) + \right.\right.$$
$$\left.\left. + \rho^2\left(\frac{\cos^2\theta}{|V_{xx}^*|} + \frac{\sin^2\theta}{|V_{yy}^*|}\right)\right]\right\}\rho\, d\rho\, d\theta . \quad (57.16)$$

From (57.9) and (57.10) we obtain

$$\begin{aligned} \xi_{mn} - \xi_0 &= \pm|V_{xx}^*|(x'_{mn} - x'), \\ \eta_{mn} - \eta_0 &= \pm|V_{yy}^*|(y'_{mn} - y'). \end{aligned} \quad (57.17)$$

We can write without any loss of generality

$$V(x, y) = \tfrac{1}{2}V_{xx}x^2 + \tfrac{1}{2}V_{yy}y^2 . \quad (57.18)$$

From (57.9), (57.10), (57.14), and (57.18), we thus find

$$\begin{aligned} x'_{mn} &= \pm \frac{p}{|V_{xx}^*|}(m\cos\psi - n\sin\psi), \\ y'_{mn} &= \pm \frac{p}{|V_{yy}^*|}(m\sin\psi + n\cos\psi). \end{aligned} \quad (57.19)$$

Using these expressions, we derive

$$I(x', y') = |1 \mp iG|^2, \quad (57.20)$$

where

$$G = \frac{e^{\pm i\pi}}{\pi}\left(\frac{1}{\sqrt{\xi}}X^2 + \sqrt{\xi}Y^2\right) \times$$
$$\times \sum_{m=-\infty}^{\infty} \sum_{n=-\infty}^{\infty} \exp\left\{\pm i\pi\left\{\mu_s^2\zeta_s^2\left[\sqrt{\xi}(m\cos\psi - n\sin\psi)^2 + \right.\right.\right.$$
$$\left. + \frac{1}{\sqrt{\xi}}(m\sin\psi + n\cos\psi)^2\right] \mp 2\mu_s\zeta_s[X(m\cos\psi - n\sin\psi) +$$
$$\left.\left. + Y(m\sin\psi + n\cos\psi)]\right\}\right\} \int_0^{\mu_s\sqrt{\pi}/2} \int_0^{2\pi} \exp\left\{\mp i\left\{\left(\sqrt{\xi}\cos^2\theta + \frac{1}{\sqrt{\xi}}\sin^2\theta\right)u + \right.\right.$$
$$+ 2\sqrt{\pi}\mu_s\zeta_s\left[\sqrt{\xi}\cos\theta\,(m\cos\psi - n\sin\psi) + \right.$$
$$\left.\left. + \frac{1}{\sqrt{\xi}}\sin\theta\,(m\sin\psi + n\cos\psi)\right]u \mp 2\sqrt{\pi}(X\cos\theta + Y\sin\theta)\,u\right\} u\,du\,d\theta\bigg\}. \quad (57.21)$$

Here

$$\mu_s = \frac{2r}{f - \Delta}\sqrt{\frac{1}{\lambda\sqrt{|V_{xx}||V_{yy}|}}}, \qquad \zeta_s = \frac{p}{2r}, \qquad \xi = \frac{V_{yy}}{V_{xx}},$$

$$X = \sqrt{\frac{\sqrt{|V_{xx}||V_{yy}|}}{\lambda}}\cdot x', \qquad Y = \sqrt{\frac{\sqrt{|V_{xx}||V_{yy}|}}{\lambda}}\cdot y' .$$

If $V_{xx}$ and $V_{yy}$ have different signs (we assume that $V_{xx} > 0, V_{yy} < 0$), we have instead of (57.20) and (57.21)

$$I_1(x', y') = |1 - G_1|^2, \tag{57.22}$$

where

$$\begin{aligned} G_1 = {} & \frac{e^{-i\pi}}{\pi}\left(\frac{1}{\sqrt{|\xi|}} X - \sqrt{|\xi|}\, Y\right) \times \sum_{m=-\infty}^{\infty} \sum_{n=-\infty}^{\infty} \exp\left\{- i\pi \left\{\mu_s^2\zeta_s^2 \times \right.\right. \\ & \times \left[\sqrt{|\xi|}(m\cos\psi - n\sin\psi)^2 - \frac{1}{\sqrt{|\xi|}}(m\sin\psi + n\cos\psi)^2\right] - \\ & \left.\left. - 2\mu_s\zeta_s[(m\cos\psi - n\sin\psi) X - (m\sin\psi + n\cos\psi) Y]\right\}\right\} \times \\ & \times \int_0^{\mu_s\sqrt{\pi}/2} \int_0^{2\pi} \exp\left\{- i\left\{\left(\sqrt{|\xi|}\cos^2\theta - \frac{1}{\sqrt{|\xi|}}\sin^2\theta\right) u^2 + \right.\right. \\ & + 2\sqrt{\pi}\mu_s\zeta_s\left[\sqrt{|\xi|}\cdot\cos\theta\,(m\cos\psi - n\sin\psi) - \frac{1}{\sqrt{|\xi|}}\sin\theta\,(m\sin\psi + \right. \\ & \left.\left.\left. + n\cos\psi)\right] u - 2\sqrt{\pi}\,(X\cos\theta + Y\sin\theta)\right\}\right\} u\,du\,d\theta. \end{aligned} \tag{57.23}$$

It follows from the above expressions that the similarity parameters of the diffraction patterns from a point grid are $\mu_s$, $\zeta_s$, $\xi$, $\psi$.

The scale of the similar patterns is proportional to the quantity

$$\frac{\lambda}{\sqrt{|V_{xx}||V_{yy}|}}. \tag{57.24}$$

It follows from (57.9) (57.10), and (57.19) that the curves bounding the geometrical shadow of the circles are ellipses with the semiaxes $r/|V_{xx}|(f - \Delta)$ and $r/|V_{yy}|(f - \Delta)$. The ellipse axes are directed along the symmetry planes of the wave surface $z = P(x, y)$. Their centers are located at the intersection points of the lines of the families

$$y' = \tan\psi \frac{V_{xx}}{V_{yy}} x' + \frac{p}{\cos\psi\, V_{yy}(f - \Delta)} n; \tag{57.25}$$

$$y' = -\frac{1}{\tan\psi}\frac{V_{xx}}{V_{yy}} x' + \frac{p}{\sin\psi\, V_{yy}(f - \Delta)} m. \tag{57.26}$$

By studying the photographs of the diffraction patterns, we determined for every value of the parameter $\zeta_s$ the values of $\mu$ for which it was still possible to identify the shadow centers. The results are summarized in Table 9. The product $\zeta_s\mu_{s0}$ remains constant, being approximately equal to 2.5.

Table 9

| $\zeta_s$ | $\mu_{s0}$ | $\zeta_s\mu_{s0}$ |
|---|---|---|
| 1.7 | 1.4 | 2.4 |
| 2.0 | 1.3 | 2.6 |
| 2.2 | 1.1 | 2.4 |
| 2.7 | 0.9 | 2.4 |
| 3.5 | 0.7 | 2.5 |

It is desirable to conduct measurements in as many points as possible. The number of measurement points is in an inverse proportion to the area $S$ of the parallelogram formed by the centers of adjacent shadows:

$$N = \frac{1}{S}. \tag{57.27}$$

Taking $|\Delta| \ll f'$, we obtain

$$S = \frac{p^2}{f^2|V_{xx}||V_{yy}|}. \tag{57.28}$$

The shadow centers can be pinpointed when

$$\zeta_s\mu_s > 2.5, \tag{57.29}$$

which may be written in the form

$$p^2 > 6.25 f\sqrt{|V_{xx}||V_{yy}|}. \tag{57.30}$$

For a plane wave front,

$$p^2 > 6.25\lambda|\Delta|. \tag{57.31}$$

The maximum number of useful shadow points in a photograph taken with an inhomogeneity in the field of view of the instrument is

$$(N_n)_{\max} = \frac{\sqrt{|V_{xx}||V_{yy}|}}{6.25\lambda}, \tag{57.32}$$

and in the zero photograph

$$(N_0)_{\max} = \frac{|\Delta|}{6.25 f^2\lambda}. \tag{57.33}$$

The random measurement error of the light deviation angle is

$$\Delta\varepsilon = | V_{ll} | \Delta l . \tag{57.34}$$

This error depends on the direction in which the displacement is measured. The average error is

$$\overline{\Delta\varepsilon} = \sqrt{| V_{xx} || V_{yy} |}\, \overline{\Delta l} . \tag{57.35}$$

The maximum number of shadow points which can be obtained for given $\overline{\Delta\varepsilon}$ and $\overline{\Delta l}$ *is*

$$(N_n)_{\max} = \frac{|\overline{\Delta\varepsilon}|}{6.25\, |\overline{\Delta l}|\, \lambda} . \tag{57.36}$$

The grid spacing for which this number of shadows are obtained is

$$p_{\min} = 2.5 f \sqrt{\frac{|\overline{\Delta\varepsilon}|}{|\overline{\Delta l}|}}\, \lambda . \tag{57.37}$$

The optimum grid parameters for studying wave fronts of complex shape, with variable curvature, are determined as in the case of a defocused line grid. The choice of the best working range depends on the specific features of the experiment.

## 58. CYLINDRICAL WAVE OF EVEN DEGREE

Our estimates of the diffraction error and the suggestions regarding the analysis of defocused-grid schlieren photographs with complex diffraction patterns assumed the illumination distribution of a wave expressible in the object plane by an equation of first or second degree in the coordinates. However, the actual wave fronts are usually more complex, and even small pieces of the front are not always representable with sufficient accuracy by a quadratic function. As a result, we have to study the diffraction of higher order waves. Due to the complexity of this problem, only one paper [53] has been published to date on the subject.

Let the wave shape in the object plane be a parabolic cylinder of even degree,

$$P_n(x) = \frac{P^{(n)}}{n!}\, x_n , \tag{58.1}$$

where $n$ is even. The wave is unbounded. A filament aligned along the wave surface generatrix is placed in the focal plane. Then

$$I_n(x') = \left| \exp\left\{ \frac{ikP^{(n)}}{n!}\, x'^n \right\} \pm \right.$$
$$\left. \pm \frac{1}{\pi} \int_{-\infty}^{\infty} \exp\left\{ ik\, \frac{P^{(n)}}{n!} \left( \frac{P(f - \Delta)}{kt} - x' \right)^n \right\} \exp\left\{ \frac{i\xi_D}{t}\, P \right\} \frac{\sin P}{P}\, dP \right|^2 . \tag{58.2}$$

We write the argument of the first exponential in the integrand in the form

$$k\, \frac{P^{(n)}}{n!} \left( \frac{P(f - \Delta)}{kt} - x' \right)^n = k\, \frac{P^{(n)}}{n!}\, x'^n \pm$$
$$\pm \frac{2}{n!} \sum_{m=0}^{n-1} (-1)^m \frac{C_n^m}{\pi^{n-m-1}} \left( \frac{f}{2t} | P^{(n)} |^{1/n} \lambda^{(n-1)/n} \right)^{n-m} \left[ x' \left( \frac{| P^{(n)} |}{\lambda} \right)^{1/n} \right]^m t^{n-m} . \tag{58.3}$$

The upper sign in (58.3) is taken for positive values of the derivative $P^{(n)}$, and the lower sign for negative values.

The geometrical axis of the shadow passes along the line $x' = x'_0$. We introduce the distance $l$ from the image point to the axis,

$$l = x' - x'_0 . \tag{58.4}$$

Then

$$k\, \frac{P^{(n)}}{n!} \left( \frac{P(f - \Delta)}{kt} - x' \right)^n = k\, \frac{P^{(n)}}{n!}\, x^n \pm$$
$$\pm \frac{2}{n!} \sum_{m=0}^{n-1} (-1)^m \frac{C_n^m}{\pi^{n-m-1}} \left( \frac{f}{2t} | P^{(n)} |^{1/n} \lambda^{(n-1)/n} \right)^{n-m} \times$$
$$\times \sum_{\delta=0}^{m} C_m^\delta \left[ x'_0 \left( \frac{| P^{(n)} |}{\lambda} \right)^{1/n} \right]^{m-\delta} \left[ l \left( \frac{| P^{(n)} |}{\lambda} \right)^{1/n} \right]^\delta P^{n-m} . \tag{58.5}$$

Putting

$$\mu_n = \frac{2t}{f} \sqrt[n]{\frac{1}{\lambda^{n-1} | P^{(n)} |}} , \qquad \gamma_n = x'_0 \sqrt[n]{\frac{| P^{(n)} |}{\lambda}} , \tag{58.6}$$

we obtain

$$k\, \frac{P^{(n)}}{n!} \left( \frac{P(f - \Delta)}{kt} - x' \right)^n = k\, \frac{P^{(n)}}{n!}\, x'^n \pm$$
$$\pm \frac{2}{n!} \sum_{m=0}^{n-1} (-1)^m \frac{C_n^m}{\pi^{n-m-1}} \frac{1}{\mu_n^{n-m}} \sum_{\delta=0}^{m} C_m^\delta \gamma_n^{m-\delta} \left[ l \left( \frac{| P^{(n)} |}{\lambda} \right)^{1/n} \right]^\delta P^{n-m} . \tag{58.7}$$

For the argument of the second exponential in the integrand, we write

$$\frac{\xi_0}{t}\, P = \frac{-f P^{(1)}(-x_0)}{t}\, P = \pm \frac{2n}{n!} \frac{1}{\mu_n}\, \gamma_n^{n-1} P . \tag{58.8}$$

We have finally

$$I_n(l) = \left| 1 - \frac{1}{\pi} \int_{-\infty}^{\infty} e^{\pm i f_n(t)} \frac{\sin P}{P}\, dP \right|^2 , \tag{58.9}$$

where

$$f_n(P) = \frac{2}{n!} \sum_{m=0}^{n-1} (-1)^m \frac{C_n^m}{\pi^{n-m-1}} \frac{1}{\mu_n^{n-m}} \sum_{\delta=0}^{m} \gamma_n^{m-\delta} \left[ l \left( \frac{|P^{(n)}|}{\lambda} \right)^{1/n} \right]^{\delta} P^{n-m} +$$

$$+ \frac{2n}{n!} \frac{1}{\mu_n} \gamma_n^{n-1} P. \qquad (58.10)$$

The illumination distribution depends on two similarity parameters, $\mu_n$ and $\gamma_n$. The width of the patterns is proportional to $\sqrt[n]{\lambda/|P^{(n)}|}$.

The only exceptions are the patterns obtained with a cylindrical wave of second degree, when the function

$$f_2(P) = \frac{1}{\pi} \frac{1}{\mu_2^2} t^2 - \frac{2}{\mu_2} l \sqrt{\frac{|P^{(2)}|}{\lambda}} P \qquad (58.11)$$

does not contain the parameter $\gamma_2$. As indicated in § 53, we have only one similarity parameter in this case:

$$\mu_2 = \frac{2t}{f} \sqrt{\frac{1}{\lambda |P^{(2)}|}}. \qquad (58.12)$$

For $n = 2$ the diffraction pattern is independent of the filament position relative to the wave apex and is symmetrical with respect to the geometrical axis.

For $n > 2$, the illumination distribution is symmetrical only if the filament middle is aligned with the rays passing through the wave apex. The shape of the pattern depends on the filament position.

The wave asymmetry can be a source of biased errors. To estimate the asymmetry error, we used a computer to calculate the illumination distribution for a fourth-degree wave [53]

$$f_4(P) = \frac{1}{12\pi^3} \frac{1}{\mu_4^4} P^4 - \frac{1}{3\pi^2 \mu_4^3} (L + \gamma_4) P^3 + \frac{1}{2\pi \mu_4^2} (L + \gamma_4)^2 t^2 -$$

$$- \frac{1}{3\mu_4} (L^3 + 3L^2\gamma_4 + 3L\gamma_4^2) t, \qquad (58.13)$$

where

$$L = l \sqrt[4]{\frac{|P^{(n)}|}{\lambda}}. \qquad (58.14)$$

The parameter $\mu_4$ was taken equal to 0.341 and 3.41, $\gamma_4 = 4.40$ and 8.80. These values of the parameters are close to the values occurring in actual measurements.

The curves in Figure 141 are asymmetrical with respect to the axis, but the asymmetry is noticeable only at a relatively large distance from the geometrical axis, being small near it. For $l = 0$, all the three curves have an extremum, but the curve $b$, unlike the curves of the second-degree waves, has at this point a small relative minimum, and not a maximum.

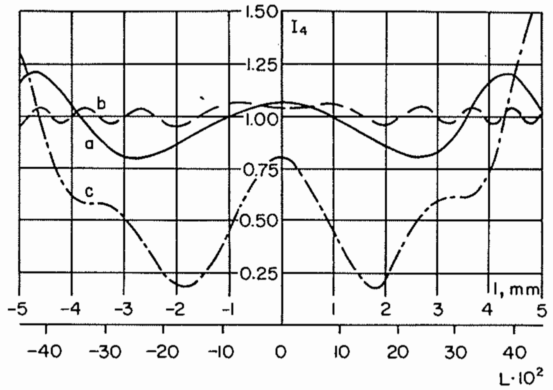

Figure 141

Illumination distribution in the filament shadow in the case of a fourth-degree wave.

$a$ $\mu_4 = 0.341, \gamma_4 = 4.40$; $b$ $\mu_4 = 0.341, \gamma = 8.80$; $c$ $\mu_4 = 3.41, \gamma_4 = 4.40$.

The deviations from symmetry at the usual measurement points of the diffraction pattern are small, and, therefore, the biased asymmetry errors can be ignored.

# XIII

# UTILIZATION OF DIFFRACTION IN MEASUREMENTS

## 59. DETERMINATION OF THE ANGLE OF INCLINATION OF THE LIGHT WAVE AT THE BORDER OF AN OPAQUE BODY

Schlieren photographs taken with a high-sensitivity instrument show a bright diffraction band near the edge of the opaque object. Schlieren measurements are impossible in the vicinity of this band, since the relationship between the angle of light deviation and the illumination derived on the basis of geometrical optics is not valid there. The higher the measurement sensitivity, the broader is the zone inaccessible to study.

Since the illumination distribution in this part of the image depends on the shape of the wave front emerging from the inhomogeneity, we may try to solve the inverse problem, namely to determine some parameters of the inhomogeneity near the opaque edge from the form of the diffraction pattern.

We shall adopt the diagram of Figure 110 as our mathematical model, and assume a point light source.

The image illumination distribution is determined by the following expression:

$$I(x') = \frac{4\pi^2(\eta_2 - \eta_1)f^4}{k^4} C^2 \left\{ \left[ \mathrm{Ci}\,\frac{k}{f}(-R + x')r - \mathrm{Ci}\,\frac{k}{f}(-R + x')\xi_0 - \right.\right.$$

$$\left. - \mathrm{Ci}\,\frac{k}{f}(R + x')r + \mathrm{Ci}\,\frac{k}{f}(R + x')\xi_0 \right]^2 + \left[ \mathrm{Si}\,\frac{k}{f}(-R + x')r - \right.$$

$$\left.\left. - \mathrm{Si}\,\frac{k}{f}(-R + x')\xi_0 - \mathrm{Si}\,\frac{k}{f}(R + x')r + \mathrm{Si}\,\frac{k}{f}(R + x')\xi_0 \right]^2 \right\}. \qquad (59.1)$$

We shall consider in our analysis the phenomena taking place near the image of one of the edges of the object plane diaphragm, for instance the edge whose image lies on the line $x' = R$. It is the diffraction from this diaphragm edge that is most important; the diffraction from the second edge ($x' = -R$) has a relatively weak effect, which can be neglected altogether if the diaphragm is sufficiently wide.

Expressed mathematically, this approximation means that $(R + x')\xi_0 k/f$ and $(R + x')rk/f$ are sufficiently large to neglect in (59.1) terms of order $f/k(R + x')\xi_0$ and $f/k(R + x')r$ which determine the maximum value of the first term in the expansions of $\mathrm{Ci}\,(R + x')\xi_0 k/f$ and $\mathrm{Ci}\,(R + x')rk/f$ and of the second term in the expansions of $\mathrm{Si}\,(R + x')\xi_0 k/f$ and $\mathrm{Si}\,(R + x')rk/f$ for large values of the arguments.

We shall examine later the smallness of these terms and the error introduced by this approximation. It is valid in practice, since the plane portion of the wave front is restricted in the object plane not only by opaque diaphragms (models, rims of the objectives and glasses, system components, etc.), but also by wave front changes due to the complexity of the inhomogeneity (shock waves, rarefaction zones, etc.). Most real objects are exceedingly complex, so that an exact calculation of the diffraction pattern is impossible, and therefore in practical work we must consider the diffraction from one edge only.

We move the origin of the coordinates to the point where the geometrical image of the diaphragm edge should be located ($x' = R$). Under the above assumptions, equation (59.1) reduces to

$$I(x') = 4\pi^2(\eta_2 - \eta_1)\frac{f^4}{k^4} C^2 \left\{ \left[ \mathrm{Ci}\,\frac{k}{f}x'r - \mathrm{Ci}\,\frac{k}{f}x'\xi_0 \right]^2 + \right.$$

$$\left. + \left[ \begin{pmatrix} 0 \\ \pi \end{pmatrix} - \mathrm{Si}\,\frac{k}{f}x'r + \mathrm{Si}\,\frac{k}{f}x'\xi_0 \right]^2 \right\}. \qquad (59.2)$$

The top term in parentheses corresponds to positive values of $\xi_0$, and the bottom term to negative values.

To determine the position of the illumination extrema in the image, we equate to zero the derivative of (59.2) with respect to $x'$:

$$\frac{dI(x')}{dx'} = \frac{4C^2}{x'} \frac{4\pi^2(\eta_2 - \eta_1)f^4}{k^4} \sin\frac{kx'}{2f}(r - \xi_0) \left\{ \sin\frac{kx'}{2f}(r + \xi_0) \times \right.$$

$$\times \left[ \mathrm{Ci}\,\frac{k}{f}x'r - \mathrm{Ci}\,\frac{k}{f}x'\xi_0 \right] - \cos\frac{k}{f}(r + \xi_0) \left[ \begin{pmatrix} 0 \\ -\pi \end{pmatrix} - \right.$$

$$\left.\left. - \mathrm{Si}\,\frac{k}{f}x'r + \mathrm{Si}\,\frac{k}{f}x'\xi_0 \right] \right\} = 0. \qquad (59.3)$$

Note that for $\xi_0 > 0$ (when the slit image is completely covered by the knife), equation (59.3) is satisfied for $x' = 0$. The negative value of the second derivative at that point indicates that in this case there is always an illumination peak at the opaque edge.

In what follows, we shall consider separately the cases $|x'| \neq 0$ and $x' \approx 0$.

Except for points near $x' = 0$, we can neglect the effect of the second edge of the focal plane diaphragm, located at $\xi = r$. In this case the argument $(k/f)x'r$ becomes sufficiently large and we may take its integral sine as equal to $\pi/2$ and its integral cosine as equal to zero (for $x' = 0.25$ mm, $\lambda = 5.5 \times 10^{-4}$ mm, $f = 1918$ mm, $r = 20$ mm we obtain $(k/f)x'r = 30$, and the deviation of the integral sines and cosines from the above values does not exceed 0.03). In this case

$$I(x') = 4\pi^2(\eta_2 - \eta_1)\frac{f^4}{k^4}C^2\left\{\mathrm{Ci}^2\frac{k}{f}x'\xi_0 + \left[\begin{pmatrix} -\frac{1}{2}\pi \\ -\frac{3}{2}\pi \end{pmatrix} + \mathrm{Si}\frac{k}{f}x'\xi_0\right]^2\right\}, \quad (59.4)$$

and the equation for the extrema reduces to

$$\tan\frac{k}{f}x'\xi_0 = -\frac{\mathrm{Ci}\dfrac{k}{f}x'\xi_0}{\begin{pmatrix} -\frac{1}{2}\pi \\ -\frac{3}{2}\pi \end{pmatrix} + \mathrm{Si}\dfrac{k}{f}x'\xi_0}. \quad (59.5)$$

The graphic solution of (59.5) is represented in Figure 142. The abscissa axis plots $P = (k/f)x'\xi_0$ and the ordinate axis gives the quantity $y$, which determines the values of the right- and the left-hand sides of (59.5). The curves $a$ plot the value of the left-hand side. These are tangent curves of the argument $P$. The other curves give the value of the right-hand side. The graph in the lower right-hand corner is the blown-up representation of the small square enclosed in a dotted line.

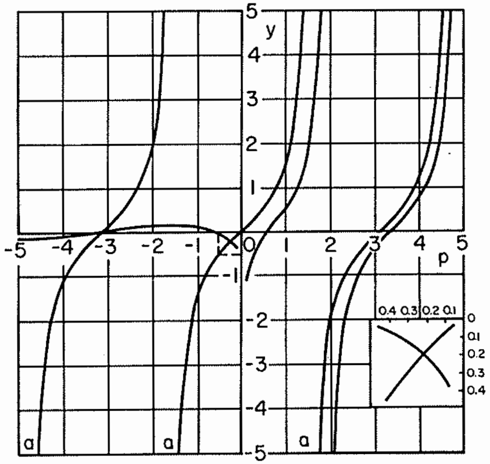

Figure 142

Graphic solution of equation (59.5).

The equation has no solution for $P > 0$, which corresponds to $\xi_0 > 0$ for $x' > 0$ (the curves do not intersect). Therefore, when the knife covers the slit image, there is a single diffraction illumination peak which coincides with one of the points of the opaque edge. This enables us to find the true position of the opaque edge, needed for the qualitative analysis of schlieren photographs. The illumination in the diffraction peak is determined from (59.2) by substituting $x' = 0$. It is equal to

$$I(0) = 4\pi^2(\eta_2 - \eta_1)\frac{f^4}{k^4}C^2\ln^2\frac{\xi_0}{r}. \quad (59.6)$$

This expression is attractively simple, and thus we can develop a method for measuring the angle of light deviation in the inhomogeneity from the illumination of the peak lying on the opaque edge. If the slit image is originally located at a point $\xi_2 - \xi_1$, and is shifted by the inhomogeneity to a new position which is to be determined, then

$$\frac{I_1}{I_2} = \left(\frac{\ln(\xi_1/2)}{\ln(\xi_2/2)}\right)^2. \quad (59.7)$$

The peak illumination ratio before and after the introduction of the inhomogeneity can be found by photometry of the "zero" and the "working" photographs:

$$\log\frac{I_1}{I_2} = \frac{D_1 - D_2}{\gamma}. \quad (59.8)$$

From (59.7) and (59.8) we find the displacement of the slit image caused by the inhomogeneity:

$$\delta = \xi_2 - \xi_1 = \xi_1\left[\left(\frac{r}{\xi_1}\right)^{1-A} - 1\right], \quad \text{where} \quad A = 10^{(D_2 - D_1)/2\gamma \log e}. \quad (59.9)$$

We shall describe the use of this method with one of the schlieren instruments [14].

A diaphragm with a straight opaque edge is placed in the object plane. A Foucault knife-edge and an illuminating slit 0.02 mm wide are set parallel to the edge. Photographs are taken for different positions of the knife-edge with respect to the slit image, which correspond to different angles of inclination of the light wave front in the object plane. When the knife covers the slit image completely, the whole field is darkened in accordance with the theory. Only a central peak located at the point where the geometrical image of the opaque edge should be situated) is observed (Figure 143, $k$ through $n$).

The photographic density at the intensity peak is determined with a microphotometer. The experimental curve was compared with the theoretical curve, calculated on the strength of (59.6) (Figure 144).

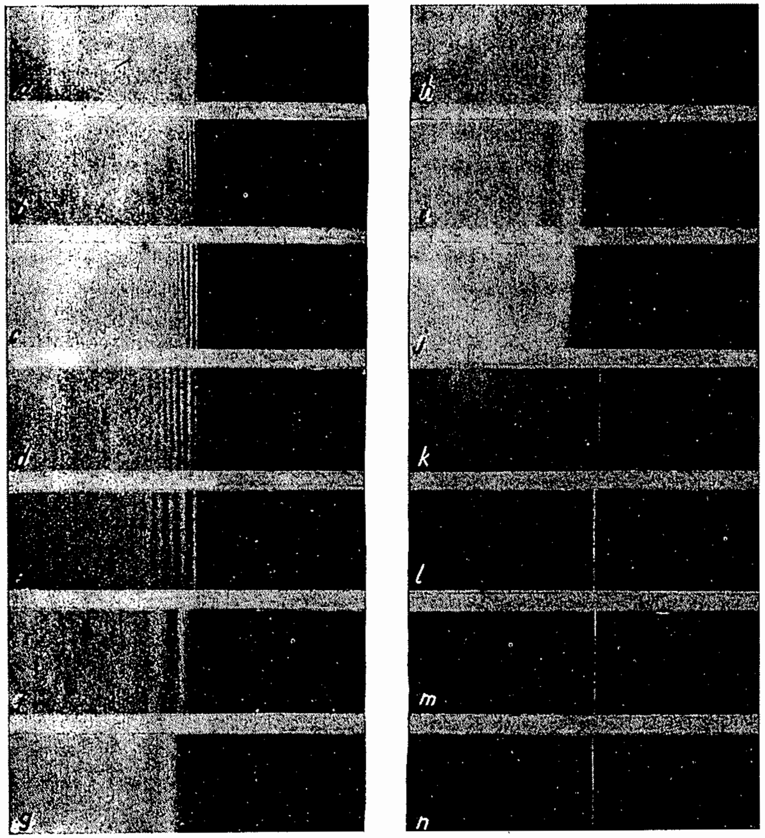

Figure 143

Series of photographs for different positions of the knife-edge relative to the slit image.

The comparison established a satisfactory fit between the experimental and the theoretical data in the range of knife-edge positions between 0.02 mm and 0.1 mm, which testifies to the validity of the above formulas and the possibility of using the method in practice.

This method can also be used for determining the emulsion characteristics. Thus, the $\gamma$ of the emulsion can be determined by measuring the optical density at the diffraction peak on two photographs:

$$\gamma = \frac{D_1 - D_2}{2\log\dfrac{\ln(\xi_1/2)}{\ln(\xi_2/2)}}, \qquad (59.10)$$

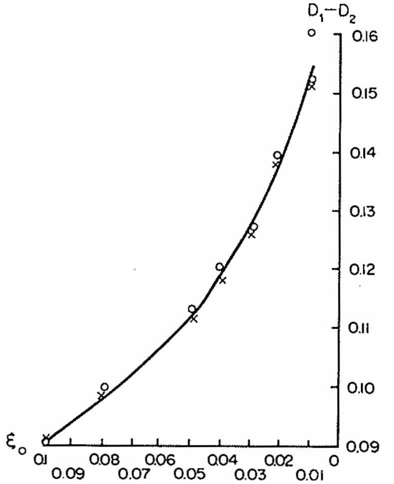

Figure 144

Check of the accuracy and the range of the diffraction method. The solid curve is theoretical, the circles and crosses represent experimental points.

where $\xi_1$ and $\xi_2$ are the knife-edge positions on the first and the second photograph. This method for determining $\gamma$ is convenient in that it is frequently possible to use the "zero" comparison photograph, thus avoiding the necessity of imprinting a stepped attenuator on the film. Another advantage is that the $\gamma$ is determined using the same light source and the same exposure as those for the working photographs.

Let us estimate the error caused by the neglect of the second edge of the object plane diaphragm. We will allow for the first terms in the asymptotic expansion of $\mathrm{Ci}\left[(k/f)R\xi\right]$ and the second terms in the expansion of $\mathrm{Si}\left[(k/f)R\xi\right]$. The illumination ratio is equal in this case to

$$\left(\frac{I_2}{I_1}\right)_{tr} = \frac{\ln^2(r/\xi_2)}{\ln^2(r/\xi_1)}\left[1 + \frac{2[\xi_2\ln(r/\xi_2) + \xi_1\ln(r/\xi_1)]}{\dfrac{k}{f}R\xi_2\xi_1\ln(r/\xi_2)\ln(r/\xi_1)}\right]. \qquad (59.11)$$

The relative error in the determination of the illuminations ratio is thus

$$\frac{\Delta I}{I} = \frac{2f\,[\xi_2\ln(r/\xi_2) + \xi_1\ln(r/\xi_1)]}{kR\xi_1\xi_2\ln(r/\xi_2)\ln(r/\xi_1)}. \qquad (59.12)$$

It follows from (59.12) that the error increases markedly when the slit image approaches the knife-edge ($\xi_1, \xi_2 \to 0$).

The error in the determination of the light deviation angle can be found from the following expression:

$$d\varepsilon = \frac{\xi_1}{2f}\sqrt{\frac{I_2}{I_1}}\left(\frac{r}{\xi_1}\right)^{1-\sqrt{I_1/I_2}} \ln\left(\frac{r}{\xi_1}\right)\frac{\Delta I}{I}, \tag{59.13}$$

which also may be written in the form

$$d\varepsilon = \frac{\left(\varepsilon + \dfrac{\xi_1}{f}\right)\ln\dfrac{r}{\xi_1}}{2\left[1 - \dfrac{\ln\left(1 + \varepsilon f/\xi_1\right)}{\ln\left(r/\xi_1\right)}\right]}. \tag{59.14}$$

If the shift of the slit image due to the inhomogeneity is much smaller than the distance from the slit image to the knife-edge in the original position, equation (59.12) can be transformed to

$$\frac{\Delta I}{I} = \frac{4f}{kR\xi_1 \ln\left(r/\xi_1\right)}. \tag{59.15}$$

The measurement error is equal in this case to

$$d\varepsilon = \frac{2}{kR}. \tag{59.16}$$

(If the allowed error is $d\varepsilon = 5 \times 10^{-6}$, $R$ should not be less than 32 mm for $\lambda = 5 \times 10^{-4}$ mm).

If the slit image is near the knife edge only in one of the two photographs (the "zero" or the working photograph), the error is half the previous value:

$$\frac{\Delta I}{I} = \frac{2f}{kR\xi_1 \ln\left(r/\xi_1\right)}. \tag{59.17}$$

The relative error in the measurement of the angle of light deviation is then

$$\kappa = \frac{f \ln\left(r/\xi_1\right)}{kR\xi_1 \ln\left(r/\xi_2\right)}. \tag{59.18}$$

With the aid of (59.16) and (59.18), we can find the experiment conditions so that the error should not exceed some specified value, and estimate the maximum possible sensitivity of the method.

The application of this computation method is inherently restricted because of the assumption of a plane wave front over the entire instrument field. In real experiments, regions of considerable wave front curvature — eddies, shock waves, rarefaction zones, etc. — exist side by side with the almost plane zones. However, zones far from the edge used in the measurements contribute less to the error, and the existence of compression shocks or other optical inhomogeneities there is much less dangerous than in near zones.

To estimate the probable error, we assume that the wave front has a kink at a point distant $x_1$ from the edge (Figure 145). In this case we have instead of (59.6):

$$I(x') = 4\pi^2(\eta_2 - \eta_1)\frac{f^4}{k^4}C^2\left\{\ln^2\frac{\xi_0}{r} + \right.$$
$$\left. + 2\ln\frac{\xi_0}{r}\left[-\operatorname{Ci}\frac{k}{f}\xi_0 x_1 + \operatorname{Ci}\frac{k}{f}(\xi_0 - b)x_1\right]\right\}, \tag{59.19}$$

where $b$ is the shift of the slit image formed by the segment $x_1R$ relative to the image formed by the segment $x_0x_1$. In deriving (59.19), just as in the derivation of (59.6), we neglected the influence of the edge at $x = R$ and of the second edge of the focal plane diaphragm at $\xi = r$.

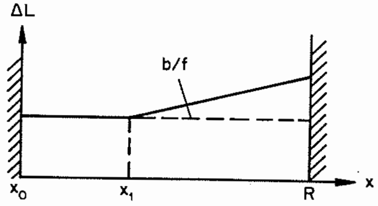

Figure 145

Wave front with a kink at point $x_1$.

Assuming that $b \ll \xi_0$, i.e., the shift of the slit image produced by the segment $x_1R$ of the wave front is considerably less than the original distance from the knife-edge to the slit image, and taking a sufficiently large $(k/f)x_1\xi_0$ (the influence of the diffraction from the kink point is small), we rewrite (59.19) in the form

$$I(x') = 4\pi^2(\eta_2 - \eta_1)\frac{f^4}{k^4}C^2\left\{\ln^2\frac{\xi_0}{r} + \right.$$
$$\left. + 2\ln\frac{\xi_0}{r}\left(-\frac{\sin\dfrac{k}{f}\xi_0 x_1}{\dfrac{k}{f}x_1\xi_0} + \frac{\sin\dfrac{k}{f}(\xi_0 - b)x_1}{\dfrac{k}{f}(\xi_0 - b)x_1}\right)\right\}. \tag{59.20}$$

Further simplification depends on the value of $(k/f)bx_1$. If this term is sufficiently large, $\sin\left[(k/f)bx\right]$ can take any value between $-1$ and $+1$. In this case we should look for the maximum error, which is attained when $\sin\left[(k/f)(\xi_0 - b)x_1\right]$ and $\sin\left[(k/f)\xi_0 x_1\right]$ are equal to 1 and $-1$ (or $-1$ and 1). Expression (59.20) reduces to

$$I(x') = 4\pi^2(\eta_2 - \eta_1)\frac{f^4}{k^4}C^2\left\{\ln^2\frac{\xi_0}{r} + \frac{4\ln\left(\xi_0/r\right)}{\dfrac{k}{f}\xi_0 x_1}\right\} \tag{59.21}$$

If the second term between braces is small compared to the first term, we can rewrite (59.21) in the form

$$\frac{I_2}{I_1} = \frac{\ln^2 (\xi_2/r)}{\ln^2 (\xi_1/r)} \left\{ 1 + \frac{4}{\frac{k}{f} \xi_2 x_1 \ln (\xi_2/r)} - \frac{4}{\frac{k}{f} \xi_1 x_1 \ln (\xi_1/r)} \right. \tag{59.22}$$

Assuming that $\delta = \xi_2 - \xi_1$ is small, we get

$$\frac{I_2}{I_1} = \frac{\ln^2 (\xi_2/r)}{\ln^2 (\xi_1/r)} \left\{ 1 - \frac{4\delta [1 + \ln (\xi_2/r)]}{\frac{k}{f} \xi_2^2 x_1 \ln^2 (\xi_2/r)} \right\}. \tag{59.23}$$

From (59.23) we obtain an expression determining the slit image shift:

$$\delta_{\text{tr}} = \frac{\left( \frac{I_0}{I_1} - 1 \right) \xi_0 \ln (\xi_0/r)}{2 \left( 1 - \frac{2[1 + \ln (\xi_0/r)]}{\frac{k}{f} \xi_0 x_1 \ln (\xi_0/r)} \right)}. \tag{59.24}$$

Comparing (59.24) with the previously used formula (for $\delta \ll \xi_0$)

$$\delta_{\text{m}} = \left( \frac{I_0}{I_1} - 1 \right) \frac{\xi_0}{2} \ln \frac{\xi_0}{r}, \tag{59.25}$$

we obtain an expression for the relative measurement error

$$\kappa = \frac{\delta_{\text{tr}} - \delta_{\text{m}}}{\delta_{\text{tr}}} = \frac{2[1 + \ln (\xi_0/r)]}{\frac{k}{f} \xi_0 x_1 \ln (\xi_0/r)}. \tag{59.26}$$

Let us estimate the numerical value of the error. For $\xi_0 = 0.1$ mm, $r = 10$ mm, $\lambda f = 1\ \text{mm}^2$, $x = 50$ mm, we have $\kappa = 0.05$. Thus if the break in the wave front (a sharp optical inhomogeneity) is located at a distance larger than 50 mm, the error in the determination of the angle of deviation near the edge will not exceed 5% even with the most unfavorable arrangement of the diffraction peaks.

The sensitivity of the method is

$$S_{\text{d}} = \frac{\gamma\, dI}{I\, d\varepsilon} = \frac{2f\gamma}{\xi_0 \ln (\xi_0/r)}. \tag{59.27}$$

Let us compare the sensitivities of the diffraction method and the photometric knife-edge and slit method. For the knife-edge and slit method

$$S_{\text{k}} = \frac{\gamma f}{\xi_0}. \tag{59.28}$$

Dividing (59.28) by (59.27), we get

$$\frac{S_{\text{k}}}{S_{\text{d}}} = \frac{\ln (\xi_0/r)}{2}. \tag{59.29}$$

For

$$\xi_0 = \frac{r}{7.5}, \tag{59.30}$$

the sensitivities are equal. For small light deviation angles, which must be measured with smaller $\xi_0$ than those given by (59.30), the diffraction method is less sensitive than the photometric method; due to the logarithmic relationship, this relative drop in sensitivity is small. Thus, for $r/\xi_0 = 10^3$, we have $S_{\text{k}}/S_{\text{d}} = 3.5$, i.e., the diffraction method is only 3.5 times less sensitive even for infinitesimal deviation angles.

In practical measurements, the knife-edge is set so as to view with maximum clarity certain regions of the inhomogeneity. The opaque edge is not necessarily parallel to the knife-edge. Furthermore, the edge is frequently of a complex shape, and measurements should be conducted at points of the image located at different parts of the edge. In this case, the diffraction pattern is determined by the parameters of the viewing diaphragm in the direction perpendicular to the portion studied complex body shapes such that the diffraction patterns from different parts of the opaque edge interact are not considered).

The same formula for the illumination distribution holds if we use a slit source, and the diaphragm is a knife-edge or a slit. However, the distances between the slit image and the diaphragm edges are multiplied by a factor of $1/\cos \alpha$. Since $r$ and $\xi_0$ multiplied by the same factor, the final formulas of the diffraction method remain the same: the illumination peak does not change. Such will be the situation until the inclination of the opaque edge to the knife-edge becomes such that the perpendicular to the edge drawn from some point of the light source image does not pass through the rectangular zone of the slit diaphragm. Starting with this inclination angle, the illumination peak begins to decrease, vanishing when this perpendicular no longer intersects the viewing diaphragm aperture.

Experiments corroborate these conclusions. The theoretical illumination distribution in the diffraction peak is plotted in Figure 146 as a function of the angle between the opaque edge and the slit. The experimental points are seen to agree with the theory. The small differences at the two ends are attributed to the averaging of the optical density during the photometric analysis.

However, although the illumination at the central diffraction peak is the same for edges parallel to the knife and those making a certain angle with it, this is not so for the other points of the diffraction pattern. The diffraction peak width decreases with the increase of $r$ and $\xi_0$, i.e., as the inclination angles of the opaque edge to the knife increases.

To determine the influence of the viewing diaphragm edge at $\xi = r$ on the measurement of the illumination at the central peak, we write the expression for

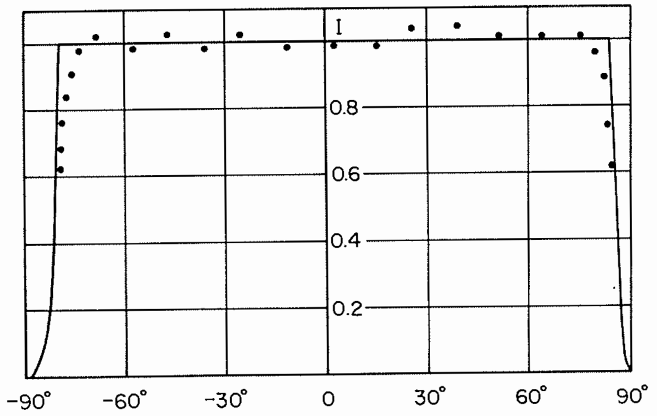

Figure 146

Theoretical distribution of the illumination in the diffraction peak at the opaque edge and experimental points.

the illumination distribution near the opaque edge when the slit image is covered by the knife in the form

$$I = \left[\operatorname{Si} a - \operatorname{Si}\frac{a}{\chi}\right]^2 + \left[\operatorname{Ci} a - \operatorname{Ci}\frac{a}{\chi}\right]^2, \qquad (59.31)$$

where

$$a = \frac{k}{f}\,rx', \qquad \chi = \frac{r}{\xi_0}.$$

Only the scale of the diffraction pattern depends on $a$, while the shape of the pattern is determined by the parameter $\chi$.

Figure 147 plots curves of the illumination distribution for different values of the parameter $\chi$. These curves describe the entire variety of patterns which can be obtained for different values of $r$ and $\xi_0$.

These curves give the half-width of the diffraction peak as a function of the parameter $\chi$ (Figure 148). The half-width is large for small $\chi$ and decreases with the increase of $\chi$; starting with $\chi = 10$, it remains constant.

During the photometry of the diffraction peak, the microphotometer slit covers a finite area of the image. This results in an averaging of the optical density. The limitations of the resolving power caused by the emulsion grain size and the aberrations of the main and the photographic objectives lead to the same effect. In order to keep the error within acceptable limits, the microphotometer slit and the quantities $1/R_a$ and $1/R_{ph}$ (see pp. 244–245) must be considerably smaller than the half-width of the peak. The particular values are determined by the allowed error and

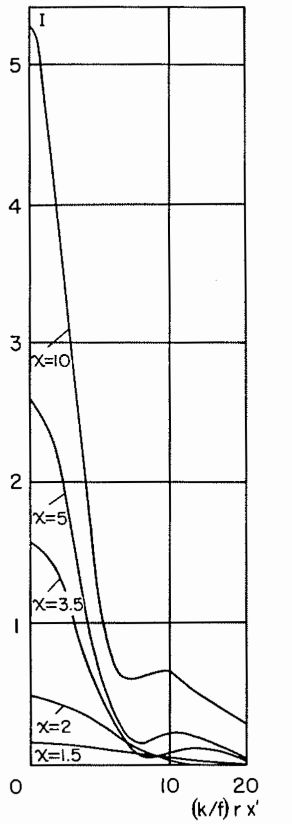

Figure 147

Illumination distribution in the diffraction peak for different values of $\chi$.

the shape of the illumination distribution curve. They can be obtained from the curves of Figure 148, which shows the size of the averaging zone for errors of 3% and 10%.

Using these curves, we can choose the experimental conditions in such a way that the measurement sensitivity is sufficiently high, while the averaging error does not exceed some specified value.

Consider now the case when the knife-edge does not cover the slit image. In this case equation (59.3) does not have a solution at the point $x' = 0$, but it is satisfied in a number of other points. The diffraction pattern represents a system of bands parallel to the opaque edge.

The graphic solution of (59.5), represented in Figure 142, shows that the first

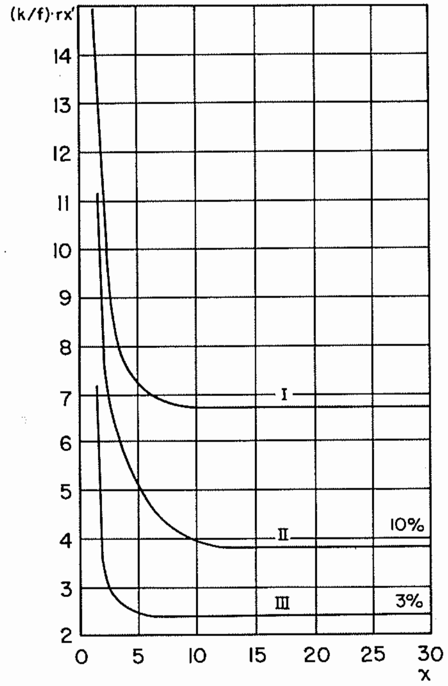

Figure 148

Half-width of the diffraction peak (I) and size of the averaging zone for errors of 10% and 3% (II and III) in units of $(k/f)r$.

peak is located at the point satisfying the condition

$$\frac{k}{f}\, x'\xi_0 = 0.204\,. \tag{59.32}$$

Since the ordinates of the curve which plots the right-hand side of equation (59.5) for $p > 0$ are small, it meets the curves $a$ near the points of intersection of the tangent curves with the abscissa axis, i.e., for

$$\frac{k}{f}\, x'\xi_0 = n\pi\,, \tag{59.33}$$

where $n = 1, 2, 3, \ldots$ the accuracy of equality (59.33) improves with the increase of $n$.

Thus if the knife-edge does not cover the slit image, the diffraction pattern constitutes a system of diffraction bands, where position depends on the distance between the knife-edge and the slit image. Having found the position of the diffraction maxima and minima in the image of the opaque edge, we can determine the angle of light deviation in the inhomogeneity (or the displacement of the slit image due to the inhomogeneity).

The deviation angle is related to the position of the first diffraction maximum by the equality

$$\varepsilon = \frac{0.204\,(x_2 - x_1)}{k x_2 x_1}\,, \tag{59.34}$$

where $x_2$ and $x_1$ are the distances from the first maximum to the opaque edge on the photographs taken before and after the introduction of the inhomogeneity.

This method is little used, since the displacement of the first peak is small and is therefore measured with a large error. It is more convenient to measure the deviation angle from the change in the distance $l$ between the first and second peaks:

$$\frac{k}{f}\, l\xi_0 = 2.9\,, \tag{59.35}$$

whence

$$\varepsilon = \frac{2.9}{k}\left(\frac{1}{l_0} - \frac{1}{l_1}\right), \tag{59.36}$$

where $l_0$ and $l_1$ are the distances between peaks on the "zero" and the working photographs. In practical work it is convenient to write (59.36) in the form

$$\varepsilon = 0.46\lambda\,\frac{l_1 - l_0}{l_1 l_0}\,. \tag{59.37}$$

Note that in this case the light intensity in each of the extrema is independent of the knife-edge position relative to the slit image. When the knife is displaced, the maxima and minima shift with respect to the opaque edge: they approach one another when the knife is moved away from the slit and recede when it is moved closer. The light intensity in each of the peaks remains constant.

The upper measurement limit is attained when the peaks become so narrow that they are not resolved by the instrument (from the diffraction point of view, the peaks are always resolvable for a thin monochromatic light source, and restrictions are imposed only by abberations and the emulsion). If we take the IAB-451 instrument with a photograph diameter of 24 mm, the resolving power (see Table 6) will be 3 lines/mm. The peaks are resolved if the spacing between them is not less than $\frac{1}{3}$ mm. We find from (59.35) that this spacing corresponds roughly to $\xi_0 = 1.5$ mm.

The lower limit is attained when the peaks become blurred and poorly distinguishable. Furthermore, for small $\xi_0$, the diffraction from the second edge of the diaphragm affects the pattern. This limit is attained roughly for $l = 15$ mm, whence $\xi_0 = 0.03$ mm. This range ($0.03\text{ mm} < \xi_0 < 1.5\text{ mm}$) can be considered as the range of this method.

The sensitivity of the method is the derivative of the displacement of the diffraction peaks with respect to the light deviation angle in the inhomogeneity:

$$S = \frac{dl}{d\varepsilon}. \tag{59.38}$$

Substituting (59.35) and (59.36) in (59.38), we get

$$S = \frac{\mu f}{\xi_0}, \tag{59.39}$$

where $\mu$ is the image scale.

The method described was tested, as in the preceding case, by photographing and measuring the diffraction patterns obtained from diaphragms with a straight edge; the only difference was that, instead of covering the slit image, the knife was set a certain distance from it. The resulting series of photographs are shown in Figure 143, *a–i*. The diffraction peaks at the opaque edge are clearly visible. The nearer the knife to the slit image, the smaller is the spacing between peaks.

Using (59.33), we can easily derive the inclination of the wave front from the position of any of the maxima or minima relative to the opaque edge or to another maximum or minimum.

The inclination of the wave front in the photographs of Figure 143 (or, equivalently, the distance between the knife-edge and the slit image) was calculated by (59.33) after the position of the first three minima ($x_1$, $x_2$, $x_3$) had been measured. The results of the measurements ($\xi_1$, $\xi_2$, $\xi_3$) were compared with the true position of the knife-edge relative to the slit image $\xi_0$. The values obtained are summarized in Table 10. We see that the measurement accuracy is between 1 and 20% in the entire range of knife-edge positions relative to the slit image ($0.05 < |\xi_0| < 1.08$). The error increases at the two ends of the range. For large $\xi_0$, it is determined by the inaccuracy in measuring the small distance between the minimum being measured and the opaque edge. For small $\xi_0$, measurements in the second and the third minima are impossible. The relative error in $\xi_0$ increases due to the blurred character of the maxima and the minima, and their position is very difficult to determine exactly.

Table 10

| $\xi_0$ | $x_1/\mu$ | $x_2/\mu$ | $x_3/\mu$ | $\xi_1$ | $\xi_2$ | $\xi_3$ | $\Delta\xi_{av}$ |
|---|---|---|---|---|---|---|---|
| −1.08 | 1.1 | 2.1 | 3.1 | −1.05 | −1.10 | −1.11 | ±0.03 |
| −0.88 | 1.3 | 2.6 | 4.0 | −0.89 | −0.89 | −0.88 | ±0.01 |
| −0.68 | 1.6 | 3.5 | 5.5 | −0.72 | −0.66 | −0.63 | ±0.04 |
| −0.48 | 2.2 | 4.8 | 7.5 | −0.52 | −0.48 | −0.46 | ±0.02 |
| −0.38 | 2.9 | 5.8 | 9.2 | −0.4 | −0.40 | −0.38 | ±0.01 |
| −0.28 | 3.8 | 8.0 | 12.5 | −0.03 | −0.29 | −0.27 | ±0.01 |
| −0.23 | 5.0 | 10 | 15.5 | −0.23 | −0.23 | −0.22 | ±0.01 |
| −0.18 | 6.0 | 12.2 | 20.0 | −0.19 | −0.19 | −0.17 | ±0.01 |
| −0.12 | 10.5 | 20 | 29 | −0.11 | −0.11 | −0.12 | ±0.01 |
| −0.09 | 11.5 | 26 | — | −0.10 | −0.09 |  | ±0.005 |
| −0.06 | 17.5 | 38 | — | −0.07 | −0.06 | — | ±0.005 |
| −0.05 | 20 | — | — | −0.06 | — | — | ±0.01 |

The measurement accuracy can be increased by using pen-and-ink recorders.

The values obtained agree well with the theoretical results; it follows that the above formulas are correct and can be used in practical work with schlieren instruments.

The methods described are applicable only when studying the angle of inclination of a plane wave front. If the wave front has a more complex structure, the methods can be used for studying almost plane sections, but in this case we must allow for possible errors due to the wave front curvature. In order to study complex inhomogeneities, we must develop methods for calculating the front shape from the parameters of the diffraction pattern, starting with quadratic-function fronts.

## 60. MEASUREMENT OF THE DISCONTINUITY OF A PLANE WAVE

In the study of optical inhomogeneities, we often deal with two-dimensional objects whose parameters are constant in one direction, i.e., with plane inhomogeneities. It is convenient to align the optical axis of the schlieren instrument in this direction, since this simplifies the mathematical processing of the results. Typical examples of such objects are the phase plates for phase-contrast microscopes and flow around wedge-shaped objects, wing profiles, and turbine blades.

When a plane model is immersed in a supersonic flow, a plane compression shock (a zone of a sharp variation of the parameters) forms near its surface. According to the geometrical theory of schlieren instruments, the image of this inhomogeneity is a narrow band, whose width is determined by the shock wave width and the instrumental image scale. However, the phase discontinuity width is small. In gas-dynamic measurements, it is equal to several free paths of the gas molecules in the flow and is generally much smaller than 0.1 mm. The width of the phase discontinuity in phase plates is of the same order of magnitude. Therefore, the width of the image of such objects lies far beyond the resolving power of the instrument, and plane phase discontinuities ought to be inaccessible to observation by schlieren instruments. This conclusion is inconsistent with the experimental results: plane discontinuities are clearly visible on schlieren photographs. The reason for this is to be sought in the wave nature of light.

The visibility of plane phase discontinuities is mainly determined by diffraction phenomena, and therefore the discontinuity parameters (the location or the additional path difference) can be determined only by analyzing and measuring the diffraction pattern on the schlieren photograph.

We shall now outline the main features of the method described in [13, 14, 19] for determining the intensity of the compression shock.

To calculate the illumination distribution, consider a wave front in the object plane, with a discontinuity at the point $x = x_0$ (Figure 149). The optical path difference between the parts of the wave front corresponding to $x < x_0$ and $x > x_0$, expressed in wavelengths, is equal to $\delta$. The object plane diaphragm is an infinitely long slit parallel to the $y$ axis, with edges at $x = R$ and $x = -R$. The light source is a luminous point. The focal plane diaphragm is a Foucault knife-edge — a slit diaphragm with edges at $\xi = \xi_0$ and $\xi = r_0$.

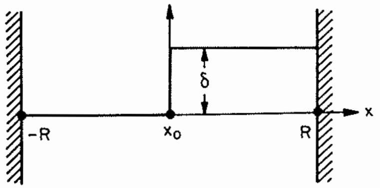

Figure 149

Wave front with a discontinuity at point $x_0$.

The illumination distribution in the image plane of the schlieren instrument is expressed by the formula [19]

$$\begin{aligned} I(x') = C^2 \Bigg\{ \Bigg[ & \mathrm{Ci}\,\frac{k}{f}(-R + x')r - \mathrm{Ci}\,\frac{k}{f}(-x_0 + x')r - \\ & - \mathrm{Ci}\,\frac{k}{f}(-R + x')\xi_0 + \mathrm{Ci}\,\frac{k}{f}(-x_0 + x')\xi_0 + \\ & + \cos\delta \Bigg( \mathrm{Ci}\,\frac{k}{f}(-x_0 + x')r - \mathrm{Ci}\,\frac{k}{f}(-x_0 + x')\xi_0 - \\ & - \mathrm{Ci}\,\frac{k}{f}(R + x')r + \mathrm{Ci}\,\frac{k}{f}(R + x')\xi_0 \Bigg) - \sin\delta \Bigg( \mathrm{Si}\,\frac{k}{f}(-x_0 + x')r - \\ & - \mathrm{Si}\,\frac{k}{f}(-x_0 + x')\xi_0 - \mathrm{Si}\,\frac{k}{f}(R + x')r + \mathrm{Si}\,\frac{k}{f}(R + x')\xi_0 \Bigg) \Bigg]^2 + \\ & + \Bigg[ \mathrm{Si}\,\frac{k}{f}(-R + x')r + \mathrm{Si}\,\frac{k}{f}(-x_0 + x')\xi_0 - \mathrm{Si}\,\frac{k}{f}(-R + x')\xi_0 + \\ & + \mathrm{Si}\,\frac{k}{f}(-x_0 + x')\xi_0 + \sin\delta \Bigg( \mathrm{Ci}\,\frac{k}{f}(-x_0 + x')r - \end{aligned}$$

$$\begin{aligned} & - \mathrm{Ci}\,\frac{k}{f}(-x_0 + x')\xi_0 - \mathrm{Ci}\,\frac{k}{f}(R + x')r + \mathrm{Ci}\,\frac{k}{f}(R + x')\xi_0 \Bigg) + \\ & + \cos\delta \Bigg( \mathrm{Si}\,\frac{k}{f}(-x_0 + x')r - \mathrm{Si}\,\frac{k}{f}\Big(-x_0 + x'\Big)\xi_0 - \\ & - \mathrm{Si}\,\frac{k}{f}(R + x')r + \mathrm{Si}\,\frac{k}{f}(R + x')\xi_0 \Bigg) \Bigg]^2 \Bigg\}. \end{aligned} \tag{60.1}$$

Assuming that the diaphragm edges $R$ and $-R$ are sufficiently far from the shock, and neglecting their influence on the illumination distribution for points near the image of the wave front discontinuity, we find (moving the origin of coordinates to $x = x_0$)

$$\begin{aligned} I(x') = 2C^2 \Bigg\{ & (1 - \cos\delta) \Bigg( \mathrm{Ci}\,\frac{k}{f}\,x'r - \mathrm{Ci}\,\frac{k}{f}\,x'\xi_0 \Bigg)^2 + \\ & + (1 - \cos\delta) \Bigg( \mathrm{Si}\,\frac{k}{f}\,x'r - \mathrm{Si}\,\frac{k}{f}\,x'\xi_0 \Bigg)^2 + (1 + \cos\delta) \begin{pmatrix} 0 \\ -\pi \end{pmatrix}^2 + \\ & + 2\sin\delta \begin{pmatrix} 0 \\ \pi \end{pmatrix} \Bigg( \mathrm{Ci}\,\frac{k}{f}\,x'r - \mathrm{Ci}\,\frac{k}{f}\,x'\xi_0 \Bigg) \Bigg\}. \end{aligned} \tag{60.2}$$

The top terms in parentheses correspond to $\xi_0 > 0$, the bottom terms to $\xi_0 < 0$.

The examination of (60.2) shows that the illumination distribution is symmetrical about the intended position of the discontinuity image according to geometrical optics. The illumination peak is always located at the center of the diffraction pattern. The symmetry is essential for finding the true position of the discontinuity.

The symmetry of the diffraction pattern of a phase discontinuity clearly distinguishes it from the pattern obtained at an opaque edge.

Let us consider the illumination distribution at points near the image of the wave front discontinuity [19].

The illumination of the central peak is obtained by substituting $x' = 0$ in (60.2):

$$I(0) = 4C^2 \left[ \sin\tfrac{1}{2}\delta \ln(r/\xi_0) + \begin{pmatrix} 0 \\ -\pi \end{pmatrix} \cos\tfrac{1}{2}\delta \right]^2. \tag{60.3}$$

Equation (60.3) suggests two methods of determination of the optical path increment (the discontinuity intensity) from the measurement of $I(0)$. The first is based on the comparison of the emulsion density on the "zero" and the working photographs at points corresponding to the position of the discontinuity [13].

In the absence of a compression shock, the image plane illumination is equal to (for $\xi_0 < 0$ and without allowing for the influence of the field boundaries)

$$I_z(0) = 4\pi^2 C^2. \tag{60.4}$$

The difference between the densities of the field points on the "zero" and the working photographs corresponding to the position of the geometrical image of the shock is determined by the formula

$$\frac{D - D_0}{\gamma} = \log \frac{I(0)}{I_z(0)}, \tag{60.5}$$

where $D$ and $D_0$ are the optical densities of the measured field point on the "zero" and the working photographs. By combining (60.4), (60.5), and (60.3) we obtain

$$\sin \frac{\delta}{2} = \frac{A \ln (r/\xi_0) - \binom{0}{\pi} \sqrt{\binom{0}{\pi}^2 + \ln^2 (r/\xi_0) - A^2}}{-\binom{0}{\pi^2} + \ln^2 (r/\xi_0)}, \tag{60.6}$$

where

$$A = \pi \cdot 10^{(D - D_0)/2\gamma} \tag{60.7}$$

If $\xi_0 > 0$ in the working position, and $\xi_0 < 0$ for the comparison photograph, then

$$\sin \frac{\delta}{2} = \frac{A}{\ln (r/\xi_0)}. \tag{60.8}$$

If the knife-edge completely covers the slit image in the working position, we can use another method, comparing the illumination peak at the compression shock with the illumination peak at the opaque edge (with both diffraction patterns obtained for the same instrument sensitivity).

If the experimental conditions permit and the image illumination is uniform over the entire instrument field, we can compare peaks on the same photograph. However, this comparison method is insufficiently accurate. It is therefore advisable to take an additional "zero" photograph, in which the opaque edge is placed at roughly the same place where the wave front discontinuity should be.

The additional path difference introduced by the discontinuity is determined from the relation

$$\frac{I}{I_1} = 4 \sin^2 \frac{\delta}{2}, \tag{60.9}$$

where $I$ and $I_1$ are the illuminations of the peaks located at the wave discontinuity and at the opaque edge. From (60.9) and (60.5) we get

$$\sin \frac{\delta}{2} = \frac{10^{(D - D_0)/2\gamma}}{2}. \tag{60.10}$$

The sensitivity of the method is

$$S = \frac{dD}{d\delta} = \frac{\gamma \ln (r/\xi_0)}{\pi}. \tag{60.11}$$

For $r = 10$ mm, $\xi_0 = 0.1$ mm, $\gamma = 2$, the sensitivity $S = 3$. This means that, for a difference of 0.03 in the measured optical densities, we can determine the magnitude of a plane discontinuity in a wave front which increments the optical path by $10^{-2}\lambda$ compared to that in the undisturbed space.

Consider the illumination distribution in the diffraction pattern outside the geometrical position of the compression shock. We can neglect the effect of the second edge of the focal plane diaphragm at $\xi_0 = r$; equation (60.1) reduces then to

$$I(x') = 2C^2 \left\{ (1 - \cos \delta) \operatorname{Ci}^2 \frac{k}{f} x'\xi_0 + (1 - \cos \delta) \left[ (\tfrac{1}{2}\pi, - \tfrac{1}{2}\pi) - \operatorname{Si} \frac{k}{f} x'\xi_0 \right]^2 + \binom{0}{-\pi}^2 (1 + \cos \delta) - 2 \binom{0}{-\pi} \sin \delta \operatorname{Ci} \frac{k}{f} x'\xi_0 \right\}. \tag{60.12}$$

The first of the two terms in the parenthetical row in (60.12) corresponds to positive values of $x'$, and the second term to negative values.

The position of the extrema is obtained by equating to zero the derivative of (60.12) with respect to $x'$; we get

$$\tan \frac{\delta}{2} = \frac{\binom{0}{-\pi}}{\operatorname{Ci} \frac{k}{f} x'\xi_0 - \left[ (\tfrac{1}{2}\pi, - \tfrac{1}{2}\pi) - \operatorname{Si} \frac{k}{f} x'\xi_0 \right] \tan \frac{k}{f} x'\xi_0}. \tag{60.13}$$

For $\xi_0 > 0$, the position of the extrema is independent of the shock intensity, and is given by the equality

$$\operatorname{Ci} \frac{k}{f} x'\xi_0 = \left[ (\tfrac{1}{2}\pi, - \tfrac{1}{2}\pi) - \operatorname{Si} \frac{k}{f} x'\xi_0 \right] \tan \frac{k}{f} x'\xi_0. \tag{60.14}$$

As we saw in the preceding section, this equation does not have a solution in the whole range of $x'$. Thus, in the case of a completely covered slit, we have a single intensity peak, coinciding with the location of the geometrical image of the plane wave-front discontinuity. Its illumination is determined from (60.3).

If the slit image is not covered by the knife-edge, the position of the extrema is determined from the equality

$$\tan \frac{\delta}{2} = \frac{-\pi}{\operatorname{Ci} \frac{k}{f} x'\xi_0 - \left[ (\tfrac{1}{2}\pi, - \tfrac{1}{2}\pi) - \operatorname{Si} \frac{k}{f} x'\xi_0 \right] \tan \frac{k}{f} x'\xi_0}. \tag{60.15}$$

Using (60.15), we can find the optical path increment in the compression shock from the position of the diffraction peaks.

As an illustration of these methods, consider the diffraction patterns obtained with the Soviet-made IAB-451 instrument (Figure 150) [14]. The light source was a narrow slit (0.02 mm) illuminated by a cineprojector lamp with a light filter having a transmission maximum in the vicinity of 6000 Å. The objects were glass plates sprayed with phase-layer coatings, introducing an additional path difference of $\lambda/2$ and $\lambda/4$.

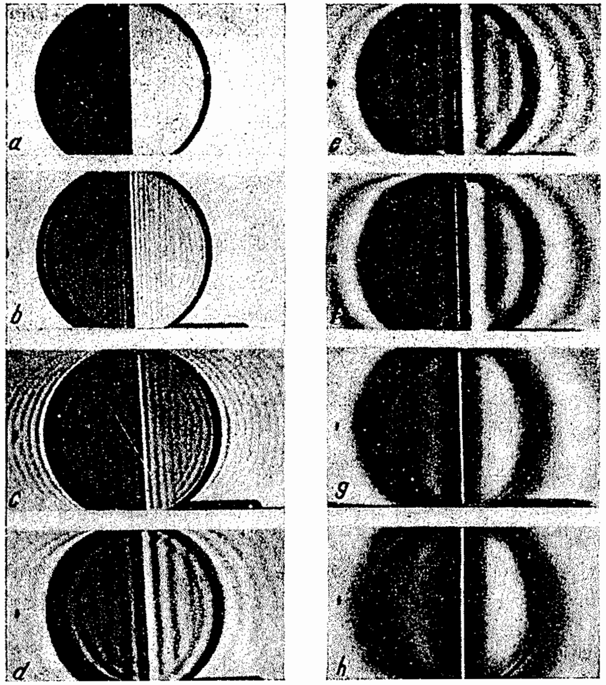

Figure 150
Diffraction photographs of a discontinuity in a plane wave front with the knife-edge gradually moved toward the illuminating slit image.

We see from the photographs that the results are in complete qualitative agreement with the theoretical conclusions. In each of the series of photographs for $\xi_0 < 0$ (completely uncovered slit), the diffraction pattern represents a system of bands, symmetrical about the position of the geometrical image of the shock. As expected, the illumination peak is always located at the center of the pattern. The distance between the diffraction peaks increases with the decrease in the distance from the knife-edge to the source image; the peaks become broader and fill a larger part of the field. The most complex phenomena take place when the knife-edge starts to cover the slit image. Inaccuracies in the manufacture of the plates begin to be felt then. The diffraction from the plate edges also has a strong effect. Therefore, in this zone ($-0.04$ mm $< \xi_0 <$ 0.02 mm), the pattern is too complex for theoretical interpretation (in particular if we take into account the complexity of the wave fronts in real optical inhomogeneities) and cannot be used in practical measurements.

When the knife-edge covers completely the slit image, the diffraction pattern is radically different. There is only one light maximum, located at the place of the shock image. Its intensity drops with the increase of the absolute value of $\xi_0$.

However, the qualitative fit is insufficient for quantitative application of the diffraction methods.

The first stage of the quantitative processing consists in measuring the distances of the illumination maxima and minima to the center of symmetry of the pattern.

The additional path difference can be determined from the position of the diffraction peaks if the product $\xi_0 x_i$ ($x_i$ is the distance from the $i$-th extremum to the axis of symmetry) is constant for each series of photographs and satisfies equation (60.15). The measurement results are summarized in Table 11. Here $x_1$ and $x_2$ are the distances corresponding to the position of the first minimum and the first maximum. The products $\xi_0 x_1$ and $\xi_0 x_2$ appear at a first glance to be fairly constant. A more comprehensive examination, however, leads to the conclusion that the difference between the mean values for the different series falls within the margin of measurement error. A relatively small error in the measurement of the position of the diffraction extrema leads to a large error in the determination of $\delta$. It follows that in order to measure reliably the intensity of a plane compression shock from the position of the maxima and minima, we have to alter the experimental technique and substantially increase the accuracy with which the distances are measured. This method cannot be used in practice at this stage.

To check the applicability of the second group of methods, the maxima were analyzed photometrically keeping the slit image covered. The results are represented in Figure 151. The solid curve is theoretical, and the dots represent the measurement results. The theoretical and experimental values of the additional path difference in the comparison shock are seen to agree satisfactorily. The measurement accuracy

Table 11

| $\xi_0$ | $x_1$ | $x_2$ | $\lvert\xi_0 x_1\rvert$ | $\lvert\xi_0 x_2\rvert$ |
|---|---|---|---|---|
| −0.94 | 0.35 | 0.7 | 0.33 | 0.66 |
| −0.49 | 0.45 | 1.25 | 0.22 | 0.61 |
| −0.39 | 0.5 | 1.5 | 0.20 | 0.59 |
| −0.29 | 0.6 | 1.9 | 0.17 | 0.55 |
| −0.21 | 0.85 | 2.5 | 0.18 | 0.53 |
| −0.12 | 1.4 | 3.7 | 0.18 | 0.45 |
| −0.07 | 1.6 | 5.5 | 0.11 | 0.39 |
|  | Average |  | 0.20 ± 0.04 | 0.54 ± 0.07 |

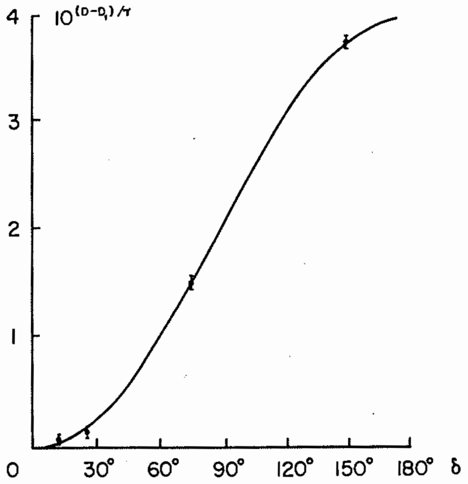

Figure 151
Results of the photometry of diffraction peaks.

for a quarter-wavelength phase plate is equal to $\pm\ \lambda/300$, which is quite satisfactory for most measurements. The measurement error increases in the case of half-wavelength phase plates, since large changes of the wave phase are accompanied by only small changes of the peak illumination.

We must emphasize one characteristic feature of the diffraction methods for determining the intensity of a plane wave-front discontinuity. The additional path difference figures in all the expressions as $\cos\delta$ or $\sin\delta$, which are functions of period $2\pi$. Therefore, compression shocks which produce optical path increments differing by a whole number of wavelengths have diffraction patterns with the same illumination distribution.

The measurement range of the diffraction methods lies within the limits of $\lambda/2$. Consequently, these methods are suitable only for measuring weak shocks, which introduce an additional path difference not larger than $\lambda/2$. In the study of strong compression shocks ($\delta > \lambda/2$), they can be used to improve on the intensity value, measured with an accuracy of $\lambda/2$ by some other method (in gas dynamics, for instance, from the angle of inclination of the adjacent compression shock).

When these methods are used in practice, the experimental conditions do not always fully correspond to the ideal mathematical model. Thus, it is very difficult to align an extended phase discontinuity strictly parallel to the optical axis of the instrument. Small deviations from the ideal model are inevitable. Furthermore, many wave-front discontinuities correspond only approximately to the rectangular phase coats for which the measurement method was created. The boundary of the

phase coats is not clear-cut. The gas-dynamic shocks near plane models are not exactly straight, either, since the flow velocity is not uniform over the wind tunnel section.

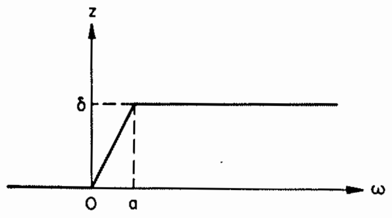

Figure 152
Wave front with an extended discontinuity.

Let us estimate the error which can be caused by this departure from the ideal model. Consider the diffraction pattern on the "extended" compression shock shown in Figure 152. As before, we assume that the instrument field is unbounded, and that the shock boundaries are parallel to the $y$ axis. The formula for the light disturbance in the image in this case is

$$S(x',y') = \frac{e^{i\omega\tau}C}{\lambda^2 f^2}\int_{-r}^{r}\left\{\int_{\xi_0}^{r}\left[\int_{-R}^{R}\left(\int_{-R}^{0}\exp\left\{\frac{ik}{f}\,\xi(x+x')\right\}dx + \right.\right.\right.$$
$$+\int_0^a \exp\left\{\frac{ik}{f}\,\xi(x+x') + \frac{ikx\delta}{a}\right\}dx +$$
$$\left.\left.\left.+\int_a^R \exp\left\{\frac{ik}{f}\,\xi(x+x') + ik\delta\right\}dx\right)dy\right]d\xi\right\}d\eta\,. \tag{60.16}$$

By integrating we get the following expression for the illumination distribution:

$$I(x') = C^2\left\{\left[-\operatorname{Ci}\frac{k}{f}\,\xi_0 x' - \cos\frac{k\delta x'}{a}\left[\operatorname{Ci}\frac{k}{f}\,(a+x')\left(\frac{\delta f}{a}+\xi_0\right) - \right.\right.\right.$$
$$\left.-\operatorname{Ci}\frac{k}{f}\,x'\left(\frac{\delta f}{a}+\xi_0\right)\right] - \sin\frac{k\delta x'}{a}\left(\operatorname{Si}\frac{k}{f}\,(a+x')\left(\frac{\delta f}{a}+\xi_0\right) - \right.$$
$$\left.-\operatorname{Si}\frac{kx'}{f}\left(\frac{\delta f}{a}+\xi_0\right)\right) + \cos k\delta\,\operatorname{Ci}\frac{k}{f}\,(x'+a)\,\xi_0 -$$
$$\left.-\sin k\delta\,\operatorname{Si}\frac{k}{f}\,(x'+a)\left(\frac{\delta f}{a}+\xi_0\right) + \sin k\delta\begin{pmatrix}\pi\\ \pi\\ 0\end{pmatrix} + \sin k\delta\left(\frac{\pi}{2},\,-\frac{\pi}{2}\right)\right]^2 +$$

$$+\left[\pm\frac{\pi}{2}-\operatorname{Si}\frac{k}{f}\xi_0x'+\frac{\pi}{2}+\left(-\frac{\pi}{2},+\frac{\pi}{2}\right)-\cos\frac{k\delta x'}{a}\operatorname{Si}\frac{k}{f}(a+x')\left(\frac{\delta f}{a}+\xi_0\right)+\right.$$

$$+\left(\pm\frac{\pi}{2}\right)\cos\frac{k\delta x'}{a}+\cos\frac{k\delta x'}{a}\operatorname{Si}\frac{k}{f}x'\left(\frac{\delta f}{a}+\xi_0\right)-\cos\frac{k\delta x'}{a}\left(\pm\frac{\pi}{2}\right)+$$

$$+\sin\frac{k\delta x'}{a}\operatorname{Ci}\frac{k}{f}(a+x')\left(\frac{\delta f}{a}+\xi_0\right)-\sin\frac{k\delta x'}{a}\operatorname{Ci}\frac{kx'}{f}\left(\frac{\delta f}{a}+\xi_0\right)+$$

$$+\cos k\delta\frac{\pi}{2}-\cos k\delta\left(+\frac{\pi}{2},-\frac{\pi}{2}\right)-\left(\pm\frac{\pi}{2}\right)\cos k\delta+$$

$$\left.+\cos k\delta\operatorname{Si}\frac{k}{f}(x'+a)\,\xi_0+\sin k\delta\operatorname{Ci}\frac{k}{f}(x'+a)\,\xi_0\right]^2\Bigg\}. \tag{60.17}$$

In deriving (60.17), we neglected the effect of the second edge of the viewing diaphragm, located at $\xi = r$. This is correct if we do not consider the illumination distribution in the immediate vicinity of the points $x = 0$ and $x = a$.

The illumination at the point $x' = a/2$ is equal to

$$I\left(\frac{a}{2}\right)=C^2\left\{\left(\operatorname{Ci}\frac{ka\xi_0}{2f}-\operatorname{Ci}\frac{kar}{2f}\right)^2 4\sin^2\frac{k\delta}{2}+\left[\operatorname{Si}\frac{k}{2f}(\delta f+a\xi_0)-\right.\right.$$

$$\left.-\operatorname{Si}\frac{k}{2f}(\delta f+ar)\right]^2\cdot 4+\left[\operatorname{Si}\frac{ka\xi_0}{2f}-\operatorname{Si}\frac{kar}{2f}\right]^2 4\cos^2\frac{k\delta}{2}-$$

$$-8\sin\frac{k\delta}{2}\left(\operatorname{Ci}\frac{ka\xi_0}{2f}-\operatorname{Ci}\frac{kar}{2}\right)\left[\operatorname{Si}\frac{k}{2f}(\delta f+a\xi_0)-\operatorname{Si}\frac{k}{2f}(\delta f+ar)\right]+$$

$$+8\sin\frac{k\delta}{2}\cos\frac{k\delta}{2}\left(\operatorname{Ci}\frac{ka\xi_0}{2f}-\operatorname{Ci}\frac{kar}{2f}\right)\left(\operatorname{Si}\frac{ka\xi_0}{2}-\operatorname{Si}\frac{kar}{2f}\right)-$$

$$\left.-8\cos\frac{k\delta}{2}\left[\operatorname{Si}\frac{k}{2f}(\delta f+a\xi_0)-\operatorname{Si}\frac{k}{2f}(\delta f+ar)\right]\left(\operatorname{Si}\frac{ka\xi_0}{2f}-\operatorname{Si}\frac{kar}{2f}\right)\right\}. \tag{60.18}$$

If $a$ is small, (60.18) can be transformed to

$$I\left(\frac{a}{2}\right)=4\sin^2\tfrac{1}{2}k\delta\ln^2(r/\xi_0)+$$

$$+\frac{ka(r-\xi_0)}{2f}\left[-8\sin\tfrac{1}{2}k\delta\ln(r/\xi_0)\frac{\sin\frac{1}{2}k\delta}{\frac{1}{2}k\delta}+8\sin\tfrac{1}{2}k\delta\cos\tfrac{1}{2}k\delta\ln(r/\xi_0)\right]+$$

$$+\left(\frac{ka}{2f}\right)^2\left[-2\sin^2\tfrac{1}{2}k\delta\ln(r/\xi_0)(r^2-\xi_0^2)+4\left(\cos\tfrac{1}{2}k\delta-\frac{\sin\frac{1}{2}k\delta}{\frac{1}{2}k\delta}\right)^2(r-\xi_0)^2-\right.$$

$$\left.-4\sin\tfrac{1}{2}k\delta\ln(r/\xi_0)\left(\frac{\cos\frac{1}{2}k\delta}{\frac{1}{2}k\delta}-\frac{\sin\frac{1}{2}k\delta}{(\frac{1}{2}k\delta)^2}\right)(r^2-\xi_0^2)\right]. \tag{60.19}$$

The illumination due to an extended shock can be represented as the illumination corresponding to a sudden unit-step shock with the same optical path difference plus some additional term. The extended shock can be regarded as ideal if the additional term is small compared to the leading term. The error in the determination of the shock intensity associated with the linear part of the additional term is given by the following expression:

$$\frac{d\delta_l}{\delta}=\frac{a(r-\xi_0)}{\delta f\ln(r/\xi_0)}\left(1-\frac{\tan\frac{1}{2}k\delta}{\frac{1}{2}k\delta}\right). \tag{60.20}$$

The error due to the quadratic term is equal to

$$\frac{d\delta_q}{\delta}=\frac{(ka)^2A}{\delta\cdot 4f^2 4k\sin\frac{1}{2}k\delta\cos\frac{1}{2}k\delta\ln^2(r/r_0)}, \tag{60.21}$$

where

$$A=-2\sin^2\tfrac{1}{2}k\delta\ln(r/\xi_0)(r^2-\xi_0^2)+4\left(\cos\tfrac{1}{2}k\delta-\frac{\sin\frac{1}{2}k\delta}{\frac{1}{2}k\delta}\right)(r-\xi_0)^2-$$

$$-4\sin\tfrac{1}{2}k\delta\ln(r/\xi_0)\left[\frac{\cos\frac{1}{2}k\delta}{\frac{1}{2}k\delta}-\frac{\sin\frac{1}{2}k\delta}{(\frac{1}{2}k\delta)^2}(r^2-\xi_0^2)\right].$$

Using (60.20) and (60.21), we can estimate the applicability of the diffraction method for different instrumental adjustment parameters and different values of the shock "width". We can also select the experimental conditions so that the error resulting from our approximation does not exceed some specified value.

A particular application of the diffraction method is described in [19]. The experiments were conducted in a shock tube. The model was a 60° wedge. The measurements were made with an IAB-451 schlieren instrument, using spark photography. The light source was synchronized to trigger the spark when the wedge was in the zone of uniform flow parameters (between the shock wave and the contact surface). Special filters transmitted the light from the source, blocking the gas glow in the instrument.

It was borne in mind when selecting the experimental conditions in the shock tube that the measurement was equal to $\lambda/2$. Figure 153 plots the theoretical values of the optical path difference in the compression shock at the wedge for a ray path of 10 mm in the inhomogeneity and various shock-tube operating conditions

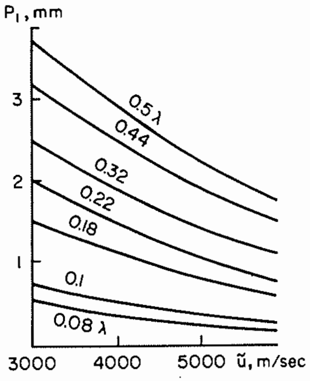

Figure 153

Range of application of the diffraction method in shock-tube measurements.

(different initial gas pressures $P_i$ and shock wave velocities $\tilde{u}$). Using the curves of Figure 153, we can select operating conditions and wedge sizes for which the shock wave strength will not exceed the measurement range.

A photograph obtained in the shock tube is shown in Figure 154. The shock wave is clearly seen in the field of view of the schlieren instrument (behind the wedge). The photographs were taken, as required, with narrow slits covered almost totally by the knife-edge. The photometry was made at the center of the diffraction peaks corresponding to the compression shock and the wedge edge. The measurement results are summarized in Table 12, together with the corresponding theoretical values. Here $\rho_0$ is the initial density of the gas, and $\rho_2/\rho_1$ is the compression shock strength. The experimental and theoretical values coincide within 15%.

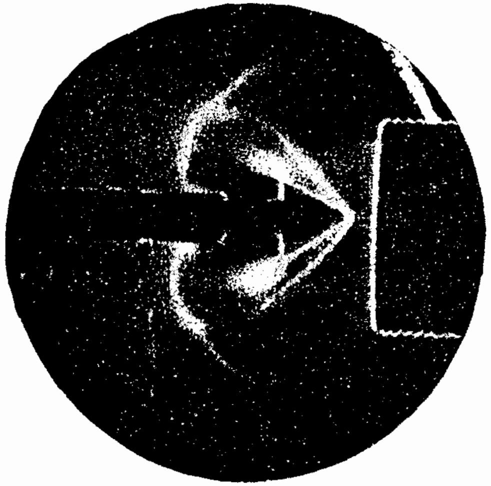

Figure 154

A schlieren photograph of shock waves at a wedge.

Table 12

| $\rho_0$, $10^{-6}$ g/cm$^3$ | $\tilde{u}$, m/sec | $\rho_2/\rho_1$ | $\delta_{ex}$ | $\delta_{th}$ |
|---|---|---|---|---|
| 0.75 | 3220 | 4.2 | 0.175λ | 0.17λ |
| 0.75 | 3300 | 4.0 | 0.167λ | 0.16λ |
| 0.75 | 4310 | 3.6 | 0.22λ | 0.26λ |
| 0.96 | 4060 | 3.8 | 0.33λ | 0.33λ |
| 0.75 | 4030 | 3.5 | 0.26λ | 0.29 |
| 0.75 | 4060 | 4.1 | 0.24λ | 0.21λ |

It was thus established that the method can be successfully used in the study of gas-dynamic flows with plane compression shocks and seems promising for the study of phenomena accompanying the propagation of shock waves.

The diffraction methods enables us to conduct schlieren studies of objects which have not been accessible to measurement before. They yield qualitatively new results and substantially broaden the scope of the schlieren technique.

## 61. DIFFRACTION SCHLIEREN INTERFEROMETER

When a narrow light source is used, and the viewing diaphragm is a thin filament, diffraction bands are reminiscent of the fringes in a two-beam interferometer. They can be employed for quantitative measurements; however, instead of the angle of light deviation, the quantitative analysis yields the path difference introduces by the inhomogeneity.

The use of a schlieren instrument in the interferometer mode considerably increases its potential and leads to substantial advantages: no additional integration is needed and, after all, schlieren instruments are much more common than the expensive interferometers.

As a result, numerous scientists have contributed to the development of the diffraction method [87]. Abrukov [1, 2] applied this method to the study of flames and gas jets. He obtained a satisfactory qualitative and quantitative agreement with the results obtained by other methods and with theoretical data.

The diffraction pattern is much more complex than the corresponding interference pattern. A splitting of the diffraction bands is frequently observed. The bands sometimes disappear when the instrument field is partially covered.

The basic features of these phenomena can be understood only from the point of view of diffraction effects. The first attempt in this direction was made in [128].

It was shown that for a certain class of inhomogeneities, the diffraction bands are indeed highly similar to the interference fringes. Many significant features of the phenomena, however, remained unexplained after this first analysis.

Let the object plane be made of two regions $\sigma_1$ and $\sigma_2$, with a common boundary described by the equation $x = \phi_2(y)$. The outer boundaries of $\sigma_1$ and $\sigma_2$ are described by the equations $x = \phi_1(y)$ and $x = \phi_3(y)$, respectively. The wave in region $\sigma_1$ is expressed by the function $P_1(x, y)$, and in region $\sigma_2$ by the function $P_2(x, y)$. A filament of width $2t$ parallel to the $\eta$ axis serves as a viewing diaphragm. The midpoint of the filament is at $\xi = \xi_1$.

The light disturbance in the image plane can thus be written

$$\begin{aligned}
S(x', y') &= \\
&= C\left\{\int_{-\infty}^{\infty}\int_{\phi_1(y)}^{\phi_2(y)}\int_{-\infty}^{\infty}\left[\int_{\xi_1+t}^{\infty}\exp\left\{\frac{ik}{f}[fP_1(x, y) + \xi(x + x') + \eta(y + y')]\right\}d\xi\,+\right.\right. \\
&\quad \left.+\int_{-\infty}^{\xi_1-t}\exp\left\{\frac{ik}{f}[fP_1(x, y) + \xi(x + x') + \eta(y + y')]\right\}d\xi\right]d\eta\,dx\,dy\,+ \\
&\quad +\int_{-\infty}^{\infty}\int_{\phi_2(y)}^{\phi_3(y)}\int_{-\infty}^{\infty}\left[\int_{\xi_1+t}^{\infty}\exp\left\{\frac{ik}{f}[fP_2(x, y) + \xi(x + x') + \eta(y + y')]\right\}d\xi\,+\right. \\
&\quad \left.\left.+\int_{-\infty}^{\xi_1-t}\exp\left\{\frac{ik}{f}[fP_2(x, y) + \xi(x + x') + \eta(y + y')]\right\}d\xi\right]d\eta\,dx\,dy\right\}.
\end{aligned} \tag{61.1}$$

Transforming the integrals in brackets, we obtain from (61.1):

$$\begin{aligned}
S(x', y') &= C\left\{\int_{-\infty}^{\infty}\int_{\phi_1(y)}^{\phi_2(y)}\int_{-\infty}^{\infty}\int_{-\infty}^{\infty}\exp\left\{\frac{ik}{f}[fP_1(x, y)\,+\right.\right. \\
&\quad \left.+\,\xi(x + x') + \eta(y + y')]\right\}d\xi\,d\eta\,dx\,dy\,+ \\
&\quad +\int_{-\infty}^{\infty}\int_{\phi_2(y)}^{\phi_3(y)}\int_{-\infty}^{\infty}\int_{-\infty}^{\infty}\exp\left\{\frac{ik}{f}[fP_2(x, y) + \xi(x + x') + \eta(y + y')]\right\}d\xi\,d\eta\,dx\,dy\,+ \\
&\quad +\int_{-\infty}^{\infty}\int_{\phi_1(y)}^{\phi_2(y)}\int_{-\infty}^{\infty}\int_{\xi_1-t}^{\xi_1+t}\exp\left\{\frac{ik}{f}[fP_1(x, y) + \xi(x + x') + \eta(y + y')]\right\}\times \\
&\quad \times\,d\xi\,d\eta\,dx\,dy - \int_{-\infty}^{\infty}\int_{\phi_2(y)}^{\phi_1(y)}\int_{-\infty}^{\infty}\int_{\xi_1-t}^{\xi_1+t}\exp\left\{\frac{ik}{f}[fP_2(x, y)\,+\right. \\
&\quad \left.\left.+\,\xi(x + x') + \eta(y + y')]\right\}d\xi\,d\eta\,dx\,dy\right\}.
\end{aligned} \tag{61.2}$$

The sum of the first two integrals gives the distribution of the light disturbance function in the image plane of the schlieren instrument when there is no screening diaphragm in the plane $\xi\eta$. It is equal to $C_1 e^{ikP_1(x_1' - y')}$ for image points corresponding to $\sigma_1$, and to $C_1 e^{ikP_2(x_1' - y')}$ for points of $\sigma_2$.

We denote by $I_1$ and $I_2$ the third and the fourth integral in (61.2). The basic condition of applicability of the method being described is

$$|I_1| \ll |I_2|. \tag{61.3}$$

Physically, this means that the filament screens much more strongly the light wave coming from $\sigma_2$ than the wave from $\sigma_1$. This condition is satisfied if the wave is plane in $\sigma_2$ and the focal-plane filament covers the image of the illuminating slit formed by rays from $\sigma_2$, without intercepting most of the rays from $\sigma_1$. The strictness of condition (61.3) and the technical means adapting this method virtually for all inhomogeneities will be described below.

Neglecting $I_1$, and writing $I_2$ in the form

$$I_2 = e^{-ikP_x x'}(a + bi), \tag{61.4}$$

we obtain an expression for the illumination in the image plane:

$$I(x', y') = 1 + a^2 + b^2 - 2a\cos kP_1(-x', -y') - 2b\sin kP_1(-x', -y'), \tag{61.5}$$

where

$$\begin{aligned}
a &= \frac{1}{2\pi}\left\{\mathrm{Si}\,\frac{k}{f}(t + P_x f)[\phi_2(-y') + x']\,-\right. \\
&\quad - \mathrm{Si}\,\frac{k}{f}(t + P_x f)[\phi_1(-y') + x'] + \mathrm{Si}\,\frac{k}{f}(t - P_x f)[\phi_2(-y') + x']\,- \\
&\quad \left.- \mathrm{Si}\,\frac{k}{f}(t - P_x f)[\phi_1(-y') + x']\right\},
\end{aligned} \tag{61.6}$$

$$\begin{aligned}
b &= \frac{1}{2\pi}\left\{-\mathrm{Ci}\,\frac{k}{f}(t + P_x f)[\phi_2(-y') + x']\,+\right. \\
&\quad + \mathrm{Ci}\,\frac{k}{f}(t + P_x f)[\phi_1(-y') + x'] + \mathrm{Ci}\,\frac{k}{f}(t - P_x' f)[\phi_2(-y') + x']\,- \\
&\quad \left.- \mathrm{Ci}\,\frac{k}{f}(t - P_x f)[\phi_1(-y') + x']\right\}.
\end{aligned} \tag{61.7}$$

Here the wave intensity in the absence of a diaphragm in the $\xi\eta$ plane is taken equal to one; the midpoint of the screening filament is placed at the origin ($\xi_1 = 0$).

Substantial simplifications are attained if the midpoint of the screening filament coincides with the midpoint of the diffraction image of the illuminating slit formed by the rays from $\sigma_2$. This is achieved when

$$P_x = \xi_1 = 0\,. \tag{61.8}$$

Then

$$a = \frac{1}{\pi}\left\{\mathrm{Si}\,\frac{k}{f}\,t[\phi_2(-y') + x'] - \mathrm{Si}\,\frac{k}{f}\,t[\phi_1(-y') + x']\right\}, \tag{61.9}$$

$$b = 0\,, \tag{61.10}$$

$$I(x', y') = 1 + a^2 - 2a\cos kP_1(-x', -y')\,. \tag{61.11}$$

Thus the light pattern formed in the image plane can be formally treated as the result of the interference of two waves: a free wave of constant unit amplitude and a wave of variable amplitude. The phase difference between the interfering waves is determined by the phase distribution function in region $\sigma_1$ of the object plane.

Let us establish in what parts of $\sigma_1$ the interference fringes are sufficiently distinct. Writing $H$ for the size of the comparison region in a given section $y =$ const and $l$ for the distance between the observation point and the common boundary of the two zones, we represent (61.9) in the form

$$a = \frac{1}{\pi}\,\mathrm{Si}\,2\pi\frac{t}{\lambda f}(l + H) - \frac{1}{\pi}\,\mathrm{Si}\,2\pi\frac{t}{\lambda f}\,l\,. \tag{61.12}$$

If $H$ is sufficiently large, we can write

$$a = \frac{1}{2} - \frac{1}{\pi}\,\mathrm{Si}\,2\pi\frac{t}{\lambda f}\,l\,. \tag{61.13}$$

The amplitude of the interfering wave coming from $\sigma_1$ thus depends only on the parameter $2\pi lt/\lambda f$.

Fringe visibility can be defined by the expression

$$K = \frac{I_{\max} - I_{\min}}{I_{\max} + I_{\min}}\,. \tag{61.14}$$

Assuming that $a$ changes negligibly between any minimum and the nearest peak of the fringe pattern, we get

$$K = \frac{2a}{1 + a^2}\,. \tag{61.15}$$

The fringe contrast is equal to 0.8 for small $l$, which corresponds to points near the boundary. The contrast vanishes for

$$l_0 = 0.31\,\frac{\lambda f}{t}, \tag{61.16}$$

then increases again, when band reversal is observed. If we take $\lambda = 5 \times 10^{-4}$ mm, $f = 2 \times 10^3$ mm, $2t = 4 \times 10^{-2}$ mm, the size of the region in which direct diffraction bands are still visible will be $l_0 = 15$ mm. A calculation of $H$ for which the size of the free field hardly affects the contrast and the arrangement of the bands shows that the comparison region can be made sufficiently narrow (Figure 155). It is definitely not a limiting factor in measurements.

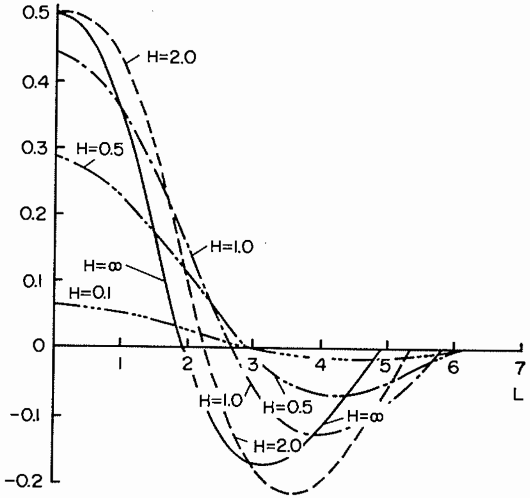

Figure 155

Estimating the width of the comparison region.

Were the value of $a$ constant over the entire field, the illumination peaks would fall exactly at the points corresponding to a change of $\lambda/2$ in the optical path. However, since $a$ is position-dependent, the light intensity maxima and minima will be located at somewhat different points.

Let us calculate this displacement. We assume that $a$ can be determined sufficiently accurately from (61.13), and that the integral sine in this expression can be replaced by the first term of the power-series expansion. We are considering a plane wave with an angle of inclination $\gamma$. Under these assumptions, the equation for the position of maxima and minima is

$$\left(\frac{1}{2} - \frac{2tl}{\lambda f}\right)\left(-\frac{2t}{\lambda f} + k\gamma\sin k\gamma l\right) + \frac{2t}{\lambda f}\cos k\gamma l = 0\,. \tag{61.17}$$

We introduce a new variable $y$, which is defined as the difference between the solution of (61.17) and the ideal position of the extrema:

$$y = l - \frac{n\lambda}{\gamma}\,. \tag{61.18}$$

Since $y$ is small, equation (61.17) can be transformed to an ordinary quadratic equation

$$y^2 - 2y\left(\frac{\lambda f}{8t} - \frac{\lambda n}{2t} + \frac{t}{\lambda f k^2 \gamma^2}\right) - \frac{2tn}{k^2\gamma^3 f} - \frac{1}{2k^2\gamma^2} = 0\,, \qquad (61.19)$$

which gives, after dropping several terms,

$$y = \frac{\lambda t(4tn + \gamma f)}{2\pi^2\gamma^2 f(\gamma f - 4tn)}. \qquad (61.20)$$

Since the principal parameter is the displacement, expressed in fractions of wavelength, it is convenient to rewrite (61.20) in the form

$$\frac{\Delta\lambda}{\lambda} = \frac{y\gamma}{\lambda} = \frac{\Pi(4\Pi n + 1)}{2\pi^2(1 - 4\Pi n)}, \qquad (61.21)$$

where $\Pi = t/\gamma f$ is a parameter which expresses the displacement of the light intensity extrema from the ideal position.

This method is not suitable for measuring inhomogeneities with $\gamma < 5 \times 10^{-5}$. For $f = 2 \times 10^3$ and $t = 2 \times 10^{-2}$, we get $\Pi = 0.2$, which even for $n = 20$ leads to an error equal roughly to a mere 0.01 $\lambda$. The error can increase substantially for extrema whose ordinal number satisfies the condition

$$\frac{4tn}{\gamma f} = 1\,. \qquad (61.22)$$

Thus the band shift from the ideal position is small and almost always lies within the margin of measurement error. We can therefore treat the diffraction pattern as if it were an ideal interference pattern.

If the field is made up of three regions, and not two as before, and the wave front shape in the middle region is described by the function $P(x, y)$, while in the two outside regions we have a plane wave, the expression for the light intensity will be

$$I(x', y') = 1 + (a_1 + a_3)^2 - 2(a_1 + a_3)\cos kP(-x', y')\,. \qquad (61.23)$$

It was assumed here, as above, that

$$|I_2| \ll |I_1|\,, \qquad (61.24)$$

$$|I_2| \ll |I_3|\,. \qquad (61.25)$$

The quantities $a_2$ and $a_3$ may have different signs. If they can be made positive, the second plane-wave region improves the visibility of the bands.

Frequently, the interfering fields in the object plane are not adjacent, being separated by an opaque space. All the formulas remain valid in this case, but the distance is measured from the boundary $x = \phi_2(-y)$ of the plane-wave zone.

The setting angle of the viewing filament is of great importance. An interference pattern will be observed at any point of the field only if the perpendicular to the viewing diaphragm drawn through this point intersects the plane-wave region. The distance $l$ and the widths of the regions $\sigma_1$ and $\sigma_2$, which affect the contrast of the interference fringes, also depend on the setting angle. They are measured in the direction perpendicular to the filament.

Furthermore, for a given function $P_1(x, y)$, $I_1$ depends on the filament setting angle. In certain directions, the rays from $\sigma_1$ create a diffraction pattern in the focal plane near the slit image formed by light from $\sigma_2$. Therefore, the filament cannot screen the slit image formed by the plane wave without altering the diffraction pattern from $\sigma_2$. As a result, for certain filament positions, the diffraction bands do not coincide with the interference fringes for some wave front shapes. It is advisable to place the filament so that the angle between the test section of the wave front and the plane comparison wave is sufficiently large.

In actual experiments, the source always has a finite width. We shall elucidate how this factor affects the diffraction pattern in the image plane. Consider two light sources, and let their images be symmetrical with respect to the filament centerline. The sources are not coherent. The light intensity in the image plane produced by each of the sources is

$$\begin{aligned} I^{(+)}(x', y') &= 1 + a^{(+)2} + b^{(+)2} - 2a^{(+)}\cos kP(-x', -y') - \\ &\qquad - 2b^{(+)}\sin kP(-x', -y'), \\ I^{(-)}(x', y') &= 1 + a^{(-)2} + b^{(-)2} - 2a^{(-)}\cos kP(-x', -y') - \\ &\qquad - 2b^{(-)}\sin kP(-x', -y')\,. \end{aligned} \qquad (61.26)$$

It follows from (61.6) and (61.7) that

$$a^{(+)} = a^{(-)}\,; \qquad b^{(+)} = -\,b^{(-)}. \qquad (61.27)$$

The total intensity is

$$J(x', y') = I^{(+)} + I^{(-)} = 2[1 + a^{(+)2} + b^{(+)2} - 2a^{(+)}\cos kP(-x', -y')]. \qquad (61.28)$$

It is seen from this result that the simultaneous action of two symmetrical light sources produces the same illumination distribution as a central point source. The only difference is a twice stronger intensity of the pattern. The interference pattern remains suitable for measurements.

The light intensity created in the image plane by an extended source of width $2\varepsilon_0$ which is symmetrical with respect to the viewing diaphragm is given by

$$J(x', y') = 2\left[\varepsilon_0 + \int_0^{\varepsilon_0} a^2\,d\varepsilon + \int_0^{\varepsilon_0} b^2\,d\varepsilon - 2\cos kP(-x', -y')\int_0^{\varepsilon_0} a\,d\varepsilon\right]. \qquad (61.29)$$

Let

$$\phi_2(-y') = \infty\,, \qquad \mathrm{Si}\,(x) = x\,, \qquad \mathrm{Ci}\,(x) = C + \ln x\,, \qquad \varepsilon_0 < t\,.$$

Then

$$a = \frac{1}{2} - \frac{kt}{\pi f} l, \qquad b = \frac{1}{2\pi} \ln \frac{t+\varepsilon}{t-\varepsilon}. \tag{61.30}$$

Setting $\alpha = \varepsilon_0/t$, we write

$$\int_0^{\varepsilon_0} b^2 d\varepsilon = \varepsilon_0 \psi(\alpha), \tag{61.31}$$

where

$$\psi(\alpha) = \frac{1}{4\pi^2 \alpha} \int_0^{\alpha} \left( \ln \frac{1+x}{1-x} \right)^2 dx. \tag{61.32}$$

Finally

$$I(x', y') = 2\varepsilon_0 [1 + a^2 + \psi(\alpha) - 2a \cos kP(-x', -y')]. \tag{61.33}$$

It is seen from (61.33) that the image shows the same bands, similar to the interference fringes. Their contrast, however, is reduced due to the additional term $\psi(\alpha)$. It is equal to

$$V = \frac{2a}{1 + a^2 + \psi(\alpha)}. \tag{61.34}$$

The function $\psi(\alpha)$ is plotted in Figure 156. It is small even for $\alpha$ close to unity. We can therefore use light sources of width comparable to that of the viewing diaphragm.

If the viewing diaphragm is a phase filament, introducing a path difference of $\lambda/2$, equation (61.11) reduces to

$$I(x', y') = 1 + 4a^2 - 4a \cos kP(-x', -y'). \tag{61.35}$$

This pattern will be better suited for measurements, since the band contrast is higher:

$$K_{\text{ph}} = \frac{4\alpha}{1 + 4a^2 + 4\psi(\alpha)}. \tag{61.36}$$

Diffraction bands are also obtained if a Foucault knife-edge is used as a viewing diaphragm, but in this case the illumination distribution is described by more complicated formulas which are difficult to use in practice.

If (61.3) is not exactly fulfilled, we can use an artificial procedure — the wave in $\sigma_1$ is given an additional rotation with the aid of an optical wedge. This method has been developed by Podkovyrin [47]. In this case, a system of interference fringes is observed in $\sigma_1$. After the introduction of the inhomogeneity, they are shifted in the same way as the fringes in a double-beam interferometer adjusted for finite-width bands. To calculate the diffraction pattern in this case, let the boundary between $\sigma_1$ and $\sigma_2$ lie along the $Oy$ axis. The viewing diaphragm is a filament of width $2t$, symmetrical with respect to the light source.

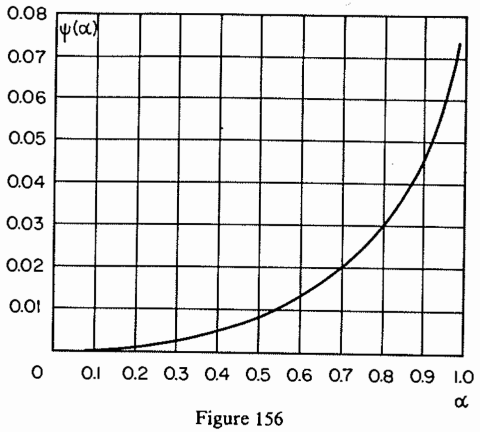

Figure 156

The function $\psi(\alpha)$ from (61.33).

If we assume that the inhomogeneity is large, the expression for the distribution of the light disturbance function is

$$S(x', y') = e^{i\omega\tau} e^{-ik(x'^2 + y'^2)/2f} \left\{ e^{-i2\pi W} \left[ 1 + \frac{i}{2\pi} \int_{2\pi(1+\mu)(V+W)}^{2\pi(1+\mu)W} \frac{e^{i\omega t}}{t} dt - \right. \right.$$

$$\left. \left. - \frac{i}{2\pi} \int_{2\pi(1-\mu)(V+W)}^{2\pi(1-\mu)W} \frac{e^{i\omega t}}{t} dt \right] - \frac{1}{\pi} \int_{2\pi\mu W}^{\infty} \frac{\sin t}{t} dt \right\}, \tag{61.37}$$

where

$$\mu = \frac{t}{P_x f}, \qquad V = \frac{P_x \phi_1(-y')}{\lambda}, \qquad W = \frac{P_x x'}{\lambda}. \tag{61.38}$$

The light intensity is a function of the variable $W$. The parameters determining the shape of the diffraction pattern are $\mu$ and $V$. Curves of the light intensity distribution for different values of the parameters are represented in Figure 157.

A visibility loss occurs for the values of $W$ such that

$$\text{Si}\, 2\pi\mu W = \pi/2. \tag{61.39}$$

The first visibility loss takes place for $W = W_0$, where

$$W_0 = \frac{0.3}{\mu}. \tag{61.40}$$

Speaking of the comparison wave, we have assumed so far that $\sigma_2$ corresponds to a plane wave. However, the method described can also be used in other cases, when the light flux from one zone in the object plane can be intercepted almost com-

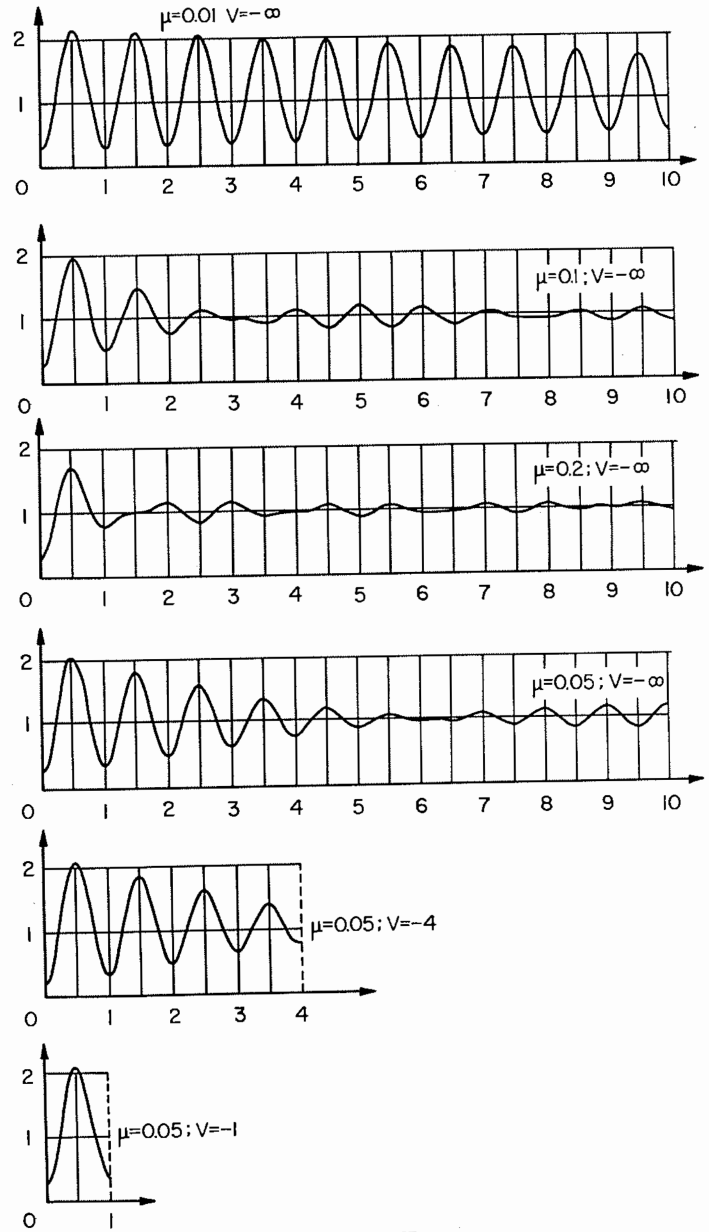

Figure 157

Light intensity distribution for different values of the parameters $\mu$ and $V$.

pletely somewhere in the instrument without affecting the light from the adjacent zone. Such is the case when wave curvature of the comparison region is constant in the direction perpendicular to the filament.

Let the shape of the light wave in region $\sigma_2$ be described by the expression

$$P_2(x, y) = P_2^x(y) + \frac{Cx^2}{2}, \tag{61.41}$$

where $P_2^x(y)$ is an arbitrary function and $C$ is a constant. Defocusing the filament by

$$\Delta = \frac{f^2C}{1 + fC}, \tag{61.42}$$

we place it in the astigmatic image of the source formed by the rays from $\sigma_2$. The light intensity in $\sigma_1$ is thus given by

$$I(x', y') = 1 + a_\Delta^2 - 2a_\Delta \cos\frac{2\pi}{\lambda}\left[P_1(-x', -y') - P_2(-x', -y')\right], \tag{61.43}$$

where

$$a_\Delta = \frac{1}{\pi}\,\mathrm{Si}\,\frac{2\pi}{\lambda}\,\frac{d}{f - \Delta}(l + h) - \frac{1}{\pi}\,\mathrm{Si}\,\frac{2\pi}{\lambda}\,\frac{d}{f - \Delta}\,l. \tag{61.44}$$

The method remains the same as before, but we measure the phase difference $(2\pi/\lambda)\left[P_1 - P_2\right]$. Usually, the introduction of $\Delta$ in (61.44) has no effect, due to its smallness compared to $f$.

We have examined only two types of viewing diaphragms — amplitude and phase filaments. More complex diaphragms were used in [54, 128]. A rectangular groove was cut on a glass plate, and its middle was made opaque. This gave a directional diaphragm, similar to echelette diffraction gratings. The displacement of such a diaphragm relative to the light source image through a distance roughly equal to half the groove width led to a substantial increase of the region with high band visibility. One of the main factors restricting the application of the diffraction schlieren interferometer was removed in this way.

The method described has been frequently used for measuring optical inhomogeneities. Gayhart and Prescott [87] used it for quantitative measurements of the temperature of the air under free convection conditions near heated plates or cylinders. Abrukov [3] was the first to use this method in the USSR for quantitative measurements in flames and for determining the temperature field around a heated cylinder.

Sukhorukikh, whose theoretical results are described in this section, used the diffraction interferometer [54] to study the gas flow density distribution in the boundary layer near a plane plate. The light source was a DRSh-250 mercury lamp. The illuminating slit width was 0.05 mm, and the width of the screening filament 0.16 mm. A light filter isolating the green mercury line was used. The part of the photograph showing the boundary-layer flow is represented in Figure 158 in blown-up form. A very bright band and several narrow dark bands are visible directly about the plate. Their appearance cannot be explained by the theory, and it is due to the complex phenomena taking place when light propagates along a plate in a medium with a large second derivative of density. To suppress these bands, the light from the collimator was not directed parallel to the plate, but at a certain angle to it. The direction and the magnitude of the rotation were selected so that the rays were stopped by the edge of the plate placed near the exit window (down along the ray in this experiment). The additional bands disappeared when the angle was 20′. The results obtained agree satisfactorily with the results of other measurement methods.

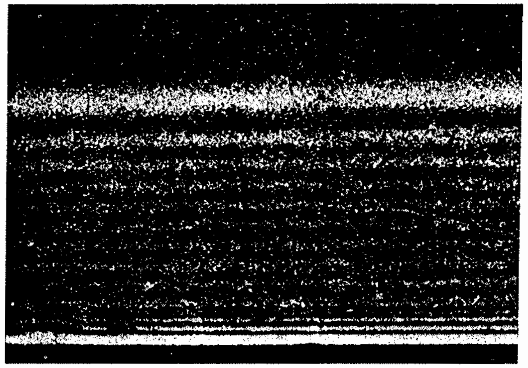

Figure 158
Diffraction bands in a boundary layer.

This method gave satisfactory results in the study of the convective flow about a heated cylinder. A typical interferogram is shown in Figure 159. The temperature field recovered from the photograph was found to coincide (within the experiment error) with the field obtained by the method of grids (cf.§ 18). The advantage of the present method is that it dispenses with integration of the temperature gradients over the entire space from the cold region far from the cylinder to the hot region near the cylinder.

The use of a knife-edge as a viewing diaphragm also yields a distinct diffraction pattern (Figure 160). However, these bands are more difficult to analyze.

## 62. DETERMINATION OF THE ANGLE OF ROTATION OF A PLANE WAVE

Diffraction is one of the main factors restricting the applicability of most schlieren methods. Therefore, it is advisable to use different variants of the conventional

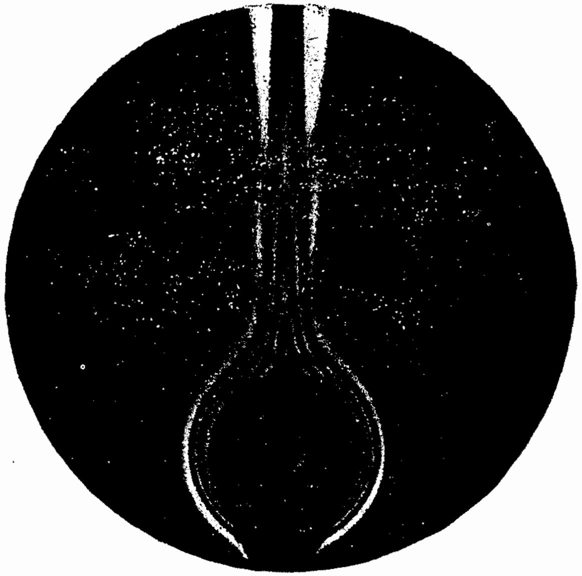

Figure 159
Diffraction bands in the image of the convective flow near a heated cylinder. Thin focal filament.

Figure 160
Diffraction bands in the image of the convective flow near a heated cylinder. Focal knife-edge.

methods in different experiments, seeking the conditions which ensure minimum diffraction errors.

Sukhorukikh proposed a modification of the defocused filament method, suitable for measuring the angle of rotation of plane light waves. A cylindrical lens is placed between the receiving and the illuminating parts of the instrument. The filament is defocused so that the wave surface is a hyperbolic paraboloid, and it is set at right angles to one of the families of the straight generatrices of this paraboloid. A rectangular aperture is provided in the object plane, two of its sides parallel to the filament.

A diffraction pattern of the filament shadow, perpendicular to the filament, is observed in the image plane. When the plane wave is rotated in the object plane, the shadow is displaced parallel to itself, and the illumination distribution in the diffraction pattern remains unchanged. This property of the diffraction pattern enables us to use it for measurements.

Let the filament be parallel to the $y$ axis. The size of the rectangular aperture in the direction perpendicular to the filament is $R$. The illumination distribution in the image plane then has the form

$$I(x', y') =$$
$$= \left| a - \frac{1}{\pi} \int_{(x'-R)\cdot kt/(f-\Delta)}^{x'\cdot kt/(f-\Delta)} \exp\left\{ \pm i \frac{f-\Delta}{t} \sqrt{|V_{xx}||V_{yy}|}\, y'P \right\} \frac{\sin P}{P}\, dP \right|^2 . \qquad (62.1)$$

The coordinate $x'$ is measured from the left edge of the aperture image, $y'$ from the middle of the diffraction shadow (from the geometrical axis); $a = 1$ inside the aperture image and $a = 0$ outside the aperture image. It follows from (62.1) that

$$I(x', y') = I(R - x', -y'), \qquad (62.2)$$

i.e., the half of the diffraction pattern lying on one side of the vertical axis of the aperture image, can be superimposed on the other half by double mirror reflection: one reflection relative to the vertical axis and another relative to the geometrical axis of the diffraction pattern of the shadow.

Expression (62.1) is independent of the filament position. This means that the diffraction pattern is only displaced when the wave is rotated, without altering its shape. The aperture edges cover the pattern as opaque blinds.

The qualitative interpretation of this diffraction pattern emerges from the fact that it is created by secondary Fresnel waves originating in the horizontal segment of the object plane limited by the edges of the rectangular aperture. The amplitude distributions in the plane of the filament from different segments are identical, but they show different shifts (without rotation) relative to the filament.

These conclusions are correct if the filament is infinitely long. In real experiments the filament is finite, but estimates show that the influence of the end-points is negligible for lengths greater than 20 mm.

We introduce new variables:

$$L = \sqrt{\frac{|V_{xx}| + |V_{yy}|}{\lambda}}\, y' ; \qquad H = \sqrt{\frac{1}{\lambda} \frac{|V_{xx}||V_{yy}|}{|V_{xx}| + |V_{yy}|}}\, x' ;$$

$$\mu = \frac{2t}{f-\Delta} \sqrt{\frac{1}{\lambda} \frac{|V_{xx}| + |V_{yy}|}{|V_{xx}| - |V_{yy}|}} ; \qquad \rho = R \sqrt{\frac{1}{\lambda} \frac{|V_{xx}||V_{yy}|}{|V_{xx}| + |V_{yy}|}} .$$

We can now write (62.1) in the form

$$I(L, H) = \frac{1}{4\pi^2} [2\pi a - \mathrm{Si}\,\pi H(2L + \mu) + \mathrm{Si}\,\pi H(2L - \mu) +$$
$$+ \mathrm{Si}\,\pi(H - \rho)(2L + \mu) - \mathrm{Si}\,\pi(H - \rho)(2L - \mu)]^2 +$$
$$+ \frac{1}{4\pi^2} [\mathrm{Ci}\,\pi H(2L - \mu) - \mathrm{Ci}\,\pi H(2L + \mu) - \mathrm{Ci}\,\pi(H - \rho)(2L - \mu) +$$
$$+ \mathrm{Ci}\,\pi(H - \rho)(2L + \mu)]^2 . \qquad (62.3)$$

$L$ and $H$ are the affine coordinates, $\mu$ and $\rho$ are the affine parameters.

The diffraction patterns are similar if $\mu$, $\rho$, and $V_{yy}/V_{xx}$ are equal. The pattern size in this case is proportional to $\sqrt{\lambda/(|V_{xx}| + |V_{yy}|)}$.

The angle $\varepsilon$ of rotation of the plane wave is related to the displacement $\delta$ of the diffraction pattern by the equality

$$\varepsilon = \pm \sqrt{|V_{xx}||V_{yy}|} \qquad (62.4)$$

The error in the measurement of the angle of light deviation depends on the error in the determination of the shadow displacement and the light wave curvature in the plane of the diaphragm. The accuracy of measurement of the displacement is increased substantially if photometry is used. The measurement error in $\delta$ then can be written in the form

$$d\delta = \sqrt{2}\, \frac{dI}{dI/dy'} , \qquad (62.5)$$

and the total measurement error is

$$d\varepsilon = \sqrt{2}\, \frac{\lambda}{R}\, f(P)\, \frac{dI}{I} , \qquad (62.6)$$

where

$$f(P) = \frac{1}{2\pi} \frac{P(\pi - \mathrm{Si}\,P)}{P - \sin P} , \qquad (62.7)$$

$$P = \pi\mu\rho = \frac{2\pi t}{f - \Delta} \cdot \frac{R}{\lambda}. \tag{62.8}$$

The curve $f(P)$ is plotted in Figure 161. It has an absolute minimum for $P = 3.9$. Substituting this value in (62.8), we can find the optimal experimental conditions.

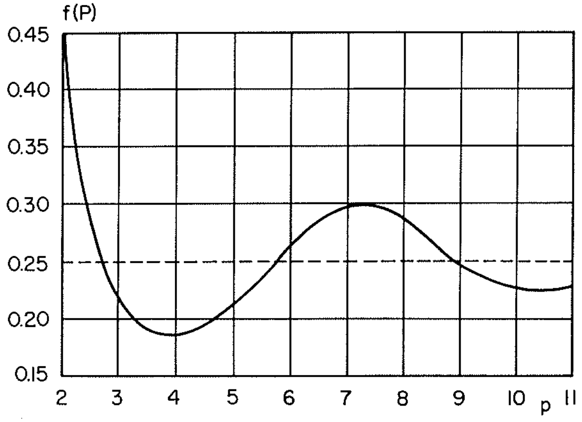

Figure 161
Curve of the function $f(P)$ from (62.7).

The error in this case is independent of the wave front curvature. This is very convenient, since it enables us to select the experimental conditions in such a way that the error is minimized.

Let us estimate the influence of the finite light source dimensions on the measurement error. As usual, the illumination in the image plane is found by integrating (62.3) over various noncoherent points of the extended light source. Seeing that in reality

$$\frac{2t}{f - \Delta} \gg \alpha_0, \tag{62.9}$$

where $\alpha_0$ is the angular half-width of the light source, we obtain

$$I = \frac{2\alpha_0}{\pi^2}\left[(\pi - \mathrm{Si}\,\pi\mu\rho)^2 + \mathrm{Si}^2\,\frac{\pi R\alpha_0}{\lambda} + \right.$$
$$\left. + \frac{2\lambda}{\pi R\alpha_0}\cos\frac{\pi R\alpha_0}{\lambda}\,\mathrm{Si}\,\frac{\pi R\alpha_0}{\lambda} - \frac{\lambda}{\pi R\alpha_0}\,\mathrm{Si}\,\frac{2\pi R\alpha_0}{\lambda}\right] \tag{62.10}$$

Substituting (62.10) in (62.5), we obtain

$$d\varepsilon = \sqrt{2}\,\frac{\lambda}{R}\,F(P, z)\,\frac{dI}{I}, \tag{62.11}$$

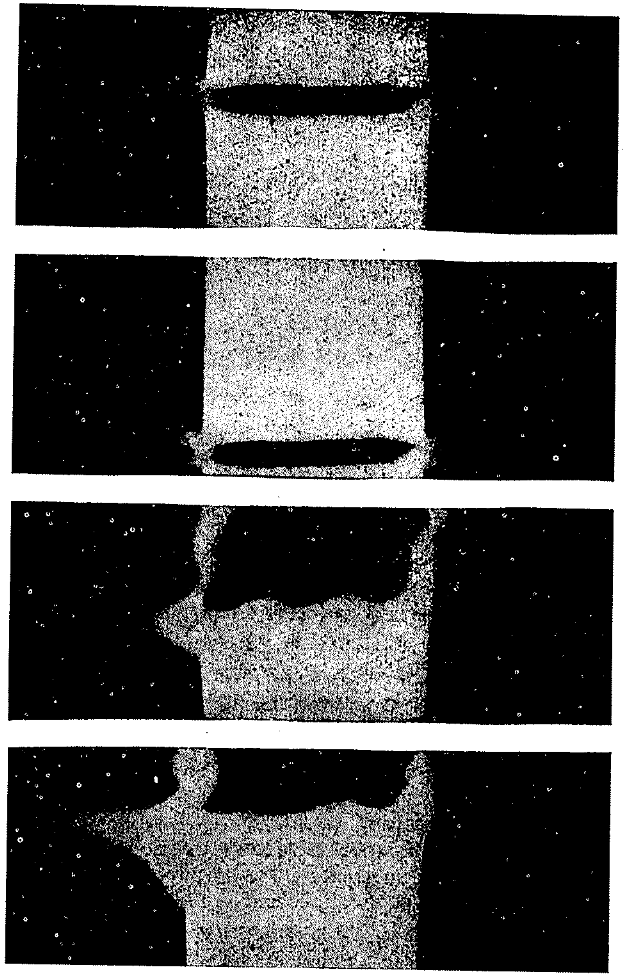

Figure 162
The shadow of the filament for a wave in the shape of a hyperbolic paraboloid.

where

$$F(P, z) = \frac{1}{2\pi}\,\frac{P[(\pi - \mathrm{Si}\,P)^2 + \mathrm{Si}^2\,z + (2/z)\cos z\,\mathrm{Si}\,z - (1/z)\,\mathrm{Si}\,2z]}{(\pi - \sin P)\,[(P/z)\,\mathrm{Si}\,z - \sin P]}, \tag{62.12}$$

$$z = \frac{\pi R\alpha_0}{\lambda}. \tag{62.13}$$

The parameter $z$ is the third affine parameter of the diffraction pattern. For $P = \infty$,

$$F(\infty, z) = \frac{z}{4\,\mathrm{Si}\,z} + \frac{z\,\mathrm{Si}\,z}{\pi^2} + \frac{2\cos z}{\pi^2} - \frac{\mathrm{Si}\,2z}{\pi^2\,\mathrm{Si}\,z}. \tag{62.14}$$

If $z$ is small, we have

$$F(P, z) = f(P) + \frac{1}{2\pi}\frac{P}{(\pi - \mathrm{Si}\,P)(P - \sin P)z^2}. \tag{62.15}$$

Passing to the limit of geometrical optics ($\lambda \to 0$, $\lambda F(P, z)/R \to \alpha_0$), we get

$$d\varepsilon = \sqrt{2}\,\alpha_0 \frac{dI}{I}. \tag{62.16}$$

$\alpha_0$ is selected in measurements so as to ensure a sufficient diffraction pattern illumination for observation or photographing; it should not be smaller than $2.5 \times 10^{-6}$ rad (slit width 0.01 mm). Then $z = 2.9$. Taking $P \gg 2.9$, we find that the measurement error is 3.5 times larger than with a point light source. If $R$ is small, smaller values of $z$ correspond to the same size of the source. The value of $P$ can be optimized, and $\alpha_0$ will hardly affect the measurement accuracy.

The light source used in the experiments was a DRSh-250 mercury lamp. A filter isolating the green mercury line was used. The slit width was 0.01 mm. A cylindrical wave was formed by means of a cuvette. The patterns obtained are shown in Figure 162. We see that the theoretical conclusions are essentially correct: the illumination distribution is independent of the filament position.

The parts of the pattern outside the rectangular aperture sometimes have the appearance of bright whiskers. They also may be used in measurements.

In practice, it is better to conduct a preliminary calibration, rather than use expression (62.4); in this calibration, one finds experimentally the proportionality coefficient between the angle of light deviation and the filament displacement by measuring the shadow position for two different settings of the filament.

# BIBLIOGRAPHY

1. Abrukov, S. A. Candidate's Thesis, Kazan University. 1953.
2. Abrukov, S. A. *Uchenye Zapiski Kazanskogo Universiteta*, **115**, No. 12, 3 (1955).
3. Abrukov, S. A. *Tenevye i interferentsionnye metody issledovaniya opticheskikh neodnorodnostei (Schlieren and Interferometric Methods for the Study of Optical Inhomogeneities)*. Kazan. 1962.
4. Abrukov, S. A. and P. V. Klevtsov. *ZhFKh*, **27**, No. 8, 1145 (1953).
5. Abrukov, S. A. and A. G. Shafigullin. *Zh. Tekh. Fiz.*, **25**, No. 3, 421 (1955).
6. Bazhenova, T. V. and Z. S. Leont'eva. In: *Gazodinamika i fizika goreniya (Gas Dynamics and Physics of Combustion)* [English translation by Israel Program for Scientific Translations, Jerusalem, 1962, p. 85].
7. Bazhenova, T. V., Z. S. Leont'eva, and V. S. Pushkin. *Ibid.*, p. 92.
8. Belotserkovskii, S. M., V. S. Sukhorukikh, and V. S. Tatarenchik. *Zhurnal Prikladnoi Mekhaniki i Tekhnicheskoi Fiziki*, No. 3, 95 (1964).
9. Born, M. *Optik*. Berlin, Springer. 1933.
10. Valeev, Kh. S., Yu. N. Vorontsov, and M. G. Morozov. *Pribory i Tekhnika Eksperimenta*, No. 2, 122 (1960).
11. Vasil'ev, L. A. *Nauchnye Doklady Vysshei Shkoly, Mashinostroenie i Priborostroenie*, No. 4, 230 (1958).
12. Vasil'ev, L. A. Soviet Patent No. 122310 of 25 August, 1959.
13. Vasil'ev, L. A. Specification of Patent Application No. 158703, Cl. $42_h$, $35_{03}$, Intern. Patent Class: $\mathrm{G01}_n$. Bulletin No. 22, 12 Nov., 1963.
14. Vasil'ev, L. A. *Doklady AN SSSR*, **157**, No. 4, 830 (1964).
15. Vasil'ev, L. A. *Zhurnal Nauchnoi i Prikladnoi Fotografii i Kinematografii* (1968).
16. Vasil'ev, L. A. and B. L. Arlov. *Zhurnal Optiko-Makhanicheskoi Promyshlennosti*, No. 9 (1962).

17. Vasil’ev, L. A., A. G. Galanin, I. V. Ershov, and G. N. Suntsov. *Pribory i Tekhnika Eksperimenta*, **5–6**, No. 3, 195 (1964).
18. Vasil’ev, L. A., I. V. Ershov, E. V. Sokolenko, and V. I. Yanichkin. *Doklady AN SSSR*, **175**, No. 6, 1245 (1967).
19. Vasil’ev, L. A. and I. V. Ershov. *Doklady AN SSSR*, **157**, No. 2, 317 (1964).
20. Vasil’ev, L. A., V. K. Efimov, N. N. Gubel’, V. G. Koskovskii, and A. V. Savin. Specification of Patent Application No. 189604, Cl. $42_h$, $35_{01}$. *Byulleten’ Izobretenii*, No. 24. 1967.
21. Vasil’ev, L. A. and V. P. Minina. *Zhurnal Nauchnoi i Prikladnoi Fotografii i Kinematografii*, **8**, No. 5, 337 (1963).
22. Vasil’ev, L. A., S. S. Semenov, and E. A. Tarantov. *Izvestiya AN SSSR*, tech. sci. sec., No. 11, 186 (1957).
23. Vasil’ev, L. A. and O. M. Sineglazov. *Optika i Spektroskopiya*, **14**, No. 4, 553 (1963).
24. Vasil’ev, L. A. and O. M. Sineglazov. *Optika i Spektroskopiya*, **18**, No. 6, 1065 (1965).
25. Vasil’ev, L. A. and M. M. Skotnikov. *Doklady AN SSSR*, **143**, No. 3, 578 (1962).
26. Vasil’ev, L. A. and V. S. Sukhorukikh. *Optika i Spektroskopiya* (1968) (in print).
27. Vertgeim, B. A. and G. A. Ostroumov. *Prikladnaya Matematika i Mekhanika*, **19**, No. 1, 109 (1956).
28. Vol’kenshtein, M. V. *Molekulyarnaya optika (Molecular Optics)*. Gostekhizdat. 1951.
29. Grodzovskii, G. L. *Izvestiya AN SSSR*, tech. sci. sec., No. 7, 119 (1955).
30. Dubovik, A. S. and N. M. Sitsinskaya. *Pribory i Tekhnika Eksperimenta*, No. 5, 166 (1961).
31. Emel’yanov, V. A. *Inzhenerno-Fizicheskii Zhurnal*, **6**, No. 1, 79 (1963).
32. Emel’yanov, V. A. and G. P. Zhavrid. *Inzhenerno-Fizicheskii Zhurnal*, No. 5, 18 (1962).
33. Levin, L. M. *Izvestiya AN SSSR*, phys. ser. **4**, 111 (1940).
34. Maksutov, D. D. *Zhurnal Optiko-Mekhanicheskoi Promyshlennosti*, No. 11 (1932).
35. Maksutov, D. D. *Tenevye metody issledovaniya opticheskikh sistem (Schlieren Methods in the Study of Optical Systems)*, *Problems in Advanced Physics* series, No. XXIII. GTTI. 1934.
36. Maksutov, D. D. *Tenevye pribory (Schlieren Instruments)*. 1935.
37. Maksutov, D. D. *Zhurnal Optiko-Mekhanicheskoi Promyshlennosti*, No. 5, 3 (1941).
38. Malakhov, L. N., V. N. Vertsner, and A. A. Lebedev. *Izvestiya AN SSSR*, phys. ser., **23**, No. 6, 770 (1959).
39. Melankholin, N. M. In: *Issledovanie mineral’nogo syr’ya (The Study of Mineral Raw Materials)*, p. 46. Moscow, Gosgeoltekhizdat. 1955.
40. Meshkov, V. V. and I. I. Sokolov. *Kurs osvetitel’noi tekhniki (A Course in Illumination Engineering)*. Moscow–Leningrad, Gosenergoizdat. 1960.
41. Obreimov, I. V. *Trudy GOI*, **3**, No. 23 (1924).
42. Ostroumov, G. A. *Doklady AN SSSR*, **81**, No. 5, 887 (1950).
43. Ostroumov, G. A. *Svobodnaya konvektsiya v usloviyakh vnutrennei zadachi (Free Convection in the Conditions of the Internal Problem)*, pp. 159–170. Gostekhizdat, 1952.
44. Ostroumov, G. A. *Zh. Tekh. Fiz.*, **24**, No. 11, 2043 (1954).
45. Papiyants, K. A. *Zhurnal Optiko-Mekhanicheskoi Promyshlennosti*, No. 6, 7 (1958).
46. Podkovyrin, I. A. *Uchenye Zapiski Kazanskogo Universiteta*, **116**, No. 5, 60 (1956).
47. Podkovyrin, I. A. Candidate’s Thesis, Kazan University. 1956.

48. Ronchi, V. *Vademecum del colaudatore ottico*. Roma, Liberia Stato. 1931.
49. Rytov, S. M. *Uspekhi Fizicheskikh Nauk*, **41**, No. 4, 425 (1950).
50. Salamandra, G. D., I. M. Naboko, and I. K. Sevast’yanova. *Pribory i Tekhnika Eksperimenta*, No. 2, 124 (1959).
51. Sukhorukikh, V. S. *Metod shcheli i niti s tochki zreniya difraktsionnoi teorii obrazovaniya izobrazhenii (The Slit and Filament Method from the Aspect of the Diffraction Image Formation Theory)*. Candidate’s Thesis, Moscow. 1948.
52. Sukhorukikh, V. S. *Optika i Spektroskopiya* (1968).
53. Sukhorukikh, V. S. *Optika i Spektroskopiya* (1968).
54. Sukhorukikh, V. S. *Zh. Tekh. Fiz.* (1968).
55. Tarantov, E. A. *Zhurnal Nauchnoi i Prikladnoi Fotografii i Kinematografii*, **4**, No. 5, 375 (1959).
56. Françon, M. *Le microscope a contraste de phase et le microscope interferential*. Paris. 1954.
57. Chiang Cheh-hsing. *Inzhenerno-Fizicheskii Zhurnal*, **4**, No. 4, 10 (1961).
58. *Fizicheskie izmereniya v gazovoi dinamike i pri gorenii (Physical Measurements in Gas Dynamics and Combustion)*. Izdatel’stvo Inostrannoi Literatury. 1957. [Russian Translation.]
59. Alpher, R. A. and D. R. White. *Phys. Fluids*, **2**, 153 (1959).
60. Anderson, J. A. and R. W. Porter. *Astrophys. J.*, **70**, 175 (1929).
61. Ascoli–Bartoli, V. In: *Plasma Physics*. Lectures held at the Seminar on Plasma Physics, Trieste, 5–31 Oct., 1964, p. 287–321. Vienna, Nat. Agency for Intern. Publications. 1965.
62. Ball, G. A. *5th Symposium on Combustion, Pittsburgh*, 1954, p. 366. New York. 1955.
63. Barer, R. *J. Roy. Microscop. Soc.*, **72** (3), No. 2, 81 (1952).
64. Barer, R. *J. Roy. Microscop. Soc.*, **73**, No. 1, 30 (1953).
65. Barer, R. *J. Roy. Microscop. Soc.*, **73** (3), No. 4, 206 (1953/1954).
66. Barnes, N. F. *J. Soc. Motion Picture and Telev. Engrs.*, **61**, No. 4, 487 (1953).
67. Barnes, N. F. and S. L. Bellinger. *J. Opt. Soc. Amer.*, **35**, No. 8, 497 (1945).
68. Barnes, N. F. and S. L. Bellinger. *J. Opt. Soc. Amer.*, **44**, No. 8 (1954).
69. Baskins, L. and L. Hamilton. *J. Opt. Soc. Amer.*, **43**, No. 9, 817 (1953).

69a. Bender, H. *Optik*, **11**, No. 5, 244 (1954).

70. Bennet, F. D., W. C. Carter, and V. E. Bergdolt. *J. Appl. Phys.*, **23**, 453 (1952).
71. Blount, G. H. and G. M. Jordan. *ISA (Instr. Soc. Am.) J.*, **4**, No. 6, 216 (1957).
72. Brinkmann, H. *Optische studie van electrische lichtboog*. Thesis, Amsterdam. 1937.
73. Burry, F. W. and G. M. Edelman. *J. Aeronaut. Sci.*, **15**, No. 6, 364 (1948).
74. Burton, R. A. *J. Opt. Soc. Amer.*, **39**, No. 11, 907 (1949).
75. Garner, F. H., R. Long, and B. Thorley. *4th Symposium on Combustion, Baltimore*, 1952, p. 386. 1953.
76. Cranz, C. and H. Schardin. *Z. Phys.*, **56**, 147 (1929).
77. De Boer, P. C. T. *Rev. Sci. Instrum.*, **36**, No. 8, 1135 (1965).
78. Eckert, E. R. G. and Th. W. Zobel. US Patent No. 2655074 of 13 Oct., 1953.
79. Egerton, A. C., O. A. Saunders, A. H. Lefebvre, and N. P. W. Moore. *4th Symposium on Combustion, Baltimore*, 1952, p. 396. 1953.
80. Euler, J. and V. Hüppner. *Optik*, **6**, No. 6, 332 (1950).
81. Faust, R. C. *Proc. Phys. Soc.*, **B68**, No. 12, 1081 (1955).

82. Fish, R. W. and K. Parnham. *Focussing Schlieren Systems. Aeron. Res. Coun. (Min. of Supply), London, Curr. Pap.*, No. 54, 1466 (1951).
83. Foucault, L. *Ann. de l'Observ. Imp. de Paris*, **5**, 203 (1858).
84. Françon, M. and G. Nomarski. *Revue d'Optique*, **31**, 510. 1952.
85. Garner, F. H., R. Long, and B. Thorley. *4th Symposium on Combustion, Baltimore*, 1952, p. 386. 1953.
86. Gascoigne, S. C. G. *Royal Astron. Soc., Monthly Notices*, **104**, No. 6, 326 (1944).
87. Gayhart, E. L. and R. Prescott. *J. Opt. Soc. Amer.*, **39**, No. 7, 546 (1949).
88. Gooderum, P. B. and G. P. Wood. *Nat. Advis. Comm. Aeron., (Nat. Aeron. Space Admin.), Tech. Note*, 2173 (1950).
89. Graindorge, R. *Rech. aeronaut.*, No. 42, 55 (1954).
90. Hett, J. H. *J. Soc. Motion Picture and Telev. Engrs.*, **56**, No. 2, 214 (1951).
91. Holder, D. W. and R. J. North. *Nature*, **169**, 466 (1952).
92. Holder, D. W. and R. J. North. *Schlieren Methods*. In: *Notes Appl. Sci., Nat. Phys. Lab. (London)*, No. 31 (1963).
92a. Holder, D. W. and R. J. North. *Aeron. Res. Counc., (Min. of Supply), London, Rep. and Mem.*, No. 2780, 13068 (1950).
93. Jeffree, H. *J. Sci. Instrum.*, **33**, No. 1, 29 (1956).
94. Kantrowitz, A. and R. L. Trimpi. *J. Aeronaut. Sci.*, **17**, No. 5, 311 (1950).
95. Keagy, W. R. and H. H. Ellis. *Application of the Schlieren Method to the Quantitative Measurements of Mixing Gases in Jets*. In: *Third Symp. Comb., Flame, Explos. Phen., Univ. of Wisconsin*, 1948.
96. Kistler, J. *Chem. Rundschau*, **13**, No. 4, 73 (1960).
97. Lamm, O., T. Svedberg, and P. O. Petersen. *The Ultracentrifuge*. Oxford Univ. Press. 1939.
98. Lamm, O. *Nature*, **132**, 820 (1933).
99. Lamplough, F. F. *Aeron. Res. Counc. (Min. of Supply), London* (1948).
100. Lamplough, M. A. *Aircraft Engng.*, **23**, No. 266, 904 (1951).
101. Linfoot, E. H. *Proc. Roy. Soc.*, **A186**, 72 (1946).
102. Linnett, J. W. In: *Voprosy goreniya i detonatsionnykh voln (Problems of Combustion and Detonation Waves)*, p. 24. Moscow, Gosudarstvennoe Izdatel'stvo Oboronnoi Promyshlennosti. 1958.
103. Liot, B. *Compt. rend.*, **222**, No. 14, 765 (1946).
104. Locquin, M. *Microscopie (Paris)*, M47, 1 (1948).
105. Lumley, E. *Atti fondaz. Giorgio Ronchi*, **15**, No. 5, 457 (1960).
106. Mahan, A. L. *J. Opt. Soc. Amer.*, **37**, 852–867 (1947).
107. Mair, W. A. *The Aeronautical Quarterly*, **4F**, 4 (1952).
108. Marton, L. *Bull. Amer. Phys. Soc.*, **23**, No. 2, 12 (1948).
109. McDonald, K. L. *J. Opt. Soc. Amer.*, **43**, No. 8 (1953).
110. Menzel, E. *J. Opt. Soc. Amer.*, **47**, No. 6, 563 (1957).
111. Mortensen, T. A. *Rev. Sci. Instrum.*, **21**, No. 1, 3 (1950).
112. Ormerod, A. O. *Aeron. Res. Counc. (Min. of Supply), Rep. and Mem.*, No. 2798 (1950).
113. Osterberg, H. and A. J. Carlan. *Trans. Amer. Microscop. Soc.*, **77**, No. 4, 340 (1958).
114. Osterstrom, G. E. *Nat. Advis. Comm. Aeron.*, Report U3835, June, 1948.
115. Philpot, J. St. L. *Nature*, **141**, 283 (1938).
116. Rayleigh, J. *Phil. Mag.*, **33**, No. 194, 161 (1917).

117. Resler, E. L. Jr. and M. Scheibe. *Industr. Engng. Chem.*, **47**, No. 6, 1182 (1955).
118. Ritchey, G. W. *Astrophys. J.*, **19**, 53 (1904).
119. Rudinger, G. and L. M. Somers. *J. Soc. Motion Picture and Telev. Engrs.*, **66**, No. 10, 622 (1957).
120. Schardin, H. *Ver. deut. Ing., Forschungsheft*, **367** (5) 1 (1934).
121. Shardin, H. *Ergeb. exakt. Naturwiss.*, **20**, 303 (1942).
122. Schardin, H. *J. Soc. Motion Picture and Telev. Engrs.*, **61**, No. 3, 273 (1953).
123. Schardin, H. *Photographie et cinematographie ultra-rapides*, pp. 301–314. Paris, Dunod. 1956.
124. Shafer, H. J. *J. Soc. Motion Picture and Telev. Engrs.*, **53**, No. 5, 524 (1949).
125. Shafer, H. J. *Phys. Rev.*, **75**, 1313 (A) (1949).
126. Svensson, H. and R. Forsberg. *J. Opt. Soc. Amer.*, **44**, No. 5, 414 (1954).
127. Taylor, E. W. *Proc. Roy. Soc.*, **A 190**, 422 (1947).
128. Temple, E. *J. Opt. Soc. Amer.*, **47**, No. 1, 91 (1957).
129. Thovert, J., *Ann. Phys.*, (9) **2**, 369–427 (1914).
130. Toepler, A. *Beobachtungen nach einer neuen optischen Methode*. Bonn, Cohen and Son. 1864.
131. Toraldo di Francia, G. *J. Opt. Soc. Amer.*, **45**, No. 7, 497 (1955).
132. Veret, C. *Rech. aeronaut.*, **IX–X**, No. 29, 3 (1952).
133. Weyl, F. J. *Nav. Ord. Rept.*, p. 211, 1945.
133a. Wolter, H. *Ann. Phys.*, **8**, No. 1–2, 1 (1950).
133b. Wranglen, G., *Acta chem. scand.*, **12**, No. 1543 (1958).
134. Zernike, F. *Roy. Astron. Soc., Monthly Notices*, **94**, No. 5, 377 (1934).
135. Zernike, F. *Physica*, **9**, 686 (1942).
136. Zobel, Th. W. US Patent No. 2642770, 1952; GFR Patent No. 175843, of 25 July, 1950.
137. Zobel, Th. W. US Patent No. 2660915, 1953; GFR Patent No. 175844, of 25 July, 1950.

## EXPLANATORY LIST OF ABBREVIATIONS OF U.S.S.R. INSTITUTIONS AND JOURNALS APPEARING IN THE BIBLIOGRAPHY

| *Abbreviation* | *Full name (transliterated)* | *Translation* |
|---|---|---|
| AN SSSR | Akademiya Nauk SSSR | Academy of Sciences of the USSR |
| GTTI | Gosudarstvennoe Izdatel'stvo Tekhniko-Teoreticheskoi Literatury | State Publishing House for Technical and Theoretical Literature |
| *Trudy GOI* | Trudy Gosudarstvennogo Opticheskogo Instituta | Transactions of the State Optical Institute |
| *ZhFKh* | Zhurnal Fizicheskoi Khimii | Journal of Physical Chemistry |
| *Zh. Tekh. Fiz.* | Zhurnal Tekhnicheskoi Fiziki | Journal of Technical Physics |

# SUBJECT INDEX